Transactions of the ASME

TRANSACTIONS OF THE AMERICAN SOCIETY OF MECHANICAL ENGINEERS

VOLUME 77 NOVEMBER 1955 NUMBER 8

Transactions

of The American Society of Mechanical Engineers

Published on the tenth of every month, except March, June, September, and December

Published monthly by The American Society of Mechanical Engineers. Publication office at 20th and Northampton Streets, Easton, Pa. The editorial department is located at the headquarters of the Society, 29 West Thirty-Ninth Street, New York 18, N. Y. Cable address, "Dynamic," New York. Price $1.50 a copy, $12.00 annually for Transactions and the *Journal of Applied Mechanics;* to members $1.00 a copy, $6.00 annually. Add $1.50 for postage to all countries outside the United States, Canada, and Pan-American Union. Changes of address must be received at Society headquarters seven weeks before they are to be effective on the mailing list. Please send old as well as new address.... By-Law: The Society shall not be responsible for statements or opinions advanced in papers or...printed in its publications (B13, Par. 4).... Entered as second-class matter March 2, 1928, at the Post Office at Easton, Pa., under the Act of August 24, 1912....

The Short Bearing Approximation for Plain Journal Bearings

By G. B. DuBOIS[1] and F. W. OCVIRK,[1] ITHACA, N. Y.

A method of analysis of short plain journal bearings is presented which eliminates the need of leakage factors and makes use of charts which have both analytical and experimental support. Eccentricity ratio, oil-film thickness, peak pressure, friction, and oil flow are obtainable for a given temperature. A method of estimating a maximum bearing operating temperature is suggested. Methods of evaluating the effect of elastic deflection and misalignment are also included. A method of determining a factor of safety is explained.

Nomenclature

The following nomenclature is used in the paper:

c_d = diametral bearing clearance, in.
c_d/D = clearance ratio, in/in. of diam
c_r = radial clearance = $c_d/2$, in.
C_n = capacity number = $\dfrac{\mu N'}{p}\left(\dfrac{D}{c_d}\right)^2\left(\dfrac{L}{D}\right)^2$
$1/C_n$ = load number = $\dfrac{p}{\mu N'}\left(\dfrac{c_d}{D}\right)^2\left(\dfrac{D}{L}\right)^2$
$1/C_{p0}$ = inlet oil-pressure number = $\dfrac{1}{C_n}\dfrac{p_0}{p}$
D = bearing diameter, in.
e = eccentricity, in.
h_{min} = minimum oil-film thickness at point of closest approach if shaft and bearing are parallel $h_{min} = c_r - e = c_r(1 - n)$, in.
k = peak pressure ratio in oil film, $k = p_{max}/p$
L = bearing length, in.
L/D = length-diameter ratio
n = eccentricity ratio = e/c_r
N = rotative speed, rpm
N' = rotative speed, rps
p = unit pressure on projected area $p = P/LD$, psi
p_0 = inlet oil pressure, psi
P = total load, lb
q = oil-flow factor from Fig. 5
Q = oil flow,

$$Q = q(\pi DLc_dN'n)/2, \text{ cu in/sec}$$

T = friction torque
stationary element, $T = T_0(T/T_0)$, lb-in.
rotating element = $T + Pc_rn_{hor}$, lb-in.
(n_{hor} from Fig. 2)
T_0 = friction torque at no load and zero eccentricity, lb-in.

$$T_0 = (\pi^2\mu N'LD^3)/c_d \text{ (Petroff)}$$

T/T_0 = friction ratio from Fig. 4
Z = viscosity in centipoises, dyne sec/cm²
μ = viscosity in reyns, lb sec/in.²
ϕ = attitude angle from Fig. 2, deg

Introduction

The following describes a method of analysis of plain journal bearings based on the "short bearing approximation" with emphasis on the use of the charts rather than on the research methods by which they were obtained. The charts are based on data and curves in two technical notes (1, 2)[2] published by the National Advisory Committee for Aeronautics which sponsored a research project conducted by the authors in the Machine Design Laboratory at the School of Mechanical Engineering at Cornell University. The charts have been replotted in reciprocal form to facilitate their use. The charts show the basic performance of the oil film in the hydrodynamic sense. Variation of clearances in manufacture, elastic deflection, and temperature reduction of viscosity may cause marginal film thickness which can be evaluated numerically by the use of the chart information. Practical considerations such as conformability of the bearing material become important. One of the objects of this paper is to obtain wider use of the charts in order to gain experience in interpreting practical operating limits of the basic variables involved.

Background of the Load Number. The charts are plotted against a basic variable, the load number, and a brief explanation of its origin may be of interest. Perhaps the oldest variable is ZN/p where Z is viscosity in centipoises. This variable is useful for a given bearing, but changing the clearance and length-diameter ratio moves the line. In the Sommerfeld number, the ZN/p variable is multiplied by the clearance ratio term $(D/c_d)^2$. In the load number, a second modification consists in multiplying by the length-diameter ratio term $(L/D)^2$ as shown in Figs. 3 and 4. In both the Sommerfeld number and load number, viscosity μ is given in reyn, the English equivalent of the metric centipoise.

The determination of the Sommerfeld number $\mu N'/p\ (D/c_d)^2$ was based on a solution of the Reynolds equation obtained by A. Sommerfeld (3) in 1904, in which the term related to the endwise flow of oil in the bearing was neglected in order to permit an integration. The Sommerfeld number theoretically applies best to a bearing of infinite axial length where the endwise flow of oil out of the ends of the bearing is negligible. The usefulness of the Sommerfeld number as a variable for plotting experimental data has become widely recognized.

The possibilty of a second solution which would include the endwise oil flow and which would apply best to narrow bearings was suggested by Michell (4) as early as 1929, but was little appreciated because it was thought that this solution neglected the entire circumferential oil flow. It was not until 1950, when it was found that dropping the other term in the Reynolds equation retained a considerable part of the circumferential flow, that this solution was completely worked out. This solution is called the short bearing approximation (1) and includes the endwise flow, and that part of the circumferential flow due

[1] NACA Plain Bearing Research Project, Machine Design Laboratories, Sibley School of Mechanical Engineering, Cornell University.

Contributed by the Research Committee on Lubrication under the auspices of the Lubrication Activity and presented at the first annual ASME-ASLE Lubrication Conference, Baltimore, Md., October 18–20, 1954, of The American Society of Mechanical Engineers.

Note: Statements and opinions advanced in papers are to be understood as individual expressions of their authors and not those of the Society. Manuscript received at ASME Headquarters, July 28, 1954. Paper No. 54—Lub-5.

[2] Numbers in parentheses refer to the Bibliography at the end of the paper.

to rotation and film thickness, neglecting only that part of the circumferential flow due to the effect of the pressure gradient on the circumferential oil flow. The relative effect of the term neglected in the short bearing approximation is minimized in narrow bearings, and the short bearing approximation is therefore especially useful in modern practice where the length to diameter ratio is 1 or less. This solution supplements the Sommerfeld solution in the narrow bearing range, and the two may be considered as two halves of the same type of solution. However, the short bearing approximation omits the negative half of the mathematical pressure distribution in the oil film which does not appear to exist experimentally.

Experimental data taken at Cornell University (2) on bearings of L/D of $^1/_4$, $^1/_2$, and 1 show reasonable agreement with the analytical curves of the short bearing approximation, as shown in Figs. 2, 3, and 4.

The Load Number. The short bearing approximation requires the inclusion of a length-diameter ratio term L/D, in the Sommerfeld number S, to give the capacity number $C_n = S\,(L/D)^2$. For use as a parameter for plotting curves, the reciprocal $1/C_n$ has the advantage of expanding the important heavy load region and making the load increase to the right. The load number is derived analytically in the following form by the short bearing approximation

$$\frac{\mu N'}{p}\left(\frac{D}{c_d}\right)^2\left(\frac{L}{D}\right)^2 = \frac{(1-n^2)^2}{\pi\, n}\left[\frac{1}{\pi^2(1-n^2)+16n^2}\right]^{1/2} \quad \ldots [1]$$

$$\text{Load number} = \frac{1}{C_n} = \frac{1}{S\,(L/D)^2} = \frac{p}{\mu N'}\left(\frac{c_d}{D}\right)^2\left(\frac{D}{L}\right)^2 \quad \ldots [2]$$

As shown by the experimental data on eccentricity ratio in Fig. 3, the experimental curve falls slightly above the analytical curve as it should theoretically. The experimental data for L/D of $^1/_4$, $^1/_2$, and 1 considered individually are practically indistinguishable. The spread of the data is reasonable considering the experimental difficulties involved.

Effect of Bearing Clearance. In the load number the bearing-clearance term is squared, so that small variations of the clearance have a considerable effect on the result. In experimental work it is difficult to obtain a bearing surface which does not depart from a true cylinder when measured with precision methods, and it is also difficult to estimate the effect of differential thermal expansion on the actual bearing clearance under operating conditions. This becomes especially important if the bearing is made of aluminum or other metal which has a higher rate of expansion than the shaft.

For a new design, some tolerance on the bearing clearance is necessary to facilitate production. In addition, some allowance for wear in service must be considered. For example, if the minimum clearance desired is 0.002 in. per in. of diameter, the tolerance might be 0.001, and the allowance for wear 0.001, making the maximum clearance ratio 0.004. This gives a two-to-one change in clearance ratio and results in a four-to-one change in the load number. To be safe, it is desirable to make calculations at both extremes of the clearance range, since the effects on temperature and oil flow are confusing.

Description of Curves

The following analysis and charts apply to plain bearings under a steady load, in the range of L/D of $^1/_4$, $^1/_2$, and 1, covered by the experimental data given in reference (2).

Fig. 1 shows a diagram of a plain bearing with the bearing clearance exaggerated so that the eccentric displacement e of the shaft in the bearing clearance can be visualized. The basic variable is the eccentricity ratio $n = e/c_r$.

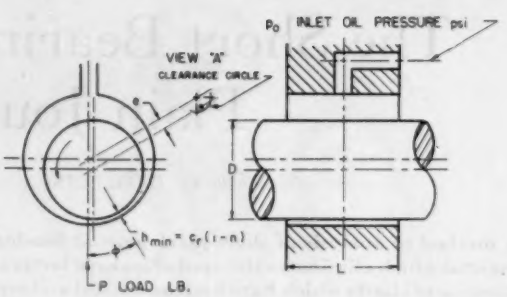

Fig. 1

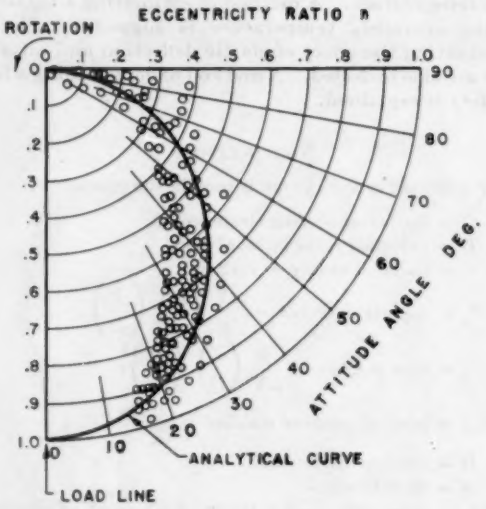

Fig. 2

In view A, Fig. 1, the eccentricity e is shown in relation to the clearance circle. When e reaches a value where $n = 1.0$, the shaft makes metallic contact with the bearing.

Fig. 2 is an enlargement of view A in Fig. 1, showing experimental data in polar co-ordinates. The experimental displacements of the shaft center are grouped around the analytical curve of the short bearing approximation. The attitude angle of the shaft displacement can be determined from this curve if n is known.

Fig. 3 shows the eccentricity ratio n plotted against the load number with experimental data shown for L/D of $^1/_4$, $^1/_2$, and 1. If the bearing dimensions, the load, viscosity, and speed are known, a practical value of the eccentricity ratio can be obtained from the experimental line rather than the analytical curve. The data represent the displacement of a shaft which remains theoretically straight and parallel with the bearing. The eccentricity ratio at the end of a bearing is increased by elastic deflection or misalignment, and calculated corrections can be introduced. The curve in Fig. 3 of eccentricity ratio at the end of a bearing is illustrative only, since the amount of correction depends on the conditions in a particular bearing.

Fig. 4 shows the variation of the friction ratio T/T_0 with the load number. Multiplying this by the Petroff friction at no load T_0, an equation for which is in the nomenclature, gives the friction torque on the stationary element, or in these experiments, the bearing friction. The friction torque on the rotating member, or journal, is larger than the bearing-friction torque, since it includes the load couple caused by the load multiplied by the lateral

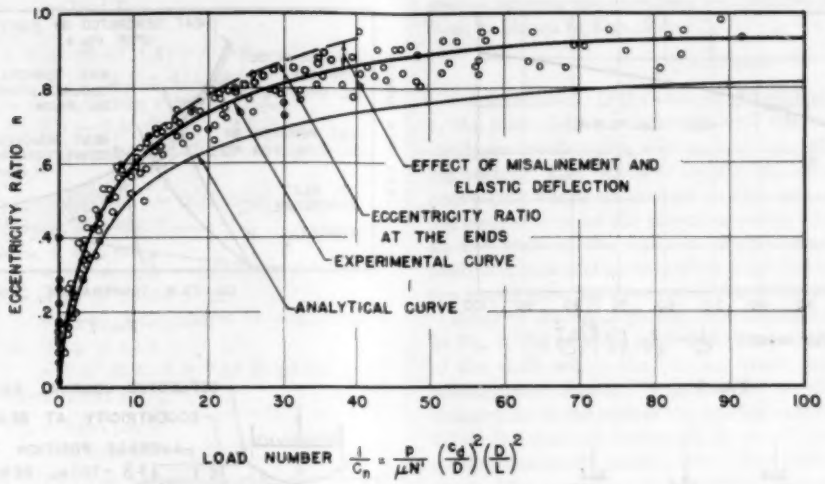

FIG. 3

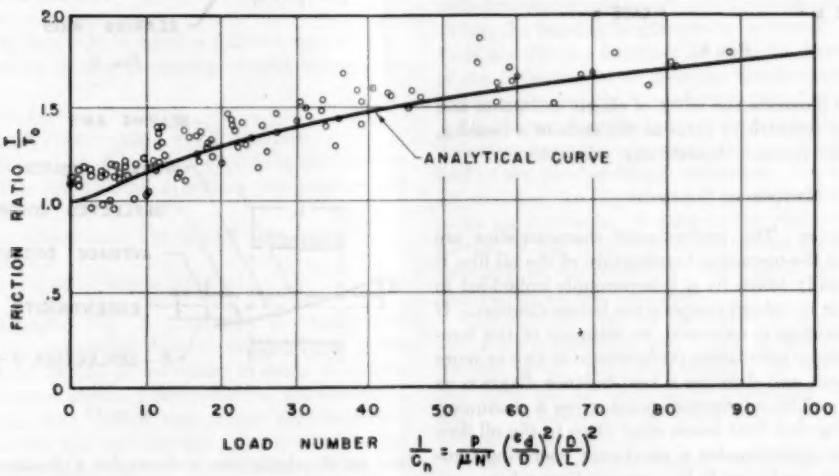

FIG. 4

component of the eccentricity. The increase can be calculated as shown in the example by using Fig. 2 to convert the polar value of n to its horizontal component. It is the larger friction torque on the rotating element which generates heat and causes power loss.

Fig. 5 gives an oil-flow factor to be multiplied by a calculated volumetric displacement of oil per second to obtain the estimated total oil flow from a pressure-lubricated bearing. The oil-flow factor is empirically obtained as shown in reference (2); the calculated volumetric displacement is the analytical net oil-flow rate issuing from the loaded half of the bearing. On the basis of experimental data from reference (2) and McKee (5), curves are shown for bearings with a single oil hole opposite the load and with an axial groove through the oil hole.

Fig. 6 gives the analytical peak pressure in the oil film in relation to the pressure on the projected area, with experimental data taken from reference (1) and McKee and McKee (6).

Fig. 7 illustrates a heat-balance diagram which is of assistance in estimating the probable maximum oil-film temperature based on the heat-generated and heat-dissipated quantities calculated from the friction and oil flow.

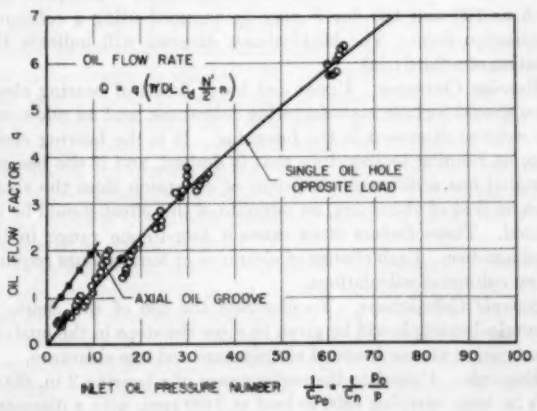

FIG. 5

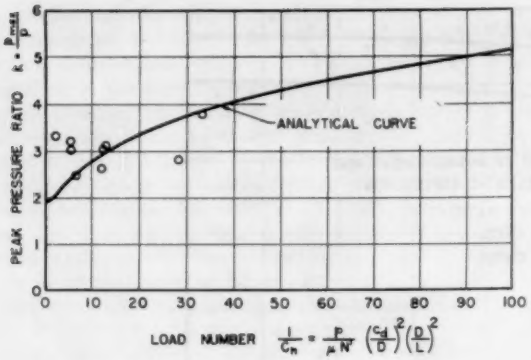

FIG. 6

FIG. 8

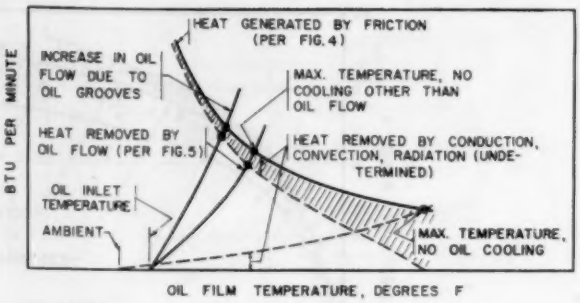

FIG. 7

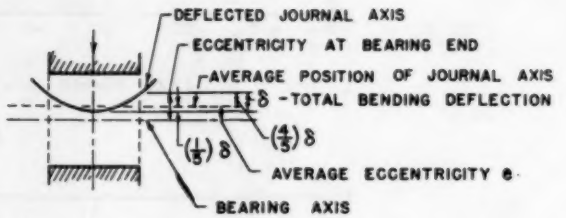

FIG. 9

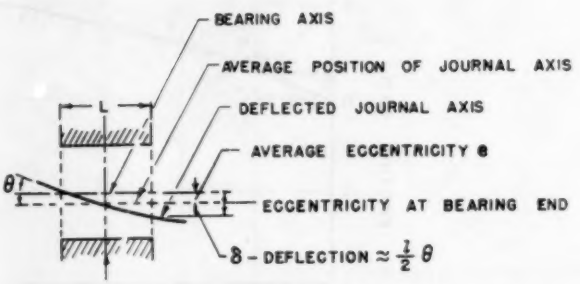

FIG. 10

Figs. 8, 9, and 10 illustrate the effect of elastic deflection and misalignment on the eccentricity ratio at the ends of a bearing, where initial metallic contact theoretically originates.

METHOD OF SOLUTION

Bearing Temperature. The performance characteristics are directly obtainable if the operating temperature of the oil film is known. This is usually taken by a thermocouple imbedded in the bearing surface or by oil-out temperature before dilution. If the operating temperature is unknown, an estimate of the temperature can be made by calculating performance at two or more assumed temperatures, and drawing a heat-balance diagram as suggested in Fig. 7. The intersection point gives a maximum temperature assuming that heat losses other than to the oil flow are negligible. This approximates a maximum operating temperature under severe conditions in hot surroundings where conduction, radiation, and convection cooling effects are small.

In the absence of a known temperature, it is suggested that the upper and lower temperature limits be assumed, representing the desired or allowable operating range. The lower temperature should be above the inlet oil temperature. Temperatures such as 100 and 180 deg F may be assumed using a columnar calculation form. The heat-balance diagram will indicate the location of a third trial.

Bearing Clearance. Upper and lower limits of bearing clearance should include manufacturing tolerances, and an allowance for wear as discussed in the foregoing. It is the bearing clearance at running temperature that is desired, and if the bearing material has a different coefficient of expansion than the shaft, such as that of aluminum, an estimate of this effect should be included. These factors often cause a four-to-one range in the load number. Each change of clearance or temperature requires a new column of calculations.

Sample Calculations. To illustrate the use of the charts, a numerical example will be given to show the steps in the analysis of a bearing at one assumed temperature and one clearance.

Example: Calculate the performance of a bearing 2 in. diam, $1^1/_2$ in. long, carrying 1800 lb load at 2400 rpm, with a diametral clearance of 0.002 to 0.003 in. To simplify the example, only one set of calculations is shown for a clearance of 0.003 in. using SAE 20 oil at 180 F

$L = 1.5$ in. $\quad D = 2$ in. $\quad L/D = {}^3/_4$

$c_d = 0.003$ in. $\quad c_r = 0.0015$ in.

$(c_d/D)^2 = (0.003/2)^2 = 2.25 \times 10^{-6}$

$N' = 40$ rps $\quad P = 1800$ lb $\quad p = 1800/2 \times 1.5 = 600$ psi

$p_0 = 40$ psi oil-inlet pressure

1 SAE 20 oil at 180 deg F, 12 centistokes

2 Viscosity in centipoises
= centistokes × specific gravity
= 12 × 0.862 = 10.33 centipoises

3 Viscosity in reyns
= centipoises × 1.45×10^{-7}
= $10.33 \times 1.45 \times 10^{-7} = 1.5 \times 10^{-6}$ reyns

4 Load number $\frac{1}{C_n} = \frac{p}{\mu N'} \left(\frac{c_d}{D}\right)^2 \left(\frac{D}{L}\right)^2$

$= \frac{600}{1.5 \times 40 \times 10^{-6}} (2.25 \times 10^{-6})(1.78) = 40$

5 Eccentricity ratio from Fig. 3, $n = 0.86$

6 Minimum oil-film thickness h_{min}
(assuming shaft and bearing remain parallel)

$h_{min} = c_r(1 - n) = 0.0015(1 - 0.86) = 0.000210$ in.

7 Friction torque at no load T_0

$T_0 = \pi^2 \mu N' L D^3 / c_d$

$= 9.87\ (1.5 \times 10^{-6})\ 40\ (1.5)\ 2^3/0.003 = 2.36$ lb-in.

8 Friction ratio (T/T_0) from Fig. 4, 1.48

9 Friction torque on stationary member, T_{bearing}

$T_{\text{bearing}} = T_0\,(T/T_0) = 2.36\ (1.48) = 3.5$ lb-in.

Load couple = $P\,c_r$ (lateral component of n from Fig. 2 for $n = 0.86$)

$= 1800\ (0.0015)\ (0.35) = 0.95$ lb-in.

Friction torque on rotating element, T_{journal}

$T_{\text{journal}} = T_{\text{bearing}} + P\,c_r\,n_{\text{hor}}$

$= 3.5 + 0.95 = 4.45$ lb-in.

10 Horsepower loss $= 2\pi\,N'T/550 \times 12$

$= 2\pi 40\ (4.45)/550 \times 12 = 0.17$ hp

11 Heat generated $=$ hp $\times$ 42.4

$= 0.17 \times 42.4 = 7.18$ Btu/min

12 Inlet oil-pressure number $1/C_{p_0}$

$1/C_{p_0} = 1/C_n\,(p_0/p)$

$= 40\ (40/600) = 2.67$

13 Oil-flow factor q from Fig. 5, 0.32

14 Oil-flow rate Q

$Q = q(\pi D L c_d N' n)/2$

$= 0.32\ (\pi \times 2 \times 1.5 \times 0.003 \times 40 \times 0.86)/2 = 0.156$ cu in/sec

In lb/min $= 0.156 \times 60 \times 0.36 \times 0.862 = 0.29$ lb/min

15 Heat removed by oil flow (assuming oil-inlet temperature of 120 F)

$H = wc(t_{\text{out}} - t_{\text{in}})$

$= 0.29\ (0.42)\ (180 - 120) = 7.3$ Btu/min

Since the heat removed by the oil flow (7.3) is larger than the heat generated (7.18), the bearing operating temperature will stabilize below 180 F.

16 Peak pressure ratio k from Fig. 6, 4.05

17 Peak pressure $p_{\max}$

$p_{\max} = kp = 4.05 \times 600 = 2430$ psi

Heat-Balance Diagram. Fig. 7 illustrates a heat-balance diagram which can be constructed from the values of heat generated and heat removed by the oil calculated in items 11 and 15. Values at three or more assumed temperatures are needed to establish the curved lines. After two points are computed, roughly sketched curves will indicate the approximate location of the intersection point to be used for the third calculation.

In some cases data may be available for estimating the heat removed by conduction, convection, and radiation by reference to the heat-balance diagram on a previous application where the running temperature is known. The data given by Lasche (7) may be useful. The portion of the heat generated that is removed by the oil flow varies from zero in bearings having no oil flow to nearly 100 per cent in some applications in internal-combustion engines where the temperature of the surrounding walls approximates the bearing temperature.

In severe applications in hot surroundings it may be acceptable to assume that all of the heat is removed by the oil flow. This gives a "maximum" operating temperature that will be reduced somewhat by any other heat transfer present. This assumption simplifies the heat-balance diagram and makes it a useful tool for analysis of bearing designs even if complete information is lacking. Unavoidable variations in bearing clearance have a marked effect on bearing temperature so that precise estimates are impractical.

Oil Grooves. Fig. 5 includes a curve based on data published by McKee (5) indicating the increase in oil flow obtained by an axial oil groove on the unloaded side. The groove increased the area for admission of oil, but was shorter than the bearing length to provide a seal to maintain oil pressure. The use of an axial oil groove reduces the operating temperature by increasing the oil flow, as shown in Figs. 5 and 7.

Discussion

Oil Starvation. If the value of the oil-flow factor q is less than 1, the inlet oil-flow rate is less than the theoretical volumetric displacement flow rate issuing from the 180 deg of the converging wedge. This means either that the entering corners of the converging wedge are unfilled, or that some oil leaving the bearing returns to enter the diverging wedge by way of a bead of oil at the ends of the bearing. Partial starvation is evidently fairly common and causes only a small loss in load capacity since the empty entering areas contribute little to the oil-film pressure.

Effect of Elastic Deflection and Misalignment. As illustrated in Fig. 8, the effect of shaft deflection may be either a curvature of the shaft within the bearing length, case *a;* or an angular misalignment, case *b.* In either case, the effect is to increase the eccentricity at the ends of the bearing as shown in Figs. 9 and 10. While this increase is numerically small, it represents an appreciable effect on the eccentricity of the shaft in the bearing clearance. The correction to be applied depends on the conditions of the particular application involved.

If the shaft is deflected in an elastic curve but remains parallel with the bearing axis as in Fig. 9, the height of the deflection curve within the bearing length can be estimated. Assuming the deflection curve is a fourth-order parabola, four-fifths of the height of the deflection curve gives the displacement from the average location of a straight line, which is that shown in Fig. 3.

For the angular misalignment case as in Fig. 10, the slope of the deflection curve may be calculated, and the displacement in one half of the bearing length estimated. For both Fig. 9 and Fig. 10, dividing the displacement by the radial clearance converts it to an increment of eccentricity ratio which then may be plotted in Fig. 3 as a point above the experimental line corresponding to the eccentricity ratio at the end of the bearing for that particular load and speed.

This method may be unnecessarily severe, considering that soft bearing materials may run-in to conform with a steady deflection curve. Also, in some cases, the deflection of the bearing mounting can be designed to counteract the deflection of the shaft. However, the deflection due to sudden increases in load evidently acts in this way.

A series of points indicating the eccentricity at the ends of a bearing will form a line above the experimental curve as indicated in Fig. 3, and will intersect the top line where $n = 1$ at a finite-load number, whereas the analytical curve extends to infinity. The intersection point with the top line is evidently related to the hook point commonly found on friction curves where metallic contact causes a sharp increase in friction.

Safety Factor for Plain Bearings. The safety factor can be defined as the ratio of the load number at failure to the load number under design conditions. The failure load number would be the load number at experimentally determined failure points. It also should be indicated in Fig. 3 by the intersection of the line indicating "eccentricity ratio at the ends of the bearing" with the top line of the chart where $n = 1.0$. The load number under design conditions can be determined without calculating deflection. Usually the normal maximum operating conditions would be chosen as the design point.

As an example of the factor of safety, the master rod bearing of certain World War II radial engines experienced experimental failures on a centrifugal test machine at a failure load number of the order of 200. The bearing was preshaped to counteract shaft deflection similar to that shown in Fig. 9. With the design load number considered to be about 60, this gives a factor of safety of 200/60 or about 3.3.

While the eccentricity ratio is the fundamental variable and could be used as a reference tool, an examination of Fig. 3 will show that a 50 per cent increase in the load number from 60 to 90 corresponds to a change in eccentricity ratio from 0.90 to about 0.93.

The load number is suggested as a better reference number. It varies in direct proportion to the unit bearing load and may be considered as the unit load properly weighted so that a fair comparison can be made between bearing applications.

Load Number for L/D Above 1. In using the load number, it should be noted that the experimental data shown in the curves is limited to the range of L/D from $^1/_4$ to 1. The range above L/D of 1 has been investigated recently as reported in reference (8) in which it is shown that Fig. 3 can be used to determine eccentricity ratios for L/D ratios between 1 and 2 by substituting 1 for the $(D/L)^2$ in the load number.

Friction Ratio Versus Friction Coefficient. The method of estimating bearing friction by multiplying the friction at no load by the friction ratio from Fig. 4 has the advantage of focusing attention on the items on which friction directly depends, including the cube of the diameter. A similar ratio, called the power-loss ratio j, was presented by Wilcock and Rosenblatt (9) in 1952. The bearing friction varies only moderately with the load as shown by Fig. 4. The journal friction has a greater dependence on the load, since it equals the bearing friction plus the load couple.

The friction shown analytically by the short bearing approximation neglects the effect of the circumferential pressure gradient in the oil film, but this effect on bearing friction is evidently small as shown by the experimental data. Raising the oil-inlet pressure at light loads will increase the friction and the eccentricity considerably, as though a load were applied.

Conclusions

It is hoped that this discussion will encourage wider use of the basic variables suggested so that experience will be gained in interpreting practical operating limits. Upper limits of eccentricity ratio or load number cannot be suggested since these evidently must be guided by experience with successful applications in service. However, the variables offer a rational method of comparison of existing experience.

BIBLIOGRAPHY

1 "Short Bearing Approximation for Full Journal Bearings," by F. W. Ocvirk, NACA TN 2808, 1952.

2 "Experimental Investigation of Eccentricity Ratio, Friction, Oil Flow of Short Journal Bearings," by G. B. DuBois and F. W. Ocvirk, NACA TN 2809, 1952.

3 "The Hydrodynamic Theory of Lubrication Friction," by A. Sommerfeld, *Zeit. Math. und Phys.*, vol. 50, nos. 1 and 2, 1904, pp. 97–155.

4 "Progress in Fluid-Film Lubrication," by A. G. M. Michell, Trans. ASME, vol. 51, 1929, pp. 153–163.

5 "Oil Flow in Plain Journal Bearings," by S. A. McKee, Trans. ASME, vol. 74, 1952, pp. 841–848.

6 "Pressure Distribution in Oil Films of Journal Bearings," by S. A. McKee and T. R. McKee, Trans. ASME, vol. 54, 1932, pp. 149–165.

7 "Bearings for High Speed," by O. Lasche, *Traction and Transmission*, vol. 6, 1903, pp. 33–64.

8 "Experimental Investigation of Eccentricity Ratio, Friction, and Oil Flow of Long and Short Journal Bearings—With Load Number Charts," by G. B. DuBois, F. W. Ocvirk, and R. L. Wehe, NACA TN 3491, 1955.

9 "Oil Flow, Key Factor in Sleeve-Bearing Performance," by D. F. Wilcock and Murray Rosenblatt, Trans. ASME, vol. 74, 1952, pp. 849–866.

10 "Analytical Derivation and Experimental Evaluation of the Short Bearing Approximation for Full Journal Bearings," by G. B. DuBois and F. W. Ocvirk, NACA Technical Report No. 1157, 1953.

Appendix

The equations of the analytical curves shown in Figs. 2, 3, 4, and 6 are the following:

Fig. 2 $$\tan \phi = \frac{\pi}{4} \frac{(1 - n^2)^{1/2}}{n}$$ from reference (1)

Fig. 3 Equation [1] reference (1)

Fig. 4 $$\frac{T}{T_0} = \frac{F}{F_0} = \frac{1}{(1 - n^2)^{1/2}}$$ reference (10)

Fig. 6 $$k = \frac{p_{max}}{p} = C_a \frac{6\pi n \sin \theta_{max}}{(1 + n \cos \theta_{max})^2}$$ reference (1)

where

$$\theta_{max} = \cos^{-1}\left[\frac{1}{4n}\left(1 - \sqrt{1 + 24n^2}\right)\right]$$

Discussion

F. T. Barwell.[a] Everyone who has given serious consideration to the problem of making bearing theory available to designers in a usable form will be grateful to the authors for their exploration of the potentialities of the narrow bearing approximation for this purpose.

It is noted that the authors find it necessary to add the load couple to the estimated bearing-friction torque in order to arrive at a value for horsepower dissipated by the shaft. Clearly, this energy must be dissipated in the viscous action of the bearing film and there is something unsatisfying about a value obtained by adding the two components as though they were mutually independent. The difficulty is a direct consequence of the assumptions of the narrow bearing analysis in so far as the pressure-induced flow in the bearing film is neglected. As shown by Reynolds this has the effect of diminishing the viscous drag on the one member and increasing it on the other member. While the writer is entirely in agreement with the authors that the difference will be equivalent to the load couple, would it not be fairer to assume that the short bearing analysis gives a mean of the bearing and shaft torque? Would the authors agree that a closer approximation to shaft torque would result if a quantity equivalent to half the load couple were added to the calculated bearing torque?

Authors' Closure

Mr. Barwell raises an interesting comment in regard to the relation of the friction torque on the rotating element, and on the stationary element, to the friction torque given by the short bearing approximation, which of necessity does not distinguish between the two, because of its fundamental assumption. This question has been studied in more detail and is reported in reference (8). Experimental data obtained by other experimenters using four-bearing-type test machines indicate that the full value of the load couple should be added to the friction torque from Fig. 4 to obtain the friction torque on the rotating element. Also, the points obtained by the relaxation method for the friction of the rotating element by Cameron and Wood at L/D of $^1/_4$, $^1/_2$, and 1 check almost exactly on the curve obtained by adding the load couple to the torque from Fig. 4, as described in the foregoing.

We were also pleased with some experimental data on peak pressure ratio supporting the curve in Fig. 6, which were presented in an oral discussion of the paper by Dr. E. R. Booser of the Thomson Laboratory of the General Electric Company, Lynn, Mass.

[a] Lubrication and Wear Division, Mechanical Engineering Research Laboratory, Thorntonhall, Glasgow, Scotland.

Studies in Lubrication—X

The Complete Journal Bearing With Circumferential Oil Inlet

By M. J. JACOBSON,[1] A. CHARNES,[2] AND E. SAIBEL[3]

An approximate pressure solution is developed for the Reynolds equation for the case of the end-lubricated complete journal bearing. This solution is used to obtain expressions for the load-carrying capacity, coefficient of friction, axial thrust, and rate of flow of lubricant. Finally, this solution is extended to the case of the circumferential oil inlet.

Nomenclature

The following nomenclature is used in the paper:

θ = polar angle of bearing measured from point of maximum clearance
y = axial variable measured from central axial section
r = radius of journal
R = radius of bearing
$2L$ = length of bearing
$c = R - r$ = radial clearance
e = eccentricity
$\eta = e/c$ = attitude
p = pressure
U = linear velocity of journal periphery
μ = viscosity

Introduction

The pressure distribution in the lubricating film of a finite journal bearing and its operating characteristics have been found to be poorly described by the solution to the infinite bearing. For example, the theory of the infinite bearing can lead to values of the load capacity that err by more than 100 per cent on the optimistic side (1).[4] Further, when side leakage is neglected, negative pressures are predicted in the film. For reasons such as these, the problem which is regarded as most important is the one which includes the effect of end flow. It is the object of the present paper to develop an approximate solution for the finite bearing when the lubricant is introduced through an end or through a circumferential inlet.

Following the approach of Charnes and Saibel (2), the basic assumption is made that the film thickness, which is expressed as a trigonometric function of the polar angle of the bearing, can be sufficiently well approximated by an exponential function of the polar angle. The pressure distribution is determined in a form which is essentially the sum of the solution to the corresponding infinite bearing and a rapidly convergent series of Whittaker functions. The mathematical solution is valid over the entire range of values of the attitude.

Pressure Solution

The Reynolds equation for the slider bearing (3), when extended to the case of the journal bearing of finite length, becomes

$$\frac{1}{r^2}\frac{\partial}{\partial\theta}\left(h^3\frac{\partial p}{\partial\theta}\right)+\frac{\partial}{\partial y}\left(h^3\frac{\partial p}{\partial y}\right)=\frac{6\mu U}{c^2 r}\frac{dh}{d\theta} \quad \ldots [1]$$

where $ch = c(1 + \eta\cos\theta)$ is the thickness of the lubricating film, see Fig. 1.

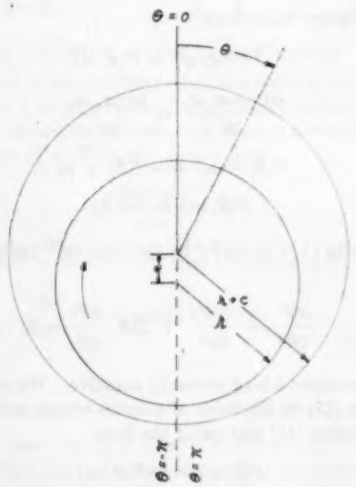

Fig. 1 Axial Section of Complete Journal Bearing

Introducing the dimensionless variable $\omega = y/r$, this becomes

$$\frac{\partial}{\partial\theta}\left(h^3\frac{\partial p}{\partial\theta}\right)+\frac{\partial}{\partial\omega}\left(h^3\frac{\partial p}{\partial\omega}\right)=\frac{6\mu U r}{c^2}\frac{dh}{d\theta} \quad \ldots [2]$$

The following boundary conditions are to be satisfied by p

$$p(-\pi,\omega)=p(\pi,\omega) \quad \ldots [3]$$

$$\frac{\partial p(-\pi,\omega)}{\partial\theta}=\frac{\partial p(\pi,\omega)}{\partial\theta} \quad \ldots [4]$$

---

[1] Member of Technical Staff, Bell Telephone Laboratories, Inc., Whippany, N. J.; formerly, Instructor, Department of Mathematics, Carnegie Institute of Technology, Pittsburgh, Pa. Part of this paper was done by this author in partial fulfillment of requirements for the degree of Doctor of Philosophy in Mathematics, Carnegie Institute of Technology, Pittsburgh, Pa.

[2] Associate Professor, Department of Mathematics, Carnegie Institute of Technology, Pittsburgh, Pa.

[3] Professor of Mechanics, Department of Mathematics, Carnegie Institute of Technology, Pittsburgh, Pa. Mem. ASME.

[4] Numbers in parentheses refer to the Bibliography at the end of the paper.

Contributed by the Research Committee on Lubrication under the auspices of the Lubrication Activity of The American Society of Mechanical Engineers and presented at the First Annual ASME-ASLE Lubrication Conference, Baltimore, Md., October 18–20, 1954.

Note: Statements and opinions advanced in papers are to be understood as individual expressions of their authors and not those of the Society. Manuscript received at ASME Headquarters, August 3, 1954. Paper No. 54—Lub-10.

$$p(\theta, -\omega_0) = p_0 \quad [5]$$

$$p(\theta, \omega_0) = 0 \quad [6]$$

In Equations [5] and [6], $\omega_0 = L/r$ where $2L$ is the length of the bearing, and p_0 is the assumed constant pressure of the inflowing lubricant. Equations [3] and [4] assure the continuity of the pressure and its first derivative in the circumferential direction, while Equation [6] states that the pressure at the free end of the bearing is atmospheric.

In order to remove the inhomogeneous term in Equation [2], set

$$p(\theta, \omega) = P(\theta, \omega) + f(\theta) \quad [7]$$

where $f(\theta)$ satisfies the equation of the infinite length journal bearing

$$\frac{d}{d\theta}\left[(1 + \eta \cos\theta)^3 \frac{df}{d\theta}\right] = \frac{6\mu U r}{c^2} \frac{d}{d\theta}(1 + \eta \cos\theta) \quad [8]$$

and satisfies the boundary conditions

$$f(-\pi) = f(\pi) \quad \text{and} \quad df(-\pi)/d\theta = df(\pi)/d\theta$$

The solution of Equation [8], subject to these conditions, is

$$f(\theta) = \frac{6\mu U r \eta}{c^2(2 + \eta^2)} \frac{(2 + \eta \cos\theta)\sin\theta}{(1 + \eta \cos\theta)^2} + K \quad [9]$$

where K is a constant The function $P(\theta, \omega)$ satisfies

$$\frac{\partial}{\partial\theta}\left[(1 + \eta \cos\theta)^3 \frac{\partial P}{\partial\theta}\right] + \frac{\partial}{\partial\omega}\left[(1 + \eta \cos\theta)^3 \frac{\partial P}{\partial\omega}\right] = 0 \quad [10]$$

and the boundary conditions

$$P(-\pi, \omega) = P(\pi, \omega) \quad [11]$$

$$\frac{\partial P(-\pi, \omega)}{\partial\theta} = \frac{\partial P(\pi, \omega)}{\partial\theta} \quad [12]$$

$$P(\theta, -\omega_0) = -f(\theta) + p_0 \quad [13]$$

$$P(\theta, \omega_0) = -f(\theta) \quad [14]$$

Approximating $(1 + \eta \cos\theta)^2$ by the form $de^{b\theta^2}$ reduces Equation [10] to

$$\frac{\partial^2 P}{\partial\theta^2} + \frac{\partial^2 P}{\partial\omega^2} + 2b\theta \frac{\partial P}{\partial\theta} = 0 \quad [15]$$

where the constant b is of necessity negative. We seek a solution of Equation [15] in the form of a series whose individual terms satisfy Equation [15] and are of the form

$$P(\theta, \omega) = Q(\theta)W(\omega) \quad [16]$$

Separating variables in the customary manner leads to

$$W'' - \lambda^2 W = 0 \quad [17]$$

and

$$Q'' - xQ' - aQ = 0 \quad [18]$$

where we have set $\theta = (-2b)^{-1/2}x$, $a = \lambda^2/2b$, and λ is a constant to be determined. From Sturm-Liouville theory, it is known that Equation [18], with the boundary conditions to be applied here, possesses a sequence of solutions Q_i corresponding to a sequence of real, non-negative eigenvalues λ_i^2 (4). For $\lambda_i \neq 0$, the solutions of Equations [17] and [18] are, respectively

$$W_i = A_i \cosh(\lambda_i\omega) + B_i \sinh(\lambda_i\omega) \quad [19]$$

and

$$Q_i = C_i O_i(x) + D_i E_i(x) \quad [20]$$

where A_i, B_i, C_i, and D_i are constants, and O_i and E_i are given by (5)

$$O_i(x) = x + \sum_{n=1}^{\infty} \frac{(a_i + 1)(a_i + 3)\ldots(a_i + 2n - 1)}{(2n + 1)!} x^{2n+1} \quad [21]$$

and

$$E_i(x) = 1 + \sum_{n=1}^{\infty} \frac{a_i(a_i + 2)\ldots(a_i + 2n - 2)}{(2n)!} x^{2n} \quad [22]$$

For $\lambda_i = \lambda_0 = 0$

$$W_0 = A_0 + B_0\omega \quad [23]$$

and

$$Q_0 = C_0 \int_0^x e^{\frac{x^2}{2}}\, dx + D_0 \quad [24]$$

where A_0, B_0, C_0, and D_0 are constants We require that each Q_i satisfy

$$Q_i|_{x=\alpha} = Q_i|_{x=-\alpha} \quad [25]$$

and

$$\left.\frac{dQ_i}{dx}\right|_{x=\alpha} = \left.\frac{dQ_i}{dx}\right|_{x=-\alpha} \quad [26]$$

where $\alpha = (-2b)^{1/2}\pi$, in order that the conditions expressed by Equations [11] and [12] be met by our solution. Noting that O_i and E_i are odd and even functions of x, respectively, we have from Equations [20], [25], and [26] for $i \neq 0$ that

$$C_i O_i(\alpha) = 0 \quad [27]$$

and

$$D_i E_i'(\alpha) = 0 \quad [28]$$

Since $f(\theta)$ is an odd function, Equations [13] and [14] require that P be an odd function at $\omega = +\omega_0$ and an odd function plus a constant at $\omega = -\omega_0$. If $C_i = 0$, then P is an even function of x so that, from Equation [27], we require

$$O_i(\alpha) = 0 \quad [29]$$

Similarly, $\partial P/\partial x$ must be an even function of x for $\omega = \pm\omega_0$. Since $E_i'(x)$ is odd, we have from Equation [28] that $D_i = 0$. Equation [29] may be solved for the eigenvalues λ_i^2 by evaluating O_i in Equation [21] at $x = \alpha$, rewriting as a series in increasing powers of a_i, and successively applying Whittaker's formula (6) for the root having the smallest value. It can be shown (7) that, for n sufficiently large, λ_n is approximately $n/2$. When Equations [25] and [26] are applied to Equation [24], it is found that $Q_0 = D_0$. If we absorb the constant D_0 into A_0 and B_0 and absorb C_i into A_i and B_i, then the function P takes the form

$$P = A_0 + B_0\omega + \sum_{i=1}^{\infty} O_i(x)[A_i \cosh(\lambda_i\omega) + B_i \sinh(\lambda_i\omega)] \quad [30]$$

The constants A_0, B_0, A_i, and B_i will now be determined by employing Equations [13] and [14]. It can be shown that the Q_i are orthogonal with respect to the weighting function $e^{-x^2/2}$ over the interval $(-\alpha, \alpha)$; that is

$$\int_{-\alpha}^{\alpha} e^{-\frac{x^2}{2}} Q_i Q_j dx = 0 \quad \text{for all } i \neq j \ldots\ldots\ldots [31]$$

Further, from Equations [18] and [26]

$$\int_{-\alpha}^{\alpha} e^{-\frac{x^2}{2}} Q_j dx = 0 \quad \text{for } j \neq 0 \ldots\ldots\ldots [32]$$

Equation [13] states that

$$A_0 - B_0\omega_0 + \bar{O}(x) + \sum_{i=1}^{\infty} O_i(x)[A_i \cosh(\lambda_i\omega_0) - B_i \sinh(\lambda_i\omega_0)] = p_0 \ldots [33]$$

while Equation [14] gives

$$A_0 + B_0\omega_0 + \bar{O}(x) + \sum_{i=1}^{\infty} O_i(x)[A_i \cosh(\lambda_i\omega_0) + B_i \sinh(\lambda_i\omega_0)] = 0 \ldots [34]$$

where $\bar{O}(x)$ denotes the trigonometric term in Equation [9]. The constant K in Equation [9] has been incorporated into A_0. If we multiply Equations [33] and [34] by $e^{-x^2/2}$, integrate over $(-\alpha, \alpha)$, and apply Equation [32], then the following two equations are obtained

$$-B_0\omega_0 + A_0 = p_0 \ldots\ldots\ldots [35]$$

and

$$A_0 + B_0\omega_0 = 0 \ldots\ldots\ldots [36]$$

Similarly, if we multiply Equations [33] and [34] by $e^{-x^2/2}O_j(x)$, integrate over $(-\alpha, \alpha)$, and make use of Equations [31] and [32], then

$$\int_{-\alpha}^{\alpha} e^{-\frac{x^2}{2}} \bar{O} O_i dx + [A_i \cosh(\lambda_i\omega_0) - B_i \sinh(\lambda_i\omega_0)] \int_{-\alpha}^{\alpha} e^{-\frac{x^2}{2}} O_i^2 dx = 0 \ldots\ldots [37]$$

and

$$\int_{-\alpha}^{\alpha} e^{-\frac{x^2}{2}} \bar{O} O_i dx + [A_i \cosh(\lambda_i\omega_0) + B_i \sinh(\lambda_i\omega_0)] \int_{-\alpha}^{\alpha} e^{-\frac{x^2}{2}} O_i^2 dx = 0 \ldots\ldots [38]$$

Adding and subtracting Equations [35] and [36] gives

$$A_0 = p_0/2 \ldots\ldots\ldots [39]$$

and

$$B_0 = -p_0/2\omega_0 \ldots\ldots\ldots [40]$$

Adding and subtracting Equations [37] and [38] gives

$$A_i = -\frac{\int_{-\alpha}^{\alpha} e^{-\frac{x^2}{2}} \bar{O} O_i dx}{\cosh(\lambda_i\omega_0) \int_{-\alpha}^{\alpha} e^{-\frac{x^2}{2}} O_i^2 dx} \ldots\ldots\ldots [41]$$

and

$$B_i = 0 \ldots\ldots\ldots [42]$$

From Equations [7], [9], [30], and the four results of Equations [39] to [42], the following expression is obtained for the pressure distribution

$$p = \frac{p_0}{2\omega_0}(\omega_0 - \omega) + \bar{O}(x) + \sum_{i=1}^{\infty} A_i \cosh(\lambda_i\omega) O_i(x) \ldots\ldots [43]$$

It should be mentioned that the power-series representation for the O_i, Equation [21], converges slowly for large values of x. If it is noted that O_i is related to the Whittaker M function (7) by

$$O_i(x) = 2^{\frac{3}{4}} x^{-1/2} e^{-\frac{x^2}{4}} M_{-\frac{ai}{2}+\frac{1}{4},\frac{1}{4}}\left(\frac{x^2}{2}\right) \ldots\ldots [44]$$

then a rapidly convergent expansion of the Whittaker function in terms of tabulated Bessel functions may be employed (7) to give

$$O_i(x) = \frac{8e^{-\frac{x^2}{4}}}{x} \sum_{n=0}^{\infty} \frac{(-1)^n(1+n)\left(1-\frac{a_i}{2}\right)_n}{\left(\frac{3}{2}\right)_n n!} {}_3F_2 I_{1+n}\left(\frac{x^2}{4}\right) \ldots\ldots [45]$$

where ${}_3F_2$ is a hypergeometric function defined by

$${}_3F_2 = \sum_{p=0}^{n} \frac{\left(-\frac{1}{2}-n\right)_p \left(\frac{a_i+1}{2}\right)_p (-n)_p}{\left(\frac{a_i}{2}-n\right)_p \left(\frac{3}{2}\right)_p p!} \ldots\ldots [46]$$

and the terms in Equations [45] and [46] with n or p subscripts are defined by

$$(\tau)_0 = 1$$
$$(\tau)_s = \tau[\tau+1][\tau+2]\ldots[\tau+(s-1)]$$

Recalling Equation [44], we may employ an asymptotic form for the M-function (8) to obtain an approximate form for the O_i which is useful when λ_i is large. It is found that O_i is given approximately by

$$\sqrt{\frac{2}{-2a_i+1}}\, e^{-\frac{x^2}{4}} \sin\left[x\sqrt{\frac{-2a_i+1}{2}}\right] \ldots\ldots [47]$$

A Condition on the Inlet Pressure

The pressure at the outflow end of the bearing has been taken to be zero and it is important to note that if $\partial p/\partial\omega > 0$ at $\omega = \omega_0$, air will be sucked into the bearing, causing a breakdown of the lubricating film (9). Thus we require that

$$\frac{\partial p(x, \omega_0)}{\partial\omega} \leq 0$$

If the solution is approximated up to the first eigenfunction, then

$$\frac{-p_0}{2\omega_0} + \lambda_1 A_1 \sinh(\lambda_1\omega_0) O_1(x) \leq 0 \ldots\ldots [48]$$

or

$$p_0 \geq 2\omega_0\lambda_1 A_1 \sinh(\lambda_1\omega_0) O_1(x) \ldots\ldots [49]$$

for all x such that $-\alpha \leq x \leq \alpha$. The condition of no air contamination of the film is therefore equivalent to the condition that the inlet pressure be greater than, or equal to, the minimum value prescribed by Equation [49]. Greater accuracy on this lower bound can be found by including higher eigenfunctions.

Load-Carrying Capacity

The components of force applied to the journal along and perpendicular to the line of centers are, respectively

$$P_V = r\int_D\int p \cos\theta\, d\theta\, dy \ldots\ldots [50]$$

and

$$P_H = r\int_D\int p \sin\theta\, d\theta\, dy \ldots\ldots [51]$$

where D represents the domain $-\pi/2 \leq \theta \leq \pi/2$ and $-L \leq y \leq L$. If p is substituted from Equation [43], and these integrals evaluated making use of the oddness of $\bar{O}$ and O_i, it results that

$$P_V = 0 \quad [52]$$

and, to one eigenfunction

$$P_H = \frac{24\pi\omega_0\mu U r^3\eta}{c^3(2+\eta^2)\sqrt{1-\eta^2}} + \frac{4(-2b)^{-\frac{1}{2}}r^2 A_1 \sinh(\lambda_1\omega_0)}{\lambda_1}\int_0^{\alpha} O_1 \sin[(-2b)^{-\frac{1}{2}}x]dx \quad [53]$$

Since $P_V = 0$, the load acts perpendicular to the ray through the sections of maximum and minimum film thickness. This same result has been found for the infinite bearing. The first term in Equation [53] arises from the term $\bar{O}(x)$, Equation [43], and therefore represents the load-carrying capacity of the corresponding infinite bearing. Therefore the second term may be regarded as a quantity which corrects for the finiteness of the bearing. It can be shown (7) that $O_1(x)$ is positive over the interval $0 < x < \alpha$ and negative over $-\alpha < x < 0$, so that the second term in Equation [53] is negative, giving the result that the load-carrying capacity of the finite bearing is less than that of the corresponding infinite one. This conclusion is consistent with that found by Muskat and Morgan (9).

Coefficient of Friction

The total frictional force F on the journal is given by

$$F = r^2\int_{-\omega_0}^{\omega_0}\int_{-\pi}^{\pi}\left[\frac{ch}{2r}\frac{\partial p}{\partial\theta} + \frac{\mu U}{ch}\right]d\theta\, d\omega \quad [54]$$

where the integrand represents the surface traction on the journal in the circumferential direction. If we integrate the first term by parts, apply Equation [3], and recall Equation [53], then

$$F = \frac{c\eta}{2r}P_H + \frac{4\pi r^2\mu U\omega_0}{c\sqrt{1-\eta^2}} \quad [55]$$

The coefficient of friction f for the journal is defined as the ratio of F to the total load. Since $P_V = 0$, the total load is simply P_H, and

$$f = \frac{F}{P_H} = \frac{c\eta}{2r} + \frac{4\pi r^2\mu U\omega_0}{cP_H\sqrt{1-\eta^2}} \quad [56]$$

Axial Thrust on Journal

The axial force G on the journal is defined by

$$G = r^2\int_{-\omega_0}^{\omega_0}\int_{-\pi}^{\pi}\left[\frac{c(1+\eta\cos\theta)}{2r}\frac{\partial p}{\partial\omega}\right]d\theta\, d\omega \quad [57]$$

where the integrand represents the axial shearing stress on the journal. Integrating and applying Equations [5] and [6] gives

$$G = crp_0\pi \quad [58]$$

so that the axial force on the journal varies linearly with the entrance pressure, the radial clearance, and the radius of the journal.

Rate of Flow of Lubricant

If τ represents the radial variable measured inward from the circumference of the bearing, and if Q denotes the rate of flow of lubricant per unit time in the axial direction, then

$$Q = \int_{-\pi}^{\pi}\int_0^{c(1+\eta\cos\theta)}\left[\frac{1}{2\mu(r+c)}\tau\{\tau - c(1+\eta\cos\theta)\}\frac{\partial p}{\partial\omega}\right](r+c-\tau)\,d\tau\,d\theta \quad [59]$$

where the quantity in square brackets is the velocity of the lubricant in the axial direction, and the remaining terms represent an element of area in polar co-ordinates. It results that

$$Q = \frac{p_0\pi}{24\mu(r+c)\omega_0}\left[-\frac{3}{8}c\eta^4 + 3r\eta^2 + (2r+c)\right] \quad [60]$$

Recall that $\eta = e/c$ and $0 \leq e < c$. The first term in the brackets is at most $-3/8c$ and the second term is at most $3r$. Neglecting all terms of order c gives

$$Q = \frac{\pi p_0}{24\mu\omega_0}(3\eta^2 + 2) \quad [61]$$

Thus the rate of flow of lubricant through the bearing is directly proportional to the inlet pressure, inversely proportional to the viscosity and bearing length, and is a quadratic function of the attitude. Note that, neglecting terms of order c, the rate of flow is a minimum when the journal and bearing are concentric ($\eta = 0$) and a maximum when the journal occupies an extreme position ($\eta = 1$). In fact

$$2 \leq \left(\frac{24\mu\omega_0}{\pi p_0}\right)Q < 5 \quad [62]$$

Equation [49] gave the minimum value of the inlet pressure for effective lubrication. Substituting this minimum value for p_0 into Equation [61] gives the minimum rate of flow of lubricant for effective lubrication for any value of the attitude

$$Q_{\min} = \frac{1}{12\mu}\pi(3\eta^2+2)\lambda_1 A_1 \sinh(\lambda_1\omega_0)[O_1]_{\min} \quad [63]$$

Complete Journal Bearing With Circumferential Oil Feed

Now that an approximate solution has been found for the end-lubricated bearing, the solution for the more general case of circumferential oil feed under constant pressure can be determined directly. Consider a bearing of length $2L_1 + 2L_2$, where a given axial section is located by the axial variable y measured from an end of the bearing. Let the lubricant be introduced at constant pressure p_0 through a circumferential groove at $y = 2L_1$. The pressure solution given by Equation [43] is applied to the two regions $0 \leq y \leq 2L_1$ and $2L_1 \leq y \leq 2L_1 + 2L_2$ to give

$$p = \frac{p_0 y}{2L_1} + \bar{O}(x) + \sum_{i=1}^{\infty} A_i O_i(x)\frac{\cosh\left[\lambda_i\left(\frac{y-L_1}{r}\right)\right]}{\cosh\left[\lambda_i\frac{L_1}{r}\right]} \quad [64]$$

for $0 \leq y \leq 2L_1$ and

$$p = \frac{p_0}{2L_2}[2(L_1+L_2) - y] + \bar{O}(x) + \sum_{i=1}^{\infty} A_i O_i(x)\frac{\cosh\left[\lambda_i\left(\frac{y-2L_1-L_2}{r}\right)\right]}{\cosh\left[\lambda_i\frac{L_2}{r}\right]} \quad [65]$$

for $2L_1 \leq y \leq 2L_1 + 2L_2$ where

$$A_i = -\frac{\int_0^{\alpha} e^{-\frac{x^2}{2}}\bar{O}(x)O_i(x)dx}{\int_0^{\alpha} e^{-\frac{x^2}{2}}O_i^2(x)dx} \quad [66]$$

The operating characteristics computed for the end-lubricated bearing may now be determined for the circumferentially lubricated bearing in an analogous fashion. It also should be mentioned that while the methods in this section have been extended only to the case of a single circumferential groove, the solution for the journal bearing with multiple grooves can be similarly obtained. The only fundamental change would occur in Equations [5] and [6] since, in the most general case, different constant pressures may be present at the ends of each region bounded by circumferential grooves.

Example

The approximate solution to one eigenfunction for a particular problem of an end-lubricated complete journal bearing will now be found. Suppose

D = 220 mm—diameter of bearing
$2L$ = 300 mm—length of bearing
$D - d$ = 0.58 mm—diametral clearance
U = 6.93 m s^{-1}—linear velocity of journal
μ = 0.005 kg m s^{-1}—mean dynamic viscosity
η = 0.50—attitude

If we match the curves

$$z = (1 + \eta \cos \theta)^3 \text{ and } z = de^{b\theta^2}$$

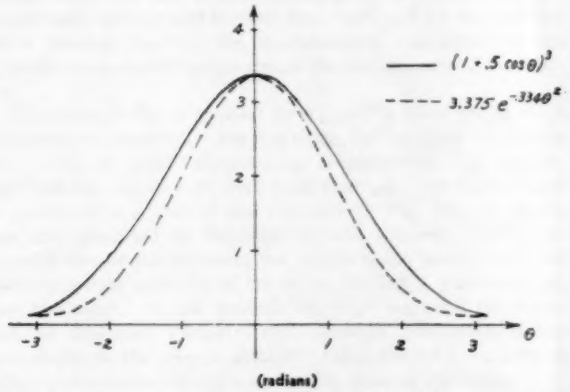

Fig. 2 A Comparison of $(1 + \eta \cos \theta)^3$ With $de^{b\theta^2}$ for the Case $\eta = 0.50$

at $\theta = 0$ and $\theta = \pi$, it is found that $b = -0.334$, Fig. 2. Substituting into Equation [29] gives $a_1 = -1.37$ and $\lambda_1 = 0.922$. From Equation [46] the values for ${}_3F_2$ are as given in Table 1.

TABLE 1 VALUES OF ${}_3F_2$

n	0	1	2	3	4	5	6
${}_3F_2$	1	1.083	1.145	1.190	1.227	1.258	1.285

Substituting into Equation [45] gives

$$O_1(x) = \frac{8e^{-\frac{x^2}{4}}}{x}\left[I_1\left(\frac{x^2}{4}\right) - 4.725I_2\left(\frac{x^2}{4}\right) + 11.85I_3\left(\frac{x^2}{4}\right) - 22.75I_4\left(\frac{x^2}{4}\right) + 37.75\,I_5\left(\frac{x^2}{4}\right) - 57.12I_6\left(\frac{x^2}{4}\right) + 81.08I_7\left(\frac{x^2}{4}\right) - \ldots\right] \ldots\ldots [67]$$

The Bessel functions I_n are fully tabulated (10). For small values of x, the power series expansion for $O_1(x)$ represented by Equation [21] is more useful

$$O_1(x) = x - 0.0617x^3 - 0.00503x^5 - \ldots\ldots [68]$$

With this information, the constant A_1 may be computed from Equation [41] using graphical or numerical integration. The pressure solution to one eigenfunction is then known from Equation [43]. This solution has been computed at the central axial section ($\omega = 0$) using an inlet pressure of 2 atm. The result is compared in Fig. 3 with the solution to the corresponding infinite bearing, as given by Equation [9], with $K = 1$.

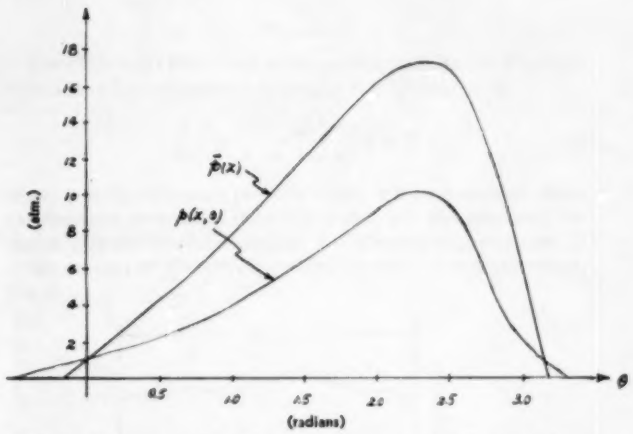

Fig. 3 A Comparison of Proposed Solution p at Central Axial Section With Solution p of Corresponding Infinite Bearing

The values for the pressure, calculated to one eigenfunction, should be reasonably accurate compared to those of the complete solution in a region about the central axial section since the function $\cosh(\lambda_i \omega)$ is small there. Also, the function $O_i(x)$ is of such an oscillatory nature for $i > 1$ as to make the numerator of Equation [41] for A_i small for $i > 1$. However, near either end of the bearing, the results are not so satisfactory and higher eigenfunctions must be included for greater accuracy.

BIBLIOGRAPHY

1 "Analysis and Lubrication of Bearings," by M. C. Shaw and E. F. Macks, McGraw-Hill Book Company, New York, N. Y., 1949, p. 242.

2 "On the Solution of the Reynolds Equation for Slider-Bearing Lubrication—I," by A. Charnes and E. Saibel, Trans. ASME, vol. 74, 1953, pp. 867–873.

3 "On the Theory of Lubrication," by O. Reynolds, Philosophical Transactions of the Royal Society of London, England, part 1, vol. 177, 1886, pp. 157–234.

4 "Ordinary Differential Equations," by E. L. Ince, Dover Publications, New York, N. Y., 1944, chapter 10.

5 "Differential Gleichungen," by E. Kamke, J. W. Edwards Company, Ann Arbor, Mich., 1945, p. 414.

6 "A Formula for the Solution of Algebraic or Transcendental Equations," by E. T. Whittaker, Proceedings of the Edinburgh Mathematical Society, vol. 36, 1917–1918, p. 103.

7 "Reynolds Theory and Journal Bearing Lubrication," by M. J. Jacobson, Doctoral Dissertation, Carnegie Institute of Technology, Pittsburgh, Pa., June, 1954, chapter 2.

8 "Special Functions of Mathematical Physics," by W. Magnus and F. Oberhettinger, Chelsea Publishing Company, New York, N. Y., 1949, p. 90.

9 "Studies in Lubrication: I—The Theory of the Thick Film Lubrication of a Complete Journal Bearing of Finite Length," by M. Muskat and R. Morgan, *Journal of Applied Physics*, vol. 9, 1938, p. 393. See also II, *Journal of Applied Physics*, vol. 10, 1939.

10 "British Association Mathematical Tables X," University Press, Cambridge, England, 1937.

On the Solution of the Reynolds Equation for Slider-Bearing Lubrication—IX

The Stepped Slider With Adiabatic Lubricant Flow

By F. OSTERLE,[1] A. CHARNES,[2] and E. SAIBEL,[3] PITTSBURGH, PA.

Treating viscosity as a function of temperature and pressure and taking approximate account of the variation of density, the load-supporting capacity of the stepped slider bearing with adiabatic lubricant flow is found. The importance of the "density-wedge" effect is noted and a numerical example is worked out illustrating the effect of different locations of the step on load capacity and comparing the performance of the stepped slider with the flat inclined-plane slider.

Introduction

IN THE slider-bearing problem the merits of many slider profiles have been investigated. In these investigations the important considerations have been the effects of the profile on (*a*) the ease of construction of the slider, (*b*) the load-supporting capacity and friction force exhibited by the resulting slider bearing, and (*c*) the mathematical tractability of the hydrodynamic equations governing the performance of the bearing.

The slider profile of stepped form (see Fig. 1) is one of those given serious attention. For one thing, as Archibald (1)[4] points out, it enjoys "great constructional simplification over the tilting-block bearing, or even over those bearings in which the taper is machined into one of the elements." The stepped profile was first suggested by Rayleigh (2) who showed that for isothermal flow of the lubricant the profile which would make the load-supporting capacity of the slider bearing a maximum was just this form. In his analysis Rayleigh neglected the variation of lubricant viscosity with pressure. However, it has been shown by the present authors (3) that when this variation is taken into account the optimum profile remains unchanged.

As pointed out previously by the authors (4) and others, the lubricant flow through a slider bearing is not isothermal but rather more nearly adiabatic, so that the "optimum" property, just mentioned, of the stepped profile is of doubtful practical significance. However, because of its constructional simplicity and the inherently simple nature of the governing hydrodynamic equations, the stepped slider bearing still warrants consideration. In the light of this, an analysis of the stepped slider bearing under the more realistic condition of adiabatic rather than isothermal lubricant flow is considered in this paper.

[1] Assistant Professor, Department of Mechanical Engineering, Carnegie Institute of Technology. Assoc. Mem. ASME.

[2] Associate Professor, Department of Mathematics, Carnegie Institute of Technology.

[3] Professor of Mechanics, Department of Mathematics, Carnegie Institute of Technology. Mem. ASME.

[4] Numbers in parentheses refer to the Bibliography at the end of the paper.

Contributed by the Research Committee on Lubrication under the auspices of the Lubrication Activity of The American Society of Mechanical Engineers and presented at the first annual ASME-ASLE Lubrication Conference, Baltimore, Md., October 18–20, 1954.

Note: Statements and opinions advanced in papers are to be understood as individual expressions of their authors and not those of the Society. Manuscript received at ASME Headquarters, August 26, 1954. Paper No. 54—Lub-11.

Theory

For a lubricant film which shows no side leakage, the Reynolds equation of hydrodynamic lubrication theory reduces to

$$\frac{d}{dx}\left(\rho\frac{Uh}{2}-\frac{\rho h^3}{12\mu}\frac{dp}{dx}\right)=0 \qquad [1]$$

where p is the lubricant pressure which will be measured above the common pressure at inlet and outlet, μ is the lubricant viscosity, ρ is the lubricant density, h is the film thickness, and U is the velocity of the moving surface (bearing) in the x-direction, Fig. 1.

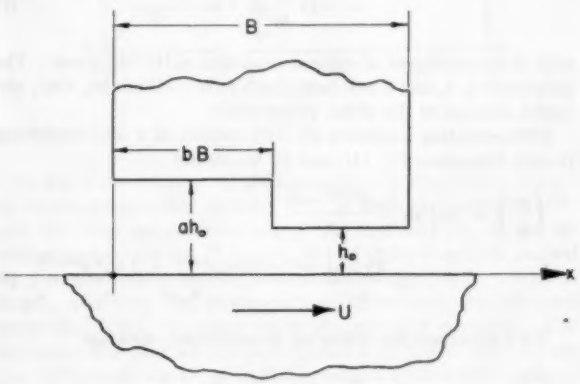

Fig. 1

The energy equation governing the adiabatic flow of the lubricant is formulated (4) by equating the work done on an element of the fluid by the shearing forces and the pressure forces to the increase in the internal energy of the element. For the case of no side leakage this energy equation is

$$\frac{\mu U^2}{h}+\frac{h^3}{12\mu}\left(\frac{dp}{dx}\right)^2=c\frac{dt}{dx}\left(\frac{\rho Uh}{2}-\frac{\rho h^3}{12\mu}\frac{dp}{dx}\right) \qquad [2]$$

where c is the lubricant specific heat, and t is the temperature of the lubricant measured above the temperature at inlet.

Integration of Equation [1] leads to

$$\frac{dp}{dx}=\frac{6\mu U}{h^3}\left(h-\frac{\rho_0}{\rho}h_m\right) \qquad [3]$$

where h_m is the constant of integration, and ρ_0 is the lubricant density at inlet. Substituting Equation [3] into the energy Equation [2] there results

$$\frac{dt}{dx}=\frac{2\mu U}{\rho_0 c h^3 h_m}\left[4h^2-6\frac{\rho_0}{\rho}h_m h+3\left(\frac{\rho_0}{\rho}h_m\right)^2\right] \qquad [4]$$

We now introduce the following viscosity variation relationship (4)

$$\mu=\mu_0 e^{\alpha p}e^{-\gamma t} \qquad [5]$$

where μ_0 is the lubricant viscosity at inlet, and α and γ are the pressure and temperature coefficients of viscosity, respectively.

The lubricant density also varies with pressure and temperature, increasing about 0.3 per cent for a pressure rise of 1000 psi, and decreasing about 2 per cent for a temperature rise of 50 deg F. It is difficult to take this density variation into account exactly. However, it was shown by the present authors (5) that the load capacity resulting from density variation (density-wedge effect) is usually equivalent to that brought about by the film-thickness variation (geometric-wedge effect) resulting from an inlet to outlet film-thickness ratio of only slightly greater than 1, and since ratios of about 2 would be reasonable for the stepped slider, the expected smallness of the density-wedge effect would seem to justify an approximate treatment. It will be assumed that the density varies exponentially with distance along the slider, i.e.

$$\rho = \rho_0 e^{-\epsilon x/B} \quad [6]$$

This variation is almost linear since ϵ is small. The reasonableness of this assumption will be checked later. The constant ϵ must be related to the outlet temperature (t_2) by

$$\epsilon \equiv \ln \frac{\rho_0}{\rho_2} \cong \beta t_2 \quad [7]$$

with β the coefficient of cubical expansion of the lubricant. The subscripts 0, 1, and 2 will henceforth refer to the inlet, step, and outlet sections of the slider, respectively.

Differentiating Equation [5] with respect to x and combining it with Equations [3], [4], and [6] we obtain

$$\frac{d}{dx}\left(\frac{\mu_0}{\mu}\right) = 6\alpha U\mu_0 \frac{h_m e^{\epsilon x/B} - h}{h^3} + \frac{2\gamma U\mu_0}{\rho_0 c} \frac{4h^2 - 6hh_m e^{\epsilon x/B} + 3h_m^2 e^{2\epsilon x/B}}{h_m h^3} \quad [8]$$

If we introduce the following dimensionless notation

$$M = \frac{\mu_0}{\mu}, \quad H = \frac{h_m}{h_0}, \quad X = \frac{x}{B} \quad [9]$$

and consider the stepped slider of Fig. 1, Equation [8] becomes

$$\frac{dM}{dX} = A \frac{He^{\epsilon X} - s}{s^3} + \Gamma \frac{4s^2 - 6sHe^{\epsilon X} + 3H^2 e^{2\epsilon X}}{s^3 H} \quad [10]$$

where $s = a, \quad 0 \leq X < b$

$= 1, \quad b < X \leq 1$

and with $A = \frac{6\alpha\mu_0 UB}{h_0^2}, \quad \Gamma = \frac{2\gamma\mu_0 UB}{\rho_0 c h_0^2}$ [11]

Equation [10] integrates to

$$M = M_\eta + A\left[\frac{H(e^{\epsilon X} - e^{\epsilon\eta}) - \epsilon s(X - \eta)}{\epsilon s^3}\right] + \Gamma\left[\frac{4\epsilon s^2(X - \eta) - 6sH(e^{\epsilon X} - e^{\epsilon\eta}) + \frac{3}{2}H^2(e^{2\epsilon X} - e^{2\epsilon\eta})}{\epsilon s^3 H}\right] \quad [12]$$

where

$\eta = 0, 0 \leq X < b$

$= b, b < X \leq 1$

Note that $M_0 = 1$. If the fact that the pressure and temperature are continuous at the step is taken into account we have that $M_b = M_1$.

Replacing the exponentials in Equation [12] by their power-series expansions and retaining only terms in the first power of ϵ (since ϵ is quite small), there results

$$M = m + \epsilon d_\eta (X^2 - \eta^2) \quad [13]$$

with

$$m = M_\eta + c_\eta (X - \eta) \quad [14]$$

where

$$c_\eta = A\frac{H - s}{s^2} + \Gamma\frac{4s^2 - 6sH + 3H^2}{s^3 H}$$

$$d_\eta = A\frac{H}{2s^2} + \Gamma\frac{3(H - s)}{s^3}$$

Note that m is the value of M when density variation is neglected and that

$$M_b = m_1 + \epsilon d_b b^2$$

For this stepped slider, the Reynolds Equation [3] becomes

$$\frac{dp}{dX} = \frac{6\mu_0 UB}{h_0^2} \frac{s - H(1 + \epsilon X)}{s^3[m + \epsilon d_\eta (X^2 - \eta^2)]} \quad [15]$$

Equation [15] must be integrated with respect to X to determine the pressure distribution. The constant H is determined by the condition that the pressure vanish at the inlet and outlet ends of the slider and be continuous at the step. With this value of H, the pressure distribution may be integrated with respect to X to determine the load capacity. The temperature rise through the bearing may then be calculated and the constant ϵ adjusted to satisfy Equation [7]. This direct procedure is tedious and quite time-consuming. A relatively simple iteration procedure for finding the load capacity will now be described, the first step of which will prove to be sufficient for almost all cases.

First Approximation

If the density variation is neglected (i.e., ϵ taken as zero), it is apparent that since there will be no density-wedge effect the resulting load capacity will bound the actual load capacity from below. For this case Equation [15] becomes

$$\frac{dp}{dX} = \frac{6\mu_0 UB}{h_0^2} \frac{s - H}{s^3 m} \quad [16]$$

Integrating Equation [16] with respect to X, we obtain

$$\left.\begin{aligned} p &= \frac{6\mu_0 UB}{h_0^2} \frac{a - H}{a^2 c_0} \ln m, \quad 0 \leq X < b \\ &= \frac{6\mu_0 UB}{h_0^2} \frac{1 - H}{c_b} \ln \frac{m}{m_2}, \quad b < X \leq 1 \end{aligned}\right\} \quad [17]$$

The condition that the pressure be continuous at the step requires that

$$\frac{a - H}{a^2 c_0} \ln m_1 = \frac{1 - H}{c_b} \ln \frac{m_1}{m_2} \quad [18]$$

Equation [18] determines the constant H. Integrating the pressure as given by Equation [17] with respect to X to obtain the load-supporting capacity W, we have

$$W = \frac{6\mu_0 UB^2}{h_0^2}\left\{\frac{a-H}{a^3c_0^2}\left[m_1 \ln m_1 - (m_1 - 1)\right] - \frac{H-1}{c_0^2}\left[m_1 \ln \frac{m_2}{m_1} - (m_2 - m_1)\right]\right\} \quad [19]$$

Thus, if the geometrical configuration of the slider is known (B, a, b), the operating conditions are known (h_0, U), and the lubricant properties are known (μ_0, α, γ, ρ_0, c), Equation [19] gives a lower bound to the load-supporting capacity W once H is determined from Equation [18].

From the definition of m_2 it is obvious that the total temperature rise experienced by the lubricant in flowing adiabatically through the stepped slider bearing is given by

$$t_2 = \frac{1}{\gamma} \ln m_2 \quad [20]$$

to this first approximation.

Second Approximation

If the temperature rise as given by Equation [20] is substituted into Equation [7] to determine an ϵ, a second approximation to the load capacity can be obtained by substituting this value of ϵ into Equation [15], integrating this equation to obtain the pressure distribution, determining H by requiring continuity of pressure at the step, and with this H integrating the pressure distribution for the load capacity. If greater accuracy is desired the cycle of operations can be repeated.

Numerical Examples

This method of successive approximations will now be illustrated by a numerical example. Consider a stepped slider with the optimum profile for isothermal flow ($a = 1.8660$, $b = 0.7182$; see reference 2 or 3) and a length B of 2 in., operating with a minimum film thickness (h_0) of 0.001 in., and a bearing velocity U of 320 ips, and using a lubricant with the following properties:

$\mu_0 = 9.25$ microreyn
$\alpha = 0.00015$ sq in. per lb
$\gamma = 0.029$ per deg F
$\rho_0 = 0.0325$ pci
$c = 4200$ in-lb per lb deg F
$\beta = 0.0004$ per deg F

By the methods of the first approximation the following results are obtained:

Load capacity (W) = 1662 lb per in. of width
Temperature rise to step (t_1) = 24.0 deg F
Pressure at step (p_1) = 1615 psi
Temperature rise to outlet (t_2) = 35.5 deg F

On the basis of the pressure and temperature distributions of this first approximation, the lubricant density is found to decrease about 1.5 per cent through the bearing, roughly one third of this decrease occurring in the first two thirds of the bearing length. Thus the density variation is not exactly linear, but in the light of the smallness of the density change the linearity assumption seems reasonable as an approximation. The second approximation to the load capacity works out to be 1680 lb, an increase of only 1 per cent. The smallness of the density-wedge effect is thus quantitatively expressed for a typical example of a stepped-profile slider bearing. It would seem therefore that the first approximation generally would be sufficient for the prediction of the load-supporting capacity of stepped sliders provided a is not too close to 1 and b is not too close to zero or 1. If a equals 1 or b equals zero or 1, the surfaces are parallel and the methods of reference (5) can be used to determine the load capacity.

Rayleigh's constant-viscosity theory (2) predicts a load of 2444 lb per in. of slider width for this stepped slider bearing, a value 45 per cent above the prediction of the variable-viscosity theory of this paper.

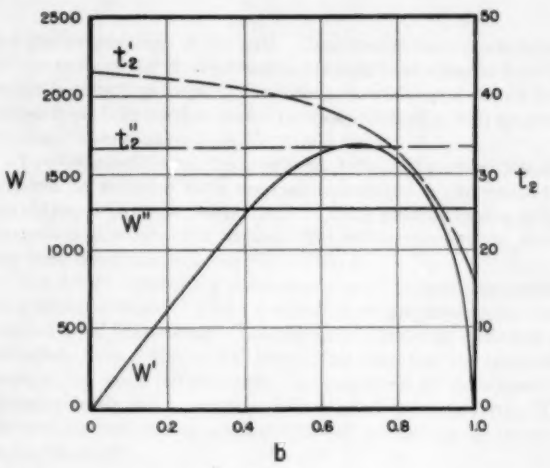

Fig. 2

In Fig. 2 the variation of the first approximation (lower bound) to the load-supporting capacity (W', in lb per in. of slider width) and the total temperature rise of the lubricant (t_2', in deg F) with the step location (b, in per cent of slider length) is plotted for a stepped slider bearing with a step ratio (a) of 2—the slider length, minimum film thickness, bearing velocity, the lubricant properties being the same as in the previous example. Also shown on this plot are the load capacity (W'') and temperature rise (t_2'') which would result if the stepped profile were replaced by a flat inclined-plane profile with the same inlet and outlet film thicknesses. These values were taken from the numerical example of reference (4).

It is evident from Fig. 2 that under these conditions it is possible to support 31 per cent more load with the stepped slider than with the flat inclined-plane slider. Another interesting observation is that the stepped slider could be made to support the same load as the flat inclined-plane slider while experiencing 19 per cent less temperature rise.

BIBLIOGRAPHY

1 "A Simple Hydrodynamic Thrust Bearing," by F. R. Archibald, Trans. ASME, vol. 72, 1950, pp. 393–400.

2 "Notes on the Theory of Lubrication," by Lord Rayleigh, *Philosophical Magazine*, vol. 35, 1918, p. 1.

3 "On the Solution of the Reynolds Equation for Slider-Bearing Lubrication—VIII. The Optimum Slider Profile for Viscosity a Function of the Pressure," by A. Charnes, F. Osterle, and E. Saibel, Trans. ASME, vol. 77, 1955, pp. 33–36.

4 "On the Solution of the Reynolds Equation for Slider-Bearing Lubrication—IV. Effect of Temperature on the Viscosity," by F. Osterle, A. Charnes, and E. Saibel, Trans. ASME, vol. 75, 1953, pp. 1117–1123.

5 "On the Solution of the Reynolds Equation for Slider-Bearing Lubrication—VI. The Parallel-Surface Slider Bearing Without Side Leakage," by F. Osterle, A. Charnes, and E. Saibel, Trans. ASME, vol. 75, 1953, pp. 1133–1136.

Measurement of Total Emissivities of Gas-Turbine Combustor Materials

By S. M. DE CORSO[1] and R. L. COIT[2]

A method of measuring total emissivity is presented with a description of the apparatus used. Data are presented showing the emissivity of several metals and ceramic coatings as functions of temperature, surface treatment, and previous history of the material.

Nomenclature

The following nomenclature is used in the paper:

e_t = total emissivity
e_λ = spectral emissivity
F = constant arising from the thermopile calibration, equal to

$$\frac{\Delta mv_b}{\left(\frac{T}{1000}\right)^4}$$

F_1 = dimensionless factor defining geometry of a particular thermopile, as it concerns radiant heat transfer
Δmv = thermopile emf in mv, corrected for the "zero" reading when viewing a hot body
Δmv_b = thermopile emf in mv, corrected for zero reading when viewing a black body
Δmv_s = thermopile emf in mv, corrected for zero reading when viewing a nonblack source
T = temperature of a body, deg R
T_a = ambient temperature, deg R
T_R = radiation temperature of a body at true temperature T, deg R
W_b = radiant flux density from a black body, Btu/ft² sec
W_s = radiant flux density from a nonblack source, Btu/ft² sec
σ = Stefan-Boltzmann constant, Btu/ft² hr deg R⁴
ρ = reflectance of a hot body for radiation at its own temperature
ρ' = reflectance of a hot body at some temperature for radiation at a different temperature

Introduction

This paper presents a means of measuring the total emissivities of various gas-turbine combustor materials and gives data obtained for some of these materials. A more thorough knowledge of this field will permit selective use and treatment of materials to take full advantage of emissive properties to reduce combustor wall temperatures. The overheating of combustor walls causing "hot spots" is one of the primary causes of combustor failure.

It is evident that the emissivities of both the inner surface (flame side) and outer surface of a combustor wall have an effect on the temperature of the wall. Combustion tests made by one of the authors (1)[3] showed that the radiant heat transfer from the flame is quite important. These tests showed that a change from diesel fuel oil to residual fuel oil caused combustor wall temperature increases ranging from 250 to 500 deg F.

To evaluate different flame-tube materials and coatings it is convenient to measure their thermal emissivities under controlled conditions which are independent of those existing during actual operation or combustion testing. The temperature range chosen for these measurements was 800 to 2100 F.

The device selected for determining total emissivities consists of a thermopile which views a radiating source through an aperture of fixed dimensions. The thermopile receives radiation alternately from a black-body source and from the test specimen, both at the same temperature. A comparison of the respective thermoelectric emf provides a value of the total emissivity. The general method and procedure followed are similar to those of Sully, et al. (2).

Theoretical Basis of Method

The total emissivity e_t is defined as the ratio of the total radiant flux from a source to that from a black body at the same temperature, i.e.

$$e_t = \frac{W_s}{W_b} = \frac{e_t T^4}{T^4} \quad [1]$$

The general arrangement of the thermopile, black-body source, and specimen is shown in Fig. 1. The thermopile emf, measured by means of a potentiometer, will be some function of the temperature difference between the hot and cold junctions of the thermopile. This temperature difference in turn is a function of the net radiant energy falling on the receiver element (which contains the hot junctions). Let T be the temperature of the source, and T_a the ambient temperature, both in degrees R, then the net radiant heat transfer to the receiver when it views a black-body source is

$$F_1\sigma(T^4 - T_a^4)$$

since the receiving element has a coating which can be considered black. This follows from the Stefan-Boltzmann law. F_1 is a geometry factor which is characteristic of the particular thermopile and aperture dimensions. As concerns the thermopile, the ambient temperature refers to the temperature of its surroundings, i.e., the thermopile housing and shutter.

The net radiant heat transfer to the receiving element when it views a nonblack body is (3)

$$F_1\sigma(e_t T^4 + \rho' T_a^4 - T_a^4) \quad [2]$$

The term $\rho' T_a^4$ represents radiation which originates from the surroundings at T_a and is reflected from the hot body to the receiving element. ρ' is the reflectance of the hot body for radiation from the ambient surroundings and, in general, differs from ρ, which is the reflectance of the hot body for radiation at its own temperature. If the hot body is assumed to be a "gray body" then ρ' is equal to ρ.

[1] Engineer, Westinghouse Research Laboratories, East Pittsburgh, Pa.

[2] Development Engineer, Steam Division, Westinghouse Electric Corporation, Essington, Pa.

Contributed by the Gas Turbine Power Division and presented at the Semi-Annual Meeting, Pittsburgh, Pa., June 20–24, 1954, of The American Society of Mechanical Engineers.

Note: Statements and opinions advanced in papers are to be understood as individual expressions of their authors and not those of the Society. Manuscript received at ASME Headquarters, March 25, 1954. Paper No. 54—SA-26.

[3] Numbers in parentheses refer to the Bibliography at the end of the paper.

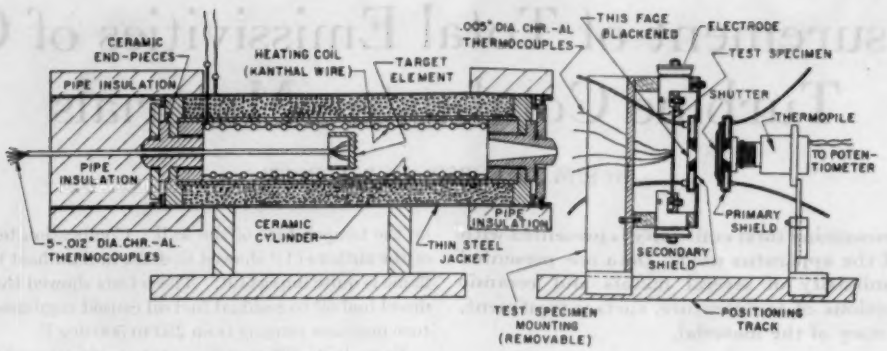

FIG. 1 ARRANGEMENT OF FURNACE, SPECIMEN, AND THERMOPILE

From Newton's law of cooling and the fact that the temperature difference between the receiver and the thermopile body is small, we may say that the temperature difference between the hot and cold junctions will vary directly with the net radiant heat transfer to the receiver. Since the emf versus temperature curve for the constantan-chromel thermocouples of the thermopile is nearly a straight line in the temperature range encountered in the thermopile, then it follows that Δmv, the emf, will be proportional to the net radiant heat transfer to the thermopile receiver.

The ratio of emf obtained from the thermopile viewing a non-black and a black-body source is then

$$\frac{\Delta mv_s}{\Delta mv_b} = \frac{F_1\sigma(e_t T^4 + \rho' T_a^4 - T_a^4)}{F_1\sigma(T^4 - T_a^4)} \quad \ldots\ldots [3]$$

This reduces to

$$\frac{\Delta mv_s}{\Delta mv_b} = e_t - \frac{(\rho - \rho')}{\left(\frac{T}{T_a}\right)^4 - 1} \quad \ldots\ldots [4]$$

If the viewed body is approximately gray or if the temperature of the source greatly exceeds the ambient temperature then the term on the right in the foregoing equation will be small and the emf ratio will represent the emissivity of the specimen.

That Equation [4] holds for the thermopile arrangement used here can be seen from the calibration curve obtained, Fig. 2. Here it was found that

$$\Delta mv_b = F\left(\frac{T}{1000}\right)^4$$

where F = const. Also we may say

$$\Delta mv_s = F\left(\frac{T_R}{1000}\right)^4 = Fe_t\left(\frac{T}{1000}\right)^4$$

and consequently

$$\frac{\Delta mv_s}{\Delta mv_b} = e_t \quad \ldots\ldots [5]$$

If F were not a constant, suitable corrections would have to be made at each value of T. While the foregoing treatment which represents an ideal thermopile leads to Equation [4], it has been found by Burgess and Foote (4) that, in general, F may vary with heat input to the thermopile, depending on the thermopile design. Thus a calibration of the thermopile over the range of use is necessary.

The value of e_t obtained in our tests is the normal emissivity of the test specimen.

If one considers absorption of radiant energy by the gas intervening between the radiating source and the thermopile, only the water vapor present in the air need be considered (5). This correction would vary with the humidity, but since it cannot exceed about 1 per cent it has been neglected.

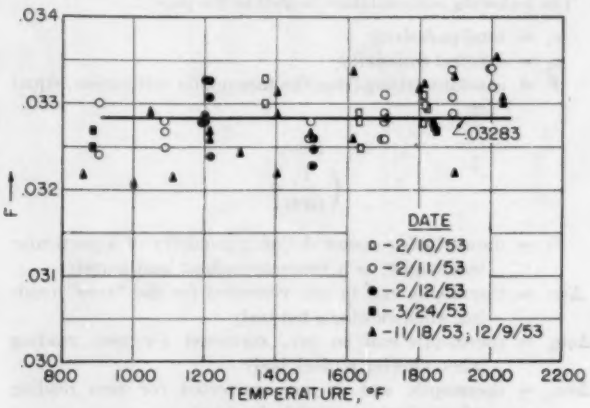

FIG. 2 PARAMETER F VERSUS TEMPERATURE IN DEG F

$$\left(\text{Where } F = \frac{\Delta mv_b}{\left(\frac{T}{1000}\right)^4}\right)$$

DESCRIPTION OF APPARATUS

Thermopile. The thermopile consists of eight thermojunctions of 3-mil-diam constantan and chromel wire, with the hot junctions fastened in good thermal contact between two thin platinum disks of $^1/_{16}$ in. diam. The face of one of the disks is blackened with a mixture of varnish and lampblack to form a black-body receiver. The cold junctions are located away from the hot junctions and are well shielded from incoming radiation. A Leeds and Northrup double-range portable millivolt-indicator Type 8662 was used to measure the emf generated by the thermopile.

Fastened to the open end of the thermopile housing was a water-cooled shield which contained a centrally located circular aperture of fixed size (0.25 in. diam for these tests). This aperture was always held in a fixed position relative to the thermopile receiving element, thereby determining the solid angle from which radiation reached the receiver. Sliding in flanges on this shield, a water-cooled shutter could be moved so as to cover the afore-mentioned aperture. Water from a constant-temperature bath was circulated continuously through the shield and shutter to insure that radiation from these parts was always at a constant intensity. When the thermopile was set to view the test strip instead of the black body, an additional water-cooled shield was interposed between the test strip and the primary

shield to reduce the cooling load on the latter. The face of this additional shield which confronts the test specimen was blackened with soot to avoid repeated reflections between the test strip and the shield. If the face were not blackened, the emissivity obtained would not be that of the strip alone but that of the strip-shield configuration.

Black-Body Source. The heating coil of the black body consisted of a spiral of Kanthal wire enclosed by insulation. The furnace is shown in Fig. 1. The Kanthal wire coil is supported by a ceramic cylinder which is insulated by magnesia held in a metal jacket. Pipe insulation was used outside the metal jacket at the ends in order to reduce the heat loss at the ends of the furnace. The inner walls of the furnace form a cylinder 3 in. in diam and 21 in. long, with a $^3/_4$-in. viewing hole at one end. A target disk was located, as shown in Fig. 1, at a distance of 13 in. from the viewing end of the furnace. The disk was made of stainless steel and the face was serrated with vee-shaped grooves having an included angle of 45 deg to increase the emissivity of the face of the disk. Since the disk was the principal source of radiation from the furnace cavity to the thermopile, it was important that its emissivity be a close approximation to that of a black body and that its temperature be uniform and accurately measured. Hence five 0.012-in-diam chromel-alumel thermocouples were peened into the target disk in order to determine the temperature. After oxidation at 2100 F the emissivity of the target disk can be taken as greater than 0.98 so that radiation from other surfaces inside the furnace is of secondary importance (6).

Test-Strip Arrangement. The test specimen was heated by passing an electrical current through it using a constant-voltage supply with a maximum power of 7000 watts at 700 amps. The arrangement of the specimen holder is shown in Fig. 1. The area viewed by the thermopile lies within a circle of $^1/_2$ in. diam at the center of the specimen. This area was kept at a minimum to reduce the possibility of large temperature gradients across it. The specimen strips are $1^1/_2$ in. wide × 5 in. long and approximately 0.040 in. thick with the ends clamped in electrodes.

Three thermocouples of 0.005-in-diam chromel-alumel wire were peened into the specimen from the side opposite the thermopile and lying within the circle which encloses the viewed area. The conduction error of the thermocouples was found to be negligible. This conduction error was determined by comparing the temperature readings of two thermocouples peened into the strip at a point from opposite sides. The leads on one of the thermocouples were led out normal to the surface while on the other they were kept close to the surface of the heated strip.

Since the thermocouple beads ranged from 20 to 30 mils and the specimen thickness ranges from 30 to 50 mils, the temperature at the bead can be taken as the temperature at the face of the specimen. When a ceramic coating was used a correction was made based on the thickness of the coating, its thermal conductivity, and the temperature of the metal strip.

The thermal conductivity of the ceramic coating was obtained in the following manner. With the test specimen heated to some arbitrary temperature a temperature reading of the coating surface was obtained using an optical pyrometer operating at 0.665 μ. A pyrometer reading also was obtained for the black or uncoated side of the specimen. Since the emissivity of the uncoated metal was known and that of the ceramic coating could be calculated approximately from the data, a correction of the readings could be made to obtain the temperatures of the coated and uncoated surfaces. The difference of these was taken as the temperature drop through the coating. The heat-transfer coefficient at the surface of the ceramic coating was calculated and the thickness of the coating was known; then equating the heat flow at the surface of the coating to the heat flow by conduction through the coating yields a value of thermal conductivity.

The two sizes of chromel-alumel thermocouples used (0.005 and 0.012 in.) were calibrated against a standard platinum-platinum 10 per cent rhodium thermocouple obtained from the National Bureau of Standards. The curve obtained is shown in Fig. 3. In this figure the sequence in which the readings were taken is indicated by the numbers next to the points. Note that upon initial heating there is only a slight correction, but at temperatures above 1800 F the correction required becomes larger. Once the thermocouples have been heated above 1800 F, the corrections required at all temperatures are larger than the initial corrections. The corrections shown in Fig. 3 were applied to all temperatures measured with chromel-alumel couples to obtain corrected temperatures. If this temperature correction is ignored a maximum error in emissivity of 1.5 per cent would result.

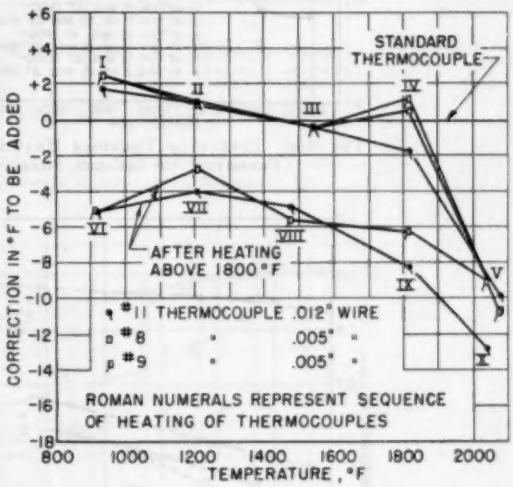

FIG. 3 CALIBRATION CURVES FOR Cr-Al THERMOCOUPLES

TEST PROCEDURE

With the thermopile in position opposite the hot radiating source the procedure followed in obtaining emf readings was to obtain successive emf readings with the shutter closed, open, and closed again. The average of the first and third readings was considered to be a zero reading. The difference of the second reading and the zero reading was Δmv, the emf due to radiation from the source.

It was found that instead of viewing alternately the black-body source and the test strip, the most convenient procedure was to view the black body over the full range of temperatures, after which the apparatus would be considered calibrated. The testing of specimens could then proceed with only an occasional return to the black body for a check of the original calibration.

The results of this calibration with the furnace as the black-body source are shown in Fig. 2 where the ordinate is

$$F = \frac{\Delta mv_b}{\left(\frac{T}{1000}\right)^4}$$

and the abscissa is the black-body temperature in degrees F.

The emf readings with the thermopile opposite the test strip were obtained in the same manner as just indicated, with the ratio of $\Delta mv_s/\Delta mv_b$ being the emissivity of the test strip.

To obtain spectral band emissivities four filters were used. These filters were CaF_2, LiF, fused quartz, and pyrex glass. From

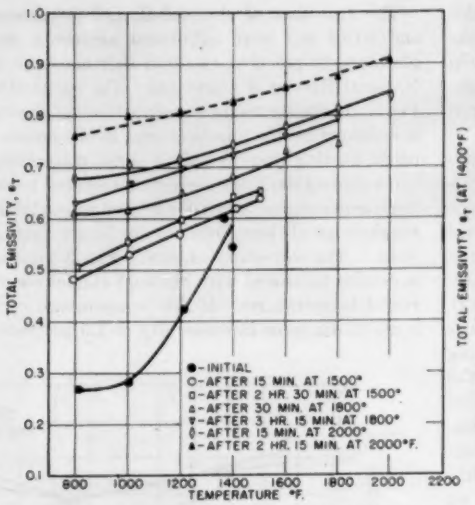

FIG. 4(a) EFFECT OF PREVIOUS HEATING UPON EMISSIVITY OF INCONEL SHEET

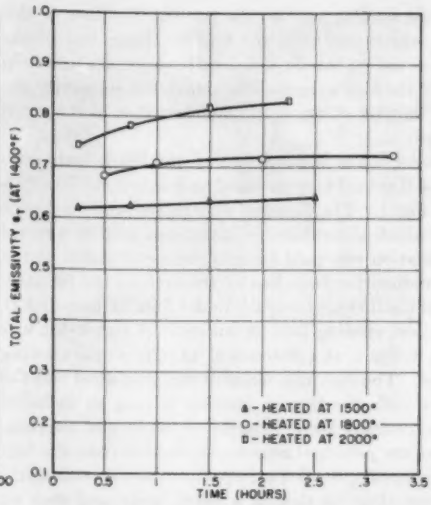

FIG. 4(b) EFFECT OF TIME AND TEMPERATURE UPON EMISSIVITY OF INCONEL SHEET AT 1400 DEG F

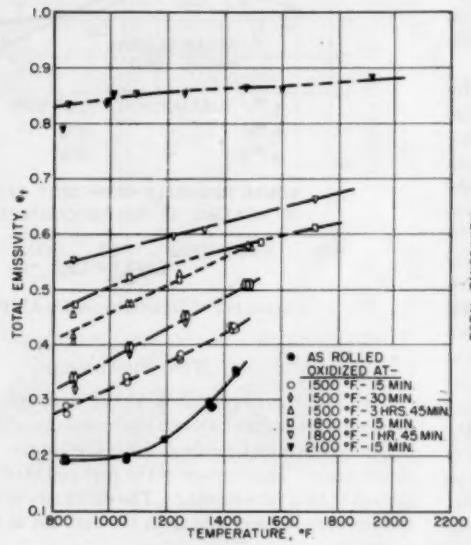

FIG. 5(a) EFFECT OF PREVIOUS HEATING UPON EMISSIVITY OF NICHROME V SHEET

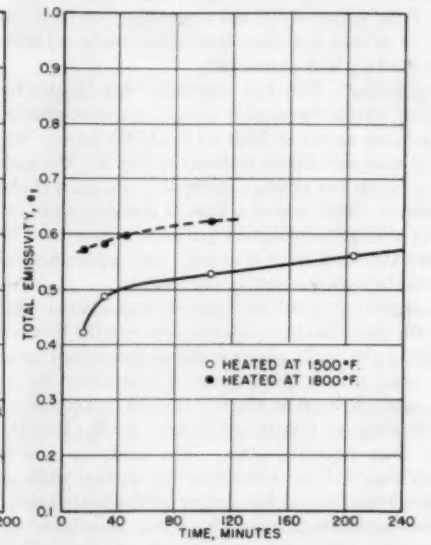

FIG. 5(b) EFFECT OF TIME AND TEMPERATURE UPON THE EMISSIVITY OF NICHROME V SHEET AT 1400 DEG F

tests with the black body, effective cutoff wave lengths of these filters were found to be 8.9, 5.8, 3.7, 2.55 μ, respectively.

DISCUSSION OF EXPERIMENTAL RESULTS

Heat-Resistant Alloys. In order to determine the effect of time and temperature upon emissivity, as-rolled specimens of Inconel, Nichrome V, and Type 310 stainless steel were tested over the range from 800 to 1500 F, then heated at 1500 F for additional time increments. After each period at 1500 F the emissivity as a function of temperature was measured. After completing the tests at 1500 F, the same specimen was heated at 1800 and 2100 F and the effect of time at these temperatures was evaluated. Results of these tests are shown in Figs. 4 and 5. Figs. 4(*a*) and 5(*a*) present the emissivity versus temperature after oxidation at 1500, 1800, and 2000, or 2100 F for various lengths of time. The effect upon emissivity at 1400 F of prolonged heating at 1500, 1800, and 1500, 1800, 2000 F is shown in Figs. 4(*b*) and 5(*b*) for Inconel and Nichrome. For the Nichrome specimen the emissivity increases only slightly after the first 40 min. For the Inconel specimen the increase in emissivity is slight after the first 15 min.

The emissivity of Nichrome V, Inconel, and Type 310 stainless steel was measured as a function of temperature, surface condition, and previous oxidation. The sequence used in obtaining the test points was as follows:

1 Obtain readings from 900 to 1500 F.
2 Oxidize at 1500 F for 15 min.
3 Obtain readings from 900 to 1500 to 1800 F.
4 Oxidize at 1800 F for 15 min.
5 Obtain readings from 900 to 1800 to 2100 F.
6 Oxidize at 2100 F.
7 Obtain readings from 900 to 2100 F.

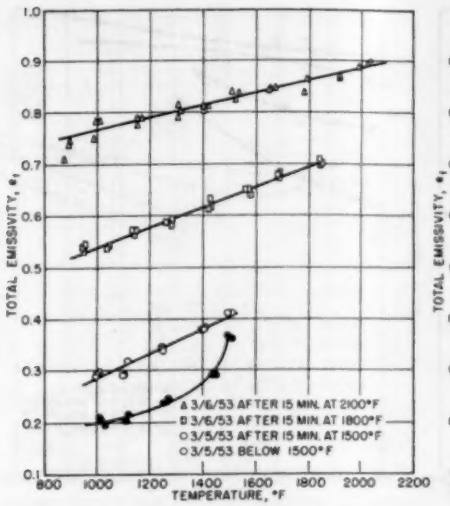

FIG. 6(a) TOTAL EMISSIVITY VERSUS TEMPERATURE, NICHROME V, AS-ROLLED

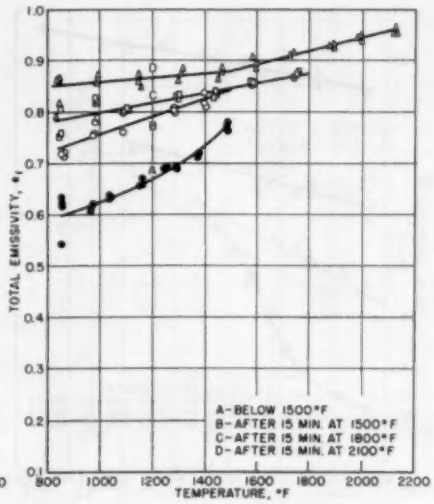

FIG. 6(b) TOTAL EMISSIVITY VERSUS TEMPERATURE, SANDBLASTED NICHROME V

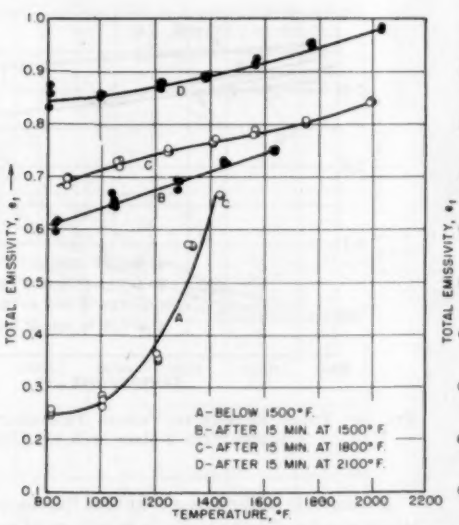

FIG. 7(a) TOTAL EMISSIVITY VERSUS TEMPERATURE FOR INCONEL, AS-ROLLED

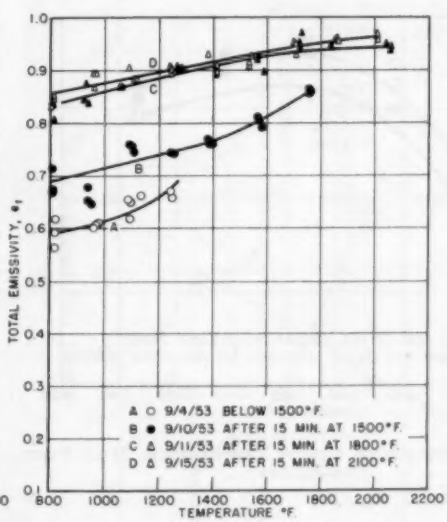

FIG. 7(b) TOTAL EMISSIVITY VERSUS TEMPERATURE, SANDBLASTED INCONEL

This procedure was used to obtain the data plotted in Figs. 6, 7, and 8. These figures provide a comparison of Nichrome V, Inconel, and Type 310 stainless steel in the as-rolled and sandblasted condition. Each of the curves except the below 1500 F curves show a nearly linear increase of emissivity with temperature with the slope of the curves decreasing as the oxidation temperature is increased. In the as-rolled condition for corresponding conditions Inconel had the highest emissivity, with Type 310 stainless next, and Nichrome V having the lowest emissivity. This effect was more pronounced the lower the temperature. In the sandblasted condition no such relationship is evident. It is evident that sandblasting increases the emissivity of the materials, there being a larger increase at the lower temperatures.

This increase due to sandblasting is greatest in the case of Nichrome with Type 310 and Inconel next in order.

DISCUSSION OF RESULTS

Table 1 gives values of emissivity increase as a result of sandblasting. These were obtained at 1300 F for Nichrome, Inconel, and Type 310 stainless steel.

TABLE 1 VALUES OF EMISSIVITY INCREASE AS A RESULT OF SANDBLASTING

	Oxidation temp, deg F	Total emissivity, ϵ_t		Emissivity increase, $\Delta\epsilon_t$
		As-rolled	Sandblasted	
Nichrome	1500	0.36	0.81	0.45
	1800	0.60	0.83	0.23
	2100	0.80	0.87	0.07
Inconel	1500	0.69	0.75	0.06
	1800	0.76	0.90	0.14
	2100	0.88	0.91	0.03
Type 310	1500	0.56	0.82	0.26
	1800	0.67	0.91	0.24
	2100	0.89	0.93	0.04

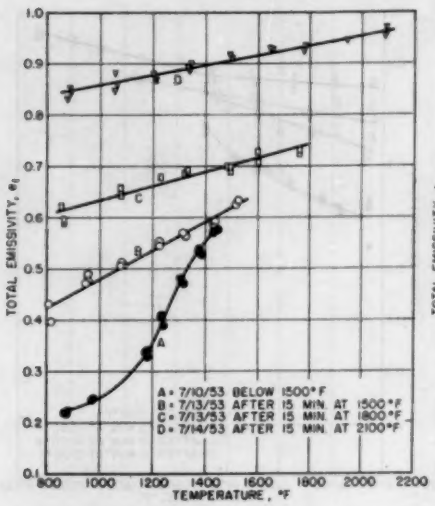

FIG. 8(a) TOTAL EMISSIVITY VERSUS TEMPERATURE, TYPE 310 STAINLESS STEEL, AS-ROLLED

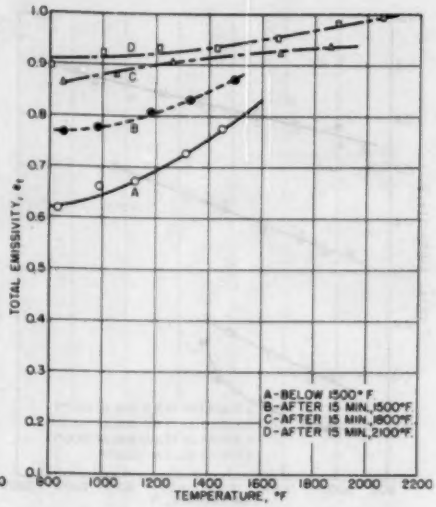

FIG. 8(b) TOTAL EMISSIVITY VERSUS TEMPERATURE, SANDBLASTED TYPE 310 STAINLESS STEEL

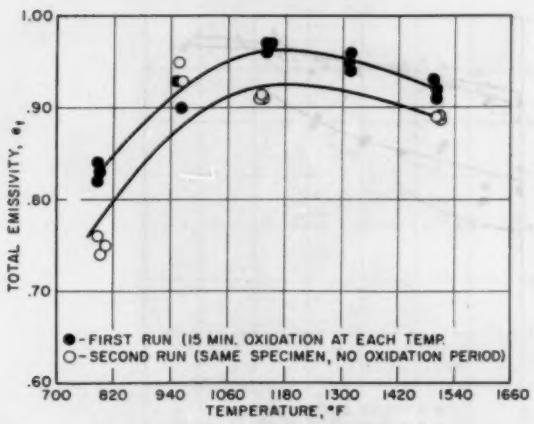

FIG. 9 TOTAL EMISSIVITY VERSUS TEMPERATURE, MILD STEEL, AS-ROLLED

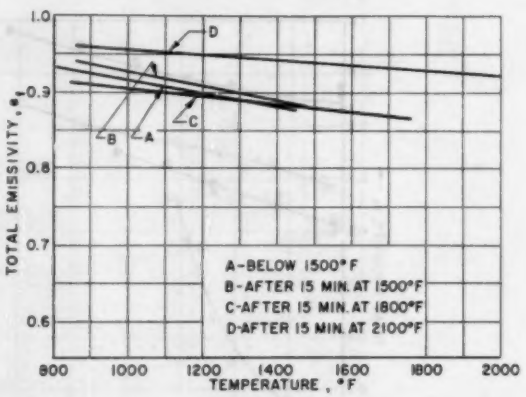

FIG. 10 TOTAL EMISSIVITY VERSUS TEMPERATURE, NICHROME V COATED WITH 2 MILS OF A-418 CERAMIC

Thus, for applications of Nichrome and Type 310 at oxidation temperatures below 1800 F, a considerable increase in emissivity can be obtained by sandblasting. The behavior of Inconel appears to be unusual in that the increase due to sandblasting was not as large as for the other two specimens. It is interesting to note that well-oxidized Type 310 sandblasted at 2100 F closely approaches a black-body radiator.

Mild-Steel Specimen. In Fig. 9 emissivity data for mild steel (SAE 1020), as-rolled, are plotted for the temperature range 800 to 1500 F. The emissivity on the initial run increases from 0.83 at 800 F to a peak of 0.97 at 1140 F and falls off to 0.92 at 1500 F. A second run on the same specimen showed that oxidation at 1500 F had lowered the emissivity slightly over the whole range.

Radiation Suppressive Coatings. Several types of ceramic coatings were evaluated with the object of obtaining a suitable coating of low emissivity. The coatings were obtained from several sources which included the Solar Aircraft Company; University of Illinois, Department of Ceramic Engineering; and the Fulmer Research Institute, England. The two latter groups have published descriptions of their coatings (7, 8).

A commonly used coating, National Bureau of Standards A-418, which was developed primarily to withstand corrosive effects, was tested and the emissivity data are shown by the curves in Fig. 10. While its emissivity decreases with increasing temperature, it did not go below 0.86 in our tests.

Fig. 11 (coating 5210-TA1K) presents the emissivity of another type of coating tested. The change in emissivity after heating is probably caused by the fusion of some elements in the coating. This type and the A-418 do not have emissivities low enough to be considered in a radiation-suppression application.

The emissivity of a third type of coating is shown in Fig. 12. The emissivity of this coating reaches a value of 0.58 at 1600 F. Upon further heating the emissivity increases, indicating that fusion of the coating is occurring. Heating to 2030 F in this case destroyed the low emissivity properties of the coating, as is shown by the upper curve of Fig. 12.

Fig. 13 presents the emissivities of a fourth group of coatings. The lowest total emissivity attained by this group is 0.42 for coating 216 at a temperature of 1800 F. The characteristics of coating 216 were not changed appreciably by heating the specimen to 2000 F as is shown by curve D, Fig. 13.

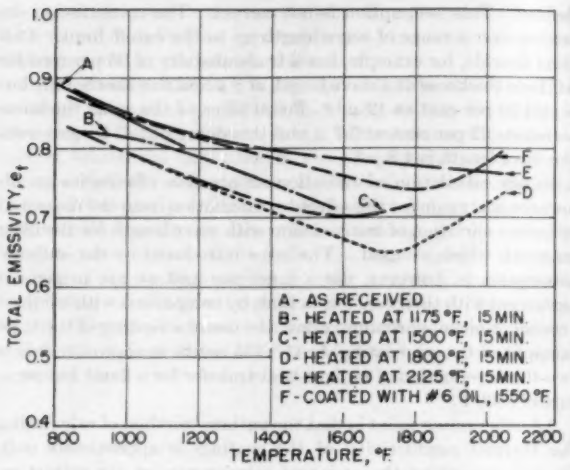

FIG. 11 TOTAL EMISSIVITY VERSUS TEMPERATURE, CERAMIC COATING 5210-TA1K

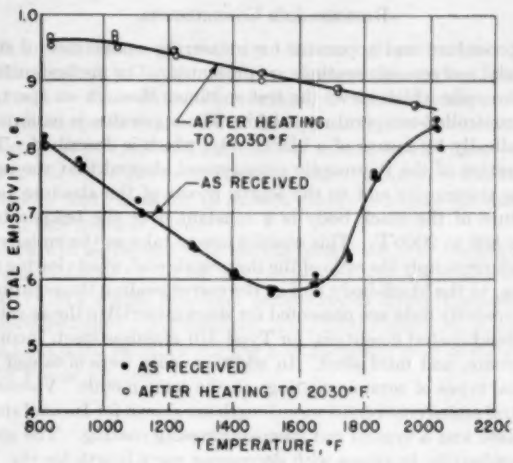

FIG. 12 TOTAL EMISSIVITY VERSUS TEMPERATURE, CERAMIC COATING 117-23

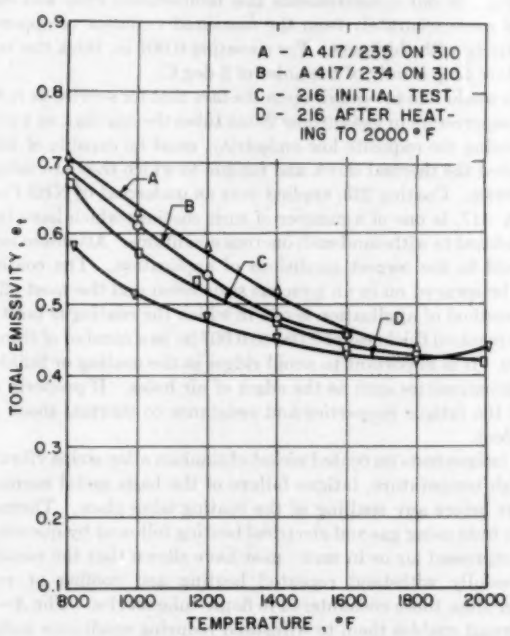

FIG. 13 TOTAL EMISSIVITY VERSUS TEMPERATURE, CERAMIC COATINGS A-417/234; A-417/235; 216

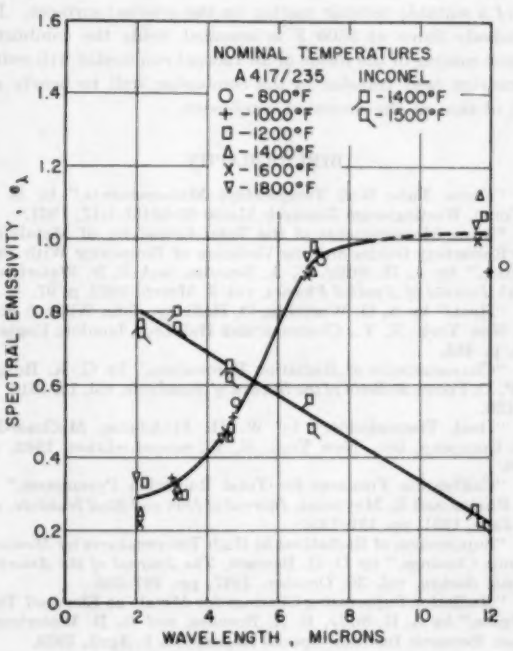

FIG. 14 SPECTRAL EMISSIVITY VERSUS WAVE LENGTH FOR INCONEL AND COATING A-417/235

Comparison of Spectral Emissivities of Inconel Sheet and Ceramic Coating A-417/235. The variation of spectral emissivity with wave length for Inconel sheet and coating A-417/235 is shown in Fig. 14. The emissivities used here were obtained for a band of wave lengths using the four filters described previously. In Fig. 14 each band emissivity is plotted at a wave length which equally divides the black-body energy in that band.

The data for Inconel were obtained at two temperatures, 1400 and 1500 F, while the data for the ceramic coating were obtained at several temperatures ranging from 800 to 1800 F. The spectral emissivity should not vary with temperature where a particular surface condition is maintained. This is seen to be true for the coating A-417/235, and constitutes a check on the method and apparatus used.

In going from 2μ to 12μ the spectral emissivity of Inconel decreases from 0.8 to 0.21 while that of coating A-417/235 increases from 0.3 to 1.0. Neither material can be considered gray over this range of wave lengths.

If the spectral distribution of the radiation from the flame is known, spectral emissivity data, such as those shown in Fig. 14, can be used to calculate the effectiveness of a radiation suppressive coating by taking $e_\lambda = \alpha_\lambda$ for the wall. For example, consider the case of a combustor wall and a flame as two large parallel surfaces, with the flame taken as a black body at 3500 F. The ratio of the net radiant heat transfer to the combustor wall for an Inconel wall to that for the ceramic (A-417/235) wall ranges from 2.1 to 2.8 for wall temperatures of 1000 and 1500 F, respectively.

Results and Conclusions

A procedure and apparatus for measuring emissivities of strip material and ceramic coatings are presented. The method utilizes a thermopile which views the test specimen through an aperture in a controlled-temperature shield. The apparatus is calibrated periodically by means of a black body, which is described. The calibration of the thermopile arrangement showed that the ratio of the thermopile emf to the fourth power of the absolute temperature of the black body is a constant over the temperature range 800 to 2000 F. This enables one to take as the emissivity of a source simply the ratio of the thermopile emf, when viewing the source, to the black-body emf at the corresponding temperature.

Emissivity data are presented for sheet material in the as-rolled and sandblasted condition, for Type 310 stainless steel, Inconel, Nichrome, and mild steel. In addition, data were obtained for several types of ceramic coatings on the same metals. Values of spectral emissivity versus wave length are shown for Inconel sheet as-rolled and a typical radiation-suppressing coating. The spectral emissivity increases with decreasing wave length for the Inconel while the opposite is true for the ceramic coating A–417/235.

The data presented show that combustor wall temperatures can be reduced by sandblasting of the external surfaces and application of a suitable ceramic coating on the internal surfaces. If a black-body flame at 3500 F is assumed inside the combustor, ceramic coating of the inside of an Inconel combustor will reduce the radiant heat transfer to the combustor wall to nearly one third of that of the uncoated combustor.

BIBLIOGRAPHY

1 "Flame Tube Wall Temperature Measurements," by S. M. De Corso, Westinghouse Research Memo 60-94451-1-17, 1951.

2 "Some Measurements of the Total Emissivity of Metals and Pure Refractory Oxides and the Variation of Emissivity With Temperature," by A. H. Sully, E. A. Brandes, and R. B. Waterhouse, *British Journal of Applied Physics*, vol. 3, March, 1952, p. 97.

3 "Heat," by A. G. Worthing, D. Halliday, John Wiley & Sons, Inc., New York, N. Y., Chapman and Hall Ltd., London, England, 1948, p. 455.

4 "Characteristics of Radiation Pyrometers," by G. K. Burgess and P. D. Foote, *Bulletin of the Bureau of Standards*, vol. 12, 1916, pp. 130–133.

5 "Heat Transmission," by W. H. McAdams, McGraw-Hill Book Company, Inc., New York, N. Y., second edition, 1942, pp. 64–66.

6 "Calibration Furnaces for Total Radiation Pyrometers," by E. J. Burton and R. Mayorcas, *Journal of Iron and Steel Institute*, vol. 168, June, 1951, pp. 151–155.

7 "Suppression of Radiations at High Temperatures by Means of Ceramic Coatings," by D. G. Bennett, *The Journal of the American Ceramic Society*, vol. 30, October, 1947, pp. 297–305.

8 "Radiation Suppressing Coatings for Metals at Elevated Temperatures," by A. H. Sully, E. A. Brandes, and R. B. Waterhouse, Fulmer Research Institute Special Report No. 1, April, 1953.

Discussion

A. H. Sully[4] and E. A. Brandes.[4] The experimental technique which the authors have adopted is similar to that used by the writers in a similar series of measurements[5] and their results are in gratifying agreement with those which we have reported on similar metals and refractory coatings.[6] The only comments which we wish to make on the experimental procedure is to point out that the measurements of emissivity in selected bands of the emission spectrum may be subject to minor errors if it is assumed that the filter materials have 100 per cent transmission at all wave lengths up to the cutoff wave length and that this is sharply defined. This assumption is not correct. The transmission decreases over a range of wave length up to the cutoff limit. Calcium fluoride, for example, has a transmissivity of 95 per cent for a 0.1-cm thickness at a wave length of 8 μ and this slowly falls but is still 30 per cent at 12 μ.[7,8] Fused silica of the same thickness transmits 82 per cent at 3.7 μ and this does not fall to zero until the wave length is 4.8 μ.[9]

In our calculation of radiation-suppression efficiencies an allowance was made for this effect by calculation from the measured or known variation of transmission with wave length for the filter materials which we used. The error introduced by the authors' assumption is, however, not a large one and we are in general agreement with their conclusion that, by comparison with oxidized Inconel or nickel-chromium alloy, the use of a coating of the type exemplified by our coating A–417/235 results in approximately a two-thirds reduction of radiant heat transfer for a flame temperature of 3500 F.

A further minor point is that the authors' method of calculating the thermal conductivity of the coatings is approximate only since in measuring the apparent temperature of the refractory surface they utilize a value for the emissivity of this surface which in itself involves an error due to the temperature drop through the coating. In our measurements this temperature drop was computed more accurately from the measured variation of apparent emissivity with thickness. For a coating 0.007 in. thick the temperature drop is only of the order of 5 deg C.

We would like to remark upon the fact that for service as radiation suppressors in gas-turbine flame tubes the coatings, as well as possessing the requisite low emissivity, must be capable of withstanding the thermal shock and fatigue to which they are subject in service. Coating 235, applied over an undercoat of NBS Coating A–417, is one of a number of such coatings which have been formulated to withstand such onerous conditions. Attention must be paid to the correct conditions of application. The coatings may be sprayed on in an aqueous suspension and the most effective method of application is one in which the coating is built up to its required thickness of 0.005 to 0.007 in. as a number of thinner layers. It is important to avoid ridges in the coating or build-up at discontinuities such as the edges of air holes. If properly applied the fatigue properties and resistance to thermal shock are excellent.

In fatigue tests on coated nickel-chromium alloy strips vibrated at high temperature, fatigue failure of the basis metal normally occurs before any spalling of the coating takes place. Thermal-shock tests using gas and electrical heating followed by quenching in compressed air or in water mist have shown that the coatings successfully withstand repeated heating and cooling at rates higher than those encountered in flame-tube service. The A–417 undercoat enables them to withstand reducing conditions such as occur when there is direct-flame impingement on the flame-tube wall, and their properties are not significantly affected by heating for periods up to at least 1000 hr.

The authors correctly point out that the heat transfer by radiation represents a higher proportion of the total heat transfer with high-flame luminosity, such as results from the combustion of marginal fuels, than with the lower-flame luminosity resulting from the combustion of distillate fuel. The degree of wall-temperature reduction in experimental combustion systems, using low-emissivity coatings in experiments with which we have been

[4] Fulmer Research Inst., Stoke Poges, Buckinghamshire, England.
[5] Reference (2) of the Bibliography of the paper.
[6] Reference (8) of the Bibliography of the paper.
[7] "Investigation of Infra-Red Spectra," by W. W. Coblentz, Carnegie Institution of Washington, part 3, 1906, p. 69.
[8] "Comparison of LiF and CaF_2 Prisms for Infra-Red Use," by R. C. Gore, et al., *Journal of the Optical Society of America*, vol. 37, 1947, p. 23.
[9] "The Infra-Red Absorption Spectra of Quartz and Fused Silica From 1 to 7.5 μ," by D. G. Drummond, Proceedings of the Royal Society of London, series A, vol. 153, 1935–1936, p. 328.

associated, has shown this correlation. Temperature reductions have varied from 90 F for kerosene flames to as much as 360 F for high-temperature marginal-fuel flames.

It is necessary, however, in this connection to utter a word of warning. The adhesion of these refractory coatings is sometimes adversely affected by contact at high temperatures with ash containing substantial quantities of vanadium pentoxide or of sulphates which results from the combustion of certain nondistillate fuels. Whenever possible it is advisable to prevent as far as possible ash deposition on the surface of the coating. No difficulty is experienced with distillate fuels. On the contrary it has been noted that the coatings appear to make a minor contribution to combustion efficiency with the result that, as we have noted, carbon deposition does not seem to occur on the surface of the low-emissivity coatings under conditions in which it occurs to some extent on the unprotected metal.

Authors' Closure

The discussion provided by Messrs. Brandes and Sully provides much valuable additional information concerning the application of low emissivity coatings, for which we are grateful.

That the error due to use of an equivalent cutoff wave length is not large is evident from the low scatter in the data points of Fig. 14. The increased scatter of the 12μ points is due to the relatively small quantity of radiant energy reaching the thermopile in this spectral region.

We are in agreement with the discussers' value of coating temperature drop of 5 C or 9 F if given at a specimen temperature of 1450 F. At higher specimen temperatures larger temperature drops were found. For example, at the 2100 F specimen temperature for a 0.007 in. thick coating a temperature drop of the order of 25 F was obtained.

Modified Residual Fuel for Gas Turbines

By B. O. BUCKLAND[1] and D. G. SANDERS,[2] SCHENECTADY, N. Y.

Sodium in gas-turbine fuel causes rapid deposit formation as well as corrosion. Besides naturally contained sodium, sea-water contamination during transportation introduces additional amounts. In order to obtain the benefits of a low-sodium fuel, 90 per cent or more of the sodium is washed out of the fuel by a scheme described. The results of the desalting show that calcium also can be reduced substantially. Turbine tests of 50 to 1500 hr duration using these desalted fuels show that deposit can be almost eliminated by keeping both the sodium and the calcium below 10 parts per million. The steady-stage decrease in turbine efficiency resulting from burning these low-sodium, low-calcium fuels is shown to be about 2 per cent and the reduction in regenerator effectiveness about 5 points. A specification is proposed, defining a fuel which can be obtained at the point of use by means of the desalting method described and by adding a water solution of magnesium sulphate to the fuel just before it is burned. Treating vanadium-containing fuels with calcium or magnesium shows that, below 1650 F, magnesium is a better inhibitor than calcium and, since magnesium does not cause deposit, it is used. Lead in the fuel in sufficient quantities is shown to spoil, somewhat, the inhibition of vanadium by means of magnesium. There now appear to be at least two methods available for modifying residual fuel to make it suitable for long-life gas turbines, one of which is described herein.

Introduction

DURING the past two years a number of General Electric gas turbines have been burning modified residual fuel with little or no corrosion of the nozzles and buckets. The units in locomotive service have accumulated in excess of 100,000 hr and have burned about 35 million gallons of this fuel. The life of the first-stage nozzles is no longer limited by oil-ash corrosion. Three units in power-generation service have burned about four million gallons of residual fuel modified at the user's plant with no apparent corrosion of the first-stage nozzles due to the fuel.

During 1952 and most of 1953 the fuel used on the locomotive units was inhibited by means of a calcium additive put in at the refinery and delivered to the railroad in the modified condition. No corrosion was detected on the 28 per cent chrome (446) nozzle partitions, but some corrosion was observed on the S-590 buckets at 5000 hr service from the use of the calcium-inhibited fuel. In addition, a great deal of deposit accumulated on the nozzles and buckets, resulting, of course, in a substantial loss in capacity.

Late in 1953 fuel was supplied to the locomotive units modified in accordance with a new specification in which magnesium was used in place of calcium to prevent vanadium-pentoxide corrosion. This change was made because it was found that in the temperature range below 1650 F magnesium is a better inhibitor for vanadium corrosion than calcium. It was found also that calcium in the oil promoted the accumulation of deposits, whereas magnesium did not, or at least did so in a much lesser degree. The deposits resulting from the magnesium-inhibited fuel on the locomotive units were minor and no appreciable loss in capacity occurred.

At present, the fuel being supplied to the locomotive units is a new kind of residual which has a very low ash. It is a heavy oil consisting of still bottoms resulting from cracking in a unit charged with distillate stock. It is ideal from a corrosion and ash-deposit standpoint because it contains only 1 or 2 ppm of sodium and vanadium. Thus far, no deposit or corrosion has occurred on the locomotive units from the use of this fuel.

All the fuel used by the locomotive units is transported by means of pipe line and tank car; hence the oil can be desalted at the refinery, and no subsequent sodium contamination will take place. The three power-generation units, however, are located in New England where the economical means of transportation is tankers. It is useless in this case to remove the sodium at the refinery because of the subsequent salt-water contamination which occurs in transport. Oil delivered in New England has been very bad from a corrosion as well as a deposit standpoint, both because of the sodium introduced during transport and because of the naturally contained sodium. This problem also plagues marine boiler users, the Navy, and those utilities burning bunker C, because of the accumulation of bad boiler and superheater deposits and, in some cases, because of superheater corrosion. Although vanadium, when uninhibited, causes corrosion, it also retards that corrosion which is due to sodium sulphate. This was the reason for proposing the requirement of having the sodium-vanadium ratio three-tenths or less. Since such a requirement was difficult to attain in some oils—particularly when salt-water contamination occurred, additives were sought to inhibit sodium-sulphate corrosion when the sodium content of the oil was high. The addition of chromic acid to a high-calcium fuel was tried on a plant scale, and although satisfactory from a corrosion standpoint, the treatment was not useful for this fuel and was discontinued because it produced extremely hard and rapidly accumulating deposit.

In order to obtain the noncorrosive benefits of a low-sodium fuel, the possibility of reducing the sodium content at the point of use by washing or other desalting means had been considered since the summer of 1951, and help from separator manufacturers was sought from time to time. After the plant-scale tests showed that sodium and chromium together caused bad deposit, and after the tests of Bowden, Draper, and Rowling[3] showed that sodium added to gas oil also caused bad deposit, it was decided to learn how to reduce the sodium content of the oil by a substantial amount at the point of use. With the co-operation of the Central Vermont Public Service Corporation and the De Laval Separator Company this has been done on a plant scale, and a method of removing the salt and reducing both the sodium and the calcium content of the oil has been found.

---

[1] Manager, Advance and Development Engineering, Gas Turbine Department, General Electric Company. Mem. ASME.

[2] Engineer, Gas Turbine Department, General Electric Company. Assoc. Mem. ASME.

Contributed by the Gas Turbine Power Division and presented at the Annual Meeting, New York, N. Y., November 28–December 3, 1954, of The American Society of Mechanical Engineers.

Note: Statements and opinions advanced in papers are to be understood as individual expressions of their authors and not those of the Society. Manuscript received at ASME Headquarters, December 7, 1954. Paper No. 54—A-246.

[3] "The Problem of Fuel-Oil Ash Deposition in Open-Cycle Gas Turbines," by A. T. Bowden, P. Draper, and H. Rowling, Proceedings of The Institution of Mechanical Engineers, London, England, vol. 167, 1953, pp. 291–300.

This paper describes the method now in use at the Rutland plant of the Central Vermont Public Service Corporation for removing most of the sodium and part of the calcium. It gives some of the modifications in the fuel obtained with the washing equipment, as well as the results of operating the turbine on oils washed by several means and having several different ash compositions. A specification is proposed to define a gas-turbine fuel which would have the beneficial features found by the turbine tests. Some pertinent data obtained on a small-burner rig[4] are presented and the proposed specification is discussed in the light of these data.

Desalting System

The scheme used for sodium removal consists of mixing the oil intimately with water or a water solution of a suitable salt and then centrifuging the mixture. The heart of the washing system is a continuously self-cleaning concentrator type of centrifuge which is shown in cross section in Fig. 1. It discharges clean oil at the top of the bowl while a sludge of wash solution, oil, and suspended solids flows out through a number of small nozzles at the periphery of the bowl. Because the solids are carried out through these nozzles by sufficient liquid, the bowl is essentially self-cleaning and can be run for many hours, if not indefinitely, without shutting down.

A diagram of the system in which the centrifuge is used is shown in Fig. 2. Raw oil is heated, mixed with an emulsion breaker to improve separation in the sludge tank and centrifuge, mixed with wash solution, passed through the centrifuges in series, and stored in a clean-oil tank. Sludge from both machines goes to a settling tank from which the upper layer is continuously pumped back to the recycle inlet at the bottom of the first centrifuge. In this way the oil-rich part of the sludge is recirculated until all the oil is finally separated from the water and solids and discharged with the clean oil. The solids collect in the bottom of the settling tank and the water is drained away. In the process the wash solution picks up most of the sodium in the oil, and with a suitable wash solution, such as magnesium sulphate, a substantial fraction of the calcium can be removed also. It is necessary to have a density difference in order of 2 to 6 per cent between the oil and the wash solution at the centrifuging temperature, depending on the viscosity of the oil and the degree of sodium reduction required. Since some bunker C oils are about as dense as water, the requirement in such cases is fulfilled by using a wash solution of some salt to provide the necessary density difference, and magnesium sulphate has been found to be very satisfactory for this purpose.

[4] "Residual Fuel-Oil Ash Corrosion," by B. O. Buckland, C. M. Gardiner, and D. G. Sanders, ASME Paper No. 52—A-161.

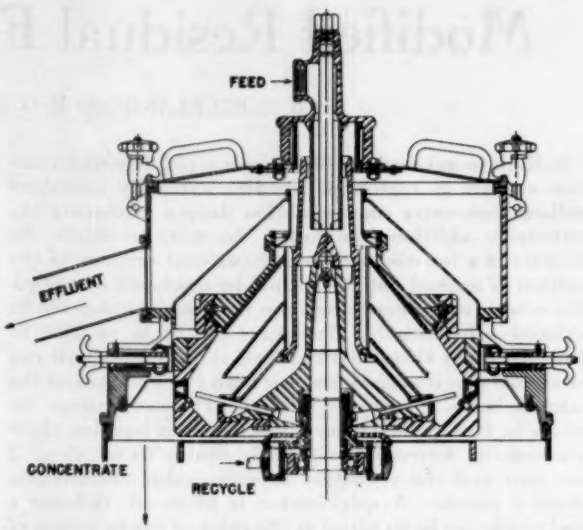

Fig. 1 Cross Section of Continuous, Self-Cleaning Concentrator of the De Laval Type

Results of Washing Tests

Including the oil washed for the turbine tests, some 200 washing tests were made. Table 1 shows a group of tests selected from these in order to show typical results over the range of variables covered. The oil viscosity varied from 12 to 28 centistokes at 210 F and the oil specific gravity varied from 0.973 to 1.018 at 60 F. The flow rates varied from 500 to 2100 gph, and solutions of calcium nitrate, aluminum sulphate, and magnesium sulphate as well as water were used for washing. In general, dur-

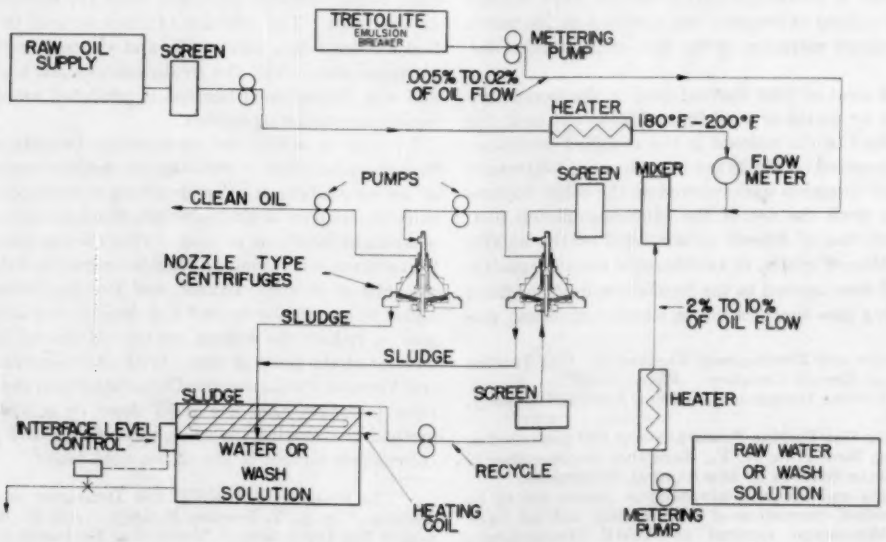

Fig. 2 Schematic Diagram of Oil-Washing System

TABLE 1 TYPICAL REDUCTION IN SODIUM AND CALCIUM OBTAINED BY WASHING SEVERAL RESIDUAL OILS

OIL						WASH SOLUTION			METALS PPM				METALS—% Remaining		
Test No.	Name	Viscosity CS 100 F	Viscosity CS 210 F	Sp. Gr. 60 F	Flow GPH	Type Sol.	% Sol. in Oil	Sp. Gr. 60 F	Before Wash Na	Before Wash Ca	After Wash Na	After Wash Ca	Na	Ca	RV* $\Delta\gamma \times 10^6$
41	O.S.	679	23	0.984	600	H_2O	1 1/4	1.0	86	225	8	139	9.3	62	0.48
41	O.S.	679	23	0.984	600	H_2O	2 1/2	1.0	86	225	7	92	8.1	41	0.48
41	O.S.	679	23	0.984	600	H_2O	5	1.0	86	225	6	83	7.0	37	0.48
41	O.S.	679	23	0.984	750	H_2O	1 1/4	1.0	86	225	10	112	11.6	50	0.61
41	O.S.	679	23	0.984	750	H_2O	2 1/2	1.0	86	225	10	90	11.6	40	0.61
41	O.S.	679	23	0.984	750	H_2O	5	1.0	86	225	7	86	8.1	38	0.61
42	O.S.	679	23	0.984	600	None	0	. . .	86	225	20	110	23.2	49	. . .
42	O.S.	679	23	0.984	750	None	0	. . .	86	225	21	111	24.4	49	. . .
47	N.S.	1170	28	1.001	720	$CaNO_3$	2 1/2	1.155	106	109	13.3	172	13	158	0.12
48	N.S.	1170	28	1.001	720	$CaNO_3$	2 1/2	1.155	102	115	19.2	212	19	184	0.12
50	O.S+10% #2 oil	270	15.7	0.974	600	H_2O	5	1.0	78.4	197	3.2	60.2	4	31	0.26
55	N.S+10% #2 oil	435	20	0.994	780	H_2O	5	1.0	96	192	10.3	81.6	11	42	0.32
58	O.S+10% #2 oil	270	15.7	0.974	780	H_2O	5	1.0	74	206	4	76	5.4	37	0.33
71	N.S+15% #2 oil	279	16	0.990	600	Al_2SO_4	10	1.02	6.2	77	2.2	1.5	35	2	0.23
89	D1	354	17.1	0.973	1080	H_2O	10	1.0	32	3	2.7	2.5	8	85	0.5
118	O.S.	679	23	0.984	1320	$MgSO_4$	6	1.03	68	220	7	41	10	19	0.52
123	O.S.	679	23	0.984	1320	$MgSO_4$	7	1.025	68	183	6.6	37.1	10	20	0.57
130	D1	354	17.1	0.973	1500	H_2O	5	1.0	24.5	5	2.5	3.8	10	76	0.69
165	D2	328	11.5	0.990	1500	H_2O	5	1.0	17	5	<2	2	10	40	0.77
176	N.S.	1170	28	1.001	1320	$MgSO_4$	5	1.05	76	143	7	25	9	17	0.60
225	D3	231	11.5	0.990	1440	$MgSO_4$	5	1.02	25	4	4	3	16	75	0.41
226	D3	231	11.5	0.990	1680	$MgSO_4$	4	1.025	27	5	4	3	15	60	0.42
235	S.C.	680	24	1.018	2100	$MgSO_4$	4	1.035	18	13	4	7	22	50	1.71
235	S.C.	680	24	1.018	2100	$MgSO_4$	2 1/2	1.04	18	12	8	10	44	80	1.71

* R = rate of oil flow, gph.
V = viscosity at 210 F, centistokes.
$\Delta\gamma$ = difference in specific gravity between oil and wash solution at 190 F.

ing both the tests and the periods of oil washing for turbine use, the system was operated so as to produce washed oil having a water content of no more than 0.2 to 0.5 per cent, depending on the sodium reduction required.

The tests have shown that for a fairly representative group of residuals, a reduction in sodium content of 10 to 1 or more can be obtained when the system is operated to give a relatively low water content in the washed oil.

Further, the tests indicate a relationship, expressed in the following formula, which might be used to establish an initial adjustment in the variables in order to start a washing test on a particular oil

$$r = 0.06 + \left(\frac{0.8}{P^{1.3}}\right)\left(\frac{VR}{\Delta\gamma \times 10^6}\right)$$

where

r = fraction of original sodium remaining
P = per cent of wash solution
V = viscosity of oil at 210 F in centistokes
R = rate of oil flow, gph
$\Delta\gamma$ = difference in specific gravity between oil and wash solution at centrifuging temperature

However, the final adjustment will have to be made by the results obtained in the washed oil for the particular case.

Turbine Tests

Procedure. After it was discovered how to reduce the sodium in the oil to 10 ppm or below by the scheme described in the foregoing, a number of turbine tests were run to assess the results of modifying the fuel. An ash was sought which would be noncorrosive and at the same time have a tolerably low rate of deposition and, if possible, be water-soluble also. The tests consisted of operating the turbine on oil washed in a given manner and observing the increase in bowl pressure. At the end of the test the combustion chambers were removed and photographs were taken of the ash deposit on the first-stage nozzle. The nozzle was then cleaned in preparation for the next test by using a jet of hot water and steam from a small portable steam boiler. This, together with some scraping with a set of screw drivers shaped for the purpose, produced a reasonably clean first-stage nozzle. Oil was washed and stored in clean tank cars until an ash analysis was made, after which the test was started.

The turbine units in this plant are two-turbine, two-compressor, intercooled and regenerative, having a 9 to 1 pressure ratio and being fired to 1500 F inlet or bowl temperature. They have been described by Howard and Walker.[5]

At intervals of about 3 hr throughout the test, readings were taken from which a nozzle-area index number was calculated. This is a number which is proportional to the first-stage nozzle effective flow area. The basic observations which determine it are the air flow and the turbine bowl pressure. However, a number of auxiliary readings are required to correct these two to constant conditions. The flow was obtained by observing the low-pressure compressor speed and the ambient conditions, and the inlet guide-vane setting at the compressor inlet. From these, and from a flow-speed curve which had previously been established on factory test by means of a flow nozzle, the flow through the unit was determined. The nozzle-area index number was plotted against time, and in the early tests, after about 60 hr of operation, the test was concluded. This is a rather short time for such a test but was sufficient to establish trends and was used in order to proceed rapidly. As the ash conditions were improved, longer time tests were run, and one test on unit No. 2, still in progress (October, 1954) has been run for a period of about 2500 hr.

Effect of Reduction of Sodium and Calcium in Fuel

Twelve such tests were run, eleven on unit No. 1 and one on unit No. 2. Typical nozzle-area index numbers for the short-time tests are shown in Figs. 3, 4, and 5, and for a longer time test in Fig. 9. The first-stage nozzle appearance at the end of three typical tests is shown in Figs. 6, 7, and 8.

The first three tests were made with an oil relatively high in calcium content, but with a sodium content of approximately 8 ppm. Test 1–2, Fig. 3, is typical of these. No tests com-

[5] "A 5000-Kw Gas Turbine for Power Generation," by Alan Howard and C. J. Walker, ASME Paper No. 48—A-83.

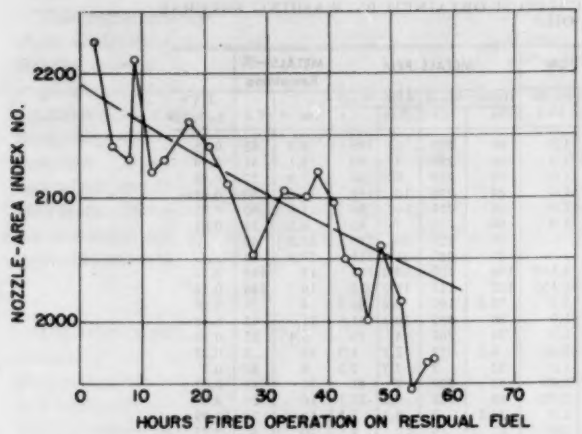

FIG. 3 VARIATION OF NOZZLE-AREA INDEX NUMBER WITH A LOW-SODIUM, HIGH-CALCIUM FUEL. TEST 1–2, CA = 150 PPM, MG = 10 PPM

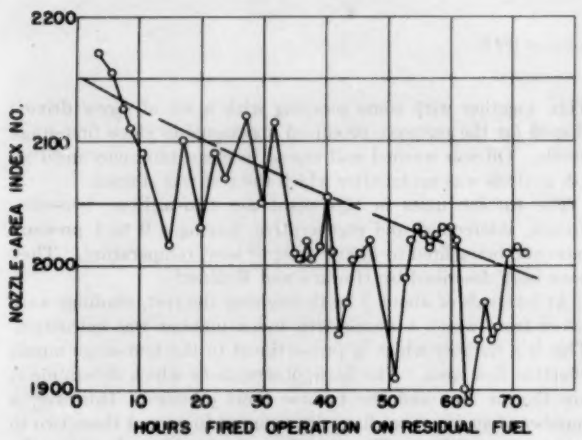

FIG. 4 VARIATION OF NOZZLE-AREA INDEX NUMBER WITH A LOW-SODIUM, MEDIUM-CALCIUM FUEL. TEST 1–5, CA = 80 PPM, MG = 100 PPM

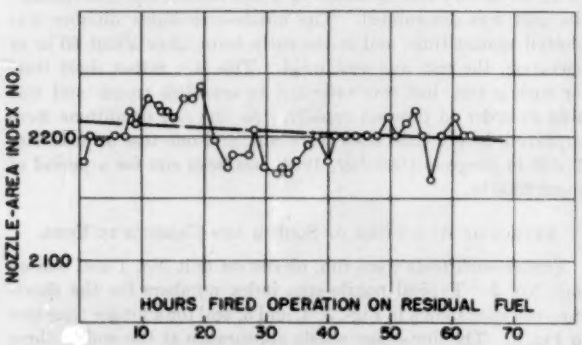

FIG. 5 VARIATION OF NOZZLE-AREA INDEX NUMBER WITH A LOW-SODIUM, LOW-CALCIUM FUEL. TEST 1–8, CA = 10 PPM, MG = 108 PPM

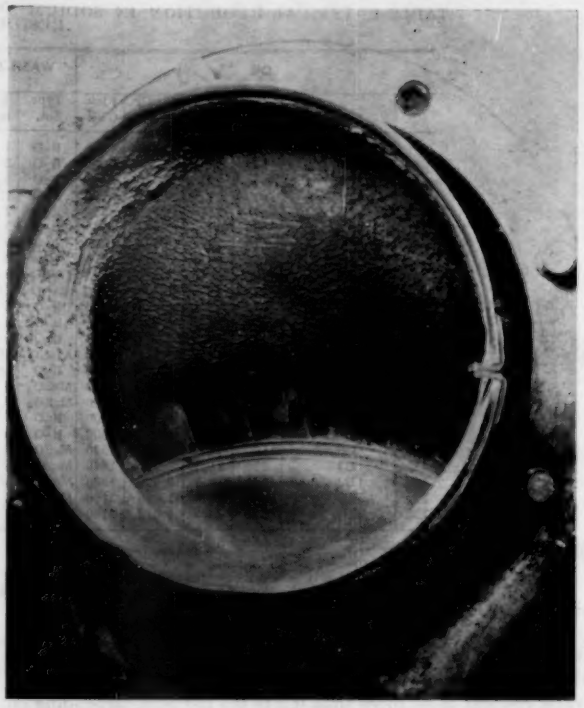

FIG. 6 FIRST-STAGE NOZZLE AFTER 60 HR OPERATION ON LOW-SODIUM, HIGH-CALCIUM FUEL. TEST 1–1, CA = 150 PPM

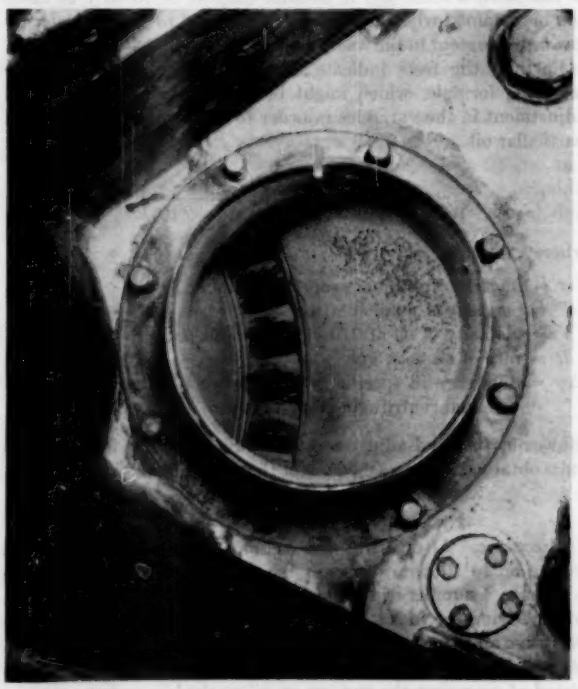

FIG. 7 FIRST-STAGE NOZZLE AFTER 67 HR OPERATION ON LOW-SODIUM, MEDIUM-CALCIUM FUEL. TEST 1–5, CA = 80 PPM

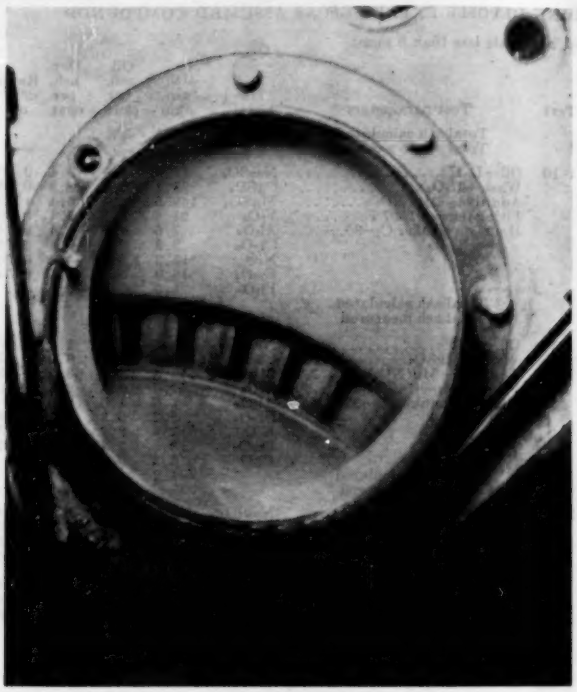

FIG. 8 FIRST-STAGE NOZZLE AFTER 63 HR OPERATION ON LOW-SODIUM, LOW-CALCIUM FUEL. TEST 1–8, Ca = 10 PPM

parable to these were made when the sodium content of the oil was high and before modification of the fuel by washing. However, it is known from operating experience on these units with the same kind of oil, but with sodium in the neighborhood of 100 ppm, that the nozzle-area index fell off 30 per cent or more in 60 hr. Thus the reduction in sodium content of the fuel resulted in a marked reduction in deposition rate.

At the end of each test, samples of the deposit were removed from the first-stage nozzle by means of a vacuum cleaner having hollow, chisel-shaped tools for scraping the deposit from the partitions with a small cotton sample bag in the hose to catch the deposit. These samples were analyzed for metallic constituents, with the results as given in Table 2. In the early tests on high-calcium oil, such as Test 1–2, approximately two thirds of the deposit appeared to be calcium sulphate; the oil ash also appeared to be two thirds calcium sulphate. For this reason, efforts were made to reduce the calcium content of the oil to determine if this would not reduce the rate of deposition. In order to keep the oil inhibited against vanadium corrosion, magnesium was substituted for the calcium removed. This was done, first, by water-washing oil that had previously been washed with calcium nitrate as in Test 1–5, and later by washing with an aluminum-sulphate solution as in Test 1–8. In addition, an entirely different oil, naturally low in calcium, was tried as in Tests 1–10 and 2–1. As already indicated in Figs. 3, 4, 5, and 9, each reduction of the calcium in the fuel resulted in a lower rate of decrease in the nozzle-area index number.

The change in nozzle-area index number due to the deposit on all of the eleven tests on unit No. 1 and the first test on unit No. 2 can be represented by the following formula

$$a = \frac{KCq\beta}{\gamma k_s}(1 - e^{-k_s t})$$

where

a = reduction in effective flow area divided by clean-nozzle area

K = product of two factors: (a) A function of nozzle geometry and (b) a ratio of average thickness of deposit in nozzle throat to average thickness of deposit over entire nozzle surface. K in this case is taken to be 86.0×10^{-4} in.$^{-2}$

C = ratio of ash which deposits on nozzle to ash which flows to nozzle

q = rate of fuel flow

β = ash as a fraction of fuel weight

γ = weight of ash deposit per unit volume (assumed to be one-half specific weight of material deposited to account for porosity)

k_s = ratio of rate at which deposit sheds off nozzle to weight of deposit on nozzle ($k_s = 0.005$ hr^{-1})

t = time from beginning of test

Such an expression for the change in nozzle area results if it is assumed that the deposit is continually laid on at a rate measured by the factor C, which is a function of the stickiness of the ash, and is continually shed at a rate equal to the product of k_s and the weight of ash deposited on the nozzle. Tests 1–2, 1–5, 1–8, and 2–1 (Figs. 3, 4, 5, and 9) are typical of the way the formula

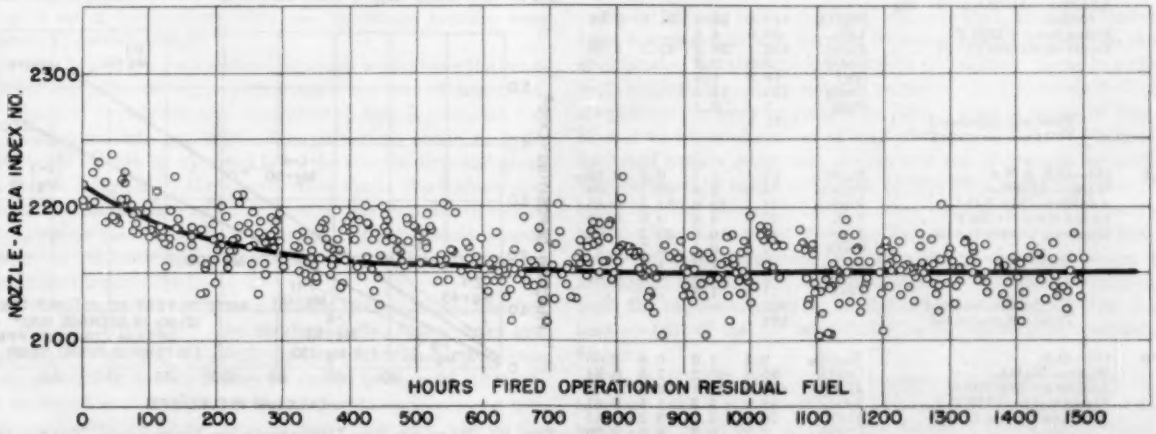

FIG. 9 LONG-TIME VARIATION OF NOZZLE-AREA INDEX NUMBER WITH A LOW-CALCIUM FUEL. TEST 2–1, Ca = 6 PPM, Mg = 45 PPM

TABLE 2 METALS MEASURED IN OIL ASH AND IN TURBINE DEPOSIT EXPRESSED AS ASSUMED COMPOUNDS

(Cu, Zn, Sn, Ti, Ag, also measured, aggregate less than 8 ppm)

Test	Test parameters	Material	Oil ash, ppm	Oil ash, per cent	Dep. ash, per cent	Ratio dep/oil
1-1	Oil—O.S.	Na_2SO_4	24.7	3.9	1.8	0.46
	Wash—$Ca(NO_3)_2$	$CaSO_4$	510.0	80.3	67.6	0.84
	Additive—none	$MgSO_4$	49.5	7.8	..	..
	Firing temp—1400 F	V_2O_5	42.8	6.7	3.6	0.54
	Hours on bunker C—60	Al_2O_3	3.8	0.6	..	..
		Cr_2O_3	2.2	0.3	2.9	9.67
		NiO	20.4	3.2	2.0	0.63
		Fe_2O_3	38.6	6.1	3.3	0.54
		PbO	5.4	0.8	..	..
	Total ash calculated		697.4			
	Total ash measured		635			
1-2	Oil—O.S.	Na_2SO_4	26.0	3.4	1.5	0.44
	Wash—$Ca(NO_3)_2$	$CaSO_4$	490.6	64.3	74.8	1.16
	Additive—none	$MgSO_4$	49.5	6.5	..	..
	Firing temp—1486 F	V_2O_5	55.3	7.2	2.3	0.32
	Hours on bunker C—57	Al_2O_3	9.4	1.2	..	..
		Cr_2O_3	2.2	0.3	0.7	2.33
		NiO	21.6	2.8	1.8	0.64
		Fe_2O_3	38.6	5.1	3.1	0.61
		PbO	5.4	0.7	..	..
	Total ash calculated		698.6			
	Total ash measured		761			
1-3	Oil—O.S.	Na_2SO_4	15.4	2.0	1.2	0.60
	Wash—two washes—$Ca(NO_3)_2$	$CaSO_4$	530.4	68.4	74.1	1.08
	Additive—none	$MgSO_4$	49.5	6.4	..	..
	Firing temp—1507 F	V_2O_5	57.1	7.4	1.8	0.24
	Hours on bunker C—45	Al_2O_3	11.3	1.5	..	..
		Cr_2O_3	2.2	0.3	1.0	3.33
		NiO	21.6	2.8	1.7	0.61
		Fe_2O_3	44.3	5.7	3.7	0.65
		PbO	4.3	0.6	..	..
	Total ash calculated		736.1			
	Total ash measured		775			
1-4	Oil—O.S.—washed with Ca-$(NO_3)_2$	Na_2SO_4	9.3	1.1	0.6	0.54
	Wash—H_2O + 10% No. 2 oil.	$CaSO_4$	326.4	36.9	39.4	1.07
	Additive—$Mg(NO_3)_2$	$MgSO_4$	445.5	50.3	47.0	0.93
	Firing temp—1412 F	V_2O_5	46.4	5.2	2.5	0.48
	Hours on bunker C—23	Al_2O_3	7.6	0.9	..	..
		Cr_2O_3	2.2	0.2	0.1	0.50
		NiO	16.5	1.9	1.3	0.68
		Fe_2O_3	32.9	3.7	2.9	0.78
		PbO	4.3	0.5	..	..
	Total ash calculated		891.1			
	Total ash measured		883			
1-5	Oil—O.S. & O.S. washed with Ca $(NO_3)_2$	Na_2SO_4	12.4	1.3	1.5	1.15
	Wash—H_2O + 10% No. 2 Oil	$CaSO_4$	276.8	28.4	31.0	1.09
	Additive—$Mg(NO_3)_2$	$MgSO_4$	495.0	50.7	55.5	1.09
	Firing temp—1530 F	V_2O_5	48.2	4.9	1.4	0.29
	Hours on bunker C—67	Al_2O_3	7.6	0.8	3.4	4.25
		Cr_2O_3	2.2	0.2	0.6	3.00
		NiO	19.1	2.0	1.5	0.75
		Fe_2O_3	42.9	4.4	3.3	0.75
		PbO	8.6	0.9	..	..
	Total ash calculated		912.8			
	Total ash measured		976			
1-6	Oil—O.S.	Na_2SO_4	6.2	0.5	0.3	0.60
	Wash—H_2O	$CaSO_4$	102.0	8.6	23.1	2.69
	Additive—$Al_2(SO_4)_3$ + Mg-$(NO_3)_2$	$MgSO_4$	410.8	35.4	34.6	0.98
	Firing temp—1524 F	V_2O_5	50.0	4.2	..	..
	Hours on bunker C—27	Al_2O_3	453.1	38.3	42.1	1.10
		Cr_2O_3	2.2	0.2	..	..
		NiO	17.8	1.5	..	..
		Fe_2O_3	134.4	11.4	..	..
		PbO	5.4	0.5	..	..
	Total ash calculated		1181.9			
	Total ash measured		..			
1-8	Oil—O.S. & N.S.	Na_2SO_4	12.4	1.4	0.3	0.21
	Wash—$Al_2(SO_4)_3$	$CaSO_4$	34.0	3.8	5.1	1.34
	Additive—$Mg(NO_3)_2$	$MgSO_4$	544.5	61.6	52.5	0.85
	Firing temp—1505 F	V_2O_5	42.8	4.8	0.9	0.19
	Hours on bunker C—63	Al_2O_3	88.7	10.0	20.2	2.02
		Cr_2O_3	2.2	0.2	0.7	3.5
		NiO	19.1	2.2	1.7	0.77
		Fe_2O_3	47.2	5.3	4.3	0.81
		PbO	11.8	1.3	..	..
	Total ash calculated		802.7			
	Total ash measured		884			
1-9	Oil—O.S.	Na_2SO_4	9.3	1.0	0.6	0.60
	Wash—$MgSO_4$	$CaSO_4$	95.2	10.2	7.5	0.74
	Additive—$Mg(NO_3)_2$	$MgSO_4$	643.5	69.1	72.8	1.05
	Firing temp—1515 F	V_2O_5	48.2	5.2	1.1	0.21
	Hours on bunker C—79	Al_2O_3	20.8	2.2	3.2	1.45
		Cr_2O_3	2.2	0.2	0.6	3.00
		NiO	17.8	1.9	1.3	0.68
		Fe_2O_3	42.9	4.6	3.4	0.74
		PbO	8.6	0.9	..	..
	Total ash calculated		888.5			
	Total ash measured		931			
1-10	Oil—D-1	Na_2SO_4	12.4	4.5	3.4	0.76
	Wash—H_2O	$CaSO_4$	27.2	10.0	8.8	0.88
	Additive—$Mg(NO_3)_2$	$MgSO_4$	148.5	54.4	66.4	1.22
	Firing temp—1507 F	V_2O_5	21.4	7.8	5.4	0.69
	Hours on bunker C—96	Al_2O_3	7.6	2.8	0.4	0.14
		Cr_2O_3	2.2	0.8	0.6	0.75
		NiO	15.3	5.6	4.2	0.75
		Fe_2O_3	16.9	6.2	3.4	0.54
		PbO	1.6	0.6	..	..
	Total ash calculated		253.1			
	Total ash measured		273			
1-11	Oil—O.S.	Na_2SO_4	9.3	1.2	1.5	1.25
	Wash—$MgSO_4$	$CaSO_4$	108.8	13.7	9.2	.67
	Additive—$Mg(NO_3)_2$	$MgSO_4$	544.5	68.5	63.9	0.93
	Firing temp—1495 F	V_2O_5	50.0	6.3	2.5	0.40
	Hours on bunker C—328	Al_2O_3	7.6	1.0	2.0	2.0
		Cr_2O_3	2.2	0.3	0.1	0.33
		NiO	17.8	2.2	1.6	0.73
		Fe_2O_3	18.6	2.3	2.0	0.87
		PbO	5.4	0.7	..	..
	Total ash calculated		764.2			
	Total ash measured		795			
2-1	Oil—D-2 and D-3	Na_2SO_4	10.8	3.4	5.9	1.74
	Wash—H_2O and $MgSO_4$	$CaSO_4$	20.4	6.4	4.8	0.75
	Additive—$MgSO_4$	$MgSO_4$	222.8	70.2	77.2	1.10
	Firing temp—1473 F	V_2O_5	20.5	6.5	3.6	0.55
	Hours on bunker C—1249	Al_2O_3	10.6	3.3	..	..
		Cr_2O_3	2.2	0.7	0.9	1.28
		NiO	12.7	4.0	3.2	0.80
		Fe_2O_3	15.6	4.9	4.1	0.84
		PbO	1.6	0.5	..	..
	Total ash calculated		317.2			
	Total ash measured		..			

fits the observed data. The factor C from this formula is plotted as a function of the calcium content of the fuel in Fig. 10. The rate of ash deposition as represented by the factor C is shown to be a marked function of the calcium content of the oil and relatively independent of the other constituents, particularly magnesium, which ranges from 10 to 130 ppm.

Most of the metallic constituents in the oil and in the nozzle deposit were found by analysis, and from these the sulphates and oxides shown in Table 2 were computed. The results scatter somewhat, but they show that the sodium, calcium, and magnesium metals appear in the deposit on the nozzle in about the same proportion as they are found in the oil ash. The fraction of vanadium pentoxide in the deposit, however, is only about 40 per cent of the fraction found in the oil ash.

Specifications for Gas-Turbine Fuel

As Fig. 10 shows, magnesium did not cause deposit, or at least did so to a lesser degree than calcium. Fortunately, it also hap-

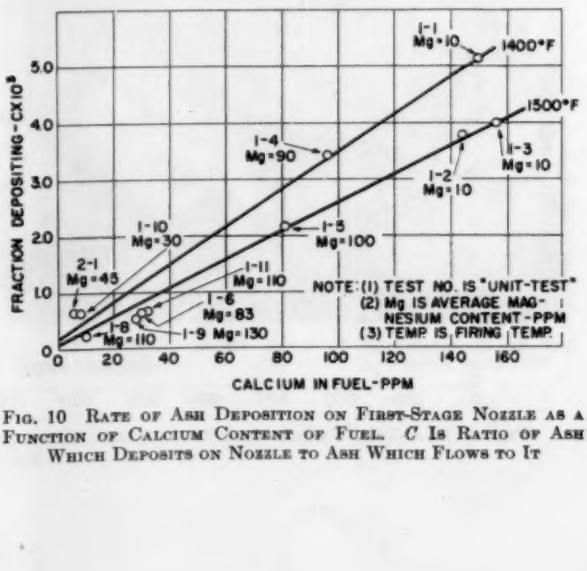

Fig. 10 Rate of Ash Deposition on First-Stage Nozzle as a Function of Calcium Content of Fuel. C Is Ratio of Ash Which Deposits on Nozzle to Ash Which Flows to It

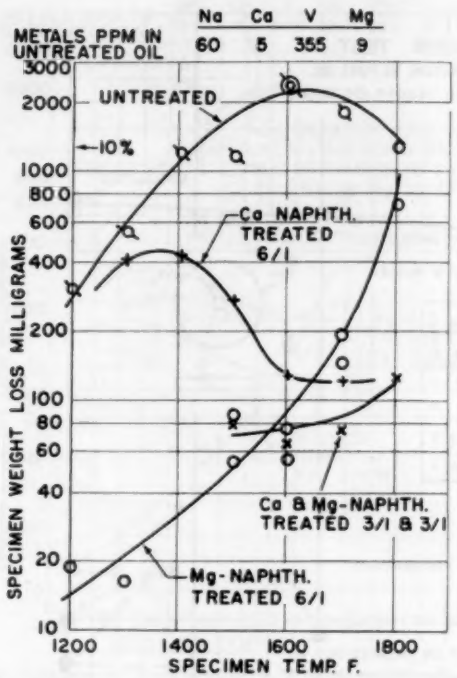

FIG. 11 CORROSION OBTAINED WITH A HIGH-VANADIUM OIL SHOWING EFFECT OF MAGNESIUM AND CALCIUM ADDITIVES. TESTS MADE ON 25 CR, 20 NI SPECIMENS FOR 100 HR IN SMALL-BURNER RIG

pens that, in the temperature range below about 1650 F, magnesium is a better inhibitor for vanadium corrosion than calcium. This is shown in Fig. 11 in which the weight loss of a 25-Cr, 20-Ni specimen tested in a small-burner rig[4] is plotted against temperature with a fuel having approximately 350 ppm of vanadium. The three bottom curves give the results for the same oil with calcium and magnesium additives used separately and in combination. It can be seen that, at approximately 1650 F, the calcium and the magnesium additives are equivalent, but that at 1500 F and below, the magnesium is considerably better.

The lack of protection in the low-temperature region when calcium is used, as shown by the small-burner tests, is borne out also by observation of buckets in service on the locomotives. When the oil was inhibited with calcium, the buckets, which are at a lower temperature than the first-stage nozzles, were observed to corrode faster.

In order to define a gas-turbine fuel which would have the beneficial features of no oil-ash corrosion and a low rate of deposition, the foregoing experience was incorporated into a proposed fuel specification in October, 1953. The paragraph concerning the character of the ash is extracted from the specification and given in Table 3. Basically, the specification limits the sodium and calcium content of the fuel to 10 ppm or less in order to reduce the deposition rate to acceptable values. It substitutes magnesium as an inhibitor against vanadium-pentoxide corrosion for the calcium formerly used.

The specification is written to include both modified residual fuels and distillate fuels. The distillate fuels contemplated are, in general, also low-ash fuels with the ash quantities ranging from values possibly as low as 3 ppm to values as high as 100 ppm. It is expected that the important considerations to prevent corrosion with distillate fuels, as with any other fuel, will be the ratios of the ash constituents as limited in the specification, even when the total quantities of these metallic materials are very low.

TABLE 3 CHARACTER OF ASH[a]

(a) The ratio of the weight of sodium in the ash to the weight of vanadium in the ash should not be greater than 0.3. If this ratio is not satisfied by the original oil, it can be obtained by removing sodium by means of washing, centrifuging, filtering, electrostatic precipitating, or by any other desalting means.

(b) The sodium content of the oil should not exceed 10 ppm, and a value of 5 or less is preferred. When the sodium content is 5 ppm or less, the foregoing weight ratio of sodium to vanadium need not be maintained.

(c) The ratio of the weight of magnesium to the weight of vanadium in the ash should not be less than 3.0. Oil-soluble materials can be added to the fuel to obtain this ratio, in case it does not satisfy the condition naturally. In cases where the oil is modified at the point of use, water solutions of suitable magnesium salts, such as magnesium nitrate or magnesium sulphate, may also be added to obtain the desired ratio, but they must be thoroughly mixed with the fuel to obtain a fine and uniform dispersion, and the oil must be burned sufficiently soon after treatment to avoid partial separation, or settling out, of the water solution.

When the vanadium content is 2 ppm or less, the foregoing weight ratio of magnesium to vanadium need not be maintained.

[a] Copied from fuel specification dated Oct. 21, 1953.

Fig. 12 shows evidence supporting this expectation. It shows the effect of varying vanadium concentration on the corrosion rate as measured by the small-burner tests for four residual oils. A rapid increase in corrosion rate occurs as the vanadium content increases, and any amount of vanadium, uninhibited, will cause a corrosion rate higher than when the vanadium is inhibited in the proper ratio by means of, say, magnesium. Thus it is believed that the best results will be obtained when the ash constituents have the ratios specified for all quantities of total ash, regardless of how small. Many distillate-type fuels will contain 2 ppm of vanadium or less. Since the rate of corrosion at these concentrations, when uninhibited, is low, the requirement of maintaining the proper magnesium-vanadium ratio is removed for this concentration of vanadium and below.

Data showing the way in which the corrosion rates increase with increasing sodium content in low-concentration ranges are being obtained. Also, corrosion by sodium sulphate is influenced strongly by the presence or absence of carbon as well, perhaps, as by the presence of chlorides. Thus there is as yet no very accurate way of specifying a value of sodium below which safety will be assured without the protection afforded by a suitable sodium-vanadium ratio. However, in some cases at least, little or no corrosion has occurred with 5 ppm of sodium when the sodium-to-vanadium ratio was not maintained; consequently, until further evidence is at hand, this concentration is chosen as the value at and below which the sodium-vanadium ratio need not be maintained. In borderline cases, where this discontinuity in the specification would be unreasonably discriminating, it may be possible to rate the oils in question by the small-burner tests.

Since October, 1953, additional evidence from the small-burner tests has shown that it may be desirable to add a clause to the specification limiting the lead content of the fuel. Lead in sufficient quantities appears to spoil, partially, the beneficial effect of magnesium, or even to corrode by itself. This is shown in Figs. 13 and 14 where the effect of lead additions to two magnesium-inhibited fuels is given, one of high and one of low-ash content. The high-ash oil seems to be able to tolerate a larger quantity of lead than the low-ash oil. The effect of lead is not sufficiently well explored to warrant changing the proposed specification now. However, such exploration is in progress and enough evidence is at hand to indicate that some modification may be required and, until the requirement is better defined, it is suggested that the lead content of the gas-turbine fuel be limited to approximately 5 ppm.

The limit of 10 ppm of calcium might also be increased to 20, together with a statement that, although a tolerable rate of deposition will result with 20 ppm, the deposit is about proportional to the calcium content and, therefore, the lower this value the better the fuel.

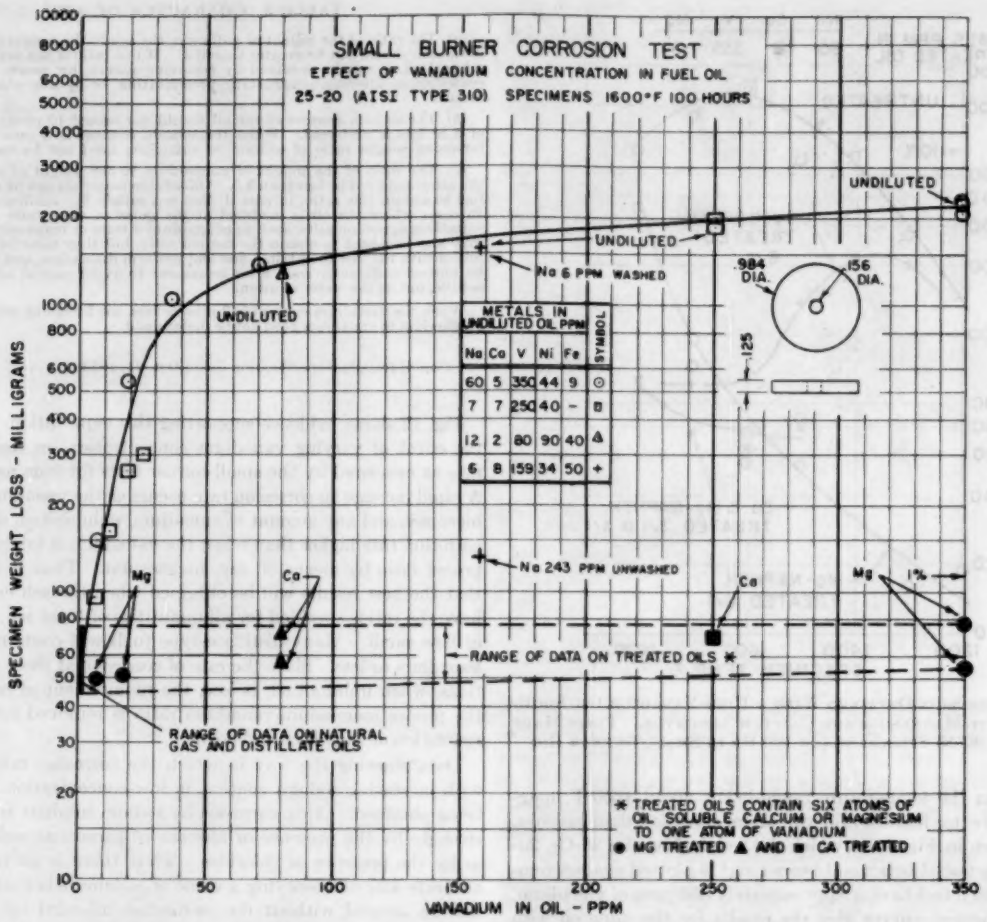

FIG. 12 CORROSION OBTAINED WITH VANADIUM-CONTAINING OILS HAVING RELATIVELY LOW-SODIUM CONTENTS, SHOWING EFFECT OF VANADIUM CONCENTRATION FOR BOTH TREATED AND UNTREATED FUELS. ONE HIGH-SODIUM OIL IS SHOWN TOGETHER WITH SAME OIL AFTER REDUCING SODIUM BY WASHING. TESTS MADE ON 25-CR, 20-NI SPECIMENS FOR 100 HR AT 1600 F IN SMALL BURNER RIG

DROP IN EFFICIENCY BETWEEN CLEANINGS WITH SPECIFICATION FUEL

In the fall of 1953, when unit No. 2 was opened up for a bearing modification, it was put in a substantially new condition. The buckets had no corrosion, and any nozzles, which were not new and uncorroded when cleaned, were replaced. When the unit was again put into service a test (2–1) was started, using oil washed to obtain low sodium and calcium contents and using magnesium-sulphate solution as an inhibitor. The test, which is still in progress, has now (October, 1954) accumulated a total time of 2500 hr. At intervals during the first 475 hr of the run, six heat-rate tests were made in order to establish the change in efficiency which occurred due to the ash deposit. The turbine efficiency, shown in Fig. 15, was found to drop approximately 1.9 per cent during this period, and it is estimated that the steady-state change will be about 2.1 per cent. A drop of 2.1 per cent in turbine efficiency corresponds to 5.7 per cent decrease in thermal efficiency and 7 per cent in output.

In addition to a change in turbine efficiency, it was noted that the regenerator effectiveness decreased approximately 4.4 points in the same period, and it is estimated that the ultimate change will be 5 points. The curve of regenerator effectiveness against time is shown in Fig. 16. A decrease in regenerator effectiveness of 5 points causes 2 per cent decrease in thermal efficiency.

The regenerator on unit No. 2 has never been cleaned or inspected. However, the regenerator on unit No. 1 was cleaned after bunker C operation, at which time the ash deposit in the regenerator was found to be confined to a distance of about 30 in. along the inlet of the tube bundle. This would seem to indicate that the deposit does not adhere at temperatures somewhat under that of the turbine exhaust. The deposit is also relatively easy to clean from this location.

CONCLUSIONS

Efforts by the authors' company to develop a completely successful residual-fuel-burning gas turbine by means of factory tests and experience in the field are continuing. In the early stages of this experience there was doubt in some minds that a cheap and practical scheme to inhibit ash corrosion or deposit, or both, could be found. It seems to the authors, however, that at least one such means is now at hand. Certain of the equipment and techniques described here are in daily use at the Rutland plant, and observations made thus far show the corrosion and deposit conditions to be good. The total cost of the fuel treatment, including the heat, most of which is required in any case, is approximately 14 cents per bbl, and an excellently cleaned oil is obtained

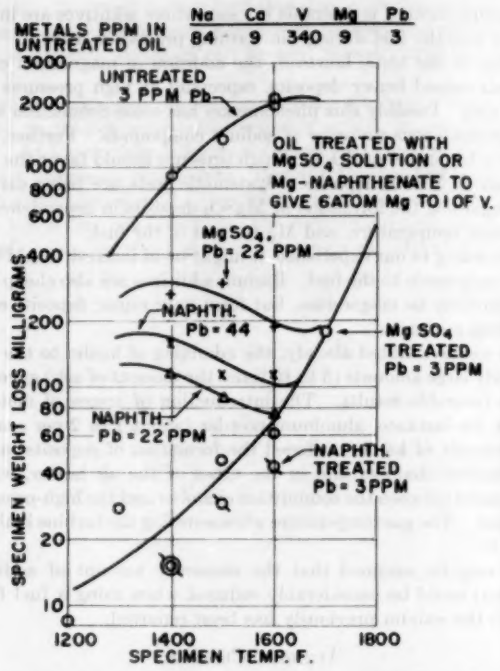

FIG. 13 CORROSION OBTAINED WITH A HIGH-ASH OIL SHOWING DETRIMENTAL EFFECT OF LEAD ADDITIONS TO TREATED FUEL. TESTS MADE ON 25-CR, 20-NI SPECIMENS FOR 100 HR IN SMALL-BURNER RIG

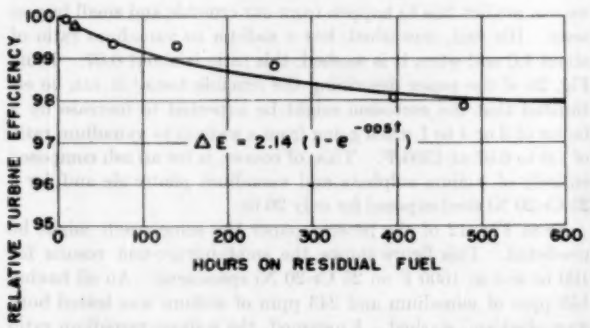

FIG. 15 CHANGE IN TURBINE EFFICIENCY DUE TO DEPOSIT FROM A LOW-SODIUM, LOW-CALCIUM RESIDUAL FUEL—TEST 2-1

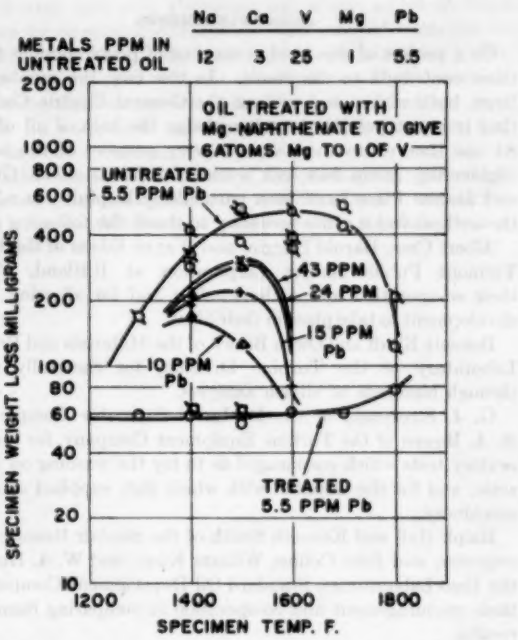

FIG. 14 CORROSION OBTAINED WITH A LOW-ASH OIL SHOWING DETRIMENTAL EFFECT OF LEAD ADDITIONS TO TREATED FUEL. TESTS MADE ON 25-CR, 20-NI SPECIMENS FOR 100 HR IN SMALL-BURNER RIG

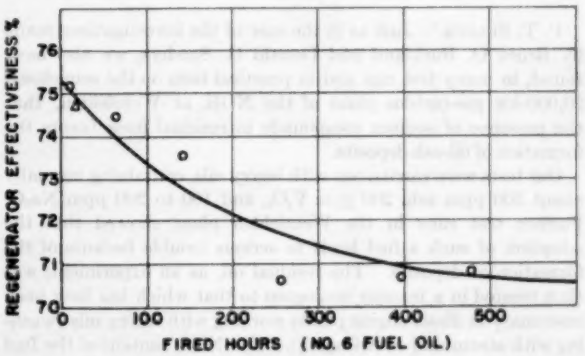

FIG. 16 CHANGE IN REGENERATOR EFFECTIVENESS DUE TO DEPOSIT FROM A LOW-SODIUM, LOW-CALCIUM RESIDUAL FUEL—TEST 2-1

for which no credit has been taken in this treatment cost.

Efforts by others also appear to have produced practical results along somewhat different lines. Dr. Peter T. Sulzer of Sulzer Brothers, Winterthur, Switzerland,[8] reports successful use of residual fuel in their gas turbine installed at Weinfelden where "Kaolin with metallic additives" was used. Details of the dispersion and emulsifying means used and the nature of the metal in the kaolin are not given, so that the method cannot be compared in detail with the scheme reported in this paper. However, costs of treatment of approximately 12 cents per bbl are given, and it is the authors' opinion that this is probably another practical scheme for using residual oil in a gas turbine.

In addition, there is the scheme probably first suggested by Bowden, Draper, and Rowling[9] of controlling deposit by producing a small amount of incomplete combustion. This scheme has been studied by Dr. Sulzer[8] and others, but it has not been used intentionally in a gas-turbine plant. It might, perhaps, be further developed to a point where it would be practical either by itself or as a supplementary measure. It seems to the authors, therefore, that there are now available at least two schemes of burning residual fuel in long-life gas turbines in a commercially acceptable manner and that, as development proceeds, more schemes may be available. It is possible, also, that with further development the cost of treatment might be reduced to 3 to 5 cents per bbl where it would be of interest to large utility users of fuel. Furthermore, when, as, and if residual oil disappears, the lessons learned in burning it can be more or less directly applied to the burning of the coke, pitch, or whatever other petroleum product appears in its place, because the product will contain the same ash constituents.

[8] "The Influence of Control of Combustion on Oil-Ash Deposition Occurring in Industrial Gas Turbines," by P. T. Sulzer, *Schweizer Archiv für angewandte Wissenschaft und Technik*, vol. 20, 1954, pp. 33–41.

Acknowledgments

On a project of this kind, a number of people besides the authors contribute to the result. In this case the number is so large, both within and without the General Electric Company, that it is not possible to acknowledge the help of all of them. At one time or another, almost every member of the authors' engineering group has lent a cheerful hand. Cecil Gardiner and Jeanne Place have been particularly helpful. In addition, the authors feel it quite necessary to thank the following people:

Albert Cree, Harold Durgin, and Wayne Edson of the Central Vermont Public Service Corporation at Rutland, Vt., for their co-operation and understanding and for allowing such a development to take place in their plant.

Bennett Kindt and Owen Brown of the Materials and Processes Laboratory of the Turbine Division, for cheerfully wading through hundreds of oil-ash analyses.

G. J. Strezynski of the De Laval Separator Company and R. A. Bowen of the Turbine Equipment Company, for their laboratory tests which encouraged us to try the washing on a plant scale, and for the dispatch with which they supplied centrifuge machinery.

Ralph Hall and Kenneth Smith of the Sinclair Research Laboratories, and John Collins, William Knox, and W. A. Herbst of the Esso Laboratories, Standard Oil Development Company, for their encouragement and co-operation in comparing burner test results.

A. B. Culbertson and M. E. Spaght of the Shell Oil Company for their interest in supplying a special test fuel.

Discussion

P. T. Sulzer.[7] Just as in the case of the investigations made by Bruce O. Buckland and Donald G. Sanders, we also have found, in many test rigs and in practical tests on the semiclosed 20,000-kw gas-turbine plant of the NOK at Weinfelden, that the presence of sodium compounds in residual fuels favors the formation of oil-ash deposits.

Our tests were carried out with heavy oils, containing normally about 500 ppm ash, 200 ppm V_2O_5, and 100 to 200 ppm Na_2O. Former test runs in the Weinfelden plant showed that the adoption of such a fuel leads to serious trouble because of the formation of deposits. The residual oil, as an experiment, was then treated in a manner analogous to that which has long been customary in diesel-engine plants working with heavy oils (washing with steam and centrifuging). The Na_2O content of the fuel could be reduced to about 10 ppm. A subsequent trial run with the plant for about 100 hr showed a greatly reduced formation of deposits, but considerably more corrosion. The mean temperature at the turbine inlet was 650 C.

A more accurate investigation gave the following results: Because of the deposits formed when burning the nontreated fuel (deposits consisting for the most part of Na_2SO_4, Fe_2O_3, and V_2O_5), the blade material is protected to a certain extent; the diffusion flow of oxygen to the metal is checked by the layers. After the sodium compounds had been washed out, the remaining V_2O_5 together with the remainder of the ash components (mainly iron and traces of calcium and silicon) formed only badly adhering deposits, which continually fell off.[8] This phenomenon appears to us to explain the considerably stronger corrosive properties of a fuel with high vanadium content and few sodium components.

Removal of the sodium components from a fuel with high vanadium content is desirable in cases where additives are introduced into the fuel during the washing process or after it. According to our tests, however, the addition of magnesium compounds caused heavy deposits, especially at high pressures (20 atm abs). Possibly this phenomenon has some connection with the simultaneous presence of sodium compounds. Further, the greater formation of SO_3 at a high pressure should favor the formation of $MgSO_4$ deposits. Systematic tests are being carried out regarding the formation of $MgSO_4$ deposits in dependence on pressure, temperature, and Mg content of the fuel.

According to our experience, it might be of interest to add barium compounds to the fuel. Barium additives are also cheap and act similarly to magnesium, but form only minor deposits even at a high pressure.

As we have stated already, the admixing of kaolin to the fuel in fairly large amounts (5 to 10 times the amount of ash) gave the most favorable results. The introduction of traces of metallic dusts, for instance, aluminum powder (about 1 to 2 per cent of the amount of kaolin) reduced the formation of deposits in the combustion chamber and in the tubes of the air heater, which is situated between the combustion chamber and the high-pressure turbine. The gas temperature when entering the turbine is about 1050 C.

It may be assumed that the necessary amount of additive (kaolin) could be considerably reduced when using a fuel from which the sodium previously has been removed.

Authors' Closure

The authors are pleased to know that Mr. Sulzer, in his plant tests, also finds that washing the sodium out of the fuel reduces the deposit. We are particularly interested to hear that this sodium reduction in his case also increases the corrosion because we can predict this to happen from our crucible and small-burner tests. His fuel, unwashed, has a sodium to vanadium ratio of about 1.0 and when it is washed, this ratio is about 0.07. From Fig. 25 of the paper describing the crucible tests,[4] it can be estimated that the corrosion might be expected to increase by a factor of 3 or 4 to 1 when going from a sodium to vanadium ratio of 1.0 to 0.07 at 1300 F. This, of course, is for an ash composed entirely of sodium sulphate and vanadium pentoxide and for a 25 Cr-20 Ni steel exposed for only 20 hr.

From Fig. 12 of the present paper the same result might be predicted. This figure shows the small-burner-test results for 100 hr and at 1600 F on 25 Cr-20 Ni specimens. An oil having 159 ppm of vanadium and 243 ppm of sodium was tested both unwashed and washed. Unwashed, the sodium-vanadium ratio was 1.63 and, washed, it was 0.04. This change produced a twelvefold increase in corrosion.

Mr. Sulzer's explanation that the layers of sodium sulphate reduce the corrosion by preventing the diffusion of oxygen to the steel seems to us not to be borne out by our tests. In the crucible the specimen is entirely surrounded by the synthetic ash and the portion thus surrounded corrodes. Furthermore, even when the oxygen is thus excluded, a substantial increase in corrosion occurs on reducing the sodium as described. In any case, the reduction in corrosion due to the vanadium pentoxide produced by having a high ratio of sodium to vanadium is not sufficient to be useful for gas turbines, especially when the metal temperatures are 1300 F or more. Additives to prevent the vanadium type of corrosion are sufficient, however, as shown by both Mr. Sulzer and ourselves.

In this case, though, it is desirable even from a corrosion standpoint alone, and if the deposit features are ignored, to have a low ratio of sodium to vanadium. It is not given in the paper, but evidence is at hand which shows that, when the vanadium is inhibited by additives such as, say, magnesium, a sodium-sulphate type of attack can occur if the sodium to vanadium ratio is

---

[7] Sulzer Brothers, Ltd., Winterthur, Switzerland.

[8] These tests are fully described in a paper by J. G. Bowen, London, England, and P. T. Sulzer, Winterthur, Switzerland, read in 1955 at a Gas-Turbine Meeting of the ASME.

too high. Our small-burner tests show that with ratios of sodium to vanadium of 1/3 or more, a 25 Cr-20 Ni specimen shows substantial sulphide attack in 600 hr with temperatures as low as 1400 F.

Barium compounds, as Mr. Sulzer suggests, have shown good ability to inhibit vanadium-pentoxide attack in our crucible tests. In the single small-burner test we ran they did not show as much promise as magnesium. Perhaps, this one test is not too conclusive and we should do further work with this additive.

As Mr. Sulzer has found, we, too, have found that aluminum and silicon are excellent in preventing deposit. In addition, in a small burner test with aluminum and silicon added in large quantities as oil-soluble compounds, a substantial reduction in corrosion of a relatively high vanadium oil was observed. We have not yet developed a means of introducing these materials in their solid and inexpensive form, however, in a manner that results in an acceptable maintenance of the fuel pumps, fuel nozzles, and other fuel-handling equipment.

This failure caused us to abandon the plant-scale tests which were started using an aluminum-oxide additive and to turn to the use of a water-soluble material which could be emulsified easily with the fuel.

Experimental Determination of the Thermal-Entrance Length for the Flow of Water and of Oil in Circular Pipes

By J. P. HARTNETT,[1] MINNEAPOLIS, MINN.

Thermal entrance-length results are presented for the flow of two different fluids, water and oil, in a ¾-in. 4-ft-long tube with a constant heat input per unit length. A hydrodynamic calming section of 97 tube diameters preceded the test section. Pressure-drop measurements in the water tests indicate that the condition of fully established flow at the test-section entrance was closely approximated, if not actually attained. Confidence in the entry-length heat-transfer results is indicated by the agreement of the asymptotic heat-transfer performance of both test fluids with the generally accepted correlation equations. The resulting thermal-entrance lengths were from 10 to 15 tube diameters over the Reynolds modulus range of 10^4 to 10^5 and agreed favorably with the analytical results of Deissler and Latzko. When compared at the same Reynolds modulus, the water and oil-entrance lengths were in excellent agreement over the range of Reynolds number common to both fluids (17,000 to 48,000), thereby indicating a negligible influence of the Prandtl modulus on the thermal-entrance length for Prandtl numbers above unity. In the transition region, experimental entry-length values are reported for the flow of oil. As the Reynolds number was increased from 2000 to 10,000, the thermal-entrance length steadily decreased from a large value representative of laminar flow down to a value of approximately 10 diameters.

Nomenclature

The following nomenclature is used in the paper:

A = heat-transfer area, sq ft
a = thermal diffusivity of fluid at t_f, ft²/sec
c_f = Fanning friction factor
c_p = specific heat of fluid evaluated at t_f, Btu/lb-deg F
D = inside diameter of test section, ft
h_x = local heat-transfer coefficient, Btu/hr-sq ft-deg F
h_a = asymptotic heat-transfer coefficient, Btu/hr-sq ft-deg F
k = thermal conductivity of fluid at t_f, Btu/hr-sq ft-deg F/ft
k_s = thermal conductivity of stainless-steel tubing at t_{ix}, Btu/hr-sq ft-deg F/ft
L = heat-transfer length of test section, ft
L_e = thermal-entry length, ft
L_e/D = dimensionless thermal-entry length, tube diameters
$(L_e/D)_{5\%}$ = dimensionless 5 per cent entry length, tube diameters
q_e = net electrical input, Btu/hr
q_f = heat gain indicated by flow rate and temperature rise of fluid, Btu/hr
Q = heat generated per unit volume of tube, Btu/hr-cu ft
r_o = radius to outer surface of heat-transfer tube, ft
r_i = radius to inner surface of heat-transfer tube, ft
t_I = temperature at entrance to calming section, deg F
t_{II} = temperature at exit of test section, deg F
t_{ix} = outside tube temperature at longitudinal position x, deg F
t_f = mean fluid temperature, arithmetic mean of inlet and exit temperatures, deg F
t_{fx} = local mean fluid temperature at longitudinal position x, deg F
t_w = test section inner wall temperature, deg F
t_{wx} = test section inner wall temperature at longitudinal position x, deg F
u = mean bulk velocity, fps
W = weight rate of flow, lb/hr
x = distance along test section, ft
μ = fluid viscosity evaluated at t_f, lb/hr-ft
ν = fluid kinematic viscosity evaluated at t_f, ft²/hr
ρ = fluid weight density evaluated at t_f, lb/ft³

Dimensionless Ratios

Nu = Nusselt number hD/k
Re = Reynolds number uD/ν
Pr = Prandtl number $c_p\mu/k$

Introduction

A thermal-entry length is present whenever a fluid is heated or cooled as it flows through a conduit. At the position where heating (or cooling) starts, the heat-transfer coefficient begins at a very high initial value and decreases in the direction of flow until, for the case of constant fluid properties, a constant value is reached. For the cases considered in this paper, the thermal-entrance length is that distance, from the start of heating, necessary to attain the constant heat-transfer coefficient and is dependent on the character of the flow and the nature of the wall-temperature variation.

The two hydrodynamic conditions of major analytical interest in the study of thermal-entry length are (*a*) when the velocity distribution is fully established at the entrance of the heated section, and (*b*) when the velocity distribution is uniform at the heated entrance, that is, a simultaneous initiation of the thermal and hydrodynamic boundary layers. The cases of constant heat rate and constant wall temperature are the most frequently imposed boundary conditions in the theoretical considerations. A specification of the thermal-entrance length for these hydrodynamic and wall-temperature conditions could be used as a guide for other conditions encountered in actual practice.

For flow in circular ducts the constant wall-temperature case has received the major consideration with theoretical analysis

[1] Assistant Professor, Department of Mechanical Engineering, University of Minnesota. Assoc. Mem. ASME.

Contributed by the Heat Transfer Division and presented at the Annual Meeting, New York, N. Y., November 28–December 3, 1954, of The American Society of Mechanical Engineers.

Note: Statements and opinions advanced in papers are to be understood as individual expressions of their authors and not those of the Society. Manuscript received at ASME Headquarters, August 26, 1954. Paper No. 54—A-184.

presented by references (1, 6, 8, 21, 28, 31, 35)[1] and experimental data reported by references (3, 14, 15, 23, 29, 37). The most extensive investigation in the case of turbulent pipe flow is that of Boelter, Young, and Iversen (3) who report results for the flow of air with many different hydrodynamic entrance conditions.

For the constant-heat-rate boundary condition few investigations are reported. Theoretical consideration of this boundary condition is available in references (5, 19, 36), while an experimental indication is obtainable from the results of (9, 12, 17, 18).

Although the foregoing experimental and analytical investigations are available, there exists no experimental study of the case of established turbulent flow at the entrance. The effect of Prandtl modulus, although indicated by theoretical considerations, has not been demonstrated experimentally. Consequently, this investigation was undertaken with the object of experimentally determining the thermal entrance for established turbulent flow in a circular pipe over a range of Reynolds and Prandtl numbers. Since it is more readily obtained experimentally, the constant-heat-rate boundary condition was imposed.

Apparatus

Separate flow systems were used for the water and oil heat-transfer tests with only the test heat exchanger and hydrodynamic entrance section being common to both systems.

The flow circuit for the oil heat-transfer tests is shown in Fig. 1. The medium-heavy crystal oil (Freezene oil) flowed by gravity from a baffled head tank to the suction side of a gear pump which pumped the oil through the calming section and into the test section. From the test section the oil flowed through a cooler and finally into a weigh tank, which normally drained into the head tank. A gate valve on the weigh tank was closed whenever a flow-rate measurement was obtained. The flow rate was controlled by adjusting a valve on a by-pass line from the discharge of the pump to the head tank.

Tap water was used for the water heat-transfer tests and was supplied directly from the city water lines. The water flowed through the calming and test sections and then into a weigh tank, which discharged into the city drain line.

[1] Numbers in parentheses refer to the Bibliography at the end of the paper.

The test section, shown in Fig. 2, was a 47½-in. length of type-304 stainless-steel tubing with 0.652-in. ID, 0.750-in. OD. The position of the test section was vertical with the fluid entrance at the bottom. At 20 positions along the tube, iron-constantan

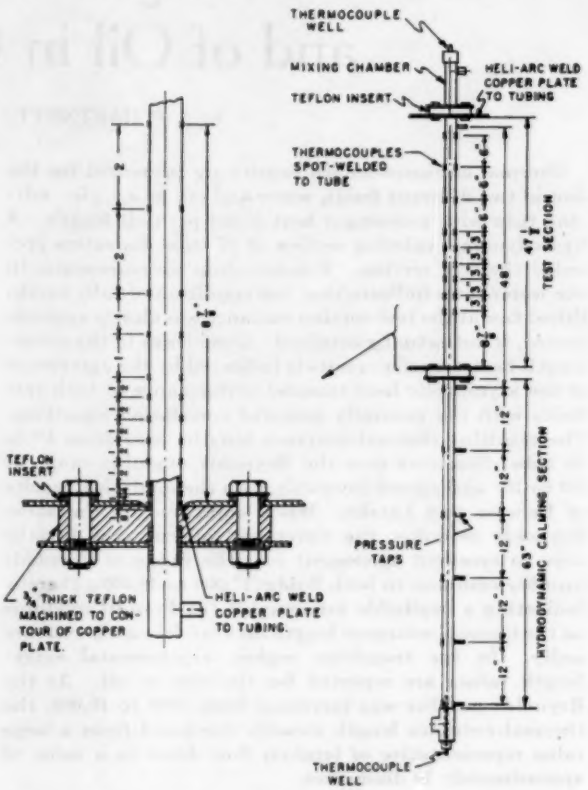

Fig. 2 Detail of Test Section and Hydrodynamic Calming Section

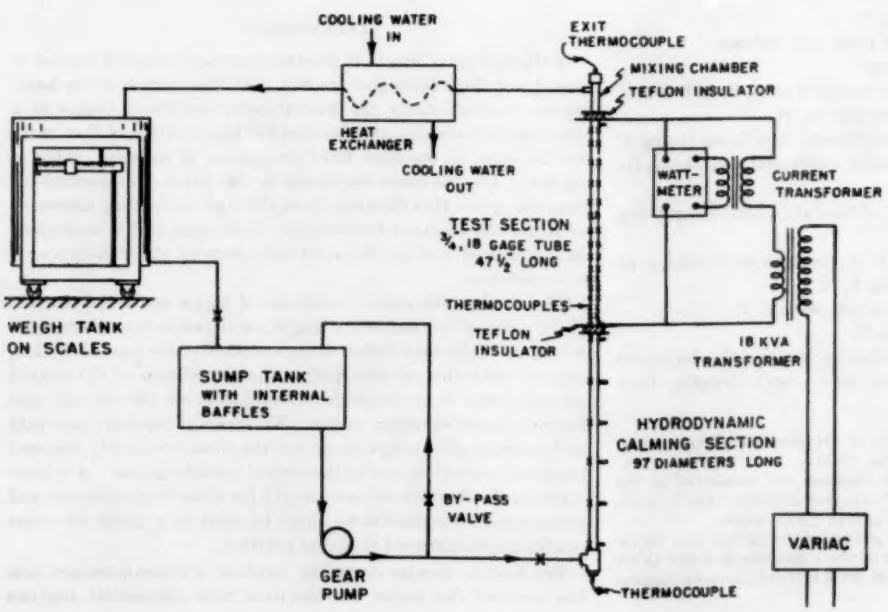

Fig. 1 Schematic Diagram of Oil Heat-Transfer System

thermocouples (No. 24 gage) were spot-welded on opposite sides of the tube, thereby allowing 40 determinations of the tube-wall external temperature. A $^1/_4$-in. pressure tap was drilled at the top of the test section, and a $^1/_4$-in. pipe stub was silver-soldered in position over the hole. Heating was accomplished by passing low-voltage high-amperage alternating current through the test section.

The two electrical terminal connections at the extremes of the test section were 10-in-square $^1/_8$-in-thick copper plates. In the center of each plate a $^3/_4$-in. hole was drilled, and the plate was placed in a press which produced a sharp edge around the periphery of the hole. As shown in Fig. 2, the sharp edge was heliarc-welded to the test section using a small welding bead, thereby yielding a well-defined entrance and exit for the current flow. Thermocouples were peened into small holes drilled in the tops of the terminal plates, with six thermocouples in the bottom plate and three in the top.

The hydrodynamic calming section which preceded the test section was 63 in. in length and was constructed of the same-size tubing as was used in the test section. An intervening Teflon insert, carefully machined to insure continuity of the flow surface, electrically and thermally isolated the entrance and test sections.

Pressure taps of $^1/_4$-in. diam were drilled at 12-in. intervals in this entrance section. The pressure drop from the last tap in the entrance section to the tap at the exit of the heat exchanger also was measured.

The temperature at the inlet to the calming section was measured in a thermocouple well positioned immediately after the 90-deg bend. Temperatures along the calming section were measured by six thermocouples spot-welded at 12-in. intervals along the length. The exit temperature was determined in a thermocouple well which was preceded by a mixing chamber.

The test-section power as supplied by an 18-kva transformer was measured on a calibrated wattmeter used in conjunction with a current transformer. As shown in Fig. 1, the input power could be controlled by a variac located on the primary side of the transformer.

Test Procedure

The thermal-entry-length experimental program consisted of 22 water runs in which both heat-transfer and pressure-drop data were obtained, followed by 21 heat-transfer tests with oil. Check runs with water were then obtained to investigate the reproducibility of test results.

A measure of the heat losses through the test-section insulation was obtained by passing current through the empty test section, the ends of which were plugged with rubber stoppers. The power input and test-section tube-wall temperatures were recorded. In this manner the losses were determined as a function of the wall-to-surroundings temperature difference.

The operational procedure for the water tests involved the initiation of circulation followed by a check of all fluid and wall temperatures, which always agreed to $^1/_2$ deg F. The test section was then energized, and the flow rate adjusted to the desired amount which could be quickly checked by weighing the discharge for a 1-min period. Approximately 2 hr were then allowed for the attainment of steady state, which was confirmed by the constancy of observed temperature readings. Several sets of temperatures, flow rate, power, and pressure-drop readings were then recorded over a 1-hr period.

The range of variables covered in the test program is given in Table 1.

TABLE 1 RANGE OF VARIABLES COVERED IN TESTS

Water Heat-Transfer Tests	
Flow rate, lb/hr	1700–9800
Asymptotic heat-transfer coefficient, Btu/hr-sq ft-deg F	700–3000
Mean fluid temperature, deg F	60–74
Fluid temperature rise, deg F	2–23
Wall-to-fluid temperature difference, deg F	8–72
Net electrical heat flux, Btu/hr-sq ft	27000–56000
Reynolds modulus	16000–89000
Prandtl modulus	6.5–8.0
Asymptotic Nusselt modulus	120–500
Oil Heat-Transfer Tests	
Flow rate, lb/hr	4800–14000
Asymptotic heat-transfer coefficient, Btu/hr-sq ft-deg F	70–870
Mean fluid temperatures, deg F	108–260
Fluid temperature rise, deg F	2–7
Wall-to-fluid temperature difference, deg F	48–390
New electrical heat flux, Btu/hr-sq ft	20000–48000
Reynolds modulus	1600–47000
Prandtl modulus	60–480
Asymptotic Nusselt modulus	50–726

Analysis of Data

The specification of the thermal-entrance length requires the knowledge of the local heat-transfer coefficients along the length of the test section. The local heat-transfer coefficient h_x is defined as

$$h_x = \frac{q_o/A}{t_{wx} - t_{fx}} \qquad [1]$$

The expression q_o/A represents the local heat input per unit area. If this quantity were constant along the length, the resulting voltage distribution would be linear. Reference to Fig. 3 reveals the linearity of the measured voltage except in the immediate vicinity of the entrance, thereby justifying the assumption that the local heat input per unit area is equal to the ratio of the total heat input to the total tube inside-surface area. Heat losses to the surroundings were measured and found to be approximately 50 watts, which is less than $^1/_3$ per cent and therefore, negligible.

The local inner-wall temperature t_{wx} is obtained from the measured outer-wall temperatures. The governing differential equation for a cylindrical tube being heated by passing current through it may be stated

$$\frac{1}{r}\frac{d}{dr}\left(kr\frac{dt}{dr}\right) + Q = 0$$

Boundary conditions $dt/dr = 0$ at $r = r_s$

$$t = t_{ix} \text{ at } r = r_o \qquad [2]$$

Since small increments of the tube are considered, the temperatures are assumed independent of the axial position, x. Test measurements indicate a circumferential temperature variation of approximately 1 to 2 deg F in the turbulent region, but this variation is neglected in the differential equation, and the outer wall temperature is assumed to be constant at the average value. Since the temperature drop through the tube wall is small, the thermal conductivity k_s is assumed independent of r and is evaluated at the local measured wall temperature.

If it is assumed that the heat generated per unit volume is independent of the radius, and further, that the mean fluid temperature increases linearly along the tube a specification of the local heat-transfer coefficient is obtainable from the solution of Equation [2] in conjunction with Equation [1]

$$h_x = \frac{q_o/A}{t_{ix} - [t_1 + x/L(t_{11} - t_1)] - \dfrac{q_o\left(r_o^2 \ln \dfrac{r_o}{r_i} - \dfrac{r_o^2 - r_i^2}{2}\right)}{2\pi(r_o^2 - r_i^2)k_s L}} \qquad [3]$$

It is essential to demonstrate that the steep temperature curve at the inlet as shown in Fig. 3 is due primarily to a thermal-entry effect and not to conduction losses. The copper terminal plate at the entrance was, therefore, instrumented to function as an

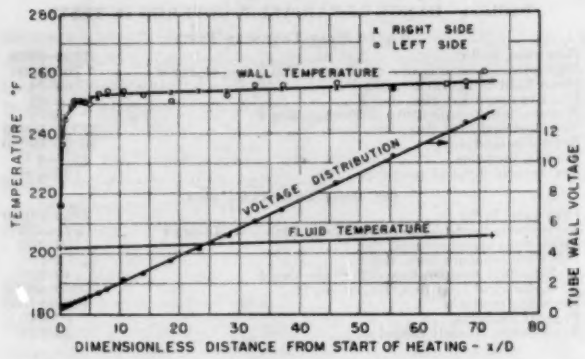

FIG. 3 TYPICAL TEMPERATURE AND VOLTAGE DISTRIBUTION

effective heat meter. These heat-flow measurements showed a loss through the terminal plate of approximately 100 Btu/hr for the oil runs and a heat gain of 30 Btu/hr for the water runs. Since the heat generated within the tube was 850 Btu/hr per inch of the tube, this heat leak influenced at most only those measurements taken over the first tube diameter. Thus the only wall temperatures which possibly include an axial conduction effect are those at x/D values of 0.19 and 0.58. These conclusions also are substantiated by reference to the simple infinite rod solution (5).

For each run the twenty local values of the heat-transfer coefficient are plotted versus the dimensionless tube length x/D and a smooth curve is drawn through the results, as shown in Figs. 8 to 12. The thermal-entrance length L_t/D is defined as the position along the tube where this curve becomes parallel to the abscissa. The asymptotic heat-transfer coefficient h_t is also selected from this curve as the value of the coefficient where the curve becomes parallel to the abscissa. The calculated coefficients are divided by this value and yield the dimensionless coefficient h_x/h_t, which is estimated to be accurate to ±5 per cent.

The specification of the thermal-entry length, as obtained in the manner indicated, is admittedly somewhat arbitrary since the position at which the heat-transfer coefficient levels off is not well defined. The values so obtained, however, are certainly indicative of the order of magnitude. A more well-defined intercept of the heat-transfer coefficient versus length curve is the position at which the local coefficient deviates 5 per cent from the ultimate value. This is designated as the 5 per cent entry length, $(L_t/D)_{5\%}$.

An increase of the local heat-transfer coefficient in the vicinity of 60 diameters from the entrance may be noted, Figs. 9 and 12. In this vicinity the tube-wall temperature deviated slightly from a linear increase with length. Since the deviation was greatest at 60 diameters and decreased at 70 diameters this is not attributed to end conduction. A local variation in tube-wall thickness appears to be the most probable explanation, and this was reflected in a slight departure from linearity of the measured local voltage in this vicinity. The results as shown are still within the probable error of 5 per cent and the influence of this local effect on the thermal-entry-length specification is considered to be negligible.

The correlating parameters, including Nusselt, Reynolds, and Prandtl numbers, are obtained in the usual manner, and all properties are evaluated at the average of the mixed mean terminal fluid temperature unless otherwise noted.

The heat-balance ratios of 1.00 ± 0.03 found for the water tests compare favorably with the computed probable error of 2 to 7 per cent at the maximum and minimum flows, respectively. The heat-balance ratios for the oil tests, except for three values, lie in the range from 0.90 to 1.02, while all values cover the range from 0.84 to 1.06.

RESULTS

The magnitude of the thermal-entrance length is dependent on the hydrodynamic condition at the entrance of the heat exchanger. A measure of the relative development of the flow in this region is indicated by the pressure-drop measurements obtained in the water test program. These results, reported as Fanning friction factors, are in Fig. 4 where separate representation is given to the three friction factors based on the individual pressure-drop measurements over the last 3 ft of the calming

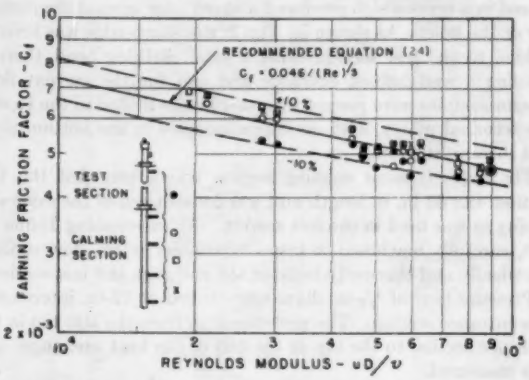

FIG. 4 FRICTION FACTORS FOR CALMING SECTION AND TEST SECTION

section. The values based on the test-section pressure-drop measurements also are presented. The three friction factors in the calming section are in agreement within ±5 per cent, with few exceptions, for any individual run; however, the values for the test-section friction factors are 10 per cent lower. Although the results are somewhat ambiguous they do indicate that the condition of a fully developed flow at the test-section entrance was closely approached.

The asymptotic water heat-transfer results are presented in Figs. 5 and 6. In Fig. 6 these experimental asymptotic coefficients are compared on a dimensionless basis with McAdams' equation (24), and, with the exception of two runs, the experimental values agree with the predicted performance within ±10 per cent. In Fig. 7 the asymptotic heat-transfer coefficients for the oil tests are compared to the prediction of Sieder and Tate (24) on a dimensionless basis. The experimental values are approximately 10 per cent higher than the prediction. In the transition region the anticipated deviation from the turbulent-flow prediction is apparent in the experimental results. This general agreement of the experimental oil results for established thermal conditions with the predicted performance, which also was found for the water heat-transfer results, lends confidence to the entry-length values reported in this investigation.

The thermal-entrance-length values, as obtained in the manner indicated in the Analysis of Data, are tabulated in Tables 2 and 3. The thermal-entrance length for water over the Reynolds-number range of 17,000 to 90,000 is approximately 10 tube diameters; the length necessary to attain a heat-transfer coefficient deviating 5 per cent from the ultimate value is approximately 2 to 3 diameters. The entry-length values for oil are longer than the tube (72 tube diameters) in the laminar range and decrease uniformly to a value of approximately 10 tube diameters for Reynolds numbers from 10,000 to 48,000; the 5 per cent entry length, $(L_t/D)_{5\%}$, decreases from 70 tube diameters down to approximately 2 to 3 tube diameters over the same range. There is no discernible effect of Prandtl number over the range of Reynolds numbers 17,000 to 48,000, which region is common to both oil and water.

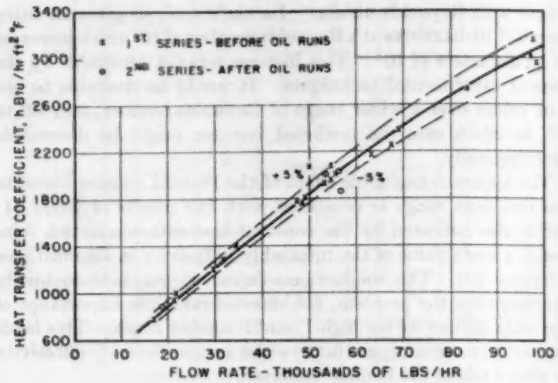

FIG. 5 WATER HEAT-TRANSFER COEFFICIENTS

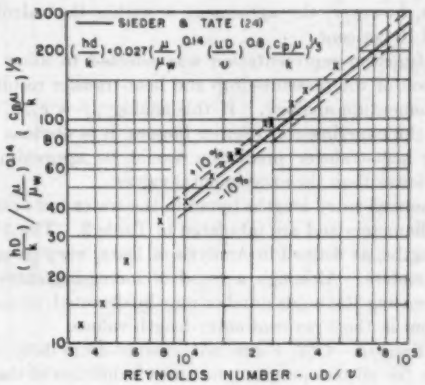

FIG. 7 DIMENSIONLESS OIL HEAT-TRANSFER RESULTS

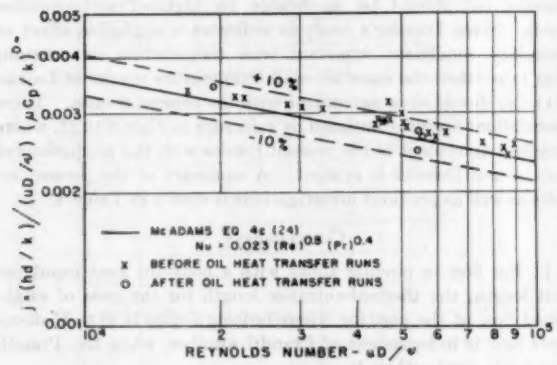

FIG. 6 DIMENSIONLESS WATER HEAT-TRANSFER RESULTS

DISCUSSION OF RESULTS

Pressure-Drop—Water. The pressure-drop measurements for the water tests are shown as friction factors in Fig. 4. The agreement of the three friction-factor values over the last 3-ft intervals of the calming section suggests that established flow conditions prevailed in this region. However, these friction-factor values in the entrance region are 10 per cent higher than the values for the test section, thereby casting some doubt on the condition of established flow. These ambiguous results may be due to the 1/4-in. pressure taps drilled in the 3/4-in. tube which are larger than good practice dictates. These large openings conceivably could have caused local disturbances which are reflected in higher friction-factor values over the 1-ft intervals of the calming section than for the 4-ft length of the test section. This interpretation of the results is complicated, however, by the agreement of the inlet-section friction factors with the predicted values. It is possible that the predicted values are not truly representative for the present tube, as there appears no other feasible explanation for the low values across the test section.

The greater deviation in the friction factors noted at the lower Reynolds-number range, Fig. 4, may be attributed to inaccuracies in the pressure measurements, since in this range the deflections on the mercury-water manometer were less than 3/4 in.

Previous investigations, both experimental and analytical, indicate that the flow should become fully established in the calming section. Experimental measurements of the velocity distribution reported by Schiller and Kirsten (33) and Folsom and Iversen (10) indicate that established conditions prevail at approximately 55 tube diameters. Analytical studies of Elser (7) and Pascucci (26) indicate a very short hydrodynamic-entrance length, approximately 10 pipe diameters.

On the basis of the present results and those reported in the foregoing, it appears reasonable to conclude that fully established flow conditions were at least closely approached.

Heat Transfer—Water. The experimental asymptotic heat-transfer coefficients for water, Fig. 6, are somewhat higher than predicted by McAdams' equation (24). With the exception of

TABLE 2 THERMAL-ENTRY-LENGTH RESULTS—WATER

uD/ν 10^3	$c_p\mu/k$	L_e/D	$(L_e/D)_{5\%}$
	Before oil tests		
16.9	6.8	10.7	5.2
21.3	6.7	7.7	3.7
22.7	6.5	7.7	3.2
28.1	7.2	7.7	3.2
30.3	7.0	7.7	2.6
33.6	7.0	7.7	2.9
44.0	7.5	9.2	2.6
44.3	7.3	9.2	2.6
45.3	7.4	9.2	2.8
45.8	8.0	9.2	2.5
46.8	7.3	6.1	1.5
46.8	8.0	10.7	2.3
50.3	7.4	13.8	3.5
50.3	7.4	9.2	2.6
51.2	7.4	10.7	2.2
57.4	7.5	10.7	2.8
59.6	7.8	12.3	3.4
62.7	7.5	10.7	2.4
75.9	7.5	11.7	2.0
84.9	7.9	13.8	2.4
86.2	7.9	13.8	3.4
89.2	7.5	15.0	3.1
	After oil tests		
19.3	6.5	10.7	3.1
54.7	6.6	9.2	1.7
55.2	6.9	10.7	2.5
54.6	7.0	14.0	3.1

TABLE 3 THERMAL-ENTRY-LENGTH RESULTS—OIL

uD/ν 10^3	$c_p\mu/k$	L_e/D	$(L_e/D)_{5\%}$
1.58	459	74*	58
1.94	480	74*	58
2.57	379	74*	69
3.44	350	41	31
4.29	336	41	28
5.50	223	29	14
7.83	260	15.3	7.2
10.1	206	13.8	5.7
13.3	170	16.9	4.6
14.8	157	13.8	4.4
16.2	90	10.7	3.7
16.3	135	7.4	4.1
17.2	138	13.8	3.7
17.3	87	13.8	3.7
22.9	98	7.7	2.2
24.6	107	10.7	2.8
24.6	107	15.3	2.6
29.8	88	7.8	2.0
34.6	63	13.8	2.8
46.4	63	6.9	1.5
46.6	61	8.4	1.7

* Thermal-entry length actually greater than tube length.

two runs, however, the agreement is within the calculated accuracy of 10 per cent.

The j-function representation was selected to allow a direct comparison of the pressure-drop and heat-transfer results by use of the momentum analogy. If this analogy, $j = c_f/2$, were applied to the experimental friction factors, it is obvious that the resulting heat-transfer prediction would be approximately 15 per cent lower than the experimental values.

The thermal-entry lengths found in the water tests range from 6 to 15 diameters and are tabulated in Table 2. The 5 per cent entry lengths, as defined in Analysis of Data, vary from 1.5 to 5 tube diameters. Although a trend of increasing entry lengths with increasing Reynolds number may be detected, no such trend is apparent in the 5 per cent entry-length values.

Heat Transfer—Oil. Since no pressure-drop data were obtained in the oil-test program, no direct indication of the relative development of the flow is available. However, it may be inferred from the water-test results that the condition of fully developed flow at the test-section entrance was closely approximated in the oil runs in the turbulent range. In the laminar range the results of analysis (32) indicate that the 63-in. (97 tube diameters) calming section is sufficient for the attainment of established flow. Even if a spinning flow is considered at the calming-section entrance, a recent analysis (38) indicates that the flow conditions at 97 diameters downstream closely approach established laminar flow. It appears reasonable to assume, therefore, that for all test runs the ideal of fully established flow at the test-section entrance was approximated.

The thermal-entry length for the oil tests, as presented in Table 3, demonstrate a marked decrease in the entry length with increasing Reynolds number in the transition region. In the laminar-flow range, the thermal-entrance length is longer than the test section (73 tube diameters), which value decreases to approximately 10 diameters at a Reynolds number of 10,000. In the Reynolds-number range from 10,000 to 40,000 the thermal-entrance length scatters from 7 to 16 diameters with no trend indicated. The 5 per cent entry length varies from 1.5 to 6 diameters over this same range—Reynolds number of 10,000 to 40,000—and a trend of decreasing length with increasing Reynolds number is detectable.

The low entry-length values found in the fully turbulent region suggest that any analysis in this range which accounts for the thermal capacity of a sublayer in which only molecular condition prevails, will yield an incorrect excessively long entrance length.

Comparison—Water and Oil-Entry Lengths. There is no discernible effect of the Prandtl modulus on the thermal-entrance length over the Reynolds-number range, 17,000 to 48,000, common to the water and oil tests. This is demonstrated in Figs. 8 to 11 where the local dimensionless heat-transfer coefficient, h_x/h_a, is shown for water and oil as a function of the position along the tube, x/D, at a constant Reynolds number.

Comparison—Present Results With Other Investigations. A comparison of the results of the present investigation with those of Boelter, Young, and Iversen (3) for air is shown in Figs. 9 to 11. Boelter and his co-workers studied the constant-wall-temperature case with a hydrodynamic calming section of 11.2 diameters in length. The present entry-length results are somewhat shorter than the values reported by Boelter, which may be due to the longer calming section of the present investigation rather than to the difference in boundary conditions. It is even more important to note that the discrepancy is small—Boelter shows entry lengths of 15 diameters—notwithstanding the difference in fluids, boundary conditions, and hydrodynamic calming length.

Theoretical considerations of Latzko (21), Berry (1), and Deissler (6) indicate a slight increase of the thermal-entrance length with Reynolds number—Latzko's analysis gives an entry length of 10 diameters at a Reynolds number of 10^4 which increases to 15 diameters at 10^5. This increase was not detectable by the present experimental techniques. It would be desirable to obtain values over a wider range of Reynolds number, say, 10^4 to 10^6, in which case the predicted increase might be discernible experimentally.

The apparent negligible effect of the Prandtl number found in the turbulent range is consistent with the results of Berry (1) and is also indicated by the constant-heat-rate conduction solution if a mean value of the total eddy diffusivity is assumed (see reference 39). The conduction-solution approach undoubtedly oversimplifies the problem, but demonstrates the importance of the eddy diffusivity for high-Prandtl-number fluids. This lends support to those analyses (6, 22) which assume the eddy diffusivity to play a role in the laminar sublayer.

If this hypothesis of the independency of the thermal-entrance length with Prandtl number is valid, then the boundary layer of Deissler (6) should be applicable to higher-Prandtl-number fluids. Since Diessler's analysis indicates a negligible effect of boundary conditions—constant wall temperature or constant heat rate—then the constant-wall-temperature results of Latzko (21) also should show agreement with the present results. These speculations are substantiated by reference to Figs. 8 to 11, where excellent agreement of the present results with the predictions of Latzko and Deissler is evident. A summary of the present results as well as previous investigations is shown in Table 4.

Conclusions

1 For flow in circular tubes with a constant heat input per unit length, the thermal-entrance length for the case of established flow at the position where heating begins is 10 to 15 diameters and is independent of Prandtl number, when the Prandtl number is greater than 1.

2 The constant wall-temperature analysis of Latzko (21) and the boundary-layer analysis of Deissler (6) yield satisfactory entry-length values for the constant-heat-rate case. Since no Prandtl effect is apparent in the Reynolds range of 10^4 to 10^5, these predictions also are valid for Prandtl numbers in excess of unity.

3 In the transition region, as the Reynolds number is increased from 2000 to 10,000 the thermal-entrance length steadily decreases from a large value representative of laminar flow down to a value of approximately 10 diameters.

Acknowledgments

The author wishes to express his appreciation to Prof. R. A. Seban, H. A. Johnson, and C. R. Wilke of the University of California, Berkeley, for their comments and criticisms during the course of this investigation; to Messrs. W. J. Clabaugh, E. D. Martin, J. Ingamells, and H. Chan for their assistance in equipment operation and data reduction, and to the Mechanical Engineering Laboratory and Shops for their aid in equipment construction.

BIBLIOGRAPHY

1 "Non-Uniform Heat Transfer to Fluids Flowing in Conduits," by V. J. Berry, Jr., *Applied Scientific Research*, section A, vol. 4, no. 1, 1953.

2 "An Investigation of Aircraft Heaters—X, Measured and Predicted Performance of a Fluted-Type Exhaust Gas and Air Heat Exchanger," by L. M. K. Boelter, H. G. Dennison, A. G. Guibert, and E. H. Morrin, NACA Wartime Report, Advanced Restricted Report, March, 1953.

3 "An Investigation of Aircraft Heaters—XXVII. Distribution of Heat Transfer Rate in the Entrance Section of a Circular Tube," by L. M. K. Boelter, D. Young, and H. W. Iversen, NACA TN 1451, July, 1948.

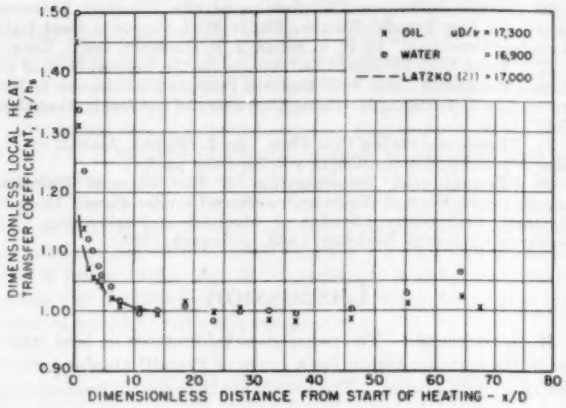

Fig. 8

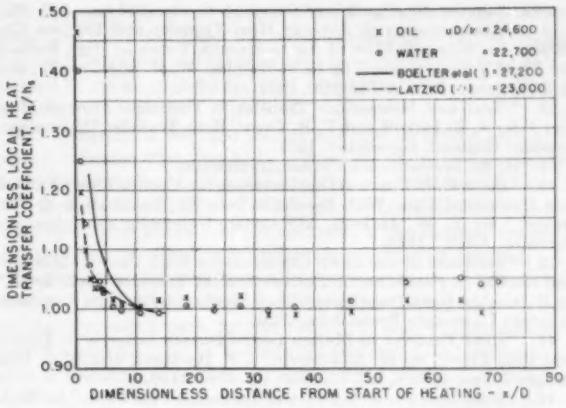

Fig. 9

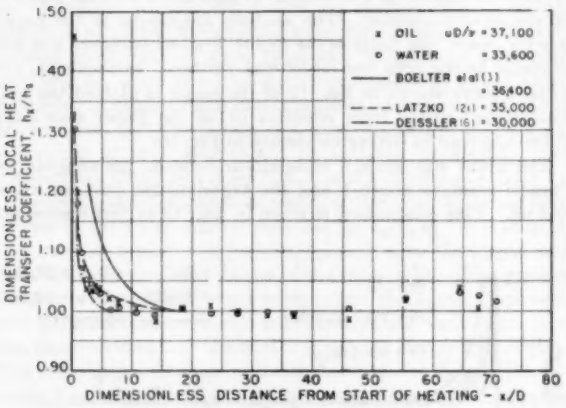

Fig. 10

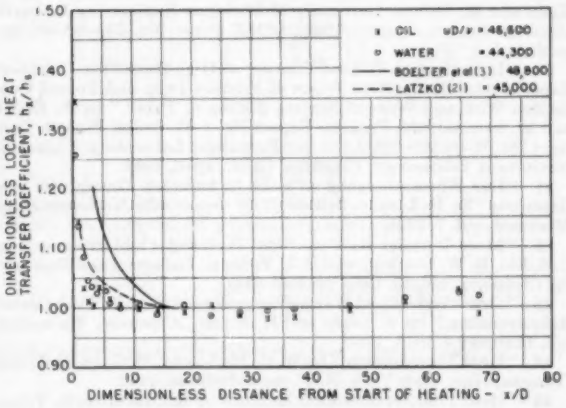

Fig. 11

FIGS. 8 to 11 COMPARISON OF PRESENT RESULTS WITH PREVIOUS INVESTIGATIONS

TABLE 4 SUMMARY OF RESULTS OF PRESENT TESTS COMPARED WITH PREVIOUS INVESTIGATIONS

Investigator	Type of investigation	Boundary condition	Prandtl number	Thermal-entrance length $Re = 10^4$	Thermal-entrance length $Re = 10^5$
Present results	Experimental	Constant heat rate	7–200	10	15
Boelter, Young, Iversen	Experimental	Constant wall temp	0.7	12[a]	
Latzko	Analytical	Constant wall temp	1.0	10	15
Deissler	Analytical	Constant heat rate	0.73	10	15
Deissler	Analytical	Constant wall temp	0.73	10	15
Berry	Analytical	Constant wall temp	1.0–100	13	17

[a] For Reynolds number of 27,200—no results available for 10^4.

4 "The Correlation of Heat and Matter Transfer With Pressure Drop," by C. H. Bosanquet, General Discussion on Heat Transfer, London, England, September, 1951.

5 "Conduction of Heat in Solids," by H. S. Carslaw and J. C. Jaeger, Oxford University Press, Oxford, England, 1948.

6 "Analysis of Turbulent Heat Transfer and Flow in the Entrance Regions of Smooth Passages," by R. G. Deissler, NACA TN 3016, October, 1953.

7 "Der Warmeübergang im Rohreinlauf," by K. Elser, *Allgemeine Warmetechnik*, Jahrgang 3, no. 2, 1952.

8 "Der Warmeübergang im der thermischen Anlaufstreck bei hydrodynamisch asgebildeter turbulenter Zustromung im Rohr," by K. Elser, *Schweizer Archiv für Angewandte Wissenschaft und Technik*, Jahrgang 15, no. 12, 1949.

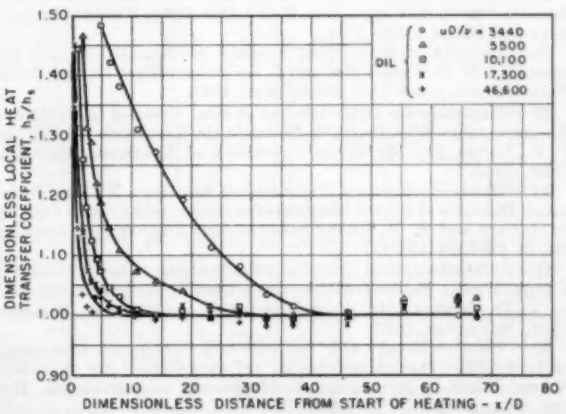

FIG. 12 THERMAL-ENTRY-LENGTH RESULTS FOR OIL FLOW IN THE TRANSITION REGION

9 "Heat Transfer Properties of Mercury," by D. English and T. Barrett, Report of Atomic Energy Research Establishment, ER 547, Harwell, Berks., England, June, 1950.

10 "Pipe Factors for Quantity Rate Flow Measurements With Pitot Tubes," by R. G. Folsom and H. W. Iversen, ASME Paper No. 48—A-35, unpublished.

11 "Über die Warmeleitungsfahigkeit von Flussigkeit," by L.

Graetz, *Annalen der Physik und Chemie*, vol. 25, 1885, pp. 337–357.

12 "Measurements of Average Heat-Transfer and Friction Coefficient for Subsonic Flow of Air in Smooth Tubes at High Surface and Fluid Temperatures," by L. V. Humble, W. H. Lowdermilk, and G. D. Desmon, NACA TR 1020, 1951.

13 "Heat and Momentum Transfer in Turbulent Flow of Mercury," by S. E. Isakoff and T. B. Drew, Heat Transfer Discussions, London, England, September, 1951.

14 H. W. Iversen, personal communication.

15 "Point Unit Thermal Conductances for Viscous Flow of an Oil in a Horizontal Tube With Parabolic Velocity Distribution at Entrance," by T. W. Jackson, MS thesis, University of California, Berkeley, Calif., 1946.

16 "Variation of the Eddy Conductivity With Prandtl Modulus and Its Use in Prediction of Turbulent Heat Transfer Coefficients," by R. Jenkins, Heat Transfer and Fluid Mechanics Institute Preprints, Stanford University Press, June, 1951.

17 "Heat Transfer to Molten Lead-Bismuth Eutectic in Turbulent Pipe Flow," by H. A. Johnson, J. P. Hartnett, and W. J. Clabaugh, Trans. ASME, vol. 75, 1953, pp. 1191–1198.

18 "Heat Transfer to Mercury in Turbulent Pipe Flow," by H. A. Johnson, W. J. Clabaugh, and J. P. Hartnett, Trans. ASME, vol. 76, 1954, pp. 505–511.

19 "Forced Convection From Nonisothermal Surfaces," by J. Klein and M. Tribus, University of Michigan Engineering Research Institute Report, August, 1952, ASME Paper No. 53—SA-45, unpublished.

20 "Investigation of Heat Transfer at High Heat Flux Densities: Experimental Study With Water of Friction Drop and Forced Convection With and Without Surface Boiling in Tubes," by F. Kreith and M. Summerfield, Progress Report No. 4-68, Ordcit Project, Contract No. W-04-200-ORD-455, Jet Propulsion Laboratory, California Institute of Technology, Pasadena, Calif., April, 1948.

21 "Der Warmeübergang an einen turbulenten Flussigkeits oder Gasstrom," by H. Latzko, *Zeitschrift für angewandte Mathematik und Mechanik*, vol. 1, 1921.

22 "Mass Transfer Between Solid Wall and Fluid Streams," by C. S. Lin, R. W. Moulton, and G. L. Putnam, *Industrial and Engineering Chemistry*, vol. 45, 1953, pp. 636–646.

23 "Druckverlust und Warmeübergang im Anlauf de Turbulenten Rohrstromung," by W. Linke and H. Kunze, *Allgemeine Warmetechnik*, Jahrgang 4, no. 4, 1953.

24 "Heat Transmission," by W. H. McAdams, McGraw-Hill Book Company, Inc., New York, N. Y., second edition, 1942.

25 "Heat Transfer to Molten Metals," by R. C. Martinelli, Trans. ASME, vol. 69, 1947, pp. 947–959.

26 "Sul Moto Di Fluidi In Regime Turbolento Nel Tratto Inisiale Dei Tubi Con Distribuzione Logaritmica Di Velocita," by L. Pascucci, *Atti di Guidonia*, vol. 4, 1953.

27 "Forced Convection Heat Transfer in Thermal Entrance Regions," by H. F. Poppendiek, Part I, Oak Ridge National Laboratory, Oak Ridge, Tenn., 1951.

28 "Forced Convection Heat Transfer in Thermal Entrance Regions," by H. F. Poppendiek and L. D. Palmer, Part II, Oak Ridge National Laboratory, Oak Ridge, Tenn., 1952.

29 "Experimental Determination of Heat Transfer to an Oil in a Horizontal Pipe With Reynolds Noduli in the Transition Region," by F. E. Romie, Jr., MS thesis, University of California, Berkeley, Calif., 1947.

30 "Phase Equilibria in Hydrocarbon Systems—X. Thermodynamic Behavior of Liquid Mixtures of n-Butane and Crystal Oil," by B. H. Sage and W. N. Lacey, *Industrial and Engineering Chemistry*, vol. 28, 1936, pp. 106–111.

31 "A Mathematical Analysis of the Turbulent Heat Transfer in a Pipe With a Surface Temperature Discontinuity at Entrance," by V. D. Sanders, MS thesis, University of California, Berkeley, Calif., November, 1946.

32 "Untersuchungen über laminare und turbulenten Strömung," by L. Schiller, Forschungsarbeiten auf dem Gebiet der Ingenieur-Wesen, *Zeitschrift für angewandte Mathematik und Mechanik*, Heft 248, 1922, p. 96.

33 "Die Entwicklung der Geschwindigkeitsverteilung bei der turbulenten Rohrstromung," by V. L. Schiller and H. Kirsten, *Zeitschrift für Technische Physik*, vol. 10, 1929, pp. 268–274.

34 "Temperature Gradients in Turbulent Gas Streams," by W. G. Schlinger, V. J. Berry, J. L. Mason, and B. H. Sage, *Industrial and Engineering Chemistry*, vol. 45, 1953, pp. 662–666.

35 "Calculations Relative to the Thermal Entry Length for Fluids of Low Prandtl Number," by R. A. Seban and T. Shimazaki, University of California, Division of Engineering Research Report, series no. 16, issue no. 4, Berkeley, Calif., January, 1950.

36 "Finite Difference Calculations of the Thermal Entrance Length for Low-Prandtl-Number Fluids With Constant Heat Rate Boundary Condition," by R. A. Seban, J. P. Hartnett, and S. Levy.

37 "Point Unit Thermal Conductance for the Viscous Flow of an Oil in a Horizontal Tube With Uniform Velocity Distribution at Entrance," by J. A. Stahn, MS thesis, University of California, Berkeley, Calif., 1946.

38 "Laminar Swirling Pipe Flow," by L. Talbot, *Journal of Applied Mechanics*, Trans. ASME, vol. 76, 1954, pp. 1–7.

39 "Experimental Determination of the Thermal Entrance Length for the Flow of Water and of Oil in Circular Pipes," by J. P. Hartnett, PhD thesis, Division of Mechanical Engineering, University of California, Berkeley, Calif., February, 1954.

Discussion

R. G. Deissler.[3] The paper gives information on heat transfer in the entrance region for a range of Prandtl numbers where few or no data existed. The results are therefore of fundamental interest.

The author's conclusion that the entrance length is unaffected by Prandtl number is not entirely in agreement with the analytical results of the writer. The analysis mentioned in the paper was for gases; the analysis for higher Prandtl numbers was not available at the time the paper was written. Incidentally, the writer's curve shown in Fig. 10 of the paper is plotted too low. The original curves from reference (6) of the paper were quite difficult to read in the region plotted in Fig. 10.

The writer has made a comparison between his analysis for Prandtl numbers above 1 and the experimental data for water and oil. This comparison is given in Fig. 13 of this discussion.

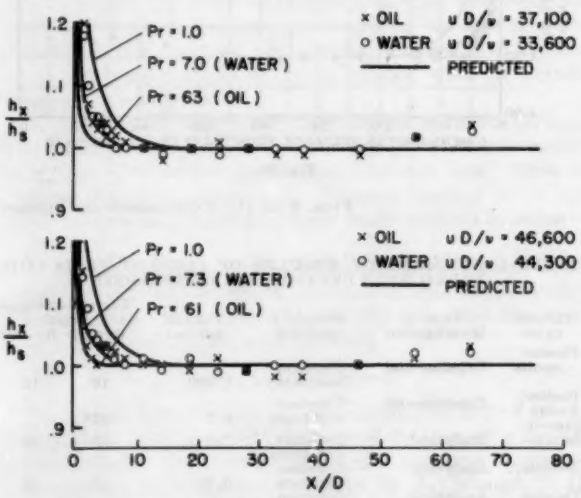

Fig. 13 Comparison of Writer's Analysis With Experimental Data for Water and Oil

Data from Figs. 10 and 11 of the paper are compared with the predicted curves for corresponding Reynolds and Prandtl numbers. The curves for a Prandtl number of 1 and a Reynolds number of 30,000 are shown for comparison. The data for water are in very good agreement with the predicted curves for water in both figures. The circles represent the water data. The data for oil in the upper figure lie above the predicted curve for oil. In the lower curve, some of the points for oil are in agreement with the predicted curve, but some lie above it. It appears that no definite conclusion can be drawn in the case of oil. In general,

[3] Research Engineer, National Advisory Committee for Aeronautics, Cleveland, Ohio. Assoc. Mem. ASME.

it would seem that the agreement between the analysis and experiment for oil is probably within the accuracy of the data. The experimental trends with Reynolds number are in agreement with those predicted; that is, the values of h_x/h_s at a given X/D decrease as Reynolds number increases, Fig. 12 of the paper.

The region very close to the entrance, that is, for X/D between 0 and 1 or 2, could be seen better by using an expanded scale on the abscissa. However, as indicated by the author, the heat losses to the electrical terminal at the entrance might be important in that region. Somewhat more accurate results very near the entrance might be obtained by using a wound wire or ribbon type of heater rather than direct resistance heating of the tube. In this way the heat loss through the electrical connection at the entrance would be reduced considerably.

S. Levy.[4] The author has made a valuable contribution in a field where experimental data are practically nonexistent. The values of thermal-entrance lengths he has presented will find major application in the design of heat-transfer equipment and in the evaluation of available theoretical studies. To obtain his experimental results the author had to distinguish between heat-transfer coefficients different from each other by 5 and 1 per cent, and his effort is all the more appreciated in a field where the spread of experimental data always exceeds 5 per cent. It is felt, however, that a more complete understanding of the contents and results of this paper would be achieved by including the original data shown in Tables 2, 3, 4, and 5 of reference (39).[5]

Tables 3 and 5 give the local values of the ratio[6] h_x/h_s and may be used to derive an explicit function for h_x/h_s in terms of x/D, with more and more weight being placed upon the larger, and therefore more accurate, values of the ratio h_x/h_s. The explicit function in turn can be used to calculate the 5 and 1 per cent entry lengths, and probably will yield values more consistent than those obtained by the author by means of a graphical plot. With more emphasis given to the higher ratios of h_x to h_s, it is expected that whenever the 5 per cent entry length will decrease from run to run the corresponding 1 per cent entry-length value will exhibit the same trend, thus eliminating some inconsistencies noted in Tables 2 and 3 of the paper.

Tables 2 and 4 of reference (39) serve to demonstrate the extent of property variation in the present study. The property variation, though major in several instances, has not been mentioned by the author. Its existence is apparent in Fig. 4 of the paper where the test-section friction factor is seen to fall consistently below the friction factor in the calming section. If the test-section values are corrected by the factor $(\mu/\mu_w)^{0.14}$ as recommended in reference (24), good correspondence is obtained between the friction factor in the test section and the corresponding value in the last section previous to start of heating. The corrections ranging from 2 to 8 per cent also lead to satisfactory agreement with the recommended equation. Because of the greater dependency of oil viscosity upon temperature the role of property variation is larger for this fluid, and the friction coefficient or wall shear stress in the test section is expected to fall from 7 to 25 per cent below the calming-section values.

In comparing the experimental data with theory it is necessary, therefore, to realize that the velocity profile though fully developed in the calming region, undergoes slight changes in the test section because of system heating. Also, examination of Tables 2 and 3 of the paper may give the reader the erroneous idea that the author was not always able to repeat his result at the same Reynolds number. In most cases where the Reynolds number was unchanged the difference in entry lengths may be explained in terms of different heat input, i.e., different property variation.

The comparison between theory and test as presented by the author indicates that the eddy diffusivity plays a major role in the laminar sublayer. Agreement with the analyses of Latzko (21), Deissler (6), and Berry (1) support this conclusion since the three theoretical studies do not account for the thermal capacity of a sublayer in which only molecular conduction prevails. In order to confirm the possible need for a re-evaluation of the existence or extent of the thermal sublayer, the writer derived the thermal-entrance length for the flow of a high-Prandtl-number fluid in a circular pipe.[7] The solution based upon a laminar sublayer of thickness y_1 is obtained readily from the book of Carslaw and Jaeger[8] if the linear-velocity profile in the sublayer is replaced by an equivalent constant-velocity distribution. The 5 per cent entry-length value becomes equal to[9]

$$\left(\frac{L_t}{D}\right)_{5\%} = 0.892\ y_1^{+3}\left(\frac{\mu C_p}{k}\right)\Big/\left(\frac{uD}{\nu}\right)\sqrt{\frac{c_f}{2}}$$

where

$$y_1^+ = \frac{y_1}{D}\,\frac{uD}{\nu}\sqrt{\frac{c_f}{2}}$$

When the variation of properties is negligible $y_1^+ = 5$ and

$$\left(\frac{L_t}{D}\right)_{5\%} = 112\left(\frac{\mu C_p}{k}\right)\Big/\left(\frac{uD}{\nu}\right)\sqrt{\frac{c_f}{2}}$$

and the numerical results given in Table 5 are obtained.

TABLE 5 NUMERICAL RESULTS

uD/ν	$C_p\mu/k$	Prediction constant property	Test results	Prediction-effect of property variation (max)
5500	223	46	14	1.6
7830	260	35	7.2	0.97
10100	206	24	5.7	0.83
13300	170	16	4.6	0.86
14800	157	14	4.4	0.75
16200	90	6.6	3.7	0.75
16300	135	9.9	4.1	0.72
17200	138	9.6	3.7	0.72
17300	87	6.0	3.7	0.71
22900	98	5.2	2.2	0.66
24600	107	5.7	2.8	0.58
24600	107	5.7	2.6	0.52
29800	88	4.1	2.0	0.43
34600	63	2.4	2.8	0.46
46400	63	1.9	1.5	0.37
46600	61	1.8	1.7	0.33

The computed and test values are seen to decrease with Reynolds number[10] in direct contrast to the predictions of Latzko (21), Deissler (6), and Berry (1). Quantitatively speaking, the present theory always yields values larger than the experimental ones. This trend is to be expected since the value of y_1^+ is not equal to 5 but continually decreases below 5 in the entrance region. The value of the term y_1^+ at the end of the entrance region may be obtained from the results of Boelter, Martinelli,

[4] Engineer, General Electric Company, Schenectady, N. Y. Assoc. Mem. ASME.

[5] All reference numbers refer to Bibliography at the end of the paper.

[6] All symbols, unless otherwise noted, are those defined in the author's nomenclature.

[7] "Heat-Conduction Methods in Forced-Convection Flow," by S. Levy, ASME Paper No. 54—A-142.

[8] Reference 5 in author's Bibliography.

[9] The 5 per cent entry length was chosen over the 1 per cent value because the experimental measurements at 5 per cent may be viewed with more confidence.

[10] The same trend is noted in results obtained by I. T. Alyadev, "Experimental Determination of Local and Mean Coefficients of Heat Transfer for Turbulent Flow in Pipes," NACA TM 1356, 1954.

and Jonassen,[11] or it may be computed from the measurements of the fully developed heat-transfer coefficient

$$\frac{hD}{k} = \frac{D}{y_1}$$

Values of y_1/D computed from the latter expression were substituted in the derived equation for $(L_e/D)_{5\%}$ and the corresponding entry lengths are tabulated with the constant property values. The two sets of predictions really represent an upper and lower limit of the term $(L_e/D)_{5\%}$ and examination of the results reveals that they play such a role. This bracketing effect coupled with the predicted decrease of entrance length with Reynolds number leads the writer to believe that the test results lend support rather than weaken the concept of laminar sublayer. Further, it is felt that a sublayer analysis accounting for the decrease in y_1 will give answers within the experimental range. With regard to the effects of Reynolds number it is interesting to note that, since at low Prandtl number the entry length is directly proportional to the Reynolds number, the entrance length must be independent of Reynolds number at some intermediate range of the Prandtl number.

The simplicity of the analytical solution at high Prandtl numbers suggests a method of measuring the thermal-sublayer thickness. By minimizing the effect of properties (fluid with relatively small property variation with temperature) or by controlling this variation so that y_1^+ remains about constant in the entrance region (test section maintained at constant temperature) the measured values of $(L_e/D)_{5\%}$ can be utilized to compute the laminar sublayer thickness y_1^+ by means of the derived expressions.[7] Such a technique may be preferable to the use of a temperature probe which disturbs the laminar nature of the sublayer and exhibits errors too close to the pipe wall. On the other hand, the entry-length measurements will require careful and complete experimentation of the type presented by the author.

[11] "Remarks on the Analogy Between Heat Transfer and Momentum Transfer," by L. M. K. Boelter, R. C. Martinelli, and F. Jonassen, Trans. ASME, vol. 63, 1941, pp. 447–455.

Author's Closure

The general agreement of the experimental results presented by the author with the analytical results of Deissler is quite satisfactory. The Prandtl-number effect predicted by Deissler will be extremely difficult to verify experimentally in any detail although there appear to be some indications of this effect in the present experimental data as discussed in detail by Deissler.

In so far as obtaining more accurate information near the very entrance, this presents a formidable problem. Regardless of the type of heating used, there will be some axial heat conduction in the fluid itself which makes impossible, in practice, the obtaining of the initial conditions imposed in the analysis.

With respect to Dr. Levy's suggestion of deriving an explicit function for h_x/h_a in terms of x/D, this could easily be accomplished and might smooth out some of the inconsistencies in the results. However, it was felt that the statement that the thermal-entrance length was approximately 10 to 15 pipe diameters over the range cited was sufficient for most applications; under those circumstances an explicit function was not considered essential.

The variation of the property values should certainly have been mentioned in the paper and the author is indebted to Levy for emphasizing this point. In particular, his suggestion that the correlation of the friction-factor results may be improved by the viscosity correction factor is a valuable criticism and results in improved agreement of the experimental values with the commonly accepted equations.

The approximate analysis proposed by Levy for high-Prandtl-number fluids predicts decreasing thermal-entrance lengths with increasing Reynolds number, and this is in agreement with the present experiment results. Contrary to the statement of Levy, this trend is also in agreement with the analysis of Deissler. However, Deissler's analysis shows decreasing thermal-entrance lengths with increasing Prandtl number, whereas Levy's approximate analysis yields the opposite trend, increasing entrance lengths with increasing Prandtl number. No conclusive evidence regarding this Prandtl-number effect is derivable from the experimental results.

Turbulent Heat Transfer and Friction in the Entrance Regions of Smooth Passages

By R. G. DEISSLER,[1] CLEVELAND, OHIO

The effect of various factors on the turbulent heat transfer and friction in the entrance regions of smooth passages is investigated analytically. The influence of Reynolds number, Prandtl number, initial velocity distribution, wall-boundary condition, passage shape, and of variable fluid properties is predicted. Integral heat-transfer and momentum equations are used for calculating the thicknesses of the thermal and flow boundary layers. The results indicate that approximately fully developed heat transfer and friction are, in general, attained in an entrance length less than 10 diameters. Substantial agreement between analysis and experiment was obtained for heat transfer to air in the entrance regions of tubes and parallel plates.

Nomenclature

The following nomenclature is used in the paper:

c_p = specific heat of fluid at constant pressure at wall, Btu/(lb)(deg F)
D = inside diameter of tube, or twice plate spacing, ft
d = exponent; value depends on variation of viscosity of fluid with temperature
g = conversion constant, 32.2 ft/sec^2
h = local heat-transfer coefficient, $q_0/(t_0 - t_b)$, Btu/(sec)(sq ft)(deg F)
k = thermal conductivity of fluid, Btu/(sec)(sq ft)(deg F/ft)
k_i = thermal conductivity of fluid evaluated at t_i, Btu/(sec)(sq ft)(deg F/ft)
n = constant
p = static pressure, psfa
p_i = static pressure at inlet, psfa
q = rate of heat transfer toward tube center per unit area, Btu/(sec)(sq ft)
q_0 = rate of heat transfer at inside wall toward tube center per unit area for a given X/D, Btu/(sec)(sq ft)
r = radius, distance from tube center, ft
r_0 = inside tube radius or one-half distance between plates, ft
t = absolute static temperature, deg R
t_b = bulk static temperature of fluid at cross section of tube, deg R
t_i = inlet static temperature of fluid, deg R
t_{δ_h} = temperature of fluid outside thermal boundary layer
t_0 = wall temperature, deg R
u = time-average velocity parallel to axis of passage, fps
u_b = bulk velocity at cross section of tube, fps
u_i = velocity of fluid at inlet, fps
u_δ = velocity outside flow boundary layer, fps
X = distance from entrance, or from point at which heat transfer begins, ft
y = distance from wall, ft
δ = flow-boundary-layer thickness, ft
δ_h = thermal-boundary-layer thickness, ft
ϵ = eddy diffusivity for momentum, sq ft/sec
ϵ_h = eddy diffusivity for heat, sq ft/sec
μ = absolute viscosity of fluid, (lb)(sec)/sq ft
μ_i = absolute viscosity of fluid evaluated at t_i, (lb)(sec)/sq ft
μ_0 = absolute viscosity of fluid evaluated at t_0, (lb)(sec)/sq ft
ρ = mass density of fluid, (lb)(sec^2)/ft^4
ρ_i = mass density of fluid evaluated at t_i, (lb)(sec^2)/ft^4
ρ_0 = mass density of fluid evaluated at t_0, (lb)(sec^2)/ft^4
τ = shear stress in fluid, psf
τ_0 = shear stress in fluid at wall, psf
f_{rd} = fully developed friction factor
f_τ = friction factor based on local shear stress at wall, $2\tau_0/\rho u_b^2$
$f_{\tau i}$ = friction factor based on local shear stress at wall and density and velocity at inlet, $\dfrac{2\tau_0}{\rho_i u_i^2}$
Gz = Graetz number, Re Pr/(X/D)
Nu = local Nusselt number, hD/k
Nu_d = fully developed Nusselt number
Nu_i = Nusselt number with conductivity evaluated at t_i
Nu_0 = Nusselt number with thermal conductivity evaluated at t_0
Pe = Peclet number, Re Pr
Pr = Prandtl number, $c_p g\mu/k$
Pr_0 = Prandtl number with properties evaluated at t_0
q_i' = heat-transfer parameter, $q_0/(c_p g \rho_i u_i t_i)$
Re = Reynolds number, $\rho u_b D/\mu$
Re_i = Reynolds number with density and viscosity evaluated at t_i, $\dfrac{\rho_i u_b D}{\mu_i}$
Re_0 = Reynolds number with density and viscosity evaluated at t_0, $\rho_0 u_b D/\mu_0$

r_0^+ = tube radius parameter, $\dfrac{\sqrt{\tau_0/\rho_0}}{\mu_0/\rho_0} r_0$

t^+ = temperature parameter, $\dfrac{(t_0 - t)c_p g \tau_0}{q_0\sqrt{\tau_0/\rho_0}} = \dfrac{1 - t/t_0}{\beta}$

t_b^+ = bulk-temperature parameter, $\dfrac{1}{\beta}\left(1 - \dfrac{t_b}{t_0}\right)$

$t_{\delta_h}^+ = \dfrac{1}{\beta}\left(1 - \dfrac{t_{\delta_h}}{t_0}\right)$

u^+ = velocity parameter, $\dfrac{u}{\sqrt{\tau_0/\rho_0}}$

u_b^+ = bulk-velocity parameter, $\dfrac{u_b}{\sqrt{\tau_0/\rho_0}}$

$u_\delta^+ = \dfrac{u_\delta}{\sqrt{\tau_0/\rho_0}}$

---

[1] Aeronautical Research Scientist and Head, Heat Transfer Section, Lewis Flight Propulsion Laboratory, National Advisory Committee for Aeronautics. Assoc. Mem. ASME.

Contributed by the Heat Transfer Division and presented at the Annual Meeting, New York, N. Y., November 28–December 3, 1954, of The American Society of Mechanical Engineers.

 Manuscript received at ASME Headquarters, September 13, 1954. Paper No. 54—A-154.

y^+ = wall distance parameter, $\frac{\sqrt{\tau_0/\rho_0}}{\mu_0/\rho_0} y$

β = heat-transfer parameter, $q_0 \sqrt{\tau_0/\rho_0}/(c_p g \tau_0 t_0)$

δ^+ = dimensionless flow-boundary-layer thickness, $\frac{\sqrt{\tau_0/\rho_0}}{\mu_0/\rho_0} \delta$

δ_h^+ = dimensionless thermal-boundary-layer thickness, $\frac{\sqrt{\tau_0/\rho_0}}{\mu_0/\rho_0} \delta_h$

Introduction

Flow and heat transfer in the entrance regions of passages have been subjects of considerable interest, both from a theoretical and a practical point of view. From a practical viewpoint it is often desirable to use short passages in heat exchangers in order to take advantage of the high heat-transfer coefficients in the entrance region. The laminar-flow case has been analyzed in references (1 to 3),[2] and the turbulent case, in references (4) and (5). In these analyses constant fluid properties were assumed, and uniform wall temperature was postulated in the cases in which heat transfer was considered. In the turbulent-flow cases the flow was assumed to be turbulent at all points along the passage. The analysis in reference (4) is based on an assumed $^1/_7$-power velocity profile and the Blasius resistance formula. The analysis given in reference (5) is applicable to cases in which the heat transferred by turbulence can be neglected, as might occur at very low Prandtl numbers.

The analysis given herein was made at the NACA Lewis Laboratory. It is an extension of the analysis given in reference (6) for fully developed turbulent heat transfer and flow with variable fluid properties to the entrance regions of smooth passages. The influence of Reynolds number, Prandtl number, initial velocity distribution, wall-boundary condition, passage shape, and of variable fluid properties is predicted. In calculating the growth of the thermal and flow boundary layers in the entrance region, integral equations for heat transfer and momentum are used. For obtaining velocity and temperature distributions in the boundary layers, the same assumptions are made for solving the turbulent transfer equations as were made in reference (6).

The flow is assumed to be turbulent at all points along the passage, as in previous analyses, so that at low Reynolds numbers it is usually necessary that a small disturbance be present at the entrance to trip the turbulent boundary layer. Experimental data for heat transfer in a tube with a smooth entrance (7) indicate that at high Reynolds numbers (Re > 50,000) the flow is turbulent near the entrance, even without artificial disturbances. When a turbulence screen was placed ahead of the entrance, the flow appeared to be turbulent at all Reynolds numbers tested. According to Prandtl's assumption, which is in reasonable agreement with experiment, in the presence of a laminar boundary layer near the entrance, the turbulent portion of the boundary layer behaves as though the boundary layer were turbulent all the way from the entrance (8). The present calculations may therefore be applicable to the turbulent portion of the boundary layer even when a laminar boundary layer exists near the entrance.

In general, the solution of the equations to obtain the results given in the present paper requires considerable numerical integration and cross-plotting. Only the basic equations and assumptions, together with the general procedures for solution are given here.

[2] Numbers in parentheses refer to the Bibliography at the end of the paper.

Velocity and Temperature Distribution in Boundary Layers

For calculating heat transfer and friction in the entrance region of ducts, the usual boundary-layer assumptions used with integral methods are made; that is, it is assumed that the effects of heat transfer and friction are confined to fluid layers close to the surface (thermal and flow boundary layers, respectively). The temperature and velocity distributions outside the boundary layers are assumed uniform, and the total temperature and total pressure are constant along the length of the duct for the region outside the boundary layers. More exact analyses (2) indicate that these assumptions are valid, even for laminar flow, except in the region at a distance from the entrance where the boundary layer fills a large portion of the tube. For that region, however, the Nusselt numbers and friction factors have values very close to the values for fully developed flow.

The effects of frictional heating are neglected throughout the analysis. For obtaining the velocities and temperatures in the flow and thermal boundary layers, the differential equations for shear stress and heat transfer can be written as follows

$$\tau = \mu \frac{du}{dy} + \rho\epsilon \frac{du}{dy} \quad [1]$$

$$q = -k \frac{dt}{dy} - \rho g c_p \epsilon_h \frac{dt}{dy} \quad [2]$$

where ϵ and ϵ_h are the eddy diffusivities for momentum and heat transfer, respectively, the values for which depend on the amount and kind of turbulent mixing at a point. When written in dimensionless form, Equations [1] and [2] become

$$\frac{\tau}{\tau_0} = \left(\frac{\mu}{\mu_0} + \frac{\rho}{\rho_0}\frac{\epsilon}{\mu_0/\rho_0}\right)\frac{du^+}{dy^+} \quad [3]$$

and

$$\frac{q}{q_0} = \left(\frac{k}{k_0}\frac{1}{\mathrm{Pr}_0} + \frac{\rho}{\rho_0}\frac{\epsilon_h}{\mu_0/\rho_0}\right)\frac{dt^+}{dy^+} \quad [4]$$

where the subscripts 0 refer to values at the wall and the dimensionless quantities are defined in the Nomenclature.

Assumptions. The following assumptions are made in the use of Equations [3] and [4] for obtaining velocity and temperature distributions in the flow and thermal boundary layers, except in the case of liquid metals:

1 The eddy diffusivities for momentum ϵ and heat transfer ϵ_h are equal. Previous analyses for fully developed flow in tubes based on this assumption yielded heat-transfer coefficients that agree with experiment for Reynolds numbers above 15,000 (6). The same assumption is made here for developing boundary layers.

2 The eddy diffusivity ϵ is given by

$$\epsilon = \epsilon(u, y, u/\rho) = n^2 u y \left(1 - e^{-\frac{n^2 u y}{\mu/\rho}}\right) \quad [5]$$

in the region close to the wall ($y^+ < 26$), and by the von Kármán relation

$$\epsilon = \epsilon(du/dy, d^2u/dy^2) = \kappa^2 \frac{(du/dy)^3}{(d^2u/dy^2)^2} \quad [6]$$

in the region at a distance from the wall ($y^+ > 26$). These expressions have been verified experimentally for fully developed boundary layers with variable properties in references (6) and (9). It is assumed here that they apply also to developing boundary layers. The quantities n and κ are experimental con-

stants having the values 0.124 and 0.36, respectively. It should be noted that the expression for the region close to the wall, Equation [5], differs from that in reference (6). Equation [5] is more general in that it contains an effect of kinematic viscosity on ϵ and is adequate for high as well as low Prandtl numbers (9).

3 The variations across the flow and thermal boundary layers of the shear stress τ and the heat transfer per unit area q have a negligible effect on the velocity and temperature distributions. It is shown in Fig. 11 of reference (6) that the assumption of a linear variation of shear stress and heat transfer across the boundary layers (τ or q = 0 at the edge of the thermal or flow boundary layer) gives very nearly the same velocity and temperature profiles as those obtained by assuming uniform shear stress and heat transfer across the boundary layers for values of δ^+ or $\delta_h{}^+$ between 500 and 5000.[3] For small values of $\delta_h{}^+$ such as occur very near the entrance, the effect of variable heat transfer across the boundary layer is checked in Fig. 9 of reference (10).

4 The molecular shear stress and heat-transfer terms in Equations [3] and [4] can be neglected in the region at a distance from the wall (reference 6, Fig. 12).

Solution of Equations. The details of the solution of Equations [3] and [4] under the foregoing assumptions are given in the Appendix. The resulting temperature and velocity distributions are given in Figs. 1, 2, and 3. Fig. 1 gives the relation between

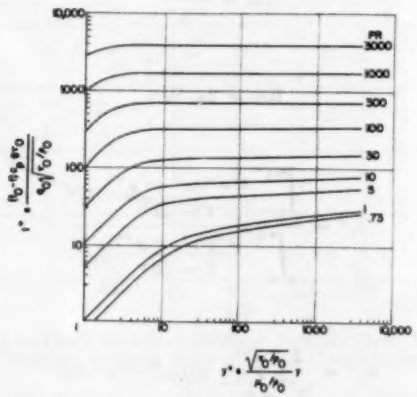

FIG. 1 PREDICTED TEMPERATURE DISTRIBUTION FOR VARIOUS PRANDTL NUMBERS FOR USE IN THERMAL BOUNDARY LAYERS ($y^+ \leq \delta_h{}^+$). CONSTANT PROPERTIES

t^+ and y^+ for various Prandtl numbers and constant fluid properties. Figs. 2 and 3 give the relations between t^+ and y^+ and u^+ and y^+ for gases (Pr = 0.73) with variable density, viscosity, and thermal conductivity (specific heat and Prandtl number considered constant). For calculating the latter curves it is assumed that $\mu/\mu_0 = k/k_0 = (t/t_0)^{0.68}$. From the perfect-gas law and the assumption of constant pressure across the passage, $\rho/\rho_0 = t_0/t$. It can be shown from the definitions of the quantities involved that $t/t_0 = 1 - \beta t^+$. Positive values of β correspond to heat addition to the gas; negative values, to heat extraction. For the cases in which the fluid properties are considered constant, the curves for $\beta = 0$ are used.[4] The plotted values of t^+ and u^+ are to be used in the thermal and flow boundary layers; that is, for values of $y^+ \leq \delta_h{}^+$ or $y^+ \leq \delta^+$. For values of

[3] Fig. 11 of reference (6) applies to developing boundary layers if the symbols $r_0{}^+$ in Fig. 11 are replaced by δ^+ or $\delta_h{}^+$.

[4] The case in which $\beta = 0$ is a limiting one which can be approached as closely as desired by making the temperature difference small. In the limit, where the temperature difference is zero or infinitesimal, the properties must be constant.

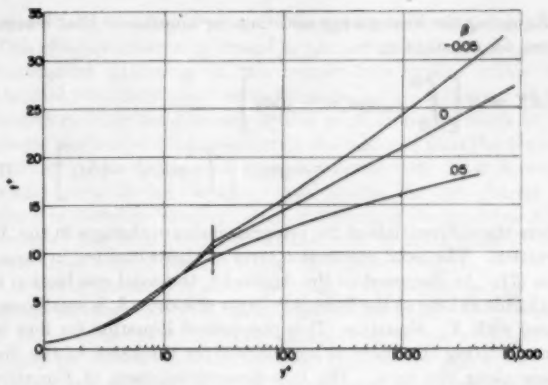

FIG. 2 PREDICTED TEMPERATURE DISTRIBUTIONS FOR GASES FOR USE IN THERMAL AND FLOW BOUNDARY LAYERS ($y^+ \leq \delta_h{}^+$). PRANDTL NUMBER, 0.73. VARIABLE PROPERTIES

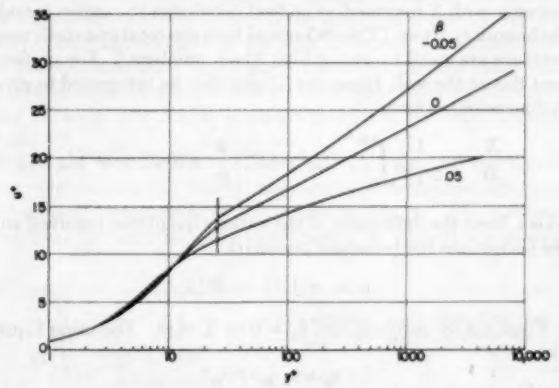

FIG. 3 PREDICTED VELOCITY DISTRIBUTIONS FOR GASES FOR USE IN FLOW AND THERMAL BOUNDARY LAYERS ($y^+ \leq \delta^+$). PRANDTL NUMBER, 0.73. VARIABLE PROPERTIES

y^+ greater than these values, t^+ and u^+ are constant and have the values at $\delta_h{}^+$ and δ^+. The relations between $\delta_h{}^+$ and X/D and δ^+ and X/D will be obtained in the following sections.

DEVELOPMENT OF THERMAL BOUNDARY LAYERS

Most of the following calculations are made for flow in a round tube, but as will be shown later, the results apply also, with small error, to parallel plates.

Heat-Flow Equation for Thermal Boundary Layers. The heat-flow equation for the thermal boundary layer in a tube can be obtained from the diagram, Fig. 4. Energy flows into the differential annulus by convection and by conduction through plane 1

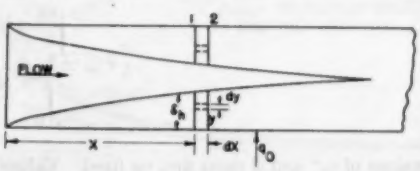

FIG. 4 DIAGRAM FOR DERIVING HEAT-FLOW EQUATION FOR TUBE

and leaves through plane 2. In addition to this energy there is a radial flow of energy (heat) from the tube surface by conduction and a radial flow by convection at δ_h. No radial heat flow due to temperature gradient takes place at δ_h because the temperature gradient is, by definition of the thermal boundary layer, zero at the edge of the boundary layer.

Equating the heat energy entering the annulus to that leaving gives, for constant c_p

$$q_0 r_0 dX = d\left[\int_0^{\delta_h} c_p g t \rho u (r_0 - y) dy\right] - c_p t_{\delta_h} g d\left[\int_0^{\delta_h} \rho u (r_0 - y) dy\right] \quad \ldots [7]$$

where the differentials of the integrals indicate changes in the X-direction. The axial conduction term has been omitted in Equation [7]. As discussed in the Appendix, the axial conduction is negligible as long as the boundary-layer thickness δ_h is small compared with X. Equation [7] is the desired Equation for flow in tubes relating the thermal boundary-layer thickness to the distance along the tube. The two-dimensional form of Equation [7] has been used extensively for calculating the growth of the thermal boundary layer on a flat plate (11).

The total temperature outside the thermal boundary layer does not vary with X inasmuch as no heat penetrates the region outside the boundary layer. (The differences between total and static temperature are small except at high Mach numbers.) For uniform heat flux at the wall, Equation [7] can then be integrated to give, in dimensionless form

$$\frac{X}{D} = \frac{1}{2 r_0^{+2}} \int_0^{\delta_h^+} (t_{\delta_h}^+ - t^+) \frac{\rho}{\rho_0} u^+ (r_0^+ - y^+) dy^+ \quad \ldots [8]$$

where, from the definitions of the various quantities involved and the perfect-gas law (constant pressure)

$$\rho/\rho_0 = 1/(1 - \beta t^+) \quad \ldots [9]$$

Equation [8] assumes that $\delta_h = 0$ at $X = 0$. For using Equation [8], values of r_0^+ and β must first be fixed. Values of X/D can then be calculated for various values of δ_h^+. The relations between t^+ and y^+ and u^+ and y^+ are obtained from Figs. 1, 2, and 3. Equation [8] is valid for $\delta_h^+ < \delta^+$ or $\delta_h^+ > \delta^+$ provided it is remembered that $u^+ = u_\delta^+$ for $y^+ > \delta^+$.

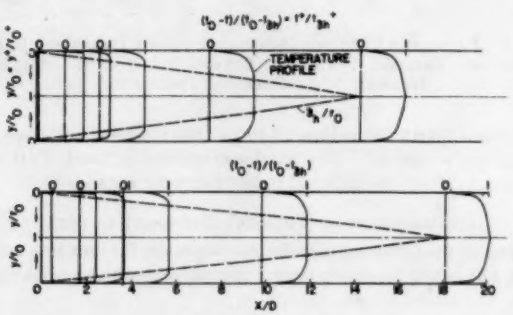

FIG. 5 DEVELOPMENT OF THERMAL BOUNDARY LAYER IN ENTRANCE REGION OF TUBE FOR A GAS. PR, 0.73
(Uniform heat flux, uniform initial temperature distribution, fully developed velocity distribution, and constant properties.)

Fig. 5 illustrates the development of the temperature profile for gas flowing in a tube with uniform wall heat flux. The profiles indicate that for a fixed tube diameter at a given distance from the entrance, the boundary-layer thickness is less for high values of r_0^+ or of Reynolds number than for low ones, or the distance required for a given degree of temperature-profile development is greater for high Reynolds numbers than for low ones. The turbulent boundary layers develop much faster than laminar boundary layers because of the rapid radial diffusion of heat by turbulence.

If the wall temperature rather than the heat flux is uniform, and the properties are constant, Equation [7] becomes

$$\frac{X}{D} = \frac{1}{2}\int_0^{[\ ]} \frac{t_{\delta_h}^+}{r_0^+} d\left[\frac{1}{r_0^+}\int_0^{\delta_h^+} \frac{t_{\delta_h}^+ - t^+}{t_{\delta_h}^+} u^+ (r_0^+ - y^+) dy^+\right] \quad \ldots [10]$$

Equation [10] can be verified by substituting the definitions of the various dimensionless quantities into the equation. This equation requires a numerical integration along the tube which was not required in Equation [8], where the wall heat flux was uniform. Equation [10] is used similarly to Equation [8].

NUSSELT NUMBERS AND REYNOLDS NUMBERS

It can easily be shown from the definitions of the quantities involved that the Nusselt number and Reynolds number (properties variable or constant) for tubes with the fluid properties evaluated at the wall temperature are given by

$$\mathrm{Nu}_0 = \frac{2 r_0^+ \mathrm{Pr}}{t_b^+} \quad \ldots [11]$$

and

$$\mathrm{Re}_0 = 2 u_b^+ r_0^+ \quad \ldots [12]$$

where

$$t_b^+ = \frac{\displaystyle\int_0^{r_0^+} \frac{t^+ u^+ (r_0^+ - y^+)}{1 - \beta t^+} dy^+}{\displaystyle\int_0^{r_0^+} \frac{u^+ (r_0^+ - y^+)}{1 - \beta t^+} dy^+} \quad \ldots [13]$$

and

$$u_b^+ = \frac{2}{r_0^{+2}} \int_0^{r_0^+} u^+ (r_0^+ - y^+) dy^+ \quad \ldots [14]$$

The foregoing equations can be used in the entrance region as well as for fully developed flow. It is, of course, necessary that $t^+ = t_{\delta_h}^+$ for $y^+ \geq \delta_h^+$ and $u^+ = u_\delta^+$ for $y^+ \geq \delta^+$. The use of Equations [13] and [14] in the entrance region might be understood more clearly by breaking the integrals up into several parts. For instance, Equation [13] can be written, for the case where $\delta_h^+ < \delta^+$, as

$$t_b^+ = \frac{\displaystyle\int_0^{\delta_h^+} \frac{t^+ u^+ (r_0^+ - y^+)}{1 - \beta t^+} dy^+ + \frac{t_{\delta_h}^+}{1 - \beta t_{\delta_h}^+} \int_{\delta_h^+}^{\delta^+} u^+ (r_0^+ - y^+) dy + \frac{t_{\delta_h}^+ u_\delta^+}{2} \frac{(r_0^+ - \delta^+)^2}{(1 - \beta t_{\delta_h}^+)}}{\displaystyle\int_0^{\delta_h^+} \frac{u^+ (r_0^+ - y^+)}{1 - \beta t^+} dy^+ + \frac{1}{1 - \beta t_{\delta_h}^+} \int_{\delta_h^+}^{\delta^+} u^+ (r_0^+ - y^+) dy^+ + \frac{u_\delta^+}{2} \frac{(r_0^+ - \delta^+)^2}{(1 - \beta t_{\delta_h}^+)}}$$

For cases where the flow boundary layer is not fully developed ($\delta^+ < r_0^+$), the relation between δ^+ and X/D will be obtained in the section, Friction with Variable Properties. For calculating values of Nu_0 and Re_0 values of δ_h^+, δ^+, r_0^+, and β must be fixed, as in Equation [8]. Values of Nu_0 and Re_0 are thus obtained for given values of X/D and β.[5]

[5] Unfortunately, β varies along the passage. It will later be seen that q_i is more convenient for use as a heat-flux parameter.

Predicted Effect of Various Factors on Heat Transfer in the Entrance Region With Constant Fluid Properties

For comparing heat transfer in the thermal-entrance region for various cases, the ratio of local Nusselt number to the fully developed Nusselt number ($\delta_h = r_0$) is plotted against X/D for each

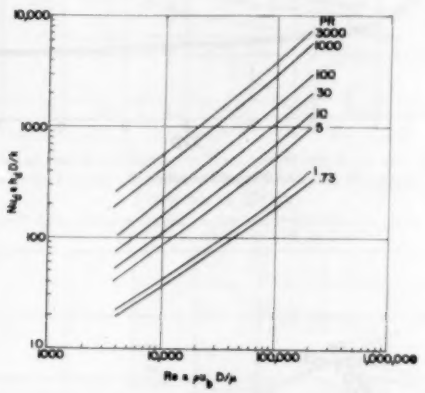

Fig. 6 Predicted Fully Developed Nusselt Numbers Against Reynolds Number for Various Prandtl Numbers. Constant Properties

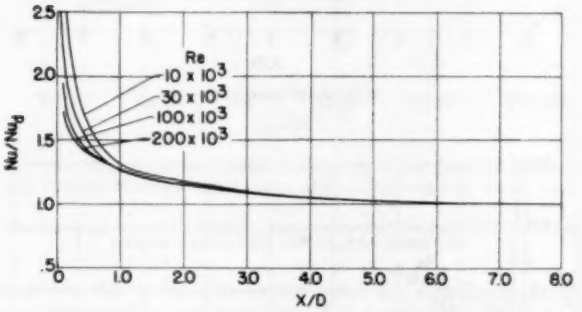

Fig. 7 Variation of Local Nusselt Number Over Fully Developed Nusselt Number With X/D for Gas Flowing in Tube. Pr, 0.73

(Uniform wall heat flux, uniform initial temperature distribution, fully developed velocity distribution and constant properties.)

case, Figs. 7 to 12. The values of local Nusselt number can then be obtained from those plots together with Fig. 6, which gives predicted fully developed Nusselt numbers for various Reynolds and Prandtl numbers (9).

Fig. 7 gives the variation of local Nusselt number with X/D and Reynolds number for uniform wall heat flux and fully developed velocity distribution ($\delta = r_0$). The curves indicate, as might be expected, that the Nusselt numbers (heat-transfer coefficients) close to the entrance are high in comparison with the fully developed values farther down the tube. The thermal boundary layer is thin and the temperature gradients consequently are severe near the entrance. At $X/D = 0$ the boundary-layer thickness is zero, so that the heat-transfer coefficient is infinite at the entrance. For uniform wall heat flux this means that the temperature difference $t_0 - t_b$ must be zero at $X/D = 0$; for a finite temperature difference at $X/D = 0$ the heat transfer per unit area could not be uniform since it would be infinite at the entrance.

Comparison of the curves in Fig. 7 with the temperature profiles in Fig. 5 indicates that the Nusselt numbers very nearly reach their fully developed values long before the boundary layers meet at the center of the tube; that is, the values of Nu/Nu_d are somewhat lower than one would expect from the variation of δ_h. This effect is apparently caused by the increase of turbulence and consequent flattening of the temperature profile within the thermal boundary layer as it develops. The flattening of the boundary-layer temperature profile as X increases tends to increase the temperature gradient at the wall and thus the Nusselt number. The decrease of Nusselt number with X or δ_h which would occur if the boundary-layer profile did not change its shape is therefore lessened by the flattening of the profile as X increases; that is, the increase of turbulence in the thermal boundary layer with X tends to lower the values of Nu/Nu_d.

Effect of Reynolds Number for Gases. The curves in Fig. 7 indicate an effect of Reynolds number on the value of Nu/Nu_d at a given value of X/D. The values close to the entrance are higher for the low Reynolds numbers than for the high ones, even though the boundary layer develops faster at the low Reynolds numbers (Fig. 5). This effect can be explained by the increase of turbulence in the thermal boundary layer as X or δ_h increases, as discussed in the preceding paragraph. The rate of increase of turbulence with boundary-layer thickness is greater for high Reynolds numbers than for low ones, inasmuch as the turbulence in the boundary layer varies from zero at the entrance to the value for fully developed flow. The effect of turbulence on decreasing the values of Nu/Nu_d is therefore greater at the high Reynolds numbers.

Effect of Wall Boundary Condition. The effect of wall boundary condition on the Nusselt numbers in the entrance region can be seen by comparison of the curves in Fig. 8. The values of Nu/Nu_d for uniform wall temperature in general are slightly

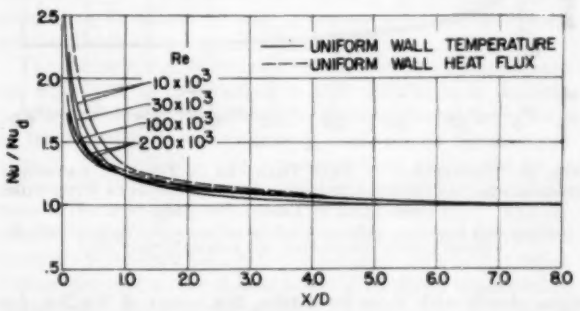

Fig. 8 Comparison of Heat Transfer in Thermal Entrance Region for Gas Flowing in Tube With Uniform Wall Temperature With That for Uniform Wall Heat Flux. Pr, 0.73

(Uniform initial temperature distribution, fully developed velocity distribution, and constant properties.)

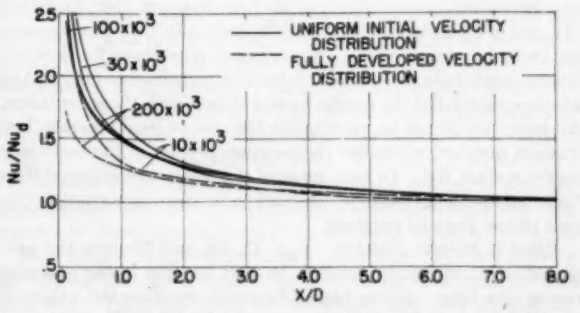

Fig. 9 Comparison of Heat Transfer in Thermal Entrance Region for Gas Flowing in Tube With Uniform Initial Velocity Distribution With That for Fully Developed Velocity Distribution. Pr, 0.73

(Uniform heat flux, uniform initial temperature distribution, and constant properties.)

lower than those for uniform wall heat flux. The heat transfer per unit area q_0 must be infinite at $X/D = 0$ for uniform wall temperature. This occurs only for an infinitesimal distance dX, however, so that a finite amount of heat is transferred.

Effect of Initial Velocity Distribution. Comparison of the curves in Fig. 9 indicates the effect of initial velocity distribution on heat transfer in the entrance region. The comparison indicates that the values of Nu/Nu_d for a uniform initial velocity distribution are higher than those for a fully developed velocity distribution. This result might be expected because of the higher friction in the case of uniform initial velocity profile.

In order to calculate the curves for uniform initial velocity distribution in Fig. 9, it is necessary to know the relation between δ^+ and X/D as well as the relation between $\delta_h{}^+$ and X/D. The relation for δ^+ will be obtained later. In most cases (for gases) it is sufficiently accurate to assume that $\delta^+ = \delta_h{}^+$.

Curves for heat transfer with a uniform initial velocity distribution and a uniform wall temperature, rather than uniform heat flux, were also calculated (10) and were found to be similar to those in Fig. 9.

Effect of Passage Shape. The effect of passage shape on the heat transfer in the entrance region can be obtained by comparing the curves in Fig. 10. The curves for flow between parallel plates

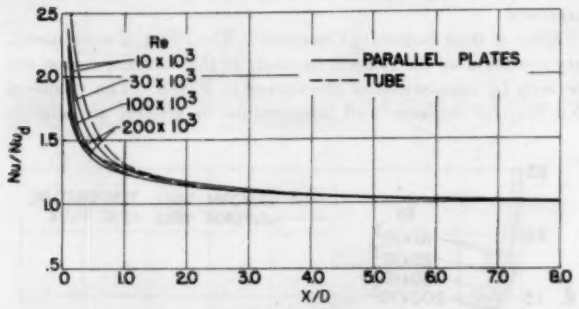

FIG. 10 COMPARISON OF HEAT TRANSFER IN THERMAL ENTRANCE REGION FOR GAS FLOWING BETWEEN PARALLEL PLATES WITH THAT FOR FLOW IN TUBE. PR, 0.73

(Uniform wall heat flux, uniform initial temperature distribution, fully developed velocity distribution, and constant properties.)

agree closely with those for a tube, the values of Nu/Nu_d for parallel plates being slightly lower than those for tubes. This agreement indicates that results for turbulent heat transfer in tubes can be used with small error for parallel plates when an equivalent diameter equal to twice the plate spacing is used.

For calculating the curves for parallel plates it was necessary to obtain two-dimensional forms of the heat-flow equation, Equation [7], and of Equations [11], [12], [13], and [14]. These equations are given in reference (10). A number of other cases for flow between parallel plates were also calculated in reference (10) and in all cases calculated the results agreed closely with those for tubes. An exception would be expected in the case of liquid metals (low Prandtl number) where the temperature profiles in the boundary layers are not flat. In fact, most of the effects investigated thus far in this section would be expected to be more important in the case of low Prandtl numbers.

Effect of Prandtl Number. Figs. 11, 12, and 13 show the predicted effect of Prandtl number on heat transfer in the entrance region of a tube. At the higher Reynolds numbers the values of Nu/Nu_d for a given X/D decrease as the Prandtl number increases above 1; that is, the effect of X/D becomes small at large values of Prandtl number. At low Reynolds numbers the variation is more complex: Values of Nu/Nu_d first decrease and then increase slightly as Prandtl number increases. In either case it

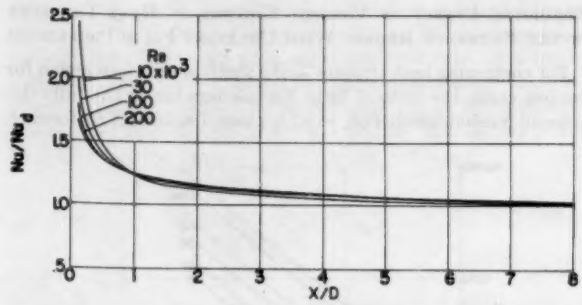

(a) Prandtl number, 1

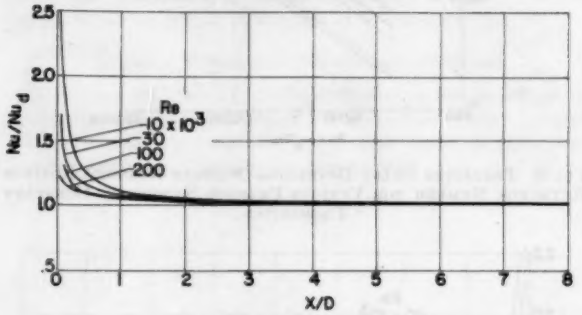

(b) Prandtl number, 10

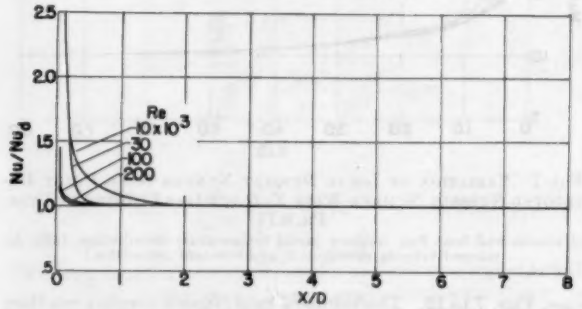

(c) Prandtl number, 100

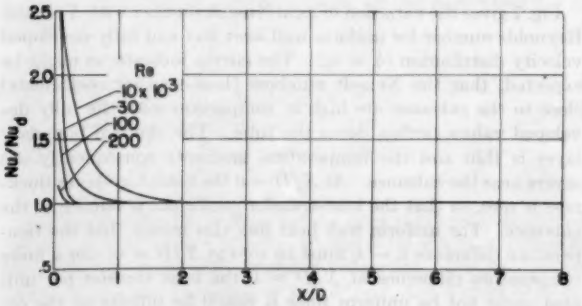

(d) Prandtl number, 1000

FIG. 11 CURVES SHOWING EFFECT OF PRANDTL NUMBER ON HEAT TRANSFER IN THERMAL ENTRANCE REGION OF TUBE

(Uniform wall heat flux, uniform initial temperature distribution, fully developed velocity distribution, and constant properties.)

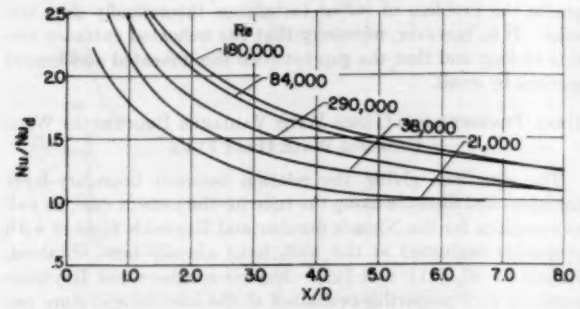

FIG. 12 VARIATION OF NUSSELT NUMBER WITH X/D AND REYNOLDS NUMBER FOR LIQUID METALS WITH PRANDTL NUMBER OF 0.01 FLOWING IN TUBE

(Uniform heat flux, uniform initial temperature distribution, fully developed velocity distribution, and constant properties.)

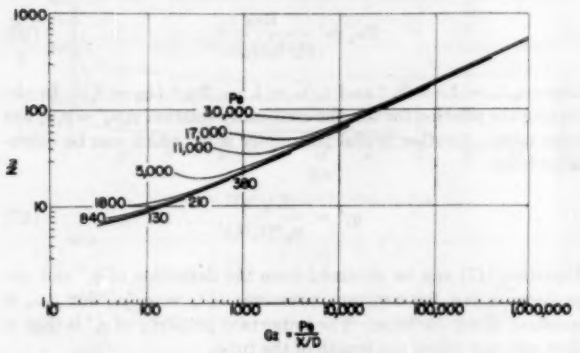

FIG. 13 VARIATION OF NUSSELT NUMBER WITH GRAETZ NUMBER AND PECLET NUMBER FOR LIQUID METAL FLOWING IN TUBE. PR, 0.01

(Uniform heat flux, uniform initial temperature distribution, fully developed velocity distribution, and constant properties.)

is evident that in the entrance region the fully developed Nusselt numbers should be multiplied by a factor which is a function of X/D, Reynolds number, and Prandtl number rather than of X/D alone; that is, a simple factor such as $(X/D)^{-n}$, which is often used for Prandtl numbers of approximately 1, is inadequate for high Prandtl numbers. The effect of Reynolds number on Nu/Nu_d in the entrance region increases with Prandtl number; that is, the separation of the curves for various Reynolds numbers increases with Prandtl number.

It is of interest to note that the Nusselt numbers for turbulent flow in Fig. 11, in general, display trends opposite to those for Nusselt numbers for laminar flow with increasing values of Prandtl number. In the case of laminar flow, the value of Nu/Nu_d at a given X/D and Reynolds number increases considerably with Prandtl number (reference 5, Fig. 3). The heat diffuses through the fluid more slowly at the higher Prandtl numbers (the thermal diffusivity is lower) so that the thermal boundary layer is thinner and Nu/Nu_d for a given X/D near the entrance and a given Reynolds number is consequently higher than for the lower Prandtl numbers. The same phenomenon also tends to increase the effect of X/D for turbulent heat transfer.

In the case of turbulent heat transfer, however, the shape of the temperature profile within the thermal boundary layer changes considerably because of the increase of turbulence in the boundary layer as X or δ_h increases. This effect was discussed in and before the section Effect of Reynolds Number for Gases, where it was found to decrease the value of Nu/Nu_d at a given X/D. The effect would be expected to be greater at high Prandtl numbers because the ratio of the turbulent to the molecular term in Equation [4] is proportional to the Prandtl number. The value of Nu/Nu_d at a given X/D and Re therefore tends to decrease as Prandtl number increases. The same effect should also explain the greater separation of curves with Reynolds number at the high Prandtl numbers.

The predicted variation of Nusselt number in the entrance region for a low-Prandtl-number fluid (liquid metal) is given in Figs. 12 and 13. As the Reynolds number increases, the value of Nu/Nu_d at a given X/D first increases and then decreases. The trend at low Reynolds numbers is opposite to that obtained for high Prandtl numbers and resembles the trend for laminar heat transfer, where the change in boundary-layer thickness with Reynolds number is the controlling factor (change of profile shape in boundary layer less important). The heat transfer is in fact almost entirely by laminar conduction at the low Reynolds numbers. The similarity to laminar heat transfer can be seen most clearly in Fig. 13, where Nusselt number is plotted against Graetz number ($Re\ Pr/[X/D]$) for various Peclet numbers. If the heat transfer contributed by eddy diffusion were neglected, the curves for various Peclet numbers would fall essentially on a single line as in reference (5). Examination of the curves in Fig. 13 indicates that for Peclet numbers below 1000 the curves could be represented approximately by a single line. This line is slightly higher than the one obtained in reference (5) inasmuch as a uniform wall temperature rather than a uniform heat flux was postulated in that reference.

For calculating the curves for low Prandtl numbers, temperature distributions for fully developed flow of liquid metals calculated as described in reference (12) were used in the thermal boundary layer. The assumptions made in the present paper for integrating Equations [3] and [4] are not valid for low-Prandtl-number fluids.

The curves in Fig. 13 indicate a slight increase of Nusselt number with X/D at large values of X/D and Peclet or Reynolds number. This effect is apparently caused by the change in shape of the boundary-layer profile as δ_h increases, as discussed previously. The effect in this case seems to be aggravated by an influence of Peclet number on ϵ_h which is included in the calculations of the temperature distributions in reference (12). The predicted trend at large X/D might be open to question because the boundary layer occupies a large portion of the tube in that region. The existence of a core of fluid which is relatively unaffected by heat transfer is therefore doubtful.

COMPARISON OF ANALYSIS AND EXPERIMENT

Experimental heat-transfer data in the entrance region are quite sparse, usually being confined to measurements with air as a fluid. Figs. 14, 15, and 16 compare three sets of data for air from references (7) and (13) with the analytical results. The experimental data in Fig. 14 from reference (7) are for air flowing in a tube at uniform wall temperature with a bellmouth entrance and a screen at the entrance. These curves should be comparable with the case analyzed in which the initial-velocity profile is uniform. The screen at the entrance should insure a turbulent boundary layer throughout the tube. The data from reference (7) taken with an approach section were not compared with the analysis, because the approach section was apparently not long enough to damp out the large disturbances at its sharp entrance.

Figs. 15 and 16 give experimental data from reference (13) for air flowing through a bank of parallel plates with uniform wall heat flux. Data are given for flow both with and without an unheated bank at the entrance (fully developed and uniform initial-velocity distributions). A $^1/_{32}$-in. gap existed between the first and second banks when the unheated bank was used (plate spacing = $^1/_4$ in.). All data were corrected for heat conduction

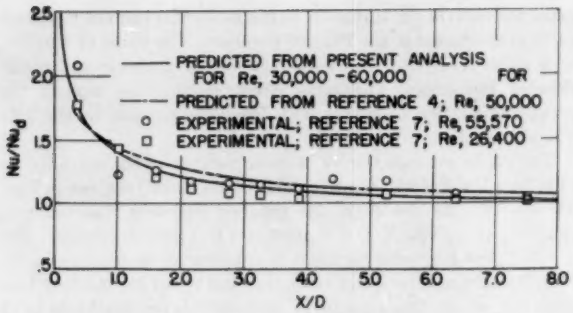

FIG. 14 COMPARISON OF ANALYSIS AND EXPERIMENT FOR AIR FLOWING IN TUBE. PR, 0.73

(Uniform wall temperature, uniform initial velocity and temperature distributions, and constant properties.)

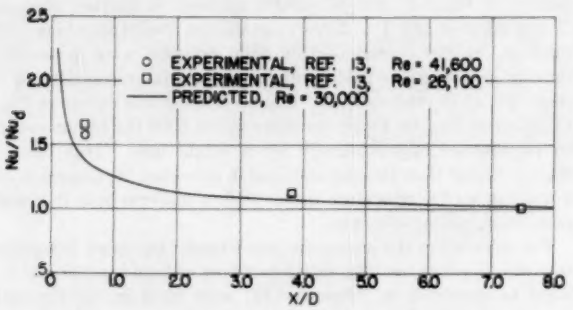

FIG. 15 COMPARISON OF ANALYSIS AND EXPERIMENT FOR AIR FLOWING BETWEEN PARALLEL PLATES. PR, 0.73

(Fully developed velocity distribution, uniform temperature distribution, uniform wall heat flux, and constant properties.)

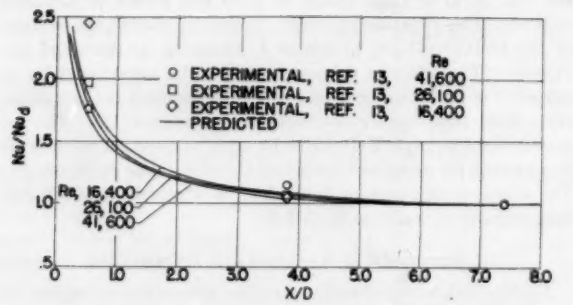

FIG. 16 COMPARISON OF ANALYSIS AND EXPERIMENT FOR AIR FLOWING BETWEEN PARALLEL PLATES. PR, 0.73

(Uniform initial velocity profile, uniform initial temperature profile, uniform wall heat flux, and constant properties.)

along the plates. Temperature differences were small enough that the effect of variable fluid properties could be neglected. For calculating the values of Nu/Nu_d in the figures it was assumed that fully developed heat transfer existed at the trailing edges of the plates ($L/D = 7.5$), as indicated by the analysis. The finite thicknesses of the plates (0.018 in.) should cause enough disturbance to produce a turbulent boundary layer at the entrance.

In all cases the agreement between analysis and experiment is considered good in view of the difficulties associated with obtaining accurate heat-transfer measurements in the entrance region. There is also a possible effect of initial turbulence which was not considered in the analysis. Strictly speaking the initial turbulence or disturbance should be just sufficient to produce transition at the entrance. In the case of a fully developed initial velocity profile the problem of initial turbulence theoretically does not exist. It is, however, necessary that the unheated entrance section be long and that the gap between the unheated and heated sections be small.

HEAT TRANSFER FOR GASES WITH VARIABLE PROPERTIES WITH UNIFORM WALL HEAT FLUX

The equations giving the relation between boundary-layer thickness and distance along the tube for the present case, as well as equations for the Nusselt number and Reynolds number with properties evaluated at the wall, have already been obtained, Equations [8], [11], and [12]. Nusselt numbers and Reynolds numbers with properties evaluated at the inlet temperature can be calculated from the following equations, which can easily be verified

$$Nu_i = \frac{Nu_0}{(t_i/t_0)^d} \quad \ldots\ldots [15]$$

$$Re_i = \frac{Re_0}{(t_b/t_0)(t_i/t_0)^d} \quad \ldots\ldots [16]$$

where $t_b/t_0 = 1 - \beta t_b^+$ and $t_i/t_0 = 1 - \beta t_{b_h}^+ (t_{b_h} = t_i)$. In obtaining the relation for Re_i the continuity relation $\rho_b u_b = \rho_i u_i$ has been used. Another useful parameter is q_i' which can be calculated from

$$q_i' = \frac{\beta(t_b/t_0)}{u_b^+(t_i/t_0)} \quad \ldots\ldots [17]$$

Equation [17] can be obtained from the definition of q_i' and the perfect-gas law for constant pressure, $t_0/t_b = \rho_b/\rho_0$, for $\rho_b u_b$ is constant along the tube. The important property of q_i' is that it does not vary along the length of the tube.

As mentioned previously, ρ, μ, and k are considered variable whereas c_p and Pr are considered constant. It is assumed that $\mu/\mu_0 = k/k_0 = (t/t)^d$, where $d \approx 0.68$ for air and most gases. In applying the results of the analysis for calculating heat-transfer coefficients it is necessary to make these same assumptions for the variation of properties.

Case of Fully Developed Velocity Profile ($\delta = r_0$). Local Nusselt numbers for this case with properties evaluated at the inlet temperature are plotted against X/D for various values for Re_i and q_i' (heat flux) in Fig. 17. Interpolation was necessary for obtaining the variation of Nu_i with X/D for constant values of Re_i and q_i'. Each curve extends to the point where $\delta_h = r_0$.

Comparison of the curves for $q_i' = 0$, 0.004, and —0.0025 indicates a decrease in Nu_i at a given X/D for heat addition to the gas and an increase for heat extraction from the gas. For both heat addition and extraction, Nu_i increases with X/D for large values of X/D. When the curves are extended beyond the entrance region as in Fig. 17(d), it is seen that Nu_i continues to increase. The increases in Nusselt number with X/D are caused by the variation of properties along the tube and across the tube. The increases are due principally to the variation of t_0/t_b, which decreases along the tube for both heat addition to and extraction from the gas.

It is clear from the foregoing discussion that fully developed heat transfer, in the sense that the heat-transfer coefficient becomes independent of X/D, cannot be obtained when the properties are variable. Fully developed heat transfer can, however, be obtained in the sense that the relation between the Nusselt number and Reynolds number becomes independent of X/D for sufficiently large values of X/D when the properties are evaluated at the proper reference temperature. It is shown in reference (6) that for fully developed heat transfer the reference temperature lies approximately halfway between the wall and bulk tempera-

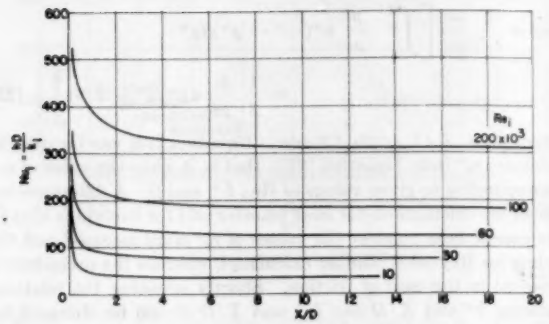

(a) $q_i' = 0$ (constant properties)

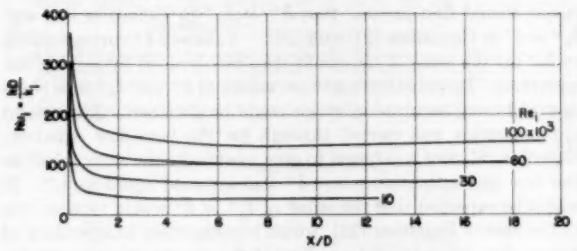

(b) $q_i' = 0.004$ (heat addition to gas)

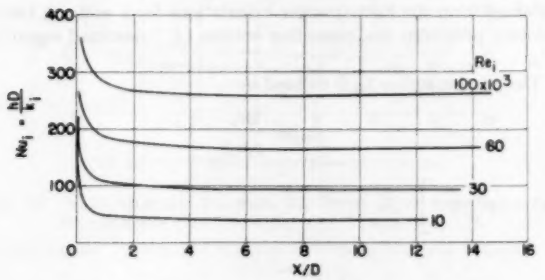

(c) $q_i' = -0.0025$ (heat extraction from gas)

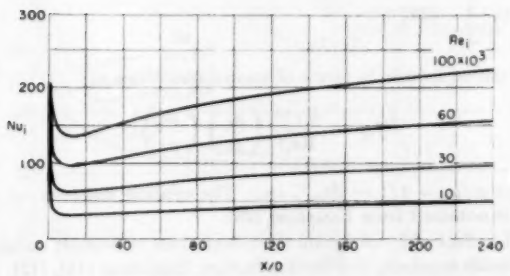

(d) $q_i' = 0.004$ (heat addition to gas, large X/D)

FIG. 17 VARIATION OF NUSSELT NUMBER Nu_i WITH X/D AND REYNOLDS NUMBER FOR GAS FLOWING IN TUBE. PR, 0.73. FULLY DEVELOPED VELOCITY DISTRIBUTION

(Uniform heat flux, uniform initial temperature distribution.)

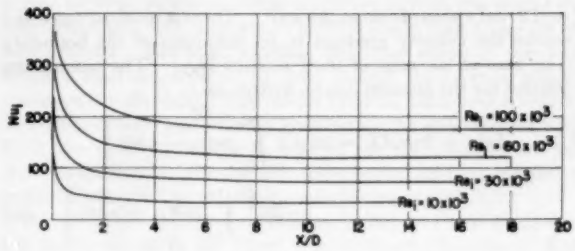

(a) $q_i' = 0$

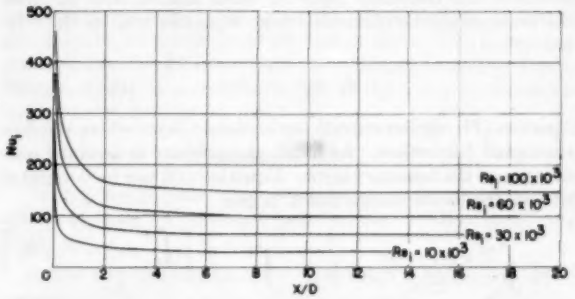

(b) $q_i' = 0.004$

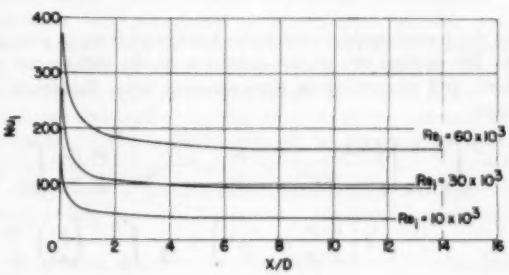

(c) $q_i' = -0.0025$

FIG. 18 VARIATION OF NUSSELT NUMBER Nu_i WITH X/D AND REYNOLDS NUMBER FOR GAS FLOWING IN TUBE. PR, 0.73. UNIFORM INITIAL VELOCITY DISTRIBUTION

(Uniform heat flux, uniform initial temperature distribution.)

tures. In reference (10) it is found that the reference temperature in the entrance region does not vary appreciably from that for fully developed heat transfer; that is, the curves in Fig. 17(*a*) for constant properties can be used for variable properties by evaluating the fluid properties in the Nusselt and Reynolds numbers at a temperature close to the average of the local wall and bulk temperatures. In using that procedure for calculating heat-transfer coefficients from the predicted curves, it is, of course, necessary to assume a constant specific heat and μ and k both proportional to $t^{0.68}$.

Case of Uniform Initial-Velocity Profile. The results for this case are plotted in Fig. 18. These curves are similar to those for a fully developed velocity profile, Fig. 17, but the Nusselt numbers at a given X/D are higher. The relation between δ^+ and X/D which is required for calculating the curves in Fig. 18, will be obtained in the next section.

FRICTION WITH VARIABLE PROPERTIES

The relation between flow-boundary-layer thickness and distance along the tube can be obtained by applying the momentum principle to the differential annulus in Fig. 4 (δ_4 replaced by δ). The X-component of the force acting on the fluid in the annulus is equated to the rate of flow of the X-component of momentum out of the annulus. The force is composed of pressure forces on planes

1 and 2 and a shear force at the wall.[6] There is no shear force at δ because the velocity gradient is, by definition of the boundary layer, zero at the edge of the boundary layer. The momentum equation for the annulus can be written as

$$\delta(2r_0 - \delta)dp + 2r_0\tau_0 dX = 2u_\delta d\left[\int_0^\delta \rho u(r_0 - y)dy\right] - 2d\left[\int_0^\delta \rho u^2(r_0 - y)dy\right] \quad \ldots [18]$$

Equation [18], in the two-dimensional form, was first obtained by von Kármán and has been used extensively for calculating the growth of the boundary layer for fluids flowing over surfaces. The pressure can be eliminated from Equation [18] by the relation

$$dp = -\rho u_\delta du_\delta \quad \ldots [19]$$

Equation [19] applies outside the boundary layer where the flow is assumed frictionless. As usual, the pressure is assumed constant across the boundary layer. Equation [18] can be integrated between the tube entrance and X to give

$$X = \int_{u_i}^{u_\delta} \frac{\delta(2r_0 - \delta)}{2\tau_0 r_0}\rho u_\delta du_\delta - \int_0^{[\ ]} \frac{d\left[\int_0^\delta \rho u^2(r_0 - y)dy\right]}{\tau_0 r_0} + \int_0^{[\ ]} \frac{u_\delta d\left[\int_0^\delta \rho u(r_0 - y)dy\right]}{\tau_0 r_0} \quad \ldots [20]$$

where the boundary-layer thickness has been taken as zero at $X = 0$. By making use of the definition of the differential of a product, and converting to dimensionless form, Equation [20] becomes

$$X/D = \int_{\mathrm{Re}_i/2}^{[\ ]} \left[\frac{\delta^+(2r_0^+ - \delta^+)}{4r_0^{+2}}\frac{\mu_i}{\mu_0}u_\delta^+ - \frac{1}{2r_0^{+2}}\frac{\rho_0}{\rho_i}\frac{\mu_i}{\mu_0}\int_0^{\delta^+}\frac{\rho}{\rho_0}u^+(r_0^+ - y^+)dy^+\right] d\left[\frac{\mu_0}{\mu_i}\frac{\rho_i}{\rho_0}u_\delta^+ r_0^+\right] + \frac{1}{2}\int_0^{[\ ]}\left(\frac{\mu_i}{\mu_0}\right)^2\frac{\rho_0}{\rho_i}\frac{1}{r_0^{+2}} d\left[\left(\frac{\mu_0}{\mu_i}\right)^2\frac{\rho_i}{\rho_0}\int_0^{\delta^+}(u_\delta^+ - u^+)u^+\frac{\rho}{\rho_0}(r_0^+ - y^+)dy^+\right] \quad \ldots [21]$$

where $\mu_i/\mu_0 = (1 - \beta t_{\delta_h}{}^+)^d$, $\rho_i/\rho_0 = 1/1 - \beta t_{\delta_h}{}^+$, etc.[7] Equation [20] can be used for $\delta^+ <$ or $> \delta_h{}^+$ if it is remembered that $\rho = \rho_{\delta_h}$ for $y^+ \geq \delta_h{}^+$ and $u^+ = u_\delta{}^+$ for $y^+ \geq \delta^+$. In general, it is sufficiently accurate, for Prandtl numbers close to 1, to assume that $\delta_h{}^+ = \delta^+$ in solving Equation [20].

In order to solve Equation [21], $r_0{}^+$ must be known in terms of Re_i. This relation can be obtained from the law of conservation of mass. For a constant area passage, this law gives

$$\rho_i u_i = \frac{2}{r_0{}^2}\int_0^{r_0}\rho u(r_0 - y)dy \quad \ldots [22]$$

Converting Equation [22] to dimensionless form and breaking the integral into two parts gives

$$\mathrm{Re}_i = \frac{4}{r_0{}^+}\frac{\mu_0}{\mu_i}\left[\int_0^{\delta^+}\frac{\rho}{\rho_0}u^+(r_0^+ - y^+)dy^+ + \frac{1}{2}\frac{\rho_i}{\rho_0}u_\delta{}^+(r_0^+ - \delta^+)^2\right] \quad \ldots [23]$$

where $\mu_i/\mu_0 = (1 - \beta t_{\delta_h}{}^+)^d$, etc. Equation [23] can be used to eliminate $r_0{}^+$ from Equation [21]; that is, it gives the value of $r_0{}^+$ corresponding to given values of Re_i, δ^+, and β. A difference between the calculations for heat transfer and for friction is that in the case of heat transfer the values of $r_0{}^+$ were assumed and the values for Reynolds number calculated, whereas the procedure is reversed in the case of friction. Strictly speaking the relations between δ^+ and X/D and $\delta_h{}^+$ and X/D should be obtained by solving Equations [8], [21], and [23] simultaneously by iteration, since both δ^+ and $\delta_h{}^+$ are required for solving each equation; that is one should first assume that $\delta^+ = \delta_h{}^+$ in Equation [8], and $\delta_h{}^+ = \delta^+$ in Equations [21] and [23]. Values of δ^+ corresponding to $\delta_h{}^+$ (at the same X/D) could then be obtained by solving the equations. By substituting these values of δ^+ and $\delta_h{}^+$ into them new and more accurate relations could be obtained. The second approximation was carried through for the heat-flow equation, Equation [8], and was found to give essentially the same result as the first approximation where δ^+ was assumed equal to $\delta_h{}^+$. It would be expected that the effect of $\delta_h{}^+ \neq \delta^+$ would be even less in the case of Equation [21], which is completely independent of $\delta_h{}^+$ for β or $q_i' = 0$. The values of β corresponding to the desired values of q_i' and Re_i for use in Equations [21] and [23] are obtained from the heat-transfer calculations for a uniform initial velocity profile in the preceding section ($\delta_h{}^+$ assumed equal to δ^+).

The friction factor $f_{\tau i}$ is defined by

$$f_{\tau i} \equiv \frac{2\tau_0}{\rho_i u_i{}^2}$$

and can be written in terms of known quantities as

$$f_{\tau i} = \frac{8r_0{}^{+2}}{\mathrm{Re}_i{}^2}\left(\frac{\rho_i}{\rho_0}\right)\left(\frac{\mu_0}{\mu_i}\right)^2 \quad \ldots [24]$$

where $\rho_i/\rho_0 = 1/1 - \beta t_{\delta_h}{}^+$, etc. The relation between $r_0{}^+$ and Re_i is obtained from Equation [23].

The effect of $\delta^+ \neq \delta_h{}^+$ on the calculations of Nusselt numbers, Reynolds numbers, and friction factors, Equations [11], [12], and [24], was checked and found to be small, although somewhat greater than the corresponding effect on the calculated values of X/D from Equations [8] and [21]. The assumption that $\delta^+ = \delta_h{}^+$ was therefore not made in calculating those quantities.

Friction factors $f_{\tau i}$ are plotted against X/D for various values of Re_i and q_i' (heat flux) in Fig. 19. The curves extend to the points where the flow is fully developed ($\delta^+ = r_0{}^+$), except those for $q_i' = 0.004$. For those curves fully developed flow is obtained at the following values of $f_{\tau i}$ and X/D: For $\mathrm{Re}_i = 10 \times 10^3$, $f_{\tau i} = 0.0104$ at $X/D = 22.9$, for $\mathrm{Re}_i = 30 \times 10^3$, $f_{\tau i} = 0.00760$ at $X/D = 31.1$, for $\mathrm{Re}_i = 60 \times 10^3$, $f_{\tau i} = 0.00631$ at $X/D = 40.6$, and for $\mathrm{Re}_i = 100 \times 10^3$, $f_{\tau i} = 0.00561$ at $X/D = 76.8$. The variations of $f_{\tau i}$ are proportional to the variations of τ_0 along the

[6] In a viscous fluid the normal stresses in planes 1 and 2 differ slightly from the pressure at those planes. For boundary-layer flow, however, the differences are negligible, being of the same order of magnitude as the axial heat-conduction term investigated in the Appendix.

[7] The effects of static pressure and temperature variation along the tube outside the boundary layer on the properties are neglected; that is, the Mach number is assumed low. The effect of Mach number is the subject of a separate investigation.

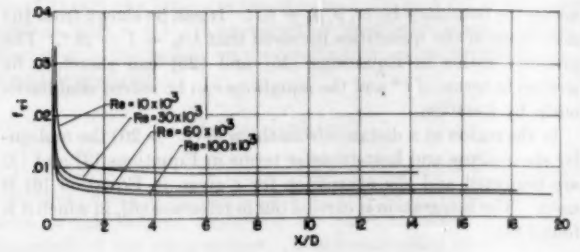

(a) $q_i' = 0$ (constant properties)

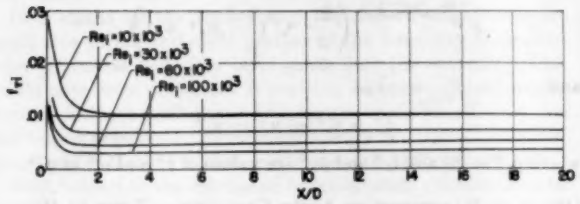

(b) $q_i' = 0.004$ (heat addition to gas)

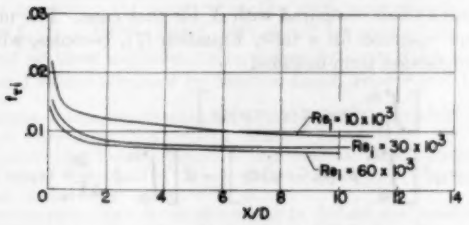

(c) $q_i' = -0.0025$ (heat extraction from gas)

FIG. 19 VARIATION OF FRICTION f_{ri} WITH X/D AND REYNOLDS NUMBER FOR GAS FLOWING IN A TUBE. PR, 0.73

(Uniform initial velocity and temperature distributions, and uniform heat flux.)

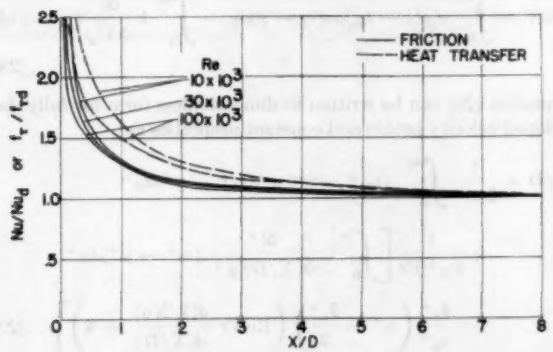

FIG. 20 COMPARISON OF FRICTION AND HEAT TRANSFER IN ENTRANCE REGION OF A TUBE. PR, 0.73

(Uniform initial velocity and temperature distributions, uniform wall heat flux, and constant properties.)

tube. In general the shear stress near the entrance is slightly higher for heat extraction ($q_i' = -0.0025$) than for heat addition to the gas, apparently because of a thinner boundary layer for heat extraction. Farther down the tube the shear stress for heat addition becomes greater than that for no heat transfer. If the curves for heat extraction were continued beyond the points for fully developed flow they would become lower than those for no heat transfer. For heat addition, the shear stress at the wall actually increases with X/D, even though the boundary-layer thickness is increasing. This occurs because, with heat addition, both the viscosity and velocity gradient at the wall increase with X/D, the latter increasing because of the expansion of the gas [$\tau_0 = (\mu\, d\mu/dy)_0$]. The opposite trend occurs for heat extraction from the gas; that is, the shear stress decreases with X/D.

Fig. 20 gives a comparison between friction and heat transfer in the entrance region for gases with constant properties. The curves for heat transfer are higher than those for shear stress. This should not, however, be taken as an indication that a gain in heat-transfer to pressure-drop ratio is necessarily obtained by using short passages, inasmuch as the curves in Figs. 19 and 20 give only the friction pressure gradient or drop. The momentum pressure drop due to velocity-profile development and to density changes should, of course, be added to this value to obtain the total pressure drop in the tube.

SUMMARY OF RESULTS

The following results were obtained from the analysis of the entrance region for turbulent heat transfer and flow in smooth passages:

1 The thin thermal boundary layers and consequently severe temperature gradients at the wall near the entrance produced high heat-transfer coefficients near the entrance. The entrance lengths required to produce fully developed turbulent heat transfer were, however, much less than those for laminar heat transfer. Approximately fully developed turbulent heat transfer was, in general, attained in an entrance length less than 10 diameters.

2 The effects of wall boundary condition (uniform wall heat flux or uniform wall temperature) and of passage shape (round tube or parallel plates) on heat transfer in the entrance region were small. This result would not be expected to apply to liquid metals.

3 The use of a uniform rather than a fully developed initial velocity profile increased the heat-transfer coefficients in the entrance region.

4 In general, the entrance effect (local Nusselt number divided by fully developed Nusselt number) for heat transfer decreased as Prandtl number increased above 1. At a low Prandtl number (Pr = 0.01) the results were given by plotting Nusselt number against Graetz number for various Peclet numbers and were found to approach a single line at low Peclet numbers.

5 Substantial agreement was obtained between analysis and experiment for heat transfer to air flowing in the entrance regions of tubes and parallel plates.

6 The effect of variable properties on the local Nusselt number correlation for gases was to decrease the Nusselt number with conductivity based on the inlet temperature for heat addition to the gas and to increase it for heat extraction from the gas at a given ratio of distance from the entrance to tube diameter X/D and inlet Reynolds number. In using the curves to obtain heat-transfer coefficients it is necessary to use the same assumptions for variation of properties as were used in the analysis; that is, constant specific heat and viscosity and thermal conductivity both proportional to the absolute temperature raised to the 0.68 power must be used.

7 In general, the shear stress near the entrance (variable properties) was slightly higher for heat extraction than for heat addition to the gas, but the trends were reversed at large values of X/D. The ratio of local shear stress to the fully developed value (constant properties) was less than the corresponding ratio for heat-transfer coefficients in the entrance region.

BIBLIOGRAPHY

1 "Modern Developments in Fluid Dynamics," by Sidney Goldstein, Clarendon Press, Oxford, England, 1938, pp. 299–310.

2 "Steady Flow in the Transition Length of a Straight Tube," by H. L. Langhaar, Trans. ASME, vol. 64, 1942, p. A-55.

3 "Heat Transfer," by Max Jacob, John Wiley & Sons, Inc., New York, N. Y., vol. 1, 1929, pp. 451–464.

4 "Heat Transfer in a Turbulent Liquid or Gas Stream," by H. Latzko, NACA TM 1068, 1944.

5 "Forced Convection Heat Transfer in Thermal Entrance Regions, Part II," by H. F. Poppendiek and L. D. Palmer, ORNL 914, Metallurgy and Ceramics, Reactor Exp. Eng. Division, Oak Ridge National Laboratory, Oak Ridge, Tenn., May 26, 1952. Contract No. W-7405, eng. 26.

6 "Heat Transfer and Fluid Friction for Fully Developed Turbulent Flow of Air and Supercritical Water With Variable Fluid Properties," by R. G. Deissler, Trans. ASME, vol. 76, 1954, pp. 73–85.

7 "An Investigation of Aircraft Heaters XXVII—Distribution of Heat Transfer Rate in the Entrance Section of a Circular Tube," by L. M. K. Boelter, G. Young, and H. W. Iversen, NACA TN 1451, 1948.

8 "Introduction to the Transfer of Heat and Mass," by E. R. G. Eckert, McGraw-Hill Book Company, Inc., New York, N. Y., first edition, 1950, p. 74.

9 "Analysis of Turbulent Heat Transfer, Mass Transfer, and Friction in Smooth Tubes at High Prandtl and Schmidt Numbers," by R. G. Deissler, NACA TN 3145, 1954.

10 "Analysis of Turbulent Heat Transfer and Flow in the Entrance Regions of Smooth Passages," by R. G. Deissler, NACA TN 3016, 1953.

11 "Introduction to the Transfer of Heat and Mass," by E. R. G. Eckert, McGraw-Hill Book Company, Inc., New York, N. Y., first edition, 1950, p. 87.

12 "Analysis of Fully Developed Turbulent Heat Transfer in Smooth Tubes at Low Peclet Numbers with Application to Liquid Metals," by R. G. Deissler, NACA RM E52F05.

13 "Experimental Heat-Transfer and Friction Coefficients for Air Flowing Through Stacks of Parallel Flat Plates," by E. W. Sams and W. F. Weiland, Jr., NACA RM E54F11.

Appendix

Solution of Equations for Shear Stress and Heat Transfer

For the region close to the wall ($y^+ < 26$), Equations [3] and [4] can be written in integral form as

$$u^+ = \int_0^{y^+} \frac{dy^+}{\frac{\mu}{\mu_0} + \frac{\rho}{\rho_0} n^2 u^+ y^+ (1 - e^{-n^2 u^+ y^+})} \quad \ldots [25]$$

and

$$t^+ = \int_0^{y^+} \frac{dy^+}{\frac{k}{k_0}\frac{1}{\mathrm{Pr}_0} + \frac{\rho}{\rho_0} n^2 u^+ y^+ (1 - e^{-n^2 u^+ y^+})} \quad \ldots [26]$$

where assumptions 1, 2, and 3 have been used. In calculating the curves for various Prandtl numbers in Fig. 1, where the properties are constant, Equation [25] must first be solved by iteration, inasmuch as u^+ occurs on both sides of the equation. By using the relation between u^+ and y^+ thus obtained, Equation [26] can then be solved.

For gases with variable viscosity, conductivity, and density (Figs. 2 and 3), it is assumed that $\mu/\mu_0 = k/k_0 = (t/t_0)^{0.68}$. From the perfect-gas law and the assumption of constant pressure across the boundary layer, $\rho/\rho_0 = t_0/t$. It can be shown from the definitions of the quantities involved that $t/t_0 = 1 - \beta t^+$. The property ratios in Equations [25] and [26] can therefore be written in terms of t^+ and the equations can be solved simultaneously by iteration.

In the region at a distance from the wall ($y^+ > 26$) the molecular shear-stress and heat-transfer terms in Equations [3] and [4] are neglected and the expression for ϵ given in Equation [6] is used. The integration is carried out in reference (6), in which it is found that

$$y^+ = \frac{y_1^+ e^{\frac{-2\kappa}{\beta}\sqrt{1-\beta(u^+-u_1^+ + t_1^+)}}\left[\frac{2\kappa}{\beta}\sqrt{1-\beta(u^+-\mu_1^+ + t_1^+)} + 1\right]}{e^{\frac{-2\kappa}{\beta}\sqrt{1-\beta t_1^+}}\left(\frac{2\kappa}{\beta}\sqrt{1-\beta t_1^+} + 1\right)}$$

and

$$t^+ = t_1^+ + u^+ - u_1^+$$

where $y_1^+ = 26$ and t_1^+ and u_1^+ are values of t^+ and u^+ at y_1^+.

Order of Magnitude of Axial Conduction Term in Heat-Flow or Energy Equation

The low-Prandtl-number case will be checked inasmuch as δ_h is not always small compared with X for that case. The integral heat-flow equation for a tube, Equation [7], becomes, with the axial conduction term included

$$q_0 r_0 dX = d\left[\int_0^{\delta_h} t\rho u c_p g(r_0 - y)dy\right] - c_p g t_{\delta_h} d\left[\int_0^{\delta_h} \rho u(r_0 - y)dy\right] - d\left[\int_0^{\delta_h} k\left.\frac{\partial t}{\partial X}\right|_y (r_0 - y)dy\right] \quad \ldots [27]$$

where the last term is the axial conduction term. Axial conduction by turbulence is not included, because, as indicated in Fig. 13, the effect of turbulence should be small at the low Peclet numbers where δ_h is not $\ll X$. Equation [27] can be integrated with respect to X for uniform heat flux to give

$$q_0 r_0 X = \int_0^{\delta_h} c_p g(t - t_{\delta_h})\rho u(r_0 - y)dy - \int_0^{\delta_h} k\left.\frac{\partial t}{\partial X}\right|_y (r_0 - y)dy \quad \ldots [28]$$

Equation [28] can be written in dimensionless form for fully developed velocity profile and constant properties as

$$X/D = \frac{1}{2r_0^{+2}}\int_0^{\delta_h^+} (t_{\delta_h}^+ - t^+)\, u^+ (r_0^+ - y^+)dy^+ + \frac{1}{4r_0^{+2}\mathrm{Pr}}\left[\int_0^{\delta_h^+} \frac{\partial t^+}{\partial (X/D)|_{y^+}} (r_0^+ - y^+)dy^+ - \frac{\delta_h^+}{u_0^+}\left(r_0^+ - \frac{\delta_h^+}{2}\right)\left(\mathrm{Re}\,\mathrm{Pr}\,\frac{d(1/\mathrm{Nu})}{d(X/D)} + 4\right)\right] \quad \ldots [29]$$

where the relation

$$\pi D q_0 = \rho g \frac{\pi}{4} D^2 u_0 c_p \frac{dt_b}{dX}$$

was used. The last term in Equation [29] is again the axial conduction term. The ratio of the last to the first term in Equation [29] was checked from the calculations for a Prandtl number of 0.01 (Figs. 12 and 13). At a Reynolds number of 13,000, the ratio was found to be 0.009 at $X/D = 1.1$. At a Reynolds num-

ber of 21,000, the ratio was found to be 0.008 at $X/D = 0.8$ and 0.002 at $X/D = 3.1$. It appears from these calculations that the effect of axial conduction on the results given in the present paper should be negligible.

Discussion

J. P. HARTNETT.[8] The present work of the author on entrance regions of pipes and channels, together with his previous contributions on this subject, represents the most extensive analytical treatment of this phenomenon. It is encouraging to the writer that the predicted thermal entrance-length results agree reasonably well with the experimental results of the writer[9] for Prandtl numbers of 7 to 50.

It is stated by the author that the present calculations are applicable to the turbulent portion of the boundary layer even when a laminar boundary layer exists near the entrance. This would offer some difficulties in practice, however. Experimental results[10] indicate a substantially longer entrance length when the flow begins as laminar, this certainly being a function of the turbulence level of the free stream and of the wall-surface conditions.

With respect to the calculated hydrodynamic entrance lengths necessary for the attainment of fully developed flow, the present constant property analysis agrees well with the analysis of Pascucci[11] who obtained $L_h/D = [3.80 \log_{10} \mathrm{Re} - 2.14]$. Both of these analyses are somewhat higher than the corrected prediction[11] of Latzko[12] $L_h/D = 0.623\ (\mathrm{Re})^{1}/_{4}$. It should be pointed out, however, that all these analyses are considerably lower than the experimental values obtained by Schiller and Kirsten[13] who found lengths of 50 diameters and greater to be necessary for the attainment of fully developed flow.

AUTHOR'S CLOSURE

It is encouraging to the author that Dr. Hartnett's experimental results for heat transfer to liquids in the entrance region are in reasonable agreement with those predicted. Those data were not available at the time of writing the paper and so could not be included.

The author's statement regarding the possibility of applying the results of the analysis to the turbulent portion of the boundary layer in the presence of a laminar boundary layer near the entrance was based on an assumption by Prandtl. That assumption, in turn, was apparently based on experimental data for flow over flat plates. It seems reasonable that the same assumption should apply also to flow in the entrance region of a tube. However, in the experiments referred to by Dr. Hartnett, it appears that, except at the highest Reynolds number (101,600), the flow was laminar throughout the entrance region, inasmuch as the friction factors were nearly all below the fully developed values. The results of an analysis for turbulent flow could therefore not be applied to those experiments. The unusually long passage length in which laminar flow occurred was apparently caused by the smooth bellmouth entrance used. On the basis of those experiments it would seem that the analysis cannot be applied at low Reynolds numbers unless a disturbance is present at the entrance.

In connection with the comparison of the analysis with the experimental results of Schiller and Kirsten it should be mentioned that the long entrance lengths obtained by those authors referred to the lengths required for the velocity profile to develop, rather than for the pressure gradient or shear stress to reach their fully developed values. They apparently did not measure pressure drops. The same result was obtained in the author's experiments,[14] where the velocity profile near the tube center was still developing slightly at values of X/D greater than 75 although the pressure gradients had long before reached their fully developed values. The predicted pressure drops of the author (10) are in good agreement with the measured values in reference (13).

---

[8] Assistant Professor, Mechanical Engineering Department, University of Minnesota, Minneapolis, Minn. Assoc. Mem. ASME.

[9] "Experimental Determination of the Thermal Entrance Length for the Flow of Water and of Oil in Circular Pipes," by J. P. Hartnett, published in this issue, pp. 1211–1220.

[10] "Druckverlust und Wärmeübergang in Anlauf der turbulenten Rohrströmung," by W. Linke and H. Kunze, Allgemeine Wärmetechnick, Jahrgang 4, no. 4. 1953.

[11] "Sul Moto di Fluidi in Regime Turbolenta Nel tratto Iniziale der con Distribuzione Logaritmica di Velocita," by L. Pascucci, atti di Guidonia, 4, 1953.

[12] "Der Wärmeübergang an einen turbulenten Flüssigkeits-oder Gasstrom," by H. Latzko, *Zeitschrift für angewandte Mathematik und Mechanik*, vol. 1, no. 4, 1921, pp. 268–290.

[13] "Die Entwicklung der Geschwindigkeitsverteilung bei der turbulenten Rohrströmung," by Ludwig Schiller and Herbert Kirsten, *Zeitschrift für technische Physik*, vol. 10, 1929, pp. 268–274.

[14] Analytical and Experimental Investigation of Adiabatic Turbulent Flow in Smooth Tubes," by R. G. Deissler, NACA TN 2138, 1950.

An Approximate Solution of Compressible Turbulent Boundary-Layer Development and Convective Heat Transfer in Convergent-Divergent Nozzles

By D. R. BARTZ,[1] PASADENA, CALIF.

A method has been derived for computing the development of the velocity boundary layer, the temperature boundary layer, and the local convective heat transfer in convergent-divergent nozzles. The method is based on approximate solutions of the integral momentum and integral energy equations for compressible turbulent boundary layers. To obtain the solutions, a flow model is adopted for which are prescribed the velocity and temperature profiles in the boundary layer, the skin-friction law, and the relation between heat and momentum transfer. The local heat-transfer coefficient is expressed as an explicit function of the boundary-layer thicknesses. The effects of nozzle size and throat radius of curvature on boundary-layer development and heat transfer are determined for certain similar nozzle contours in common use. The results of the solution are demonstrated by a sample calculation for a conventional rocket nozzle operating under typical conditions. The computed local heat fluxes were found to be in approximate agreement with those measured during rocket-motor tests using a nozzle of the same contour.

Nomenclature

The following nomenclature is used in the paper:

- a = constant in temperature-distribution equation, defined by Equation [45]
- A = local channel-flow area
- b = constant in temperature-distribution equation, defined by Equation [45]
- b' = constant in temperature-distribution equation, defined by Equation [53]
- c = constant in temperature-distribution equation, defined by Equation [45]
- c' = constant in temperature-distribution equation, defined by Equation [53]
- C_f = local coefficient of skin friction
- C_h = local coefficient of heat tranfer
- C_p = specific heat at constant pressure
- C_v = specific heat at constant volume
- F = area-ratio-derivative proportionality factor, defined by Equation [33]
- h = local enthalpy in the temperature boundary layer
- h_g = local heat-transfer coefficient
- h_L = coolant heat-transfer coefficient
- H = local enthalpy at the outer edge of temperature boundary layer
- I_1, I_2, I_1', I_2' = definite integrals used for evaluating the boundary-layer shape parameters, defined by Equations [47], [49], [54], and [55], respectively.
- k = thermal conductivity
- l = nozzle wall thickness
- M = Mach number
- p = pressure
- Pr = Prandtl number = $\mu C_p/k$
- q = local heat-transfer rate
- r = local distance from axis to wall
- r_t = radius of curvature at nozzle throat
- Re = Reynolds number
- t = local static temperature in boundary layer
- t_0 = local stagnation temperature in boundary layer
- T = local static temperature at outer edge of temperature boundary layer
- T_L = coolant bulk temperature
- T_0 = local stagnation temperature at outer edge of temperature boundary layer
- T_w = local wall temperature
- u = local velocity in the x-direction in velocity boundary layer
- U = local velocity in x-direction at outer edge of velocity boundary layer
- v = local velocity in y-direction in velocity boundary layer
- x = distance along wall in direction of flow
- x_n = distance along nozzle wall from entrance to exit
- y = distance normal to wall
- Z = velocity-distribution variable defined by Equation [45]
- Z' = temperature-distribution variable defined by Equation [52]
- α = nozzle-divergence half angle, deg
- β = nozzle-convergence half angle, deg
- γ = ratio of specific heats = C_p/C_v
- δ = local velocity boundary-layer thickness
- δ^* = local velocity boundary-layer displacement thickness
- Δ = local temperature boundary-layer thickness
- Δ^* = local temperature boundary-layer displacement thickness

[1] Research Engineer, Jet Propulsion Laboratory, California Institute of Technology. Assoc. Mem. ASME.

Contributed by the Heat Transfer Division and presented at the Annual Meeting, New York, N. Y., November 28–December 3, 1954, of The American Society of Mechanical Engineers.

Note: Statements and opinions advanced in papers are to be understood as individual expressions of their authors and not those of the Society. Manuscript received at ASME Headquarters, September 21, 1954. Paper No. 54—A-153.

ϵ = eddy viscosity
θ = local velocity boundary-layer momentum thickness
κ = eddy conductivity
λ = boundary-layer shape parameter, defined by Equation [29]
μ = local viscosity in boundary layer
μ' = local viscosity at outer edge of temperature boundary layer
ρ = local density in boundary layer
ρ' = local density at outer edge of temperature boundary layer
σ = skin-friction-coefficient factor, defined in Equation [16]
τ = shear stress
ϕ = local temperature boundary-layer energy thickness
Φ = the dissipation function, defined by Equation [19]

Subscripts

e = exit end of nozzle
i = incompressible
w = related to conditions at wall
x = based on length along wall
xy = in x-direction, along x,z-plane
δ = based on boundary-layer thickness
θ = based on momentum thickness
* = related to conditions at $M = 1$
0 = related to conditions at $M = 0$
1 = computed nozzle
2 = nozzle to be computed

Introduction

The current widespread interest in high-speed aerodynamics and jet propulsion has focused attention on the problem of boundary-layer development and heat transfer in nonadiabatic compressible flow with streamwise gradients of velocity, pressure, and temperature. Since extremely high heat flux associated with this type of flow has frequently limited the operation of such devices, there is a need for a solution of the heat-transfer problem to guide designers in this field.

Solutions of boundary-layer development and heat transfer exist for such flow with laminar boundary layers, having been fairly well established by recent papers based on the von Kármán-Polhausen method (1, 2, 3, and 4).[1] However, for two specific applications of this type of flow, namely, hypersonic wind-tunnel nozzles and rocket-motor nozzles, the Reynolds numbers are generally too high to expect laminar boundary layers to persist through the nozzle. Furthermore, in the case of rocket-motor-nozzle flow, it is expected that, from its turbulent origin, the transition Reynolds numbers would be somewhat lower than normal. Experimental evidence of turbulent boundary layers existing in the divergent portions of nozzles has been obtained from the velocity-profile measurements of Wegener, Winkler, and Sibulkin (5) in a hypersonic wind-tunnel nozzle and from the heat-transfer measurements of Saunders and Calder (6) in a rocket-type nozzle.

It is evident from the few locally measured experimental data obtained in the presence of strong velocity, pressure, and temperature gradients that conventional turbulent-flow heat-transfer correlations, based on measurements on flat plates and in pipes, are inadequate for this purpose. The high maximum values and large gradients of heat transfer observed near the throats of convergent-divergent nozzles have made it extremely difficult to obtain reliable local measurements on which to establish a new correlation.

[1] Numbers in parentheses refer to the Bibliography at the end of the paper.

Methods for computing the turbulent boundary-layer development in compressible adiabatic flow in the presence of axial velocity and pressure gradients have been developed by Tucker (7), Gomf (8), and Tetervin (9) for the purpose of determining wind-tunnel-nozzle boundary-layer corrections. These analyses are based on solutions of the von Kármán integral momentum equation only. The present analysis is based on solutions of both the integral momentum and integral energy equations. It is assumed that the nozzle flow is both one-dimensional and isentropic except for very thin velocity and temperature boundary layers which are nonadiabatic, compressible, and turbulent, and which in general are not the same thickness. In order to solve these equations, it is necessary to prescribe velocity and temperature profiles in the boundary layer, a skin-friction law, and a relation between skin friction and heat transfer. Since there is a lack of information regarding the nature of these relationships in the presence of streamwise pressure, velocity, and temperature gradients, a model having the following assumed characteristics was adopted to permit solution of the equations:

1 There exists throughout the nozzle a fully developed turbulent boundary layer having $^1/_7$-power-law profiles both of velocity and of the difference between stagnation temperature and wall temperature.

2 The local skin-friction coefficients in the nozzle are the same as would exist on a flat plate for the same boundary-layer thickness.

3 Reynolds analogy between momentum transfer and heat transfer exists for the nozzle boundary-layer flow under consideration.

Solution of the integral momentum equation (a linear first-order differential equation having variable coefficients) gives the distribution of the velocity boundary-layer thickness through the nozzle. Substituting these results in the integral energy equation and solving the resulting variable-coefficient linear differential equation, the distribution of the ratio of the temperature boundary-layer thickness to the velocity boundary-layer thickness is obtained. Finally, the heat-transfer coefficient is expressed as an explicit function of the boundary-layer thicknesses, the function resulting from the assumed analogy between heat transfer and momentum transfer.

Analysis

Basic Equations of Axially Symmetric Compressible Boundary-Layer Flow

For very thin axially symmetric boundary layers, Goldstein (10) shows that the boundary-layer approximation forms of the momentum and energy equations are the same as for two-dimensional boundary layers if the co-ordinate system is taken as shown

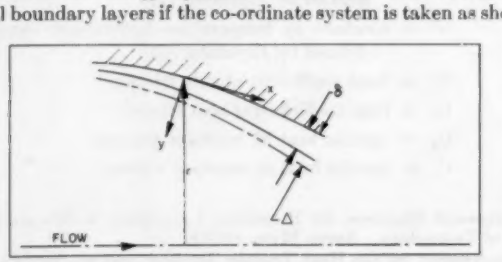

Fig. 1 Co-Ordinate System

in Fig. 1. The steady-state forms of these equations are

$$\rho u \frac{\partial u}{\partial x} + \rho v \frac{\partial u}{\partial y} = -\frac{\partial p}{\partial x} + \frac{\partial}{\partial y} \mu \left(\frac{\partial u}{\partial y}\right) \quad \text{[1]}$$

$$\rho u \frac{\partial h}{\partial x} + \rho v \frac{\partial h}{\partial y} = u \frac{\partial p}{\partial x} + \frac{\partial}{\partial y} k \left(\frac{\partial t}{\partial y} \right) + \Phi \quad [2]$$

The continuity equation for axially symmetric boundary layers is

$$\frac{\partial \rho u}{\partial x} + \frac{\partial \rho v}{\partial y} + \frac{\rho u}{r} \frac{\partial r}{\partial x} = 0 \quad [3]$$

If these equations are considered to be expressed in terms of the temporal mean values of the variables ρu, u, ρv, p, h, and t, the equations can be applied to turbulent boundary layers. Such a procedure results in neglecting the Reynolds normal stress and in using the molecular coefficients μ and k rather than the sums of the molecular and eddy coefficients $(\mu + \epsilon)$ and $(k + \kappa)$ (11). However, in the present analysis, using the integrated momentum and energy equations, μ and k are used only in computing the shear stress and heat transfer at the wall.

The Integral Momentum Equation

Derivation. Extending the derivation of the integral momentum equation given by Goldstein[3] to the case of a compressible axially symmetric boundary layer, the form of the integral momentum equation obtained by integrating Equation [1] over the velocity boundary-layer thickness δ is

$$\frac{d\theta}{dx} + \theta \left[\frac{1}{\rho' U^2} \frac{d\rho' U^2}{dx} + \left(\frac{\delta^*}{\theta} \right) \frac{1}{U} \frac{dU}{dx} + \frac{1}{r} \frac{dr}{dx} \right] = \frac{(\tau_{xy})_{y=0}}{\rho' U^2} \quad [4]$$

where for compressible boundary layers the definitions of θ and δ^* are

$$\theta \equiv \int_0^\delta \frac{\rho u}{\rho' U} \left(1 - \frac{u}{U} \right) dy \quad \text{(momentum thickness)} \quad [5]$$

$$\delta^* \equiv \int_0^\delta \left(1 - \frac{\rho u}{\rho' U} \right) dy \quad \text{(displacement thickness)} \quad [6]$$

Equation [4] can be put into a form more convenient for computation by noting that from the definition of the velocity of sound and the equations of one-dimensional isentropic-flow theory

$$d(\rho' U^2) = \rho' U^2 (2 - \mathbf{M}^2) \frac{dU}{U} \quad [7]$$

and

$$\frac{dU}{U} = \frac{-1}{(1 - \mathbf{M}^2)} d \ln \frac{A}{A_*} \quad [8]$$

and noting that for an axially symmetric nozzle where $A/A_* = (r/r_*)^2$

$$\frac{dr}{r} = \frac{1}{2} d \ln \frac{A}{A_*} \quad [9]$$

$$\frac{d\theta}{dx} + \frac{\theta}{2} \left[\frac{\mathbf{M}^2 - 2(\delta^*/\theta) - 3}{1 - \mathbf{M}^2} \right] \frac{d}{dx} \ln \frac{A}{A_*} = \frac{C_f}{2} \quad [10]$$

where

$$\frac{(\tau_{xy})_{y=0}}{\rho' U^2} \equiv \frac{C_f}{2}$$

At $\mathbf{M} = 1$, the form of the coefficient of θ in Equation [10] is indeterminant but can be shown to equal

$$\frac{1 + (\delta^*/\theta)}{\sqrt{\left(1 + \frac{\gamma - 1}{2} \right) (r_* r_c)}} \quad [11]$$

Solution. The distributions of A/A_* and $\mathbf{M}$ are known from the nozzle geometrical configuration and the assumption that outside of the boundary layer the flow is both isentropic and one-dimensional.

To evaluate the boundary-layer shape parameters δ^*/θ and θ/δ (which will appear in the $C_f/2$ equation) from Equations [5] and [6], only the velocity and temperature distributions through the boundary layers must be prescribed. In the absence of evidence to indicate the possible changes in the boundary-layer velocity distribution due to a strong favorable pressure gradient, it was assumed, as one characteristic of the model, that the $1/7$-power velocity profile persists throughout the nozzle. Velocity profiles of the $1/7$ power

$$\frac{u}{U} = \left(\frac{y}{\delta} \right)^{1/7} \quad [12]$$

have been found to fit velocity distributions measured in low-speed turbulent boundary layers on flat plates except very near the wall. This power-law velocity profile also was found to fit a velocity distribution measured near the working section of a hypersonic wind-tunnel nozzle at $\mathbf{M} = 7$ (reference 5). Although Equation [12] does not satisfy the actual velocity gradient at the wall, it gives results which generally agree with experimental results when integrated over the boundary-layer thickness, as in Equations [5] and [6]. Although the selection of $1/7$ as the power of the velocity distribution is arbitrary, it is significant to note that boundary-layer shape parameters evaluated by Tucker (7) were fairly insensitive to changes in the power from $1/6$ to $1/11$.

The assumption of a $1/7$-power distribution of the difference between stagnation temperature and wall temperature in the boundary layer

$$\frac{t_0 - T_w}{T_0 - T_w} = \left(\frac{y}{\Delta} \right)^{1/7} \quad [13]$$

as one of the characteristics of the model, was made with much the same justification as that used for the velocity profile. Expressed in terms of static temperatures, the distribution given by Equation [13] is

$$\frac{t}{T} = \frac{T_w}{T_0} \left(1 + \frac{\gamma - 1}{2} \mathbf{M}^2 \right) + \left(1 - \frac{T_w}{T_0} \right) \left(1 + \frac{\gamma - 1}{2} \mathbf{M}^2 \right) \left(\frac{y}{\Delta} \right)^{1/7} - \left(\frac{\gamma - 1}{2} \mathbf{M}^2 \right) \left(\frac{\Delta}{\delta} \right)^{1/7} \left(\frac{y}{\Delta} \right)^{2/7} \quad [14]$$

For flow on a flat plate with $\mathrm{Pr} = 1$, it was shown by Rubesin (12) that $\Delta = \delta$. For these conditions, making use of Equation [12], Equation [14] reduces to

$$\frac{t}{T} = \frac{T_w}{T_0} \left(1 + \frac{\gamma - 1}{2} \mathbf{M}^2 \right) + \left(1 - \frac{T_w}{T_0} \right) \left(1 + \frac{\gamma - 1}{2} \mathbf{M}^2 \right) \frac{u}{U} - \left(\frac{\gamma - 1}{2} \mathbf{M}^2 \right) \left(\frac{u}{U} \right)^2$$

which is the Crocco (13) temperature relation for flat-plate flow with $\mathrm{Pr} = 1$. Since the values of the boundary-layer shape parameters are known to be dependent only on the velocity and temperature distributions in the boundary layer, it is apparent

[3] Reference (10), pp. 131–134.

from Equations [12] and [14] that the parameters must be functions of the four variables $\mathbf{M}$, T_w/T_0, γ, and Δ/δ. In the Appendix it is shown that for any combination of these four variables the boundary-layer shape parameters can be computed directly from tabulated numerical values of two definite integrals I_1 and I_2. The values tabulated in Tables 1 and 2 as functions of two variables b and c, which are simple analytical functions of the four variables $\mathbf{M}$, T_w/T_0, γ, and Δ/δ, are the results of Simpson's rule calculations on a digital computer. The ranges of the variables b and c are such that, for $T_w/T_0 = 1$ and $\gamma = 1.4$, boundary-layer shape parameters can be evaluated to values of $\mathbf{M}$ as high as 14; and, for low-speed flow, they can be evaluated for temperature ratios T_w/T_0 from 0.09 to 5 for Δ/δ of 1.

TABLE 1 VALUES OF RECIPROCAL OF DEFINITE INTEGRAL I_1

$$I_1 = \int_0^1 \frac{Z^3(1-Z)\,dZ}{1+bZ-cZ^2}$$

$\frac{c}{b+1}$	b = −1.0	−0.8	−0.6	−0.4	−0.2	0	2.0	4.0	6.0	8.0	10.0
0	8.000	24.33	36.92	48.93	60.68	72.28	185.7	297.9	409.8	521.6	633.4
0.10	8.000	23.18	34.84	45.94	56.81	67.53	172.2	275.8	379.0	482.2	585.3
0.20	8.000	22.09	32.72	42.92	52.88	62.71	158.6	253.4	348.0	442.4	536.8
0.30	8.000	20.80	30.56	39.84	48.89	57.82	144.9	230.9	316.6	402.3	487.9
0.40	8.000	19.56	28.35	36.69	44.82	52.84	130.9	208.0	284.9	361.7	438.5
0.50	8.000	18.27	26.07	33.46	40.66	47.74	116.7	184.8	252.7	320.5	388.3
0.60	8.000	16.93	23.70	30.11	36.35	42.49	102.2	161.1	219.8	278.5	337.1
0.70	8.000	15.50	21.21	26.61	31.86	37.02	87.20	136.7	186.0	235.2	284.5
0.75	8.000	14.74	19.90	24.77	29.51	34.17	79.43	124.0	168.5	213.0	257.3
0.80	8.000	13.94	18.52	22.85	27.06	31.20	71.40	111.0	150.5	190.0	229.4
0.85	8.000	13.09	17.06	20.82	24.47	28.07	63.02	97.48	131.8	166.1	200.4
0.90	8.000	12.16	15.47	18.61	21.68	24.69	54.06	83.03	111.9	140.7	169.6
0.95	8.000	11.11	13.65	16.09	18.49	20.86	44.01	66.89	89.70	112.5	135.3
0.975	8.000	10.51	12.58	14.60	16.60	18.58	38.07	57.39	76.66	95.92	115.2
1.00	8.000	9.431	10.85	12.26	13.68	15.08	29.22	43.17	57.21	71.23	85.22

TABLE 2 VALUES OF RECIPROCAL OF DEFINITE INTEGRAL I_2

$$I_2 = \int_0^1 \frac{Z^2\,dZ}{1+bZ-cZ^2}$$

$\frac{c}{b+1}$	b = −1.0	−0.8	−0.6	−0.4	−0.2	0	2.0	4.0	6.0	8.0	10.0
0	0	2.175	3.683	5.142	6.581	8.009	22.12	36.16	50.18	64.20	78.21
0.10	0	2.027	3.411	4.746	6.061	7.366	20.25	33.06	45.85	58.64	71.43
0.20	0	1.879	3.135	4.345	5.536	6.717	18.36	29.94	41.50	53.06	64.62
0.30	0	1.726	2.855	3.940	5.006	6.062	16.47	26.81	37.13	47.45	57.77
0.40	0	1.570	2.570	3.528	4.468	5.398	14.56	23.65	32.73	41.80	50.88
0.50	0	1.409	2.278	3.107	3.920	4.724	12.62	20.46	28.28	36.10	43.92
0.60	0	1.240	1.976	2.675	3.359	4.034	10.66	17.22	23.78	30.32	36.87
0.70	0	1.062	1.660	2.226	2.778	3.322	8.643	13.91	19.17	24.43	29.68
0.75	0	0.9672	1.495	1.992	2.476	2.952	7.609	12.22	16.82	21.41	26.01
0.80	0	0.8668	1.322	1.748	2.163	2.571	6.548	10.48	14.41	18.33	22.25
0.85	0	0.7584	1.138	1.491	1.834	2.170	5.447	8.685	11.91	15.14	18.37
0.90	0	0.6360	0.9350	1.211	1.478	1.739	4.278	6.783	9.282	11.78	14.27
0.95	0	0.4805	0.6924	0.8826	1.064	1.243	2.965	4.662	6.354	8.044	9.733
0.975	0	0.3606	0.5247	0.6657	0.7987	0.9279	2.165	3.381	4.593	5.804	7.014
1.00	0	0	0	0	0	0	0	0	0	0	0

It was assumed as another characteristic of the model that the skin-friction coefficient $C_f/2$ is the same in a nozzle as it would be on a flat plate for equal boundary-layer thicknesses. The Blasius skin-friction equation for incompressible turbulent boundary-layer flow at moderate Reynolds numbers was chosen for the purpose of evaluating $C_f/2$ because of the simplicity of the equation and its reasonable agreement with recent shear-plate measurements (14, 15, 16). The Blasius equation for incompressible flow expressed in terms of boundary-layer thickness given by Eckert[4] is

$$\left(\frac{C_f}{2}\right)_i = 0.0228\left(\frac{\mu'}{\rho' U\delta}\right)^{1/4} \qquad [15]$$

Adopting the method used by Tucker (7), this equation was extended (18) for nonadiabatic compressible boundary layers by evaluating ρ and μ at a temperature which is the arithmetic mean between the free-stream and wall temperatures

$$\frac{C_f}{2} = 0.0228\,\sigma\left(\frac{\mu_0}{\rho' U\delta}\right)^{1/4} \qquad [16]$$

where $\sigma \equiv$

$$\frac{1}{\left[\frac{1}{2}\left(\frac{T_w}{T_0}\right)\left(1+\frac{\gamma-1}{2}\mathbf{M}^2\right)+\frac{1}{2}\right]^{0.60}\left(1+\frac{\gamma-1}{2}\mathbf{M}^2\right)^{0.15}}$$

which is based on the assumption that $\mu \sim T^{0.68}$ as suggested by the high-temperature viscosity data reported by Hilsenrath and Touloukian (19). A similar procedure has been used successfully by Humble, Lowdermilk, and Desmon (20) to modify Reynolds numbers for the purpose of improving correlations of turbulent heat-transfer and friction data measured in highly nonadiabatic pipe flow. The effect of $\mathbf{M}$ on the ratio C_f/C_{fi} for $T_w/T_0 = 1$, $\gamma = 1.4$ predicted by Equation [16] was found to agree within 5 per cent with the experimental data of Coles (16) up to $\mathbf{M}$ of 4.5 for a constant Re_θ of 7000.

Substituting this result in Equation [10], multiplying through by $\theta^{1/4}$, and introducing the boundary-layer shape parameter θ/δ, the equation becomes

$$\frac{d\theta^{5/4}}{dx} + \frac{5}{8}\theta^{5/4}\left[\frac{\mathbf{M}^2 - 2(\delta^*/\theta) - 3}{1-\mathbf{M}^2}\right]\frac{d}{dx}\ln\frac{A}{A_*} = \frac{5}{4}(0.0228)\sigma\left[\left(\frac{\mu_0}{\rho_* U_*}\right)\left(\frac{\theta}{\delta}\right)\left(\frac{A}{A_*}\right)\right]^{1/4} \qquad [17]$$

It can be seen from this form of the momentum equation and from subsequent forms of the energy and heat-transfer equations that there is an interdependence of the equations on the parameters T_w/T_0 and Δ/δ. Therefore, strictly speaking, these equations should be solved simultaneously. Although in principle a simultaneous solution is possible, in practice the mathematics would be overly burdensome. However, an approximate independent solution of the momentum equation is made possible by making reasonable assumptions of distributions of T_w/T_0 and Δ/δ. Since in the momentum equation the boundary-layer shape parameters and the skin-friction coefficients depend on T_w/T_0 and Δ/δ only indirectly, little error is introduced by such a first approximation.

Hence, making initial assumptions of T_w/T_0 and Δ/δ distributions in order to evaluate the boundary-layer shape parameters and skin-friction coefficients, the development of the velocity boundary layer is computed by solving Equation [17].

The Integral Energy Equation

Derivation. Starting with the form of the energy equation given by Equation [2], adding the momentum equation, Equation [1], multiplied through by u, the pressure-gradient terms cancel, giving

$$\rho u\frac{\partial}{\partial x}\left(h+\frac{1}{2}u^2\right) + \rho v\frac{\partial}{\partial y}\left(h+\frac{1}{2}u^2\right) = \frac{\partial}{\partial y}k\left(\frac{\partial t}{\partial y}\right) + \Phi + u\frac{\partial}{\partial y}\mu\left(\frac{\partial u}{\partial y}\right) \qquad [18]$$

[4] Reference (17), p. 73.

Even for compressible flow it can be shown that a reasonable approximation of the dissipation function Φ is given by

$$\Phi = \tau_{xy} \frac{\partial u}{\partial y} \quad [19]$$

Substituting Equation [19] into [18] and making use of Newton's shear-stress equation

$$\rho u \frac{\partial}{\partial x}\left(h + \frac{1}{2}\mu^2\right) + \rho v \frac{\partial}{\partial y}\left(h + \frac{1}{2}u^2\right) = \frac{\partial}{\partial y} k \left(\frac{\partial t}{\partial y}\right) + \frac{\partial u \tau_{xy}}{\partial y} \quad [20]$$

integrating over the temperature boundary-layer thickness Δ and evaluating the integrated functions at the limits following a procedure similar to that used in deriving the integral momentum equation, an integral energy equation can be obtained.[5] From the assumed velocity distribution, Equation [12], $u\tau_{xy}$ evaluated at the wall is exactly zero, as it is at Δ when $\Delta > \delta$. When Δ is less than δ, $u\tau_{xy}$ at y equals Δ is not zero; however, it can usually be neglected with respect to q_w except for very high velocities, very low differences between wall and stagnation temperature, and very thin boundary layers. The form of the integral energy equation is

$$\frac{d\phi}{dx} + \phi\left[\frac{d}{dx} \ln \rho' U r C_p (T_0 - T_w)\right] - \frac{\phi}{C_p(T_0 - T_w)}\left[\frac{d}{dx}(C_p T_0)\right]\left(\frac{\Delta^*}{\phi} - \frac{\Delta}{\phi}\right) = C_h \quad [21]$$

where

$$\phi \equiv \int_0^\Delta \frac{\rho u}{\rho' U}\left(1 - \frac{t_0 - T_w}{T_0 - T_w}\right) dy \text{ (energy thickness)} \quad [22]$$

$$\Delta^* \equiv \int_0^\Delta \left(1 - \frac{\rho u}{\rho' U}\right) dy$$

(temperature boundary-layer displacement thickness) [23]

$$C_h \equiv \frac{q_w}{\rho' U C_p (T_0 - T_w)} \quad [24]$$

and where it is assumed that C_p is constant in the boundary layer so that $h + {}^1/_2 u^2 = C_p t_0$ and $H + {}^1/_2 U^2 = C_p T_0$.

Solution. By the assumption of one-dimensional isentropic flow outside of the boundary layer, T_0 does not vary through the nozzle. If C_p is assumed constant through the nozzle, then the third term of Equation [21] vanishes. Such an assumption is quite reasonable in some cases, such as constant composition rocket-nozzle expansions, where the variation in C_p is only about 10 per cent. For cases when C_p and T_0 cannot be assumed constant and it becomes necessary to evaluate the temperature boundary-layer shape parameters Δ^*/ϕ and Δ/ϕ, the values can be computed from the tabulated integrals I_1 and I_2 by making slight changes in the definitions of b and c (Appendix).

The distribution of T_w/T_0 assumed for solving the integral momentum equation is also used in solving the integral energy equation. However, since the latter equation is considerably more dependent on T_w/T_0, an iterative process is required to obtain the correct solution.

For the type of flow under consideration, no correlation of C_h as a function of ϕ, Δ, or other known parameters has been established. To obtain such a relation, it was assumed as one characteristic of the model that the Reynolds analogy between heat and momentum transfer is valid for this type of flow. The fundamental equation expressing Reynolds analogy is

$$\frac{q}{\rho C_p \dfrac{dt_0}{dy}} = \frac{(\tau_{xy})}{\rho \dfrac{du}{dy}} \quad [25]$$

Substituting into this equation the derivatives of the assumed velocity and temperature profile Equations [12] and [13], making use of Rubesin analysis of Δ/δ on a flat plate (12) and the von Kármán modification of Reynolds analogy,[6] an expression for C_h is obtained for Re^δ near 10^4 and Pr from ${}^1/_2$ to 1[7]

$$C_h = \frac{C_f/2}{(\Delta/\delta)^{1/7}\,\mathrm{Pr}^{0.46}} \quad [26]$$

(For Re_x near 10^6 the Pr exponent would be 0.36, and for 10^3 it would be 0.62.) For the special case of $\mathrm{Pr} = 1$ and $\Delta = \delta$, note that Equation [26] reduces to the familiar $C_h = C_f/2$.

Substituting Equation [26] into Equation [21] for the case when $C_p T_0$ remains constant through an axially symmetric nozzle, the integral energy equation reduces to

$$\frac{d\phi}{dx} + \phi \frac{d}{dx} \ln \frac{C_p(T_0 - T_w)}{r} = \frac{C_f/2}{(\Delta/\delta)^{1/7}\,\mathrm{Pr}^{0.46}} \quad [27]$$

Using Equation [16] to evaluate $C_f/2$ in Equation [27], the resulting equation contains two dependent variables, ϕ and Δ/δ (the initially assumed distribution of Δ/δ is not used in this equation, having been assumed only for the purpose of evaluating the boundary-layer shape parameters)

$$\frac{d\phi}{dx} + \phi \frac{d}{dx} \ln \frac{C_p(T_0 - T_w)}{r} = \frac{0.0228\,\sigma \left[\left(\dfrac{\mu_0}{\rho_* U_*}\right)\left(\dfrac{\theta}{\delta}\right)\left(\dfrac{A}{A_*}\right)\right]^{1/4}}{\theta^{1/4}(\Delta/\delta)^{1/7}\mathrm{Pr}^{0.46}} \quad [28]$$

The equation can be reduced to the single dependent variable Δ/δ by expressing ϕ in terms of θ and Δ/δ through the relation

$$\phi = \lambda \left(\frac{\Delta}{\delta}\right)^{9/7} \theta \quad [29]$$

The factor λ, a boundary-layer shape parameter, is a function of $\mathbf{M}$, T_w/T_0, γ, and Δ/δ, and hence can be evaluated from the definite integrals of the Appendix, Equation [57]. Since the value of λ is fairly insensitive to changes in Δ/δ, the use of the assumed Δ/δ distribution to evaluate λ does not particularly impair the validity of Equation [29]. Substituting Equation [29] in Equation [28], the resulting equation is linear in $(\Delta/\delta)^{9/7}$ with variable coefficients and is of the same form as Equation [17]

$$\frac{d}{dx}\left(\frac{\Delta}{\delta}\right)^{9/7} + \frac{9}{8}\left(\frac{\Delta}{\delta}\right)^{9/7} \frac{d}{dx}\left[\ln \frac{\lambda\theta C_p(T_0 - T_w)}{r}\right] = \frac{9}{8}(0.0228\,\sigma)\frac{\left[\left(\dfrac{\mu_0}{\rho_* U_*}\right)\left(\dfrac{\theta}{\delta}\right)\left(\dfrac{A}{A_*}\right)\right]^{1/4}}{\theta^{5/4}\,\mathrm{Pr}^{0.46}\,\lambda} \quad [30]$$

Using the distribution of θ which results from the solution of the integral momentum equation, the ratio of the temperature boundary-layer thickness to the velocity boundary-layer thickness is obtained by solving Equation [30].

[5] Reference (10), pp. 613–615, and reference (18).

[6] Reference (17), p. 124.

[7] Reference (18), Appendix A.

Heat-Transfer Coefficient

Having solved Equations [17] and [30] for θ and Δ/δ, respectively, the local heat-transfer coefficient h_g derived from Equation [26] is

$$h_g = \left[\frac{0.0228(\rho_* U_*)^{3/4}\mu_0^{1/4}C_p}{\mathrm{Pr}^{0.46}}\right]\left[\sigma\left(\frac{\theta}{\delta}\right)^{1/4}\left(\frac{A_*}{A}\right)^{3/4}\right]\left[\left(\frac{\delta}{\Delta}\right)^{1/7}\left(\frac{1}{\theta}\right)^{1/4}\right] \quad [31]$$

where $h_g \equiv q_w/(T_0 - T_w)$. The quantities in the first bracket remain constant throughout the nozzle, whereas those in the second bracket are principally functions of the local **M**. The equation expressed in terms of the two fundamental boundary-layer thicknesses δ and Δ is

$$h_g = \left[\frac{0.0228(\rho_* U_*)^{3/4}\mu_0^{1/4}C_p}{\mathrm{Pr}^{0.46}}\right]\left[\sigma\left(\frac{A^*}{A}\right)^{3/4}\right]\left[\left(\frac{1}{\Delta}\right)^{1/7}\left(\frac{1}{\delta}\right)^{3/28}\right] \quad [32]$$

Nozzle Similarity

Once Equations [17], [30], and [31] have been solved numerically for one nozzle contour, it is not necessary to solve them again for a second nozzle contour operating with the same or only moderately different reservoir conditions, provided the following restrictions are satisfied

$$\left(\frac{d}{dx}\ln\frac{A}{A_*}\right)_2 = F\left(\frac{d}{dx}\ln\frac{A}{A_*}\right)_1 \quad [33]$$

where F is constant for all values of A/A_* (subscript 1 referring to the computed nozzle, and subscript 2 referring to the nozzle to be computed); and

$$\theta_2^{3/4} = \frac{1}{F}\theta_1^{3/4} \quad [34]$$

at some common A/A_* near the nozzle entrances. If both these restrictions are satisfied, it can be shown from the general solution of Equation [17][8] that Equation [34] holds for all values of A/A_* of the nozzles. It can be shown from the general solution of Equation [30] that, if Equation [34] holds for all values of A/A_*, then

$$\left(\frac{\Delta}{\delta}\right)_2^{3/7} = \left(\frac{\Delta}{\delta}\right)_1^{3/7} \quad [35]$$

for all values of A/A_*. Although Equations [34] and [35] require that the gas-flow conditions ($\rho_* U_*$, γ, μ, C_p, Pr, T_w/T_0, and $T_0 - T_w$) be the same for both nozzles, these parameters appear only indirectly or are raised to small powers in the momentum and energy equations; hence it is expected that moderate differences in their values would introduce very little error. In the heat-transfer-coefficient expression Equation [31], the parameter C_p appears directly and $\rho_* U_*$ appears to the $^3/_4$ power; hence differences in their values have nearly a direct effect. However, since h_g is given by an explicit algebraic expression, it is quite easy to account for these differences. Thus, from Equations [31], [34], and [35], the equation which relates the heat-transfer coefficients of two nozzles satisfying Equations [33] and [34] is

$$h_{g2} = \frac{[(\rho_* U_*)^{3/4}C_p]_2}{[(\rho_* U_*)^{3/4}C_p]_1}(F)^{1/3}\, h_{g1} \quad [36]$$

For two nozzles that are geometrically similar, it is easily shown that Equation [33] is satisfied at all values of A/A_*, the value of F being given by the equation

$$F = \frac{r_{*1}}{r_{*2}} \quad [37]$$

Geometrically similar nozzles are not the only nozzles which can satisfy Equation [33], since it is the differential equation of the contours of a whole family of nozzles which are geometrically dissimilar but whose area-ratio derivatives at each area ratio are related by the constant F. The equation of one of these nozzle contours for particular values of F and r_* can be obtained by expressing the area-ratio derivative of the computed nozzle contour in terms of x and by integrating Equation [33].

A particular family of geometrically dissimilar nozzle contours which are of practical interest because of their wide use in rocket nozzles, is that which consists of (*a*) a conical convergence section, (*b*) a throat region generated by revolving an arc of a circle about the nozzle axis, and (*c*) a conical divergence section. (The conical sections join the throat region tangentially so that there is no discontinuity in the area-ratio derivative with respect to x.) Only geometrically similar nozzle contours of this family were found to satisfy Equation [33] exactly. However, it was found that certain nozzle contours of this family, which are geometrically dissimilar, can exactly satisfy Equation [33] in the conical regions and at the throat and very nearly satisfy Equation [33] in the intermediate regions, provided certain relations between the parameters r_*, r_c, β, and α are maintained. Between any given limiting area ratios, the nozzle contour is completely specified by these four parameters. The relations are obtained from the equations of the area-ratio derivatives for each of the nozzle regions as follows

$$\frac{d}{dx}\ln\frac{A}{A_*} = -\frac{2}{r_*}\left(\frac{A_*}{A}\right)^{1/2}\sin\beta \text{ (convergence cone)} \quad [38]$$

$$\frac{d}{dx}\ln\frac{A}{A_*} = +\frac{2}{r_*}\left(\frac{A_*}{A}\right)^{1/2}\sin\alpha \text{ (divergence cone)} \quad [39]$$

$$\frac{d}{dx}\ln\frac{A}{A_*} = \pm\left[\left(\frac{A_*}{A}\right) - \left\{\left(\frac{A_*}{A}\right)^{1/2}\left(1 + \frac{r_*}{r_c}\right) - \left(\frac{r_*}{r_c}\right)\right\}^2\right]^{1/2} \text{ (throat region)} \quad [40]$$

and at the throat

$$\frac{1}{1 - \mathbf{M}^2}\frac{d}{dx}\ln\frac{A}{A_*} = \frac{1}{r_*}\left[\left(\frac{2}{\gamma + 1}\right)\frac{r_*}{r_c}\right]^{1/2} \quad [41]$$

Combining Equations [38], [39], and [41], the two relations which must be satisfied are

$$\left(\frac{\sin\beta}{\sin\alpha}\right)_2 = \left(\frac{\sin\beta}{\sin\alpha}\right)_1 \quad [42]$$

and

$$\left[\left(\frac{r_c}{r_*}\right)^{1/2}\sin\beta\right]_2 = \left[\left(\frac{r_c}{r_*}\right)^{1/2}\sin\beta\right]_1 \quad [43]$$

If Equations [42] and [43] are satisfied by some nozzle contour of the family to be computed, the value of F at all values of A/A_* in the conical sections and at the throat is given by

$$F = \frac{(r_* r_c)_1^{1/2}}{(r_* r_c)_2^{1/2}} = \left(\frac{r_{*1}}{r_{*2}}\right)\frac{(r_c/r_*)_1^{1/2}}{(r_c/r_*)_2^{1/2}} \quad [44]$$

Comparing a nozzle having $\beta = 10$ deg with one having $\beta = 30$

[8] Reference (21), p. 284.

deg, F increases about 5 per cent in the region between the conical sections and the throat. Such a variation is expected to introduce only a small error in the computed heat-flux distribution. Substituting Equation [44] in Equation [36], it is found that h_g is inversely proportional to $(r_c r_t)^{1/2}$.

Sample Calculation

In order to demonstrate the type and magnitudes of the results that can be obtained from the present solution, first-approximation calculations were made of the boundary-layer development and heat transfer in a specific rocket-type nozzle, Fig. 2, operating

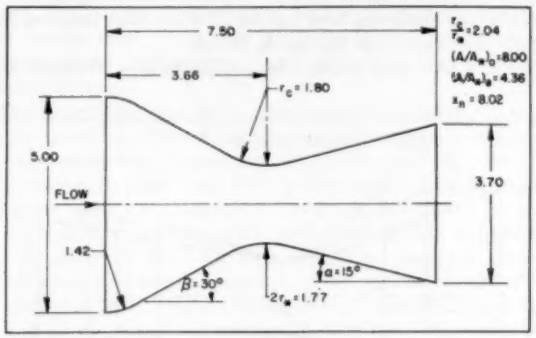

Fig. 2 Nozzle Contour

under conditions of temperature and pressure typical of rocket motors, Table 3. A comparison is made between the computed heat-transfer results and those measured in a sectionally cooled rocket nozzle having the same inner contour (22).

Constant values of T_0, T_w/T_0, and Δ/δ were assumed, Table 3, for evaluating σ, $d/dx \ln (T_0 - T_w)$, and the boundary-layer shape parameters in obtaining the first-approximation solutions. Distributions other than constant could have been assumed without adding much additional computation, since the form of the differential equations would remain unchanged. The local heat flux was computed from the equation

$$q_w = \frac{T_0 - T_L}{\frac{1}{h_g} + \frac{l}{k_w} + \frac{1}{h_L}}$$

which was selected since T_L, h_L, and l/k_w can usually be computed quite accurately from known or assumed coolant-passage conditions. Values of l, k_w, and effective diameter of the coolant passage, corresponding to those of the nozzle of reference (22), were selected for the sample calculation, Table 3. The coolant-passage heat-transfer coefficient h_L was computed by assuming the coolant to be water having a constant velocity over the entire nozzle.

TABLE 3 GAS-FLOW AND COOLANT-FLOW CONDITIONS ASSUMED FOR SAMPLE CALCULATIONS

Parameter	Value
p_0-reservoir pressure	300 psi
T_0	4500 deg R
Mean molecular weight of gas flow	21
γ	1.2
$(\rho_e U_e)$	1.92 lb/sq in. sec
μ_0	3.48 × 10^{-6} lb/sec in.[a]
Pr	0.83[b]
C_p	0.567 Btu/lb deg F
T_w/T_0	0.25[c]
Δ/δ	1.00[c]
T_L	560 deg R
l	0.090 in.
k_w (type AISI 502 stainless steel)	4.65 × 10^{-4} Btu/in. sec deg F[d]
hL	0.0133 Btu/sec sq in. deg F[d]

[a] Evaluated from viscosity equation of Bird, Hirschfelder, and Curtiss (23), using values of force constants which are numerical averages of those of H_2, O_2, N_2, CO, NO, H_2O, CO_2, N_2O, and air.
[b] Evaluated from the equation $\mathrm{Pr} = 4\gamma/(9\gamma - 5)$, which can be derived from the simplified kinetic-theory relation for thermal conductivity in terms of C_p and μ (reference 24).
[c] These constant values used only in evaluating σ and boundary-layer shape parameters.
[d] Evaluated from Dittus-Boelter equation (cf. p. 115 of ref. 17) for water assuming constant velocity of 25 fps, average bulk temperature 100 F, and coolant-passage characteristic dimension, 0.115 in., equal to 4 times hydraulic radius of coolant passage of nozzle of reference (22).

Boundary-Layer-Thickness Distributions. It was expected that the distributions of θ and Δ/δ determined by solving Equations [17] and [30] might be strongly dependent on the boundary-layer thicknesses at the nozzle entrance, which must be specified to solve the equations. For that reason, widely different values were selected in order to determine the effect. Case 1 was selected as that case when both δ and Δ at the nozzle entrance are zero. However, the ratio of Δ/δ at $x = 0$, the initial condition required for solving Equation [30], is left indeterminant by such assumed conditions. Rubesin (12) showed that Δ/δ is constant everywhere on a uniform temperature flat plate in incompressible flow. Assuming the boundary-layer growth near $x = 0$ to be the same as near the leading edge of such a flat plate, and making use of the von Kármán modification of Reynolds analogy, it was shown (18) that the constant value of Δ/δ is $\mathrm{Pr}^{-0.36}$. Case 2(a) was arbitrarily selected as that case when $\delta = 0.188$ in. and $\Delta = 0.201$ in. at $x = 0$. These are the thicknesses that would exist at the end of a cooled flat plate equal in length to the nozzle of Fig. 2 for the same free-stream flow and wall temperature as those at the nozzle entrance. Case 2(b) was arbitrarily selected as that case when $\delta = 0.188$ in. and $\Delta = 0$ at $x = 0$. Such a case applies to adiabatic boundary-layer development ahead of the nozzle, with cooling suddenly initiated at the nozzle entrance.

The computed first-approximation distributions of δ and Δ are shown in Fig. 3. Note that the distributions of δ for Cases 2(a) and 2(b) are identical.

Although δ of Case 2 shrinks by a factor of 10 from the nozzle entrance to the throat, its value at that point is only 9 per cent higher than δ of Case 1, which grows from zero to a maximum value about half way to the throat and then also shrinks. A short distance beyond the throat both distributions merge; hence beyond this region the effect of the differences in initial thicknesses vanishes.

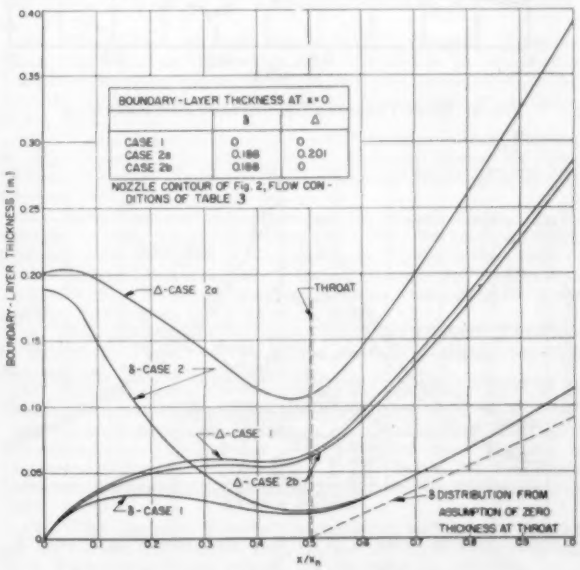

Fig. 3 Boundary-Layer-Thickness Distributions

The three distributions of Δ shown in Fig. 3 indicate that there is a similar tendency for the effects of initial differences in Δ to diminish as the temperature boundary layer developed in the nozzle. Although such a tendency is demonstrated, the three distributions do not merge as did the δ-distributions.

Also shown in Fig. 3 is a comparison between the computed δ distribution beyond the throat and that suggested by Saunders and Calder (6) from their heat-transfer measurements. They found that measurements of local heat fluxes in the divergent portion of a rocket nozzle having a low divergence angle ($\alpha = 0.6$ deg) were correlated quite well by the equation $C_h = 0.0285 (\mu'/\rho' U x)^{1/5}$ for Re_x from 10^5 to 10^6, taking x as the distance from the nozzle throat and using appropriate local values of $\rho' U$ along the nozzle. Since this equation results from applying Reynolds analogy to turbulent boundary-layer flow over a flat plate, Saunders and Calder suggested that the boundary-layer growth in the divergent section of their nozzle was probably similar to that on a flat plate if the boundary-layer thickness is assumed to be zero at the throat. The comparison in Fig. 3 shows that even for a nozzle having $\alpha = 15$ deg, such a distribution is not appreciably different from that determined from the present solution except near the throat.

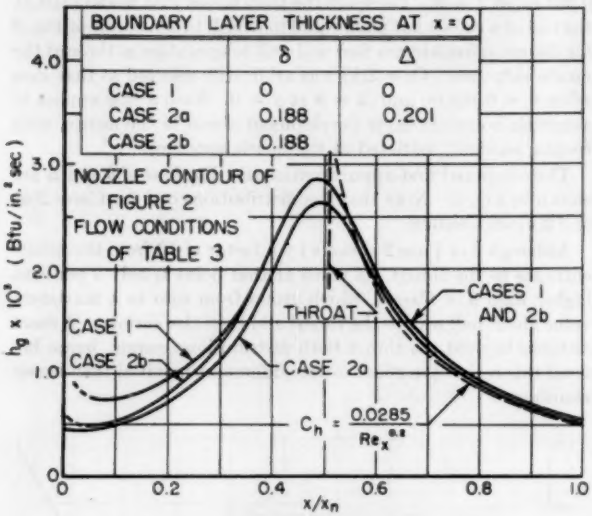

FIG. 4 HEAT-TRANSFER COEFFICIENT DISTRIBUTIONS

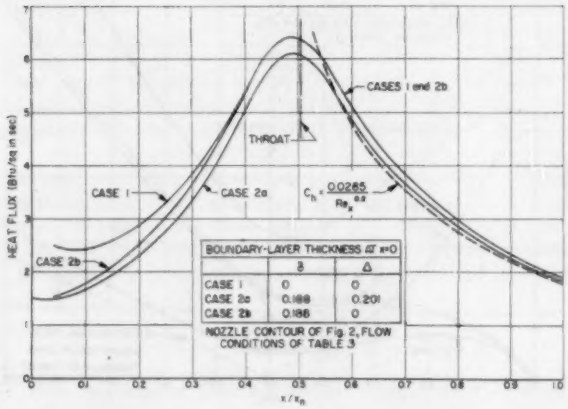

FIG. 5 HEAT-FLUX DISTRIBUTIONS

Heat-Flux Distributions. The heat-transfer coefficient and heat-flux distributions computed for the three cases are compared in Figs. 4 and 5. As might be expected from the fact that h_g depends on $\delta^{1/10}$ and on $\Delta^{1/7}$, the differences in the distributions for the three cases are not large. This fact reduces the importance of accurate knowledge of the boundary-layer thicknesses at the nozzle entrance. For rocket-motor nozzles preceded by cylindrical chambers the assumptions of Case 2(a) would probably be most nearly correct. From the equation for h_g, Equation [32], it is evident that the most significant factor determining the heat-flux distribution is the distribution of $\rho' U$ through the nozzle, since $\rho' U$ appears raised to the $^3/_4$ power. It is significant to note that the maximum heat flux for all three cases occurred just slightly upstream from the nozzle throat.

In Fig. 6, two other nozzle contours having $\beta = 20$ and 40 deg,

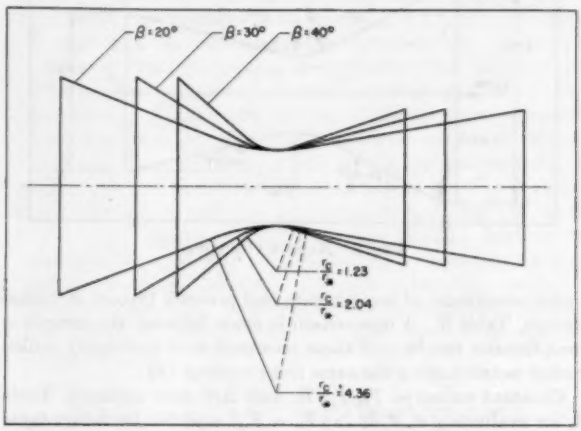

FIG. 6 NOZZLE CONTOURS HAVING SIMILAR AREA-RATIO DERIVATIVE DISTRIBUTIONS

which satisfy Equations [57] and [58], are compared with the nozzle of Fig. 2. If the initial values of the momentum thicknesses were the same and all were operating under the same gas-flow conditions, the local heat-transfer coefficients of the 20-deg-convergence-angle nozzle having $r_c/r_* = 4.36$ would be 7.3 per cent lower than those of the 30-deg-convergence-angle nozzle having $r_c/r_* = 2.04$. The local heat-transfer coefficients of the 40-deg-convergence-angle nozzle having $r_c/r_* = 1.23$ would be 5.2 per cent higher. A nozzle geometrically similar to but ten times larger than the nozzle of Fig. 2 would have local heat-transfer coefficients which would be 37 per cent lower than those of Fig. 4 for similar relative initial boundary-layer thickness.

Comparison with Experiment. At present, it is not possible to make a conclusive comparison of the results of the present heat-transfer solution with those of rocket-motor experiment because of (a) the uncertainty in evaluating the transport properties of combustion-gas mixtures and (b) the lack of locally measured nozzle-heat-transfer data obtained in the absence of phenomena, other than convection, which affect heat transfer. Such phenomena as deposition of insulating solids on nozzle walls, radiation, incomplete combustion in the chamber, and recombination of free atoms and radicals have generally confused the picture of heat transfer in rocket nozzles.

Perhaps Saunders' and Calder's measurements (6) are the best experimental data available for comparison, since they were obtained under conditions in which the effects of the extraneous phenomena mentioned were probably negligible. In Fig. 4 is shown an h_g distribution beyond the throat computed over the Re_x range

from 10^5 to 10^6 from the simple correlation equation $C_h = 0.0285 (\mu'/\rho' U x)^{1/5}$ used by Saunders and Calder. The agreement of the present solution with this equation is very good between $x/x_n = 0.55$ where Re_x is 1.8×10^5 and $x/x_n = 1.0$ where Re_x is 5×10^5. Such an equation, however, is of no use in predicting the heat flux in the convergent section or at the throat.

The computed q_w distributions of Fig. 5 were found to be in qualitative agreement with the q_w distributions measured semilocally by Boden (22) in a nozzle of the same inner contour having eight separate cooling sections of about equal axial length. A valid quantitative comparison cannot be made with the data reported in reference (22), however, because of wide variations of heat-transfer rates, which were attributed to contaminants in the propellants and thick deposits of metallic salts on the nozzle-heat-transfer surface.

The unpublished results of more recent tests using the same apparatus with a different propellant combination are considerably more applicable for comparison with the results of the sample calculation. In these tests there was no material deposition on the walls, radiation accounted for probably less than 5 per cent of the heat flux measured in the throat section, and combustion was generally 92 to 98 per cent complete. However, present knowledge of heat flux due to atomic or free radical recombination is insufficient to determine whether or not it was significant with respect to the calculated convective heat flux. Therefore the comparison of the computed results with experimental results is necessarily made without resolving this question. To make the comparison, the maximum q_w value calculated for Case 2(a) was adjusted for small differences in mass-flow rate, specific heat, and chamber temperature between those of the sample calculation and those of the tests. From the calculated q_w distribution of Case 2(a) it is estimated that the maximum heat flux in the throat cooling section of the nozzle was probably 4 per cent higher than the measured average value. The adjusted maximum computed values were found to be from 6 per cent lower to 15 per cent higher than the maximum experimental values obtained by increasing by this 4 per cent the average heat fluxes measured in the throat section. The reproducibility of the experimental data was about ±5 per cent.

Conclusions

Insufficient knowledge of turbulent processes, in general, and of those occurring in the presence of streamwise pressure gradients, in particular, makes an exact solution of the problem of turbulent boundary-layer heat transfer in convergent-divergent nozzles impossible. As an alternative, an approximate solution has been obtained for a flow model having assumed characteristics amenable to analysis. Solutions of velocity and temperature boundary-layer development were found to be obtainable from linear differential equations having variable coefficients, whereas the local heat flux was expressed as an explicit algebraic function. It was shown that numerical results from these equations can easily be extended to geometrically similar nozzles and to certain other nozzles which are geometrically dissimilar. The results of sample calculations of the boundary-layer development and heat transfer in a conventional rocket-motor nozzle operating under typical conditions show (a) that both the velocity boundary layer and the temperature boundary layer reach minimum thicknesses slightly upstream from the nozzle throat, (b) that these minimum thicknesses are fairly insensitive to the boundary-layer thicknesses at the nozzle entrance, (c) that the boundary-layer growth is nearly linear in the divergent portion of the nozzle, and (d) that the maximum heat flux occurs very close to the throat. The computed values of heat flux were found to be in approximate agreement with experimental data available to the author.

Acknowledgment

This paper presents the results of one phase of research carried out at the Jet Propulsion Laboratory, California Institute of Technology, under Contract DA-04-495-Ord. 18, sponsored by the Department of the Army Ordnance Corps. The author gratefully acknowledges the helpful suggestions and assistance of the staff of the Jet Propulsion Laboratory.

Bibliography

1 "Method for Calculation of Compressible Laminar Boundary Layer With Axial Pressure Gradient and Heat Transfer," by P. A. Libby and M. Morduchow, Technical Note No. 3157, National Advisory Committee for Aeronautics, Washington, D. C., January, 1954.

2 "The Compressible Laminar Boundary Layer With Arbitrary Pressure and Surface Temperature Gradients," by D. N. Morris and J. W. Smith, *Journal of the Aeronautical Sciences*, vol. 20, 1953, pp. 805–818.

3 "Skin Friction and Heat Transfer for Laminar Boundary-Layer Flow With Variable Properties and Variable Free-Stream Velocity," by S. Levy and R. A. Seban, *Journal of Applied Mechanics*, Trans. ASME, vol. 75, 1953, pp. 415–421.

4 "Heat Transfer and Skin Friction by Integral Method in Compressible Laminar Boundary Layer With Streamwise Pressure Gradient," by I. E. Beckwith, Technical Note No. 3005, National Advisory Committee for Aeronautics, Washington, D. C., September, 1953.

5 "A Measurement of Turbulent Boundary-Layer Profiles and Heat Transfer Coefficient at $M = 7$," by P. P. Wegener, E. M. Winkler, and M. Sibulkin, *Journal of the Aeronautical Sciences*, vol. 20, 1953, pp. 221–222.

6 "Heat Transfer in a Nozzle at Supersonic Speeds," by O. A. Saunders and P. H. Calder, *Engineering*, vol. 174, 1952, pp. 281–284.

7 "Approximate Calculation of Turbulent Boundary-Layer Development in Compressible Flow," by Maurice Tucker, Technical Note No. 2337, National Advisory Committee for Aeronautics, Washington, D. C., April, 1951.

8 "Supersonic Nozzle Design for Viscous Fluids" (Thesis in Aeronautical Engineering), by G. E. Gomf, California Institute of Technology, Pasadena, Calif., 1949.

9 "Approximate Formulas for the Computation of Turbulent Boundary-Layer Momentum Thicknesses in Compressible Flows," by Neal Tetervin, Wartime Report No. L119, National Advisory Committee for Aeronautics, Washington, D. C., March, 1946.

10 "Modern Developments in Fluid Dynamics," edited by S. Goldstein, Oxford Press, London, England, 1938.

11 "Turbulent Boundary Layer in Compressible Fluids," by E. R. Van Driest, *Journal of the Aeronautical Sciences*, vol. 18, 1951, pp. 145–160.

12 "The Effect of Arbitrary Surface-Temperature Variation Along Flat Plate on Convective Heat Transfer in Incompressible Turbulent Boundary Layer," by M. W. Rubesin, Technical Note No. 2345, National Advisory Committee for Aeronautics, Washington, D. C., April, 1951.

13 "Transmission of Heat from a Flat Plate to a Fluid Flowing at High Velocity," by Luigi Crocco, Technical Memo No. 690, National Advisory Committee for Aeronautics, Washington, D. C., October, 1932.

14 "New Frictional Resistance Law for Smooth Plates," by F. Schultz-Grunow, Technical Memo No. 986, National Advisory Committee for Aeronautics, Washington, D. C., September, 1941.

15 "Direct Measurements of Skin Friction," by S. Dhawan, Technical Note No. 2567, National Advisory Committee for Aeronautics, Washington, D. C., January, 1952.

16 "Measurements of Turbulent Friction on a Smooth Flat Plate in Supersonic Flow," by D. Coles, *Journal of the Aeronautical Sciences*, vol. 21, 1954, pp. 433–448.

17 "Introduction to the Transfer of Heat and Mass," by E. R. G. Eckert, McGraw-Hill Book Company, Inc., New York, N. Y., 1950.

18 "An Approximate Solution of Compressible Turbulent Boundary-Layer Development and Convective Heat Transfer in Convergent-Divergent Nozzles," by D. R. Bartz, Jet Propulsion Laboratory, Pasadena, Calif., Progress Report No. 20-234, July 9, 1954.

19 "The Viscosity, Thermal Conductivity, and Prandtl Number for Air, O_2, N_2, NO, H_2, CO, H_2O, He, and A," by J. Hilsenrath and Y. S. Touloukian, Trans. ASME, vol. 76, 1954, pp. 967–985.

20 "Measurements of Average Heat-Transfer and Friction Coefficients for Subsonic Flow of Air in Smooth Tubes at High Surface

and Fluid Temperatures," by L. V. Humble, W. H. Lowdermilk, and L. G. Desmon, Report No. 1020, National Advisory Committee for Aeronautics, Washington, D. C., 1951.

21 "Higher Mathematics for Engineers and Physicists," by I. S. Sokolnikoff and E. S. Sokolnikoff, McGraw-Hill Book Company, Inc., New York, N. Y., second edition, 1941.

22 "Heat Transfer in Rocket Motors and the Application of Film and Sweat Cooling," by R. H. Boden, Trans. ASME, vol. 73, 1951, pp. 385–390.

23 "The Theoretical Calculation of the Equation of State and Transport Properties of Gases and Liquids," by R. B. Bird, J. C. Hirschfelder, and C. F. Curtiss, Trans. ASME, vol. 76, 1954, pp. 1011–1038.

24 "Kinetic Theory of Gases," by E. H. Kennard, McGraw-Hill Book Company, Inc., New York, N. Y., first edition, 1938.

Appendix

Evaluation of Boundary-Layer Shape Parameters

The boundary-layer shape parameters appearing in the momentum and energy equations are θ/δ, δ^*/δ, δ^*/θ, ϕ/Δ, Δ^*/Δ, Δ^*/ϕ, and λ. The parameters are defined by Equations [5], [6], [22], [23], and [29]. Details of the method used for evaluating θ/δ and ϕ/Δ are given, whereas only the final equations are given for the other parameters.

The parameter θ/δ is obtained directly by substituting Equations [12] and [14] into Equation [5]. For convenience, Equation [14] is rewritten as

$$\frac{t}{T} = a[1 + bZ - cZ^2] \quad \ldots\ldots [45]$$

where

$$a = \frac{T_w}{T_0}\left(1 + \frac{\gamma - 1}{2}\mathbf{M}^2\right);\ b = \left(\frac{T_0}{T_w} - 1\right)\left(\frac{\delta}{\Delta}\right)^{1/7}$$

$$c = \frac{\frac{\gamma - 1}{2}\mathbf{M}^2}{1 + \frac{\gamma - 1}{2}\mathbf{M}^2}\left(\frac{T_0}{T_w}\right);\ \text{and } Z = \frac{u}{U} = \left(\frac{y}{\delta}\right)^{1/7}$$

Substituting these expressions into Equation [5] and noting that $\rho/\rho' = T/t$

$$\frac{\theta}{\delta} = \frac{7}{a}\int_0^1 \frac{Z^7(1 - Z)dZ}{1 + bZ - cZ^2} \quad \ldots\ldots [46]$$

Hence θ/δ, which is known to be a function of the four variables $\mathbf{M}$, T_w/T_0, γ, and Δ/δ, can be calculated directly from a simple algebraic expression after the integral I_1 is evaluated as a function of the two variables b and c. Making the definition

$$I_1 \equiv \int_0^1 \frac{Z^7(1 - Z)d\mathbf{Z}}{1 + bZ - cZ^2} \quad \ldots\ldots [47]$$

then

$$\frac{\theta}{\delta} = \frac{7}{a} I_1 \quad \ldots\ldots [48]$$

In evaluating δ^*/δ, a similar integral I_2 is required, where

$$I_2 \equiv \int_0^1 \frac{Z^7 dZ}{1 + bZ - cZ^2} \quad \ldots\ldots [49]$$

and

$$\frac{\delta^*}{\delta} = 1 - \frac{7}{a} I_2 \quad \ldots\ldots [50]$$

and

$$\frac{\delta^*}{\theta} = \frac{\frac{a}{7} - I_2}{I_1} \quad \ldots\ldots [51]$$

Evaluating ϕ/Δ by substituting Equations [12], [13], and [14] into Equation [22], using the notation of Equation [45], the resulting equation is

$$\frac{\phi}{\Delta} = \frac{7}{a}\int_0^1 \frac{Z(1 - Z')Z'^6 dZ'}{1 + bZ - cZ^2} \quad \ldots\ldots [52]$$

where

$$Z' = \left(\frac{y}{\Delta}\right)^{1/7} = \frac{t_0 - T_w}{T_0 - T_w} \quad \text{and} \quad Z = Z'\left(\frac{\Delta}{\delta}\right)^{1/7}$$

Expressing Equation [52] in terms of Z' only

$$\frac{\phi}{\Delta} = \frac{7\left(\frac{\Delta}{\delta}\right)^{1/7}}{a}\int_0^1 \frac{Z'^7(1 - Z')dZ'}{1 + b'Z' - c'Z'^2} \quad \ldots\ldots [53]$$

where

$$b' = \frac{b}{\left(\frac{\delta}{\Delta}\right)^{1/7}} = \frac{T_0}{T_w} - 1 \quad \text{and}$$

$$c' = \frac{c}{\left(\frac{\delta}{\Delta}\right)^{2/7}} = \frac{\frac{\gamma - 1}{2}\mathbf{M}^2}{1 + \frac{\gamma - 1}{2}\mathbf{M}^2}\left(\frac{T_0}{T_w}\right)\left(\frac{\Delta}{\delta}\right)^{2/7}$$

hence

$$\frac{\phi}{\Delta} = \frac{7\left(\frac{\Delta}{\delta}\right)^{1/7}}{a} I'_1 \quad \ldots\ldots [54]$$

where $I_1' = I_1(b', c')$

In a similar fashion it can be shown that

$$\frac{\Delta^*}{\Delta} = 1 - \frac{7\left(\frac{\Delta}{\delta}\right)^{1/7}}{a} I_2' \quad \ldots\ldots [55]$$

where $I_2' = I_2(b', c')$

and

$$\frac{\Delta^*}{\phi} = \frac{\frac{a}{7}\left(\frac{\delta}{\Delta}\right)^{1/7} - I_2'}{I'_1} \quad \ldots\ldots [56]$$

Combining Equations [48] and [54], λ can be evaluated as

$$\lambda = \frac{\phi}{\theta}\left(\frac{\delta}{\Delta}\right)^{2/7} = \frac{I_1'}{I_1} \quad \ldots\ldots [57]$$

Values of I_1 and I_2 have been computed on an IBM digital computer by means of Simpson's rule calculations for values of b from -1 to 10 and of $c/(b + 1)$ from 0 to 1. The results are tabulated as the reciprocals of I_1 and I_2 versus the parameters b and $c/(b + 1)$ in Tables 1 and 2. The values were tabulated in this form because it was found that the curves of the reciprocal values plotted versus either parameter b or $c/(b + 1)$ for constant values of the other parameter were very nearly linear. Linear interpolation in either direction in the tables should yield results well within 1 per cent accuracy except in the regions between $c/(b + 1)$ from 0.9 to 1, and b from -0.8 to -1, where the curves become somewhat nonlinear. The values of θ/δ and δ^*/δ computed by Tucker (7) for T_w/T_0 of 1, γ of 1.4, and Δ/δ of 1 for $\mathbf{M}$ from 0 to 10 were compared with values computed from Tables 1 and 2 and were found to agree within 0.8 to 0.1 per cent over the Mach-number range.

Discussion

ELI RESHOTKO.[9] The paper is one of the first to consider compressible turbulent boundary-layer development with pressure gradient and heat transfer. As such it is an extremely useful contribution. Although the calculation procedure is specifically developed for flow in an axially symmetric nozzle, the same concepts could be employed in handling more general problems of turbulent boundary-layer development in favorable pressure gradient.

The energy equation is solved by the author in order to determine the variation of thermal boundary-layer thickness for use in obtaining the heat-transfer coefficient through the Reynolds analogy relation, Equation [26]. Because the ratio of thermal to dynamic thicknesses appears as $(\Delta/\delta)^{1/7}$ in Equation [31], the heat-transfer coefficient h_g is not particularly sensitive to the variation of (Δ/δ). Thus the prescribed calculation of h_g can be approximated closely, without solving the energy equation, through the assumption of a single reasonable value of $(\Delta/\delta)^{1/7}$.

Although not presented, it is interesting to note that the displacement thickness obtained for a portion of the nozzle including the throat would be negative. This result has also been obtained assuming laminar flow in a similar nozzle.[10] The negative displacement thickness is associated with the high density (relative to the free stream) in the cooled boundary layer.

Although the local heat-transfer rates in the divergent portion of the calculated nozzle (α = 15 deg) compare favorably with the experimental determination of Saunders and Calder (α = 0.6 deg), it is not reasonable to expect the results to fully indicate the effects of pressure gradient, especially in the convergent portion of the nozzle and in the vicinity of the throat because of the use of flat-plate relationsips for skin friction and Reynolds analogy.

The proposed method of extending the results of the boundary-layer calculation for a single nozzle to nozzles of similar or related geometric shapes is potentially very useful. It should reduce the work required for calculating large numbers of problems and provide a means for quickly estimating the effects of simple geometric changes on the nozzle boundary-layer development and heat transfer.

[9] Aeronautical Research Scientist, NACA-Lewis Flight Propulsion Laboratory, Cleveland, Ohio. Assoc. Mem. ASME.

[10] "The Compressible Laminar Boundary Layer with Heat Transfer and Arbitrary Pressure Gradient," by C. B. Cohen and Eli Reshotko, NACA TN 3326, 1955.

AUTHOR'S CLOSURE

The author wishes to thank Mr. Reshotko for his interesting comments. As was pointed out by the discusser, the value of h_g depends on the solution of the energy equation only through the factor $(\Delta/\delta)^{1/7}$. Specifically, the maximum values of $(\Delta/\delta)^{1/7}$ resulting from the solution of the energy equation for Cases 1, 2(a), and 2(b) of the paper (cf. Fig. 3) were 1.19, 1.27, and 1.17, respectively, near the throat. If, instead of solving the energy equation, a constant value of $(\Delta/\delta)^{1/7}$ of one was assumed for each case, the computed values of h_g would be from 17 to 27 per cent too high near the throat. It should be noted that in Equation [32] h_g is actually more sensitive to the development of the temperature boundary layer than to the development of the velocity boundary layer since the exponent of Δ is 1/7, whereas that of δ is only 3/28. Solution of the energy equation may become particularly important for cases with certain wall-temperature distributions which could exert a strong effect on the development of the temperature boundary layer.

The discusser is quite correct about negative displacement thicknesses resulting over part of the nozzle. Using the values of Δ/δ and T_w/T_0 resulting from the first approximation results to compute second approximation values of δ^*/θ from Equation [51], negative values were calculated over the range of x/x_n from 0.24 to 1 for Case 1, from 0.12 to 1 for Case 2(a), and from 0.54 to 1 for Case 2(b). As a result of the calculated boundary-layer development for the two cases in which δ^*/θ was negative at the throat, the effective throat areas were found to be 0.0027 per cent and 0.055 per cent greater than the geometrical areas, and for the other case 0.0094 per cent less than the geometrical area. Negative-displacement thicknesses are to be expected where the temperature boundary layer is much thicker than the velocity boundary layer because much higher densities in the boundary layer relative to those in the free stream result in higher boundary-layer values of ρu. The fact that δ^*/θ does go negative does not particularly retard the convergence of the momentum-equation solutions since δ^*/θ enters into the momentum equation only through the variable coefficient $\left[\frac{\mathbf{M}^2 - 2(\delta^*/\theta) - 3}{1 - \mathbf{M}^2}\right]$. In making a second approximation calculation, revised values of

$$\theta/\delta,\ \lambda,\ \sigma,\ \text{and}\ \frac{d}{d_x}\ln(T_0 - T_w)$$

must also be used.

The Influence of Curvature on Heat Transfer to Incompressible Fluids

By FRANK KREITH,[1] BETHLEHEM, PA.

The analogy between momentum transfer and heat transfer has been extended to flow channels with heating surfaces of either a convex or a concave curvature in the direction of flow. Using experimental results of wall shear and velocity distribution obtained by Wattendorf, Nusselt numbers have been calculated for Reynolds numbers ranging from 10^4 to 10^6 and Prandtl numbers ranging from 0.01 to 100, and for radii of curvature ranging from 0.12 to 1.2 ft. It was found that the heat-transfer coefficient from a heating surface with a concave curvature is considerably higher than for a heating surface of the same curvature in a convex configuration under similar conditions of flow-cross-sectional area and flow rate. The calculated results are in agreement with results from heat-transfer experiments using flow channels with convex and concave heating surfaces in the direction of flow.

Nomenclature

The following nomenclature is used in the paper:

a = thermal diffusivity of fluid
A = $r\Delta\theta$ = area per unit width through which q flows
A_1 = $R_1\Delta\theta$ = area per unit width at the convex (inner) surface through which q_1 flows
A_2 = $R_2\Delta\theta$ = area per unit width at the concave (outer) surface through which q_2 flows
b = half-depth of channel
c_p = heat capacity of fluid at constant pressure
D_H = hydraulic diameter
h = heat-transfer coefficient
g = gravitational force per unit mass
k = thermal conductivity of fluid
q = heat flow rate at any area, A
q_1 = heat flow rate at convex surface, A_1
q_2 = heat flow rate at concave surface, A_2

$$Q_1 = \frac{q_1}{A_1 \alpha c_p \gamma \sqrt{\tau_w/\rho}}$$

$$Q_2 = \frac{q_2}{A_2 \alpha c_p \gamma \sqrt{\tau_w/\rho}}$$

r = radius
R_c = radius of curvature
R_1 = radius at convex surface
R_2 = radius at concave surface
T = temperature at any r
T' = turbulent fluctuation of temperature
T_1 = temperature at R_1
T_2 = temperature at R_2
T_m = mixed mean fluid temperature
u = steady velocity in axial direction for straight duct
V_θ = tangential velocity in curved channel
$\bar{V}_\theta$ = average tangential velocity in curved channel (based on rate of flow and flow area)
v'_θ = turbulent fluctuating component in tangential direction in curved flow
v_θ = $V_\theta + v'_\theta$
x = distance from outer wall ($R_2 - r$)
y = distance from inner wall ($r - R_1$)
γ = ρg = weight density of fluid
ϵ_H = eddy diffusivity for heat
ϵ_M = eddy diffusivity for momentum
ν = kinematic viscosity of fluid
ρ = mass density of fluid
τ = shearing stress at any point r
$\bar{\tau}_w$ = shear between wall and fluid in a straight duct
τ_1 = shear between wall and fluid at a convex surface
τ_2 = shear between wall and fluid at a concave surface

$$\alpha = \frac{\epsilon_H}{\epsilon_M}$$

f = Fanning friction factor defined by $\frac{dp}{dl} = 4f \frac{\gamma}{D_H} \frac{u^2}{2g}$

$$\eta_1 = \sqrt{\bar{\tau}_w/\tau_1}$$

$$\eta_2 = \sqrt{\bar{\tau}_w/\tau_2}$$

$$N_{Nu} = \frac{h4b}{k} = \text{Nusselt modulus based on hydraulic diameter}$$

$$N_{Re} = \frac{u4b}{\nu} = \frac{\bar{V}_\theta 4b}{\nu} = \text{Reynolds number based on hydraulic diameter}$$

$$N_{Pr} = \frac{\nu}{a} = \text{Prandtl number}$$

$$N_{Pe} = N_{Re} N_{Pr} = \text{Peclet number}$$

$$u^+ = u/\sqrt{\bar{\tau}_w/\rho}$$

$$V_{\theta 1}{}^+ = V_\theta/\sqrt{\tau_1/\rho}$$

$$V_{\theta 2}{}^+ = V_\theta/\sqrt{\tau_2/\rho}$$

$$x^+ = \frac{x\sqrt{\tau_2/\rho}}{\nu}$$

$$y^+ = \frac{y\sqrt{\tau_1/\rho}}{\nu}$$

$$\xi_1 = \int_0^2 \frac{V_\theta}{\bar{V}_\theta} d\left(\frac{y}{b}\right)$$

$$\xi_2 = \int_0^2 \frac{V_\theta}{\bar{V}_\theta} d\left(\frac{x}{b}\right)$$

$$F_1\left(\frac{y}{b}\right) = \epsilon(y)/\sqrt{\bar{\tau}_w/\rho}\, b$$

$$F_2\left(\frac{x}{b}\right) = \epsilon(x)/\sqrt{\bar{\tau}_w/\rho}\, b$$

$$R = N_{Nu2}/N_{Nu1}$$

[1] Associate Professor of Mechanical Engineering, Lehigh University. Assoc. Mem. ASME.

Contributed by the Heat Transfer Division and presented at the Annual Meeting, New York, N. Y., November 28–December 3, 1954, of The American Society of Mechanical Engineers.

Note: Statements and opinions advanced in papers are to be understood as individual expressions of their authors and not those of the Society. Manuscript received at ASME Headquarters, August 6, 1954. Paper No 54—A-55.

Introduction

In numerous heat-transfer devices an incompressible fluid is heated or cooled while flowing in a channel along a surface which is curved in the direction of flow. In the design of such equipment it is important to evaluate the heat-transfer coefficient, but heretofore there has been only scant information (1, 2)[1] available to determine the effect of curvature. It was therefore deemed desirable to study the effect of curvature by comparing heat-transfer coefficients for fluids flowing along a heating surface of concave curvature in the direction of flow with the heat-transfer coefficients for a convex heating surface and for a flat heating surface.

For the purpose of this analysis an idealized system is postulated. This system consists of a flow channel formed by the annulus between two concentric cylinders with the fluid flowing in a direction perpendicular to their common axis.

Theoretical Derivation of the Nusselt Number

The heat-transfer equation in cylindrical polar co-ordinates for incompressible fully developed turbulent flow with constant fluid properties in a curved channel as shown in Fig. 1 is (3)

Fig. 1 Schematic Sketch of Idealized System

$$\frac{\partial T}{\partial t} + V_r \frac{\partial T}{\partial r} + \frac{V_\theta}{r}\frac{\partial T}{\partial \theta} + V_z \frac{\partial T}{\partial z} = \frac{1}{r}\frac{\partial}{\partial r}\left(ra\frac{\partial T}{\partial r} - r\overline{v_r'T'}\right) + \frac{1}{r}\frac{\partial}{\partial \theta}\left(a\frac{\partial T}{\partial \theta} - \overline{v_\theta'T'}\right) + \frac{\partial}{\partial z}\left(a\frac{\partial T}{\partial z} + \overline{v_z'T'}\right) \quad [1]$$

Assuming that $V_r = 0$, $V_z = 0$, and $\partial/\partial t = 0$, Equation [1] reduces to

$$V_\theta \frac{\partial T}{\partial \theta} = \frac{\partial}{\partial r}\left(ra\frac{\partial T}{\partial r} - r\overline{v_r'T'}\right) \quad [2]$$

Utilizing Prandtl's concept of mixing length and eddy diffusivity (4), Equation [2] becomes

$$V_\theta \frac{\partial T}{\partial \theta} = \frac{\partial}{\partial r}\left[r(a + \epsilon_H)\frac{\partial T}{\partial r}\right] \quad [3]$$

A heat balance or a fluid element of unit width for heat flow from the convex (i.e., inner) surface only gives

$$V_\theta \frac{\partial T}{\partial \theta} = -\frac{\partial q}{\partial r}\frac{1}{\gamma c_p \Delta\theta} \quad [4]$$

Substituting Equation [4] into Equation [3] and integrating of the resulting equation with the boundary condition that at $r = R_2$, $q = 0$, and $\partial T/\partial r = 0$, yields

$$\frac{q}{A\gamma c_p} = -(a + \epsilon_H)\frac{\partial T}{\partial r} \quad [5]$$

The total heat flow per unit width from the inner surface is carried away by the fluid. Denoting average quantities by bars one obtains

$$q_1 = \bar{V}_\theta 2b\gamma c_p \left(\overline{\frac{\partial T}{\partial \theta}}\right)\Delta\theta \quad [6]$$

Equation [6] can be simplified without introducing a serious error (5) by assuming that $V_\theta = \bar{V}_\theta$ at all r. Postulating that $\overline{\partial T/\partial\theta} = \partial T/\partial\theta$, combining Equations [6] and [4] and integrating from R_2 to r gives

$$\frac{q}{A} = \frac{q_1}{A_1}\frac{R_1}{2b}\left(\frac{R_2}{r} - 1\right) \quad [7]$$

Defining a new variable, $y = r - R_1$, Equation [7] becomes

$$\frac{q_1}{\gamma c_p A_1}\frac{y/2b - 1}{1 + y/R_1} = (a + \epsilon_H)\frac{\partial T}{\partial y} \quad [8]$$

where $2b = R_2 - R_1$.

A separation of variables yields the temperature distribution across the channel

$$\int_{T_1}^{T} dT = \frac{q_1}{\gamma c_p A_1}\int_{y=0}^{y}\frac{1}{a + \epsilon_H}\frac{y/2b - 1}{1 + y/R_1}\,dy \quad [9a]$$

By definition, the heat-transfer coefficient and the Nusselt number (based on the hydraulic diameter) are, respectively

$$h_1 = \frac{q_1}{A_1}\frac{1}{T_1 - T_m} \quad [10]$$

$$N_{Nu1} = \frac{h_1 4b}{k} \quad [11]$$

Utilizing the quantities Q_1 and α (see nomenclature) and defining $\bar{\tau}_w$ as the tractive force at the wall of a straight channel having a flow-cross-sectional area geometrically equal to that of the curved channel, the Nusselt number can be expressed as

$$N_{Nu1} = \frac{Q_1 \alpha N_{Re}\sqrt{f/2}}{T_1 - T_m} \quad [12]$$

By definition

$$T_1 - T_m = \frac{\int_0^2 \frac{V_\theta}{\bar{V}_\theta}(T_1 - T)\,d(y/b)}{\int_0^2 \frac{V_\theta}{\bar{V}_\theta}\,d(y/b)} \quad [13]$$

Equation [9] supplies the expression for $T_1 - T$ and thus the Nusselt number can be evaluated once the velocity and the eddy diffusivity are determined as a function of the radius. The equation to be solved is

$$N_{Nu1} = \frac{\alpha N_{Re}\sqrt{f/2}\int_0^2 \frac{V_\theta}{\bar{V}_\theta}\,d\left(\frac{y}{b}\right)}{\int_0^2 \frac{V_\theta}{\bar{V}_\theta}\left\{\alpha\sqrt{\frac{\bar{\tau}_w}{\rho}}\int_{\frac{y}{b}=0}^{\frac{y}{b}}\frac{b}{a + \epsilon_H}\frac{\frac{y}{2b} - 1}{1 + \frac{2b}{R_1}\frac{y}{2b}}\,d\left(\frac{y}{b}\right)\right\}d\left(\frac{y}{b}\right)} \quad [14a]$$

[1] Numbers in parentheses refer to the Bibliography at the end of the paper.

In a similar manner, the Nusselt number for heat flow from the concave (i.e., outer) surface can be derived and the expressions for the temperature distribution and Nusselt number, respectively, are

$$\int_{T_1}^{T} dT = \frac{q_2}{\gamma c_p A_2} \int_{x=0}^{x} \frac{\frac{x}{2b} - 1}{1 - x/R_2} \frac{1}{(a + \epsilon_H)} dx \quad \ldots [9b]$$

Convex surface

$$T_{y^+=30} - T_1 = -5Q_1\eta_1[\alpha N_{Pr} + \ln(5\alpha N_{Pr} + 1)] \quad \ldots [15a]$$

Concave surface

$$T_{x^+=30} - T_2 = -5Q_2\eta_2[\alpha N_{Pr} + \ln(5\alpha N_{Pr} + 1)] \quad \ldots [15b]$$

Adding to Equations [15a] and [15b] the temperature drop in the turbulent core (Equations [9a] and [9b]) and substituting the resulting expressions into Equations [14a] and [14b] yields upon some simplification the following expressions for the Nusselt numbers for heat flow from the convex and concave surface, respectively

$$N_{Nu2} = \frac{\alpha N_{Pe}\sqrt{f/2}\int_0^2 \frac{V_\theta}{\overline{V}_\theta} d\left(\frac{x}{b}\right)}{\int_0^2 \frac{V_\theta}{\overline{V}_\theta}\left\{\alpha\sqrt{\frac{\overline{\tau}_w}{\rho}}\int_{\frac{x}{b}=0}^{\frac{x}{b}} \frac{b}{a+\epsilon_H}\frac{\frac{x}{2b}-1}{1-\frac{2b}{R_2}\frac{x}{2b}} d\left(\frac{x}{b}\right)\right\} d\left(\frac{x}{b}\right)} \quad \ldots [14b]$$

For the purpose of analysis (5), the flow field is subdivided into three regions, the laminar sublayer, the buffer layer, and the turbulent core. Experimental data obtained by Wattendorf (6) indicate that in the region adjacent to a convex or concave wall the velocity distribution may be correlated by dimensional parameters similar to those used for straight channels or circular pipes. In fact, if the shearing stress τ is taken at the value corresponding to the conditions at the wall, the curves u^+ versus y^+ for a straight channel (5, 7) are identical in the buffer layer to the curves obtained by plotting V_θ^+ versus x^+ for a curved channel, Fig. 2. The edge of the laminar boundary layer was therefore taken at values of y^+ or x^+ equal to 5, respectively, and the buffer layer was assumed to extend from the edge of the laminar boundary layer to a distance at which x^+ or y^+ have values of 30, respectively, in agreement with previous analyses for flow in straight ducts (5, 7). It should be noted, however, that even though the correlating equations are similar, the physical thickness of the laminar boundary layer and the buffer layer depend upon the geometry of the channel as a result of the dependence of the wall shearing stress on the curvature.

In the laminar boundary layer $x/2b$ and $y/2b$ are very small compared to unity and heat is only transferred by conduction (i.e., $\epsilon_H = 0$). In the buffer layer $x/2b$ and $y/2b$ are still negligible compared to unity; also it may be assumed that V_θ/r is negligible compared to $\partial V_\theta/\partial r$ (less than 1 per cent error for the geometry of the channel used in reference 2), and that the shearing stress remains constant (5). Postulating the usual relationship between heat and momentum (or vortex) diffusivity, $\epsilon_H = \alpha\epsilon_M$, Equations [9a] and [9b] give the following expressions for the temperature drops through the laminar boundary layer and the buffer layer in series for heat flow from a convex or concave wall, respectively.

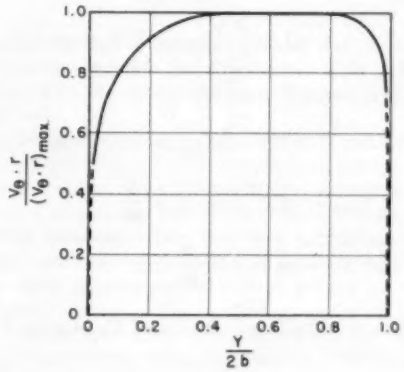

FIG. 2 DIMENSIONLESS VELOCITY DISTRIBUTION IN A CURVED CHANNEL

$$N_{Nu1} = \frac{\alpha N_{Pe}\sqrt{12.5f}}{[\alpha N_{Pr} + \ln(1 + 5\alpha N_{Pr})]\,\eta_1 + \frac{1}{5\xi_1}\int_{\left(\frac{y}{b}\right)_{y^+=30}}^{2} \frac{V_\theta}{\overline{V}_\theta}\left[\int_{\left(\frac{y}{b}\right)_{30}}^{y/b} \frac{1 - y/2b}{1 + \frac{2b}{R_1}\frac{y}{2b}} \frac{d(y/b)}{F_1\left(\frac{y}{b}\right) + \frac{4}{\alpha N_{Pe}\sqrt{f/2}}}\right] d\left(\frac{y}{b}\right)} \quad \ldots [16a]$$

$$N_{Nu2} = \frac{\alpha N_{Pe}\sqrt{12.5f}}{[\alpha N_{Pr} + \ln(1 + 5\alpha N_{Pr})]\,\eta_2 + \frac{1}{5\xi_2}\int_{\left(\frac{x}{b}\right)_{x^+=30}}^{2} \frac{V_\theta}{\overline{V}_\theta}\left[\int_{\left(\frac{x}{b}\right)_{30}}^{\frac{x}{b}} \frac{1 - x/2b}{1 - \frac{2b}{R_2}\frac{x}{2b}} \frac{d(x/b)}{F_2\left(\frac{x}{b}\right) + \frac{4}{\alpha N_{Pe}\sqrt{f/2}}}\right] d\left(\frac{x}{b}\right)} \quad \ldots [16b]$$

NUMERICAL EVALUATION OF THE NUSSELT NUMBER

The numerical evaluation of Equations [16a] and [16b] for a given geometry and flow condition resolves into:

1 Determination of the velocity distribution.
2 Evaluation of the shearing stress at each wall.
3 Determination of the eddy diffusivity in a curved channel.
4 Evaluation of the last integral in the denominator.

1 The velocity distribution in the curved channel can be

estimated closely from data which were obtained by Wattendorf (3) at Reynolds numbers ranging from 30,000 to 120,000 and for radii of curvature ranging from 0.65 ft to 1.3 ft. These data were correlated, Fig. 3, by plotting $V_\theta r/(V_\theta r)_{max}$ versus $y/(2b)$, but for practical purposes the term $(V_\theta r)_{max}$ may be replaced without serious error by $\bar{V}_\theta R_2$ within the range of the experimental data.

2 The distribution of the shearing stress τ, for fully developed turbulent flow, can be obtained from the Navier-Stokes equations (3). If turbulence is introduced into the Navier-Stokes equation as a fluctuation of the variable around the average (e.g., $v_\theta = V_\theta + v_\theta'$, etc.) and the time averages of all fluctuating terms of the variables as well as their derivatives are neglected as compared to averages of products of such fluctuating variables, one obtains the following set of equations

$$\left.\begin{aligned}
\rho\frac{\partial V_r}{\partial t} &= \frac{\partial}{\partial r}\left(\tau_{rr} - \rho V_r^2 - \rho\overline{v_r'^2}\right) + \frac{\partial}{r\partial\theta}\left(\tau_{r\theta}\right.\\
&\quad \left. - \rho V_r V_\theta - \rho\overline{v_r' v_\theta'}\right) + \frac{\partial}{\partial z}\left(\tau_{rz} - \rho V_r V_z - \rho\overline{v_r' v_z'}\right)\\
&\quad + \frac{1}{r}\left[\left(\tau_{rr} - \rho V_r^2 - \rho\overline{v_r'^2}\right)\right.\\
&\quad \left. - \left(\tau_{\theta\theta} - \rho V_\theta^2 - \rho\overline{v_\theta'^2}\right)\right]\\
\rho\frac{\partial V_\theta}{\partial t} &= \frac{\partial}{r\partial\theta}\left(\tau_{\theta\theta} - \rho V_\theta^2 - \rho\overline{v_\theta'^2}\right) + \frac{\partial}{\partial r}\\
&\quad \left(\tau_{r\theta} - \rho V_r V_\theta - \rho\overline{v_r' v_\theta'}\right) + \frac{\partial}{\partial z}\left(\tau_{\theta z}\right.\\
&\quad \left. - \rho V_z V_\theta - \rho\overline{v_z' v_\theta'}\right) + \frac{2}{r}\left(\tau_{r\theta} - \rho V_r V_\theta - \rho\overline{v_r' v_\theta'}\right)\\
\rho\frac{\partial V_z}{\partial t} &= \frac{\partial}{\partial z}\left(\tau_{zz} - \rho V_z^2 - \rho\overline{v_z'^2}\right) + \frac{\partial}{\partial r}\left(\tau_{rz}\right.\\
&\quad \left. - \rho V_r V_z - \rho\overline{v_r' v_z'}\right) + \frac{1}{r\partial\theta}\left(\tau_{\theta z}\right.\\
&\quad \left. - \rho V_\theta V_z - \rho\overline{v_\theta' v_z'}\right)
\end{aligned}\right\} \ldots [17]$$

where

$$\tau_{rr} = -p + 2\mu\frac{\partial v_r}{\partial r} \qquad \tau_{r\theta} = \mu\left[r\frac{\partial}{\partial r}\left(\frac{v_\theta}{r}\right) + \frac{1}{r}\frac{\partial v_r}{\partial\theta}\right]$$

$$\tau_{\theta\theta} = -p + 2\mu\left(\frac{1}{r}\frac{\partial v_\theta}{\partial_\theta} + \frac{v_r}{r}\right) \qquad \tau_{\theta z} = \mu\left[\frac{\partial v_\theta}{\partial z} + \frac{1}{r}\frac{\partial v_z}{\partial\theta}\right]$$

$$\tau_{zz} = -p + 2\mu\frac{\partial v_z}{\partial z} \qquad \tau_{rz} = \mu\left[\frac{\partial v_r}{\partial z} + \frac{\partial v_z}{\partial r}\right]$$

Under the assumptions made previously for Equation [2], the set of Equations [17] reduces to

$$\frac{1}{r}\frac{\partial\bar{p}}{\partial\theta} = \frac{\partial}{\partial r}\left(\tau_{r\theta} - \rho\overline{v_r' v_\theta'}\right) + \frac{2}{r}\left(\tau_{r\theta} - \rho\overline{v_r' v_\theta'}\right) \ldots [18]$$

Defining the total stress (viscous + turbulent) $\bar{\tau}_{r\theta} = \tau_{r\theta} - \rho\overline{v_r' v_\theta'}$, the distribution of shearing stress across the channel can be obtained by integrating Equation [18]. This yields

$$\tau(r) = \frac{1}{2}\frac{dp}{d\theta}\left[1 - \left(\frac{R_m}{r}\right)^2\right] \ldots [19]$$

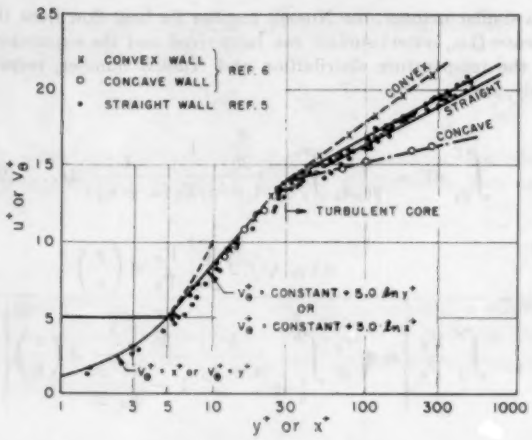

FIG. 3 DIMENSIONLESS VELOCITY DISTRIBUTION NEAR CONVEX, CONCAVE, OR STRAIGHT WALL

where R_m is the radius at which the shearing stress vanishes. Experimental data (6 and 8) indicate that $\tau(r) = 0$ at the point where $\partial V_\theta/\partial r = V_\theta/r$ and can be found geometrically by drawing a tangent from the center of curvature to the velocity profile. The frictional pressure drop in the curved channel can be determined (6) from the relation

$$\frac{dp}{d\theta} = \frac{R_1 + R_2}{2}\frac{f}{b}\frac{\rho\bar{V}_\theta^2}{2} \ldots [20]$$

where f is the Fanning friction factor. The foregoing relations permit the evaluation of the shear stress ratios η_1^2 and η_2^2 in the absence of secondary vortices of a three-dimensional mean flow such as is encountered in sharp pipe bends.

3 To determine the shape of the eddy-diffusivity curved channel, it is necessary to find a pertinent transport property. Considering the transfer of a property P in the direction of r when the mean value of P is constant over cylindrical surfaces perpendicular to r, the mean rate of transfer S of P across a unit area can be obtained by expansion in a Taylor series. Neglecting all but the first term one obtains

$$S = -\overline{v_r' \Delta r}\frac{dP}{dr} \ldots [21]$$

Introducing a mixing length L_r in the direction of r, the effect of turbulence on the transfer of a property may be written as

$$S = -\overline{v_r' L_r}\frac{dP}{dr} \ldots [22]$$

For the case of fully developed turbulent curved flow there are several properties which could be transferable. They are as follows:

Momentum: ρv_θ

Moment of momentum: $r\rho v_\theta$

Vorticity: $\rho\frac{1}{r}\frac{\partial}{\partial r}(rv_\theta)$

Forced vortex parameter: $\rho\frac{v_\theta}{r}$

Substituting these properties into Equation [22] and noting that $\tau_{r\theta} = \rho\,\overline{v_r' v_\theta'}$, the stresses due to turbulent fluctuations for the four cases are as follows:

Momentum transferable: $\tau_{r\theta} = \rho\,\overline{L_r v_r'}\left(\frac{\partial V_\theta}{\partial r}\right)$

Moment of momentum transferable:

$$\tau_{r\theta} = \rho\,\overline{L_r v_r'}\left(\frac{\partial V_\theta}{\partial r} + \frac{V_\theta}{r}\right)$$

Vorticity transferable:

$$\tau_{r\theta} = \rho\,\overline{L_r v_r'}\left(\frac{\partial^2 V_\theta}{\partial r^2} + \frac{1}{r}\frac{\partial V_\theta}{\partial r} - \frac{V_\theta}{r^2}\right)$$

Forced vortex parameter transferable:

$$\tau_{r\theta} = \rho\,\overline{L_r v_r'}\left(\frac{\partial V_\theta}{\partial r} - \frac{V_\theta}{r}\right) \quad \ldots\ldots\ldots\ldots\ldots\ldots [23]^3$$

Experimental data (6 and 8) agree with the hypothesis that the turbulent shearing stress depends on the vortex parameter rather than the physically equally plausible moment of momentum as has been assumed by Prandtl (9).

Postulating the similarity between the diffusivity, $\overline{L_r v_r'} = \epsilon$, for the heat content and the pertinent flow property, the heat content per unit volume transferred in Equation [2] is

$$\rho c_p\,\overline{v_r' T'} = -\overline{v_r' L_r}\rho c_p\frac{dT}{dr} = \rho\epsilon c_p\frac{dT}{dr} \quad \ldots\ldots\ldots [24]$$

Data obtained by Wattendorf (6) show that in the vicinity of a curved wall, the velocity distribution in the turbulent core can be represented by a dimensionless equation of the type

$$V_{\theta 1}^{+} = \text{const}\,(y^{+})^{1/n} \quad \text{or} \quad V_{\theta 2}^{+} = \text{const}\,(x^{+})^{1/n} \ldots [25]$$

However the exponent n depends on the curvature parameter, $\left(\nu/R_c\sqrt{\tau_w/\rho}\right)$ as shown in Fig. 4, which is taken from reference (6). (It may be noted that the abscissa in the original reference is in error.) The constant in Equation [25] can be evaluated by joining the velocity profile in the turbulent core to that in the buffer layer (i.e., $V_\theta^{+} = 14$ when x^{+} or $y^{+} = 30$). The velocity gradient can be obtained by differentiating Equation [25], and can be expressed as

$$\text{Convex:} \quad \frac{\partial V_\theta}{\partial y} = \frac{(\tau_1/\rho\,\overline{V}_\theta)\ \text{const}}{n\left(\frac{\sqrt{\tau_1/\rho}\ y}{\nu}\right)^{\frac{n-1}{n}}} \quad \ldots\ldots [26a]$$

$$\text{Concave:} \quad \frac{\partial V_\theta}{\partial y} = \frac{(\tau_2/\rho\,\overline{V}_\theta)\ \text{const}}{n\left(\frac{\sqrt{\tau_2/\rho}\ x}{\nu}\right)^{\frac{n-1}{n}}} \quad \ldots\ldots [26b]$$

Equations [26a] and [26b] upon substitution into Equation [23] yield the eddy diffusivity from the respective walls to a distance where a maximum is reached. The value of the eddy diffusivity in the vicinity of the point in the channel where the shearing stress approaches zero is uncertain because the equation for the eddy diffusivity becomes indeterminate. This difficulty has been discussed by Harrison and Menke (10) and their comments also apply here.

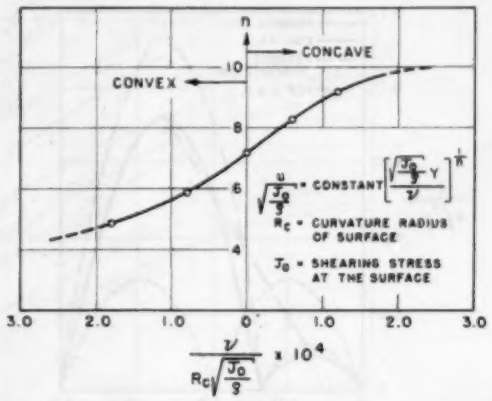

FIG. 4 RECIPROCAL OF EXPONENT FOR POWER LAW OF VELOCITY DISTRIBUTION IN A CURVED CHANNEL VERSUS CURVATURE PARAMETER

For the purpose of numerical calculations it was assumed that the shape of the eddy-diffusivity curve in a curved channel is similar to that observed by Nikuradse in a straight pipe (7) and tends toward zero at the point where the shearing stress disappears. This assumption may lead to a maximum error in the calculated Nusselt modulus of about 20 per cent at Prandtl numbers near unity as compared to a shape joining the peaks by a straight line.

4 The last integral in the denominator can be evaluated numerically or graphically using the velocity distribution and the eddy-diffusivity curve determined previously (see items 1 and 3).

An important point to note in the evaluation of this integral is that the lower limit of integration (i.e., the edge of the buffer layer where y^{+} or $x^{+} = 30$) is inversely proportional to the viscosity. Physically, this means, of course, that a more viscous fluid has a thicker boundary layer. In view of the fact that the local value of the integral, especially for large values of N_{Pe}, is very large for small values of ϵ_M (i.e., near the wall and in the region $\tau \to 0$) a thick buffer layer will result in a smaller numerical value for the integral than a thin buffer layer. Hence the choice of the fluid or the viscosity will influence the Nusselt modulus even at a specified Peclet number. This effect of viscosity is in addition to its influence on the curvature parameter $\left(\nu/R_c\sqrt{\bar{\tau}_w/\rho}\right)$ which determines the value of the exponent n used in Equations [26a] and [26b].

CALCULATIONS

Nusselt numbers, Equations [16a] and [16b], have been evaluated numerically for conditions of heat flow from the convex or concave surface for flow channels having geometries similar to those used in references (2) and (6) (i.e., $R_1 = 0.655$ ft, $R_2 = 0.820$ ft for Case I, and $R_1 = 0.1250$ ft, $R_2 = 0.1305$ ft for Case II). For the numerical calculations, a value of viscosity equal to that of standard air has been used for Case I and a viscosity equal to that of water ($\nu = 1.0 \times 10^{-5}$ lb-sec/ft^2) for Case II. The selection of ν for Case II was dictated by the available experimental data. The calculations have been extended over a Prandtl-number range from 0.01 to 100 and a Reynolds-number range from 10^4 to 10^5. For Case I, the calculations have been performed for eddy-diffusivity curves based on Equation [23] as well as the assumption that the moment of momentum is conserved, in order to determine the

[3] It is interesting to note that the viscous stress is

$$\tau_{r\theta} = \mu\left(\frac{\partial V_\theta}{\partial r} - \frac{V_\theta}{r}\right)$$

and therefore $\rho\,\overline{L_r v_r'}$ is virtually a viscosity coefficient similar to the case of straight flow.

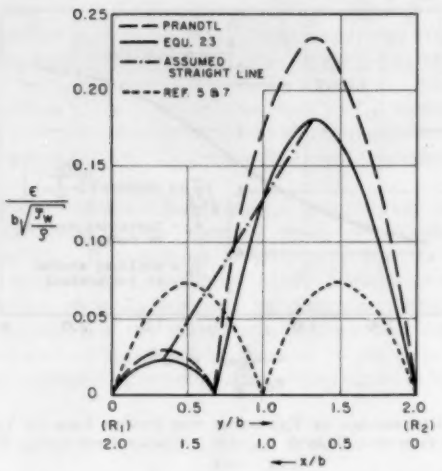

FIG. 5 EDDY-DIFFUSIVITY DISTRIBUTION FOR CHANNEL I

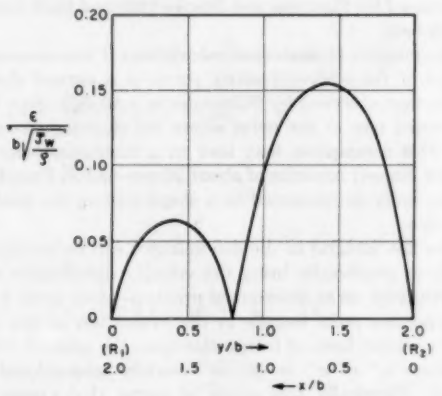

FIG. 6 EDDY-DIFFUSIVITY DISTRIBUTION FOR CHANNEL II

TABLE 1 NUSSELT NUMBERS CALCULATED FOR CONVEX AND CONCAVE WALL OF CHANNEL I (R_1 = 0.655 ft, R_2 = 0.820 ft)

N_{Re}	N_{Pr}	N_{Pe}	Nusselt number — N_{Nu} Convex wall	Straight[a] wall	Concave wall	N_{Nu} Concave / N_{Nu} Convex (R)	Eddy diffusivity based on
1.0×10^4	0.01	1.0×10^2	5.4	5.5	5.5	1.02	Eq. [23] or ref. (7)
1.0×10^4	0.10	1.0×10^3	6.65	...	8.05	1.21	
1.0×10^4	1.0	1.0×10^4	18.0	...	26.1	1.45	
1.0×10^4	10.0	1.0×10^5	57.5	...	80.0	1.40	
1.0×10^4	50.0	1.0×10^6	90.0	...	116.0	1.29	
5.0×10^4	0.01	5.0×10^2	6.9	7.0	7.1	1.03	
5.0×10^4	0.10	5.0×10^3	14.7	19.0	22.6	1.54	
5.0×10^4	0.70	3.5×10^4	54.3	...	88.8	1.62	
5.0×10^4	1.00	5.0×10^4	59.0	...	98.0	1.64	
5.0×10^4	10.00	5.0×10^5	244.0	...	333.0	1.36	
5.0×10^4	100.00	5.0×10^6	400.0	...	510.0	1.28	
2.0×10^5	0.01	2.0×10^3	9.0	11.0	13.5	1.50	
2.0×10^5	0.10	2.0×10^4	36.2	...	61.0	1.66	
2.0×10^5	0.70	1.4×10^5	147.0	...	260.0	1.77	
2.0×10^5	1.00	2.0×10^5	179.0	...	306.0	1.71	
2.0×10^5	10.0	2.0×10^6	780.0	...	1090.0	1.39	
1.0×10^6	0.01	1.0×10^4	21.0	24.4	33.8	1.61	
1.0×10^6	0.05	5.0×10^4	65.6	90.0	122.0	1.86	
1.0×10^6	0.10	1.0×10^5	115.0	...	217.0	1.89	
1.0×10^6	0.70	7.0×10^5	500.0	700.0	930.0	1.86	
1.0×10^6	1.00	1.0×10^6	653.0	...	1117.0	1.80	
5.0×10^4	0.01	5.0×10^2	6.9	7.0	7.1	1.03	Ref. (9)[b]
5.0×10^4	0.10	5.0×10^3	12.3	19.0	29.5	2.40	Ref. (9)[b]
5.0×10^4	1.00	5.0×10^4	50.3	...	108.0	2.05	Ref. (9)[b]
5.0×10^4	10.0	5.0×10^5	198.0	...	322.0	1.62	Ref. (9)[b]

[a] Harrison and Menke (reference 10).

[b] $\epsilon = \dfrac{\tau/\rho}{\dfrac{\partial}{\partial r}(rV_\theta)}$

effect of Prandtl's hypothesis on the Nusselt modulus. In addition, for Case I the Nusselt numbers at a Prandtl number of unity also were calculated on the assumption that the eddy diffusivity follows a straight-line relationship between the maxima calculated from Equation [23]. The eddy-diffusivity curves used for these calculations are shown in Fig. 5 for Case I and Fig. 6 for Case II. For all calculations α was assumed to be unity.

The Nusselt numbers calculated for Case I are shown in Table 1, both for a convex and a concave curvature. For comparison also the results obtained by Harrison and Menke (10) for a straight channel are included in this tabulation. Their Nusselt numbers extend only over a limited range of Reynolds numbers, but where a comparison can be made the agreement with the results of reference (10) is excellent. Fig. 7 shows these results for Case I as a plot of Nusselt number versus Prandtl number for Reynolds number of 1.0×10^4, 5.0×10^4, 2.0×10^5, and 1.0×10^6.

The Nusselt numbers calculated for Case II are shown in Table 2. The results of this theoretical analysis have been compared in Fig. 8 with the results of heat-transfer experiments in curved flow channels. The experimental phase of the work (11) is described in the Appendix.

Discussion of Effect of Curvature on Nusselt Number

The analysis leading to Equations [16a] and [16b] shows that the degree of curvature affects the tractive forces at the wall as well as the shape of the eddy-diffusivity curve. The first phenomenon directly affects only the thermal resistances of the laminar sublayer and the buffer layer because their respective thicknesses are inversely proportional to the square root of the wall shear. Hence this mechanism is most important for fluids having Prandtl numbers larger than unity because for such fluids the thermal resistance in the turbulent core is relatively small. As a rule of thumb, the ratio of the Nusselt number for a concave wall to the Nusselt number for a convex wall under similar flow conditions is equal to the square root of the ratio of the respective shearing stresses. For geometries encountered in practical applications the Nusselt number for a concave surface is from 25 to 60 per cent larger than for a convex surface at the same Reynolds number, when the Prandtl number of the fluid is larger than unity.

For fluids having Prandtl numbers of unity or less, the shape of the eddy-diffusivity curve may affect greatly the value of the Nusselt number. However, the influence of curvature is important only for large values of the Peclet number. If the Peclet number is small, then the heat transfer by conduction in the turbulent core is more important than the convective mechanism, and consequently the value of the last integral in the denominator of Equations [16a] and [16b] is not materially affected by the shape of the eddy-diffusivity curve since

$$F_1 \text{ or } F_2 \ll \frac{4}{N_{Pe}\sqrt{f/2}}$$

For Peclet numbers less than 10^3 Equations [16a] and [16b] yield values of Nusselt numbers which are in agreement with those for a straight heating surface (10). On the other hand, for va ues of

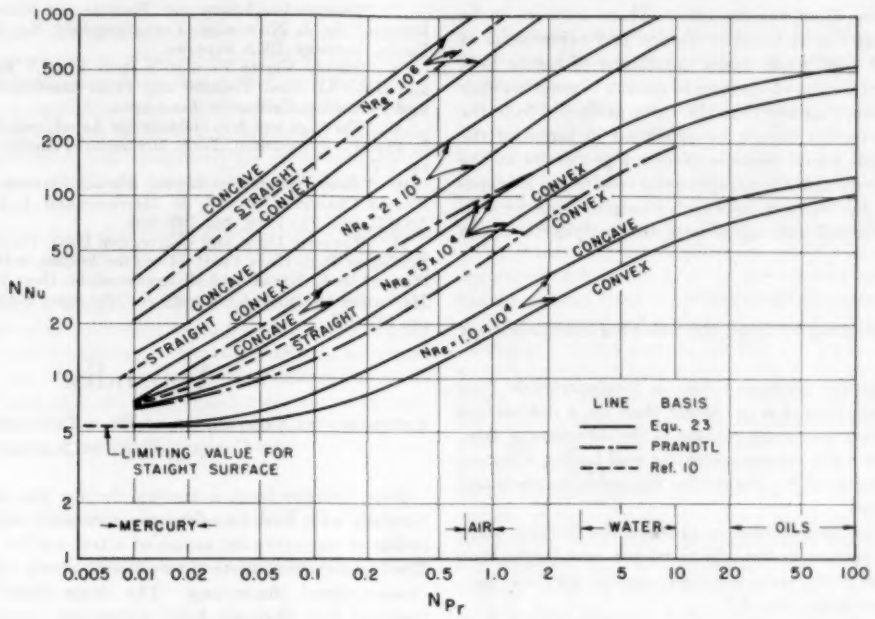

FIG. 7 NUSSELT NUMBER AT CONCAVE, CONVEX, AND STRAIGHT SURFACE FOR CHANNEL I

TABLE 2 NUSSELT NUMBERS CALCULATED FOR CONVEX AND CONCAVE WALL OF CHANNEL II (R_1 = 0.1250 ft, R_2 = 0.1305 ft)

N_{Re}	N_{Pr}	N_{Pe}	N_{Nu} (convex)	N_{Nu} (concave)	$\frac{R}{N_{Nu\ concave}}{N_{Nu\ convex}}$
1.0×10^4	0.1	1.0×10^3	7.2	10.0	1.39
1.0×10^4	1.0	1.0×10^4	22.1	32.8	1.48
1.0×10^4	10.0	1.0×10^5	65.5	88.0	1 34
1.0×10^4	50.0	5.0×10^5	95.0	119.0	1.25
3.0×10^4	1.0	3.0×10^4	56.0	87.5	1.55
3.0×10^4	10.0	1.0×10^5	176.0	240.0	1.35
5.0×10^4	0.01	5.0×10^3	7.1	8.9	1.25
5.0×10^4	0.1	5.0×10^3	19.7	32.2	1.64
5.0×10^4	1.0	5.0×10^4	79.0	128.0	1.62
5.0×10^4	10.0	5.0×10^5	256.0	352.0	1.38
5.0×10^4	50.0	2.5×10^6	378.0	482.0	1.27
5.0×10^4	100.0	5.0×10^6	415.0	512.0	1.23
2.0×10^5	1.0	2.0×10^5	56.0	87.5	1.55
2.0×10^5	10.0	2.0×10^6	176.0	240.0	1.35

the Peclet number larger than 10^3, the shape of the eddy-diffusivity curve becomes increasingly important and essentially controls the value of the Nusselt number. For instance, in the case of a molten metal at a Reynolds number of 10^6, an almost twofold increase in the heat-transfer coefficient could be attained for a wall of concave curvature, compared to the heat-transfer coefficient for a convex wall of similar curvature. Since this increase in heat-transfer rate can be achieved without an increase in pumping requirements, special geometries might be considered in heat-exchange equipment for molten metals where a high heat flux in a small space is desired.

To determine the effect of Prandtl's hypothesis of the exchange mechanism on the Nusselt number in a curved channel, Equations [16a] and [16b] were re-evaluated at a Reynolds number of 5×10^4, using values of the eddy diffusivity calculated on the basis that the moment of momentum instead of the vortex parameter is the transfer property. The results of these calculations are presented in Fig. 7, and an inspection of these curves shows that the effect of curvature would be even more pronounced if the moment of momentum is used as the transfer property. For instance, at a Prandtl number of 0.7 the ratio of concave to convex Nusselt number is 2.2 according to Prandtl's hypothesis, as compared to 1.6 for the vortex parameter theory.

In view of the fact that there exists considerable uncertainty regarding the shape of the eddy-diffusivity curve in the neighborhood of the point where the shearing stress becomes zero, the Nusselt numbers also were evaluated using an assumed straight-line relationship for the eddy diffusivity between the peaks calculated from Equation [23]. This shape of the curve represents only a hypothetical extreme, indicating the smallest possible effect of curvature. At a Reynolds number of 5×10^4 and a Prandtl number of 0.7, the minimum Nusselt number ratio is 1.4 as compared to 1.6 for the analysis based on the vortex parameter and 1.5 for the experimental results.

The analytical results have been compared in Fig. 8 with experimental results obtained with a test section whose geometry

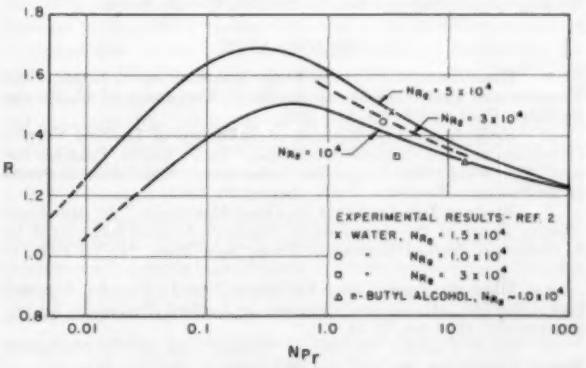

FIG. 8 COMPARISON OF EXPERIMENTAL AND CALCULATED RATIO OF CONCAVE TO CONVEX NUSSELT NUMBER FOR CHANNEL II
(N_{Nu2}/N_{Nu1} versus N_{Pr} for various N_{Re})

corresponds to Case II of the analysis. There appears to be reasonable good agreement between theory and experiment at low values of heat flux, while under conditions of higher heat flux, the experimental ratio of concave to convex Nusselt number was found to be somewhat less than the value predicted from the analysis. This deviation cannot be explained in terms of the theoretical approach which assumes constant properties in the flow channel. However, if the experimental results are extrapolated to zero heat flux so as to approach constant property conditions the experimental data agree with the analysis to within 10 per cent.

Conclusions

Based on the foregoing analysis, the following conclusions are made:

1 The heat-transfer coefficient for an incompressible fluid flowing in a curved channel is (*a*) larger than for a flat surface along the wall having a concave surface in the direction of flow, (*b*) smaller than for a flat surface along the wall having a convex surface in the direction of flow for similar Reynolds numbers and similar cross sections.

2 For geometries encountered in practice the Nusselt number for a concave surface is from 25 to 60 per cent larger than for a convex surface at the same Reynolds number for fluids having Prandtl numbers larger than 0.7.

3 For fluids having a Prandtl number below 0.02 the influence of curvature is insignificant at Reynolds numbers below 10^5, but at Reynolds numbers above 10^6 a twofold increase of the Nusselt number along a concave surface over that of a convex surface is predicted by the analysis. There are no experimental data available for such fluids to verify this result.

4 Experimental results with water and alcohol in a heat-transfer test section having a radius of curvature of 1.5 in. agree within 10 per cent with the theoretical analysis.

5 Assuming that the forced vortex parameter, $\rho(v_\theta/r)$, is a transferable property in curved flow, the turbulent and viscous stresses in the equations of motion may be superimposed in direct analogy with the mixing-length theory for straight flow.

6 Additional experiments should be performed with various radii curvature and with different fluids to verify the theoretical results over wider ranges of the variables.

Acknowledgments

Appreciation is expressed to Prof. Luigi Crocco of Princeton University and to Prof. Lawrence Grossman of the University of California for valuable suggestions, and to Mr. N. Van De Verg, Jet Propulsion Laboratory, California Institute of Technology, for help and encouragement in the experimental work.

BIBLIOGRAPHY

1 "Heat Transfer in Curved Flow Channels," by F. Kreith, Heat Transfer and Fluid Mechanics Institute, University of California, Berkeley, Calif., 1953, pp. 111–122.

2 "Preliminary Investigation of Influence of Heating Surface Curvature on Heat-Transfer Coefficient," by F. Kreith, Progress Report No. 4-115, Jet Propulsion Laboratory, California Institute of Technology, Pasadena, Calif., August 25, 1945.

3 "Modern Developments in Fluid Mechanics," by the Fluid Motion Panel of the Aeronautical Research Committee, edited by S. Goldstein, Oxford University Press, New York, N. Y., 1938, p. 647.

4 "Über die Ausgebildete Turbulenz," by L. Prandtl, Proceedings of the 2nd International Congress for Applied Mechanics, Zurich, Switzerland, 1926, pp. 62–74.

5 "Heat Transfer to Molten Metals," by R. C. Martinelli, Trans. ASME, vol. 69, 1947, pp. 947–959.

6 "A Study of the Effect of Curvature on Fully Developed Turbulent Flow," by F. L. Wattendorf, Proceedings of the Royal Society of London, England, series A, vol. 148, February, 1934, pp. 565–598.

7 "Gesetzmässigkeiten der Turbulenten Strömung in Glatten Rohren," by J. Nikuradse, Forschungsheft No. 356, VDI Verlag, Berlin, Germany, 1932, 36 pages.

8 "Steady Vortex Flow in a Real Fluid," by H. A. Einstein and Huon Lá, Heat Transfer and Fluid Mechanics Institute, Stanford University, California, June, 1951.

9 "Vorträge aus dem Gebiete der Aerodynamik Aachen Ks," by L. Prandtl, Symposium, Tech. Hochschule, Aachen, Germany, 1929, pp. 1–7.

10 "Heat Transfer to Liquid Metals Flowing in Asymetrically Heated Channels," by W. B. Harrison and J. R. Menke, Trans. ASME, vol. 71, 1949, pp. 797–803.

11 "Pressure Drop and Convective Heat Transfer With Surface Boiling at High Heat Flux: Data for Aniline, n-Butyl Alcohol, and Water," by F. Kreith and M. Summerfield, Heat Transfer and Fluid Mechanics Institute, University of California, Berkeley, Calif., 1949, pp. 127–138.

Appendix[4]

Experimental Comparison of Heat Transfer From Convex and Concave Heating Surfaces

Heat transfer from a convex surface was compared experimentally with heat transfer from a concave surface of the same radius of curvature by means of a test section shown in Fig. 9. The test section consists of two flow channels which are of similar cross-sectional dimensions. The inner (concave) and outer (convex) flow channels have a common central dividing wall. This wall presents a concave surface to the coolant in the inner flow channel and a convex surface to the coolant in the outer flow channel. The central wall also serves as a resistance heating element for the liquids in both channels, since it is heated by electric current. The combined central-wall heating element

[4] This Appendix presents the results of one phase of research carried out at the Jet Propulsion Laboratory, California Institute of Technology, under Contract Number W-04-200-Ord-455, sponsored by the Department of the Army, Ordnance Corps.

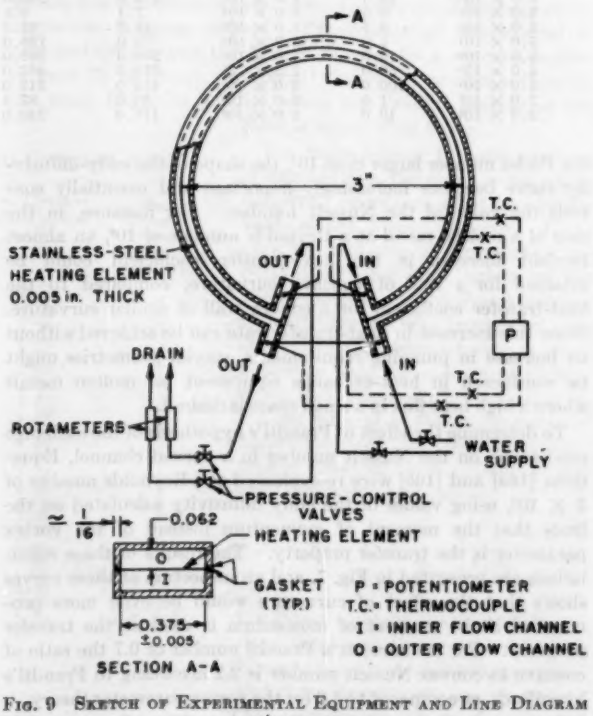

Fig. 9 Sketch of Experimental Equipment and Line Diagram of Apparatus

is insulated from the walls of the inner and outer channels by insulating gaskets as shown in detail A-A of Fig. 9. Provisions were made to use both water and n-butyl alcohol as coolants.

During each test, equal flow rates were maintained in the inner and outer channels and the respective temperature differences between inlet and outlet were measured for given heat input. The inlet temperatures of both streams were identical since a common inlet line was used.

Calculations of temperature gradients compatible with known heat-transfer rates in the 0.005-in.-thick heating element showed that the surface temperatures of the concave and convex surfaces must be within 1 deg F at heat fluxes below 1 Btu/in.^{2} sec. The bulk temperature rise of the coolant was less than 25 deg F in both channels, and it could be assumed without introducing an appreciable error (less than 3 per cent), that the temperature potentials between wall and bulk of liquid were equal for the inner and outer flow channels.

The heat-transfer coefficient is given by

$$h = \frac{q}{A(T_{wall} - T_{bulk})} \quad \ldots\ldots [27]$$

The rate of heat transfer from the entire heating strip is given for each flow channel by

$$q = wc_p (T_{out} - T_{in}) \quad \ldots\ldots [28]$$

where w is the fluid flow rate.

Therefore the following relationship between the heat-transfer coefficient of the concave and that of the convex surface is approximately correct

$$\frac{h_{concave}}{h_{convex}} = \frac{(T_{out} - T_{in})_{concave}}{(T_{out} - T_{in})_{convex}} \quad \ldots\ldots [29]$$

By means of this equation, it is possible to compare the heat-transfer coefficients of the convex surface with those of the concave surface.

Experimental results (2 and 11) at Reynolds numbers of 1×10^4, 1.5×10^4, and 3×10^4 for water and n-butyl alcohol were obtained at various heat fluxes between 1×10^5 and 8×10^3 Btu/hr-sq ft. In all cases the ratio $h_{concave}/h_{convex}$ was found to decrease slightly with increasing heat flux. The ratios of $h_{concave}/h_{convex}$ for each Reynolds number were plotted versus heat flux and the curves were extrapolated to zero heat flux to correspond with the assumption made in the analysis. The results of these tests are shown in Fig. 8.

The equipment used for these tests unfortunately did not permit the quantitative determination of the heat-transfer coefficient. Additional tests would be desirable to determine the heat-transfer coefficient and extend the range of variables.

Discussion

KURT GOLDMANN.[5] The author is to be congratulated for a very good paper which presents another valuable contribution to the knowledge of heat-transfer characteristics for fluids flowing through curved channels.

One may perhaps point toward the need for further work to increase the usefulness of the results and to ascertain the effects of certain simplifying assumptions.

The author presents results for two geometries (Cases I and II). It should be possible to define a curvature parameter (b/R or a similar expression) which allows a presentation of the results as a function of this parameter. It would be of interest to observe the effect of the amount of curvature on heat-transfer coefficients.

The author has assumed that the eddy diffusivity is zero in laminar sublayers adjacent to walls. While errors introduced by this assumption are small for fluids with Prandtl numbers less than unity, they do become significant for fluids with higher Prandtl numbers. Thus the results presented in Fig. 7 for water and particularly those for oils may not be valid.

An interesting consequence of curved channel flow is the centrifugal field which is set up by the fluid motion. The writer has carried out some work to confirm his postulate that it is possible to "centrifuge" boundary layers to increase heat-transfer coefficients under certain conditions. Such conditions prevail at high-rotational fluid velocities and simultaneously high-heat fluxes. The high-heat fluxes establish temperature differences through boundary layers that are large enough to be associated with significant density differences for all common fluids. For concave surfaces and heating of the fluid, the centrifugal field set up by the fluid motion will exert forces that tend to replace low-density particles in the boundary layer by higher-density particles of the fluid bulk. The converse is true for convex surfaces and fluid cooling. The expected effect in either case is a continuous breaking up of boundary layers by centrifuging with an attendant increase of heat-transfer coefficients.

AUTHOR'S CLOSURE

The author agrees with Mr. Goldmann that further work on the influence of curvature on heat transfer should be done in order to verify the results presented in this paper over wider ranges of the variables and also to explore the potential applications of the phenomena associated with convection in the presence of a centrifugal-force field.

The author originally intended to investigate a wide range of curvature radii and channel widths in the hope of finding some kind of generalized curvature parameter which would allow a simple correlation of the results. The only reason the numerical computations are limited to two geometries is that no mechanical computing equipment was available and the computations are extremely time-consuming without it. The author would like to take this opportunity to encourage someone who has access to mechanical computing equipment to continue the calculations. Mr. Goldmann has used IBM equipment successfully on a similar problem (12)[6] and the same general method should be applicable to the calculations of Nusselt numbers in curved channels.

The second point raised in the discussion concerns the assumption that laminar flow exists in a fluid layer adjacent to the wall. Deissler (13) recently measured the velocity distribution during turbulent flow in the vicinity of a pipe wall and found that the velocity distribution in the region between $y^+ = 0$ and $y^+ = 26$ can be correlated by a single equation. His results, however, do not eliminate the possibility of the existence of a thin laminar layer as was originally postulated by Prandtl. Some direct evidence for the existence of a laminar layer was obtained by Fage and Townend (14) who observed no velocity fluctuations in a radial direction near the wall during turbulent flow in a tube. On the other hand, Deissler (15) obtained excellent agreement with experimental data at high Prandtl numbers by assuming that the diffusivity can be represented by a continuous function which approaches zero at the wall. It should not be overlooked, however, that similar correlation between theory and experiment can be obtained without abandoning the laminar sublayer concept by simply allowing for a variation in the layer thickness (16).

[5] Research Engineer, Nuclear Development Associates, Inc., White Plains, N. Y. Assoc. Mem. ASME.

[6] Numbers in parentheses refer to Bibliography at the end of the closure.

To determine the effect of turbulence in the laminar sublayer, Deissler's equation 17 in reference (15)

$$\frac{\epsilon}{\nu} = n^2 u^+ y^+ (1 - e^{-n^2 u^+ y^+}) \quad [30]$$

was used in the region between $y^+ = 0$ and $y^+ = 5$ to calculate the Nusselt numbers for channel I at Re = 25,000 and Pr = 10. The Nusselt numbers calculated in this manner were found to be about 12 per cent larger than before. At very high Prandtl numbers, however, the assumption that purely laminar flow exists up to $y^+ = 5$ will yield Nusselt numbers considerably smaller than those predicted by Deissler's equation. An equally important factor at high Prandtl is the variation of properties under severe temperature gradients. This effect was not considered in this paper but could be included in the analysis (12, 13).

Mr. Goldmann's last comment is extremely interesting. Experiments are presently also under way at Lehigh University to determine the effect of large centrifugal forces on heat transfer by forced convection. Preliminary results indicate that in a strong centrifugal-force field it may indeed be possible to break up the boundary layer and increase heat-transfer coefficients appreciably. This technique has potential applications in heat exchangers where high heat-transfer rates per unit area in single-phase flow are desired and it may also be used to replace finned surfaces in certain compact heat exchangers.

BIBLIOGRAPHY

12 "Heat Transfer to Supercritical Water and Other Fluids With Temperature Dependent Properties," by K. Goldmann, presented at the International Congress on Nuclear Engineering, AIChE, Ann Arbor, Michigan, June 22, 1954.

13 "Analytical and Experimental Investigation of Adiabatic Turbulent Flow in Smooth Tubes," by R. G. Deissler, NACA Technical Note 2138, July, 1950.

14 "An Examination of Turbulent Flow With an Ultramicroscope," by A. Fage and H. C. Townend, Proceedings of the Royal Society of London, England, series A, vol. 135, 1932, p. 656.

15 "Analysis of Turbulent Heat Transfer, Mass Transfer, and Friction in Smooth Tubes at High Prandtl and Schmidt Numbers," by R. G. Deissler, NACA Technical Note 3145, May, 1954.

16 "Remarks on the Analogy Between Heat Transfer and Momentum Transfer," by L. M. K. Boelter, R. C. Martinelli, and Finn Jonassen, Trans. ASME, vol. 63, 1941, pp. 447–456.

Heat Transfer and Pressure Drop for Viscous-Turbulent Flow of Oil-Air Mixtures in a Horizontal Pipe

By H. A. JOHNSON,[1] BERKELEY, CALIF.

The heat transfer and static pressure drop for two-phase, two-component flow of oil and air were measured for flow in a steam-heated horizontal 15-ft length of 3/4-in. extra-heavy copper pipe. This is a second part of a two-phase heat-transfer program for which the first part, on water-air mixtures, was reported in reference (1).[2] Tentative correlations are presented and used in a comparison of the oil-air and water-air results for heat transfer and nonisothermal pressure drop in the same test system.

Nomenclature

The following nomenclature is used in the paper:

A = inside surface heat-transfer area of tube, sq ft
c = specific heat of single-phase fluid, Btu/lb deg F
D = inside diameter of the tube, ft
f = Weisbach single-phase pipe friction factor defined by

$$\Delta P = f \frac{L}{D} \rho \frac{u^2}{2g}$$

G_L, G_G = single-phase weight rates of flow per unit of tube cross-sectional area, lb/sq ft hr
g = gravitational force per unit mass, 32.2 ft/sec²
h_L, h_G = calculated single-phase heat-transfer coefficient based on tube dimensions, Btu/sq ft hr deg F
h_{TP} = two-phase heat-transfer coefficient, Btu/sq ft hr F, defined by

$$q_{TP} = h_{TP} A (t_2 - t_1)/\ln (t_w - t_1)/(t_w - t_2)$$

k = thermal conductivity of single-phase fluid, Btu/ft hr deg F
L = tube test section length, ft
P_1, P_m, P_2 = static pressures, psia
ΔP_L, ΔP_G = calculated single-phase pressure drop based on tube dimensions and neglecting momentum effects, psi
ΔP_M = calculated momentum change pressure drop, psi
ΔP_{TP} = two-phase pressure drop = $(P_1 - P_2) - \Delta P_M$, psi
q_L, q_G = calculated single-phase heat-transfer rate based on tube dimensions, Btu/hr
q_f, q_{TP} = single-phase and/or two-phase heat-transfer rate equal to enthalpy increase of fluid mixture, Btu/hr
q_s = heat-transfer rate based on steam-condensate rate, Btu/hr
q_u, q_d = upstream and downstream heat-transfer rates determined as fractions of q_f by first and second test section condensate collection rates, Btu/hr
R_L, R_G = liquid and gas (vapor) volume fractions, respectively, fraction of tube volume occupied by one phase
t_1, t_2 = mixed mean temperatures at entrance and exit, deg F
t_m = arithmetic mean of t_1 and t_2, deg F
t_w, T_{ww}, t_{wd} = average inside tube-wall surface temperatures for total upstream and downstream sections of heated lengths, respectively, deg F
u_L, u_G = actual single-phase velocities, fps
W_L, W_G = weight rates of single-phase flow, lb/hr
μ = viscosity of the single-phase fluid, lb/hr ft
ρ = density of single-phase fluid, pcf

Dimensionless Groups:

$G_L D/\mu_{Lm}$, $G_G D/\mu_{Gm}$ = single-phase pipe flow Reynolds moduli
$G_L D^2/(k/c)_{Lm} L$ = liquid-phase modified Graetz modulus
$\Delta P_{TP}/\Delta P_L$ and $\sqrt{\Delta P_L/\Delta P_G}$ = Martinelli-Lockhart (7) two-phase flow correlation parameters. Other dimensionless ratios of h, q, and ΔP are arbitrary parameters suggested by Martinelli-Lockhart procedure
hD/k = single-phase Nusselt modulus
$c\mu/k$ = single-phase Prandtl modulus

Subscripts:

1, 2 = positions at entrance and exit of test section
d = downstream or second condensate collection section of heated test length
f = fluid, single-phase and/or two-phase mixture
L, G = liquid and gas (vapor) phases, respectively
m = mean of states 1 and 2 or temperature at which a property is evaluated
M = momentum effects
s = steam condensate
TP = two-phase
u = upstream or first condensate collection section of heated test length
w = inside tube-wall surface or temperature at which a property is evaluated

Introduction

This paper on heat transfer and nonisothermal pressure drop of oil-air mixtures in horizontal pipe flow is the second part of a

---

[1] Professor, Mechanical Engineering, University of California. Mem. ASME.

[2] Numbers in parentheses refer to the Bibliography at the end of the paper.

Contributed by the Heat Transfer Division and presented at the Annual Meeting, New York, N. Y., November 28–December 3, 1954, of The American Society of Mechanical Engineers.

Note: Statements and opinions advanced in papers are to be understood as individual expressions of their authors and not those of the Society. Manuscript received at ASME Headquarters, August 26, 1954. Paper No. 54—A-150.

continuing two-phase two-component flow heat-transfer program at the University of California. The first part, on water-air mixtures, has been reported by Johnson and Abou-Sabe (1), King (2), and Fried (3). With the annular flow analysis by Levy (4) and the results for air-water mixtures in a vertical pipe by Verschoor and Stemerding (5), this appears to be the present extent of the two-phase two-component flow heat-transfer literature. There is, however, considerable published information on isothermal two-phase pressure drop which has been reviewed recently by Baker (6) in a paper on oil and gas-pressure drop for large-diameter pipes.

The interpretation and attempts at correlating the experimental results presented here parallel the isothermal two-phase flow procedures suggested by Martinelli and Lockhart (7) who characterize the essential features of the flow with the three parameters:

1 Two-phase pressure-drop ratios defined as $\Delta P_{TP}/\Delta P_L$ or $\Delta P_{TP}/\Delta P_G$.

2 Single-phase pressure-drop ratio parameter defined as $\sqrt{\Delta P_L/\Delta P_G}$.

3 Volume fraction R defined as the fraction of conduit volume containing one phase.

They also indicate four modes of flow, grouped according to viscous or turbulent single-phase flow for each fluid, and for each mode several flow patterns arbitrarily characterized by such terms as stratified, bubble, slug, annular, and others. Of the four possible modes, the previous results for heat transfer to water-air mixtures (1) were in the turbulent-turbulent regime while the present oil-air results are for the viscous-turbulent regime.

The alternative procedure for treating the mixture as the flow of a homogeneous fluid (8, 9) has not been investigated here. Ludwig (8) shows this procedure to be in substantial agreement with the Martinelli-Lockhart turbulent-turbulent two-phase pressure-drop correlations, and reports good design results for the relation

$$f = \frac{2gD\rho}{G^2}\frac{\Delta P}{L} = \phi\left[\frac{Du}{\mu_L/\rho_L}\right]$$

where

f = effective pipe-friction factor

$$G = (W_L + W_G)/\frac{\pi}{4}D^2$$

$$\rho = (W_G + W_L)/(W_G/\rho_G + W_L/\rho_L)$$

$$u = G/\rho$$

However, the analytic development for idealized annular flow by Levy (4) shows the Martinelli-Lockhart parameters to be fundamental though not necessarily complete, i.e., not independent of the flow pattern.

Apparatus and Oil Properties

The apparatus is essentially the same as described in reference (1), although it has been completely rebuilt. The test section was changed to a $^3/_4$-in. extra heavy-wall copper pipe (0.737 in. ID) in which the 24 wall thermocouples are imbedded and made flush with the outside tube surface. The test-section lengths are 193.6 in. between pressure taps, the center pressure tap of the first system having been removed, and 186.6 in. of heated length. Since the heated length was short for oil and long for air, satisfactory heat-transfer data required complete mixing and careful measurement of the inlet and outlet fluid temperatures. This was done by installing an outlet mixing chamber in which the baffles and screens could be changed readily and by comparing the average of three inlet and three outlet thermocouples with a threefold temperature-difference thermocouple pile. The observed deviations in the fluid temperature rise seldom exceeded 0.2 deg F. The steam condensate streams were collected separately for upstream and downstream heated lengths of 92.7 and 93.9 in., respectively. The quick-closing-valve system for measuring the volume fraction R_L was removed so that data were not obtained. Dependent on the results of a current study for the effect of the system pressure level, it is believed that further investigations of the volume fraction eventually will be necessary.

The oil was substantially equivalent to the crystal mineral oil used by Sage and Lacey (10) for their properties studies. Purchase specifications were: Freezene heavy SP, specific gravity at 60 F 0.875 to 0.885, viscosity at 100 F 200 to 210 SUS, flash 400 F, fire 455 F, and pour —30 F. The properties given in Table 1 were obtained in the petroleum inspections laboratory of the University of California for this investigation; however, the specific heats were adjusted to favor the Sage and Lacey values since our number of determinations was minimal.

TABLE 1 PHYSICAL PROPERTIES OF THE OIL

Temperature	80 F	140 F	200 F
Thermal conductivity, Btu/ft hr deg F	0.0075	0.0732	0.0689
Spec grav ref to water at 60 F	0.873	0.852	0.831
Specific heat, Btu/lb deg F	0.464	0.504	0.543
Viscosity, lb/hr ft $\mu = \frac{92.88}{(t/100)^{2.72}}$	60 F < t < 220 F		

As a check on the stability of the oil, the viscosity was measured after approximately 400 hr of operation with air. These results, supplied by courtesy of the Shell Development Company, are compared with our original measurement, i.e., foregoing formula, in Table 2.

TABLE 2 USED OIL VISCOSITY, LB/HR FT

Temperature	100 F	210 F
New oil original values (as received)	92.9	12.2
After 3 years in storage	91.7	11.7
Used oil after 400 hr of operation with air	95.8	12.0

Although the used oil showed some color change, the 5 per cent viscosity variation in Table 2 is considered to be within the accuracy of sampling and measurement.

Also, after the 400 hr of operation with air, only minor losses due to leakage and entrainment were observed, so there is no evidence of any mass-transfer effects for these tests.

Single-Phase Tests

A series of single-phase flow tests for both oil and air were made to establish the validity of the system instrumentation and testing techniques. That these results are satisfactory is revealed in Fig. 1. In correlating the oil-flow results the Sieder and Tate viscosity corrections (11) were used. An alternative, more complex laminar-flow correlation procedure proposed by Yamagata (12) was found to be unsatisfactory. It is interesting to note that these laminar-flow heat-transfer data lie between predicted values based on the Leveque constant of 1.615 and McAdams, recommended constant of 1.86 (11). The apparent high-transfer value at a Reynolds modulus of 135 is attributed to experimental error since the total temperature rise here was only 3 deg F, and the high value at the Reynolds modulus of 2200 may be due to the onset of transition flow. Since the heated section was too long for air only, it was necessary to apply a heat-loss temperature correction for the short section of piping between the end of the heated section and the point of outlet-temperature measurement. This correction, while negligible for high air rates, is substantial for Reynolds moduli values below 15,000 and is the probable cause of the large deviations there shown in Fig. 1.

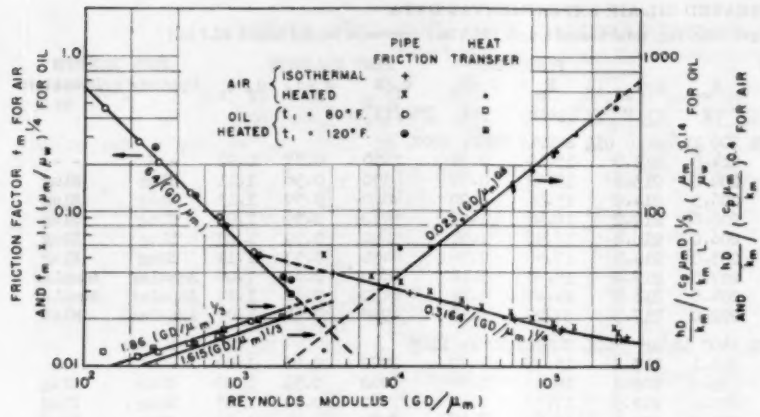

FIG. 1 COMPARISON OF PREDICTED SINGLE-PHASE PIPE FRICTION AND HEAT-TRANSFER PERFORMANCE OF SYSTEM FOR BOTH AIR AND OIL

TWO-PHASE FLOW TEST PROCEDURE

The two-phase test series were conducted at approximately constant oil rates of 700, 1400, 2100, 3500, and 5000 lb/hr with the oil, prior to mixing with the air, controlled at a supply temperature of 120 F. For each liquid rate the air rates were approximately 4, 8, 15, 22, 35, 56, 130, and 280 lb/hr, the highest air rate for any liquid rate being determined by capacity limitations of the air-supply system. On completion of this test series, in which the system pressure level was determined by discharge flow conditions, a discharge valve was installed and two runs made at average system pressures of 30 and 60 psia for oil and air rates of 1400 and 35 lb/hr, respectively. This was done as a trial of the assumption that the system pressure may be an independent parameter having a significant effect on the flow pattern; i.e., some quantitative measure of the flow pattern appears necessary (see Baker, reference 6).

Isothermal pressure-drop runs included a test series for oil rates of 700, 2100, and 5000 lb/hr with air rates of 4, 15, 35, 130, and 280 lb/hr, and two runs at an oil rate of 1400 lb/hr and air rate of 35 lb/hr for system pressures of 22 and 60 psia. These isothermal runs were not planned originally but appeared necessary when the heated pressure drop showed unexpected decreasing values at high air rates.

The flow patterns upstream and downstream of the test section were observed and recorded for each run; however, these patterns are reported here by an arbitrary choice of single words, it being understood that the appearance was often different in the upstream and downstream observation glasses and that in all cases the flow was stratified; i.e., approximately one half or more of the oil always flowed along the bottom of the tube. The difference in appearance usually showed the oil to be transparent or clear upstream and opaque or white downstream. No attempt has been made to include the flow-pattern information in the correlation of results.

RESULTS AND DISCUSSION

For the heated two-phase runs the experimental data are presented in Table 3 and Figs. 2 and 3, while calculated results are in Table 4 and Fig. 4. The two-phase isothermal data and calculated results are presented in Table 5 and Fig. 4.

Considering first the two-phase pressure-drop results in Fig. 4 and the comparison with previous water-air results for the same system shown in Fig. 5, all values have been corrected for momentum effects by subtracting from the measured two-phase pressure drop $(P_1 - P_2)$ a momentum pressure drop ΔP_M calculated in the following manner:

If the liquid and gas (vapor) are assumed to have steady and uniform but not necessarily the same actual velocities u_L and u_G, the momentum pressure drop would be expressed by the relation

$$\Delta P_M = \frac{G^2_{L2}}{\rho_{L2} g R_{L2}} - \frac{G_{L1}{}^2}{\rho_{L1} g R_{L1}} + \frac{G_{G2}{}^2}{\rho_{G2} g R_{G2}} - \frac{G_{G1}{}^2}{\rho_{G1} g R_{G1}}$$

in which it is understood that the liquid and gas properties and flow rates at stations 1 and 2 are corrected to include mass-transfer effects. While not necessary for the oil-air mixtures, this was

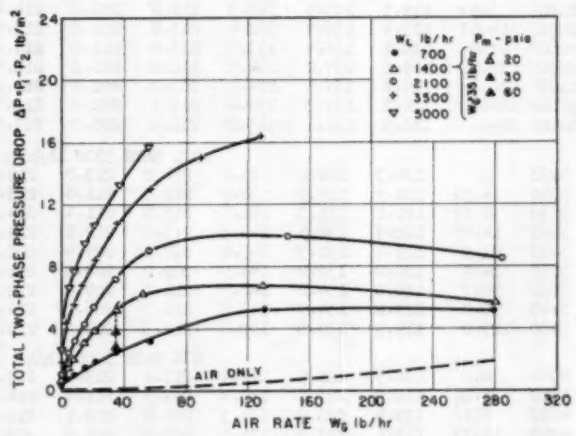

FIG. 2 MEASURED TWO-PHASE PRESSURE DROP FOR HEATED OIL-AIR FLOW

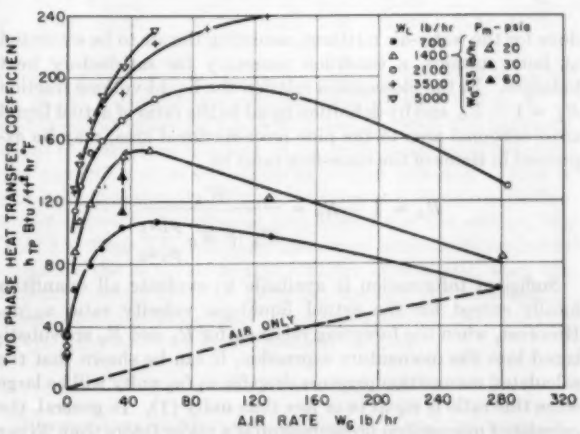

FIG. 3 MEASURED HEAT-TRANSFER COEFFICIENTS FOR OIL-AIR FLOW

TABLE 3 HEATED OIL-AIR EXPERIMENTAL DATA

(0.737-in-ID tube; pressure-drop length 193.6 in.; total heated length 186.6 in.; upstream heated length 92.7 in.)

OIL RATE	AIR RATE	TEMPERATURES						PRESSURES		HEAT TRANSFER			FLOW PATTERN	
		t_1	t_m	t_2	t_w	t_{wu}	t_{wd}	P_m	P_1-P_2	q_t/A	q_t/q_r	q_t/q_s	Upstrm.	Downstrm.
lb/hr	lb/hr	F	F	F	F	F	F	psia	psi	Btu/ft^{2}hr				
					OIL RATE 700 lb/hr		OIL SUPPLY TEMP. 120F							
683	0	117.6	125.8	134.1	215.2	214.8	215.6	15.19	0.35	1850	0.57	0.92	- -	- -
678	4.32	117.7	137.9	158.1	211.2	208.8	213.6	15.72	0.77	4590	0.56	1.11	Slug	Slug
675	7.74	117.7	138.8	160.0	210.5	206.5	214.0	15.86	1.00	4820	0.59	1.15	Slug	Slug
675	14.75	117.5	141.4	165.3	213.0	208.6	217.2	16.48	1.47	5470	0.59	1.07	Slug	Slug
675	21.9	117.2	142.7	168.2	211.2	206.0	216.4	16.96	1.91	5890	0.59	1.07	Slug	Slug
694	35.2	116.4	143.3	170.2	208.9	203.0	214.8	17.66	2.56	6430	0.57	1.12	Slug	Slug
683	56.9	115.8	144.4	173.1	212.6	207.5	217.4	18.78	3.16	6860	0.60	1.06	Annular	Annular
658	131.2	114.7	141.4	168.0	211.4	204.6	218.0	24.47	5.21	6430	0.62	1.12	Annular	Annular
673	279.	113.5	131.9	150.4	209.9	202.0	217.3	37.29	5.18	4950	0.66	1.09	Annular	Mist
					OIL RATE 1400 lb/hr		OIL SUPPLY TEMP. 120F							
1370	0	117.8	122.4	127.0	212.1	211.1	213.2	15.73	0.70	2070	0.69	1.04	- -	- -
1380	4.45	118.7	131.9	145.1	200.7	199.0	202.2	16.83	1.57	6060	0.55	1.20	Slug	Slug
1370	7.79	118.6	135.9	153.3	211.3	209.6	212.9	17.37	2.10	7970	0.54	1.05	Slug	Slug
1390	14.68	118.5	135.9	153.3	205.5	201.8	209.1	18.54	3.08	8120	0.54	1.09	Slug	Slug
1390	22.0	118.1	137.1	156.1	207.0	203.1	210.6	19.53	3.86	8910	0.55	1.06	Slug	Slug
1390	35.9	117.8	138.6	159.4	207.0	201.3	211.8	21.30	5.21	9850	0.54	1.07	Slug	Slug
1380	55.0	118.1	139.4	160.7	215.0	212.7	217.2	31.01	3.85	9980	0.57	1.03	Slug	Slug
1420	35.4	117.6	136.1	154.6	215.0	212.6	217.2	59.56	2.54	8870	0.55	1.03	Slug	Slug
1390	53.1	117.1	137.9	158.7	204.8	199.2	209.9	22.98	6.26	9870	0.55	1.08	Slug	Slug
1390	130.5	116.7	134.5	152.4	206.2	202.7	209.5	28.92	6.76	8600	0.54	1.08	Annular	Annular
1380	281.	115.8	130.1	144.4	216.4	213.0	219.8	42.82	5.63	7200	0.70	1.02	Mist	Mist
					OIL RATE 2100 lb/hr		OIL SUPPLY TEMP. 120F							
2090	0	118.8	122.6	126.4	215.8	214.7	216.8	16.60	1.02	2640	0.60	1.05	- -	- -
2080	4.48	119.7	133.0	146.4	214.5	213.2	215.6	18.14	2.40	9260	0.51	1.05	Slug	Slug
2100	7.93	119.5	133.9	148.3	212.8	210.8	214.4	19.12	3.22	10110	0.52	1.13	Slug	Slug
2090	14.67	119.4	135.9	152.4	213.2	211.6	215.6	20.66	4.30	11570	0.52	0.99	Slug	Slug
2080	21.8	119.2	136.4	153.7	213.0	211.0	215.2	22.10	5.41	12030	0.54	1.16	Slug	Slug
2090	35.2	119.5	137.0	154.5	210.0	207.2	212.5	24.72	7.20	12320	0.54	1.02	Slug	Slug
2100	56.4	119.2	137.1	154.9	207.0	202.8	211.0	27.62	9.04	12720	0.53	1.04	Annular	Annular
2080	146.2	118.2	137.3	156.4	212.1	210.6	213.7	35.46	9.90	13700	0.54	1.00	Annular	Annular
2100	284.	116.9	131.1	145.2	212.9	208.0	217.9	50.9	8.45	10510	0.57	0.99	Annular	Mist
					OIL RATE 3500 lb/hr		OIL SUPPLY TEMP. 120F							
3450	0	120.3	122.9	125.6	214.8	213.8	215.6	18.88	1.79	3000	0.60	1.01	- -	- -
3500	4.36	120.9	129.9	138.9	212.3	211.6	213.6	21.89	4.39	10450	0.51	1.03	Slug	Slug
3530	8.19	121.1	131.3	141.8	213.0	211.4	214.4	23.51	5.46	12150	0.51	1.01	Slug	Slug
3520	14.85	120.7	132.5	144.3	213.2	212.2	214.0	25.6	6.94	13830	0.51	1.01	Slug	Slug
3450	21.9	119.4	131.3	143.2	207.1	205.4	208.7	27.93	8.39	13670	0.52	1.05	Slug	Slug
3550	34.9	120.0	132.2	144.5	209.2	206.3	212.1	31.58	10.70	14500	0.52	1.03	Slug	Slug
3520	56.7	120.0	134.2	148.5	211.1	209.4	212.9	35.94	13.00	16870	0.53	1.08	Annular	Annular
3440	90.0	119.2	134.3	149.3	210.5	206.2	214.8	43.53	15.00	17470	0.53	1.01	Annular	Annular
3480	129.0	119.9	135.3	150.6	212.3	208.5	216.0	49.67	16.30	18170	0.55	1.02	Annular	Annular
					OIL RATE 5000 lb/hr		OIL SUPPLY TEMP. 120F							
4940	0.	120.5	121.9	124.4	215.4	213.6	217.2	22.31	2.61	3160	0.60	1.01	- -	- -
4810	5.21	119.9	126.8	133.7	212.5	211.0	214.0	27.06	6.64	10970	0.52	1.01	Bubble	Ann. Slug
4810	8.16	119.4	126.9	134.3	209.8	209.1	210.7	27.60	7.70	11870	0.52	1.01	Bubble	Ann. Slug
4910	14.79	119.1	127.3	135.5	209.0	208.9	209.2	31.96	9.51	13320	0.52	1.02	Bubble	Slug
4840	21.7	119.1	128.4	138.6	212.1	211.1	212.9	34.22	10.62	15630	0.52	1.01	Bubble	Ann. Slug
4810	36.7	120.1	130.5	140.9	211.1	209.8	212.2	39.12	13.23	16630	0.52	1.01	Annular	Ann. Slug
4805	56.3	121.2	132.5	143.8	211.3	209.7	212.7	44.93	15.76	18170	0.53	1.02	Wave	Ann. Slug

done for the water-air mixtures, assuming the air to be saturated at both stations, a condition necessary for satisfactory heat balances. In the momentum relation the liquid-volume fraction $R_L = 1 - R_G$, and by definition equal to the ratio of actual liquid cross-sectional area to the pipe cross-sectional area, may be expressed in terms of the mass-flow rates by

$$R_L = 1 - R_G = \frac{W_L}{W_L + W_G \dfrac{\rho_L u_L}{\rho_G u_G}}$$

Sufficient information is available to evaluate all quantities locally except for the actual liquid-gas velocity ratio u_L/u_G. However, when the foregoing relations for R_L and R_G are substituted into the momentum expression, it can be shown that the calculated momentum pressure drop for u_L/u_G unity will be large since this ratio is equal to or less than unity (1). In general, the calculated momentum pressure drop is a major (more than 25 per cent) correction only for the heated water-air flows where mass transfer was important, i.e., at water rates of 2000 lb/hr or less. Thus the error in the corrected two-phase pressure drop due to the assumption of unity for u_L/u_G is considered negligible for results presented to date, and the results presented in Figs. 4 and 5 are believed to represent the two-phase friction pressure drop.

In the evaluation of the nonisothermal pressure-drop ratios $\Delta P_{TP}/\Delta P_L$ and $\sqrt{\Delta P_L/\Delta P_G}$, the oil single-phase pressure drop ΔP_L was calculated with and without the Sieder and Tate viscosity correction and results are given in Table 4. The effect of this correction is to increase ΔP_L, causing the pressure-drop results to lie higher and to the left of the uncorrected values which are used in Figs. 4, 5, and 6. Since this relocation is not favorable for the Martinelli-Lockhart correlation, it is suggested that the viscosity correction is not appropriate for the dispersed and therefore probably turbulent oil-air flows. This is of course inconsistent with the concept that ΔP_L should represent the actual oil only pressure drop.

Referring to Fig. 4, it is seen that at low air rates, i.e.,

TABLE 4 HEATED OIL-AIR CALCULATED RESULTS FOR TOTAL TUBE LENGTH

(S and T designate Sieder and Tate viscosity correction.)

AIR RATE	ΔP_M	ΔP_{TP}	h_{TP}	$\frac{G_L D}{\mu_{Lm}}$	$\frac{G_L D^2}{(k/c)_m L}$	$\frac{G_G D}{\mu_{Gm}}$	$\frac{h_{TP}}{h_L}$	$\sqrt{\frac{\Delta P_L}{\Delta P_G}}$	$\frac{\Delta P_{TP}}{\Delta P_L}$	$\frac{h_{TP}/h_L}{\Delta P_{TP}/\Delta P_L}$	$\sqrt{\frac{\Delta P_L}{\Delta P_G}}$	$\frac{\Delta P_{TP}}{\Delta P_L}$	$\frac{h_{TP}/h_L}{\Delta P_{TP}/\Delta P_L}$	$\frac{h_L}{h_G}$	$\frac{q_L}{q_G}$	$\frac{q_{TP}}{q_L}$
lb/hr	psi	psi	Btu/ft²hrF	10^{-3}x	10^{-3}x	10^{-3}x		ΔP_L based on S and T			ΔP_L based on μ_m					
OIL RATE 700 lb/hr OIL SUPPLY TEMP. 120F																
0	0	0.35	20.8	0.287	0.373	- -	1.20	- -	1.15	- -	- -	- -	- -	- -	- -	1.18
4.32	0.01	0.76	64.2	0.364	0.380	1.86	3.89	9.04	2.93	1.33	11.0	1.99	1.96	7.43	44.3	3.18
7.74	0.02	0.98	69.3	0.370	0.380	3.32	4.23	5.38	3.89	1.09	6.50	2.66	1.59	4.62	24.8	3.39
14.76	0.04	1.43	79.3	0.389	0.382	6.31	4.87	3.05	5.94	0.82	3.68	4.08	1.19	2.76	12.8	3.77
21.9	0.08	1.83	90.2	0.398	0.383	9.35	5.57	2.17	7.65	0.73	2.60	5.32	1.05	1.98	8.69	4.15
35.2	0.15	2.41	104.0	0.414	0.394	15.05	6.38	1.49	9.80	0.65	1.78	6.88	0.93	1.36	5.47	4.60
56.9	0.25	2.91	107.1	0.417	0.388	24.2	6.61	0.92	12.86	0.52	1.17	8.96	0.74	0.920	3.39	4.68
131.2	0.51	4.70	96.7	0.378	0.372	56.1	5.97	0.54	19.74	0.30	0.66	13.6	0.44	0.48	1.49	4.39
279.	0.60	4.58	63.7	0.321	0.372	120.4	3.82	0.39	16.36	0.23	0.48	10.8	0.36	0.27	0.74	3.31
OIL RATE 1400 lb/hr OIL SUPPLY TEMP. 120F																
0	0	0.70	23.1	0.532	0.742	- -	1.06	- -	1.06	- -	- -	- -	- -	- -	- -	1.05
4.45	0.02	1.55	89.2	0.660	0.763	1.92	4.29	13.91	2.63	1.63	16.8	1.80	2.38	9.21	59.6	3.72
7.79	0.05	2.05	107.7	0.707	0.765	3.36	5.13	8.16	3.84	1.34	9.96	2.38	1.98	5.91	32.3	4.28
14.68	0.11	2.97	119.1	0.717	0.775	6.33	5.70	4.95	5.38	1.05	5.99	3.68	1.55	3.53	17.2	4.67
22.0	0.18	3.68	130.9	0.735	0.778	9.46	6.29	3.48	7.00	0.90	4.20	4.81	1.31	2.54	12.0	5.03
35.9	0.32	4.89	148.9	0.759	0.780	15.40	7.19	2.36	9.26	0.78	2.84	6.41	1.12	1.72	6.98	5.60
35.0	0.13	3.72	135.5	0.766	0.776	15.10	6.48	2.84	7.36	0.88	3.42	4.98	1.30	1.76	7.20	5.15
35.4	0.04	2.50	114.3	0.736	0.791	15.30	5.35	4.06	4.59	1.17	5.00	3.05	1.75	1.79	7.31	4.46
53.1	0.49	5.77	152.7	0.745	0.779	22.8	7.38	1.75	10.74	0.69	2.11	7.45	0.99	1.25	4.71	5.70
130.5	0.86	5.90	122.7	0.700	0.773	56.2	5.87	0.92	10.52	0.56	1.12	7.16	0.82	0.62	1.99	4.86
281.	0.82	4.81	84.0	0.633	0.760	122.	3.89	0.58	8.33	0.47	0.726	5.34	0.73	0.34	0.96	3.50
OIL RATE 2100 lb/hr OIL SUPPLY TEMP. 120F																
0	- -	1.02	28.0	0.817	1.130	- -	1.10	- -	1.05	- -	- -	- -	- -	- -	- -	0.90
4.48	0.04	2.36	114.5	1.023	1.154	1.94	4.61	15.60	2.75	1.68	19.3	1.80	2.56	10.85	66.3	4.11
7.93	0.08	3.14	129.8	1.049	1.167	3.42	5.33	10.79	3.78	1.41	13.3	2.50	2.13	6.74	37.5	4.60
14.67	0.17	4.13	152.0	1.083	1.164	6.33	6.25	6.29	5.14	1.22	7.72	3.42	1.83	4.14	20.6	5.28
21.8	0.27	5.14	159.1	1.099	1.162	9.38	6.63	4.57	6.51	1.02	5.58	4.37	1.51	2.96	14.1	5.31
35.2	0.45	6.75	172.0	1.118	1.168	15.13	7.18	3.20	8.52	0.84	3.89	5.77	1.24	2.02	8.65	5.67
56.4	0.73	8.31	186.3	1.121	1.175	24.2	7.78	2.27	10.34	0.75	2.75	7.09	1.10	1.38	5.45	6.03
146.2	1.35	8.55	187.5	1.121	1.165	63.0	7.78	1.09	10.95	0.71	1.33	7.36	1.06	0.64	2.12	6.12
284.	1.18	7.25	130.1	0.989	1.160	123.1	5.28	0.772	8.36	0.63	0.96	5.45	0.97	0.39	1.11	4.61
OIL RATE 3500 lb/hr OIL SUPPLY TEMP. 120F																
0	- -	1.79	32.6	1.388	1.866	- -	1.10	- -	1.13	- -	- -	- -	- -	- -	- -	0.91
4.36	0.07	4.32	127.2	1.612	1.926	1.89	4.36	25.6	2.43	1.49	31.8	1.91	2.28	13.05	85.5	3.99
8.19	0.14	5.32	149.5	1.701	1.949	3.54	4.99	14.6	3.62	1.38	18.1	2.36	2.12	7.99	43.7	4.60
14.85	0.26	6.68	172.7	1.724	1.950	6.42	5.94	9.28	4.74	1.25	11.5	3.11	1.91	4.89	24.0	5.29
21.9	0.39	8.00	181.9	1.662	1.903	9.50	6.33	6.90	5.60	1.13	8.46	3.74	1.69	3.55	16.2	5.55
34.9	0.64	10.05	190.3	1.744	1.962	15.11	6.67	4.90	7.28	0.92	6.01	4.84	1.38	2.46	10.3	5.79
56.7	1.00	12.00	222.	1.781	1.958	24.5	7.72	3.36	8.65	0.89	4.12	5.76	1.34	1.65	6.34	6.26
90.0	1.25	13.75	232.	1.720	1.920	39.0	8.12	2.44	10.01	0.81	2.96	6.80	1.19	1.13	4.01	6.85
129.0	1.53	14.77	239.	1.775	1.940	55.7	8.33	1.92	10.66	0.78	2.35	7.11	1.17	0.85	2.68	7.01
OIL RATE 5000 lb/hr OIL SUPPLY TEMP. 120F																
0	0	2.61	34.0	1.89	2.67	- -	1.00	- -	1.11	0.92	- -	- -	- -	- -	- -	1.01
5.21	0.10	6.54	128.0	2.06	2.63	2.27	3.90	29.2	3.05	1.28	36.4	1.97	1.98	12.79	77.0	3.70
8.16	0.19	7.51	143.5	2.06	2.63	3.56	4.39	20.1	3.48	1.26	25.0	2.26	1.94	8.90	49.0	4.10
14.79	0.31	9.20	163.1	2.12	2.69	6.45	4.98	13.0	4.19	1.19	16.1	2.72	1.83	5.54	27.2	4.53
21.7	0.45	10.17	187.9	2.17	2.65	9.43	5.78	9.23	4.86	1.19	11.6	3.15	1.83	4.03	18.6	5.26
36.7	0.73	12.50	207.	2.23	2.65	15.50	6.44	6.18	6.15	1.05	7.67	4.01	1.60	2.68	11.1	5.78
56.3	1.02	14.74	230.	2.32	2.67	24.4	7.18	4.50	7.49	0.96	5.55	4.97	1.45	1.86	7.38	6.37

$\sqrt{\Delta P_L/\Delta P_G} > 2$, both the nonisothermal and isothermal pressure drops increase with increasing air and oil rates, and the maximum deviation from the Martinelli-Lockhart isothermal viscous-turbulent line is +50 per cent. Note also here that increasing system pressure for a given oil and air rate causes the deviation from that reference line to change sign. In the same low air-rate range, Fig. 5 reveals only a slight tendency for the oil-air results to favor the viscous-turbulent line by lying only a little below the turbulent-turbulent water-air results. The trend of increasing pressure drop with increasing oil rate, however, is reversed for increasing water rates.

Referring again to Fig. 4 and considering the range of high air rates, $\sqrt{\Delta P_L/\Delta P_G} < 2$, where the flow pattern is increasingly annular for low oil rates, see Table 3, the nonisothermal pressure drop is seen to depart radically from the trend of the viscous-turbulent reference line. This behavior is indicated, to a lesser degree, for the isothermal pressure drop at an oil rate of 2100 lb/hr, but is not observed for the isothermal oil rate of 700 lb/hr or for any of the nonisothermal water-air results shown in Fig. 5. A comparison of values in Tables 3, 4, and 5 reveals that the cause cannot be attributed to either an excessive momentum pressure-drop correction or to differences in system pressure. There is some indication that the effect may be due to a change in the flow pattern between the entrance and exit of the test section, see Table 3. Thus it is clear that much more analysis is needed to rationalize the behavior of this complex system and, since the analytical model used by Levy (4) appears too idealized at present, an empirical approach is indicated, possibly one including the system pressure as an independent variable.

Two-Phase Heat Transfer

The two-phase heat-transfer performance is, as in reference (1), again represented in Figs. 3, 4, 5, and 6 by ratios of heat-transfer coefficients based on the total heated length and logarithmic

TABLE 5 ISOTHERMAL OIL-AIR DATA AND RESULTS

OIL RATE	AIR RATE	TEMP. t_m	PRESSURES P_m	P_1-P_2	ΔP_M	ΔP_{TP}	$\frac{G_L D}{\mu_{Lm}}$	$\frac{G_G D}{\mu_{Gm}}$	$\sqrt{\frac{\Delta P_L}{\Delta P_G}}$	$\frac{\Delta P_{TP}}{\Delta P_L}$	FLOW PATTERN Upstream	Downstream
lb/hr	lb/hr	F	psia	psi	psi	psi	10^3x	10^3x				
					OIL RATE 700 lb/hr		OIL SUPPLY TEMP. 120F					
660	4.46	117.1	15.82	1.10	0.01	1.10	0.221	1.96	13.75	1.88	Slug	Slug
684	14.40	116.8	16.89	2.18	0.03	2.15	0.228	6.44	5.12	3.48	Slug	Slug
670	35.1	116.2	18.34	3.56	0.11	3.45	0.224	15.5	2.42	5.82	Slug	Slug
688	133.	115.6	25.60	7.05	0.47	6.58	0.230	57.0	0.92	10.76	Annular	Annular
680	276.	110.0	38.66	10.36	0.75	9.61	0.227	121.5	0.59	15.90	Annular	Annular
					OIL RATE 1400 lb/hr		OIL SUPPLY TEMP. 120F					
1380	35.5	117.6	22.39	6.62	0.27	6.35	0.462	15.5	3.92	5.16	Slug	Slug
1380	35.8	117.9	60.47	3.46	0.02	3.44	0.462	15.3	6.36	2.82	Slug	Slug
					OIL RATE 2100 lb/hr		OIL SUPPLY TEMP. 120F					
2080	4.45	118.6	18.95	3.48	0.04	3.44	0.695	1.96	26.3	1.86	Slug	Slug
2090	14.50	118.8	21.77	5.73	0.15	5.58	0.698	6.38	10.10	3.01	Slug	Slug
2060	33.8	118.3	25.70	8.80	0.40	8.40	0.688	14.87	5.18	4.60	Annular	Annular
2100	129.	117.6	36.29	10.57	0.96	9.61	0.702	56.8	1.93	5.16	Annular	Annular
2090	131.	117.1	36.21	10.35	1.24	9.11	0.698	57.6	1.91	4.92	Annular	Annular
2110	278.	116.5	53.79	11.97	1.13	10.84	0.705	122.3	1.21	5.80	Annular	Annular
					OIL RATE 5000 lb/hr		OIL SUPPLY TEMP. 120F					
4770	4.64	119.2	27.86	8.49	0.10	8.39	1.594	2.04	46.6	1.98	Annular	Annular
4840	14.52	120.9	33.06	11.93	0.33	11.60	1.614	6.39	19.1	2.71	Annular	Annular
4860	35.6	119.6	40.93	16.47	0.73	15.74	1.622	15.66	9.57	3.65	Annular	Annular
4860	56.1	119.4	47.17	19.49	1.03	18.46	1.622	24.7	7.54	4.29	Annular	Annular

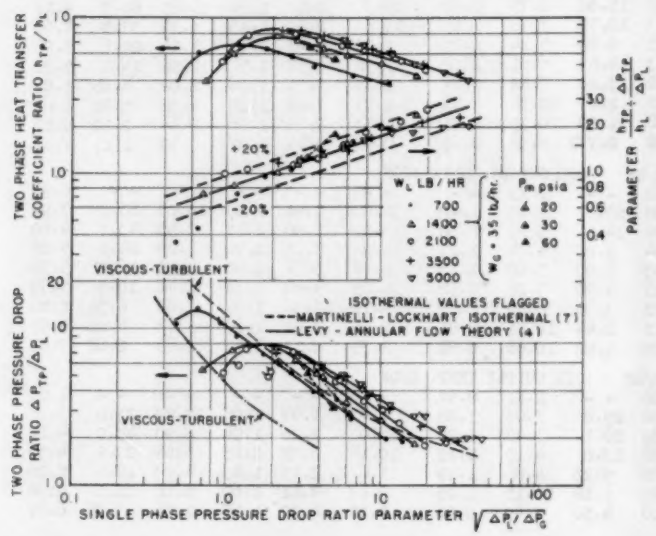

FIG. 4 OIL-AIR HEAT-TRANSFER COEFFICIENT AND TWO-PHASE PRESSURE DROP

mean temperature differences referred to averaged wall temperatures. Of course the temperature rise was usually small enough for all the oil-air mixtures that the difference between the arithmetic and logarithmic mean temperature differences was negligible. Selection of the heat-transfer-coefficient ratios for this purpose of correlation was an arbitrary choice, since corresponding graphs of the heat-transfer rates (see Table 4) revealed no promise for improved correlation and the alternative of an effective Nusselt modulus is believed to be of potential value only if an appropriate and meaningful thermal conductivity were devised.

Fig. 3 reveals the two-phase heat-transfer coefficients as forming a consistent pattern for increasing air and liquid rates. The curve for the 700-lb/hr oil rate is of particular interest since it shows a maximum and the limiting single-phase values. It is probably well for the author that the limiting capacity of the air-supply system was 280 lb/hr. Again, it is noted that the system pressure level at a given oil and air rate effectively influences the heat-transfer performance; i.e., increasing system pressure reduces the liquid displacement and thus the liquid velocity, causing a lowered heat-transfer performance.

In Fig. 4 the two-phase heat-transfer-coefficient ratios exhibit a curve shape and pattern similar to that shown and discussed for the two-phase pressure drop. Because this is consistent with the momentum-heat-transfer analogy the heat-transfer coefficient-pressure drop ratio, shown in Figs. 4 and 6, is selected as appropriate and more convenient than the alternate Equation [1] correlation suggested in reference (1). Although Fig. 4 indicates a ±20 per cent correlation for this ratio, it should be noted that the liquid rate appears as an irregular parameter with unfavorable trends at the limiting air-flow rates.

That the similarity of variation in the oil-air heat-transfer coefficients and pressure drop is not present for the water-air mixtures may be seen in Fig. 5. In fact, Fig. 5 reveals the water-air

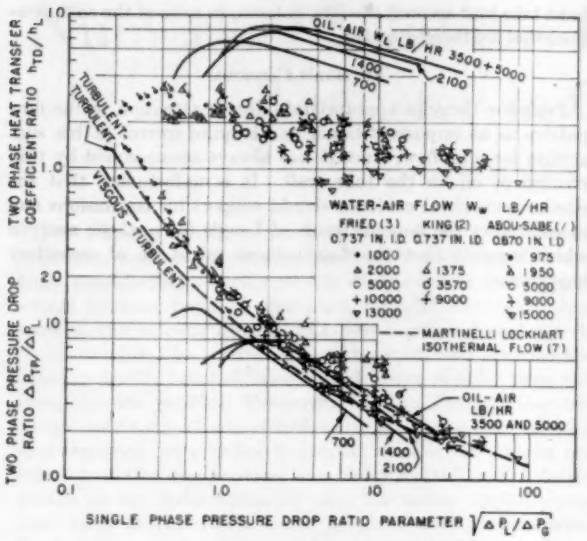

FIG. 5 COMPARISON OF OIL-AIR AND WATER-AIR HEAT TRANSFER AND NONISOTHERMAL PRESSURE DROP

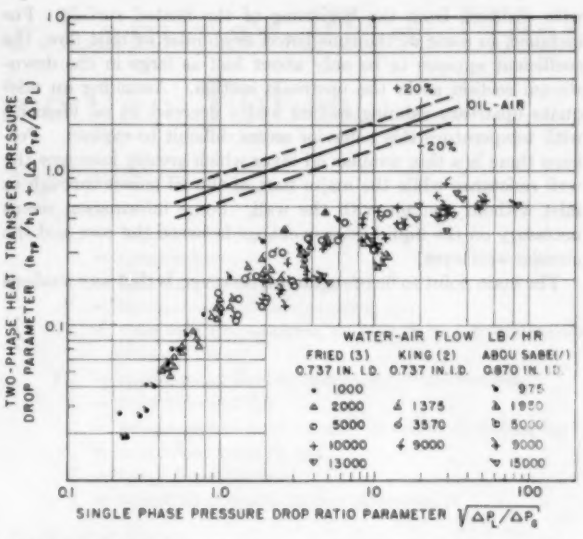

FIG. 6 COMPARISON OF OIL-AIR AND WATER-AIR TWO-PHASE HEAT TRANSFER—PRESSURE-DROP RATIOS FOR PRESENT FLOW SYSTEM

heat-transfer coefficients as being less dependent on the $\sqrt{\Delta P_L/\Delta P_G}$ abscissa than upon the water rate, contributing to the greater (±40 per cent) correlation variation shown in Fig. 6. Finally, it is observed in Figs. 5 and 6 that the oil heat-transfer performance increase due to air addition is roughly 2 to 4 times as great as that for water.

The two-phase, two-component flow system is thus shown to be of such complexity that much more analysis and experimental work must be done to develop an acceptable design procedure for two-phase heat transfer and pressure drop. It is hoped that these data and results will encourage others to perform similar investigations and to develop more effective analyses.

ACKNOWLEDGMENT

The author wishes to acknowledge the financial assistance of the University of California Faculty Research Fund and the services of the student aids, shop, and laboratory staff who participated in this investigation. Appreciation and much credit are due Mr. E. H. Phillips, who, as a student aid, did an excellent and competent job in collecting the experimental data, and to Mr. A. W. Cauwenbergh for the assembly, instrumentation, and operation of the system, which included his many excellent suggestions.

BIBLIOGRAPHY

1 "Heat Transfer and Pressure Drop for Turbulent Flow of Water-Air Mixtures in a Horizontal Pipe," by H. A. Johnson and A. H. Abou-Sabe, Trans. ASME, vol. 74, 1952, pp. 977–987.

2 "Heat Transfer and Pressure Drop for Water-Air Mixtures Flowing in a 0.737 Inch ID Horizontal Pipe," by C. D. G. King, MS thesis, University of California, Berkeley, Calif., 1952, and author's closure of reference (1), pp. 986–987.

3 "Pressure Drop and Heat Transfer for Two-Phase Two-Component Flow," by Lawrence Fried, Chemical Engineering Progress Symposium Series, vol. 50, 1954, pp. 47–51.

4 "Theory of Pressure Drop and Heat Transfer for Annular Steady State Two-Phase Two-Component Flow in Pipes," by Salomon Levy, Proceedings of the Second Midwestern Conference on Fluid Mechanics, Ohio State University, 1952.

5 "Heat Transfer in Two-Phase Flow," by H. Verschoor and S. Stemerding, The Institution of Mechanical Engineers, General Discussion on Heat Transfer, London, England, September 11–13, 1951, section 2, p. 27.

6 "Designing Pipelines for Simultaneous Flow of Oil and Gas," by Ovid Baker, *Oil and Gas Journal*, vol. 53, July 26, 1954, pp. 185–190, 192, 195.

7 "Proposed Correlation of Data for Two-Phase, Two-Component Flow in Pipes," by R. W. Lockhart and R. C. Martinelli, *Chemical Engineering Progress*, vol. 45, 1949, pp. 39–48.

8 Personal communication from Milton Ludwig, Standard Oil Company of California, San Francisco, Calif., September, 1952 (data available from author).

9 "University of Oklahoma Visual Studies of Two-Phase Flow in Horizontal and Vertical Pipes," by R. L. Huntington, presented at the 1954 Heat Transfer and Fluid Mechanics Institute, University of California, Berkeley, Calif., July 1, 1954.

10 "Phase Equilibria in Hydrocarbon Systems—Thermodynamic Behavior of Liquid Mixtures of n-Butane and Crystal Oil," by B. H. Sage and W. N. Lacey, *Industrial and Engineering Chemistry*, vol. 28, January, 1936, pp. 106–111.

11 "Heat Transmission," by W. G. McAdams, McGraw-Hill Book Company, Inc., New York, N. Y., 1942, pp. 121, 168, 188, 190.

12 "A Contribution to the Theory of Non-Isothermal Laminar Flow of Fluids in a Straight Tube of Circular Cross Section," by Kiyosi Yamagata, Memoirs of the Faculty of Engineering, Kyushu Imperial University, Fukuoka, Japan, vol. 8, no. 6, 1940.

Discussion

O. P. BERGELIN.[3] This paper presents, the writer believes, the first data on heat transfer to gas-liquid mixtures without appreciable mass transfer (and change of phase). The physical processes are so complicated that this simplification is welcome, but even so, it does not leave the process simple enough for complete analysis at this time. Anyone with experience in this field will appreciate the difficulties of the author and agree that more data are needed before an effective analysis can be developed. The experimental equipment and methods of the author appear excellent and these data should serve as a good standard for future work.

The effect of flow pattern seems worthy of some additional comments: (1) The highest rates of heat transfer, for a given oil rate, usually were obtained during slugging flow. For these cases the heat-transfer coefficient remained nearly constant along the heated section. This maximum during slugging flow agrees with the previous observations of Verschoor and Stemerding. (2) At high air rates and low oil rates the rate of heat transfer becomes less and the heat-transfer coefficient decreases

[3] Professor of Chemical Engineering, University of Delaware, Newark, Del. Mem. ASME.

with distance from the beginning of the heated surface. For instance, in some of the runs listed as annular or mist flow, the coefficient appears to be only about half as large in the downstream section as in the upstream section. Assuming an adequate upstream calming section and a decrease in oil viscosity with temperature this behavior seems difficult to explain. Perhaps there is a thin annular oil layer which greatly increases the wall resistance while the major part of the oil passes through as mist without contact with the wall. Some information seems necessary on the liquid mass exchange between the core and the annular wall layer.

The main point to be brought out, however, is that any analysis must take into account the flow pattern, in spite of the complications that are thereby added.

Author's Closure

Professor Bergelin appropriately directs attention to the flow pattern as an important factor and is quite correct in his suggestion for mist flow, since it was always accompanied by thin rivulets of oil on the tube wall. It is unfortunate that the cited experimental evidence should support his conclusions and so contradict the hopeful result of Levy's (4) analytic analysis which suggests that the flow pattern might be of secondary importance.

Numerical Solutions for Laminar-Flow Heat Transfer in Circular Tubes

By W. M. KAYS,[1] STANFORD, CALIF.

The existing solutions for laminar-flow heat transfer in a circular tube are generally based on the assumption of a fully established velocity profile at the point in the tube where heating begins. For high Prandtl number fluids, such as the viscous liquids, this idealization does not seriously restrict the usefulness of the solutions because the velocity profile is established much more rapidly than the temperature profile. However, for the Prandtl number range near 1.00, which includes the gas range, the velocity and temperature profiles develop at similar rates along the tube, and the assumption of a fully established velocity profile at the tube entrance can, for many applications, lead to a considerable error in predicted performance. In this paper, numerical solutions are presented for a number of heating conditions for the case of a fluid of $N_{Pr}=0.7$ with both velocity and temperature uniform at the tube entrance. The solution of Langhaar (1)[2] is employed to provide the velocity profiles which are introduced into the energy equation. Experimental data for laminar air flow in circular tubes are presented for two heating conditions, constant wall temperature and constant heat input per unit of tube length. These data correspond closely to the numerical solutions based on the Langhaar velocity profiles, while differing considerably from solutions based on a parabolic profile throughout the tube. All of the solutions and experimental data are presented in the form of either a local or mean Nusselt number as a function of a modified Graetz number, $N_R N_{Pr}/(x/D)$.

Nomenclature

The following nomenclature is used in the paper:

English Letter Symbols

- c = specific heat, Btu/(lb deg F)
- D = tube diameter, ft
- f_1, f_2, f_3 = constants in computing procedure defined by Equation [11]
- G = mass velocity, lb/(hr sq ft)
- h = unit conductance for convection heat transfer, Btu/(hr sq ft deg F)
- $I_n(\gamma)$ = $i^{-n}J_n(i\gamma)$, where J_n is nth order Bessel function
- k = unit thermal conductivity, Btu/(hr sq ft deg F/ft)
- L = tube-length parameter in energy equation, $4(x/D)/N_R N_{Pr}$
- R = nondimensional tube-radius position, r/r_0, measured from center line
- r = tube-radius position measured from center line, ft
- r_0 = total tube radius, ft
- t = temperature, deg F
- t_1 = initial fluid temperature, deg F.
- T = nondimensional temperature, t/t_1
- T_w = tube wall temperature, or T at $R = 1.0$, dimensionless
- T_m = mixed mean fluid temperature, dimensionless
- v = fluid velocity, fps
- v_r = component of fluid velocity in radial direction, fps
- v_m = mean fluid velocity, fps
- V = v/v_m, dimensionless
- x = length co-ordinate in flow direction, ft

Greek Letter Symbols

- γ = a parameter in Langhaar's solution, dimensionless
- Δ = prefix, denoting "final minus initial"
- ρ = fluid density, pcf
- μ = fluid viscosity, lb/(hr ft)

Nondimensional Groups

- $N_{Nu,x}$ = local Nusselt number, hD/k
- $N_{Nu,m}$ = mean Nusselt number defined by Equation [1]
- N_{Pr} = Prandtl number, $\mu c/k$
- N_R = Reynolds number based on tube diameter, DG/μ

Introduction and Objectives

Background to the Problem. Interest in laminar-flow heat transfer in tubes has arisen in the past primarily in connection with heat-exchanger applications involving oils. More recently, laminar gas flow has become of technical interest in high-temperature, compact heat-exchanger applications where tube diameters are small (less than $^1/_4$ in.) and densities are low.

All of the published solutions for laminar-flow heat transfer in a tube are based on the idealization of either a fully established velocity profile, or a uniform velocity profile (slug flow or rod-like flow). For high Prandtl number fluids, such as oils, an assumption of a fully established parabolic velocity profile, even though both velocity and temperature are uniform at the tube entrance, does not lead to significant error because the velocity profile is established much more rapidly than the temperature profile. In contrast, for very low Prandtl number fluids, such as the liquid metals, the temperature profile is established much more rapidly than the velocity profile. However, for Prandtl numbers near unity, as for gases, both temperature and velocity profiles develop at a similar rate along the tube (assuming uniform velocity and temperature at the entrance), and neither the assumption of a fully developed parabolic velocity profile, nor uniform velocity, is satisfactory. As a result, experimental data on laminar gas flow in circular tubes indicate considerably higher Nusselt numbers than would be predicted on the assumption of a fully developed velocity profile throughout the tube.[3]

Most of the published solutions for laminar-flow heat transfer in a circular tube have been obtained for a constant wall temperature, as would be approximated closely in a condenser or evaporator. Methods are now available for extending such solutions to any kind of wall-temperature variation (3). In Fig. 1

[1] Associate Professor of Mechanical Engineering, Department of Mechanical Engineering, Stanford University. Mem. ASME.

[2] Numbers in parentheses refer to the Bibliography at the end of the paper.

Contributed by the Heat Transfer Division and presented at the Annual Meeting, New York, N. Y., November 28–December 3, 1954, of The American Society of Mechanical Engineers.

Note: Statements and opinions advanced in papers are to be understood as individual expressions of their authors and not those of the Society. Manuscript received at ASME Headquarters, September 21, 1954. Paper No 54—A-151.

[3] See, for example, reference (2), fig. 61, p. 105.

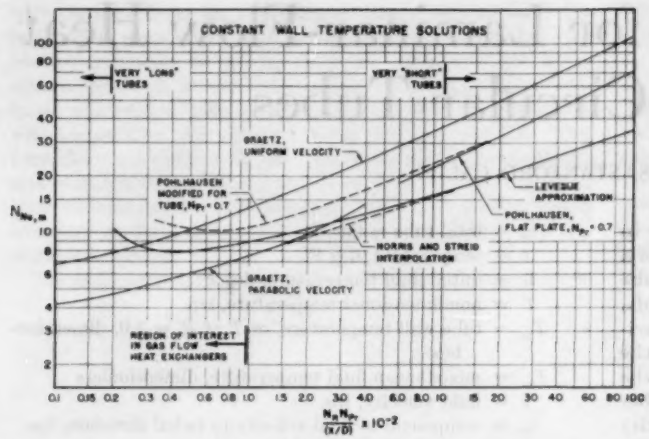

FIG. 1 CONSTANT WALL-TEMPERATURE SOLUTIONS FOR LAMINAR-FLOW HEAT TRANSFER IN CIRCULAR TUBE. UNIFORM FLUID TEMPERATURE AT TUBE ENTRANCE ASSUMED FOR ALL CASES

some of the available constant wall-temperature solutions are plotted. All of these solutions are based on a uniform temperature profile at the tube entrance.

The ordinate is the mean Nusselt number, $N_{Nu,m}$, which is often termed the log-mean Nusselt number since it can be used directly in the log-mean-rate equation heat-exchanger analysis. Actually, it is the mean of the local Nusselt numbers, $N_{Nu,x}$, averaged with respect to tube length, i.e.

$$N_{Nu,m} = \frac{1}{x}\int_0^x N_{Nu,x}\,dx \quad \ldots\ldots\ldots\ldots [1]$$

The abscissa is a modified Graetz number, $N_R N_{Pr}/(x/D)$, which is the inverse tube-length variable in the energy equation. As $N_R N_{Pr}/(x/D)$ approaches zero, $N_{Nu,x}$ and $N_{Nu,m}$ approach limiting minimum magnitudes if the surface temperature remains constant (3.66 for parabolic velocity, 5.75 for uniform velocity). These limiting magnitudes can be readily evaluated directly upon the assumption of a fully established generalized temperature profile.

The Graetz uniform-velocity solution shown in Fig. 1, is complete for all magnitudes of Graetz number (4). This solution provides an upper limit Nusselt number for constant wall temperature, since it is what would be obtained as Prandtl number approaches zero; i.e., the temperature profile becomes established much more rapidly than the velocity profile. As such it approximates what would be obtained for a liquid metal near the tube entrance.

The Graetz parabolic-velocity-profile solution, from (4), is in the form of an infinite series of which only the first three terms have been evaluated. For $N_R N_{Pr}/(x/D) < 100$ the series converges sufficiently rapidly so that this is adequate, but for higher magnitudes of $N_R N_{Pr}/(x/D)$ it yields magnitudes of $N_{Nu,m}$ that are quite obviously high because of insufficient terms.

For high magnitudes of $N_R N_{Pr}/(x/D)$, with parabolic velocity distribution, the Leveque approximation is most generally employed (4). The Leveque approximation yields adequate Nusselt numbers only for $N_R N_{Pr}/(x/D) > 1000$. In the intermediate region between the Leveque approximation and the Graetz parabolic-velocity-profile solution, Norris and Streid (5) proposed a straight-line interpolation shown in Fig. 1.

The parabolic-velocity solutions in Fig. 1 provide a lower limit Nusselt number for constant wall temperature. They are what would obtain for the case of both uniform temperature and velocity at the tube entrance as Prandtl number becomes very large; for in this case the velocity profile is established very much more rapidly than the temperature profile.

Thus the true solution for any real fluid for the technically interesting case of both velocity and temperature uniform at the tube entrance must lie somewhere between the extremes shown in Fig. 1, the exact position depending upon the Prandtl number of the fluid. Near the tube entrance (high Graetz number) the Pohlhausen flat-plate solution should closely approximate actual performance as long as the displacement thickness of the boundary layer is small relative to tube diameter. The following equation is obtained from the Pohlhausen solution when it is converted to the parameters of Fig. 1

$$N_{Nu,mi} = \frac{0.664}{N_{Pr}^{0.167}}\left[\frac{N_R N_{Pr}}{(x/D)}\right]^{0.5} \quad \ldots\ldots\ldots [2]$$

However, this Nusselt number is based on the initial tube-to-fluid temperature difference. The following relates the Nusselt number based on the initial temperature difference to the Nusselt number based on log-mean-temperature difference

$$N_{Nu,m} = \frac{\left[\frac{N_R N_{Pr}}{(x/D)}\right]}{4}\ln\left[1 - \frac{1}{4N_{Nu,mi}\left[\frac{N_R N_{Pr}}{(x/D)}\right]}\right] \quad \ldots\ldots\ldots [3]$$

It will be noted that when Equation [2] is plotted in Fig. 1, the Prandtl number is a parameter. Equation [2], modified by Equation [3], is plotted in Fig. 1 for $N_{Pr} = 0.7$. In order to determine approximately the limits of applicability of Equations [2] and [3], the mass velocity in the Reynolds number in Equation [2] has been modified to account for the displacement thickness of a laminar boundary layer, and the result is the dashed line shown in Fig. 1. These results indicate that for $N_R N_{Pr}/(x/D) >$ about 600 the flat-plate approximation, modified for boundary-layer displacement thickness, should be accurately applicable to the circular tube, but for lower magnitudes of $N_R N_{Pr}/(x/D)$ approximations of this type are apparently not going to be suitable. Unfortunately it is this latter region that is of greatest interest in heat-exchanger analysis and design.

In order to have adequate design data in the laminar-flow region for gas-flow heat exchangers, a direct solution of the energy differential equation, with both temperature and velocity uniform at the entrance, will evidently be necessary.

Objectives of This Paper. The energy equation can be solved quite readily by numerical means and, at the same time, any desired velocity distribution may be introduced into the problem. The solution of Langhaar (1) for the velocity profiles in the entrance region of a circular tube in laminar flow provides a convenient source of velocity data for a numerical solution for the case of both uniform temperature and velocity at the tube entrance. Solutions can be obtained for any type of wall-temperature variation. The specific objectives of this paper are to describe and present the following solutions obtained by numerical integration and, in addition, to present a limited amount of experimental confirmation obtained with air-flow in circular tubes:

1 Constant wall temperature, parabolic velocity profile throughout, temperature uniform at tube entrance. This numerical solution is presented as a check on the adequacy of the numerical method, since it can be compared with the Graetz parabolic-velocity solution.

2 Constant wall temperature, velocity and temperature uni-

form at the tube entrance. The velocity profiles from Langhaar's solution (1) are employed. $N_{Pr} = 0.7$ is specified.

3 Constant wall-to-fluid temperature difference, velocity and temperature uniform at tube entrance. The velocity profiles from Langhaar's solution are employed. $N_{Pr} = 0.7$ is specified.

4 Constant heat input per unit of tube length, parabolic velocity profile throughout, temperature uniform at the tube entrance.

5 Constant heat input per unit of tube length, velocity and temperature uniform at tube entrance. The velocity profiles from Langhaar's solution are employed. $N_{Pr} = 0.7$ is specified.

Energy Equation and Boundary Conditions

If the only heat-transfer mechanism in the tube is conduction (laminar flow), if fluid properties are constant, and if conversion of mechanical to thermal energy is neglected (low velocities), the following differential equation[4] obtains for heat transfer in a circular tube

$$\frac{\partial^2 t}{\partial r^2} + \frac{1}{r}\frac{\partial t}{\partial r} + \frac{\partial^2 t}{\partial x^2} = \left(\frac{\rho c}{k}\right)\left[v\frac{\partial t}{\partial x} + v_r\frac{\partial t}{\partial r}\right] \quad [4]$$

For the typical gas-flow problem it may be assumed safely that conduction in the direction of flow is negligible, and thus the $\partial^2 t/\partial x^2$ term is eliminated. If the velocity distribution is fully established the radial component of the velocity, $v_r = 0$, and the term involving v_r is eliminated. However, this paper is primarily concerned with those situations where the velocity profile is established simultaneously with the temperature profile and, in this case, the radial component of the velocity is not zero. An investigation of the relative magnitudes of the various terms of Equation [4] reveals that near the tube entrance the term involving v_r is of considerable importance, but that its importance diminishes rapidly away from the entrance.

At $N_R N_{Pr}/(x/D) = 1000$ the v_r term is 10 per cent of the other term on the right-hand side of Equation [4] at one point in the flow cross section. For lower magnitudes of $N_R N_{Pr}/(x/D)$ this term becomes of rapidly decreasing importance, and for $N_R N_{Pr}/(x/D) < 100$, which is the region of primary interest in gas-flow heat-exchanger design, the effect is quite negligible. If the v_r term is neglected the local Nusselt number evaluated from calculated temperature profiles will tend to be low, but an error of greater than 5 per cent at $N_R N_{Pr}/(x/D) = 1000$ appears unlikely, with the error becoming quite small at 100 and lower. To include the v_r term greatly complicates a numerical solution to Equation [4], so for all of the solutions to be considered here the v_r term has been omitted. For those solutions where it is desired to evaluate a mean Nusselt number with respect to tube length in addition to local Nusselt number, Equation [1], the Pohlhausen flat-plate solution is employed from the beginning of the tube to $N_R N_{Pr}/(x/D) = 1000$, and the numerical solution only thereafter.

From its reduced form, Equation [4] can then be put into a more convenient form by the introduction of nondimensional variables

$$\frac{\partial^2 T}{\partial R^2} + \frac{1}{R}\frac{\partial T}{\partial R} = V\frac{\partial T}{\partial L} \quad [5]$$

or

$$\frac{\partial\left(R\dfrac{\partial T}{\partial R}\right)}{\partial R} = VR\frac{\partial T}{\partial L} \quad [5a]$$

where

$$R = r/r_0 \qquad T = t/t_1$$

$$V = v/v_m \qquad L = kx/(v_m \rho c r_0^2) = 4(x/D)/(N_R N_{Pr})$$

Integration of Equation [5] for given boundary conditions yields $T = T(R,L)$. Then the mixed mean temperature is determined from

$$T_m = 2\int_0^1 V\,T\,R\,dR \quad [6]$$

Finally, the local Nusselt numbers are evaluated from

$$N_{Nu,x} = \frac{2\left(\dfrac{\partial T}{\partial R}\right)_{R=1}}{(T_w - T_m)} \quad [7]$$

For those solutions where the mean Nusselt number is desired

$$N_{Nu,m} = \frac{1}{L}\int_0^L N_{Nu,x}\,dL \quad [8]$$

The parabolic velocity profile for fully established flow in a circular tube is expressed by

$$V = 2\,[1 - R^2] \quad [9]$$

For the case of uniform velocity profile at the tube entrance the velocity is a function of both R and L, and is expressed, from Langhaar's solution (1), as

$$V = \frac{I_0(\gamma) - I_0(\gamma R)}{I_2(\gamma)} \quad [10]$$

where

$$\gamma = \phi\left(\frac{4x/D}{N_R}\right) = \phi(LN_{Pr})$$

γ is tabulated in Langhaar's paper. It will be noted that in order to establish V as a function of R and L for insertion into Equation [5], a Prandtl number must be specified. For the solutions considered in this paper $N_{Pr} = 0.7$ is specified so that the solutions may be applicable to gases.

With a numerical method of solution any kind of wall-temperature variation or heating rate can be handled with equal ease. Consideration has been restricted to those wall-temperature variations most commonly encountered in heat-exchanger design. One of the most common cases met in design is constant wall temperature; the fluid-temperature variation for this case is shown in Fig. 2(*a*). An essentially constant wall temperature occurs not only in condensers and evaporators, but also is often approximated in parallel-flow heat exchangers, especially where the two fluid capacity rates and heat-transfer resistances are nearly the same. For this boundary condition $N_{Nu,x}$ is of secondary importance, and $N_{Nu,m}$ is desired so that the temperature of the fluid leaving the heat exchanger may be evaluated.

If the tube is electrically resistance heated, or is heated by other means that provide a constant heat input per unit of tube length, a wall-temperature variation, such as shown in Fig. 2(*b*), will be approximated. The surface reaches the fluid temperature right at the tube entrance, and finally assumes a linear variation as the local Nusselt number approaches a constant magnitude. For this case $N_{Nu,m}$ has no particular use, and the local Nusselt number, $N_{Nu,x}$, is desired so that the wall temperature can be evaluated at any point in the heat exchanger.

Constant Wall-to-Fluid Temperature Difference. A third temperature-boundary condition that is approximated in many heat exchangers is a constant wall-to-fluid temperature difference along the flow tube. This occurs approximately in counterflow

[4] See, for example, reference (4), equations (3–24), p. 22.

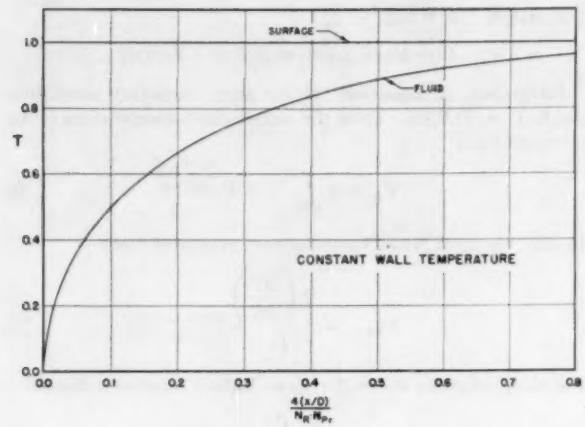

(a)

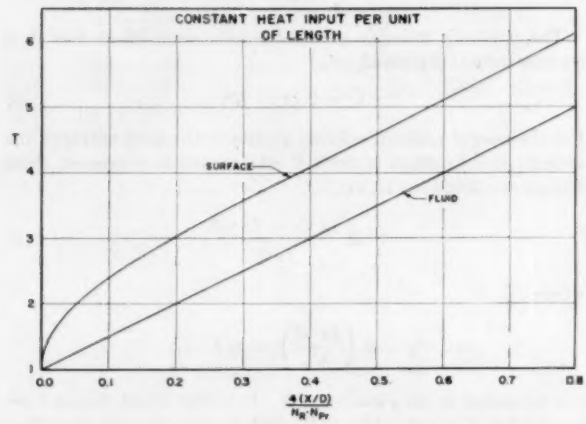

(b)

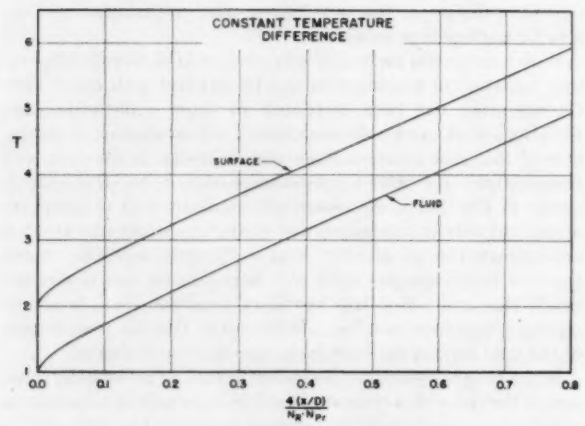

(c)

FIG. 2 TYPICAL TEMPERATURE BOUNDARY CONDITIONS ENCOUNTERED IN HEAT EXCHANGERS

heat exchangers where the two fluids have close to the same capacity rates and heat-transfer resistances. Fig. 2(*c*) shows the surface and fluid-temperature variation obtained. The surface temperature tends to drop near the entrance, and the assumption of a constant wall-to-fluid temperature difference is close to what is often encountered. For this case $N_{Nu,m}$ is of primary interest so that the over-all performance of the heat exchanger may be evaluated. For large magnitudes of $4(x/D)/N_R N_{Pr}$ this case approaches constant heat input per unit of length, and $N_{Nu,x}$ would be expected to approach the same minimum limit as for constant heat input, while near the entrance the behavior is more like the constant wall-temperature case.

The constant wall-temperature and constant temperature-difference solutions represent the extremes encountered in most two-fluid heat-exchanger applications. Constant heat input is a situation of more restricted usefulness.

FINITE-DIFFERENCE SOLUTION

The partial differential Equation [5] can be expressed in finite-difference form, for the interior points of the tube, as follows

$$T_{R+\Delta L} = f_1 T_{R+\Delta R} + f_2 T_R + f_3 T_{R-\Delta R} \quad \ldots\ldots [11]$$

where

$$f_1 = \left(\frac{1}{V}\right)\left(\frac{\Delta L}{\Delta R}\right)\left[\frac{1}{\Delta R} + \frac{1}{2R}\right]$$

$$f_2 = 1 - \left(\frac{1}{V}\right)\left(\frac{2\Delta L}{\Delta R^2}\right)$$

$$f_3 = \left(\frac{1}{V}\right)\left(\frac{\Delta L}{\Delta R}\right)\left[\frac{1}{\Delta R} - \frac{1}{2R}\right]$$

ΔL and ΔR are the arbitrarily chosen increments in tube length and tube radius, respectively. For all of the solutions ΔR was specified at 0.1; thus the radius was divided into 10 equal increments. With ΔR chosen, the choice of magnitude of ΔL is not entirely arbitrary, because if ΔL is chosen such that f_2 becomes negative the solution will not converge. This is similar to behavior encountered in finite-difference solutions of transient conduction problems in solid bodies (4). It will be noted that f_1, f_2, f_3 are functions of velocity V, as well as R, and it is here that the velocity profiles, Equation [9] or [10], are introduced into the problem. For the solutions involving the Langhaar velocity profiles, $\Delta L = 0.001$ was employed for $L = 0$ to $L = 0.010$, and $\Delta L = 0.002$ for $L = 0.010$ to $L = 0.200$. At $L = 0.200$, f_2 becomes equal to zero for the Langhaar velocity profiles, but in all cases the temperature profile becomes sufficiently near fully established at $L = 0.200$, $N_R N_{Pr}/(x/D) = 20$, so that this is as far as any of the solutions were carried.

The computing procedure involves calculation of the temperature profiles at successive increments of L, employing Equation [11] to extrapolate to the new temperatures $T_{R+\Delta L}$ from the previous temperatures T_R. At the same time the appropriate boundary conditions are applied to each profile.

The local Nusselt numbers are evaluated from Equation [7]. The wall temperature T_w is taken directly from the temperature profile. The mixed mean temperature is evaluated from Equation [6], using Simpson's rule for the integration. The temperature gradient at the wall is best evaluated by fitting a curve to the temperatures at $R = 0.8$, 0.9, and 1.0, of the type

$$T = T_w + a(1 - R) + b(1 - R)^2 \quad \ldots\ldots [12]$$

After evaluation of a and b, this equation is differentiated and R is set equal to zero to provide the slope at $R = 1.0$. These operations are combined into the following convenient computing equation

$$\left(\frac{\partial T}{\partial R}\right)_{R=1} = 5[4T_{R=0.9} - T_{R=0.8} - 3T_{R=1.0}] \quad \ldots\ldots [13]$$

For those solutions where the mean Nusselt number is desired, Equation [8] is employed. For the solutions where the Langhaar velocity profiles are used (constant wall temperature and constant

temperature difference) the Pohlhausen flat-plate solution (see Fig. 1) is used to provide $N_{Nu,m}$ from the tube entrance to $N_R N_{Pr}/(x/D) = 1000$, corresponding to $L = 0$ to $L = 0.004$, for reasons previously discussed. The integration of Equation [8] is started at this point.

In order to check the adequacy of the numerical method, a solution was obtained for the case of constant wall temperature and a fully established parabolic velocity profile, since the Graetz solution for this condition is already available. The results of this solution are presented in Table 1. The mean Nusselt number was evaluated from Equation [8], using the Leveque approximation,

TABLE 1 SUMMARY OF NUMERICAL SOLUTION CONSTANT WALL TEMPERATURE, PARABOLIC VELOCITY

$4(x/D)/(N_R N_{Pr})$	$N_{Nu,x}$	$N_{Nu,m}$	$N_R N_{Pr}/(x/D)$
0.004	10.91		1000
0.010	7.77	11.83	400
0.020	6.12	9.43	200
0.030	5.39	8.20	133.3
0.040	4.96	7.44	100.0
0.050	4.67	6.91	80.0
0.060	4.47	6.52	66.7
0.070	4.32	6.22	57.2
0.080	4.18	5.97	50.0
0.090	4.09	5.77	44.4
0.100	4.02	5.60	40.0
0.110	3.96	5.45	36.4
0.120	3.90	5.32	33.3
0.160	3.78[a]	4.95	25.0
0.200	3.72[a]	4.71	20.0
0.400	3.67[a]	4.19	10.0
0.800	3.66[a]	3.93	5.0
∞	3.66	3.66	0.0

[a] By interpolation.

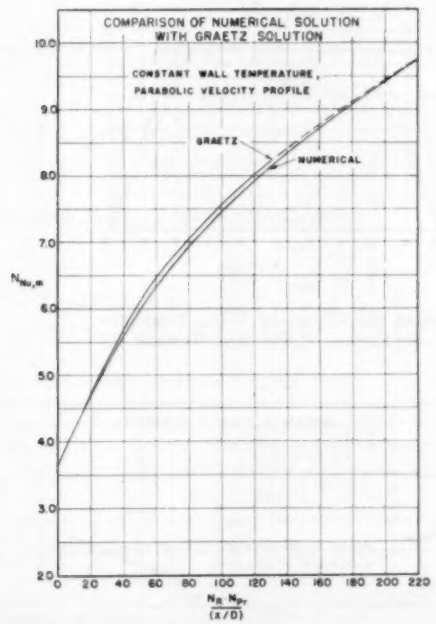

FIG. 3 COMPARISON OF NUMERICAL SOLUTION FOR PARABOLIC VELOCITY PROFILE, CONSTANT WALL TEMPERATURE, WITH GRAETZ SOLUTION FOR SAME CASE

Fig. 1, as a start at $N_R N_{Pr}/(x/D) = 1000$. In Fig. 3 the results of this numerical solution are compared with the Graetz solution. The maximum deviation is 2 per cent, which provides a measure of confidence in the technique employed, and hence in the other solutions to be presented.

TABLE 2 SUMMARY OF NUMERICAL SOLUTION CONSTANT WALL TEMPERATURE, LANGHAAR VELOCITY, $N_{Pr} = 0.7$

$4(x/D)/(N_R N_{Pr})$	$N_{Nu,x}$	$N_{Nu,m}$	$N_R N_{Pr}/(x/D)$
0.004	18.46		1000
0.010	11.31	17.44	400
0.020	7.90	13.36	200
0.030	6.53	11.28	133.3
0.040	5.82	10.00	100.0
0.050	5.34	9.12	80.0
0.060	5.02	8.46	66.7
0.070	4.75	7.95	57.2
0.080	4.57	7.53	50.0
0.090	4.42	7.19	44.4
0.100	4.29	6.91	40.0
0.110	4.18	6.67	36.4
0.120	4.09	6.45	33.3
0.130	4.03	6.27	30.8
0.140	3.97	6.11	28.6
0.150	3.91	5.96	26.7
0.160	3.88	5.83	25.0
0.170	3.85	5.72	23.5
0.180	3.82	5.61	22.2
0.190	3.79	5.52	21.1
0.200	3.77	5.43	20.0
0.400	3.67[a]	4.56	10.0
0.800	3.66[a]	4.11	5.0
∞	3.66	3.66	0.0

[a] By interpolation.

TABLE 3 SUMMARY OF NUMERICAL SOLUTION CONSTANT TEMPERATURE DIFFERENCE, LANGHAAR VELOCITY, $N_{Pr} = 0.7$

$4(x/D)/(N_R N_{Pr})$	$N_{Nu,x}$	$N_{Nu,m}$	$N_R N_{Pr}/(x/D)$
0.004	18.80		1000
0.010	11.80	17.81	400
0.020	8.36	13.76	200
0.030	7.11	11.73	133.3
0.040	6.40	10.48	100.0
0.050	5.95	9.62	80.0
0.060	5.62	8.98	66.7
0.070	5.38	8.48	57.2
0.080	5.21	8.08	50.0
0.090	5.06	7.75	44.4
0.100	4.94	7.48	40.0
0.110	4.85	7.24	36.4
0.120	4.77	7.04	33.3
0.130	4.70	6.86	30.8
0.140	4.64	6.71	28.6
0.150	4.59	6.57	26.7
0.160	4.56	6.44	25.0
0.170	4.53	6.33	23.5
0.180	4.51	6.23	22.2
0.190	4.49	6.14	21.1
0.200	4.48	6.06	20.0
0.400	4.41[a]	5.24	10.0
0.800	4.39[a]	4.82	5.0
∞	4.364	4.364	0.0

[a] By interpolation.

TABLE 4 SUMMARY OF NUMERICAL SOLUTION CONSTANT HEAT INPUT, PARABOLIC VELOCITY

$4(x/D)/N_R N_{Pr}$	$N_{Nu,x}$	$N_R N_{Pr}/(x/D)$
0.005	13.81	800
0.010	10.40	400
0.020	8.06	200
0.030	7.05	133.3
0.040	6.56	100.0
0.050	6.07	80.0
0.060	5.76	66.7
0.070	5.54	57.2
0.080	5.37	50.0
0.090	5.24	44.4
0.100	5.11	40.0
0.110	5.00	36.4
0.120	4.95	33.3
0.130	4.88	30.8
0.140	4.83	28.6
0.150	4.79	26.7
0.160	4.74	25.0
0.170	4.70	23.5
0.180	4.66	22.2
0.190	4.64	21.1
0.200	4.59	20.0
0.400	4.45[a]	10.0
0.800	4.40[a]	5.0
∞	4.364	0.0

[a] By interpolation.

TABLE 5 SUMMARY OF NUMERICAL SOLUTION CONSTANT HEAT INPUT, LANGHAAR VELOCITY, $N_{Pr} = 0.7$

$4(x/D)/(N_R N_{Pr})$	$N_{Nu,x}$	$N_R N_{Pr}/(x/D)$
0.004	21.62	1000
0.010	14.53	400
0.020	10.54	200
0.030	8.76	133.3
0.040	7.80	100
0.050	7.16	80
0.060	6.70	66.7
0.070	6.31	57.2
0.080	6.08	50.0
0.090	5.80	44.4
0.100	5.64	40.0
0.110	5.48	36.4
0.120	5.32	33.3
0.130	5.22	30.8
0.140	5.12	28.6
0.150	5.04	26.7
0.160	4.97	25.0
0.170	4.92	23.5
0.180	4.87	22.2
0.190	4.82	21.1
0.200	4.78	20.0
0.400	4.54[a]	10.0
0.800	4.45[a]	5.0
∞	4.364	0.0

[a] By interpolation.

Solutions for Various Boundary Conditions

The complete solutions for all of the conditions outlined in the objectives to this paper are presented in Tables 2, 3, 4, and 5. The local Nusselt numbers are plotted in Fig. 5. The mean Nusselt numbers for the constant wall-temperature and constant temperature-difference solutions are plotted in Fig. 6. It will be noted in Fig. 6 that, as anticipated, the constant wall temperature mean Nusselt numbers based on the Langhaar velocity profiles lie considerably above the mean Nusselt numbers obtained on the assumption of a fully established parabolic velocity profile. In the range of greatest interest in heat-exchanger design, $20 < N_R N_{Pr}/(x/D) < 100$, this difference amounts to 12 to 25 per cent.

It will be noted that, in addition to the solutions for a uniform velocity at the tube entrance, a solution for constant heat input, parabolic velocity profile, is included, Table 4. This solution was run off numerically because the author is aware of no published solutions for this case.

The solutions based on the Langhaar velocity profiles should be applicable to the Prandtl number range of gases; the parabolic velocity solutions are applicable to high Prandtl number fluids, unless a starting length of tube is used.

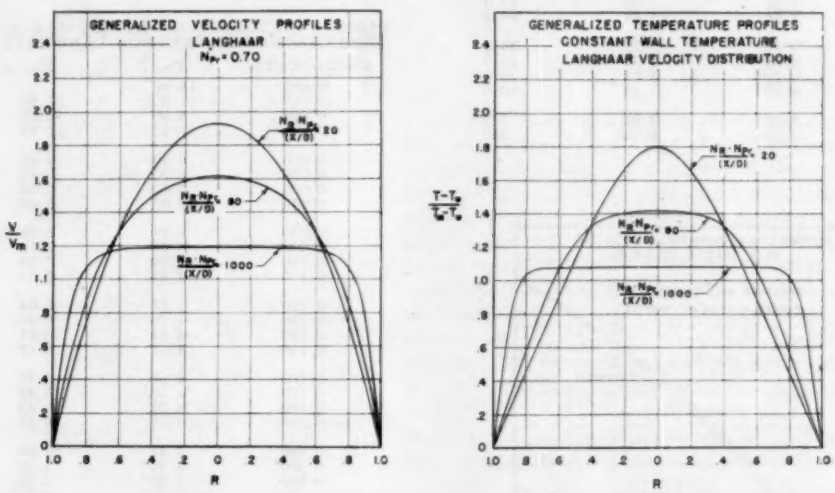

FIG. 4 GENERALIZED VELOCITY AND TEMPERATURE PROFILES FOR CONSTANT WALL TEMPERATURE, UNIFORM VELOCITY, AND FLUID TEMPERATURE AT TUBE ENTRANCE, PRANDTL NUMBER, 0.7

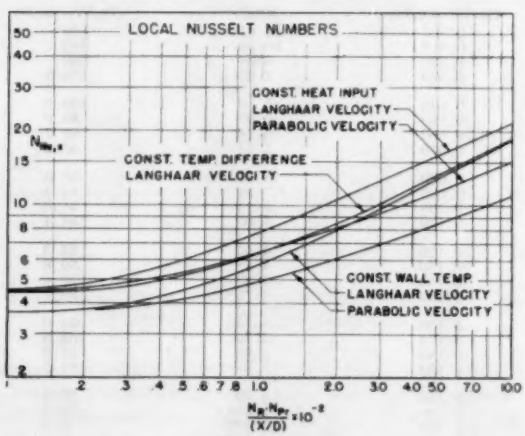

FIG. 5 LOCAL NUSSELT NUMBERS OBTAINED FROM NUMERICAL SOLUTIONS

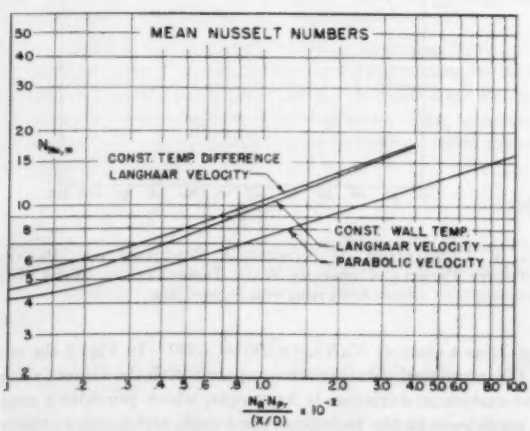

FIG. 6 MEAN NUSSELT NUMBERS WITH RESPECT TO TUBE LENGTH

As a matter of further interest, some of the velocity and temperature profiles are shown in Figs. 4(*a*) and 4(*b*). The velocity profiles in Fig. 4(*a*) are those of Langhaar and are direct plots of Equation [10]. The temperature profiles in Fig. 4(*b*) are taken from the numerical solution for constant wall temperature in which the Langhaar profiles are used for velocity.

It is sometimes convenient to the designer to have such solutions as these expressed as equations rather than in tabular or graphical form. Hausen (2) has proposed the following equation as an empirical representation of the Graetz solution for constant wall temperature, parabolic velocity profile

$$N_{Nu,m} = 3.66 + \frac{0.0668\left[\frac{N_R N_{Pr}}{(x/D)}\right]}{1 + 0.04\left[\frac{N_R N_{Pr}}{(x/D)}\right]^{2/3}} \quad \ldots\ldots [14]$$

Equation [14] fits the best interpretation for the useful regions of the Graetz, Leveque, and the Norris and Streid interpolation, all within about ±6 per cent out to $N_R N_{Pr}/(x/D) = 1000$, Fig. 1.

Empirical equations of the same general form can be employed to approximate the other solutions presented here. The following equations fit the indicated solutions with a maximum discrepancy of about ±3 per cent over the range of $N_R N_{Pr}/(x/D)$ covered by Figs. 5 and 6.

Constant Wall Temperature, Langhaar Velocity Profiles

$$N_{Nu,m} = 3.66 + \frac{0.104\left[\frac{N_R N_{Pr}}{(x/D)}\right]}{1 + 0.016\left[\frac{N_R N_{Pr}}{(x/D)}\right]^{0.8}} \quad \ldots\ldots [15]$$

Constant Temperature Difference, Langhaar Velocity Profiles

$$N_{Nu,m} = 4.36 + \frac{0.10\left[\frac{N_R N_{Pr}}{(x/D)}\right]}{1 + 0.016\left[\frac{N_R N_{Pr}}{(x/D)}\right]^{0.8}} \quad \ldots\ldots [16]$$

Constant Heat Input, Parabolic Velocity Profile

$$N_{Nu,x} = 4.36 + \frac{0.023\left[\frac{N_R N_{Pr}}{(x/D)}\right]}{1 + 0.0012\left[\frac{N_R N_{Pr}}{(x/D)}\right]} \quad \ldots\ldots [17]$$

Constant Heat Input, Langhaar Velocity Profiles

$$N_{Nu,x} = 4.36 + \frac{0.036\left[\frac{N_R N_{Pr}}{(x/D)}\right]}{1 + 0.0011\left[\frac{N_R N_{Pr}}{(x/D)}\right]} \quad \ldots\ldots [18]$$

Comparisons With Experimental Data

Good laminar-flow test data for gases in circular tubes are not easy to obtain. Because of the uncertain effects of natural convection, consideration must be limited to rather small diameter tubes, i.e., ¼ in. or less. Most of the available data have been obtained with a constant wall temperature, since most often condensing steam has been used as a heating medium. With constant wall temperature it is necessary to operate the test heat exchanger at very high effectiveness to obtain low magnitudes of $N_R N_{Pr}/(x/D)$, and the results become very sensitive to small temperature-measurement errors. There is, however, a small amount of approximately constant heat-input data obtained with electric heating.

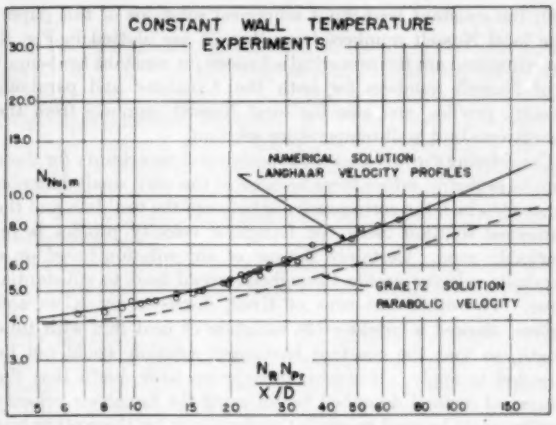

Fig. 7 Comparison of Constant Wall-Temperature Experiments With Constant Wall-Temperature Analytical Solutions

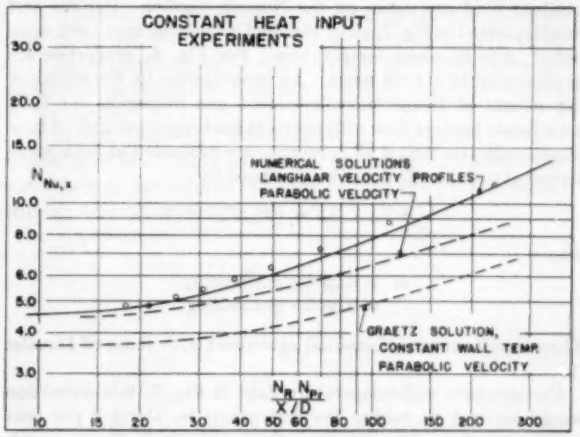

Fig. 8 Comparison of Constant Heat-Input Experiments With Constant Heat-Input Analytical Solutions

In (6) the author presented laminar-flow data obtained from tests with air flow in steam-heated small-diameter tubes. Part of these data were obtained by the author personally; the remainder by Green and King (7), and by Godfrey and Saunders (8). The experimental uncertainty for these data has been estimated at less than ±5 per cent. Fig. 7 shows a plot of the results of these tests. Superimposed is the numerical solution of this paper for constant wall temperature with Langhaar velocity profiles, and the Graetz parabolic-velocity solution. The comparison between the experiments and the numerical solution is excellent. It is quite evident that the Graetz solution underestimates the Nusselt number for laminar gas flow by a substantial amount.

It should be added that approximately half of these data were obtained with tubes with a sharp-edged entry, while the other half had entries that had been expanded to a hex shape. No apparent effect of entry type is noticeable. Values of (x/D) for the tubes ranged from 42 to 80. It is quite probable that the behavior of very short tubes would be much more sensitive to the character of the entry.

Klein and Tribus (3) discuss some laminar air-flow data obtained by Kroll of M.I.T. These data were obtained in an electrically heated system where the local Nusselt number could be determined at points along the tube. Of the three test runs discussed, one, Run 54, showed very close to constant heat input per unit of tube length, and thus should form a basis of comparison

with the constant heat-input numerical solutions of this paper. The local Nusselt numbers from Run 54 are plotted in Fig. 8. Superimposed are the numerical solutions for constant heat-input local Nusselt numbers for both the Langhaar and parabolic velocity profiles, and also the local Nusselt numbers from the Graetz constant wall-temperature solution.

Considering the fact that the experimental uncertainty for these data is probably rather large because of the very small-diameter tubes ($^1/_{16}$ in.), the correspondence between the test data and the numerical solution using the Langhaar velocity profiles is remarkably good. Certainly the use of any solution based on a parabolic velocity profile throughout would lead to substantial error. The other test runs of Kroll, discussed by Klein and Tribus, showed a considerable variation of heat flux with tube length, so that the constant heat-input solution would not be expected to apply. However, there seems little doubt that the numerical method described herein using the Langhaar velocity profiles could be used to predict performance for these other test runs as well.

Mention should be made of the effects of temperature-dependent fluid properties on the Nusselt number. For the test results plotted in Fig. 7, all of the fluid properties have been evaluated at bulk mean temperature. For Fig. 8, properties are evaluated at local bulk mean. An investigation by the author of the effects of temperature-dependent gas properties for fully established laminar flow with constant heat input per unit of tube length indicates that if all properties are evaluated at bulk mean temperature, the effect can be expressed by

$$h/h_{\text{isothermal}} = (T_w/T_m)^{-m} \quad [19]$$

where

$m = 0.25$ for gas heating
$= 0.08$ for gas cooling

These results are in substantial agreement with those of Diessler (9).

For constant wall-temperature data in Fig. 7, this correction would amount to raising the test points by about 3 per cent and would, if anything, improve the correlation between experiment and analysis. The indicated correction to the data in Fig. 8 is about 10 per cent; i.e., the data points would be raised about 10 per cent. However, the analysis upon which Equation [19] was based was for a fully established velocity and temperature profile. An examination of the temperature-dependent property correction indicated by Crocco's solution for the laminar boundary layer on a flat plate (10) shows only a very small correction, $m = 0.08$ for gas heating. The experimental data in Figs. 7 and 8 would be expected to lie between these extremes.

Summary and Conclusions

It has been shown that for fluids in laminar flow in the Prandtl number range of gases, the assumption of a fully established parabolic-velocity distribution for heat-transfer calculations can result in a substantial underestimation of the Nusselt number if heat transfer starts at the tube entry. The velocity profiles of Langhaar have been employed in numerical solutions of this problem for three boundary conditions, constant wall temperature, constant wall-to-fluid temperature difference, and constant heat input per unit of tube length. Local Nusselt numbers have been evaluated for all three cases, and mean Nusselt numbers with respect to tube length have been evaluated for the first two. In addition, a numerical solution for constant heat input with a fully established parabolic-velocity distribution has been obtained.

Simplifying assumptions made in the numerical solutions where the Langhaar velocity profiles are employed are believed to introduce only small error. Experimental data for the two cases of constant wall temperature and constant heat input are shown to be in good agreement with the numerical solutions, while differing substantially from solutions based on the parabolic-velocity-profile assumption.

Acknowledgments

The Office of Naval Research is currently sponsoring a research program on compact heat-transfer surfaces at Stanford University. The author prepared this paper as a part of this program and expresses his appreciation to the sponsoring organization.

The author also is grateful for the assistance of Mr. A. L. Holiday, Mr. I. S. Bjorklund, Mr. P. L. Dawson, and Mr. W. C. Reynolds, Stanford University Mechanical Engineering students.

Bibliography

1 "Steady Flow in the Transition Length of a Straight Tube," by H. L. Langhaar, *Journal of Applied Mechanics*, Trans. ASME, vol. 64, 1942, p. A-55.

2 "Introduction to the Transfer of Heat and Mass," by E. R. G. Eckert, McGraw-Hill Book Company, Inc., New York, N. Y., 1950.

3 "Forced Convection From Nonisothermal Surfaces," by John Klein and Myron Tribus, ASME Paper No. 53—SA-46 (unpublished).

4 "Heat Transfer," by Max Jakob, John Wiley & Sons, Inc., New York, N. Y., vol. 1, 1949.

5 "Laminar Flow Heat-Transfer Coefficients for Ducts," by R. H. Norris and D. D. Streid, Trans. ASME, vol. 62, 1940, pp. 525–533.

6 "Convective Heat-Transfer and Flow-Friction Behavior of Small Cylindrical Tubes—Circular and Rectangular Cross Sections," by W. M. Kays and A. L. London, Trans. ASME, vol. 74, 1952, pp. 1179–1189.

7 "The Influence of Tube Shape on Heat-Transfer Coefficients in Air to Air Heat Exchangers," by F. H. Green and L. S. King, Trans. ASME, vol. 68, 1946, pp. 115–122.

8 "Steam to Air Tests of Small Round Tubes With Hex Ends," by J. W. Godfrey and L. P. Saunders, Report No. RER-58, Harrison Radiator Division Research Engineering Department, April 11, 1943.

9 "Analytical Investigation of Fully Developed Laminar Flow in Tubes With Heat Transfer With Fluid Properties Variable Along the Radius," by R. G. Diessler, NACA TN 2410, July, 1951.

10 "Critical Review of Skin-Friction and Heat-Transfer Solutions of the Laminar Boundary Layer of a Flat Plate," by M. W. Rubesin and H. A. Johnson, Trans. ASME, vol. 71, 1949, pp. 383–388.

Discussion

Robert Lipkis.[6] As a check on his numerical method, the author compares his result for the uniform wall-temperature parabolic-velocity case with the well-known Graetz solution, as given by Norris and Streid (author's reference 5). This latter solution can be put into the form

$$N_{\text{Nu},Z} = \frac{\sum_{n=0}^{\infty} G_n e^{-\lambda^2_n Z}}{2\sum_{n=0}^{\infty} \frac{G_n}{\lambda^2_n} e^{-\lambda^2_n Z}} \quad [20]$$

where Z is the dimensionless length parameter ($= L/2$ in the author's notation) and the coefficients G_n are functions of the eigenvalues λ_n and the eigenfunctions occurring in the Graetz solution. The author states that, for low values of Z, high magnitudes of $N_R N_{Pr}/(x/D)$, the series yields magnitudes of N_{Nu} that are obviously high because of insufficient terms (only the first three terms were known to the author). This statement is in error; the effect of taking insufficient terms is to give too low a magnitude. This is apparent from Equation [20] of this discussion when it is realized that the successive terms of the two series are of decreasing magnitude, all are positive, and the denominator converges much more rapidly than the numerator.

[6] University of California, Los Angeles, Calif.

The writer recently has calculated the first five terms of the series accurate to 5 significant digits.[6] These, together with additional terms available from asymptotic expressions given by Lauwerier,[7] and Sellars, Tribus, and Klein,[8] permit extending the Graetz solution as close to the inlet as desired. Table 6, herewith, compares the more exact values, calculated by the writer, with the author's results, taken from his Table 1.

TABLE 6 VALUES CALCULATED BY WRITER COMPARED TO AUTHOR'S RESULTS

$4(x/D)/(N_R N_{Pr})$	$N_{Nu,x}$ (Kays)	$N_{Nu,x}$ (Lipkis)
0.004	10.91	10.12
0.010	7.77	7.471
0.020	6.12	6.002
0.040	4.96	4.9169
0.100	4.02	4.0050
0.200	3.72	3.7101

The writer's calculations appear to have sufficient internal checks to establish their correctness. Thus, near the tube inlet, the author's numerical method yields results approximately 8 per cent too high; farther downstream the agreement is excellent.

The Leveque asymptotic approximation for uniform wall temperature can be put into the form

$$N_{Nu,Z} = 1.357Z^{-1/3} \quad \ldots\ldots [21]$$

or

$$N_{Nu,Z} = 1.357Z^{-1/3}/(1 - 4.070Z^{1/3}) \quad \ldots\ldots [22]$$

where the conductance is based on the fluid entrance temperature in Equation [21] and on the local mixed mean fluid temperature in Equation [22]. Even at $Z = 0.001$ (somewhat closer to the inlet than the closest point calculated by Kays) these solutions are still 7 and 11 per cent, respectively, above the exact solution, Equation [20], for which 13 terms suffice for convergence.

To examine how closely the exact solution approaches the Leveque approximation, it is noted that the denominator of Equation [20] converges to within 1 or 2 per cent of 0.250 at a value of Z somewhat below 0.001. Then, in terms of the appropriate asymptotic expressions

$$N_{Nu,Z} = 4\sum_{n=0}^{\infty} G_n e^{-\lambda^2 nZ}$$

$$= 4\sum_{n=5}^{\infty} C\left(4n + \frac{8}{3}\right)^{-1/3} e^{-\left(4n+\frac{8}{3}\right)^2 Z} + 4\sum_{n=0}^{4} G_n e^{-\lambda^2 nZ}$$

where the first five terms are retained in exact form since they are known. Expanding

$$N_{Nu,Z} = 4C\sum_{n=0}^{\infty}\left(4n + \frac{8}{3}\right)^{-1/3} e^{-\left(4n+\frac{8}{3}\right)^2 Z}$$

$$+\left[4\sum_{n=0}^{4} G_n e^{-\lambda_n^2 Z} - 4C\sum_{n=0}^{4}\left(4n + \frac{8}{3}\right)^{-1/3} e^{-\left(4n+\frac{8}{3}\right)^2 Z}\right]$$

For $Z \leq 10^{-3}$ the bracketed term can be shown to be equal to 0.1. If the first summation is approximated by an integral, the equation can be shown to reduce to

$$N_{Nu,Z} = 1.357Z^{-1/3} - 1.7 \quad \ldots\ldots [23]$$

This is the Graetz solution extended to the region of the tube inlet ($Z < 4 \times 10^{-3}$), eliminating the need for summing the series of Equation [20]. It may be compared with the corresponding Leveque approximation, Equation [22]. The two solutions agree within 3 per cent at $Z = 10^{-3}$, and within 7 per cent at $Z = 10^{-4}$. Note that the region of applicability of this (and the Leveque) solution is very short; for example, for a fluid with $N_{Pr} = 100$ flowing with $N_{Re} = 1000$, the solution applies only for the first few tube diameters.

The writer is indebted to Dr. Myron Tribus for suggesting and aiding in this extension of the Graetz solution to small values of Z.

JOHN SELLARS,[9] JOHN KLEIN,[9] AND MYRON TRIBUS.[10] The author's Fig. 9 of this discussion is taken from a paper recently submitted to the Society and shows the variation in Nusselt modulus with Graetz modulus for three different wall-boundary conditions. This figure was prepared from equations which utilize all of the Graetz problem eigenvalues and coefficients. These eigenvalues and coefficients were determined by Dr. John Sellars at the University of Michigan and form a part of the paper referred to in the first sentence of these comments. The paper would have been submitted much earlier but delays were encountered in getting permission from the U. S. Air Force to publish the report.[11]

The Norris and Streid extrapolation to join up the Leveque solution with the Graetz solution is not correct. The infinite-series solution does not join smoothly to the Leveque approximation even when 22 terms are used ($x^+ > 10^{-3}$).

The equations used to prepare Fig. 9 are as follows

$$x^+ = \frac{2x}{D}(N_{Re}N_{Pr})^{-1}$$

$$q(x^+) = \int_{\xi=0}^{x^+} h(\xi, x^+)dT_w(\xi) \quad \ldots\ldots [24]$$

$$T_w(x^+) - T_i = \int_{\xi=0}^{x^+} g(\xi, x^+)q(\xi)d\xi \quad \ldots\ldots [25]$$

$$h(\xi, x^+) = -\frac{4k}{D}\sum_{n=0,1,2,\ldots}^{\infty}\frac{C_n}{2}R_n'(1)e^{-\lambda_n^2(x^+-\xi)} \quad \ldots\ldots [26]$$

$$g(\xi, x^+) = \frac{D}{2k}\left\{4 - \sum_{m=1,2,\ldots}^{\infty} B_m e^{-\gamma_m(x^+-\xi)}\right. \quad \ldots [27]$$

$$\lambda_n = 4n + \frac{8}{3}, \quad n = \text{integer}, \; n \geq 3 \quad \ldots\ldots [28]$$

$$-\frac{C_n}{2}R_n'(1) = 1.01276\lambda_n^{-1/3}, \quad n \geq 3$$

m	γ_m	B_m
1	25.639	4.405
2	84.624	5.7308
3	176.40	6.0084

$\ldots\ldots [29]$

If the wall-temperature variation is known, Equation [24] of this discussion is to be used with Equation [26] and the constants of Equation [28] to determine the wall heat flux. For values of n

[6] "Heat Transfer to an Incompressible Fluid in Laminar Motion," by Robert Lipkis, Master's Thesis, University of California, Los Angeles, Calif., August, 1954.

[7] "Use of Confluent Hypergeometric Functions, Mathematical Physics and Solution of Eigenvalue Problem," by H. A. Lauwerier, *Applied Scientific Research*, vol. A2, 1950, pp. 184–204.

[8] "Heat Transfer in a Round Tube or Flat Duct," by J. Sellars, M. Tribus, and J. Klein, University of Michigan, Ann Arbor, Mich., 1954.

[9] University of California, Los Angeles, Calif.

[10] Associate Professor, University of California, Los Angeles, Calif. Mem. ASME.

[11] "Heat Transfer to Laminar Flow in a Round Tube or Flat Conduit, the Graetz Problem Extended," by J. R. Sellars, M. Tribus, and J. Klein, University of Michigan, Engineering Research Institute, WADC Contract No. AF 18 600-51.

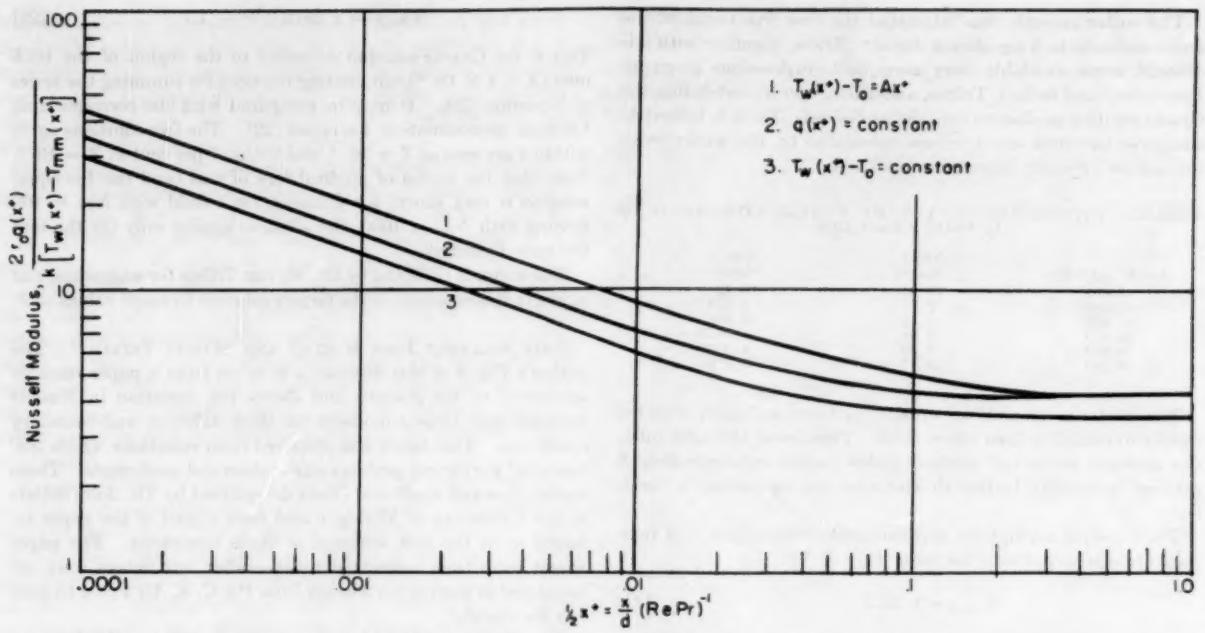

Laminar Flow of a Constant Property Fluid in a Round Tube

FIG. 9

= 0, 1, and 2 the coefficients reported by Jakob (author's reference 4) should be used, though even for $n = 1$ the approximation formulas given are sufficiently accurate for most purposes. If the wall heat flux is given then Equation [25] with Equation [27] and the data of [29] are to be used.[12]

The Leveque approximation can be extended to cover the cases of variable wall temperature or heat flux. For the three cases at hand

$Nu = 1.3565x^{+-1/3}$ Isothermal $x^+ \leq 10^{-4}$ . . [30]

$Nu = 1.6393x^{+-1/3}$ Constant (q/A) $x^+ \leq 10^{-4}$ . . [31]

$Nu = 2.0348x^{+-1/3}$ Linearly varying wall temperature $x^+ \leq 10^{-5}$ . . [32]

In the paper mentioned at the beginning of these comments details are given for the preparation of the asymptotic solution for any wall-temperature variation or heat-flux distribution.

The author's correlation of Run 54 (see his Fig. 8) clears up some interesting points in regard to Kroll's thesis. As was pointed out in reference (3)[13] of his paper, even when corrections for the nonisothermal wall were applied to Kroll's data, agreement with the Graetz solution could not be obtained. It was not noticed then for this run that the Reynolds modulus was 2850 and therefore the "entry length" should be quite large. The agreement with the author's calculations is most gratifying. We note that at low values of the Reynolds modulus the agreement between the solution with parabolic velocity distribution is much better, thus fortifying the author's conclusions concerning the use of the Langhaar velocity distributions.

If the wall shear stresses had been inserted in the integrating kernels proposed by Lighthill it would probably have been possible to avoid the numerical integration of the energy equation. These kernels and their uses have been discussed elsewhere.[13]

[12] The author's reference (3) is no longer in print. The same information appears in the book "Heat Transfer—A Symposium," University of Michigan Press, Ann Arbor, Mich., 1953, p. 211.

AUTHOR'S CLOSURE

Mr. Lipkis' discussion concerning the effect of insufficient terms in the Graetz solution indicates that there is apparently an error in the original paper by Norris and Streid (5),[2] since the authors' statement in this regard was based simply upon a replot of their curves.

It is gratifying to learn that the Graetz solution has now been extended to include all the eigenvalues and coefficients. Together with the method proposed by Sellars, Klein, and Tribus for applying the Graetz solution to any kind of wall-temperature variation, it now appears that the Graetz problem has been pretty well cleaned up. It should be remembered, however, that the Graetz solution is based on an assumption of parabolic velocity distribution throughout, whereas the major concern of the present paper is for those cases where such an assumption is not valid.

In regard to Mr. Lipkis' comparison, Table 6, of the exact solution and the author's numerical solution for constant wall temperature and parabolic velocity, it is worth noting that the numerical method error of 8 per cent at $4(x/D)/(N_{Re}N_{Pr}) = 0.004$ occurs after only four steps in the numerical integration. Considering the relatively coarse grid used, this is not bad, and the solution converges very rapidly thereafter. After 20 steps the error is less than 2 per cent, and it was for this latter region that the numerical grid was set up. Thus Table 6 provides an even better verification of the numerical method than does Fig. 3.

It appears that there must be an error in the abscissa of Fig. 9 presented by Sellars, Klein, and Tribus. In order for curve 3 to check with Table 6, the abscissa would have to be x^+ rather than $x^+/2$.

The author would like to thank the various discussers for their substantial contribution to the paper.

[13] An article published in the *Journal of the Aeronautical Sciences*, Readers' Forum, January, 1955.

An Interferometric Study of Free-Convection Heat Transfer From Enclosed Isothermal Surfaces

By C. D. JONES[1] and D. J. MASSON[2]

Variations of point and average heat-transfer coefficients with spacing are presented for (*a*) horizontal isothermal cylinders near plane partial enclosures and (*b*) vertical isothermal prisms of small height in a duct.[3]

Nomenclature

The following nomenclature is used in the paper:

Gr = Grashof number
h = heat-transfer coefficient, Btu per hr-sq ft-deg F
h' = heat-transfer coefficient, pure conduction
h'' = heat-transfer coefficient, pure convection
k = thermal conductivity, Btu per hr-ft-deg F
Nu = Nusselt number
Pr = Prandtl number
t = temperature, deg F

Applying to Cylinders Only

a = peripheral position on cylinder reading clockwise with zero at top of vertical axis, deg
a' = peripheral position on cylinder, radians
D = diameter, ft
x = perpendicular distance from vertical wall to vertical center line of cylinder, ft
x' = minimum horizontal distance from cylinder to wall, in.
X = x/D
y = perpendicular distance from horizontal wall to horizontal center line of cylinder, ft
y' = minimum vertical distance from cylinder to wall, in.
Y = y/D
a = (subscript) refers to point value on cylinder

Applying to Prisms Only

d = distance between top of prism and top of duct, ft
L = total height of prism, ft
n = exponent
w = distance between side of prism and side of duct, ft
x = co-ordinate normal to heated vertical surface, ft
y = co-ordinate parallel to heated vertical surface, ft
θ = temperature difference ($t_w - t_s$), deg F
dt/dx = temperature gradient, deg F per ft
m = (subscript) mean value
s = (subscript) refers to cooled surface of duct
w = (subscript) refers to heated surface of prism
y = (subscript) refers to point value

Introduction

When any heat-dissipating surface is placed in close proximity to an enclosing structure at a lower temperature, some effect upon the local and average free convection may be expected. It was the purpose of these investigations to provide such data, and to correlate them with those of unconfined surfaces, for horizontal cylinders and the vertical surfaces of prisms of small height.

The effects of plane enclosures on the average free-convection coefficients of cylinders (1)[4] and on local surface temperatures of cylindrical fixed-composition resistors (2) have been reported for a limited number of configurations and temperatures. Some results for free-convection coefficients in enclosed-plane gas layers greater than $^1/_2$ in. in thickness also have been reported (3).

Heat-Transfer Mechanism

When the heated bodies are unconfined, the conventional parameters of Nusselt, Grashof, and Prandtl should define the heat-transfer process where the characteristic dimensions are the diameter of the cylinder and the height of the vertical surface. However, when the body is in close proximity to an enclosure at a lower temperature, the size of the intermediate space also becomes significant because reduction of this dimension below that of the velocity boundary-layer thickness around the heated body may be expected to restrict the free-convective fluid flow. Since the free-convection heat-transfer process involves both conduction, through the fluid layers adjacent to the heated surface, and convection, it is, therefore, convenient to separate these two basic phenomena since gaseous conduction is predominant at small spacings and convection is most significant at large spacings. When the heated and cooled surfaces are parallel, this separation of processes can be made easily. However, in the case of a cylindrical surface adjacent to a plane wall, the problem becomes quite complex since the conduction path is nonlinear and varies in length from point to point. For this latter case, a dimensionless parameter equal to the perpendicular distance between the wall and the center line of the cylinder parallel to the wall per unit cylinder diameter has been suggested (1).

Test Models and Apparatus

The outer surfaces of the 10-in-long test models were made of $^1/_8$-in-thick copper attached to transite cores which contained closely spaced heating elements. Several independent circuits provided separate control of the heat dissipation of various portions of the surfaces to insure a closely isothermal condition. The distances between the models and the surrounding surfaces could be varied by screw adjustments.

The cylindrical model was 2 in. in diam and was mounted adjacent to the water-cooled walls as shown in Fig. 1. The

[1] Research Associate Supervisor, Mechanical Engineering Department, The Ohio State University, Columbus, Ohio. Assoc. Mem. ASME.

[2] Engineer, Frame and Auxiliaries Engineering, Guided Missiles Department, General Electric Company, Schenectady, N. Y. Mem. ASME.

[3] The results of prisms in ducts were obtained in the course of research sponsored by the United States Air Force, Wright Air Development Center, under Contract No. W33-038ac-14987, while the author[2] was Instructor in Mechanical Engineering at The Ohio State University.

Contributed by the Heat Transfer Division and presented at the Annual Meeting, New York, N. Y., November 28–December 3, 1954, of The American Society of Mechanical Engineers.

Note: Statements and opinions advanced in papers are to be understood as individual expressions of their authors and not those of the Society. Manuscript received at ASME Headquarters, August 27, 1954. Paper No. 54—A-147.

[4] Numbers in parentheses refer to the Bibliography at the end of the paper.

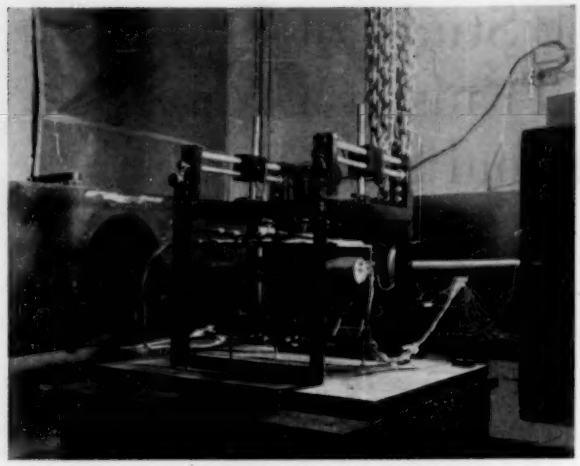

FIG. 1 CYLINDER-STUDY TEST APPARATUS IN LIGHT PATH OF INTERFEROMETER

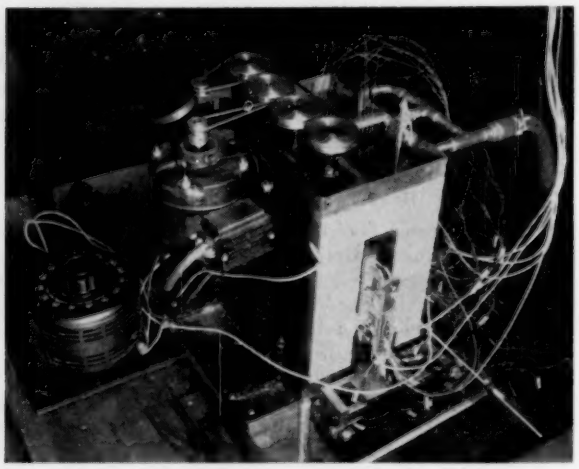

FIG. 2 PRISM-STUDY TEST APPARATUS

prismatic models, 3/4 in. thick, were mounted on an insulated base plate within a water-cooled duct as shown in Fig. 2. Most data were obtained with a 4-in-high model. A 2-in-high model also was studied to confirm the established correlations.

All temperature-gradient data were obtained with a Zehnder-Mach interferometer (4) which had an elliptical field of view with dimensions 7.44 × 4.50 in.

END EFFECTS

The heat-transfer coefficients were evaluated from the interferograms by the usual transformation equations (5, 6); these equations assume that the temperature of the air within the length of the model along any line parallel to the light beam of the interferometer is constant. Typical temperature fields adjacent to and beyond the ends of the test models were measured by very fine thermocouple probes and the resulting temperature gradients compared with those indicated by the interferograms. In the case of the cylinder studies the error was approximately 2 to 5 per cent which fell within the over-all reproducibility of a given set of test conditions and was thus neglected. For the prism studies it is desirable to change as abruptly as possible the air temperature in the end planes of the duct, to a uniform temperature within the duct length along any line parallel to the duct axis. In order to create the change it was found desirable to round the ends of the confining top surfaces and to introduce a series of horizontal heating wires of 0.004 in. diam (spaced at 3/8-in. intervals) in each vertical end plane of the duct. This decreased the heat loss from the end of the model and the inflow and outflow of air at the ends of the duct.

SCOPE AND PROCEDURE

The variables investigated and the range of each are shown in Fig. 3 and Table 1 for cylinders; Fig. 4 and Table 2 for prisms.

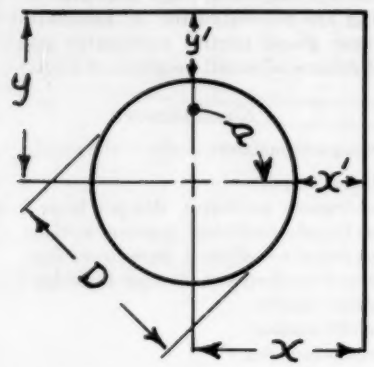

FIG. 3 DIAGRAM OF CYLINDER CONFIGURATION

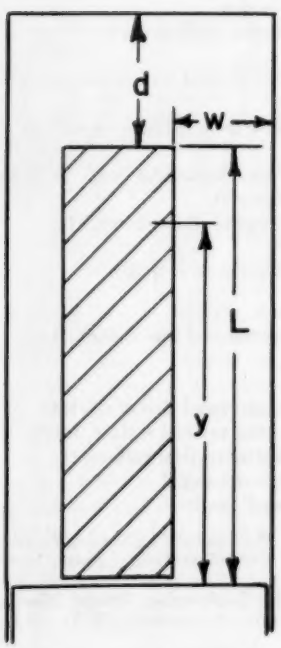

FIG. 4 DIAGRAM OF PRISM CONFIGURATION

In each case the model surface was maintained at one uniform temperature and the walls at a lower uniform temperature. All interference photographs of the cylindrical model were made with the interferometer mirrors adjusted to produce no fringes when the temperature field was uniform. Using this method, the fringes appearing around the heated model may be interpreted as isotherms as shown in Figs. 5 (*a*, *b*, and *c*). With the prism studies, it was most convenient to adjust the mirrors to produce horizontal fringes when no temperature gradient existed as shown in Fig. 6 (*a*). A typical fringe pattern produced by a heated model is shown in Fig. 6 (*b*).

Heat-transfer coefficients reported are defined in terms of the temperature difference between the heated and cooled surfaces. The water-cooled walls were at all times maintained at the ambient-air temperature.

TABLE 1 RANGE OF CYLINDER TEST DATA

Confined Cylinder. Sixteen combinations of x' and y' at each θ for both wall-floor and wall-ceiling enclosures for total of 128 runs.

Variable	Number of settings	Range of settings
x'	6	1/16 to 3/4 in.
y'	6	1/16 to 3/4 in.
θ	4	40 to 200 F
Free cylinder		
θ	18	26 to 368 F

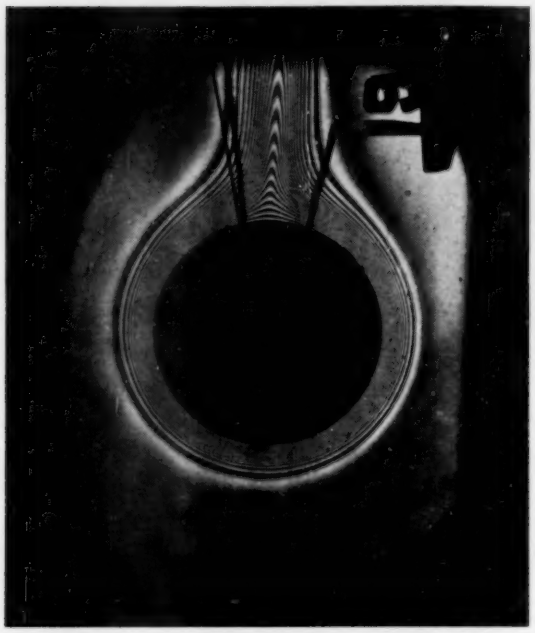

(*a*) Free cylinder, temperature difference equals 110 F

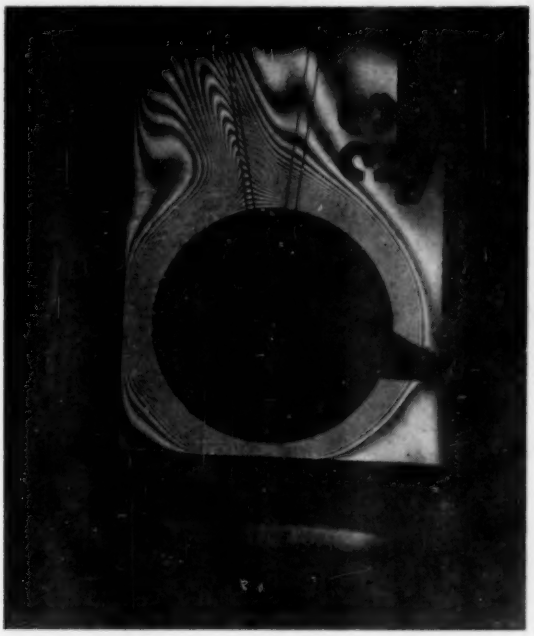

(*b*) Cylinder in vicinity of wall-floor corner

(*c*) Cylinder in vicinity of wall-ceiling corner

FIG. 5 INTERFEROGRAMS OF CYLINDER CONFIGURATION

TABLE 2 RANGE OF PRISM TEST DATA

Model height, in.	Variable	Number of settings	Range of settings
4	w	14	0.135 to 1.015 in.
4	d	4	0.125 to 1.866 in.
4	θ	4	50 to 112 F
2	w	14	0.125 to 0.875 in.
2	d	4	0.125 to 1.8 in.
2	θ	2	100 F (70 and 108 F for one distance d each)

EXPERIMENTAL RESULTS—PRISMS

Typical temperature gradients at the surface of the heated prism, which are directly proportional to the local heat-transfer coefficients, are shown in Fig. 7 for various wall-to-wall spacings. The experimentally determined local heat-transfer coefficients may conveniently be described as the sum of a pure conduction and pure convection coefficient as shown in

$$h_y = h_y' + h_y'' \quad \ldots\ldots [1]$$

where $h_y' = (k_m/w)$. This is shown graphically in Fig. 8 where the calculated conductive temperature gradient curve is tangent to the experimentally determined curve at low values of w, and the convective gradient is the difference between the two.

Point Coefficients. Fig. 9 shows the local Nusselt number, based on h_y'', as a function of the Grashof number and spacing. The linear curves for the large top distances may be empirically correlated by Equation [2] in which the n is described by Equation [3]

$$\mathrm{Nu}_y'' = 0.37 \tanh 36w\,(\mathrm{Gr}_y)^n \quad \ldots\ldots [2]$$

$$n = 0.25 - 0.0008w^{-1.43} \quad \ldots\ldots [3]$$

The expression for the total heat-transfer coefficient is as follows

$$h_y = (k_m/w) + (k_a/y)0.37 \tanh 36w\,(\mathrm{Gr}_y)^n \quad \ldots\ldots [4]$$

The experimentally determined values of h_y are predicted with good accuracy by Equation [4] except for values of y less than 0.1 in. The deviations from a straight line for small top distances, as shown in Fig. 9, are not taken into account in Equation [4] and therefore a correction factor must be applied. This factor (7) was found to be dependent on the values d, w, y, and total model height, L. It should be noted that, since the Prandtl number variation was only about 1 per cent, it is included in the constants of the foregoing equations.

Average Coefficients. Integration of Equation [4] over the height of the model gives an expression for the average heat-transfer coefficient

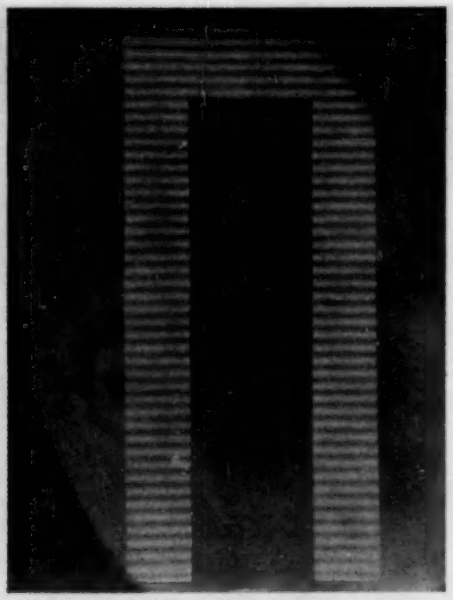

(*a*) Field at uniform temperature

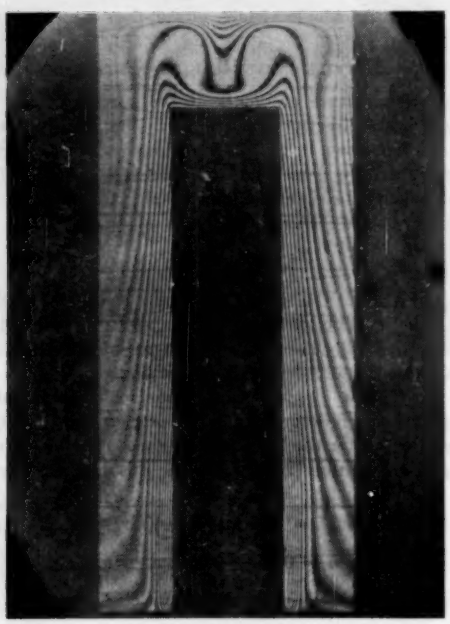

(*b*) Field with heated model

Fig. 6 Interferograms of Prism Configuration

$$h = (k_m/w) + (k_m/3nL)\,(0.37 \tanh 36w)\,(\mathrm{Gr}_L)^n \ldots . \quad [5]$$

It is recommended that this equation be used for values of w greater than 0.025 ft since it fits the experimentally determined values of h. For smaller values, it will be observed that Equation [5] yields heat-transfer coefficients that are not rational. For values of w smaller than 0.025 ft, Equation [5] should read $h = (k_m/w)$ which fits the experimentally determined values to within less than 6 per cent.

Free Vertical Plate. For large values of w, Equation [4], when rearranged, approaches

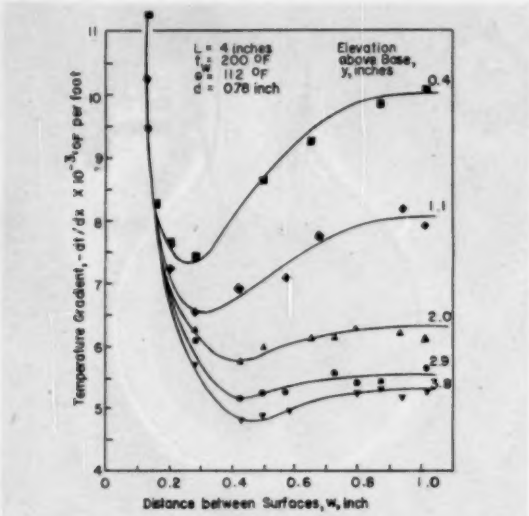

Fig. 7 Variation of Air Temperature Gradient at Prism Surface With Distance Between Model and Duct for Points of Different Elevation

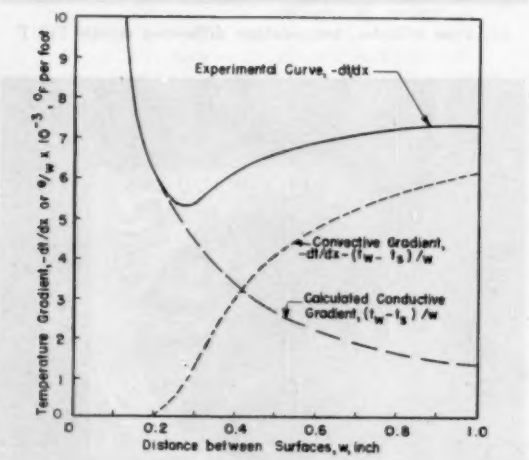

Fig. 8 Analysis of Temperature-Gradient Variation for Conductive and Convective Effects

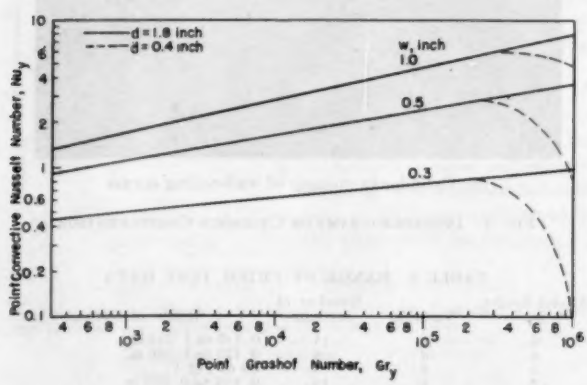

Fig. 9 Plot of Point Convective Nusselt Numbers Versus Point Grashof Numbers for Prisms

$$Nu_y = 0.37(Gr_y)^{0.25} \quad [6]$$

which is in good agreement with both theoretically derived (8) and experimentally measured (9) values; namely, constants of 0.378 and 0.36, respectively.

The average heat-transfer Equation [5] reduces to

$$Nu = 0.493\,(Gr_L)^{0.25} \quad [7]$$

for large values of w. The constant in Equation [7] may be compared with typical experimentally determined values of 0.48 (9) and 0.503 (10) and a theoretically determined value of 0.501 (10).

Experimental Results—Cylinder

Point Coefficients. Peripheral variation of the local Nusselt number on a cylinder in the neighborhood of the enclosures studied is shown in Figs. 10 and 11 for various spacings. The notable trends in these figures are the maximum values which occur at the peripheral locations closest to the enclosure, attributable to the predominance of gaseous conduction, and the minimum values which always occur approximately 45 peripheral degrees "upstream" from a narrow spacing (e.g., at a = 225 deg in Fig. 10, and a = 135 and 320 deg in Fig. 11.) It should be noted that the curves in Fig. 10 for the largest values of Y and X are applicable to cylinders near a wall only and floor only, respectively, since at these distances the effect of the adjoining wall is negligible.

The curves of Figs. 10 and 11 are drawn through the average of the available test data for which the maximum deviation from the curves is approximately $(Nu_a/Gr^{0.25}) = 0.05$. As noted in

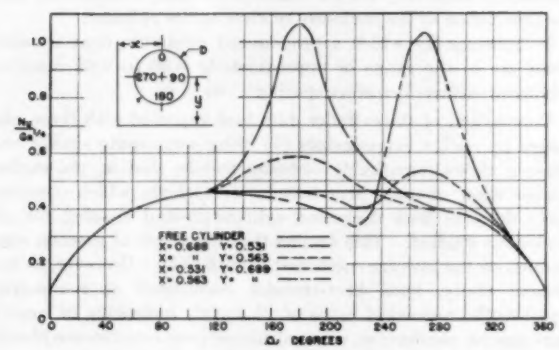

Fig. 10 Correlation of Point Heat-Transfer Coefficients on a Cylinder Near a Wall-Floor Corner

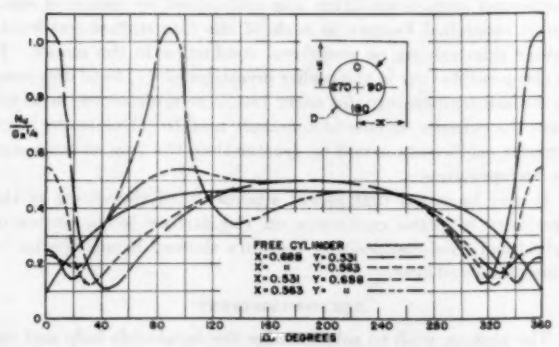

Fig. 11 Correlation of Point Heat-Transfer Coefficients on a Cylinder Near a Wall-Ceiling Corner

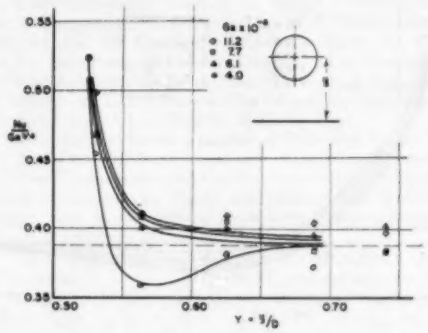

Fig. 12 Effect of a Floor-Type Enclosure on Average Nusselt Number of a Cylinder

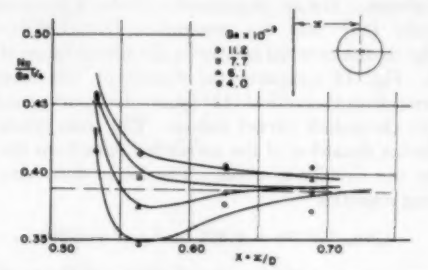

Fig. 13 Effect of a Wall-Type Enclosure on Average Nusselt Number of a Cylidner

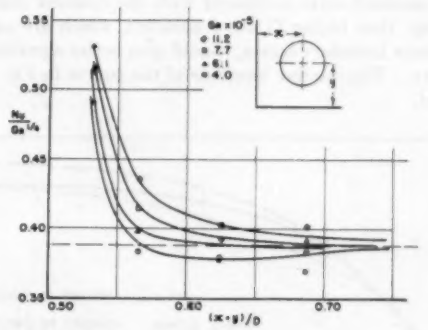

Fig. 14 Effect of a Wall-Floor Corner on Average Nusselt Number of a Cylinder

the next section, the heat-transfer coefficients generally tend to increase with temperature difference, however, at points where gaseous conduction is predominant, the reverse is true.

Average Coefficients. The effects of the various enclosures investigated on the average heat-transfer coefficients are shown in Figs. 12 through 15. The general trends shown are a decrease in the heat-transfer parameter with decreased spacing, indicative of decreased fluid velocities between the cylinder and enclosure, followed by an increased heat-transfer coefficient which may be attributed to gaseous conduction. The remarkable effect of an increase in the parameter $(Nu/Gr^{0.25})$ with increasing Grashof number for a given spacing probably may be attributed to the fact that the larger Grashof numbers, with which are associated larger buoyant forces, promote greater local air velocities through a given-size cylinder-to-enclosure space. The relative significance of the foregoing trends is shown to depend upon the number of walls in the enclosure and the relative location of the enclosure with respect to the cylinder.

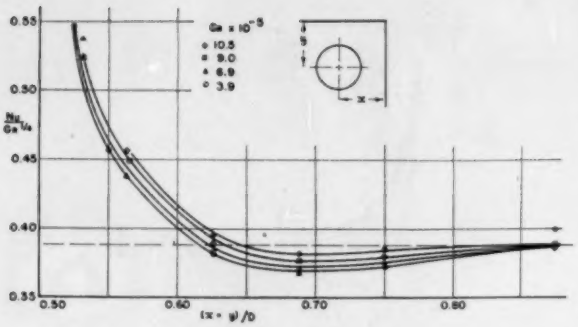

FIG. 15 EFFECT OF A WALL-CEILING CORNER ON AVERAGE NUSSELT NUMBER OF A CYLINDER

Free Cylinder. For an unconfined cylinder it has been shown theoretically (11) that the parameter $(Nu_a/Gr^{0.25})$ depends only on the circumferential position a for a large range of Grashof numbers. Fig. 16 compares the results of this investigation (solid curve) with theoretical (11) (short-dash curve) and experimental (5) (long-dash curve) values. The cross symbols show the maximum deviation of the correlated data from the average shown by the circular symbols. The latter data may be empirically expressed by

$$(Nu_a/Gr^{0.25}) = 0.463 \tanh (a' + 0.22) \quad [8]$$

It has been suggested (5) that the deviation of the experimental from the theoretical heat-transfer distribution, as shown in Fig. 16, is probably due to the fact that the thickness of the boundary layer is assumed small compared with the cylinder diameter in the theory, thus higher Grashof numbers, which are associated with thinner boundary layers, should give better agreement with the theory. The relative locations of the curves in Fig. 16 show this trend.

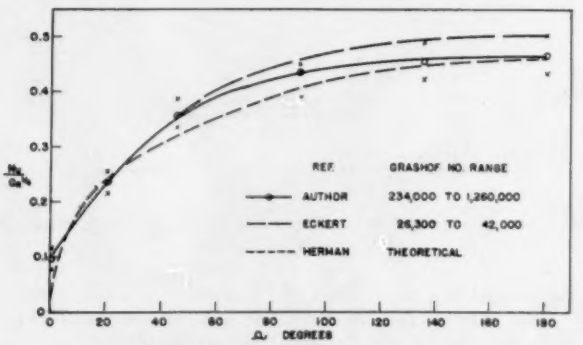

FIG. 16 POINT HEAT-TRANSFER CORRELATION OF FREE-CYLINDER DATA

Integration of Equation [8] for the average heat-transfer parameters yields

$$Nu = 0.388\ Gr^{0.25} \quad [9]$$

if the Prandtl number is assumed constant at 0.70, or

$$Nu = 0.424(Gr \cdot Pr)^{0.25} \quad [10]$$

The constants in Equations [9] and [10] may be compared with 0.401 (5) and 0.45 (12), respectively, where similar physical property data (13) were used.

A constant of 0.37 in Equation [9] has been determined from theoretical considerations (11).

CONCLUSIONS

In addition to the previously mentioned trends, the following pertinent conclusions are drawn from the results of this investigation.

Vertical Prisms

1 The free-convection heat-transfer equations for unconfined vertical surfaces are not applicable when a parallel surface is within a distance of approximately 1 in.

2 The occurrence of a minimum heat-transfer coefficient is dependent upon the values of y and θ.

3 For conditions which produce a pronounced minimum heat-transfer coefficient, the spacing w would be in the range of $^1/_4$ to $^1/_2$ in.

4 For any particular prism height L, there is a limiting value of the Grashof number below which the value of w for minimum heat transfer is infinite.

5 The effect of reducing the distance between the top of the prism and the top of the duct d is to decrease the local heat-transfer coefficients in the upper portion of the vertical surface while those near the bottom remain unaffected.

6 The height of the prism L has no effect on the local heat-transfer coefficients for top distances d exceeding $^3/_4$ in. For smaller top distances, the prism height affects only the heat transfer from the upper portion of the model.

Horizontal Cylinders

1 The free-convection heat-transfer equations for unconfined horizontal cylinders are not applicable when a plane partial enclosure is within a distance of approximately 0.75 diam, a minimum surface-to-surface spacing of $^1/_2$ in.

2 The occurrence of a minimum heat-transfer coefficient is dependent upon the Grashof number (or temperature rise) and the orientation of the enclosure relative to the cylinder.

3 Spacings for which a pronounced minimum heat transfer occur are in the range of approximately 0.56 to 0.68 diam; a minimum surface-to-surface spacing $^1/_8$ to $^3/_8$ in.

Comparison of the cylinder data here reported with those obtained by earlier investigators (1) using some quite similar enclosures shows remarkably opposite trends; that is, the earlier studies show average heat-transfer coefficients which continuously decrease with decreased cylinder-to-wall spacing for all enclosures studied. This implies that the effect of gaseous conduction on the average coefficient is negligible. However, in the present study, local heat-transfer coefficients approximately equal to the numerical value of 12 k_m/x', indicative of nearly pure gaseous conduction, were calculated from interference photographs of small spacings.

The foregoing inconsistencies may possibly arise from experimental differences. For example, in the present study, a closely isothermal surface condition was maintained by means of separately controlled heaters in each of the four surface quadrants rather than relying on peripheral conduction in the model. It is also possible that in the earlier investigation (1) local decreases in surface temperature did occur but were undetected, in which case, the cylinder surface temperature used to calculate the heat-transfer coefficients would be greater than the true average surface temperature.

It may be noted that recent studies (2) of the effects of the proximity of plane enclosures on the surface temperatures of cylindrical fixed-composition resistors showed trends similar to those presented here.

ACKNOWLEDGMENT

The authors wish to acknowledge the invaluable help and encouragement received from Profs. W. Robinson and S. M. Marco. The data presented on prisms are the results of an in-

vestigation sponsored by Wright Air Development Center, United States Air Force, under Contract W33-038ac-14987 with the Ohio State University. The authors wish to thank the Air Force for permission to publish this material.

BIBLIOGRAPHY

1 "The Measurements of Heat Transfer by Free Convection From Cylindrical Bodies by the Schlieren Method," by L. M. Boelter and V. H. Cherry, Trans. ASHVE, vol. 44, 1938, pp. 499–512.

2 "Thermodynamics of Resistors," by T. K. Slawecki, et al., University of Pennsylvania Research Division Report No. 53–24, Contract No. AF33(038)-18417, Wright Air Development Center, Dayton, Ohio, 1953, pp. 78–80.

3 "Heat Transfer," by M. Jacob, John Wiley & Sons, Inc., New York, N. Y., 1949.

4 "Manufacture of a Zehnder-Mach Interferometer," by E. R. G. Eckert, R. M. Drake, and E. Soehngen, U. S. Air Force Technical Report No. 5721, Air Materiel Command, Dayton, Ohio, 1948.

5 "Studies on Heat Transfer in Laminar Free Convection With the Zehnder-Mach Interferometer," by E. R. G. Eckert and E. Soehngen, U. S. Air Force Technical Report No. 5747, Air Materiel Command, Dayton, Ohio, 1948.

6 "Free-Convection Cooling in Air of Confined Small Bodies Similar to Electronic Components," by D. J. Masson and W. Robinson, Report No. 43, Contract W33-038ac-14987, U. S. Air Force, Wright Air Development Center, Dayton, Ohio, January, 1952.

7 "Free-Convection Heat Transfer From a Vertical Surface in an Enclosure," by D. J. Masson, The Ohio State University Graduate School, Columbus, Ohio, March, 1952.

8 "Introduction to the Transfer of Heat and Mass," by E. R. G. Eckert, McGraw-Hill Book Company, Inc., New York, N. Y., 1950.

9 "Das Temperatur und Geschwindigkeitsfeld vor einer Wärme abgebenden senkrechten Platte bei natuerlicher Konvektion," by E. Schmidt and W. Beckman, *Technische Mechanik und Thermodynamik*, vol. 1, 1930, pp. 341–364.

10 "Heat Transmission," by W. H. McAdams, McGraw-Hill Book Company, Inc., New York, N. Y., second edition, 1942, p. 243.

11 "Wärmeubergang bie Frier Strömung am Waguchton Zylinder in Zweiatomigen Gasen," by R. Herman, *Forschung auf dem Gebiete des Ingenieurwesens*, Forschungsheft 379, 1936.

12 "Introduction to Heat Transfer," by A. I. Brown and S. M. Marco, McGraw-Hill Book Company, Inc., New York, N. Y., second edition, 1951, p. 136.

13 "Gas Tables," by J. H. Keenan and J. Kaye, John Wiley & Sons, Inc., New York, N. Y., 1948.

Free-Convection Heat Transfer From a Rotating Horizontal Cylinder to Ambient Air With Interferometric Study of Flow[1]

By G. A. ETEMAD,[2] BUFFALO, N. Y.

Free-convection heat-transfer correlation for a rotating horizontal cylinder in air was evaluated experimentally for a range of Reynolds numbers from 0 to 65,400. The stability of flow around the rotating cylinder and the transition from laminar Couette flow to fully developed secondary flow were investigated with the aid of a Zehnder-Mach interferometer. The heat-transfer data obtained agree well with the experimental results of Anderson and Saunders (1).[3] The experimental results for the models in the stationary state exhibited substantial correlation with published data.

Nomenclature

The following nomenclature is used in the paper:

C_p = specific heat of air at constant pressure, Btu/lb deg F
D = outside diameter of the test cylinder, ft
g = acceleration of gravity, ft/hr²
Gr = Grashof number = $\beta g \Delta t D^3 \rho^2 / \mu^2$
h = heat-transfer coefficient at the surface of the rotating cylinder, Btu/hr sq ft deg F
k = thermal conductivity of air, Btu/hr ft deg F
Nu = Nusselt number = hD/k
Pr = Prandtl number = $C_p \mu / k$
Re = Reynolds number = $VD\rho/\mu$
t = temperature, deg F
t_f = arithmetic mean temperature of test cylinder and ambient air, deg F
t_w = temperature of test-cylinder surface, deg F
t_a = temperature of ambient air, deg F
V = peripheral velocity of test cylinder, fph
β = coefficient of volumetric expansion, $\frac{1}{v}\left(\frac{\partial v}{\partial t}\right)_p$
μ = viscosity of air, lb/hr ft
ρ = weight density of air, pcf
Δt = temperature difference between surface of the test cylinder and the ambient air, deg F

Introduction

Free-convection heat transfer from horizontal cylinders has been the subject of many investigations, both from a theoretical and from an experimental point of view. McAdams (9) and Jakob (7) have presented the results of numerous theoretical and experimental investigations which yield a host of data on free-convection heat transfer from wires and horizontal cylinders of different sizes and in various fluids.

On the other hand, relatively little attention has been given to the prediction of heat transfer from rotating models. Millsaps and Pohlhausen (10) investigated the problem of heat transfer from a rotating plate in an ambient fluid with laminar flow. Taylor (12) investigated the velocity and temperature distribution between concentric rotating cylinders at different temperatures. The problem of flow between two rotating cylinders also has been considered by several other investigators (3, 13, 14). Their efforts have been concerned mostly with measurement of drag and with the study of stability of viscous flow between rotating cylinders.

When the present investigation was initiated there was no published information concerning free-convection heat transfer from a rotating cylinder. Anderson and Saunders (1) recently investigated heat transfer by convection from an isolated heated horizontal cylinder rotating about its axis in air. In this paper the results of their study will be compared with those of the author.

The primary purpose of this investigation was to obtain experimental data on free-convection heat transfer from a rotating horizontal cylinder in air. A second purpose was to study the flow and the stability of the Couette motion around the rotating cylinder and, specifically, to visualize the changes that occur in the type of flow around the rotating cylinder. Extensive preliminary experimentation was conducted to determine a satisfactory means of measuring the surface temperature of the cylinder rotating at high speeds. A method of measuring the surface temperature of the rotating cylinder by means of calibrated and carefully aged thermistor beads was developed, and with this method—plus other improvements—the experimental measurements were extended up to a rotational speed of 5250 rpm.

Experimental Equipment

The test program involved the use of a $2^3/_8$-in-OD copper model and a $2^1/_2$-in-OD bakelite model. The copper model was used primarily as a preliminary test cylinder; secondarily, as a means of obtaining a higher cylinder-surface temperature than could be obtained with the bakelite model. The bakelite model was used to extend the tests into higher rotational speeds and also to permit interferometric study of flow around the cylinder.

The details of the construction of the copper model are shown in Fig. 1. The heater consisted of No. 22 nichrome wire wound around a threaded transite tube and inserted in the copper cylinder. The surface temperature of the cylinder was measured by means of thermocouples. The thermocouple wires and the electrical power leads were led through the hollow shaft to a brush and slip-ring arrangement.

The bakelite model comprised a central rotating cylinder and two stationary end cylinders which housed the ball bearings and brush mountings. The central rotating cylinder, $14^1/_8$ in. long,

---

[1] This paper is based on the author's PhD dissertation at the University of California, Berkeley, Calif.

[2] Assistant Professor of Engineering, Department of Mechanical Engineering, The University of Buffalo. Mem. ASME.

[3] Numbers in parentheses refer to the Bibliography at the end of the paper.

Contributed by the Heat Transfer Division and presented at the Annual Meeting, New York, N. Y., November 28–December 3, 1954, of The American Society of Mechanical Engineers.

Note: Statements and opinions advanced in papers are to be understood as individual expressions of their authors and not those of the Society. Manuscript received at ASME Headquarters, August 3, 1954. Paper No. 54—A-74.

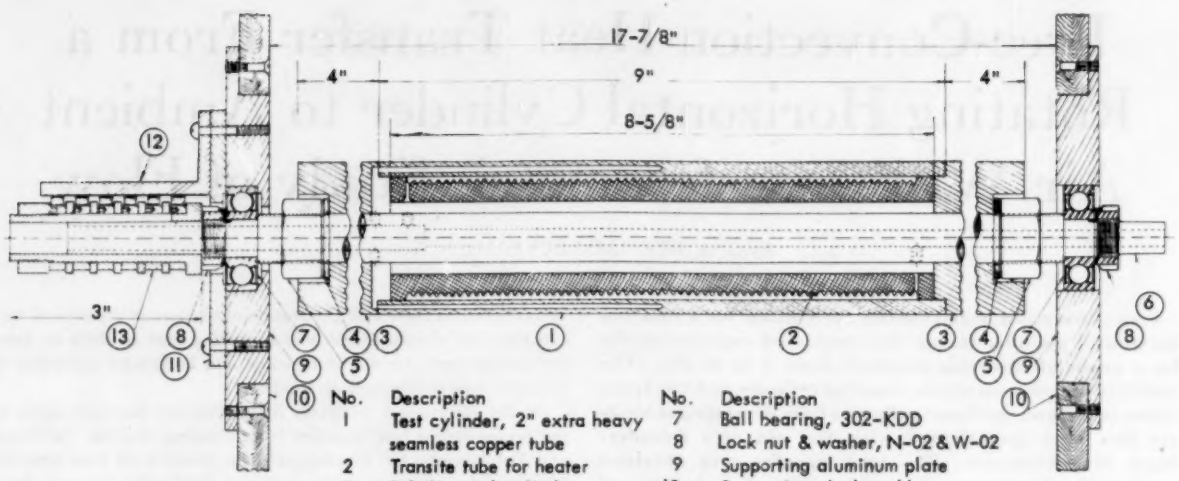

No.	Description	No.	Description
1	Test cylinder, 2" extra heavy seamless copper tube	7	Ball bearing, 302-KDD
2	Transite tube for heater	8	Lock nut & washer, N-02 & W-02
3	Bakelite end-cylinder	9	Supporting aluminum plate
4	Hard-rubber washer	10	Supporting ply-board box
5	Support nut, 3/4" bore, N. F.	11	Aluminum disk for bearing support
6	Hollow shaft, 1/2" double extra strong steel pipe	12	Brush assembly
		13	Slip-ring system

FIG. 1 DETAILS OF CONSTRUCTION OF COPPER MODEL

consisted of a $13^1/_2$-in-long bakelite tube and two end pieces which supported the central tube and held the end shafts. The heating element consisted of six turns of 0.002 × 1.0-in. nichrome ribbon wound helically around the middle $7^1/_8$ in. of the bakelite tube. The ends of the nichrome ribbon were brought inside through thin slots in the tube wall and held tight by means of two coil springs. The surface temperature of the test cylinder was measured by means of two preaged and calibrated glass-coated thermistor beads. The thermistor beads, 0.045 in. diam with opposite platinum leads, were installed 90 deg apart in angular position under the surface of the mid-section of the nichrome ribbon in the following manner.

Two holes $^1/_{64}$ in. diam were drilled $^3/_8$ in. apart at each thermistor location. These holes were joined by an axial slot cut in the surface of the bakelite tube to a depth of 0.005 in. The middle of this slot was enlarged to the size of the thermistor beads. Thermistors were laid in the enlarged part of the slot, and their end wires were led through the holes to the inside of the cylinder. In order to calibrate the thermistors under operating conditions, two iron-constantan thermocouples were placed each next to a thermistor underneath the ribbon and the end wires were led through a new set of holes to the inside of the cylinder.

In order to estimate the conduction losses to the interior and axially along the test cylinder, two more thermocouples were fitted to the inside wall of the bakelite tube, each one being located directly behind a corresponding thermocouple on the surface. The conduction losses were reduced greatly by filling the interior of the rotating bakelite tube with glass wool. Details of the construction are shown in Fig. 2.

The driving mechanism was a variable-speed a-c motor with variable pulleys arranged so that any speed was obtainable from 15 to 10,000 rpm.

TEST PROCEDURE

For each run throughout the experiment, the surface temperature of the test cylinder, the temperature of the ambient air, the rotational speed, and the rate of heat input to the test cylinder were measured. Experimentation covered the following ranges:

Grashof numbers from 1.5×10^5 to 1.7×10^6
Reynolds numbers from 0 to 65,400
Nusselt numbers from 7.8 to 179

The total number of runs made was 196. They were performed at various levels of approximately constant surface temperature of the test cylinder. For each series of runs, the rotational speed was varied in such a way that the correlation of Nu with Gr × Pr at constant Re was possible.

SURFACE-TEMPERATURE MEASUREMENT

The surface temperature of the copper model was measured by means of thermocouples, and slip rings were used to transmit the thermocouple emf. This method of transferring thermocouple voltages gave satisfactory results at rotational speeds up to 600 rpm. At higher rotational speeds the frictional heating of the brush and ring, caused by rotation, generated considerable extraneous emf in the thermocouple circuit. This extraneous emf was due to the difference between the temperature at the contact point of the leading wire and the ring and the temperature at the contact point of the brush and the wire going to the potentiometer. The magnitude of this error was measured by insulating the test cylinder and bringing it to a steady-state temperature without any heating. The maximum error involved in the thermocouple readings at rotational speeds up to 600 rpm was 0.01 millivolt; it was 0.03 millivolt at 750 rpm and increased very rapidly beyond 750 rpm. This method of temperature measurement would entail considerable error in the determination of heat-transfer coefficients at higher rotational speeds. For this reason, the experimentation with the copper model was not continued beyond 700 rpm.

The surface temperature of the bakelite model was measured by means of thermistors. Briefly, a thermistor, or thermally sensitive resistor, is a type of circuit element made of a semiconductor whose electrical resistance decreases rapidly as temperature rises. Because of the high resistance of the thermistors, the contact resistance of the brush-and-slip-ring system and the lead resistances are not bothersome. The important problems in the

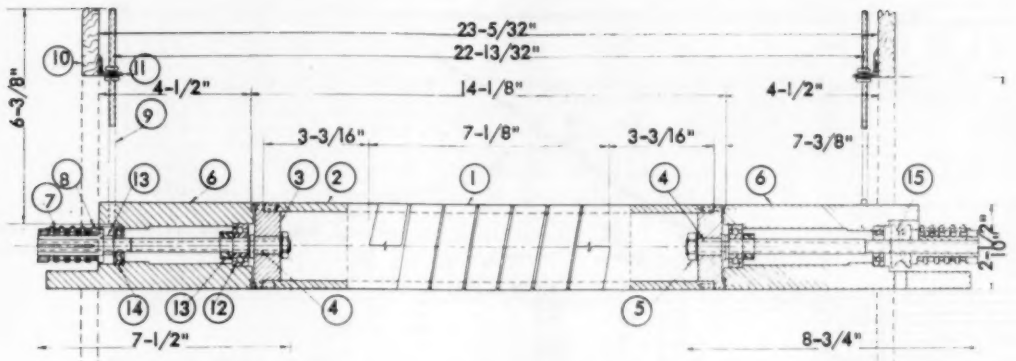

No.	Description	No.	Description
1	Nichrome ribbon, 0.002 x 1.0"	9	Supporting steel rods, 3/16" diam.
2	Canvas base bakelite tube	10	Supporting ply-board box
3	End shaft-holder	11	Supporting steel angles
4	Hollow steel shaft	12	Center bearing, 201-KDD
5	Shaft lock nut	13	Bearings' lock nut and washer
6	Stationary end bakelite cylinder	14	End bearing, 200-SFF
7	Slip-ring assembly	15	Alluminum pulley for 3/16" linen belt
8	Carbon-copper brushes		

FIG. 2 DETAILS OF CONSTRUCTION OF BAKELITE MODEL

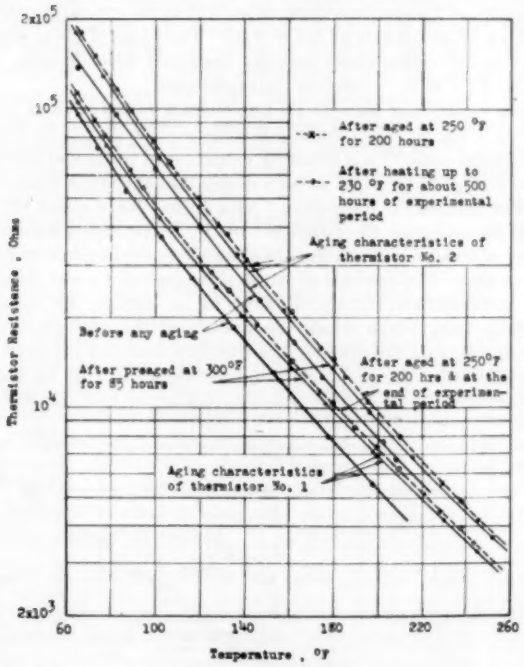

FIG. 3 AGING CHARACTERISTICS OF THERMISTORS

application of thermistors to temperature measurement are the aging characteristics and the calibration of the thermistors.

The thermistors used were preaged at 300 F for 85 hr, and after they were placed in the test cylinder they were aged at 250 F for 200 hr. Fig. 3 shows aging data for both thermistors. The curves demonstrate that remarkably good stabilities were obtained. The change in resistance during 500 hr of the experimental period was only about 0.8 per cent of the resistance after aging. This change in resistance corresponds to a temperature change of about 1 deg F. However, the effect of this change was eliminated by calibrating the thermistors by means of the thermocouples in the test cylinder before each series of runs.

The thermistor resistances were measured by a Wheatstone bridge. The bridge current was supplied by a 1.25-volt air cell. The current through the thermistors was kept below 5 microamp; therefore the power dissipated in the thermistor produced no appreciable heating, and the thermistor resistance was solely dependent upon its ambient temperature.

DISCUSSION OF RESULTS

The experimental results are presented graphically in Figs. 4 to 7. In Fig. 4 the values of heat-transfer coefficient calculated from the experimental data are plotted against the rotational speed of the cylinder for the different values of the temperature difference between the surface of the test cylinder and the ambient air. The heat-transfer coefficient decreases slightly with speed until it reaches a minimum at a critical rotational speed somewhere between 70 and 100 rpm, depending on the surface temperature of the cylinder, then increases rapidly at higher rotational speeds. The effect of the cylinder-surface temperature on the relation of the heat-transfer coefficient to rotational speed is significant at rotational speeds below the critical value but it becomes negligible at higher rotational speeds. The variation of the heat-transfer coefficient with rotational speed, for the range of the cylinder-surface temperatures covered in this experiment, becomes independent of the cylinder-surface temperature at speeds greater than 750 rpm. The experimental results in this range can be represented by the equation

$$h = 0.0336\ (\text{rpm})^{0.70}$$

In Figs. 5 to 7 the experimental results are presented in terms of Nusselt, Grashof, Prandtl, and Reynolds parameters. The calculation of Reynolds numbers was based on the outside diameter and the peripheral velocity of the rotating cylinder. The physical properties of air were evaluated at the average of the surface and surrounding air temperatures. Fig. 5 shows the correlation of Nu as a function of Gr × Pr for the different values

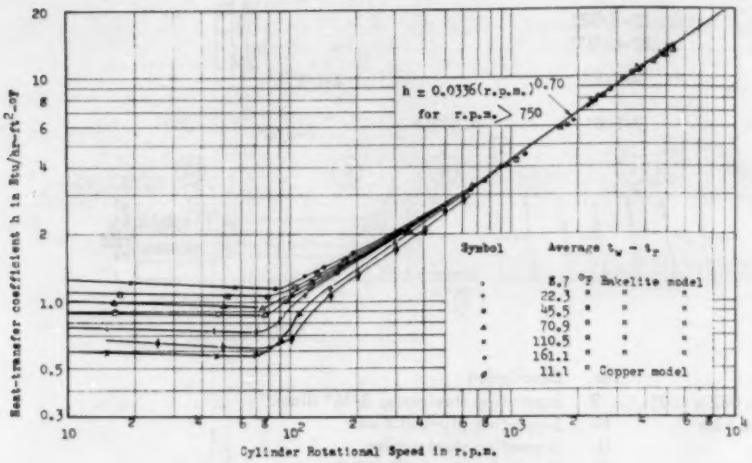

FIG. 4 VARIATION OF HEAT-TRANSFER COEFFICIENT WITH ROTATIONAL SPEED

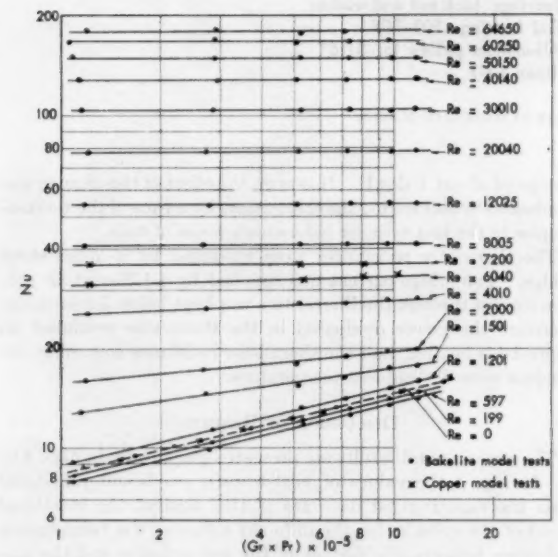

FIG. 5 NU VERSUS GR × PR FOR VARIOUS MAGNITUDES OF RE

of Re. The dashed line in this figure represents data obtained from testing the models in a stationary state and can be represented by the equation

$$Nu = 0.456\ (Gr \times Pr)^{0.25}$$

The curves of Nu versus Gr × Pr for Re below the critical value are parallel to and slightly below the data obtained for Re = 0. The slope of these curves varies from 0.25 at the critical Reynolds number to almost zero at Re = 8000. The value of Re at which the free-convection effect becomes negligible depends upon the range of Gr × Pr covered in the experiment.

The variation of Nu with Re for constant values of Gr × Pr is shown in Fig. 6. The curves of this figure show that at Re below the critical value, Nu is inversely proportional to Re and directly proportional to Gr × Pr in such a way that the latter (free-convection transfer) is controlling. At a critical Re of about 800 to 1200 depending on the magnitude of Gr, Nu reaches a minimum value of about 5 per cent less than the corresponding free-convection value. The decrease of Nu in this range of Re was seen, in the interferometric study of flow, to be due to the laminar Couette flow, which winds the hot air of the free-convection chimney around the cylinder and therefore increases the effective free-convection thermal-boundary-layer thickness. At Re above the critical value, the effect of free convection on heat transfer de-

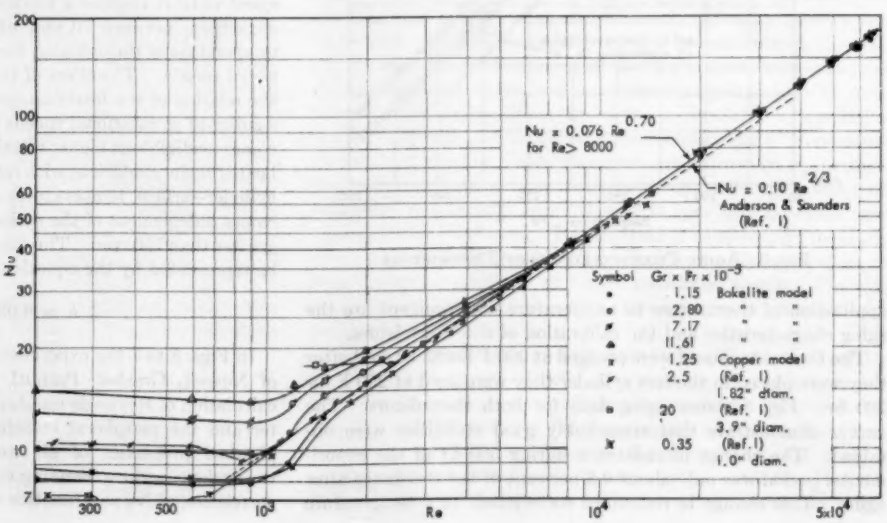

FIG. 6 NU VERSUS RE FOR VARIOUS MAGNITUDES OF GR × PR

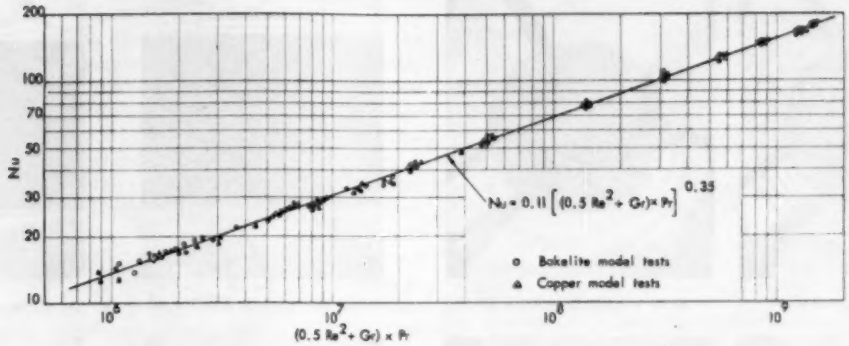

FIG. 7 NU VERSUS $(0.5\ Re^2 + Gr) \times Pr$ FOR REYNOLDS NUMBERS ABOVE CRITICAL VALUE

creases with increase in Reynolds number, and it becomes almost negligible at Reynolds numbers above 8000. In this region the centrifugal and shearing forces caused by rotation are, together with the thermal buoyancy forces, responsible for the thermal convection flow; however, when the rotational speed becomes sufficiently large the free-convection transfer becomes negligible. At Reynolds numbers above 8000, the correlation of Nu versus Re can be represented by the empirical equation

$$Nu = 0.076\ Re^{0.70}$$

Fig. 6 also includes some of the experimental results of Anderson and Saunders (1). The present results are in remarkably good agreement with the results of Anderson and Saunders at Reynolds numbers below the critical value and also at Reynolds numbers above 6000, at which the free-convection effect is diminished. At Reynolds numbers between these two values, the present results are 10 to 25 per cent, depending on the value of Grashof number, above the results of Anderson and Saunders. The dashed line in Fig. 6 shows the values based on the theoretical equation given by Anderson and Saunders as

$$Nu = 0.10\ Re^{2/3}$$

This curve compares favorably with the empirical equation given in the present investigation.

Fig. 7 shows the correlation of Nu as a function of $(0.5\ Re^2 + Gr) \times Pr$ parameter which combines the effect of rotation and free convection. This parameter is found by assuming that the work done when the buoyant force acts on the horizontal cylinder, i.e., $\rho\beta\Delta tD$ is converted into kinetic energy, $\rho V^2/2g$, in producing a velocity V. From this assumption it results that Gr is analogous to $0.5\ Re^2$ and by plotting Nu as a function of $(0.5\ Re^2 + Gr) \times Pr$ for Reynolds numbers above the critical value the following empirical equation is yielded

$$Nu = 0.11[(0.5\ Re^2 + Gr) \times Pr]^{0.35}$$

This equation can be reduced to the previous empirical equation at higher values of Reynolds number where the term Gr can be neglected.

INTERFEROMETRIC STUDY OF FLOW

The stability of flow around the rotating cylinder and, more especially, the process involved in the transition from laminar Couette flow to fully developed secondary flow were investigated with the aid of a Zehnder-Mach interferometer. The interferometer used was of the kind described by Eckert, Drake, and Söhngen (6). The boundary layer investigated was built up around the heated rotating cylinder, which was placed in the object light path of the interferometer, and the flow was studied from interference photographs. The mirrors of the interferometer were made parallel to one another and the optical path lengths were made equal, so that the interference lines in the pictures represent the constant-density lines. In the case of laminar Couette flow, which is a two-dimensional flow, the interference lines are also the constant-temperature lines. A number of photographs are shown in Figs. 8 to 11, and the corresponding values of Reynolds and Grashof numbers are noted. These photographs present an instructive view of the transition process and clearly show the changes that occur in the type of flow around the heated rotating cylinder.

The interference photographs in Fig. 8 were taken at a constant Grashof number and at Reynolds numbers from 180 to 1140. The interference lines around the rotating cylinder for Reynolds numbers from 180 to 840 are similar to the interference lines of a cylin-

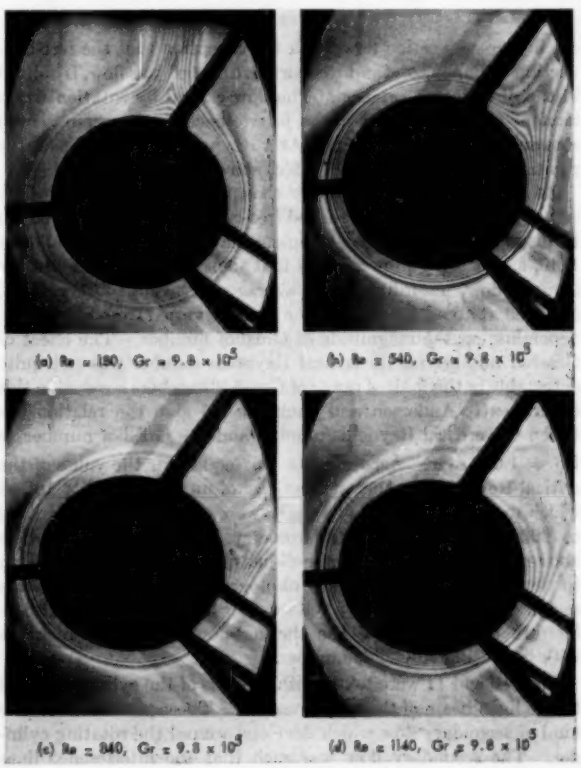

FIG. 8 INTERFERENCE PHOTOGRAPHS OF $2^1/_2$-IN. HORIZONTAL CYLINDER HEATED TO 65 DEG F ABOVE SURROUNDING AIR, WITH CLOCKWISE ROTATION

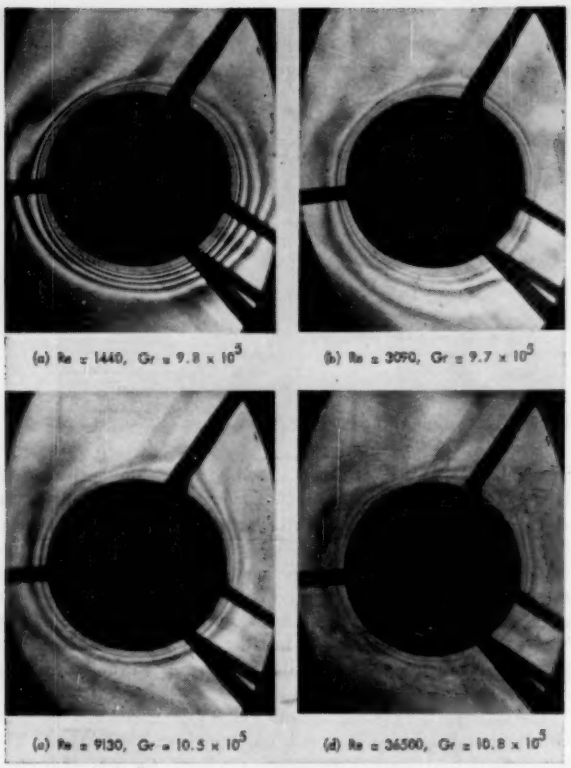

FIG. 9 INTERFERENCE PHOTOGRAPHS SHOWING VARIATION OF THERMAL-BOUNDARY-LAYER THICKNESS WITH ROTATIONAL SPEED

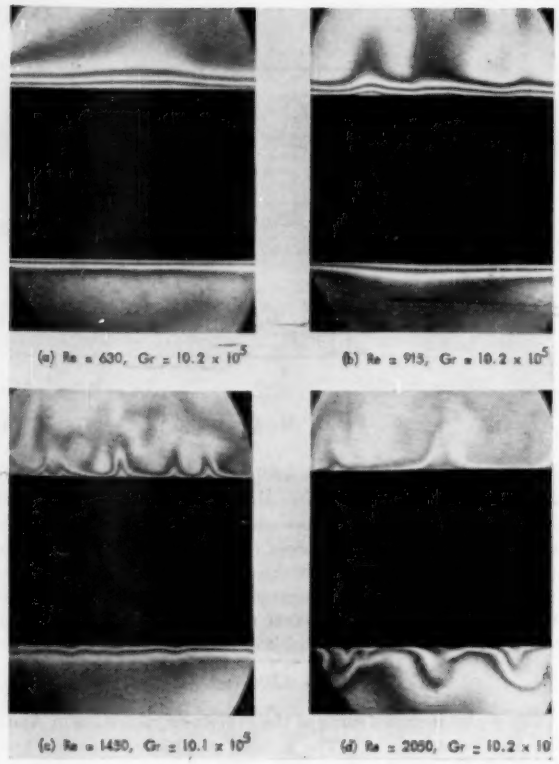

FIG. 10 INTERFERENCE PHOTOGRAPHS SHOWING DEVELOPMENT OF SECONDARY FLOW

der in free-convection flow, with the exception that the free-convection chimney, or the breakaway region of the flow, is shifted in the direction of rotation. The flow caused by rotation was a laminar Couette flow, and the interference lines were observed rotating around the cylinder. At a Reynolds number of 840, the position of breakaway, as Fig. 8(*c*) shows, was horizontal.

At Reynolds numbers greater than 840, the interference lines began to oscillate and the shifted free-convection chimney started to disappear; it vanished completely at a Reynolds number of 1140, as Fig. 8(*d*) shows. The first signs of unsteadiness in the laminar flow, according to an average of several observations, occurred at about Re = 900; the number varied from 880 to 915, depending on the magnitude of Grashof number. The effect of Grashof number on the critical Reynolds number was not quite detectable in the limited range of Grashof numbers covered in this experiment. Anderson and Saunders (1) give the relation between the critical Reynolds number and the Grashof number as $\mathrm{Re} = 1.09\sqrt{\mathrm{Gr}}$. According to this equation, the value of the critical Reynolds number at the Grashof number of 9.8×10^5, at which the interference photographs were taken, is 1080 compared to 900 determined by interferometry. At Reynolds numbers above the critical value, a three-dimensional secondary flow began to develop. The interference photographs of Fig. 9 show this region of flow up to a Reynolds number of 36,500. They also illustrate the decrease of the thermal-boundary-layer thickness with increasing Reynolds number.

Figs. 10 and 11 were taken with the axis of the cylinder normal to the light beam of the interferometer. These pictures show the kind of secondary flow which develops around the rotating cylinder. The secondary flow was such that the interference lines around the rotating cylinder were confined to a series of symmetrical compartments. The size of these compartments increased with increases in Reynolds number. Up to a Reynolds

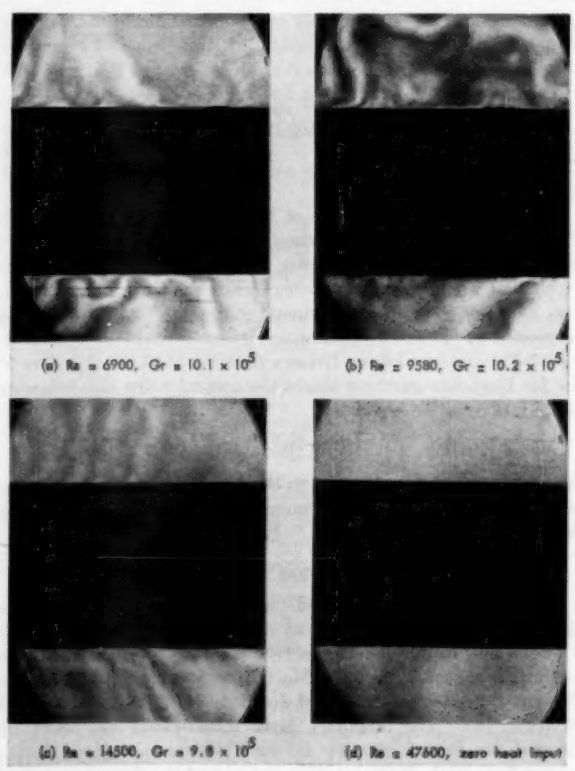

FIG. 11 INTERFERENCE PHOTOGRAPHS SHOWING BEGINNING OF TURBULENT FLOW

number of about 14,500 it was found that if Re and Gr were kept constant, the oscillations of the interference lines around the rotating cylinder were permanent and remained in perfectly steady motion. Increasing the Reynolds number beyond 14,500 caused the steady symmetrical oscillations of the interference lines to break down into some kind of unsteady irregular oscillations, and the flow became turbulent, as shown in Fig. 11 (*c*).

It should be noted that the transition from laminar Couette flow to secondary flow and also the transition from secondary flow to turbulent flow observed in this investigation occurred first along the top of the rotating cylinder and then spread downward as the Reynolds number was increased. Fig. 11 (*a*) was taken at zero heat input and at the highest Reynolds number at which pictures were obtainable, in order to discover any density field that might be due to pressure variation around the cylinder. There was no significant density field.

It is interesting to note that the secondary flow which develops around the rotating cylinder shows some resemblance to the secondary flow between two concentric cylinders when the inner cylinder is rotated, a flow observed by Taylor (13). It is also somewhat similar to the cellular motion between two horizontal plates heated from below, a motion observed by Schmidt and Saunders (11).

Acknowledgments

The author wishes to express his appreciation to Prof. Harold A. Johnson, who suggested the subject of this paper, for his valuable advice and his lasting interest throughout this investigation. Appreciation is also extended to Prof. Ralph A. Seban for his assistance and valuable suggestions during the investigation.

BIBLIOGRAPHY

1 "Convection From an Isolated Heated Horizontal Cylinder Rotating About Its Axis," by J. T. Anderson and O. A. Saunders, Proceedings of the Royal Society of London, England, vol. 217, series A, 1953, pp. 555–562.

2 "Properties and Uses of Thermistors—Thermally Sensitive Resistors," by J. A. Becker, C. B. Green, and G. L. Pearson, *Electrical Engineering*, vol. 65, 1946, pp. 711–725.

3 "Stability of a Viscous Compressible Flow Between Rotating Cylinders," by P. L. Chambre, PhD dissertation, University of California, 1951.

4 "The Flow Due to a Rotating Disc," by W. G. Cochran, Proceedings of the Cambridge Philosophical Society, vol. 30, 1934, pp. 365–375.

5 "Manufacture of a Zehnder-Mach Interferometer," by E. R. G. Eckert, R. M. Drake, and E. E. Söhngen, Technical Report No. 5721, Air Materiel Command, Wright-Patterson Air Force Base, Ohio, August, 1948.

6 "Studies in Heat Transfer on Laminar Free Convection With the Zehnder-Mach Interferometer," by E. R. G. Eckert and E. E. Söhngen, Technical Report No. 5747, Air Materiel Command, Wright-Patterson Air Force Base, Ohio, December, 1948.

7 "Heat Transfer," by M. Jakob, John Wiley & Sons, Inc., New York, N. Y., vol. 1, 1949, pp. 525–529.

8 "Das Temperatur und Geschwindigkeitsfeld um ein geheistes Rohr bei freier Konvektion," by K. Jodlbauer, *Forschung auf dem Gebiete des Ingenieurwesens*, vol. 4, July-August, 1933, pp. 157–172.

9 "Heat Transmission," by W. H. McAdams, McGraw-Hill Book Company, Inc., New York, N. Y., second edition, 1942, p. 243.

10 "Heat Transfer by Laminar Flow From a Rotating Plate," by K. Millsaps and K. Pohlhausen, *Journal of the Aeronautical Sciences*, vol. 18, 1951, pp. 354–355.

11 "On the Motion of a Fluid Heated From Below," by R. J. Schmidt and O. A. Saunders, Proceedings of the Royal Society of London, England, vol. 165, series A, 1938, pp. 216–228.

12 "Distribution of Velocity and Temperature Between Concentric Rotating Cylinders," by G. I. Taylor, Proceedings of the Royal Society of London, England, vol. 151, series A, 1935, pp. 494–512.

13 "Stability of a Viscous Liquid Contained Between Two Rotating Cylinders," by G. I. Taylor, Philosophical Transactions of the Royal Society of London, vol. 223, 1923, pp. 289–343.

14 "Turbulente Strömung Zwischen Zwei Rotierenden Konaxialen Zyl.," by F. Wendt, *Ingenieur Archiv*, 1933, p. 577.

Through-Flow in Concentric and Eccentric Annuli of Fine Clearance With and Without Relative Motion of the Boundaries

By L. N. TAO[1] and W. F. DONOVAN[2]

The problem of the through-flow across annuli of fine clearance has been investigated both theoretically and experimentally. The study includes the effects due to the relative motion of the walls and to varying degrees of eccentricity of the bounding surface. The experimental work was carried up to a Reynolds number, based on the diametral clearance, of 30,000. The theoretical results are presented both graphically and in the form of equations. Nomographs are included for rapid solution of certain engineering problems.

Nomenclature

The following nomenclature is used in the paper:

c	= radial clearance, in.	L
d	= diametral clearance, in.	L
e	= eccentricity, in.	L
f	= friction factor defined in Equation [7], dimensionless	1
g	= gravitational constant = 386 in/sec^2	LT^{-2}
l	= length of passage, in.	L
n	= coefficient or exponent	1
r	= mean radius of annulus, in.	L
r_1	= inner radius of annulus, in.	L
r_2	= outer radius of annulus, in.	L
v	= mean velocity, ips	LT^{-1}
w	= local velocity, ips	LT^{-1}
A	= cross-sectional area, sq in.	L^2
C	= constant	1
D	= mean diameter of annulus, in.	L
D_1	= inner diameter of annulus, in.	L
D_2	= outer diameter of annulus, in.	L
P	= pressure, psi	FL^{-2}
ΔP	= pressure difference, psi	FL^{-2}
Q	= through-flow, cu in/sec	L^3T^{-1}
S	= wetted surface of annulus, sq in.	L^2
Re	= Reynolds number $\frac{dv\rho}{\mu}$ or $\frac{dv'\rho}{\mu}$, dimensionless	1
α	= angle between absolute and axial velocities	1
ρ	= mass density of the fluid $\frac{\gamma}{g}$, slugs/cu in.	$FL^{-4}T^2$
γ	= density of the fluid, pci	FL^{-3}
η	= eccentricity ratio	1
μ	= dynamic or absolute viscosity, lb-sec/in.^{2}	$FL^{-2}T$
ν	= kinematic viscosity, in^2/sec	L^2T^{-1}
ξ	= ratio of flows or axial velocities between eccentric and concentric cases	1
ω	= angular velocity of the boundary wall, radians/sec (rad/sec)	T^{-1}

Superscript prime refers to rotational case

Subscript e refers to eccentric case

Introduction

An important problem associated with the design and application of certain types of journal bearings and pressure-reducing bushings as employed in turbomachinery in the form of wearing rings, labyrinth seals, balancing drums, and pressure-breakdown devices, involves the determination of the fluid flow through annuli of fine clearance, i.e., one or more spaces bounded axially by two cylindrical bodies of slightly different diameters nesting with varying degrees of eccentricity. A search of the published information reveals that many factors have an effect on the magnitude of the flow through these passages, the most significant ones being clearance, length, rotation, eccentricity, surface condition, and fluid properties.

Some restricted cases of flow through an annulus have been treated both theoretically and experimentally by several investigators. Based on the fundamental concepts of Newtonian viscous shear the expression for flow through an annulus bounded by two concentric cylinders has been derived and was given by Becker (1)[3] and Lamb (2). But these early analyses were concerned with laminar flow of stationary and concentric annuli. Cornish (3) reported his results for flow with relative motion of the walls. Taylor (4) undertook an analysis and conducted experimental studies of the effects of rotation without through-flow. Schneckenberg (5) analyzed the problem of flow through a stationary annulus with fine clearance for concentric and for fully eccentric cylinders. And Davis (6) compiled the available information on the pressure drop through a stationary and concentric annulus by various investigators and suggested an empirically determined configuration factor to modify the "friction-factor" equation

$$f = \frac{d}{l}\,\frac{\Delta P}{\rho}\,\frac{2}{v^2}$$

Nootbaar and Kintner (7) explored the range up to a Reynolds number of 10,000 for the flow through stationary and concentric annuli with fine clearances, and presented their results by equations of the form

$$f = C/\mathrm{Re}^n$$

with rationalized coefficients and constants. Their work was carried out on small-diameter rods and tubing. In the field of centrifugal pumps Stepanoff (8) has performed and reported numerous experiments on the flow through wearing rings. In the

[1] Assistant Professor, Department of Mechanics, Illinois Institute of Technology, Chicago, Ill.; formerly Engineer, Research and Development Department, Worthington Corporation, Harrison, N. J. Assoc. Mem. ASME.

[2] Group Engineer, Research and Development Department, Worthington Corporation, Harrison, N. J. Assoc. Mem. ASME.

Contributed by the Hydraulic Division and presented at the Annual Meeting, New York, N. Y., November 28–December 3, 1954, of The American Society of Mechanical Engineers.

Note: Statements and opinions advanced in papers are to be understood as individual expressions of their authors and not those of the Society. Manuscript received at ASME Headquarters, September 21, 1954. Paper No. 54—A-175.

[3] Numbers in parentheses refer to the Bibliography at the end of the paper.

theory of lubrication a relation has been developed (12) for the flow of oil through a journal bearing which is essentially the expression for the laminar flow of a fluid through an eccentric annulus.

In this investigation the problem has been attacked both theoretically and experimentally. The principal interest has been in the turbulent region, with consideration given to the relative motion of the boundaries and the full range of eccentricity ratio. The theoretical and experimental investigations reported at this time are limited to annuli of smooth surfaces and of fine clearance handling a single-phase fluid.

Analyses

For the mathematical treatment the fluid is assumed to be incompressible and the process isothermal and steady. This implies constant density and viscosity of the fluid.

Stationary and Concentric. First, consider a steady flow of fluid through a concentric annulus with no motion of the boundaries. The equation for the flow in the laminar range has been derived (1, 2), Fig. 1

$$w = -\frac{\Delta P}{4\mu l} r^2 + A \log r + B \quad \ldots\ldots [1]$$

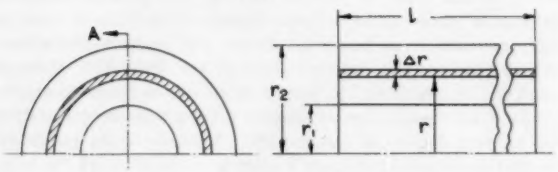

Fig. 1

In order to determine the integration constants A and B, the boundary conditions $w = 0$ at $r = r_1$ and $r = r_2$ are substituted in the equation

$$w = \frac{\Delta P}{4\mu l}\left(r_1^2 - r^2 + \frac{r_2^2 - r_1^2}{\log \frac{r_2}{r_1}} \log \frac{r}{r_1}\right) \quad \ldots\ldots [2]$$

The flux or through-flow is

$$\int_{r_1}^{r_2} 2\pi r w \, dr = \frac{\pi \Delta P}{8\mu l}\left[r_2^4 - r_1^4 - \frac{(r_2^2 - r_1^2)^2}{\log \frac{r_2}{r_1}}\right] \quad \ldots\ldots [3]$$

If a mean velocity v is used, the flux or through-flow will be

$$\int_{r_1}^{r_2} 2\pi r v \, dr = \pi v (r_2^2 - r_1^2) \quad \ldots\ldots [4]$$

Therefore

$$\pi v (r_2^2 - r_1^2) = \frac{\pi \Delta P}{8\mu l}\left[r_2^4 - r_1^4 - \frac{(r_2^2 - r_1^2)^2}{\log \frac{r_2}{r_1}}\right] \quad \ldots\ldots [5]$$

$$v = \frac{\Delta P}{8\mu l}\left[r_2^2 + r_1^2 - \frac{r_2^2 - r_1^2}{\log \frac{r_2}{r_1}}\right] \quad \ldots\ldots [6]$$

Now introduce the dimensionless quantities, Reynolds number Re and friction factor f. The Reynolds number is by definition the ratio of the product of a velocity and a linear dimension to the kinematic viscosity. Since in this investigation the entire passage is considered, the mean velocity v through the passage as calculated from the measurement of flow is used as the velocity, and the diametral clearance d is used as the linear dimension. The friction factor is defined as[4]

$$f = \frac{4A}{S} \frac{\Delta P}{\rho} \frac{2}{v^2} \quad \ldots\ldots [7]$$

In an annulus

$$A = \frac{\pi}{4}(D_1 + D_2)d$$

and

$$S = \pi(D_1 + D_2)l$$

which gives

$$f = \frac{d}{l} \frac{\Delta P}{\rho} \frac{2}{v^2} \quad \ldots\ldots [8]$$

By substituting ΔP of this equation into Equation [5] and solving for f

$$f = \frac{64\mu}{\rho d v} g\left(\frac{r_1}{r_2}\right) = \frac{64}{\mathrm{Re}} g\left(\frac{r_1}{r_2}\right) \quad \ldots\ldots [9]$$

where

$$g\left(\frac{r_1}{r_2}\right) = \frac{\left(1 - \frac{r_1}{r_2}\right)^2}{1 + \left(\frac{r_1}{r_2}\right)^2 + \frac{\left(1 - \frac{r_1}{r_2}\right)^2}{\log \frac{r_1}{r_2}}}$$

This equation also applies to circular pipes, where $r_1/r_2 = 0$ and parallel flat plates, where $r_1/r_2 = 1$. It shows

$$\lim g\left(\frac{r_1}{r_2}\right) = 1 \quad \text{when} \quad \frac{r_1}{r_2} = 0 \text{ (circular pipe)}$$

$$\lim g\left(\frac{r_1}{r_2}\right) = 1.5 \quad \frac{r_1}{r_2} = 1 \text{ (parallel flat plates)}$$

$$g\left(\frac{r_1}{r_2}\right) = 1.0 \text{ to } 1.5 \quad 0 < \frac{r_1}{r_2} < 1 \text{ (annulus)}$$

So the equation for laminar flow, Equation [9], is reduced to

$$f = 64/\mathrm{Re} \quad \text{for a circular pipe} \quad \ldots\ldots [10a]$$

and

$$f = 96/\mathrm{Re} \quad \text{for parallel flat plates} \quad \ldots\ldots [10b]$$

In the annular-flow channel here considered the diametral clearance is small in comparison with the diameter of the annulus or the shaft. Hence r_1/r_2 is in the range of 0.99 to unity and $g(r_1/r_2)$ is essentially 1.5 in value. Taking $g(r_1/r_2)$ equal to 1.5, Equation [9] is reduced to

$$f = \frac{96}{\mathrm{Re}} \quad \ldots\ldots [10c]$$

for the annulus of fine clearance with laminar flow. Note that this equation is the same as Equation [10b] and implies that the flow through a stationary annulus can be treated as flow between flat plates.

[4] Some writers divide the left-hand side by 4 or 2 which changes the numerical value of the friction factor.

For turbulent flow through a circular pipe the friction-factor equation, the Blasius law of turbulence, may be written as

$$f = \frac{C}{\mathrm{Re}^n} \quad [10d]$$

Since the fluid-dynamic characteristics are conformal on both the circular pipe and the annular flow channel it follows that the friction-factor equation for the annular flow channel would take the same form. The constant C and the exponent n would be determined from experiments.

Rotational and Concentric. The preceding analysis was limited to steady flow through a concentric annulus having stationary boundaries. If one boundary of the passage, say, the inner wall, is rotating at an angular speed ω, then the peripheral velocity of the flow is no longer zero and the analysis must be revised to include this additional parameter.

As mentioned previously, the problem of an annulus with small clearance may be considered as two flat plates separated by a distance equal to the radial clearance. According to Pai (9), who applied the mathematical statistical principles and perturbation method to the fluid flow between two parallel flat plates with one plate moving at velocity U, the velocity distributions for the laminar and turbulent regions are of the forms shown in Fig. 2.

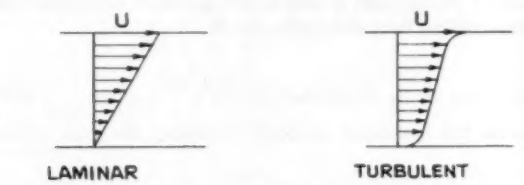

FIG. 2

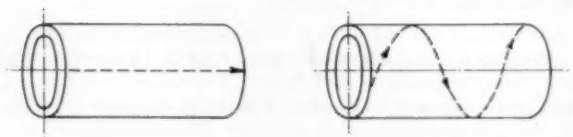

FIG. 3

From this analysis it may be deduced that the mean velocity for both laminar and turbulent flow in these cases may be taken as $U/2$. Thus the mean peripheral component of the fluid velocity in an annulus will be assumed to be $\omega r/2$ and the mean absolute fluid velocity v' will be the vector sum of $\omega r/2$ and v, the through-flow component. If the annular passage is then unwrapped it will form two parallel flat plates, as in Fig. 4, and the flow problem will be two-dimensional.

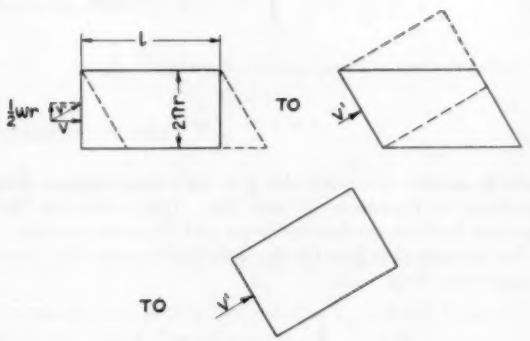

FIG. 4

By this transformation the flow through the annulus with the inner wall rotating can be treated as a higher flow velocity through an annulus with stationary walls of greater length.

Let the annulus through-flow before and after transformation be the same. Then

$$f' = \frac{4A'}{S'}\frac{\Delta P'}{\rho}\frac{2}{v'^2} \quad [11]$$

$$A' = \pi(D_1 + D_2)l\frac{\sec\alpha}{4} = A\sec\alpha$$

and

$$S' = \pi(D_1 + D_2)l = S$$

$$v' = v\sec\alpha \quad [12]$$

Therefore

$$f' = \frac{4A}{S}\frac{2\Delta P'}{v^2\rho}\frac{1}{\sec\alpha}$$

$$= f\left(\frac{\Delta P'}{\Delta P}\right)\cos\alpha \quad [13]$$

or

$$\frac{\Delta P'}{\Delta P} = \frac{f'}{f}\sec\alpha \quad [14]$$

$$f = \frac{C}{\mathrm{Re}^n} \text{ and } f' = \frac{C}{(\mathrm{Re}')^n} \quad [15]$$

or

$$\frac{f'}{f} = \left(\frac{\mathrm{Re}}{\mathrm{Re}'}\right)^n \quad [16]$$

where C is an arbitrary constant and n a constant exponent. So, by substituting Equations [16] and [12] into Equation [14]

$$\frac{\Delta P'}{\Delta P} = \left(\frac{\mathrm{Re}}{\mathrm{Re}'}\right)^n\sec\alpha = (\sec\alpha)^{1-n} \quad [17]$$

Eccentric. If a concentric annulus is unwrapped into a plane and the X-Y-Z axes taken as shown in Fig. 5, by equating the viscous and pressure forces of laminar flow

$$\mu\frac{\partial^2 w}{\partial y^2} = \frac{\partial P}{\partial x} \quad [18]$$

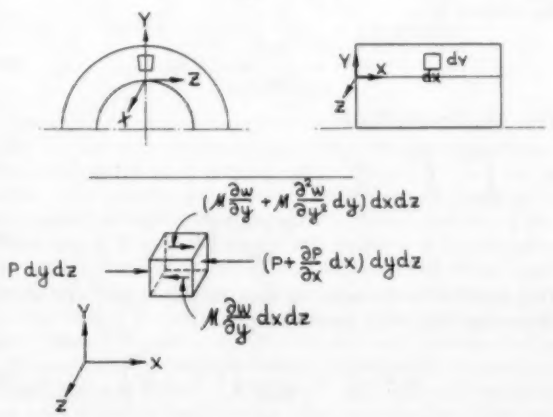

FIG. 5

Integrating with respect to y

$$w = \frac{1}{2\mu}\frac{\partial P}{\partial x}y^2 + C_1 y + C_2 \quad [19]$$

Since $\partial P/\partial x$ across the whole sleeve is $-\Delta P/l$, and the annulus is concentric and stationary, $w = 0$ at the boundaries $y = 0$ and $y = c$, respectively. Substituting these boundary conditions into Equation [19]

$$w = -\frac{1}{2\mu}\frac{\Delta P}{l}y(y - c) \quad [20a]$$

Then the through-flow is

$$Q = \int_A w dA = \int_0^{2\pi r}\int_0^c -\frac{1}{2\mu}\frac{\Delta P}{l}y(y - c)dydz = \frac{\pi r c^3 \Delta P}{6\mu l} \quad [21]$$

and the mean axial velocity is

$$v = \frac{Q}{A} = \frac{c^2\Delta P}{12\mu l} \quad [22]$$

$$f = \frac{2c}{l}\frac{\Delta P}{\rho}\frac{2}{v^2} = \frac{8c^2\Delta P}{\mu l(\mathrm{Re})v} \quad [23]$$

Substituting v of Equation [22] into Equation [23]

$$f = \frac{8c^2\Delta P}{\mu l(\mathrm{Re})}\frac{12\mu l}{c^2\Delta P} = \frac{96}{\mathrm{Re}} \quad [24]$$

This is the same result as given in Equation [10c].

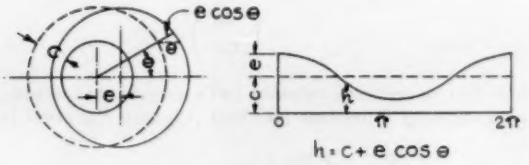

FIG. 6

If the annulus is eccentric, the unwrapped space is as in Fig. 6, the boundaries are $y = 0$ and $y = h$. Here h is not a constant but is equal to

$$h = c + e\cos\theta = c(1 + \eta\cos\theta) \quad [25]$$

with $\eta = e/c$ = eccentricity/clearance. Here the equation for the velocity is

$$w = -\frac{\Delta P}{2\mu l}y(y - h) \quad [20b]$$

Then the through-flow is

$$Q_e = \int_0^{2\pi r}\int_0^h -\frac{\Delta P}{2\mu l}y[y - c(1 + \eta\cos\theta)]dydz = \frac{\pi r c^3\Delta P}{6\mu l}\left(1 + \frac{3}{2}\eta^2\right) \quad [26]$$

This equation is the same as that developed in the theory of lubrication (12). The mean velocity is

$$v_e = \frac{Q_e}{A} = \frac{c^2\Delta P}{12\mu l}\left(1 + \frac{3}{2}\eta^2\right) \quad [27]$$

The ratio of flow between the two cases is found to be

$$\xi = \frac{Q_e}{Q} = \frac{v_e}{v} = 1 + \frac{3}{2}\eta^2 \quad [28]$$

When the flow is in the turbulent range, the previous analyses no longer hold. As in the previous section the turbulent flow can be governed by an equation of the form similar to that for laminar flow

$$f = \frac{C}{\mathrm{Re}^n} \quad [29]$$

By substituting the definition terms of f and Re into the equation and transposing the terms

$$v^{2-n} = \frac{2^{2+n}\Delta P c^{1+n}}{Cl\rho^{1-n}\mu^n} = K'c^{1+n} \quad [30a]$$

or

$$v = Kc^{\frac{1+n}{2-n}}$$

with

$$K = K'^{\frac{1}{2-n}} = \left(\frac{2^{2+n}\Delta P}{Cl\rho^{1-n}\mu^n}\right)^{\frac{1}{2-n}} \quad [30b]$$

In order to find the ratio of flow between eccentric and concentric cases, all parameters except the eccentricity are maintained constant. Hence both K and K' are arbitrary constants; and the through-flow for a concentric case is

$$Q = Av = 2\pi r K c^{\frac{3}{2-n}} \quad [31a]$$

When the flow is through an eccentric annulus, the axial velocity is

$$v_e = Kh^{\frac{1+n}{2-n}} \quad [30c]$$

So the through-flow for this case is

$$Q_e = \int_A Kh^{\frac{1+n}{2-n}}dA \quad [32a]$$

and $dA = h\,r\,d\theta$ where $h = c(1 + \eta\cos\theta)$

Thus

$$Q_e = Krr^{\frac{3}{2-n}}\int_0^{2\pi}(1 + \eta\cos\theta)^{\frac{3}{2-n}}d\theta \quad [32b]$$

This equation also can be used to check the derivations for laminar flow in which the exponent n is unity

$$Q = 2\pi r K' c^3 = \frac{\pi r c^3\Delta P}{6\mu l} \quad [31b]$$

and

$$\xi = \frac{Q_e}{Q} = \frac{1}{\pi}\int_0^\pi (1 + \eta\cos\theta)^3 d\theta \quad [33]$$

By using the binomial expansion and integrating

$$\xi = 1 + \frac{3}{2}\eta^2 \quad [34]$$

Both Equations [31b] and [34] give the same results as derived previously by Equations [21] and [28]. This verifies the relating equation between the friction factor and Reynolds number.

For the turbulent flow the exponent in Equation [33] is not an integer but is $3/(2 - n)$

$$\xi = \frac{1}{\pi}\int_0^\pi (1 + \eta\cos\theta)^{\frac{3}{2-n}}d\theta \quad [35]$$

Introducing

$$\zeta^2 = \frac{1}{1-\eta^2} \quad \text{or} \quad \eta^2 = \frac{\zeta^2 - 1}{\zeta^2}$$

and

$$t = \frac{3}{2-n}$$

Equation [35] becomes

$$\xi = \frac{1}{\pi}\,\zeta^{-t}\int_0^{\pi}(\zeta + \sqrt{\zeta^2-1}\cos\theta)^t\,d\theta = \zeta^{-t}\,\mathbf{P}_t(\zeta) \ldots [36]$$

The expression

$$\mathbf{P}_t(\zeta) = \frac{1}{\pi}\int_0^{\pi}(\zeta + \sqrt{\zeta^2-1}\cos\theta)^t\,d\theta \ldots [37]$$

is known as the Laplacian form of Legendre function of degree t (10), and the solution can be expressed as an infinite series (if t is not an integer), which is known as the hypergeometric series denoted as $F(a, b; c; z)$

$$\frac{1}{\pi}\int_0^{\pi}(1+\eta\cos\theta)^t\,d\theta = F\left(-\frac{t}{2}, \frac{1-t}{2}; 1; \eta^2\right) = \sum_{m=0}^{\infty}\binom{t}{2m}\binom{2m}{m}\left(\frac{\eta}{2}\right)^{2m} \ldots [38]$$

where $\binom{t}{2m}$ and $\binom{2m}{m}$ are the coefficients of the binomial expansion

$$(a+b)^t = \sum_{m=0}^{\infty}\binom{t}{m}a^m b^{t-m}$$

The flow ratio based on this series is plotted in Fig. 11 as curve B.

Schneckenberg's work on eccentricity (5) is based on an assumption that friction factor is independent of the eccentricity. By employing the graphical integration for a fully eccentric case ($e = c$), he obtained $\xi = 1.21$. However, by working from the derived equations an expression is possible for the complete range of eccentricity with Schneckenberg's assumption. Thus

$$f = \frac{4c}{l}\frac{\Delta P}{\rho}\frac{1}{v^2} \text{ or } v = \sqrt{\frac{4c\Delta P}{\rho l f}} \ldots [39]$$

Similarly

$$v_e = \sqrt{\frac{4\Delta P h}{\rho l f}} = \sqrt{\frac{4\Delta P c(1+\eta\cos\theta)}{\rho l f}}$$

So the ratio of flow is

$$\xi = \frac{\int_A v_e\,dA}{Av} = \frac{1}{\pi}\int_0^{\pi}(1+\eta\cos\theta)^{3/2}\,d\theta$$

By recurrence formula

$$\xi = \frac{2}{3\pi}\left[\eta\sin\theta(1+\eta\cos\theta)^{1/2}\Big|_0^{\pi} + 2\int_0^{\pi}(1+\eta\cos\theta)^{1/2}\,d\theta - \frac{1}{2}(1-\eta^2)\int_0^{\pi}\frac{d\theta}{(1+\eta\cos\theta)^{1/2}}\right] \ldots [40]$$

The substitution of $\theta = 2\alpha$, $\cos\theta = 1 - 2\sin^2\alpha$ and $k^2 = 2\eta/(1+\eta)$ gives

$$\int_0^{\phi}(1+\eta\cos\theta)^{1/2}\,d\theta = 2(1+\eta)^{1/2}\int_0^{\phi/2}(1-k^2\sin^2\alpha)^{1/2}\,d\alpha = 2(1+\eta)^{1/2}E\left(k, \frac{\phi}{2}\right)$$

$$\int_0^{\phi}\frac{d\theta}{(1+\eta\cos\theta)^{1/2}} = \frac{2}{(1+\eta)^{1/2}}\int_0^{\phi/2}\frac{d\alpha}{(1-k^2\sin^2\alpha)^{1/2}} = \frac{2}{(1+\eta)^{1/2}}F\left(k, \frac{\phi}{2}\right)$$

Therefore

$$\xi = \frac{2}{3\pi}\left[4(1+\eta)^{1/2}\mathbf{E} - \frac{1-\eta^2}{(1+\eta)^{1/2}}\mathbf{K}\right] \ldots [41]$$

where $\mathbf{K} = F(k, \pi/2)$ and $\mathbf{E} = E(k, \pi/2)$ are the complete elliptical functions of first and second kinds, respectively. Their numerical values are tabulated in reference (11). For the fully eccentric case, $\eta = 1$, and $k = 1$, then $(1-\eta^2)/(1+\eta)^{1/2} = 0$ and $\mathbf{K}$ approaches ∞, so the value of ξ is undetermined. Fortunately this function changes to a circular function

$$\xi = \frac{1}{\pi}\int_0^{\pi}(1+\cos\theta)^{3/2}\,d\theta \ldots [42]$$

By multiplying both numerator and denominator of Equation [42] by $(1-\cos\theta)^{1/2}$

$$\xi = \frac{1}{\pi}\left[\int_0^{\pi}\frac{\sin\theta\,d\theta}{(1-\cos\theta)^{1/2}} + \int_0^{\pi}\frac{\sin\theta\cos\theta\,d\theta}{(1-\cos\theta)^{1/2}}\right] = \frac{2}{\pi}\left[(1-\cos\theta)^{1/2} + \cos\theta(1-\cos\theta)^{1/2} + \frac{2}{3}(1-\cos\theta)^{3/2}\right]_0^{\pi} = \frac{8\sqrt{2}}{3\pi} \ldots [43]$$

This is the result for a fully eccentric case as obtained by Schneckenberg (5). For purposes of comparison, the flow ratio for the complete range of eccentricity based on his assumption is also plotted in Fig. 11 as curve C.

Considering relative motion of walls, it was stated previously that the problem with rotation can be treated as stationary by making an adjustment of velocity and flow configuration. Hence the flow ratio for two cases with the same speed or rotation has the same functional relationship as a stationary one, namely

$$\left.\begin{aligned}\frac{Q_e'}{Q'} &= 1 + \frac{3}{2}\eta^2 \quad \text{(laminar)}\\ &= F\left(-\frac{t}{2}, \frac{1-t}{2}; 1; \eta^2\right) \text{(turbulent)}\end{aligned}\right\} \ldots [44]$$

Experiments

The apparatus employed for these tests is shown schematically in Fig. 7. This was a recirculating system with temperature regulation maintained by admitting cold water to the flow as required. The pressure source was a vertical-triplex pump of 90-gpm capacity operating from a suction tank and discharging into a surge tank. A surge suppressor was installed at the discharge elbow of the pump to absorb some of the surge before the water passed to the large surge tank. The main stream fluid went from the surge tank to the tester where it passed through a strainer and thence through the test unit. The test unit itself is shown in Fig. 8. It consisted of a rotating assembly in a housing of adequate strength and was driven at 3580 rpm. The shaft was overhung from a set of double ball bearings. The bearings were lubricated by an oil bath.

High-pressure water entered the test unit and was distributed around the rotating shaft by an annular recess. The clearance between the rotating shaft sleeve and the stationary sleeve formed the annular flow channel. This clearance could be changed by installing different diameter shaft sleeves. The length of the flow channel was adjusted by shifting the stationary sleeve axially.

Calibrated Bourdon-type pressure gages were used to measure the pressure, and mercury manometers were used in conjunction with the venturi meters to measure the flow. The high-pressure tap was located radially from the annular inlet recess and the discharge pressure tap was on the discharge pipe section of the test unit.

The range of the principal experimental variables was as follows:

Fluid	water at 70 F
Through-flow	0 to 80 gpm
Reynolds number	800 to 30,000
Radial clearance	0.003 to 0.015 in. in 0.003-in. increments
Sleeve diameter	3.00 in. nominal
Sleeve length	2 to 4 in. in 1/2-in. increments
Eccentricity ratio	0 to 1
Surface finish	140±10 microinches
Pressure difference	0 to 800 psi
Shaft speed	0 to 3580 rpm

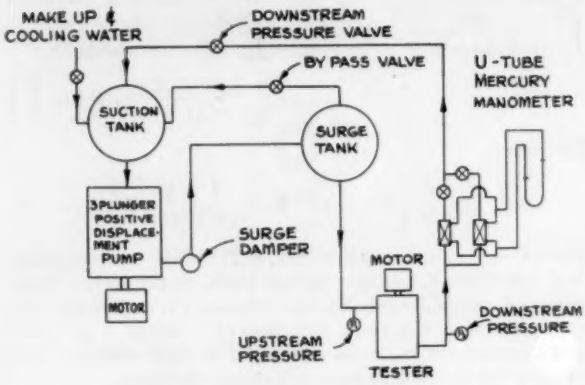

Fig. 7 Schematic Diagram of Test Setup

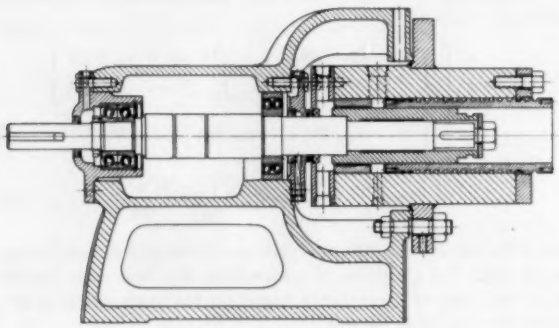

Fig. 8 Test Unit

Results and Discussion

From the test data of the stationary, concentric, and smooth-sleeve runs, the values of f and Re are calculated and plotted in log-log scale, Fig. 9. The curve may be considered to be composed of two straight lines with a slope change in the region of Re = 1500 to 2500. This region is generally known as the transition region in pipe work with laminar flow below and turbulent flow above this Reynolds number range. From the diagram it is seen that the laminar flow can be represented by an equation of the form

$$f = \frac{C}{\mathrm{Re}^n}$$

with $C = 170$ and $n = 1.03$.

Turbulent flow within the range considered also can be represented by

$$f = \frac{C}{\mathrm{Re}^n}$$

with $C = 0.316$ and $n = 0.21$.

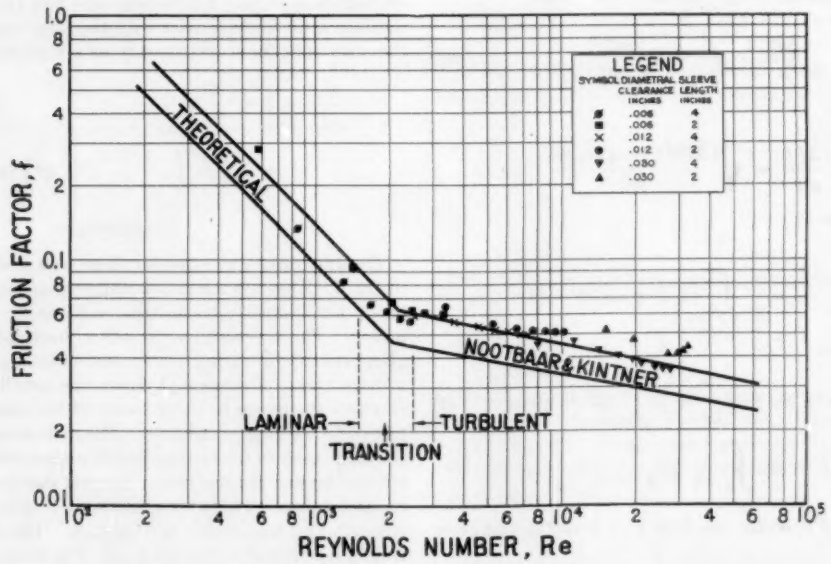

Fig. 9 Friction Factor Versus Reynolds Number (Without Rotation)

For laminar flow n is very close to 1, which is the exponential coefficient of the theoretical analysis. This value of n checks well with all other investigations (1, 5, 7). For turbulent flow, n is approximately 0.21, and is in agreement with Schneckenberg, Nootbaar-Kintner, and Davis. The over-all friction factor is different than that of Nootbaar-Kintner or Schneckenberg. This is believed due to the inclusion in the present investigation of entrance and exit losses while the Nootbaar-Kintner and the Schneckenberg data did not.

For relative motion of the walls (inner wall rotated), the values of f' and Re′ are calculated and plotted in Fig. 10. The relation between f' and Re′ based on the fictitious transformation should have the same relationship as the stationary wall case. In Fig. 10 the solid line was transferred from Fig. 9. The values of f' fall on this line and indicate that the theoretical assumption and analysis are in conformance with the experiments.

It has been shown that

$$\frac{\Delta P'}{\Delta P} = \left(\frac{f}{f'}\right) \sec \alpha = (\sec \alpha)^{1-n}$$

for two cases of the same through-flow or, in other words, the same axial or through-flow velocity. And we have obtained $n = 1$ for laminar flow and 0.21 for turbulent flow

$$\frac{\Delta P'}{\Delta P} = 1 \qquad \text{(laminar)}$$

$$= (\sec \alpha)^{0.79} \qquad \text{(turbulent)}$$

This result is in good agreement with other investigations. Here $\Delta P' = \Delta P$ for laminar flow and $\Delta P' = \Delta P\ (\sec \alpha)^{0.79}$ for turbulent flow. Cornish (3) stated that up to a certain critical speed or rotation the resistance to flow is unaffected, but above this speed the resistance increases as the speed increases. The foregoing equations show an excellent agreement with this observation. The rotation does not affect the pressure drop in the laminar region ($\Delta P' = \Delta P$); while in the turbulent region it increases with the factor $(\sec \alpha)^{0.79}$. The larger the rotational speed, the larger is the secant value and the $\Delta P'/\Delta P$ ratio.

Figs. 9 and 10 also indicate that the experimental data for both the low and high through-flows of individual runs deviate from the average line. For the low-velocity points, an erratic measurement of 0.1 or 0.2 gpm, which may only represent an error of flow measurement of about 5 per cent, will result in a 20–30 per cent deviation of the results. This is due to the fact that the Reynolds number is directly proportional and the friction factor is inversely proportional to the square of the flow velocity. Both deviations are in the same direction and consequently a larger deviation in f should be observed. For the high-velocity points, since higher entrance and exit losses should be expected, a higher pressure drop should be required.

In the eccentric case the flow ratio between eccentric and concentric cases at otherwise identical conditions as calculated from the test data are plotted versus the eccentricity ratio, Fig. 11.

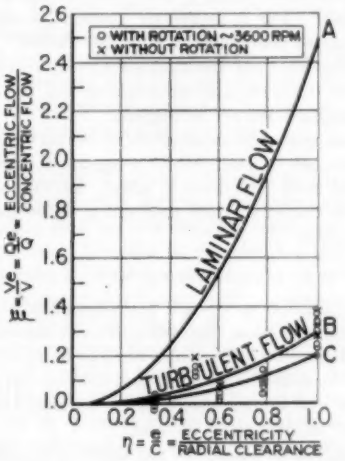

A: $\xi = 1 + 1.5\eta^2$

B: $\xi = F\left(-\frac{1}{2}, \frac{1-1}{2}; 1; \eta^2\right)$

C: $\xi = \frac{2}{3\pi}\left[4\sqrt{1+\eta}\,\mathbf{E} - \frac{1-\eta^2}{\sqrt{1+\eta}}\,\mathbf{K}\right]$

Fig. 11 Flow Ratio Versus Eccentricity Ratio

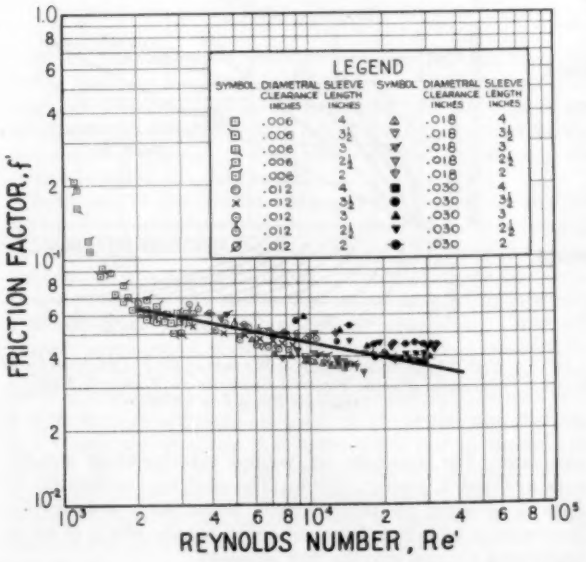

Fig. 10 Friction Factor Versus Reynolds Number (With Rotation)

In the laminar-flow range no data are available; however, the theoretical analyses are well established in the theory of lubrication. Also, the equations in the analyses of turbulent flow can be verified for the laminar range by changing the numerical coefficients and constants as derived in the analyses. Hence, once the solution for turbulent flow is established, the solution for laminar flow is also available. In the turbulent-flow regime the experimental results show considerable scatter. This is believed to result from small uncontrolled variations in the radial clearances and eccentricities. However, the results demonstrate a general trend which is in agreement with the theoretical analyses.

Also, the assumption made by Schneckenberg that the friction factor is independent of the eccentricity, Equation [39], cannot be generally accepted. Actually, the result based on his assumption is a special case of the present investigation. At the higher Reynolds number the friction factor will probably approach a constant, independent of the Reynolds number as indicated by pipe-flow practice; hence the exponent n in Equation [29] or Equation [35] approaches zero; then the exponent t in Equation [36] will be 1.5. With $t = 1.5$ the result of the hypergeometric series, Equation [38], can be verified as the expression of complete elliptical functions given by Equation [41].

The defining equation as employed for these data makes no

specific or separate allowances for area change losses at the entrance and exit from the flow channel. This is significant but necessary since the primary object of this investigation was the determination of the fluid flow across an annular-flow channel due to the total pressure difference available. By comparison with other investigators (5, 7) the present data show a larger C and a smaller n in Equation [10d], i.e., a flatter slope and a higher value of f, Fig. 10. This is expected since the pressure drop at the entrance and exit is included.

One limitation of this work is that the results of this investigation apply only to smooth-walled annuli. In a typical experiment a commercial surface finish of 140 ± 10 microinches was measured. For flow along rough or serrated sleeves, the results of the present investigation must be modified.

One other limitation of the present data is that a single-phase fluid is assumed. For a two-phase system (water flashing to steam), revisions to the equations must be effected.

For a compressible fluid, the analysis is theoretically consistent. Becker (1) and Davis (6) also have stated that the compressible and incompressible flows are analogous.

If the process cannot be assumed to be isothermal, the friction-factor equation can be modified to recognize the thermal effect. The additional term will directly affect the viscosity as μ_a/μ_w where μ_w is the viscosity at the wall and μ_a is the mean viscosity across the channel.

Applications

For the application to design, the theoretical equations and diagrams of dimensionless quantities are not convenient. They require the calculations of Reynolds number Re and friction factor f. Also, to determine the through-flow velocity for a given pressure difference and known size, either a tedious calculation or a "cut-and-trial" method must be used.

The information as based on the derived equation has been projected onto special charts for concentric and smooth sleeves with water at 68 F, Fig. 12 (turbulent) and Fig. 13 (laminar). These diagrams have pressure difference ΔP, radial clearance c, sleeve length l, shaft radius r, and shaft speed N as parameters. The axial velocity can be read directly from the chart, and hence, when multiplied by the cross-sectional area of the annulus, the flow is determined. If the annulus is eccentric, the flow is found from the product of the flow through the concentric annulus and the flow ratio from Fig. 11. To clarify the use of the chart, consider a smooth surface sleeve having a shaft radius of 1.75 in., length 3.5 in., and radial clearance 0.006 in. It is desired to determine the through-flow for a pressure drop of 500 psi, when the shaft is rotating at 3600 rpm and the eccentricity is 0.003 in. Starting from l = 3.5 in., a horizontal line is drawn which intersects the pressure-difference line of 500 psi. At this intersection a vertical line is drawn which intersects the radial clearance line of 0.006 at a point. This point is read from the velocity axis (stationary) and is equal to 72.2 fps, which is the required value for a stationary and concentric case. Thus for this case

$$Q = vA = 0.0330 \text{ cu ft per sec} = 14.8 \text{ gpm}$$

When the shaft rotates at 3600 rpm the chart is entered from the left side with r = 1.75 in. A horizontal line is drawn which intersects the shaft-speed line of 3600 rpm where a vertical line is constructed intersecting the horizontal line from the right-hand side at a point. Then this point is read from axial velocity lines and the numerical value, 70 fps, is found. The through-flow for this rotational and concentric case is

$$Q' = vA = 0.032 \text{ cu ft per sec} = 14.36 \text{ gpm}$$

When the eccentricity is 0.003 in., the eccentricity ratio is 0.5. With this ratio, the through-flow ratio of 1.07 is found from Fig. 11. Thus for this eccentric case

$$Q_a' = Q' \times 1.07 = 0.034 \text{ cu ft per sec} = 15.37 \text{ gpm}$$

Such a procedure is also shown in the diagram with broken lines and arrows. The accuracy of the charts depends on the validity of the derived equations. In most cases values read from the chart are in good agreement with experiment. The deviations are less than 5 per cent, which is within the experimental accuracy.

Conclusions

This paper presents an analysis of the effect of several parameters on the flow through a smooth annular flow channel of fine clearance. The equations are verified experimentally and the results offered in graphical form. The analysis considers the effects of pressure, clearance, length, eccentricity, and rotation. Previous available data have not correlated the effects of eccentricity and rotation into the flow equation.

Future results will assay the accuracy of the theoretical analysis and the experimental methods in terms of lasting quality. De-

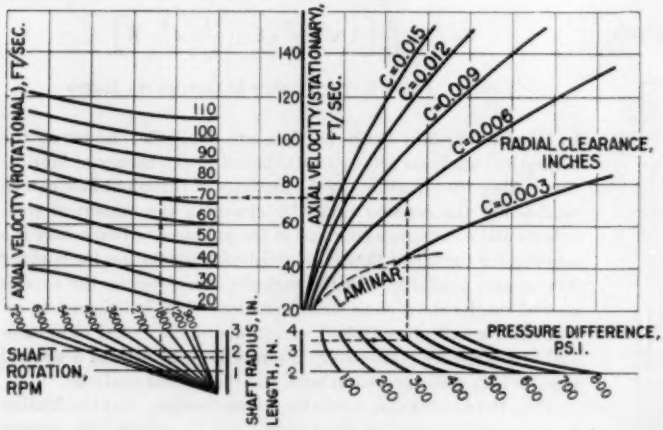

Fig. 12 Nomograph for Water at 68 F Through Concentric, Plain, Smooth Sleeves in Turbulent Region

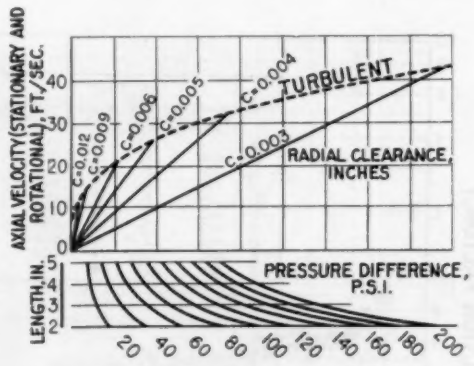

Fig. 13 Nomograph for Water at 68 F Through Concentric, Plain, Smooth Sleeves in Laminar Region. Derived From $f = 96/Re$

ficiencies are apparent (thermal, phase change, etc.) and it is hoped that in lieu of perpetual constancy, the conclusions will stimulate and justify additional work in the same field by other investigators.

Acknowledgment

The contributions of F. Mannuzza in obtaining the experimental data and of W. C. Osborne in the writing of this paper are gratefully acknowledged.

BIBLIOGRAPHY

1 "Stromungsvorgange in Ringformigen Spalten," by E. Becker, *Zeitschrift des Vereines deutscher Ingenieure*, vol. 51, 1907, pp. 1133–1141.

2 "Hydrodynamics," by Sir H. Lamb, Dover Publications, New York, N. Y., sixth edition, 1932, p. 586.

3 "Flow of Water Through Clearances With Relative Motion of the Boundaries," by R. J. Cornish, Proceedings of the Royal Society of London, series A, vol. 140, 1933, pp. 227–240.

4 "Stability of a Viscous Liquid Contained Between Two Rotating Cylinders," by G. I. Taylor, *Philosophical Transactions*, vol. 223, 1923, pp. 289–243.

5 "Der Durchfluss von Wasser durch konzentrische und exzentrische zylindrische Drosselspalte mit und ohne Ringnuten," by E. Schneckenberg, *Zeitschrift für angewandte Mathematik und Mechanik*, vol. 11, 1931, pp. 27–40.

6 "Heat Transfer and Pressure Drop in Annuli," by E. S. Davis, Trans. ASME, vol. 65, 1943, pp. 755–760.

7 "Fluid Friction in Annuli of Small Clearance," by R. F. Nootbaar and R. C. Kintner, Proceedings of Second Midwestern Conference on Fluid Mechanics, Ohio State University, Engineering Experimental Station Bulletin No. 149, September, 1952, pp. 185–199.

8 "Leakage Loss and Axial Thrust in Centrifugal Pumps," by A. J. Stepanoff, Trans. ASME, vol. 54, 1932, pp. 65–111.

9 "On Turbulent Flow Between Parallel Plates," by S. I. Pai, *Journal of Applied Mechanics*, Trans. ASME, vol. 75, 1953, pp. 109–114.

10 "A Course of Modern Analysis," by E. T. Whittaker and G. N. Watson, Cambridge University Press, London, England, fourth edition, 1927, pp. 281 and 312.

11 "Tables of Functions With Formulae and Curves," by E. Jahnke and F. Emde, Dover Publications, New York, N. Y., 1945, pp. 52–100.

12 "Analysis and Lubrication of Bearings," by M. C. Shaw and E. F. Macks, McGraw-Hill Book Company, Inc., New York, N. Y., first edition, 1949, pp. 257–259.

Discussion

H. E. Brandmaier.[5] Prior to his entry into the Navy the writer was very interested in the analysis of flow through close clearance pressure breakdowns, particularly in the work of the authors on that subject. They are to be complimented for the mathematical elegance of their presentation of the effect of eccentricity in the turbulent region.

In the way of criticism the writer feels that the authors' analytical treatment of the effect of rotation of one of the boundaries of the annulus is not altogether satisfactory. The conclusion that the addition of a rotational velocity component to the axial component has no effect in laminar flow can be deduced directly from a consideration of the Navier-Stokes' equations. Using the authors' assumptions, these equations reduce to two independent differential equations for the rotational and axial velocities. This result is independent of the geometrical transformation used and, if cylindrical co-ordinates are used, of the assumption that the flow closely approximates that between flat parallel plates. In addition, it has been the writer's experience that the addition of a rotational velocity component to a laminar flow in the breakdown usually changes the flow to transitional or turbulent flow. This restricts the applicability of the authors' Equation [17] to those cases where the flow is turbulent before and after the addition of the rotational component.

The writer would appreciate a more detailed evaluation of the effects of inlet and exit losses and methods of distributing the flow to the inlet (single and multiple holes feeding directly to the inlet or to an annular groove in one of the boundaries preceding the inlet, etc.) on the applicability of the results to cases where these factors are not the same as in the authors' experiments. In the case of centrifugal-pump wearing rings these effects may be equally as important as surface-friction effects.

Referring to the authors' Figs. 9 and 10, very little change in f is indicated for a fivefold relative roughness variation. In addition, the change appears to be in the wrong direction in Fig. 10 if a comparison is made with pipe-friction data.

The writer cannot agree with the authors that a 140-microinch finish with a 0.006-in. diametral clearance constitutes a hydraulically smooth surface.

In conclusion, the writer expresses the hope that the authors will extend their excellent work to include flow through serrated breakdowns which, in the turbulent region, are usually more effective than smooth-walled breakdowns.

O. E. Teichmann.[6] The authors are to be commended for a fine piece of experimental investigation that has yielded additional interesting data on flow through concentric and eccentric annular clearances. The idea of summarizing the results in the form of nomograms is certainly a lucky one and will be appreciated by the design engineer who needs a quick answer to the questions of leakage flow through annular gaps.

The presented experimental data are of special interest to the writer who took part in a similar investigation—although only on stationary arrangements without rotation of the shaft—which was carried out at Armour Research Foundation under an Air Force contract and which is planned for publication in the near future. Since this investigation centered around leakage flow in sleeve valves for control applications, radial clearances from 0.0003 to 0.002 in. were studied and it can be stated that, under laminar flow regime, the friction factor of 96/Re could always be verified experimentally when the entrance losses were not included in the measurement and true concentricity was established. For the turbulent region, the Blasius formula gave good agreement with the experimental values. In general, the experimental data recorded in the earlier literature were mostly carried out with considerable care and, occasionally, with more painstaking care than we are ready to apply today.

There is, of course, always the question whether we are looking for applied or fundamental data. The authors have chosen to investigate the applied case, limiting themselves to length/diameter ratios, clearances, roughness, and entrance conditions as practically encountered. This increases the value of the obtained data for the design engineer, but detracts from their value as basic information.

With regard to the mathematical analysis of the flow through an annular gap with rotational motion of the boundaries, it appears to the writer that the authors have made certain assumptions which would deserve closer scrutiny.

To clarify the picture, let us restate the various cases considered in the paper. We have a combination of two geometries (concentric and eccentric), two conditions at the boundaries (stationary and rotating), and, let us say, two flow regimes (laminar and turbulent), as shown in Table 1.

There are no reservations for any of the cases (marked with X) except for the eccentric cases (marked with ?). For the station-

[5] Ensign, USNR, USS *Newport News* CA-148, New York, N. Y. Assoc. Mem. ASME.

[6] Associate Manager, Heat and Power Research Department, Armour Research Foundation of Illinois Institute of Technology, Chicago, Ill. Mem. ASME.

TABLE 1

		Laminar	Turbulent
Stationary	Concentric	X	X
	Eccentric	?	Becker developed equation but did not integrate it Schneckenberg integrated equation graphically Tao and Donovan: mathematical integration
Rotating	Concentric	X	X
	Eccentric	?	?

ary-eccentric-turbulent case, the authors have integrated mathematically the equations which had been previously set up by Becker (1907) and graphically integrated by Schneckenberg (1931). It is gratifying to have this mathematical solution recorded in the hydraulic literature.

For the concentric case, the combination of axial flow and rotational drag represents the actual flow phenomena quite adequately (helical flow path instead of straight axial flow).

For the eccentric case, however, the situation is more involved. Even with the boundaries stationary, the flow may be turbulent in the wide portions of the gap and change to laminar in the narrow portions. The friction coefficient, therefore, may not be consistent around the periphery. The error in axial leakage flow, however, may be negligible because only a small percentage of the total flow passes through the narrow regions of the gap.

If rotation is introduced in addition to the eccentric position and a generally turbulent flow regime, the picture gets considerably complicated. Assuming the flow moves along helical streamlines, the width of the flow passage, the velocity distribution, and the mean flow velocity in the gap, as well as the friction factor, will change along the path and the flow regime may change accordingly. The statement that "the problem with rotation can be treated as stationary by making an adjustment of velocity and flow configuration" is somewhat nebulous, and if the authors mean "an adjustment as used in the concentric case with rotation," the statement would be incorrect. It is, furthermore, not clear to the writer whether the authors wish to imply that the velocity distribution shown according to Pai for the concentric rotational gap also can be applied for the eccentric rotational case, which would definitely lead to basic contradictions (see velocity distribution in journal bearings).

In conclusion, it appears to the writer that the authors were more ambitious than necessary in adding to the very significant and valuable experimental investigation, an attempt of an analytical treatment of the eccentric case with rotation that is oversimplified to the extent where it cannot be expected to offer more than a very rough check of the experimentally determined data.

Authors' Closure

The authors thank Messrs. Brandmaier and Teichmann for their comments and compliments. To answer their questions and discussion the following explanation is offered.

It is true that the statement that the addition of a rotational-velocity component to the axial component has no effect in laminar flow can be deduced from a consideration of the Navier-Stokes equations. It happens that in the case of laminar flow the pressure drop is linearly proportional to the mean velocity, or, we may say, "the linearity rule" is applicable in the laminar-flow regime. But it is not applicable to the turbulent-flow regime. The approach used by the authors was based on the change of the flow configuration due to the addition of the rotational velocity. This method of determining the mean velocity has been checked with the mathematical average obtained from the local resultant velocities and also affirmed by experiment. With the integration of the local resultant velocities of both tangential and axial-velocity components, the mean velocity of laminar-flow regime across the annular space has been calculated as a function of the ratio of the velocity components in both tangential and axial direction, which is plotted in Fig. 14 as curve *A*. This was compared with the approach adopted in the paper, which is plotted as curve *B* in Fig. 14. The agreement between the curves appears to justify the authors' simplified approach. Unfortunately, a similar computation for the turbulent zone was not possible due to the lack of available information.

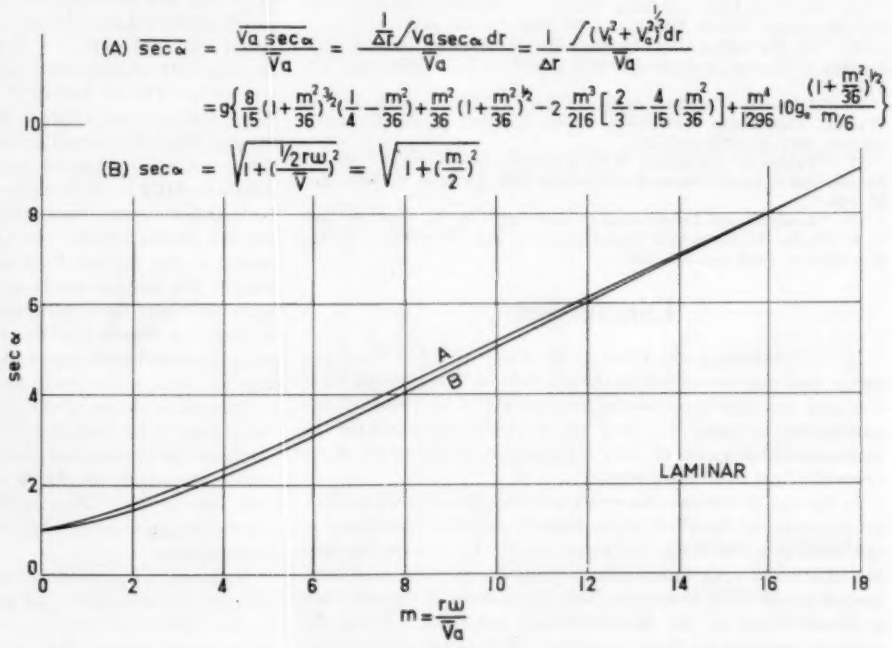

Fig. 14

Equation [17] is valid, of course, only so long as Equation [15] is true. This requires that the *n*-value with and without rotation be identical if the form of Equation [17] is employed. This will not hold for the case where the flow condition is changed from one to the other but if necessary, Equation [15] is available for this case.

Regarding the inclusion of entrance and exit losses in the investigation, it has been stated in the paper that this is signifi-

cant but necessary since the primary object of this investigation was the determination of the fluid flow across an annular-flow channel due to the total pressure difference available. During the course of the investigation the authors felt that for the cases without the inclusion of the entrance and exit losses the results for the rather simple case can be either directly or indirectly deduced from the known results in literature, e.g., in the stationary and concentric cases they can be obtained from the equation $f = 96/\mathrm{Re}$ in laminar-flow regime and from the Blasius formula of friction in the turbulent regime. While on the other hand there is no well-established information available for the case with the inclusion of the entrance and exit losses. This led to the primary objective of the present investigation. Furthermore, the mathematical derivations have no restriction whatsoever to the length-diameter, entrance, roughness, and some other conditions, if the proper constants and coefficients are inserted.

Mr. Teichmann's point on the flow in the eccentric annular channel with rotation is well taken. The authors agree that the flow analysis for a rotating eccentric channel is very complicated and the dangers of overgeneralization are always present. However, for an idealized case where the effect of rotation is not to change the over-all n-value, the results as presented in the paper are believed to be consistent and applicable to many actual design problems. The adoption of the velocity profile for the eccentric annular space with rotation given in the paper is practically feasible. Strictly speaking, the velocity in the tangential direction should be the superposition of the velocity due to the rotation and that due to the pressure gradient along the circumferential direction created by the variation of the local gap. But the term of this pressure gradient is small compared to the terms of drag and the pressure gradient in the axial direction, and it is negligible from the consideration of the order of magnitude. This notion has been employed by Ocvirk[7] in the lubrication study of journal bearings and its result was affirmed by experiment (for detail the work by Ocvirk and the references therein may be referred to).

It was commented that 140 microinches would not constitute an hydraulically smooth surface. This was the authors' semantics. What the authors want is to define a smooth surface as distinguished from a serrated surface.

The change of slope in Fig. 10 has been discussed during the presentation of the paper. As we all know that, in the turbulent pipe-friction data, the slope for the perfectly smooth surface should be at an angle of arctan 0.25 in a logarithmic f-Re diagram and horizontal for the surface of extremely high roughness, i.e., the n-value of Equation [10d] in the paper should be 0.25 for the former and zero for the latter. For all other roughnesses n should fall between these two extreme values. In the present problem with 140 microinches, it is expected that the n-value will fall between zero and 0.25.

---

[7] "Short-Bearing Approximation for Full Journal Bearings," by F. W. Ocvirk, NACA Technical Note 2808, October, 1952.

A Theory of the Fluid-Dynamic Mechanism of Regenerative Pumps

By W. A. WILSON,[1] M. A. SANTALO,[2] AND J. A. OELRICH[3]

A hypothesis of operation of the regenerative pump is presented which reflects the experimentally observed characteristics of the flow inside the pump. An analysis based on the hypothesis leads to a series of expressions for pump performance over the entire operating range in terms of only three empirical constants. The relationship of these parameters to the prior art of hydrodynamic machinery and to those geometric features peculiar to regenerative pumps is developed. Experimental corroborations of the results are presented.

Nomenclature

The following nomenclature is used in the paper:

a = cross-sectional area of impeller vane
A = cross-sectional area of open channel, area in general
b, c, d, f, h = pump dimensions, Fig. 3
D = impeller diameter
H = head and head loss
k = head-loss coefficient
K = dimensionless constants
p = pressure
P = power input
Q = flow
r = radius
R = radius to centroid of impeller vane
T = torque
U = tangential velocity of impeller
V = absolute velocity of fluid
Z = number of impeller vanes
α = ratio V_t/U at point 1, Fig. 3
η = efficiency
θ = angle measured from pump inlet, radians
ρ = density, mass per unit volume
σ = ratio V_t/U at point 2, Fig. 3
ω = angular speed in radians per unit time
ϕ = dimensionless flow coefficient, $Q/\omega D^3$
ψ = dimensionless head and head-loss coefficient, gH/ω^2D^2
¶ = dimensionless power, $P/\rho\omega^3D^5$

Subscripts

c = circulatory flow
G = centroid of open channel
t = tangential or through flow
s = solid-body rotation
o = open channel
i = impeller
l = leakage

Introduction

The term "regenerative pump" is used in this paper to denote a hydrodynamic unit often referred to in the literature as periphery pump, turbulence pump, friction pump, turbine pump, etc. The main feature of this unit is that it develops in a single rotor high heads at low flow rates. Although its efficiency is not impressive, it is very good compared to other hydrodynamic pumps of comparable specific speeds, and it has found many applications in industry. The very low specific speeds of the regenerative pump have made it particularly attractive for lubrication, control, filtering, and booster systems.

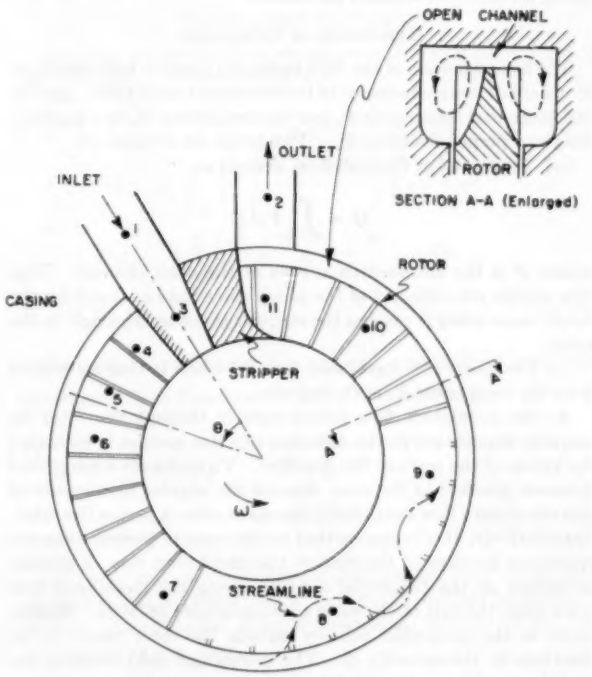

Fig. 1 Schematic Drawing of Regenerative Pump
(Numbers indicate pressure taps.)

The unit studied is shown schematically in Fig. 1. In this design the impeller has radial teeth or vanes machined into each side at its periphery. The fluid passes through an open annular chamber and circulates repeatedly through the impeller vanes. It is from this internal "multistaging" or regenerative-flow pattern, that the pump properly derives its name. Closing the circuit between inlet and discharge is the stripper or septum. In this region the open channel closes to within a few thousandths of an inch of the sides and tip of the rotor and allows only the fluid within the impeller to pass through to the suction.

[1] Associate Professor of Mechanical Engineering, Massachusetts Institute of Technology, Cambridge, Mass. Mem. ASME.
[2] Instructor in Mechanical Engineering, Massachusetts Institute of Technology, Cambridge, Mass. Assoc. Mem. ASME.
[3] Assistant Research Engineer, Research and Development Department, Worthington Corporation, Harrison, N. J. Assoc. Mem. ASME.

Contributed by the Hydraulic Division and presented at the Annual Meeting, New York, N. Y., November 28–December 3, 1954, of The American Society of Mechanical Engineers.
Note: Statements and opinions advanced in papers are to be understood as individual expressions of their authors and not those of the Society. Manuscript received at ASME Headquarters, August 4, 1954. Paper Nos. 54—A-59 and 54—A-60.

Preliminary experiments indicated that the few previously reported analyses are not compatible with direct observation of the pump mechanics. Yasutoshi Senoo (1)[4] considers turbulent friction between the moving impeller and the fluid as the primary force causing the pumping action. For this turbulent process Mr. Senoo applies Prandtl's mixing length theory, thus estimating the turbulent viscosity. This analysis and the analyses presented by W. E. Wilson (2), A. Miyadzu (3), and H. W. Iversen (4), ignore the circulatory motion induced by the centrifugal field.

Lazo and Hopkins (5) and Lutz (6) conducted experiments with a small thread probe to determine the direction of the velocity at different points in a section of the annular flow passage of the pump. They were able to corroborate an expectation that the fluid follows helical streamlines as shown in Fig. 1. This flow pattern is the basis for the present analysis.

Empirical parameters are introduced in the analysis. These parameters are rationalized on the basis of the flow pattern described and in terms of previous work done on losses in other hydrodynamic units. Experimental data were obtained from a commercial 5.4-in. impeller-diameter unit and from a 19-in. impeller-diameter model the casing geometry of which was varied by means of inserts. The flow parameters are correlated empirically as functions of the two major casing dimensions defining six different channel geometries.

Hypothesis of Operation

The helical motion of the fluid inside the pump is best described by means of two components of the velocity at each point, namely the tangential component V_t and the component V_e in a meridional plane perpendicular to V_t. Two terms are introduced:

(a) Tangential or through flow, defined as

$$Q = \int_A V_t dA$$

where A is the cross-sectional area of the open channel. This flow equals the capacity of the pump since fluid enclosed by the rotor vanes when it reaches the stripper is carried through to the inlet.

(b) Circulatory or meridional flow Q_e which is that associated with the component V_e of the velocity.

As the circulatory flow passes radially through the rotor its angular momentum in the direction of rotor motion is increased by virtue of the work of the impeller. To maintain a tangential pressure gradient in the open channel the angular momentum of the circulatory flow continually decreases after it leaves the rotor. Qualitatively, this indicates that an increase in pressure rise requires an increase in the rate of the circulatory flow, a greater reduction of the tangential velocity along the meridional flow path from the exit of the rotor to its entrance, or both. Reductions in the tangential velocity outside the rotor result in reductions in the capacity Q. The centrifugal field creating the radial pressure gradient inside the rotor is constant at a given speed while the centrifugal field due to the external flow weakens as the tangential velocities decrease; therefore the circulatory flow rate may be expected to increase as we approach zero through-flow. Both these effects lead to the observed inverse relation between flow and head.

Experimental results also show that power requirements increase with decreasing capacity. The hypothesis of operation stated satisfies this condition. The change in angular momentum per unit of circulatory flow which the rotor must produce increases with reduced capacity and there is a simultaneous increase in Q_e. The product of these two quantities is proportional to the power input.

Fig. 2 reproduces typical experimental curves of head variation of the fluid as it circulates through the pump for various capacities. These curves suggest five regions in the pump operation:

(a) Inlet region, from 1 to about 4.

(b) Acceleration region, from 4 to 6.

(c) Linear region, from 6 to 10. Note that here the head rise per unit of angle, that is, the slope $dH/d\theta$, is essentially constant.

(d) Deceleration region, from 10 to 11.

(e) Outlet or discharge region, from 11 to 2.

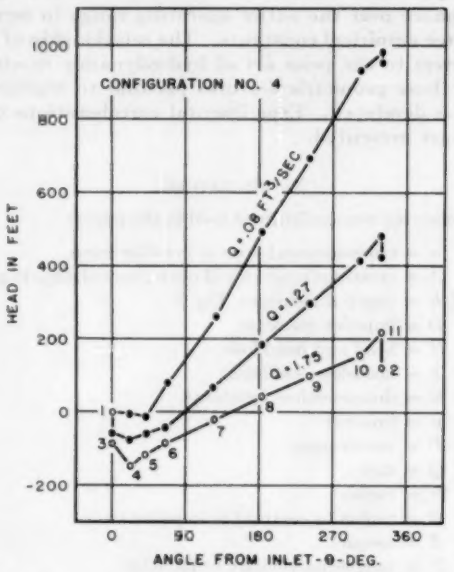

Fig. 2 Head Distribution in 18.9-In. Pump at Various Flows (1000 rpm. Numbers refer to pressure taps indicated in Fig. 1.)

Basic Hypothetical Model

To permit the development of a theoretical analysis of this complicated three-dimensional fluid motion a simplified model must be developed. The basic model used in this paper to represent the phenomenon in the linear region incorporates the following assumptions:

1 Flow is steady if time averages are used for pressures and velocities.

2 Fluid is incompressible.

3 There is no internal leakage.

4 All processes are adiabatic.

5 There are no end effects due to suction and discharge.

6 The entire pump flow may be characterized by the velocities V_t and V_e along a mean streamline.

7 Tangential pressure gradient is independent of radius.

8 Tangential pressure gradient is constant throughout the linear region.

9 All the circulatory flow leaves the impeller at the tip of the blades.

Assumptions 7 and 8 were corroborated experimentally (5, 6) and Fig. 2. These experiments also showed that part of the fluid leaves the impeller at the side of the blades. The discrepancy between assumption 9 and this observed characteristic of the pump flow is accounted for by a slip factor which reflects the degree of guidance provided by the vanes.

[4] Numbers in parentheses refer to the Bibliography at the end of the paper.

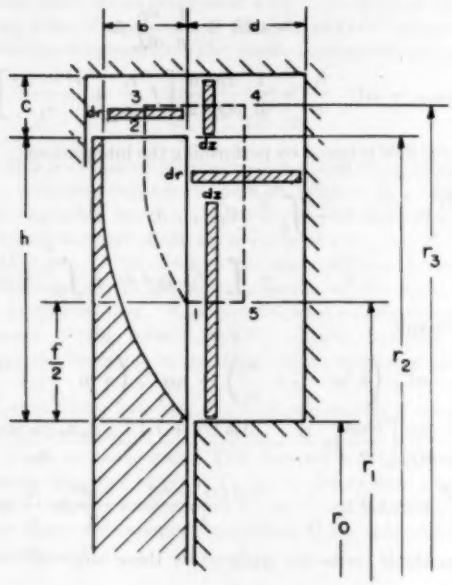

$A_1 = \frac{bc}{2}$ $\quad A_t = A_1 + A_2$

$A_2 = \frac{b+d}{2} c$ $\quad A_s = A_3 + A_4$

$A_3 = (r_3 - r_1) \cdot d$

$A_4 = \frac{f d}{2}$ $\quad A = A_t + A_s$

FIG. 3 SYMBOLS FOR OPEN CHANNEL AND IMPELLER DIMENSIONS

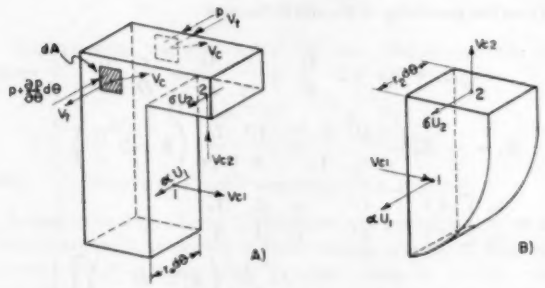

FIG. 4 CONTROL VOLUMES REPRESENTING SECTION $d\theta$ OF OPEN CHANNEL AND IMPELLER

In view of assumption 8, the analysis of any meridional section will give the equations of motion characteristic of the linear region. We therefore select for analysis an arbitrary element of the pump, as shown in Fig. 4. This analysis applies to a single-flow pump or half of a commercially typical double-flow unit, Fig. 3.

The dimensions of the impeller and open flow channel are given symbolically in Fig. 3 where points 1 and 2 denote the locations at which the assumed mean streamline of the circulatory flow enters and leaves the impeller, respectively. At these points the tangential and meridional velocity components are designated by

$$V_{t2} \equiv \sigma U_2, \; V_{t1} \equiv \alpha U_1$$

$$dQ_c = V_{c1} r_1 f d\theta = V_{c2} r_2 b \, d\theta$$

where

dQ_c = circulatory flow rate for section of width $d\theta$ considered
σ = "slip factor" mentioned previously and is assumed to be constant
α = defined as indicated and depends on flow
f = defined by Fig. 3

The dynamic equations of fluid mechanics are applied to this model. For simplicity in the presentation of the analysis, wall friction and other irreversibilities are introduced as head losses.

TANGENTIAL PRESSURE RISE

Applying angular momentum relations to the control volume of Fig. 4(*a*)

$$\int_A pr \, dA - \int_A \left(p + \frac{dp}{d\theta} d\theta \right) r \, dA = \rho \, dQ_c \, (\alpha U_1 r_1 - \sigma U_2 r_2)$$

Simplifying according to the assumptions made for the model, and dividing by

$$r_G A = \int_A r \, dA$$

$$\frac{dp}{\rho} = \frac{dQ_c \, \omega \, (\sigma r_2^2 - \alpha r_1^2)}{r_G A} - g \, dH_t \ldots\ldots\ldots\ldots [1]$$

where H_t is the head loss due to tangential shear forces on the open channel walls.

CIRCULATORY FLOW LOSSES

Applying the steady-flow energy equation in integral form to the same control volume of Fig. 4(*a*)

$$0 = \int_A \left(\frac{V_t^2}{2} + \frac{V_c^2}{2} + \frac{p}{\rho} + \frac{1}{\rho} \frac{dp}{d\theta} \right) \rho \, V_t \, dA - \int_A \left(\frac{V_t^2}{2} + \frac{V_c^2}{2} + \frac{p}{\rho} \right) \rho \, V_t \, dA + \left(\frac{V_{c1}^2}{2} + \frac{\alpha^2 U_1^2}{2} + \frac{p_1}{\rho} \right) \rho \, dQ_c - \left(\frac{V_{c2}^2}{2} + \frac{\sigma^2 U_2^2}{2} + \frac{p_2}{\rho} \right) \rho \, dQ_c$$

Simplifying according to the original assumptions and substituting dp from Equation [1] and Q for $\int_A V_t \, dA$

$$\frac{p_2 - p_1}{\rho} = \frac{Q\omega(\sigma r_2^2 - \alpha r_1^2)}{r_G A} + \frac{V_{c1}^2}{2} - \frac{V_{c2}^2}{2} + \frac{\alpha^2 U_1^2}{2} - \frac{\sigma^2 U_2^2}{2} + g H_{ce} \ldots\ldots [2]$$

$(p_2 - p_1)$ represents the meridional pressure drop in the open channel and is increased by the term H_{ce} to account for irreversibilities. Applying the angular-momentum relation to the control volume of Fig. 4(*b*)

$$dT = \rho \, dQ_c \, (r_2 \sigma U_2 - r_1 \alpha U_1) + Ra \frac{dp}{d\theta} d\theta$$

Since $\omega \, dT = dP$ represents the power input to the differential control volume

$$dP = \rho \, dQ_c \, (\sigma U_2^2 - \alpha U_1^2) + Ra\omega \, dp \ldots\ldots [3]$$

Applying Bernoulli's equation to the control volume of Fig. 4(*b*)

$$0 = -dP + \rho \, dQ_c \left(\frac{\sigma^2 U_2^2}{2} + \frac{V_{c2}^2}{2} + \frac{p_2}{\rho} - \frac{\alpha^2 U_1^2}{2} - \frac{V_{c1}^2}{2} - \frac{p_1}{\rho} \right) + Ra\omega \, dp$$

Substituting dP from Equation [3] and rearranging

$$\frac{p_2 - p_1}{\rho} = \sigma U_2^2 - \alpha U_1^2 + \frac{\alpha^2 U_1^2}{2} - \frac{\sigma^2 U_2^2}{2} + \frac{V_{e1}^2}{2} - \frac{V_{e2}^2}{2} - gH_{ei} \quad \ldots\ldots [4]$$

where H_{ei} is a measure of the irreversibilities due to the passage of the circulatory flow through the impeller. Equating Expressions [2] and [4], calling $H_e = H_{eo} + H_{ei}$ the total head loss in the circulatory flow, and rearranging

$$gH_e = \omega^2 (\sigma r_2^2 - \alpha r_1^2) \left(1 - \frac{Q}{r_G A \omega}\right) \quad \ldots\ldots [5]$$

Tangential Flow Equation

The variation of the tangential velocity V_t in the open channel may be derived if the mean streamline in the outside passage is assumed to be of the form shown in Fig. 3. This corresponds to dividing the open channel included in a section of width $d\theta$ into four subdivisions for each of which the differential equations can be set up by considering a typical differential control volume. Typical meridional surfaces of the differential control volumes are shown in Fig. 3. The control volumes have differential extent in the meridional and tangential directions, e.g., dr and $r\,d\theta$, and a finite meridional width based on the local dimension normal to the circulatory flow path, e.g., d in the main section of the open channel. For simplicity, the projection of the meridional mean stream surface is taken as rectilinear. Analysis of the control volume $b\,dr\,d\theta$ between points 2 and 3 is presented by

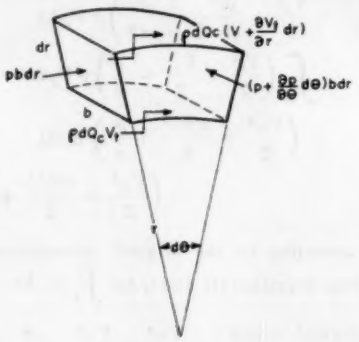

Fig. 5 Differential Control Volume Between Points 2 and 3 in Open Channel
(Only terms affecting angular momentum are included.)

way of Fig. 5. Neglecting second-order terms, the angular momentum relation leads to

$$\frac{dV_t}{dr} + \frac{V_t}{r} = -\frac{1}{\rho}\frac{dp}{d\theta}\frac{d\theta}{dQ_c} b$$

Solving this differential equation with the condition that $V_{t2} = \sigma U_2$ when $r = r_2$, we find the tangential velocity as a function of radius between points 2 and 3

$$V_{t(2-3)} = \frac{r_2}{r}\sigma U_2 - \frac{1}{\rho}\frac{dp}{dQ_c}\frac{b}{2}\left(\frac{r^2 - r_2^2}{r}\right)$$

Proceeding in a similar way between 3 and 1, matching velocities at points 3 and 5, and remembering that $V_{t1} = \alpha U_1$, successive applications of the angular momentum relation yield

$$V_{t(3-4)} = \frac{r_2}{r_3} U_2 - \frac{1}{\rho}\frac{dp}{dQ_c}\left[\frac{b(r_3^2 - r_2^2)}{2r_3} - cz\right]$$

$$V_{t(1-3)} = \alpha U_1 + \frac{1}{\rho}\frac{dp}{dQ_c} fz$$

$$V_{t(3-4)} = \alpha U_1 \frac{r_1}{r} + \frac{1}{\rho}\frac{dp}{dQ_c}\frac{d}{2}\left[f\frac{r_1}{r} + \frac{r^2 - r_1^2}{r_1}\right]$$

The total flow is found by performing the integrations

$$Q = \int_{r_1} V_{t(2-3)}\, b\, dr + \int_0^{\frac{b+d}{2}} V_{t(3-4)}\, c\, dz + \int_{r_1} V_{t(3-4)}\, d\, dr + \int_0^{\frac{d}{2}} V_{t(5-1)}\, f\, dz$$

with the result

$$Q = r_2\sigma U_2\left(b \ln\frac{r_3}{r_2} + \frac{A_2}{r_3}\right) + r_1\alpha U_1\left(d \ln\frac{r_3}{r_1} + \frac{A_1}{r_1}\right) + \frac{1}{\rho}\frac{dp}{dQ_c}\left[\frac{b^2 r_2^2}{2}\ln\frac{r_3}{r_2} - \frac{A_1 b\,(r_3 + r_2)}{4} - \frac{A_1 A_2\,(r_3 + r_2)}{2r_3} - \frac{A_2^2}{2} + r_1 A_4 d \ln\frac{r_3}{r_1} + \frac{A_3 d\,(r_3 + r_1)}{4} - \frac{r_1^2 d^2}{2}\ln\frac{r_3}{r_1} + \frac{A_4^2}{2}\right]$$

The logarithmic terms are replaced by three terms of the series

$$\ln x = (x - 1) - \tfrac{1}{2}(x - 1)^2 + \tfrac{1}{3}(x - 1)^3 - \ldots.$$

when $x = r_3/r_1$ and by two terms when $x = r_3/r_2$.

Making these substitutions and replacing dp/dQ_c from Equation [1] leads to

$$Q = \frac{1}{2}\frac{r_2}{r_G} Q_o\left(K_1\sigma + \frac{r_1^2}{r_2^2} K_2\alpha\right) \quad \ldots\ldots [6]$$

where $Q_o = r_G A\omega$ denotes the flow associated with solid-body rotation and K_1 and K_2 are dimensionless coefficients depending only on the geometry of the open channel

$$\left.\begin{aligned} K_1 &= K_3 + 2\frac{A_t}{A} - \frac{c}{r_3}\frac{A_2}{A} - \frac{c}{D}\frac{A_1}{A} \\ K_2 &= -K_3 + \frac{D}{r_1}\frac{A_s}{A} - \frac{A_2^2}{A}\frac{D}{6r_1^2 d}\left(5 - 2\frac{r_3}{r_1}\right) \\ K_3 &= \frac{r_2}{r_G}\left[\frac{A_s^2}{A^2} - \frac{A_t^2}{A^2} + \frac{c}{r_3}\frac{A_1}{A}\frac{A_2}{A} - \frac{1}{3r_1 d}\left(A_s - fd\frac{r_3}{r_1}\right)\right] \end{aligned}\right\} \quad \ldots [6a]$$

Six equations have been derived for the hypothetical model. Their significance is discussed in the following section as they are applied to the calculation of the pump-performance characteristics.

Equation [6] as stated may be used to evaluate the pump flow for a given value of α. In determining the pump performance the independent variable may be taken to be the flow Q or the parameter α since both are related by Equation [6] once the slip factor σ is known. α is the most convenient variable, but it must be remembered that the final results are head rise, power, and efficiency as functions of the flow.

Discussion of Irreversibilities

The effect of wall shear forces opposing the tangential flow is to decrease the tangential pressure gradient associated with the momentum transfer from the circulatory flow. Strictly speaking, these forces should be evaluated as the tangential components of

the total shear forces associated with the combined flow; however, an order of magnitude of the total of these components can be determined by applying the classic pipe-loss formula

$$\frac{dp}{dL} = \frac{4\rho f}{D_h}\frac{V^2}{2g}$$

When this is evaluated for the open channels of the pumps tested in the operating regimes of greatest interest it is found to be almost negligibly small. Consequently, we have hypothesized that this component of the shear forces is zero; i.e., H_t in Equation [1] is zero. The effect of this assumption is to attribute all the irreversibilities of the working section of this pump to losses in the circulatory flow. Losses in the inlet and discharge may be considered of the form $k_t(Q/D^3)^2$. These, however, will not influence the operation in the linear region in view of assumption 5.

The circulatory flow loss, H_c, of Equation [5], is considered to comprise two terms:

(*a*) Blade entrance loss. This loss arises when the velocity relative to the rotor at point 1, Fig. 3, differs from purely axial and has a tangential component $U_1 - V_{t1} = (1 - \alpha)U_1$.

These losses are evaluated according to the form suggested by Spannhacke (7)

$$\frac{(1 - \alpha)^2 U_1^2}{2}$$

(*b*) Friction losses, turning losses in the open channel, and turbulence losses due to separation inside the impeller and at the tip of the impeller. All these losses are considered proportional to V_c^2. Taking the velocity at the tip of the impeller as characteristic of the flow in the open channel, we may write the losses as

$$k_c\left(\frac{dQ_c}{r_2 b\, d\theta}\right)^2$$

Summarizing, we may write for the total circulatory flow losses

$$H_c = \frac{(1 - \alpha)^2 U_1^2}{2} + k_c\left(\frac{dQ_c}{r_2 b\, d\theta}\right)^2 \quad \ldots\ldots\ldots [7]$$

Over-All Pump-Performance Equations

Referring to Figs. 1 and 2, the flow from pump inlet 1, to impeller entrance 4, is similar to that through a series of pipes and elbows. The corresponding pressure drop is of the form $k_i(Q/D^3)^2$.

At point 4 the flow enters the working section of the pump with a velocity and direction dependent largely on the inlet port. Until the flow reaches the uniform pattern of the linear region the circulatory flow rate will increase.

The head distributions show the existence of a region (10 to 11) where a deceleration probably occurs and some of the kinetic energy of the circulatory flow is recovered as a pressure rise.

In the discharge region (11 to 2) a loss similar to that at the inlet occurs and may be incorporated with the $k_t(Q/D^3)^2$ term.

At any given point the flow is steady and has associated with it fixed values of the parameters Q_c and α. In view of this, Equation [1] is valid in the entire working section of the pump. Integrating this equation, setting H_t equal to zero, and deducting the inlet and discharge losses, $k_t(Q/D^3)^2$, leads to an expression for the head rise of the over-all pump

$$gH = \frac{\Delta P}{\rho} = \frac{Q_c}{Q_e}(\sigma U_2^2 - \alpha U_1^2) - k_i\left(\frac{Q}{D^3}\right)^2 \quad \ldots\ldots [8]$$

The system of Equations [5] through [8] involves four variables, Q, H, H_c, and Q_c. If specific values are assigned to k_i, k_c, and σ, these equations lead to the head-flow characteristics of the pump.

The integration of Equation [3] leads to an expression for the work input to the pump. The last term, namely, $Ra\omega\ \Delta p$, represents the work done in raising the pressure of the fluid between the impeller blades. This pressure rise is utilized across the stripper to perform a turbine work. Neglecting the losses associated with this process the last term of Equation [3] is dropped in determining the net power input. Combining the resulting expression with Equation [8]

$$P = \rho Q_e\left[gH + k_i\left(\frac{Q}{D^3}\right)^2\right] \quad \ldots\ldots\ldots [9]$$

Defining pump efficiency, substituting Equation [9], and rearranging

$$\eta = \frac{\rho g Q H}{P} = \frac{Q/Q_c}{1 + k_i Q^2/gHD^4} \quad \ldots\ldots\ldots [10]$$

Experimental Corroboration of Over-All Performance Analysis

Equations [5] through [10] determine the complete performance characteristics of the hypothetical model in terms of the parameters k_c, k_i, and σ. One correlation of these expressions with the experimental results obtained for a commercial unit (5)[5] has been made. The dimension f, Fig. 3, was arbitrarily set equal to the impeller vane width b, and values of the parameters were chosen to give the best over-all match. The results are shown in Fig. 6 in conventional dimensionless terms

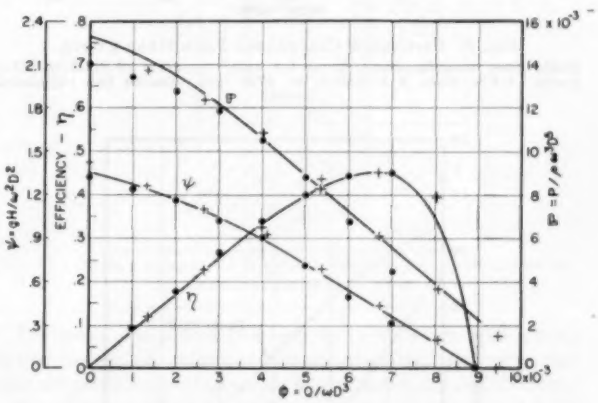

Fig. 6 Dimensionless Performance Characteristics of Sta-Rite TH-7 Pump

(Solid lines, calculated performance. $k_i = 3160$, $k_c = 110$, $\sigma = 0.85$. Dots, points from tests with air, reference 5. Crosses, manufacturer's points for water.)

$$\text{Dimensionless head} \quad \psi = \frac{gH}{\omega^2 D^2}$$

$$\text{Dimensionless flow} \quad \phi = \frac{Q}{\omega D^3}$$

$$\text{Dimensionless power} \quad \P = \frac{P}{\rho\omega^3 D^5}$$

[5] Sta-Rite Th-7 pump, 5.4 in. impeller diameter, $c = 0.181$, $d = 0.308$, $b = 0.230$, $h = 0.860$ in., double flow unit, $A = 0.36$ sq in.

The dimensionless plots are used to illustrate that the regenerative pump is a hydrodynamic unit obeying the same similitude laws as centrifugal and axial pumps, turbines and compressors. In this figure are recorded experimental points obtained at seven different speeds with air as the working fluid (5) and the performance data given by the manufacturer for water. A negligible influence of Reynolds number is indicated by these results which encompass a 2000 to 1 range of that parameter.

Inspection of Equation [10] indicates the possibility of calculating the entire efficiency curve in terms of the head-flow characteristic and of the loss coefficient k_t. These calculations have been made for a typical commercial unit. The coefficient k_t was evaluated from the experimental maximum efficiency point. The calculated and experimental efficiency curves are compared

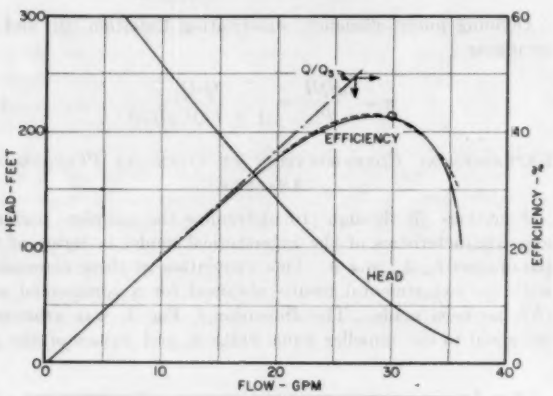

FIG. 7 EFFICIENCY CALCULATED FROM HEAD CURVE
(Solid lines, manufacturer's curves for water operation of Sta-Rite TH-4 pump. 5.4 in. diam, A = 0.40 sq in., 1750 rpm. Dotted line, calculated curve.)

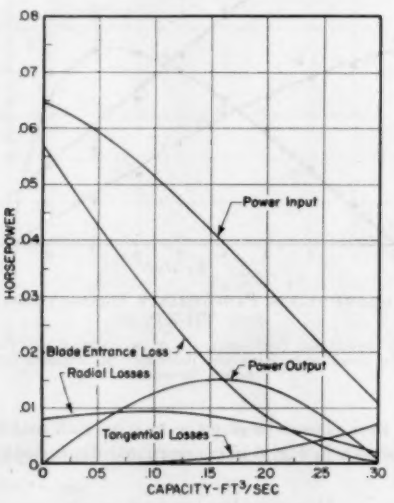

FIG. 8 THEORETICAL POWER DISTRIBUTION
(Air operation of Sta-Rite TH-7 pump; 3600 rpm, k_t = 3160, k_e = 110 σ = 0.85.)

in Fig. 7. As anticipated from Equation [10], at low flows $k_t Q^2$ is very small compared with gH, and the efficiency curve follows approximately the straight line Q/Q_s. (Recall that $Q_s = r_0 A \omega$.)

The agreement between the calculated curves and the experimental points in Figs. 6 and 7 is such as to lend considerable confidence to the hypothesized fluid-dynamic mechanism. The values of k_e, k_t, and σ obtained from the match of the performance curves are used to calculate the losses. The power-distribution curves of Fig. 8 show the magnitude of the calculated losses as a function of the pump flow. The equations give at low flows values of α of the order of -1 indicating a reversal in the direction of the velocity V_t between the tip and root of the impeller. This characteristic of the internal flow, observed experimentally (5), explains the large magnitude of the blade-entrance loss at low flows.

RATIONALIZATION OF EMPIRICAL PARAMETERS

The utility of the hypothesis developed in the foregoing depends upon our capacity to predict the parameters σ, k_t, k_e, and f in terms of the design variables. In developing this capacity we have drawn upon previous experience with similar parameters for other hydrodynamic devices. In each instance this experience has been adapted to this particular problem by appropriate experiments. Our work thus far has been limited to prediction of head-flow characteristics in the linear region.

The factor σ is introduced to account for the lack of perfect guidance to be expected from a finite number of blades. It is defined as the ratio of the average absolute tangential velocity of the fluid leaving the impeller to the tip speed of the impeller

$$\sigma = V_{t2}/U_2$$

Busemann (8) evaluated the factor σ considering the potential two-dimensional flow between the blades of a centrifugal impeller. He showed that σ is a strong function of the number of vanes Z, as that number approaches zero and a strong function of r_1/r_2 as this ratio approaches unity, Fig. 9. In view of the large number of vanes in a typical regenerative-pump impeller, the latter influence, i.e., $\sigma \to 0$ as $r_1/r_2 \to 1.0$, is the more significant.

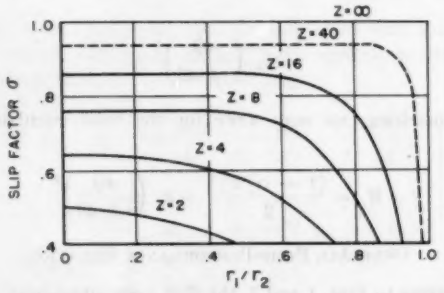

FIG. 9 DEPARTURE FROM PERFECT BLADE GUIDANCE—SLIP FACTOR σ
(After Busemann.)

The flow between the blades of the regenerative pump differs from the case of radial blades considered by Busemann mainly because the tip clearance is finite, the inlet flow is not radial, the rotor is unshrouded, and irreversibilities are present.

The selection of the parameter f is tantamount to the assignment of a value to the dimension r_1 which is defined as the radius at which the assumed mean streamline of the circulatory flow enters the blade, Fig. 3. It is to be expected that r_1 is a function of the open-channel geometry and might vary for a given geometry as the flow through the pump is changed. A further simplification is made in this analysis by neglecting the latter possibility; i.e., r_1 is a constant for a given geometry:

(a) As $c/d \to \infty$, $r_1 \to r_2$, $f \to 0$

(b) As $c/d \to 0$, $r_1 \to r_0$, $f \to 0$

Between these limiting cases a value of c/d, say, $(c/d)^*$ will exist for which $r_1 = (r_0 + r_2)/2$ and the flow enters over the whole

height of the blade, $f = h$. The value of $(c/d)^*$ is believed to be mainly a function of the impeller geometry. It is recognized that the model is actually invalid for c/d approaching either zero or infinity. Consistent with these conditions, r_1 is assumed to vary according to the relations

$$\left.\begin{aligned} r_1 &= r_0 + \frac{f}{2}; \quad f = h\,\frac{c/d}{(c/d)^*} \text{ if } c/d \leq (c/d)^* \\ r_1 &= r_2 - \frac{f}{2}; \quad f = h\,\frac{(c/d^*)}{c/d} \text{ if } c/d \geq (c/d)^* \end{aligned}\right\} \quad [11]$$

Referring to the previous discussion of irreversibilities, the parameter k_i can, for practical purposes, be connected exclusively with the inlet and discharge losses. It is therefore assigned a value of zero in the linear region.

The complex nature of the circulatory flow makes the loss coefficient k_e a complicated function of the open channel and rotor geometries. A simple and satisfactory relation for this parameter in terms of previous work on friction and turning losses could not be developed. The evaluation of this parameter in the linear region will therefore be done from experimental data noticing that if most of these losses are associated with the turning of the flow, it seems reasonable that k_e should be a minimum for some critical values of the dimensions c and d.

Experimental Investigation of Influence of Pump Geometry

As indicated in the foregoing, the general validity of the hypothesis has been verified by tests of a commercial unit having an impeller diameter of 5.4 in. The small dimensions of this unit made

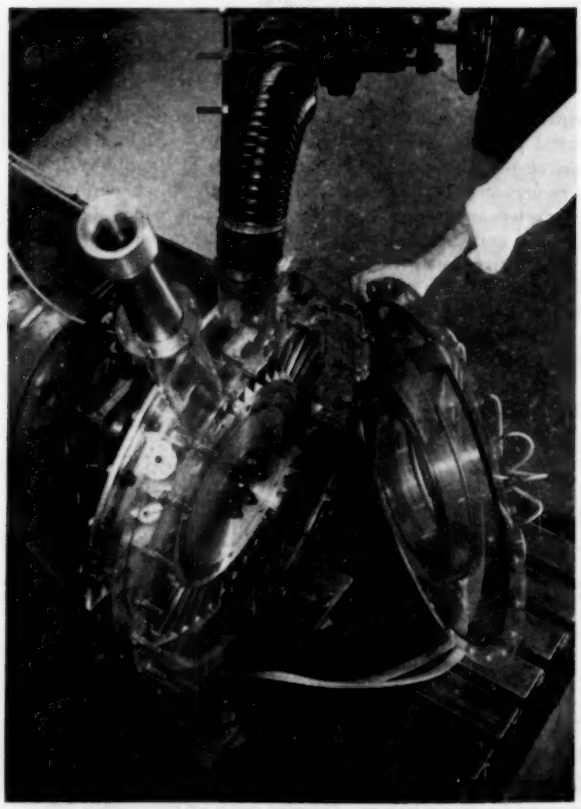

Fig. 10 Photograph of Test Model With Front Cover Off

TABLE 1 CONFIGURATIONS OF THE PUMP OPEN CHANNEL

Configuration no.	c, in.	d, in.	c/d	A, sq in.
1	0.875	1.700	0.515	7.38
2	0.365	1.700	0.215	6.12
3	1.130	1.410	0.802	6.80
4	0.620	1.060	0.585	4.39
5	0.875	0.760	1.150	3.68
6	0.365	0.760	0.480	2.89

measurements in the open channel extremely difficult. A larger, $3^1/_2$:1, scale model, shown in Fig. 10, was built to facilitate measurements and permit easy changes in some of the geometrical characteristics of the unit. The model is a single-flow pump whereas commercial units are characteristically double flow; that is, they consist of two single-flow units back to back working in parallel. The casing of the model is fabricated from lucite and designed to accommodate six lucite fillers, three flat disks, and three wide rings, Fig. 11. Six of sixteen possible configurations were selected for test. They are listed in Table 1.

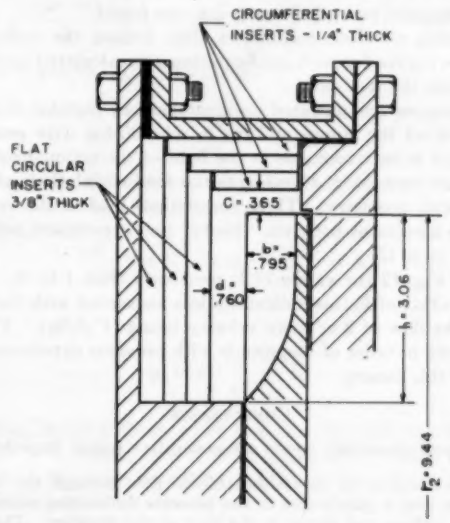

Fig. 11 Open Channel in Working Section and Major Dimensions of Experimental Unit

The model was driven at speeds up to 2000 rpm with a 5-hp dynamometer. A relatively simple and fragile experimental unit is feasible since dynamic similarity makes practicable operation with air as the fluid medium rather than water. At 2000 rpm pumping *water* this unit would require about 3500 hp and develop some 2000 psi pressure rise at shutoff.

Standard test procedures were followed. Capacity was measured by an inlet venturi, and the various static pressures for internal and over-all performance were measured by flush wall taps connected to water manometers. All tests reported were conducted at 1000 rpm, although runs at other speeds were made to verify similitude. The data showed that Reynolds number and compressibility effects are substantially negligible. (At 1000 rpm the shutoff pressure ratio is approximately 1.05.)

During the test runs the clearance between the front cover and the impeller was held to about 0.010 in. In the stripper section, clearance was harder to control and was measured to be of the order of 0.020 in.

Influence of Pump Geometry on Empirical Parameters

Figs. 13 to 15 show the internal head-flow characteristics of the six configurations tested. Figs. 13 and 14 suggest very strongly that the shutoff head is moderately dependent on tip clearance

in an inverse sense. On the other hand, the maximum flow rate is practically directly proportional to the cross-sectional area of the open channel. These two influences are shown in combination in Fig. 15. The points on the curves are the experimental data. The solid curves are the result of introducing empirically correlated performance parameters into Equations [1], [5], [6], and [7]. The procedure for securing a correlation of the parameters comprised the following steps:

(*a*) The measured flow rates were increased by calculated leakages to approximate the internal flow.[6]

$$\phi_0 = \phi + \phi_l$$

(*b*) Some sort of hypothesis for r_1 is tentatively selected, e.g., Equation [11] with a particular value of $(c/d)^*$.

(*c*) σ is tentatively selected in accordance with Busemann's work.

(*d*) Using the values of r_1 and σ from (*b*) and (*c*), values of k_e which force a match of the internal performance curves at $\alpha = 0$ (approximately best efficiency point) are found.

(*e*) Using all three parameters thus defined the entire performance curves for each configuration are calculated and compared with the test data.

The process was repeated until satisfactory matches were obtained for all the pumps and the k_e relationship with geometry was found to be reasonable in the light of the rationalization of the parameters. Fig. 12 presents the final correlations of r_1, σ, and k_e with geometry. These correlations lead to the very acceptable agreement between "theory" and experiment indicated by Figs. 13 to 15.

From Fig. 12 the values of k_e used vary from 1 to 8. From the definition of k_e this indicates a loss associated with the turning of the flow of 2 or more velocity heads ($V_{c2}^2/2g$). This result agrees in order of magnitude with previous experience with losses of this nature.

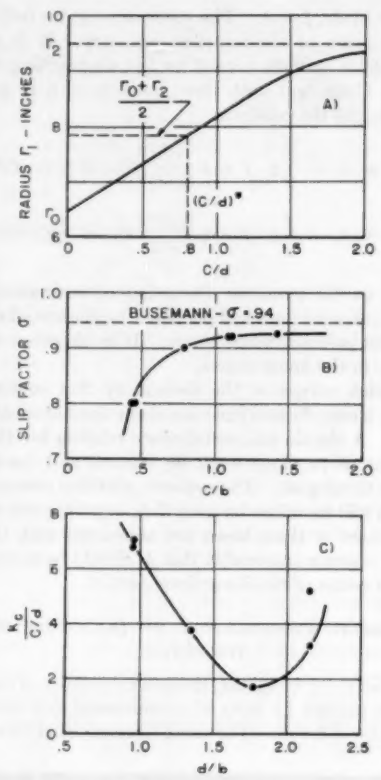

FIG. 12 VARIATION OF INTERNAL FLOW PARAMETERS WITH OPEN CHANNEL GEOMETRY

CONCLUSIONS

A hypothesis which treats a regenerative pump impeller as a centrifugal device has been shown to be consistent with the observed performance of commercial pumps. Qualitatively, the derived relations satisfy the major details of the observed flow phenomenon. It is remarkable that only three performance parameters are necessary to describe the performance of a hydrodynamic unit throughout its complete range of operation.

The correlation with the work of Busemann shows that the regenerative pump impeller performs like other centrifugal units. Radial clearance beyond the impeller tip is the major geometrical feature modifying the theoretical slip factor determined by Busemann.

One of the important irreversibilities associated with the circulatory flow can be evaluated as a Spannhacke "shock loss."

[6] ϕ_l is assumed to be attributable to flow through the stripper clearance and is partly due to the pressure differential acting on a series of orifices and partly to the drag of the impeller. This leads to the relation

$$\phi_l = \frac{(h+b)e}{2D^2}\left[1 + 1.70\sqrt{\frac{2\theta_p}{Z_s}}\sqrt{\frac{d\psi}{d\theta}}\right] - \frac{he}{4D^2}\left(1 - 2\frac{r_3}{D}\right)$$

where an orifice coefficient of 0.85 has been assumed. In this expression, θ_p is the equivalent working section of the pump in radians, Z_s is the average number of blades in the stripper at one time, and e is the average clearance at the side and tip of the rotor through the stripper. Values used for the unit tested are $\theta_p = 5.42$ radians, $Z_s = 3$, and $e = 0.020$ in.

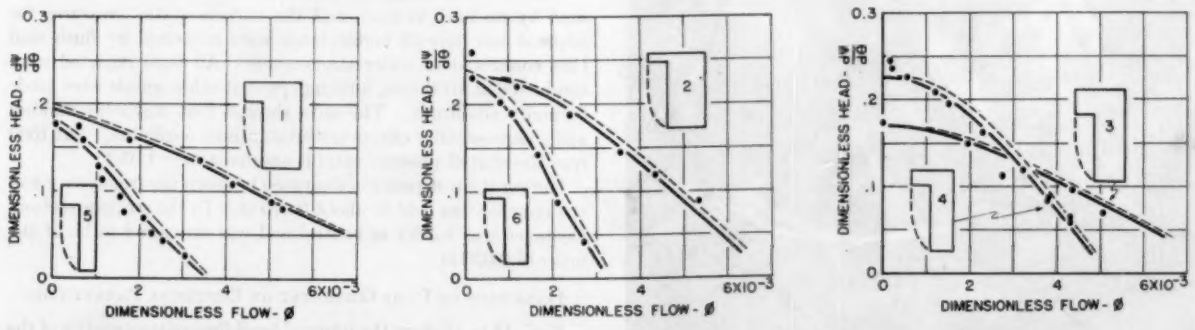

FIGS. 13–15 COMPARISON OF CALCULATED INTERNAL PERFORMANCE WITH EXPERIMENTAL RESULTS

(Dashed lines, calculated performance; solid lines, calculated performance corrected for stripper leakage. Indicated points are experimental data. Numbers within channel configurations refer to geometries listed in Table 1.)

Additional turbulent-type losses proportional to the square of the circulatory flow have been related to the casing geometry for the particular rotor tested. The losses associated directly with through-flow are found to be due principally to turbulent losses in inlet and outlet.

ACKNOWLEDGMENTS

The authors express their gratitude to the Worthington Corporation for sponsoring this project through a grant-in-aid to the Massachusetts Institute of Technology. Sta-Rite Products was most co-operative in providing both equipment and dimensional and performance data for their commercial units.

BIBLIOGRAPHY

1 "Theoretical Research on Friction Pump," by Yasutoshi Senoo, Reports of the Research Institute for Fluid Engineering, Japan, vol. no. 1, 1948. "Researches on Peripheral Pump," and "Influences of the Suction Nozzle on the Characteristics of a Peripheral Pump and an Effective Method of Their Removal," Reports of Research Institute for Applied Mechanics, Kyushu University, Japan, vol. 3, no. 11, 1954.

2 "Analysis of Turbine Pumps," by W. E. Wilson, *Product Engineering*, vol. 18, October, 1947, pp. 163–166.

3 "Theory of Westco-Type Rotary Pump," by A. Miyadzu, Transactions of the Society of Mechanical Engineers of Japan, vol. 5, no. 18, February, 1939, pp. 109–115.

4 "Performance of the Periphery Pump," by H. W. Iversen, Trans. ASME, vol. 77, January, 1955, pp. 19–22.

5 "Theoretical and Experimental Analysis of a Regenerative Turbine Pump," by L. Lazo and T. Hopkins, senior thesis, Massachusetts Institute of Technology, Cambridge, Mass., January, 1953.

6 "Experimental Investigation of the Pressure Distribution in a Regenerative Turbine Pump, the Sta-Rite TH-7," by G. F. Lutz, senior thesis, Massachusetts Institute of Technology, Cambridge, Mass., May, 1953.

7 "Centrifugal Pumps, Turbines and Propellers," by W. Spannhacke, The Technology Press, Cambridge, Mass., 1943, p. 140.

8 "Das Forderhohenverhaltnis Radialer Kreiselpumpen mit Logarithmishspiraligen Schaufein," by A. Busemann, *Zeitschrift für angewandte Mathematik und Mechanik*, vol. 8, 1928, pp. 372–384.

Discussion

H. W. IVERSEN.[7] The authors' hypothesis leads to some interesting relationships which, for the record, should be compared to other expressions applied to the pumping action of the regenerative pump. The writer[8] presented some thoughts on the prediction of the shapes of the performance curves which did not include any detailed specification of the fluid motion within the pump but merely specified a pumping shear between the impeller and the fluid in the open channel and a retarding shear between the fluid and the channel walls. The final expressions, in terms of the authors' symbols, unless otherwise defined, were

$$H = \frac{C_i a_i U^2}{2gA}\left[\left(1 - \frac{Q}{UA}\right)^2 - \frac{C_e a_e}{C_i a_i}\left(\frac{Q}{UA}\right)^2\right] \quad [12]$$

$$P = \frac{C_i a_i \rho U^3}{2}\left(1 - \frac{Q}{UA}\right)^2 \quad [13]$$

where

C_i = impeller shear coefficient
a_i = impeller shear area
C_e = casing shear coefficient
a_e = casing shear area
U = effective impeller velocity

The end points of the head-capacity curve and the end point of the power curve at zero flow were used to obtain three equations to evaluate the two shear coefficients and the effective impeller velocity. The complete performance curves were then predicted and were shown to match the test curves of one pump.

Before a comparison between Equations [12] and [13] and the authors' results can be made, a question must be raised as to the validity of the authors' Equation [7]. When Equations [7] and [5] are combined by eliminating gH_c, and with $Q_c = r_G A\omega$ and $U_1 = r_1\omega$, there results

$$Q_c^2 = \frac{\omega^2(r_2 b\theta)^2}{k_c}\left[(\sigma r_2^2 - \alpha r_1^2)\left(1 - \frac{Q}{Q_c}\right) - \frac{1}{2}(1-\alpha)^2 r_1^2\right] \quad [14]$$

A further simplification may be made for purposes of discussion by assuming σr_2^2 is approximately equal to r_1^2. This approximation is reasonable since r_2 is greater than r_1 and σ is somewhat less than unity. Then

$$Q_c^2 = \frac{(\omega r_1 r_2 b\theta)^2}{k_c}\left[(1-\alpha)\left(1 - \frac{Q}{Q_c}\right) - \frac{1}{2}(1-\alpha)^2\right] \quad [15]$$

From Equation [6] of the paper

$$\alpha = \frac{Q}{Q_c}\frac{2r_G}{r_1^2 K_2} - \frac{\sigma r_2^2 K_1}{r_1^2 K_2} \quad [16]$$

For simplicity in discussion, since the coefficients are constants let

$$\frac{2r_G}{r_1^2 K_2} = K' \quad \text{and} \quad \frac{\sigma r_2^2 K_1}{r_1^2 K_2} = K''$$

Then

$$\alpha = K'\frac{Q}{Q_c} - K'' \quad [17]$$

According to the authors, when $Q = 0$, α is of the order of -1. Then $K'' = 1$. Also, when $Q = Q_c$ (all the fluid rotates with the impeller at the mean impeller velocity), $\alpha = 1$. Then $K' = 2$. Then Equation [17] of this discussion reduces to

$$\alpha = 2\frac{Q}{Q_c} - 1 \quad [18]$$

Substitution of Equation [18] into Equation [15] yields

$$Q_c^2 = \frac{(\omega r_1 r_2 b\theta)^2}{k_c}\left[2\left(1 - \frac{Q}{Q_c}\right)^2 - 2\left(1 - \frac{Q}{Q_c}\right)^2\right] \quad [19]$$

Equation [19] shows $Q_c = 0$ for all values of Q, or no circulatory flow is present at any pumping condition. This condition violates the flow pattern upon which the authors' analysis is based.

Admittedly, certain assumptions have been made in arriving at Equation [19]. However, the authors' Fig. 8 indicates somewhat the same conclusion when the curve of radial losses is considered. It is assumed this curve is that which represents

$$k_c\frac{Q_c^2}{(r_1 r_2 b\theta)^2}$$

in which k_c is considered a constant. Therefore the radial loss in proportional to Q_c^2. The curve shows, as the capacity Q is decreased toward shutoff, that the radial-flow losses reach a maximum, then decrease, which means that the circulatory flow follows the same trend, a trend which negates the statement by the authors, "an increase in pressure rise requires an increase in the rate of circulatory flow, a greater reduction of the tangential

[7] Associate Professor, Division of Mechanical Engineering, University of California, Berkeley, Calif. Assoc. Mem. ASME.

[8] See reference (4) of the paper.

velocity along the meridional flow path from the exit of the rotor to its entrance, or both. . . . ."

If the last term of Equation [15], or the term containing α of Equation [7], representing the so-called blade-entrance loss, is dropped, then, with the approximation

$$\sigma r_2^2 = r_1^2$$

$$Q_c^2 = \frac{(\omega r_1 r_2 b\theta)^2}{k_c} 2\left(1 - \frac{Q}{Q_s}\right)^2 \quad \ldots\ldots\ldots [20]$$

Substitution of Equation [20] in the authors' Equation [1], along with Equation [18], results in

$$H = \frac{2\omega^2 r_1^2 r_2 b\theta}{k_c^{1/2} g r_G A}\left(1 - \frac{Q}{Q_s}\right)^2 - k_t\left(\frac{Q}{D^2}\right)^2 \quad \ldots\ldots\ldots [21]$$

Equation [21] is of the same form as Equation [12] of this discussion, relating the pump performance to shear coefficients which are, as the authors show, primarily the result of the momentum interchanges in the pumping action.

The authors' detailed analysis of relative geometry of the flow-channel cross section should lead to design criteria when sufficient correlations are available with other pump-impeller dimensions and flow-channel areas. However, some further substantiation of the circulatory flow "shock loss at entrance" in Equation [7] appears to be necessary before the analysis is accepted.

YASUTOSHI SENOO.[9] It is quite reasonable to suppose that there is a circulatory flow between the impeller vanes and the open annular channel in the regenerative pump and that the circulatory flow is the governing mechanism of pumping action. The method of approach adopted by the authors seems to be the most straightforward one handling the circulatory flow. No one has analyzed the characteristics of a pump by this method. Because the mechanism is too complicated to formulate, several hypotheses must be adopted, which may lead to wrong conclusions unless the hypotheses are selected properly.

Some researchers have analyzed the phenomena in the pump with a theory of turbulence. In the open channel, as the authors mention, a quantity of fluid which has gained momentum from the impeller conveys the momentum to the fluid in the channel which flows against the pressure gradient and friction force on the wall. Therefore the phenomenon in the channel probably could be approximately analyzed by a method like the classic theory of turbulence based on momentum transfer. On the other hand, the spaces between the vanes of the impeller are always filled with fluid, not only when they move from the suction port to the discharge port but also from the discharge port to the suction port; that is, these spaces do not contribute to the transport of the fluid from the suction port to the discharge port in the sense of a positive-displacement pump. Therefore it seems to be permissible to consider that the impeller is simply a source of momentum which will be conveyed to the fluid in the open channel. Accordingly, in the turbulent theory which is adopted for the analysis of the pump characteristics, the circulatory flow is not ignored but simplified as a form of turbulence.

In the open channel, as just mentioned, the transfer of momentum is induced by the impeller. Therefore the phenomenon is quite different from the turbulent flow in a pipe. Accordingly, the turbulent theory should be modified by adopting some hypothesis and coefficients which will be obtained by experiments. In the writer's analysis (1), for example, the whole performance of a pump is described by equations with a significant coefficient which indicates the intensity of turbulence, or circulatory flow. Although this coefficient depends slightly on the geometry of the impeller and open channel, the performance of a new pump will be described accurately by the characteristic equations if the geometry is not completely different from conventional ones. However, it is difficult to find the best shape and the optimum combination of impeller and open channel from this turbulent theory, unless many experiments are available which cover various kinds of geometry.

The authors have analyzed the secondary flow directly. The results and further improvements in the future may be expected to provide clues to the discovery of some factors which will improve the performance of a regenerative pump, such as the best shape and the optimum combination of impeller and open channel. Therefore this method of approach has certain significance even though the characteristic equations are complicated.

A few comments would seem to be in order:

1 The input power is easily calculated from Equation [9], but the relationship between head and rate of flow is a combination of Equations [5], [6], [7], and [8] which are too complicated to see the general tendency of the characteristics due to the change of the shape of the pump. It appears to be impossible to simplify this relationship without reducing the accuracy. However, the relationship between the head and the rate of flow is approximately linear, so the characteristics will be roughly predicted by the performances at a few particular conditions. For example, the rate of flow at zero head, the shutoff head, and the head and the rate of flow at $\alpha = 0$, seem to be shown by simpler formulas. It would be desirable if the authors' analysis could be modified or simplified to explain the change of characteristics due to the change of the shape and the dimensions of parts of pump.

2 In this paper the dimensionless flow coefficient ϕ is defined by $Q/\omega D^3$ and the head-loss coefficient k is defined by $gH/(Q/D^2)^2$. It seems to be desirable to define these dimensionless parameters so that they have direct physical meanings, e.g., $\phi = Q/Q_s$, $k = 2g\Delta H/(Q/A)^2$, etc., where A is the cross-sectional area of the open channel. Then, the head-loss coefficient will be comparable to that of the pipe flow, and the values of ϕ at $\psi = 0$ in Figs. 13, 14, and 15 will approximately coincide with each other.

3 The performance of the regenerative pump can be improved in two ways. One is an increase of the circulatory flow which results in a higher head at a constant rate of flow. This can be done by a good combination of the open channel and the impeller geometries as well as by reducing the head-loss of the circulatory flow. The other is a reduction of the tangential head-loss. The latter is not so effective as the former for a small rate of flow but is very effective for a large rate of flow. For an improvement of the performance, the mechanism of these losses should be studied and measures should be taken to meet these situations. That is, the circulatory loss coefficient k_c should be separated into shock loss and friction loss coefficients, the tangential loss coefficient k_t should be separated into friction loss, inlet loss, and discharge loss coefficients. If the magnitudes of some of these coefficients are unreasonable, there may be a possibility of improvement. For example, according to many experimental data, the input power at zero head is equivalent to the power which corresponds to 3 to 4 times the velocity head of the through flow. In one case this coefficient was reduced from 3.4 to 2.5 by an alteration of the suction-port geometry as will be explained later. Even in this case the tangential loss coefficient k_t appears to be bigger than the loss coefficient in ordinary pipe flow, but it might be reasonable for a flow with circulatory motion. It is expected that further research will either justify the magnitude of the loss coefficient or suggest a method for an improvement of the performance.

4 The writer has conducted a series of experiments (1) which verified serious influence of the inlet port on the performance of the pump. It is shown in the pressure-distribution curves along the

[9] Kyushu University, Fukuoka, Japan.

channel in Fig. 2 that the pressure of fluid decreases as soon as fluid enters the channel. This kind of pressure distribution is recognized in almost all regenerative pumps. If the pressure decrease at the entry is removed, the performance of the pump will improve. Considering the mechanism of pumping action, the writer enlarged the cross-sectional area of the channel near the inlet port. As a result of this alteration, pressure did not appreciably decrease in the channel, and cavitation was prevented. In addition, total head increased for any rate of flow, or rate of flow increased for any total head. For example, the shutoff head increased by 20 per cent and the maximum rate of flow increased by 10 per cent. On the other hand, the relationship between power and total head hardly changed; accordingly, the maximum efficiency increased from 33 to 42 per cent.

W. E. Wilson.[10] This paper is a welcome addition to the literature on the peripheral pump, pioneering as it does in a new direction in the formulation of a theoretical approach to an explanation of the operation of this controversial mechanism. The writer is particularly interested since he has been, for several years, an adherent of the Japanese school of thought which has envisaged the pump as a turbulence device. Last year the subject was covered by Professor Iversen of the University of California, in a paper at the ASME Annual Meeting and the writer expressed himself as a supporter of Professor Iversen's views.

The paper under discussion presents a fresh viewpoint and one deserving of careful and thorough consideration. It appears that there is a necessity for added investigation of an analytical and experimental nature before it will be possible to assess accurately the roles of turbulence and dynamic action and their relative importance.

In order to bring into sharper focus the significance of the hypothesis advanced in this paper, the following equations, two of which are modifications of those of the authors, are presented. Numerical designation is the same as in the paper, and the letter *b* has been added to differentiate them from the originals

$$\frac{dp}{\rho} = \frac{dQ_e\omega^2 r_2^2\left(\sigma - \alpha\frac{r_1^2}{r_2^2}\right)}{Q_s} \quad \ldots\ldots [1b]$$

$$\left(\sigma - \alpha\frac{r_1^2}{r_2^2}\right)\left(1 - \frac{Q}{Q_s}\right) = 0 \quad \ldots\ldots [5b]$$

$$Q = \frac{1}{2}\frac{r_2}{r_G}Q_s\left[K_1\sigma + \frac{r_1^2}{r_2^2}K_2\alpha\right] \quad \ldots\ldots [6]$$

In each case the equation has been written for a perfect fluid. Under these circumstances, there would be no frictional losses. These equations should then describe the ideal performance, not actually attainable, but useful as a guide in analysis and discussion.

It will be noted that Equation [5*b*] places severe limitations on the performance. It is required that either $Q/Q_s = 1$ or $\sigma = \alpha(r_1^2/r_2^2)$.

If $Q = Q_s$, then there is no variation of delivery with pressure which is obviously not in accordance with the observed facts.

On the other hand, if $\sigma = \alpha(r_1^2/r_2^2)$, Equation [1*b*] indicates that dp will be zero. This is also not in agreement with the experimental evidence.

It is apparently necessary, therefore, that the background of Equation [5*b*] be examined critically. In the authors' development the conservation of energy was assumed but modified by the introduction of losses in the form of the head loss H_c. Omission of the head loss as indicated in Equation [5*b*] assumes, simply, no energy loss in the flow due to the circulatory motion. Quite obviously, there would be energy losses in transferring momentum from the liquid ejected from the impeller into the slower moving main stream. It is pertinent, therefore, to inquire carefully into the meaning of this situation. The writer wishes, therefore, to request the authors' interpretation of the failure of the perfect-fluid equations to describe properly the performance.

It is the writer's suggestion that the mechanism of momentum exchange in this pump may be of a nature similar to that found in the "Borda tube" or the hydraulic jump. In each case a high-velocity stream mixes with a low-velocity stream and there is an accompanying loss of energy which is readily calculated by applying successively the principles of the conservation of momentum and the Bernoulli equation. Perhaps a similar analysis of the flow pattern in the pump would make possible an evaluation of the energy loss gH_c of the authors' Equation [5].

Consideration of Equation [1*b*] in the ideal form given here reveals clearly the physical picture envisioned by the authors. The pressure developed is directly proportional to the intensity of the circulatory flow as measured by the ratio dQ_e/Q_s. The quantity $r_2^2\omega^2[\sigma - \alpha(r_1^2/r_2^2)]$ describes directly the centrifugal pumping action in the conventional manner.

Equation [6] describes a linear relationship between Q and α provided σ is constant. This relationship may be introduced in Equation [1*b*] to provide an expression for dp as a function of the delivery Q if desired.

Equations [1*b*], [5*b*], and [6] are independent relationships obtainable from the hypothesis advanced by the authors. It is obviously impossible to obtain from these a complete solution to the problem of predicting the ideal performance since the unknown quantities dp, dQ_e, α, and Q exceed the number of equations. It is to be hoped that an additional hypothesis regarding the nature of the flow, gleaned from the experience of the authors, might be useful in extending the predictive power of the theory.

Consideration of Equations [9] and [10] of the paper is disappointing to the reader since it is not apparent that these necessarily follow only from the hypothesis advanced by the authors but rather could be written directly from the definition of efficiency and the concept that the power required to drive the pump is the ideal power $\rho Q_s gH$ plus a power loss proportional to the square of the mean velocity of the liquid, $\rho Q_s K(Q/D_2)^2$.

The statement, "The dimensionless plots are used to illustrate that the regenerative pump is a hydrodynamic unit obeying the same similitude laws as centrifugal and axial pumps, turbines and compressors," is not entirely satisfying in that it is not apparent that these plottings and this quotation establish clearly the distinction between the peripheral pump as a turbulence unit and a dynamic unit.

Considerations that would assist in the clarification of the nature of the pump are concerned with extreme conditions. For example, the situation at shutoff is of great interest. Reference to Equation [6] reveals that at shutoff when the delivery is zero, the following relationship between α and σ must exist

$$\alpha = -\frac{k_1}{k_2}\frac{r_2^2}{r_1^2}\sigma$$

Apparently α must be negative and indeed such would be expected since a backflow is necessary to maintain continuity.

Under these conditions, Equation [1*b*] yields the following value of the pressure differential

$$\frac{dp}{\rho} = \frac{dQ_e\omega^2 r_2^2}{Q_s}\sigma\left(1 + \frac{k_1}{k_2}\right)$$

This indicates that the shutoff pressure depends only upon the

[10] George Westinghouse Professor of Engineering Education, The Pennsylvania State University, University Park, Pa. Mem. ASME.

ideal pressure $(\rho r_2^2\omega^2)/2$, the geometry of the pump $[1 + (k_1/k_2)]$ the quantity σ, and the ratio (dQ_c/Q_e). The latter ratio is, of course, the critical distinguishing feature of the authors' concept. If σ remains essentially constant, the shutoff head coefficient $(2dp)/(\rho r_2^2\omega^2)$ should be directly proportional to (dQ_c/Q_e). This shows the necessity for an increasing value of dQ_c with decreasing delivery Q since the maximum value of dp is a shutoff; i.e., $Q = 0$. Experimental data related to this observation are of significant importance.

Another extreme condition of interest is that of zero pressure increase. Equation [1*b*] indicates that under these circumstances either $dQ_c = 0$ or $\sigma = \alpha(r_1^2/r_2^2)$. Experimental evidence on this point would be pertinent.

It is the writer's hope that additional study and experimentation may result in a complete theory of the peripheral pump that will provide a sound basis for design improvement.

G. F. Wislicenus.[11] This is a thought-provoking paper on a thought-provoking subject. In the opinion of this reader the authors have made a distinct contribution to the theory of Regenerative Pumps by attempting to describe the flow on the basis of a steady-flow hypothesis similar to that of the ordinary centrifugal-pump theory. The most immediate practical result of this contribution should be a renewed and increased effort to improve the hydrodynamics of the impeller and perhaps the surrounding fluid passages of regenerative pumps. It is indeed somewhat surprising to find no signs of major improvements in the experimental unit described by the authors unless this design was frozen prior to the establishment of the working hypothesis described in the present paper.

It is because the writer is convinced of the intrinsic value of this paper that he feels compelled to point out a few facts that may well be regarded as shortcomings of the present treatment.

The writer feels that the value of this paper could be distinctly enhanced if its principal line of reasoning were compared clearly with the more or less established theory of this type of pumps which may be described here as "turbulent-drag theory." In fact, the present treatment appears to depart from the turbulent-drag theory principally by the attempt to calculate, by means of the theory of centrifugal pumps, the mass exchange between the rotor and the stationary passages in terms of steady fluid motions, in contrast to the random-mass-exchange concept of the turbulent-drag theory. This attempt of rationalization is unquestionably valuable and appears, by the comparison with test results, as more or less successful although it still necessitates the use of empirical factors (such as the circulatory flow loss, etc.). Nevertheless, there is no reason why the new theory cannot be reconciled with the turbulent-drag theory, and may perhaps be recognized as its logical extension.

To make this point clearer it is necessary to mention a few concepts and results of the turbulent-drag theory. To do so the writer has, so to speak, started from scratch as he feels there are others far more qualified than he is to present the *existing* background of past work in this field.

It will be assumed the turbulent shear stress is proportional to the peripheral velocity of the runner U times the difference between that velocity and the mean peripheral velocity of the flow outside of the runner $(U - V_t)$. This shear stress acts on an area proportional to the radius of the runner squared r^2, whereas the opposing peripheral pressure gradient acts on the cross-sectional area of the stationary passage A. On the basis of this simple concept one arrives at the following results

$$\frac{\psi}{K_1} = \left[\frac{r^2}{A}\left(1 - \frac{Q}{Q_e}\right)\right]\left[1 - K_2\frac{(Q/Q_e)^2}{1 - Q/Q_e}\right] \quad [22]$$

and

$$\eta = \frac{Q}{Q_e}\left[1 - K_2\frac{(Q/Q_e)^2}{1 - Q/Q_e}\right] \quad [23]$$

The constant K_1 is, so to speak, a turbulent-drag coefficient and includes also constants dictated by the chosen definition of the pressure (or head) coefficient ψ. Q/Q_e has the same meaning as in the paper and is used here as a dimensionless expression of the pump capacity (in preference to ϕ). The constant K_2 is essentially the peripheral head-loss coefficient k of the paper divided by K_1 and a numerical as well as a form coefficient.

The efficiency, Equation [23], herewith, expresses primarily the simple fact that the hydrodynamic force is applied at the peripheral velocity of the runner but is made effective only at the peripheral velocity V_t of the flow in the casing passage. This simple effect of the "slip" of a turbulent-drag pump is also expressed by the corresponding Equation [10] of the paper; i.e., this principle is maintained by the centrifugal-pump theory presented by the authors except that the physical simplicity of this principle is less evident in the centrifugal-pump theory than in the drag theory.

What, then, are the differences between the centrifugal-pump and the turbulent-drag theories? The writer is convinced there are important differences and is asking the question only to stimulate the search for a comprehensive answer. One difference can be pointed out here; namely, the conditions at the extreme capacity $Q = Q_e$ for which the drag theory gives, with $K_2 = 0$ (no through-flow head loss), the familiar limit of $\psi = 0$ (zero pump head) at $\eta = 100$ per cent. The centrifugal-pump theory approaches (under the same idealizing condition) the limit of standard centrifugal-pump operation with $Q_e = Q$ and $gH = \sigma U_2^2 - \alpha U_1^2$ (see Equation [8] of the paper for $k = 0$), thus expressing correctly the effect of admitting the flow at the inner radius r_1 of the impeller and discharging from its outer periphery, r_2.

The derivations given in this paper reveal another fact of great potential significance; namely, that the flow outside of the impeller is necessarily "rotational" in the sense of an inherent departure from the potential flow pattern, going completely beyond the familiar effects of fluid friction. This fact is expressed by the first equation following Equation [5] of the paper, but one does not receive the impression that its importance has been fully appreciated. It should be noted that the vorticity of this flow, given by $\frac{dV_t}{dr} + \frac{V_t}{r}$, is of first order of magnitude, expressing indeed the very difference in action between the regenerative pump and the standard centrifugal pump for which $dp/d\theta = 0$. The writer suspects that this vorticity is responsible for the fact that the pump model suggested by the authors does not approach 100 per cent efficiency with diminishing flow losses (H_e and H_t), except in the limit of $Q = Q_e$. In other words, it is felt that H_t and H_e, as defined and used in this paper, do not give a complete picture of the mechanism of hydrodynamic losses in this type of pump.

The uniform distribution of vorticity as given in the paper goes together with the somewhat questionable assumption of continuous distribution of $dp/d\theta$ made in the derivation of Equations [2], [3], and [4]. Considering the inlet and discharge configurations, this condition cannot be satisfied for any flow condition where $Q/Q_e > 0$ and becomes increasingly inaccurate with increasing values of Q/Q_e. Correspondingly, the vorticity $(dV_t/dr) + (V_t/r)$ is really not uniformly distributed but appears primarily in form of vortex sheets separating the successive loops of

[11] Director and Professor, Garfield Thomas Water Tunnel Division, Ordnance Research Laboratory, The Pennsylvania State University, University Park, Pa. Mem. ASME.

the helically winding flow through the pump. This realization invites, of course, the thought of return vanes in the stationary passages of the pump, replacing the "free" vortex sheets by "bound" vorticity at the vanes. The most immediate application of this thought should be an analysis of a pump with stationary vanes which, in the opinion of the writer, would contribute much to the clarification of the theory of regenerative pumps, dividing it into three related lines of approach, namely, the turbulent-drag theory, the centrifugal-pump theory with continuous stationary passage, and the theory of a re-entrant centrifugal pump with separated return passages.

In closing, the writer would like to express the hope that this paper will stimulate further investigations of the theory and flow mechanism of regenerative pumps, as one cannot help but feel that this general type of turbomachinery is as yet quite far from its ultimate state of development. However, it is felt that such advancements cannot be completed by intuitive invention only but are in need of guidance by rigorous analysis such as initiated by this paper.

Authors' Closure

The discussers have been unanimous in their concerns with the relationship of our hypothesis of regenerative-pump operation to previously published theories. They have, in fact, made substantial contributions to the clarification of this relationship for which the authors are grateful, because there is some justice in Professor Wislicenus' suggestion that this was properly our task. At a recent meeting, Dr. Senoo contributed a very complete comparison of the several hypotheses that have been advanced. We need to add only a few words to this rather extensive treatment of the topic:

If the hypotheses are in competition they must be compared as to (1) their practical utility in predicting the performances of new pumps and (2) their contributions to a detailed understanding of the internal phenomena which will lead to design optimizations or useful fundamental modifications. We hold that our theory is at least an aid to prediction having a very direct applicability to geometries which can be interpolated between those tested and affording a high level of qualitative guidance outside the regime. (Unfortunately, no "complete" theory which is independent of empirical data has yet been offered.) A comparative weakness of our method in this first respect is its relative complexity. This defect has been remedied in part[12] but it is, at best, more involved than the simple theories.

On the other hand, this greater complication is viewed as an inevitable price for superiority in the second respect, i.e., in the development of a more precise understanding of the pump's mechanics. The quite detailed picture provided of the fluid kinematics and of the several resistances to flow are thought to be indicative of means for improving the pump and for adapting it to new applications. In contrast, the turbulence and shear theories merely suggest that greater roughness or turbulence-intensification are desirable without defining the means for improvement.

This claimed superiority actually exists *if* the flow pattern hypothesized is really a good approximation to what goes on within the pump. The data presented are thought to afford a reasonable verification of the basic soundness of the concept; however, Professor Iversen has argued the existence of the circulatory flow which is central to our theory. Since we have "seen" this flow we are skeptical of any demonstration of its nonexistence. The argument presented depends on the introduction of simplifications of the analysis, namely, the assumptions that $\sigma r_2^2 = r_1^2$, and that $k_1/k_2 = 1$. These plausible approximations wash out the driving potential for the circulatory flow which depends upon a relatively small difference between large quantities.

An equally effective simplification having a more rational basis than the substitution of an equal sign for the phrase "is of the order of" is that the average tangential velocity in the open channel equals the arithmetic mean of V_{t_1} and V_{t_2} or

$$Q = 1/2\, Q_s \left(\sigma + \frac{r_1}{r_2}\,\alpha\right)$$

If this expression is compared with Equation [6] of the paper it is seen that this assumption is equivalent to the simplifications

$$K_1 = \frac{r_0}{r_2} \text{ and } \frac{K_2}{K_1} = \frac{r_2}{r_1}$$

The equalities are closely checked by numerical evaluations of Equations [6a].

Professor Iversen calls attention to the maximum in the circulatory-flow losses and correctly attributes this to a reduction in circulatory-flow rate at lower flows. This is accounted for by the fact that when α becomes negative the centrifugal field in the open channel increases rather than decreases with algebraically decreasing α; thus the driving potential and the circulatory flow decreases as shutoff is approached. The statement "an increase in pressure rise requires an increase in the rate of circulatory flow, a greater reduction of the tangential velocity from the exit of the rotor to its entrance or both" is not, however, negated, because the tangential velocity at the entrance to the rotor continues to decrease algebraically as the shutoff is approached.

Dr. Senoo's correlation of our analysis and his on the grounds of momentum exchange is appreciated. The complication of Equation [6] may be simplified without much loss in accuracy by using the above approximation. The definition of dimensionless parameters suggested in point 2 of his discussion has been found to be more appropriate, than the ones defined in the paper. The possibility of improvements of pump performance by modifying the inlet and exhaust ports as suggested is very interesting and apparently consistent with our hypothesis.

Professor Wilson is grappling with a dilemma which plagued the authors for some time. The same issue can be raised in another form: without reference to the detailed kinematics of flow the limiting efficiency of the pump can be shown to be Q/Q_s; where, then, in the assumptions underlying our hypothesis is the inevitability of losses implied? The answer is in assumption 8, $dp/d\theta$ = constant. This assumption has the corrolary $dQ_c/d\theta$ = constant which is to say that there is no acceleration of the circulatory flow in the linear region. In the absence of parasitic resistance to the circulatory flow the postulated spatial steadiness would not exist. This means that a restriction is placed on the degree of idealization which is consistent with our hypothesis. On the other hand, we do not agree that "— obviously there would be energy losses in transferring momentum from the liquid ejected from the impeller into the slower moving main stream." Although we have spoken of the circulatory flow and the tangential flow in a way which suggests that they are distinct, V_t and V_c are actually defined as components of the helical flow. This helical flow is the *entire* flow and no mixing of circulatory and tangential flows is implicit in the hypothetical model. There seems to be no inevitability of losses associated with tangential deceleration as a consequence of the tangential pressure gradient.

It is suggested that Equation [9] and [10] could be more simply derived from the hypothesis that the power required to drive the pump is the "ideal" value plus a loss proportional to the flow

[12] Discussion by M. A. Santalo of "A Comparison of Regenerative Pump Theories Supported by New Experimental Data," by Y. Senoo, ASME Paper No. 55—SA-44.

squared. This is surely true, and although Professor Wilson has not indicated its derivation, his definition of "ideal" power can be arrived at more directly than indicated in the paper.

The term "hydrodynamic" used in connection with the reference to the conformance of regenerative-pump performance to familiar similitude relationships was not intended as a differentiation from the "Turbulent" characterization. If the turbulence hypothesis was truly descriptive of the pumping mechanism the affinity laws would be just as applicable, as Professor Iversen indicated in his paper.

The authors hope that they or some other investigators will have the opportunity to follow up on Professor Wilson's several interesting suggestions for further experimental investigations.

We must apologize to Professor Wislicenus (and others) for not having wrought significant improvements in the pump. Our efforts will be of little value until they lead to such improvement. This apology does not extend to our failure to investigate the benefits of stationary vanes. This is certainly a challenging topic, but the introduction of vanes into the open channel will so alter the character of the pump as to constitute a really distinct area of investigation. The distinction is more profound, we think, than merely effecting a binding of vortexes. The question of the significance of this vorticity is related to Professor Wilson's comments which have already been discussed. It is to be expected that if a complete momentum balance of the control volume of Fig. 5 were developed based on an absence of radial shear forces, the vorticity would disappear. So would the assumptions that $dQ_e/d\theta$ is a constant. Our hypothesis is tied to "real" pumps through this implicit assumption of radial losses. We believe, therefore, that the losses associated with the vorticity are, in fact, incorporated in the H_e and "shock" losses. On the other hand, the question of how the relationship of these losses to those experienced in other fluid dynamic devices is influenced by the vorticity remains unanswered and intriguing.

Predictor Control Optimalizes Control-System Performance

By L. M. SILVA,[1] FULLERTON, CALIF.

A new technique for the design of automatic-control systems with nearly optimum transient response has been developed. The fundamental concept in the new method is that the control or forcing of the output member must be performed in such a manner that the error or deviation and its derivatives should be reduced to zero in three steps for third and higher-order systems. These three steps consist of a single period of maximum corrective action which forces the controlled variable in the direction of decreasing error or deviation, a single period of maximum corrective action in the opposite sense to decelerate the controlled variable, and finally a force-free period at the end of which the error and its derivatives simultaneously go to zero. In the practical embodiment of this mode of control a proportional control action exists during the final phase. During this proportional control period, the controller corrects any errors introduced by the instrumentation during the initial phases. In addition to the superior transient performance, a predictor-control system has the advantage that its response is not affected by variations in gain, if the gain is sufficiently large, and that the allowable gain in the proportional region is considerably in excess of that permitted in conventional linear-type systems. As a result, the steady-state accuracy which can be obtained is not dependent on a critical gain setting and the system response and accuracy are not degraded by the incorporation of variable gain elements.

Introduction

AUTOMATIC-CONTROL systems are essentially devices for controlling the source of power which is supplied to the load or output member. The classical automatic-control-system design techniques are based on considerations of stability and disregard the power limitations of the source, despite the fact that the size of the source is the basic economic factor in the design of the system. The transient and steady-state performance of an automatic-control system is fundamentally limited by the characteristics and limitations of the power source and the nature of the load. The specification of the power source and the load represent the "fixed elements" of the system which have to be accepted in the design. Given these fixed elements, then the design of an optimum control system requires the synthesis of an operator which controls the power supplied to the load and which will provide for the maximum utilization of the power source.

The design of a predictor-control system is based on the foregoing considerations and will result in an optimum system with minimum time response for input or load disturbances. In order to gain insight into the mode of operation of a predictor-control system, assume that an error or a deviation of the controlled variable from the controlling variable exists. If this error is to be reduced to zero in a minimum time, the controller must apply a maximum corrective action to the process to reduce this error to zero as rapidly as possible. Since the process contains energy-storage elements, it is necessary to remove the corrective action before the error is reduced to zero to prevent the controlled variable from overshooting the desired reference value. If, during this second phase, a maximum negative corrective action is applied to the process, then it can be shown that the control system (1 to 3)[2] has an optimum transient response. The block diagram of a second-order predictor-control system is given in Fig. 1(*a*).

In this paper the order of the control system refers to the order of the differential equation describing the dynamics of the process. Fig. 1(*b*) illustrates the response of the system for a sudden change in the reference value, and Fig. 1(*c*) describes the corrective action which is applied to the process to correct for the error introduced by the change in the magnitude of the controlling variable or reference.

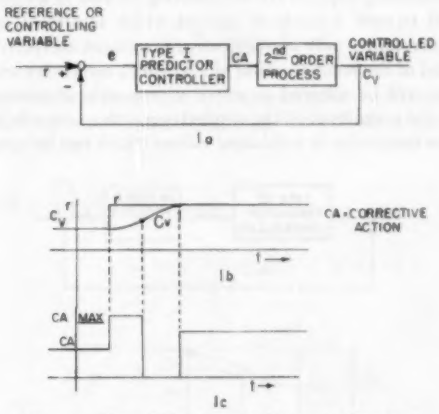

FIG. 1 TYPE I PREDICTOR-CONTROL SYSTEM

From Figs. 1(*b* and *c*) it can be seen that the predictor controller applies a sustained maximum corrective action in order to reduce the deviation to zero as rapidly as possible. During the second phase a maximum negative corrective action is applied. At the end of the second phase the error or deviation is zero and the controller furnishes the output necessary to maintain the controlled variable at the new reference level.

A Mechanical Analogy. A mechanical analogy of the control action just described can be obtained from the following simple example: Assume that the objective of the control system is the maintenance of a fixed relation between an automobile and a reference line drawn across the road. For example, let the condition of zero deviation be represented by the vertical alignment of the bumper on the automobile with the reference line. Now, if it is assumed that a new reference line is introduced which is at some distance from the present position of the automobile, the

[1] Senior Engineer, Beckman Instruments, Inc.

Contributed by the Instruments and Regulators Division and presented at the Annual Meeting, New York, N. Y., November 28–December 3, 1954, of THE AMERICAN SOCIETY OF MECHANICAL ENGINEERS.

NOTE: Statements and opinions advanced in papers are to be understood as individual expressions of their authors and not those of the Society. Manuscript received at ASME Headquarters, August 26, 1954. Paper No. 54—A-132.

[2] Numbers in parentheses refer to the Bibliography at the end of the paper.

driver of the automobile must reduce the deviation to zero by means of a single period of maximum acceleration (accelerator on floor board) and a single period of maximum braking. The driver is thus faced with the problem of predicting when he should remove his foot from the accelerator and apply the brakes. In order to determine this point, he requires a knowledge of the magnitude of the braking force, the distance of the bumper from the reference line, the mass of the automobile, and the effects of windage and friction. If he had this information at his disposal, it is conceivable that he could perform the necessary computations and determine when to apply the brakes. In the control system described in Fig. 1 the controller is furnished the necessary information and the system operates in the described manner.

Higher-Order Control Systems. For a general nth order control system, it can be shown that the total number of periods of maximum corrective action are equal to the order of the differential equation of the process. Thus a fourth-order process ideally would require four periods of alternate corrective action in order optimally to reduce to zero deviations due to the excursions of the controlling variable. Although it is possible to construct a controller which will perform in this ideal manner for 3rd and higher-order systems, the cost and the amount of equipment required become prohibitive. In the case of these higher-order systems, it is found that the complexity of controller instrumentation is the result of demanding theoretically optimum performance.

In particular, it is usually found that only the first two or three of the n-periods of corrective action are long and that the $(n-2)$ or $(n-3)$ remaining periods are successively shorter in length. Thus one is led to seek a mode of control which is almost optimum and which requires only two periods of maximum corrective effort. At the end of the second period of maximum corrective action the controller will be allowed to enter a proportional-control mode in which the magnitude of the applied corrective action is less than either the maximum or minimum values which can be applied.

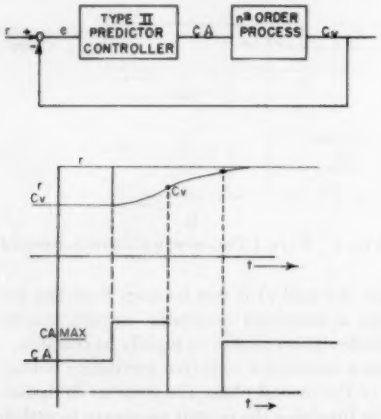

Fig. 2 Type II Predictor-Control System

Types of Predictor-Control Systems. Fig. 2 illustrates this type of predictor-control system which will be referred to as Type II. For purposes of identification a predictor-control system which operates in the optimum manner (n-corrective action periods for an nth-order system) will be called a Type I predictor controller. Although the Type II control mode is not theoretically optimum, it is found that in practical applications the response of the Type II controller is as good or better than its optimum Type I counterpart. This situation results from the fact that it is practically impossible to reverse the corrective action at exactly the correct time, due either to errors in the information furnished to the controller or to errors introduced by the controller itself.

In a Type I controller these errors are corrected after the n-corrective action periods with the result that the response time can be degraded seriously. In the case of the Type II controller the final phase is theoretically force free (no corrective action) and it is found that the controller corrects its error during this final phase by entering a proportional-control mode and that the performance of a practical controller is in close agreement with its theoretical analysis.

Type II Predictor Controller

In the previous section a Type II predictor controller was defined and it was pointed out that the control action for an nth-order system consists of two periods of maximum corrective action followed by a force-free or proportional phase. The functions performed by the controller may be subdivided into two convenient parts. The A part of the controller is a device for furnishing information about the error and its derivatives to the B part. The B part consists of a nonlinear network or mechanism which determines the polarity of the corrective action applied to the process. In addition, it is necessary to incorporate amplification means for driving the element which furnishes power to the process. These elements are illustrated in Fig. 3. The term

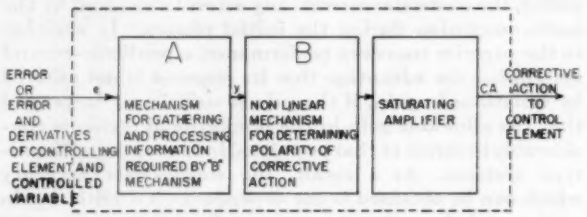

Fig. 3 Elementary Predictor Controller

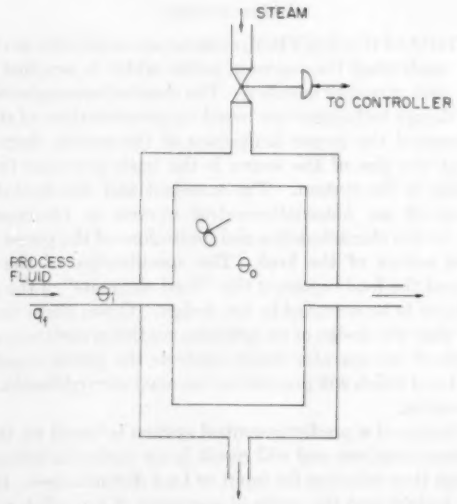

Fig. 4 Heat Exchanger

"saturating amplifier" is used to denote a means of amplification which has a maximum and a minimum output level and which can provide any output intermediate to these two extremes.

In order to illustrate the technique for deriving the operations which must be performed by the A and B mechanisms, consider a third-order system consisting of a heat exchanger and a steam

valve, illustrated in Fig. 4. The differential equation for this system is derived in the Appendix. In the block diagram given in Fig. 5 the saturation or limiting characteristic of the valve has been replaced by the saturation levels of the amplifying means in the controller. It is assumed that these saturation levels coin-

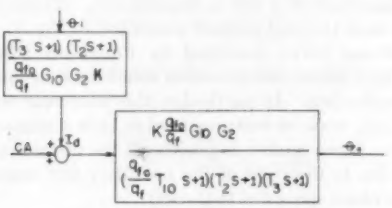

θ_o = OUTPUT TEMPERATURE, CONTROLLED VARIABLE.
θ_i = INPUT TEMPERATURE, °C.
q_f = VOLUMETRIC FLUID FLOW m^3/sec
q_{fo} = MEAN FLOW RATE.
T_{10}, T_2, T_3 = SYSTEM TIME CONSTANTS.
K, G_{10} = GAIN CONSTANTS.

FIG. 5 HEAT EXCHANGER AND VALVE—BLOCK DIAGRAM

cide with the energization required to position the valve to its two extreme positions. Under these circumstances the maximum and minimum levels of corrective action exist when the steam valve is either wide open or closed, and the nonlinear limiting characteristic of the valve does not appear in the block diagram or in the differential equation of the process. In order to discuss the effects of load changes, the volumetric fluid-flow coefficient q_f has been retained in the transfer functions of the system.

From the block diagram in Fig. 5 the differential equation of the system can be written down in operational form

$$\left(\frac{q_{fo}}{q_f} T_{10}S + 1\right)(T_2S + 1)(T_3S + 1)\theta_o(S) = K \frac{q_{fo}}{q_f} G_{10}G_2(CA + I_d) \quad [1]$$

Let

r = reference or controlling variable
e = deviation or error

Then

$$e = r - \theta_o \quad [2]$$

If the relation given in Equation [2] is substituted into Equation [1] the differential Equation [3] for the error is obtained

$$\left(\frac{q_{fo}}{q_f} T_{10}S + 1\right)(T_2S + 1)(T_3S + 1)e(S) = -K \frac{q_{fo}}{q_f} G_{10}G_2(CA + I_d) + f(S)r \quad [3]$$

where

$$f(S) = \left(\frac{q_{fo}}{q_f} T_{10}S + 1\right)(T_2S + 1)(T_3S + 1) \quad [4]$$

Equation [3] indicates that the error or deviation of the process is described by the same differential operator as that of the controlled variable θ_o and that the corrective action applied to the error equation consists of the negative of the actual corrective action, $CA + I_d$, applied to the process plus a term consisting of the reference or input quantity and its derivatives. In most process applications, the reference is a fixed quantity and hence its derivatives are zero.

Thus

$$f(S)r = r \text{ (for regulatory systems)} \quad [5]$$

Type II Predictor-Control System. In a Type II predictor-control system it can be shown that an operator for the B mechanism can be derived from any two of the n-system time constants and that the operator for the A mechanism or the information required by the B mechanism is derived from the remaining $(n-2)$ time constants. The technique for deriving the B operators analytically has been presented in the various references (4, 5, 6.) In this paper a derivation will be presented by means of the two dimensions y-$\dot{y}$ phase plane, where the variable y represents the information required by the B section.

Since the system under consideration has three time constants (3rd-order differential equation) it will be necessary to choose two of these for the derivation of the B operator. In general, it is found that the two longest-system time constants should be used for the B operator. The use of any other combination of two of the time constants also will yield a Type II predictor operator. However, the transient response of the control system will be appreciably slower than that which is obtained if the two longest time constants are employed in the B part. If it is assumed that the two longest time constants are

$$\frac{q_{fo}}{q_f} T_{10} \text{ and } T_2$$

then the remaining time constant T_3 will appear in the A operator in the following simple manner.

Let

$$y = (T_3 S + 1)e(S) \quad [6]$$

$$y = T_3 \frac{de}{dt} + e \quad [7]$$

If the relations given in Equations [5] and [6] are substituted into Equation [3] the differential Equation [8] for the y variable is obtained

$$\left(\frac{q_{fo}}{q_f} T_{10}S + 1\right)(T_2 S + 1)y(S) = -K \frac{q_{fo}}{q_f} G_{10}G_2(CA + I_d) + r \quad [8]$$

Let

$$\left.\begin{aligned} F &= +K \frac{q_{fo}}{q_f} G_{10}G_2(CA + I_d) - r \\ T_1' &= \frac{q_{fo}}{q_f} T_{10} \end{aligned}\right\} \quad [9]$$

Then

$$T_1'T_2 \frac{d^2y}{dt^2} + (T_1' + T_2) \frac{dy}{dt} + y = -F \quad [10]$$

Since

$$\frac{d^2y}{dt^2} = \ddot{y} = \dot{y} \frac{d\dot{y}}{dy} \text{ where } \dot{y} = \frac{dy}{dt}$$

Then

$$T_1'T_2\dot{y} \frac{d\dot{y}}{dy} = -F - (T_1' + T_2) \frac{dy}{dt} - y \quad [11]$$

$$\frac{d\dot{y}}{dy} = \frac{-F - (T_1' + T_2) \frac{dy}{dt} - y}{T_1'T_2\dot{y}} \quad [12]$$

Equations [10], [11], [12] are second-order differential equations which can be solved analytically. However, it is convenient at present to consider the solutions of Equation [12] in the y-$\dot{y}$ phase plane.

Equations in Phase Plane. The solutions of an equation in the phase plane are given by the trajectories of the system. In particular, since the corrective action which is to be applied to the process and which is included in the F-term can only assume either one of two values F_{max} or F_{min} during transient disturbances, all of the solutions of this equation can be represented by two families of curves in the y-$\dot{y}$ phase plane. The symbols F_{max} and F_{min} refer to the magnitude of the term F when the corrective action is a maximum (valve wide open) or a minimum (valve closed).

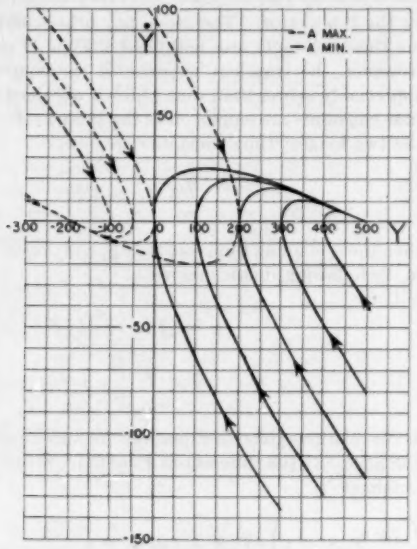

FIG. 6 TRAJECTORIES OF SYSTEM IN y-$\dot{y}$ PHASE PLANE

Fig. 6 illustrates the solution of Equation [12] for

$$\begin{aligned} T_1' &= +10 \text{ sec} \\ T_2 &= 5 \text{ sec} \\ F_{max} &= +500 \\ F_{min} &= -200 \end{aligned}$$

The analytic expression which describes the curves in Fig. 6 which pass through the origin is

$$\left.\begin{aligned} (y + 5\dot{y})^2 - Fy &= 0 \\ (y + 5\dot{y})^2 - 500y &= 0 \quad F_{max} \\ (y + 5\dot{y})^2 + 200y &= 0 \quad F_{min} \end{aligned}\right\} \quad \ldots\ldots\ldots\ldots [13]$$

The trajectories of the system which are given in Fig. 6 describe the instantaneous value of the variable y and $\dot{y}$. If the initial values of y and $\dot{y}$ and the magnitude of the corrective term F are specified then this locates the system on the particular trajectory in the phase plane which it will follow as long as the magnitude of F remains fixed. Of all the possible trajectories of the system only two, those which pass at some future time through the origin of the phase plane, are of interest. The significance of these trajectories lies in the fact that if the initial value of the variables y and $\dot{y}$ coincides with either of these trajectories and if the indicated corrective action is applied, then the system will at some future time pass through the origin of the co-ordinates at which time $y = \dot{y} = 0$. If the corrective action is removed at this time $F = 0$

$$(\text{note } CA = -I_d + \frac{q_f}{q_{fo}} \frac{\tau}{KG_{1c}G_2})$$

then the magnitude of y and $\dot{y}$ remains zero. These two trajectories have been isolated and are presented in Fig. 7.

The nonlinear curve described by Equations [13] and presented in Fig. 7 defines the operation which must be instrumented in the B mechanism. In particular, this nonlinear relation of y and $\dot{y}$, $NL(y\dot{y})$, must be instrumented in such a manner that the output of the B mechanism is positive if the instantaneous value of y and $\dot{y}$ lies to the right of the boundary and negative if the point in the phase space lies to the left.

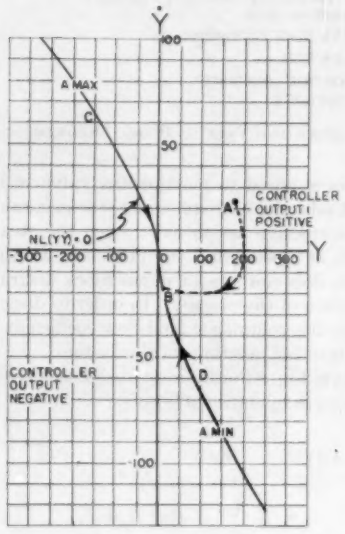

FIG. 7 NONLINEAR POLARITY DETERMINING BOUNDARY IN y-$\dot{y}$ PHASE PLANE

Next, it is necessary to investigate the relationship between the y-variable and the error or deviation and to consider how the foregoing results can be applied. The y-variable was defined in terms of the error in Equation [7]

$$y = T_3 \frac{de}{dt} + e, \quad \dot{y} = T_3 \ddot{e} + \dot{e} \ldots\ldots\ldots\ldots [7]$$

From Equation [7] it is evident that if the error, error derivative, and error acceleration are positive then y and $\dot{y}$ are positive. Under these circumstances, the point y-$\dot{y}$ will lie to the right of the boundary and the B mechanism in conjunction with the high-gain amplification means will apply the maximum positive corrective action to the process. This will cause the operating point of the system in the y-$\dot{y}$ phase plane to follow one of the trajectories of Fig. 6 toward the boundary in the phase plane. This is illustrated in Fig. 7 by the trajectory labeled AB. However, as soon as the AB trajectory crosses the COD boundary the corrective action will reverse itself and the system will follow the DBO trajectory into the origin. At this time the output of the B mechanism will go to zero and remain zero as long as the values of y and $\dot{y}$ remain zero (no new disturbances).

Thus far it has been demonstrated that, if the information contained in y is furnished to the B mechanism, it is possible to apply corrective action to the process in an optimum manner in order to

reduce y and $\dot{y}$ to zero as rapidly as possible. In addition, it was shown that y and $\dot{y}$ would remain zero if the corrective action was removed at the time $y = \dot{y} = 0$. In order to illustrate the manner in which the error goes to zero after the total corrective action is removed

$$CA = -I_d + \frac{r}{KG_{10}G_2}\frac{q_f}{q_{fo}}$$

it is necessary to include the initial conditions in Equation [3] and investigate the results

$$\left.\begin{aligned}(T_1'S+1)(T_2S+1)(T_3S+1)e(S) &= T_3[T_1'T_2S^2 + (T_1'+T_2)S+1]e(0)\\ &+ (T_1'+T_2)[T_3\dot{e}(0)+e(0)]\\ &+ T_1'T_2S[T_3\dot{e}(0)+e(0)]\\ &+ T_1'T_2[T_3\ddot{e}(0)+\dot{e}(0)]\end{aligned}\right\} \ldots [14]$$

If the initial conditions, Equation [15], are substituted into Equation [14], Equation [16] is obtained.

$$\left.\begin{aligned} y(0) &= 0 \quad T_3\dot{e}(0)+\dot{e}(0) = 0\\ \dot{y}(0) &= 0 \quad T_3\ddot{e}(0)+\dot{e}(0) = 0\\ F &= 0\end{aligned}\right\} \ldots\ldots [15]$$

$$e(S) = \frac{T_3(T_1'S+1)(T_2S+1)e(0)}{(T_1'S+1)(T_2S+1)(T_3S+1)} = \frac{T_3}{(T_3S+1)}e(0) \quad [16]$$

Thus Equations [14], [15], [16] indicate that if $y = \dot{y} = 0$ and if $F = 0$, then the error goes to zero with a single time-constant response. It should be noted that the time constant in this response is the same one, T_3, that appeared in the A-network or mechanism. In general, it can be shown that the response of the system during the final phase ($F = 0$) is described by the inverse of the linear differential operator appearing in the A-network or mechanism.

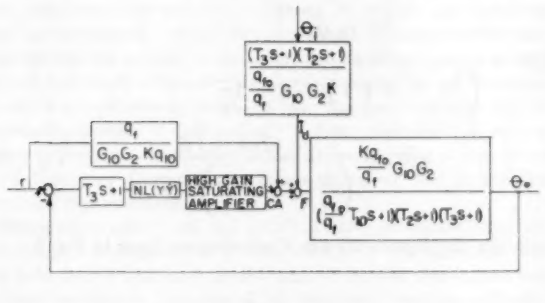

FIG. 8 TYPE II PREDICTOR-CONTROL SYSTEM

The block diagram of the complete predictor-control system is given in Fig. 8. In the figure an additional parallel or feedforward path has been added to the output of the amplifier. The purpose of this branch is to supply the corrective action necessary to maintain the steady-state value of θ_o. Thus, since $F = 0$ during steady-state operation

$$F = CA - \frac{q_f r}{G_1G_2Kq_{fo}} + I_d = 0 \ldots\ldots [17]$$

and since $CA = 0$, it is necessary to furnish an additional corrective action equal to

$$+\frac{q_f r}{G_1G_2Kq_{fo}} - I_d \ldots\ldots [18]$$

to the process. In practice, it is found that these extra terms can be ignored and that the controller will furnish the required energization.

PERFORMANCE AND CHARACTERISTICS OF A PREDICTOR-CONTROL SYSTEM

One of the interesting characteristics of the ideal predictor-control system illustrated in Fig. 8 is the fact that the performance of the ideal system is predicated on the existence of infinite gain around the loop. This condition results from the fact that it was assumed the corrective action would reverse itself for an arbitrarily small displacement of the operating point from the boundary in the y-$\dot{y}$ phase plane. In practice, it has been possible to build these systems with loop gains (for zero error) of the order of 10 to 100 times that which is permissible for an equivalent linear-control system which is stable. In addition, it was found that the system performance was not affected by variations in loop gain of the order of 10 to 1. The actual amount of loop gain which can be employed is influenced by the method of instrumenting the various operators.

In all of the systems that have been built the operations indicated by the blocks in the controller were performed with passive RC networks and thyrite resistors. Since these passive networks introduce phase lag it is to be expected that they will restrict the amount of gain which can be employed. However, in all of the applications to date the gain was limited by the combined action of noise and the saturation characteristic of the amplifier and it was not possible to obtain an unstable configuration.

If the performance of a Type II predictor controller is compared with that of the best linear system which operates with the same power limitation as the predictor controller, it is found that the transient-response time to 2 per cent error for the predictor controller is from 30 to 60 per cent shorter than that of the linear system. This figure applies for input disturbance or a change in the value of the reference. In the case of load disturbances, it is not possible to quote a theoretical figure since the predictor performance in this respect is closely related to the mode of instrumentation and the loop gain (for zero error). The ideal predictor-control system would have zero displacement or deviation for load changes since it would be able to detect these changes instantly and apply appropriate corrective action. In the practical systems which have been built the derivation of the controlled variable has been less than 1 per cent of its magnitude for load changes of 20 to 30 per cent (e.g., $q_{fo}/q_f = 1.30 = 30$ per cent load change).

CONCLUSION

A new technique for the design of automatic-control systems with nearly optimum transient response has been developed. The fundamental concept in the new method is that the control or forcing of the output member must be performed in such a manner that the error or deviation and its derivatives should be reduced to zero in three steps for third and higher-order systems. These three steps consist of a single period of maximum corrective action which forces the controlled variable in the direction of decreasing error or deviation, a single period of maximum corrective action in the opposite sense to decelerate the controlled variable, and finally a force-free period at the end of which the error and its derivatives simultaneously go to zero. In the practical embodiment of this mode of control a proportional-control action exists during the final phase. During this proportional-control period, the controller corrects any errors introduced by the instrumentation during the initial phases.

In addition to the superior transient performance, a predictor-control system has the advantage that its response is not affected by variations in gain, if the gain is sufficiently large, and that the allowable gain in the proportional region is considerably in excess

of that permitted in conventional linear-type systems. As a result, the steady-state accuracy which can be obtained is not dependent on a critical gain setting and the system response and accuracy are not degraded by the incorporation of variable gain elements.

BIBLIOGRAPHY

1 "A Phase Plane Approach to the Compensation of Saturating Servomechanisms," by A. M. Hopkins, AIEE Technical Paper 51-103, 1951.

2 "Multiple Mode Operation of Servomechanisms," by Donald McDonald, Cook Research Laboratories Report, 1953.

3 "The Application of Non-Linear Techniques to Servomechanisms," by K. C. Mathews and R. C. Boe, Cook Research Laboratories Report, 1953.

4 "Non-Linear Optimization of Relay Servomechanisms," by L. M. Silva, MS thesis, University of California, Department of EE, Berkeley, Calif., 1953.

5 "Non-Linear Optimization of Relay Servomechanisms," by L. M. Silva, University of California, Institute of Engineering Research Report, series 60, issue 106, April 15, 1954.

6 "Predictor Servomechanisms," by L. M. Silva, Trans. IRE, Circuit Theory, vol. CT-1, no. 1, March, 1954, pp. 56–70.

Appendix

In order to derive the differential equation for the heat exchanger and steam valve define the following variables:

ϕ = temperature of steam chamber
C_f = specific heat of process fluid, cal/kg deg C
d_f = density of fluid, kg/m³
V = volume of fluid chamber
θ_o = temperature of outgoing fluid
= temperature of fluid in chamber
θ_i = temperature of incoming fluid
q_f = volumetric fluid flow, cu m/sec
q_{fo} = mean fluid flow rate, cu m/sec
α = over-all heat-transfer coefficient, cal/m² deg C sec
A = area of walls of fluid chamber, m²

$$T_1 = \frac{V}{q_f} = \frac{T_{10}q_{fo}}{q_f}$$

$$T_{10} = \frac{V}{q_{fo}}$$

$$G_1 = \frac{\alpha A}{q_f d_f c_f} = \frac{G_{10}q_{fo}}{q_f}$$

$$G_{10} = \frac{\alpha A}{q_{fo} d_f c_f}$$

L = latent heat of steam, cal/kg
q_s = steam flow, kg/sec
C = equivalent heat capacity of steam chamber, cal/deg C

$$T_2 = \frac{+C}{\alpha A}$$

K = gain constant in valve equation

$$G_2 = \frac{L}{\alpha A}$$

If it is assumed that the energy leaving the system in the condensate is negligible and that the fluid is agitated so that the temperature in the chamber is uniform, then the energy input per unit time due to the steam flow must equal the rate of increase of energy stored in the chamber plus the rate at which energy is carried out of the chamber by the flow of the process fluid

$$c_f d_f V \frac{d\theta_o}{dt} + q_f d_f c_f (\theta_o - \theta_i) = \alpha A(\phi - \theta_o) \quad [19]$$

Equation [19] can be written in terms of the parameters T_1 and G_1 in the following manner

$$\frac{T_1}{1 + G_1}\frac{d\theta_o}{dt} + \theta_o = \frac{G_1}{1 + G_1}\phi + \frac{1}{1 + G_1}\theta \quad [20]$$

A similar expression is obtained from the energy relations existing in the steam chamber

$$C\frac{d\phi}{dt} + \alpha A(\phi - \theta_o) = q_s L \quad [21]$$

Equation [21] can be expressed in terms of the parameters T_2 and G_2

$$T_2\frac{d\phi}{dt} + \phi = G_2 q_s + \theta_o \quad [22]$$

If ϕ is eliminated from Equations [20] and [22], the second-order differential equation of the heat exchanger is obtained

$$T_1T_2\ddot{\theta}_o + [(1 + G_1)T_2 + T_1]\dot{\theta}_o + \theta_o = G_1G_2q_s + T_2\dot{\theta}_i + \theta_i \quad [23]$$

If the T_1 ti ne constant is expressed in terms of T_{10}, q_{fo}, and q_f, and if it is assumed that G_1 is small compared to unity, then Equation [23] can be written

$$T_2T_{10}\frac{q_{fo}}{q_f}\ddot{\theta}_o + \left(T_2 + T_{10}\frac{q_{fo}}{q_f}\right)\dot{\theta}_o + \theta_o = \frac{q_{fo}}{q_f}G_{10}G_2q_s + T_2\dot{\theta}_i + \theta_i \quad [24]$$

If Equation [24] is written in terms of Laplace transform operator S and the initial conditions are assumed zero, then the transfer function of the heat exchanger is obtained

$$\theta_o(S) = \frac{\frac{q_{fo}}{q_f}G_{10}G_2}{\left(\frac{q_{fo}}{q_f}T_{10}S + 1\right)(T_2S + 1)}q_s(S) + \frac{(T_2S + 1)\theta_i}{\left(\frac{q_{fo}}{q_f}T_{10}S + 1\right)(T_2S + 1)} \quad [25]$$

Equation [25] is presented in block-diagram form in Fig. 9.

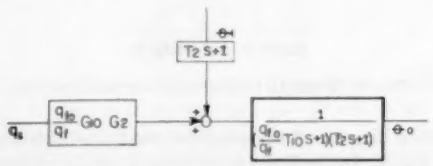

FIG. 9 BLOCK-DIAGRAM REPRESENTATION OF HEAT EXCHANGER

If it is assumed that the motion of the valve can be described by a first-order differential equation characterized by a time constant T_3, then the relation between the controller output x and the steam flow q_s can be written

$$T_3\frac{dq_s}{dt} + q_s = Kx \quad [26]$$

where

x = input to valve motor
q_s = steam flow

If Equations [24] and [26] are combined, the single third-order differential equation for the process is obtained. The block diagram for the process including the steam valve and its limiting

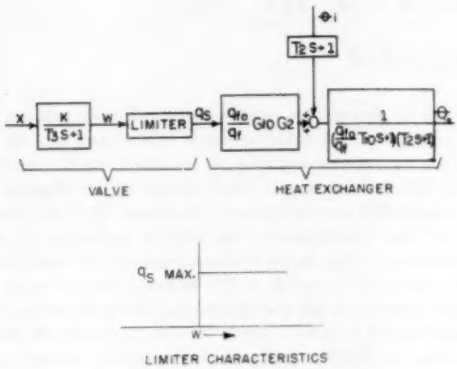

FIG. 10 PROCESS BLOCK DIAGRAM

characteristics is given in Fig. 10. If the value of the x-variable is restricted to the range

$$0 \leq x \leq \frac{q_{s\,max}}{K}$$

then it is possible to place the limiter ahead of the block representing the transfer function of the valve.

Discussion

RUFUS OLDENBURGER.[3] In studying this excellent paper, I was very interested to note the manner in which the nonlinear field has developed. Some 10 years ago I began work in this field, establishing the nature of the optimum transients for an aircraft propeller control, where during the transients the servo runs at all times at full speed, in which case the governor operates for practical purposes at full power. A few years ago I developed rather extensively the theory of this approach, and at the Woodward Governor Company we made what we feel is a rather thorough experimental study of it.

Three years ago I told the ASME-IRD Executive Committee that I hoped eventually to write a book on a new automatic-control field that I had been developing. I do not now expect ever to have the time to take out of my industrial work to write that book. This year I suggested to the ASME-IRD Executive Committee that the 1956 IRD conference be devoted to nonlinear theory partly because I felt that the work we had been doing, which is proprietary, would be at the point where we would be willing to publish a paper on it; and a number of others, also active in the nonlinear approach, would be ready to report. This proposal was approved by the committee. The conference will be held in the spring of 1956.

I wish to make some general remarks on the power-saturation approach. For third-order systems there are optimum transients for which the controller power must not be a maximum. By "optimum transient" I mean one where equilibrium is reached in a minimum time after a sudden disturbance, with a minimum overswing, etc. Fortunately, for the kinds of transients that occur normally, optimum power is indicated. For the third-order case one must control on the basis of two functions. I call these functions Σ_1 and Σ_2. I proved by mathematical techniques that one can, for practical purposes, replace Σ_1 by Σ_2, so that the control is based on one controlling function.

If a system has very small lags the writer's nonlinear approach is effective in improving the performance of a linear system over linear controls involving the same derivatives in the controlling function. If the lags are larger, this approach gives satisfactory results except that if the lags are great enough, or at least if the lag T_3 is great enough, a linear controlling function involving the same derivatives will give just as good transients as the nonlinear function. It takes an extra operation to form the nonlinear function. If the lags are great enough a linear one is what one should use; that is, the linear function is a good enough approximation to the nonlinear function so that a linear controlling function should be employed. This does not mean that for large disturbances one will not be operating at full power.

In our experimental work instability due to extra lags was a major limitation. Noise was also a serious limitation.

As I see it there are two new promising areas of automatic control. They are the nonlinear theory which Hopkins, MacDonald, Silva, Bogner and Kazda, others and myself have been developing; and the statistical approach so well publicized by Wiener. I include the information theory of Shannon in the statistical approach. Eventually these approaches may be combined.

O. J. M. SMITH.[4] The author has done an excellent job of presenting the nonlinear predictor control of a three-time-constant process. The second-order control of a higher-order process uses only two maximum force trajectories, at the end of which it leaves the process with no transient energy stored in two of the dynamic time constants. All other time constants have energy and contribute to the force-free transient.

The two time constants which should be controlled are those with the maximum K^2T, where T is the time constant and K is the root-locus or s-plane residue at the pole $s = 1/T$. These two are not always the two longest time constants, as assumed in Equations [6] and [7].

When there are three or more time constants of almost equal K^2T (equal transient energy storage) the system error at the end of the two maximum force trajectories is not small enough for the start of a force-free transient, and there will be two or more additional maximum force trajectories. In this case, Type II control may not be so good as the more complicated Type I control.

AUTHOR'S CLOSURE

Mr. Oldenburger's discussion of the third-order case using Σ_1 and Σ_2 is true for systems which possess an integral term.

The next problem discussed involves the situation in which the T_3 lag is large. If the magnitude of T_3 is less than, or equal to, T_1 or T_2 then the response of the predictor system is in all instances superior. In the event T_3 is larger than T_1 or T_2, it is necessary to alter the instrumentation and to include the two longest-system time constants in the nonlinear B mechanism of the control and put the shortest of the three time constants in the A mechanism. These same considerations are amplified in Professor Smith's comments.

[3] Director of Research, Woodward Governor Company, Rockford, Ill. Mem. ASME.

[4] Instituto Tecnológico de Aeronáutica, São Paulo, Brazil.

The Effect of Wheel-Work Conformity in Precision Grinding

By R. S. HAHN,[1] WORCESTER, MASS.

The conformity between wheel and work is defined in terms of the trochoidal work surface at the region of engagement. Experimental results are presented for a variety of wheels which show that the rate of metal removal varies as the 0.18 power of the curvature difference. Two modes of grinding action are recognized, one in which stock removal is proportional to work speed and independent of wheel speed and the other where the reverse is true. A mechanism of grinding action is proposed and a theoretical formula relating rate of stock removal to normal force and curvature difference is derived which in certain respects agrees remarkably well with experiment.

Nomenclature

The following nomenclature is used in the paper:

- Δ = curvature difference
- R_t = radius of curvature of trochoid
- N = rotary speed of wheel
- n = rotary speed of work
- $\eta = N/n$ = speed ratio
- R = work radius
- a = wheel radius
- $\rho = R/a$ = work-wheel ratio
- S = $\frac{\text{wheel surface speed}}{\text{work surface speed}}$ in surface grinding
- γ = experimentally determined exponent of Δ
- σ = grain-surface density (grains per unit of wheel area)
- ξ = variable thickness of interference region (Fig. 11)
- F_n = normal force on wheel
- ν = fraction of grains that carry load
- $\mathfrak{R}$ = rate of metal removal
- p_0 = maximum penetration
- k = spring constant of grain mounting

Introduction

The main purpose of precision-grinding operations, carried out in the machine shop, is to produce accurate workpieces all of a uniform size and in a reasonably short time. On certain types of automatic precision-grinding machines the finished size of the workpiece is indirectly related to the stock-removing ability of the grinding wheel. In other words, if the grinding wheel acts more free-cutting at one time than another, there is likely to be a small and unwanted fluctuation in workpiece size. In internal grinding it is known that a wheel which nearly fills the hole acts differently from a smaller wheel in the same hole. The purpose of this paper is to present experimental and analytical results concerning the action of grinding wheels under various conditions of conformity.

[1] Consulting Engineer, The Heald Machine Company. Mem. ASME.

Contributed by the Research Committee on Metal Processing and presented at the Annual Meeting, New York, N. Y., November 28–December 3, 1954, of The American Society of Mechanical Engineers.

Note: Statements and opinions advanced in papers are to be understood as individual expressions of their authors and not those of the Society. Manuscript received at ASME Headquarters, September 20, 1954. Paper No. 54—A-178.

Wheel-Work Conformity

A measure of the wheel-work conformity is the difference in curvature of the wheel and of the workpiece in the region of contact upon which the wheel is operating. Since the locus of a point on the wheel relative to the workpiece is either a prolate hypotrochoid or epitrochoid (depending upon whether external, internal, climb grinding, or conventional grinding) the wheel is actually being pressed against a trochoidal surface. Consequently, let Δ, the curvature difference, be defined by

$$\Delta = \frac{1}{a} - \frac{1}{R_t} \quad \ldots\ldots [1]$$

where R_t is the radius of curvature of the trochoidal surface. Figs. 1 and 2 show the motion of a grinding grit relative to the workpiece for the external and internal grinding processes. The generating circles are shown for both conventional and climb grinding. Since the arc of contact between wheel and work is very small the parametric equations for the trochoidal path can be reduced to

$$\text{External} \qquad \frac{y}{a} = \frac{(1-\eta)^2 - (1+\rho)}{2(\rho+\eta)^2}\left(\frac{x}{a}\right)^2 \quad \ldots\ldots [2]$$

$$\text{Internal} \qquad \frac{y}{a} = \frac{(1+\eta)^2 - (1-\rho)}{2(\rho+\eta)^2}\left(\frac{x}{a}\right)^2 \quad \ldots\ldots [3]$$

$$\text{Surface} \qquad \frac{y}{a} = \frac{S^2}{2(1+S)^2}\left(\frac{x}{a}\right)^2 \quad \ldots\ldots [4]$$

where η and S are positive for conventional grinding and negative for climb grinding. From these equations the radius of curvature of the trochoidal path is readily found and when substituted in Equation [1] yields the following expressions for the curvature difference

$$\text{External} \qquad \Delta_e = \frac{1}{a}\left[\frac{(\rho+1)(\rho+2\eta)}{(\rho+\eta)^2}\right] \quad \ldots\ldots [5]$$

$$\text{Internal} \qquad \Delta_i = \frac{1}{a}\left[\frac{(\rho-1)(\rho+2\eta)}{(\rho+\eta)^2}\right] \quad \ldots\ldots [6]$$

$$\text{Surface} \qquad \Delta_s = \frac{1}{a}\left[\frac{1+2S}{(1+S)^2}\right] \quad \ldots\ldots [7]$$

It will be readily appreciated that at very low work speeds ($\eta \to \infty$) the wheel tends to grind its own curvature into the workpiece thereby making the difference in curvature Δ approach zero. On the other hand, we should expect that as the work speed increases ($\eta \to 0$) to very high values the curvature difference Δ should approach the simple geometric value of

$$\Delta = \frac{1}{a} \pm \frac{1}{R}$$

where R is the geometric radius of the workpiece. Formulas [5], [6], [7] behave in exactly this way. Fig. 3 illustrates the variation of Δ_i with speed ratio η for a specific wheel and work size. In the experimental work that follows it will be shown that the cutting rate of the wheel is a function of the curvature difference.

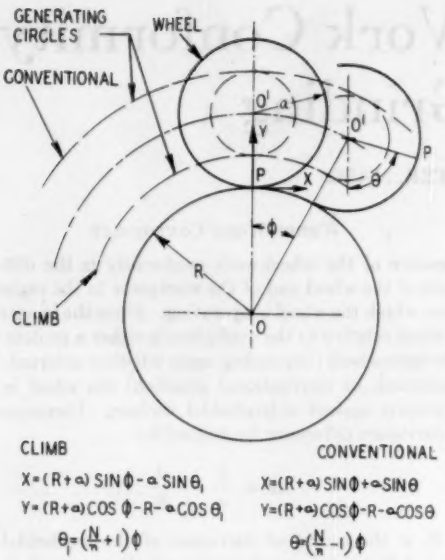

FIG. 1 TROCHOIDAL LOCUS OF GRAIN RELATIVE TO WORK—EXTERNAL GRINDING

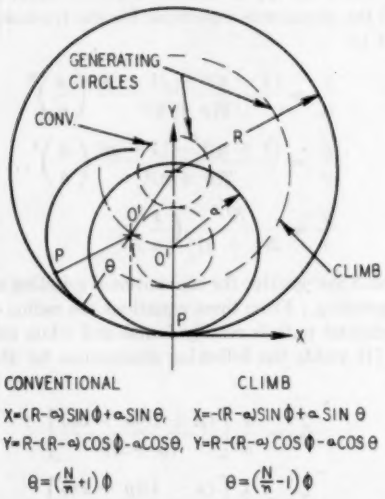

FIG. 2 TROCHOIDAL LOCUS OF GRAIN RELATIVE TO WORK—INTERNAL GRINDING

EXPERIMENTAL RESULTS

Several years ago extensive tests were made covering a variety of wheels and work materials and ranging from internal grinding through external grinding. In these tests the wheel was pressed against the workpiece with a prescribed force. In order to minimize the effect of changes in wheel surface during grinding the tests were arranged so that any point on the wheel did not work for more than about 100 revolutions. The arrangement is shown in Fig. 4. By using narrow workpieces combined with relatively long (wide) wheels, sufficient change in work size occurred, as the wheel progressed axially through or across the work, permitting the rate of metal removal to be calculated with reasonable accuracy. The wheel was gently released radially onto the work and retracted from the work at the beginning and end of the stroke. Repeat passes of the wheel across the workpiece could be made to assess the progressive changes in the cutting ability of the wheel. For example, Fig. 5 shows the progressive dulling of a coarsely dressed wheel compared with the progressive self-sharpening of the same wheel when dressed very slowly.

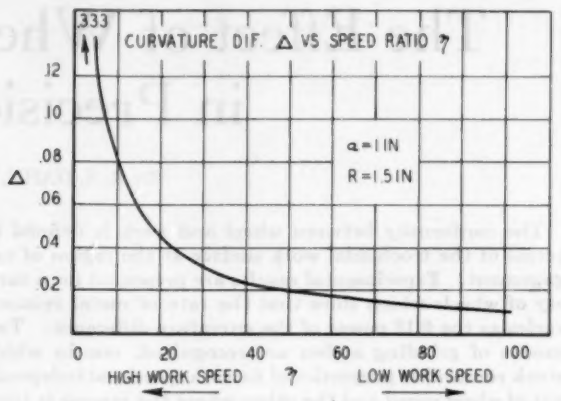

FIG. 3 ILLUSTRATION SHOWING VARIATION OF CURVATURE DIFFERENCE WITH SPEED RATIO FOR 2-IN. WHEEL GRINDING IN 3-IN. HOLE

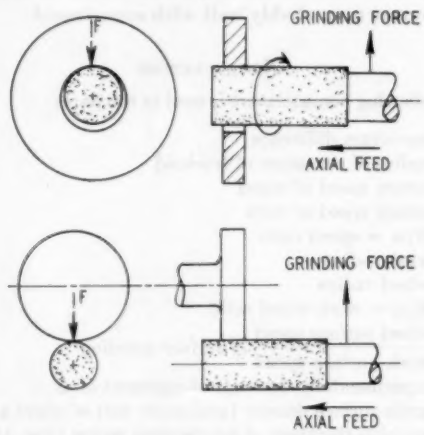

FIG. 4 ARRANGEMENT FOR INTERNAL AND EXTERNAL GRINDING WITH MINIMUM OF WHEEL DULLING

The results of a typical run from internal grinding through external grinding are shown in Fig. 6. Here nine passes are made through the hole starting with a wheel that barely enters the hole. The rate of metal removal is shown plotted against curvature difference on log-log paper. The next group of points represents five passes through a larger hole. The last two groups of points at the right represent five passes apiece across two external workpieces. In this way it was found that the rate of metal removal varied with curvature difference in a linear manner when plotted on log-log paper.

Fig. 7 shows similar data for three values of normal force. It will be noticed that the slope of each line is essentially equal and it will be recalled that the slope on log-log paper is equivalent to the exponent γ to which the curvature difference must be raised in the relation

$$\Re = f(F_n \Delta^{\gamma}) \quad [8]$$

A set of carefully controlled aluminum-oxide wheels was furnished by the Norton Company. These wheels were tested as described and a graph similar to Fig. 6 was made for each type

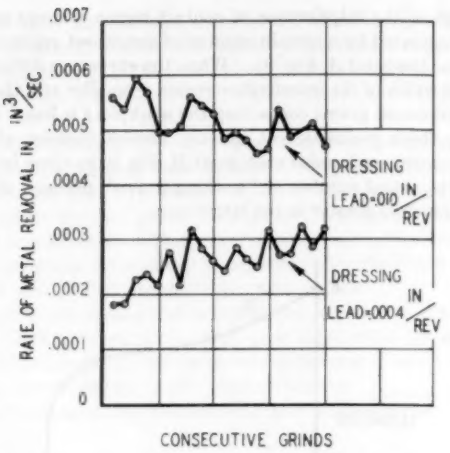

FIG. 5 PROGRESSIVE CHANGES IN CUTTING ABILITY OF GRINDING-WHEEL SURFACE; WORK—SAE 4150, 47-52C; WHEEL—38A60-LSVBE

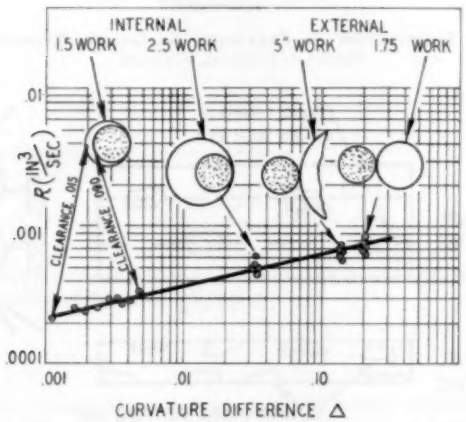

FIG. 6 RATE OF METAL REMOVAL VERSUS CURVATURE DIFFERENCE WHERE WORK SIZE IS CHANGED FROM INTERNAL TO EXTERNAL GRINDING

of wheel. The exponent γ was measured from these graphs and the results are summarized in Table 1.

TABLE 1 SUMMARY OF EXPONENT γ MEASUREMENTS

Wheel	Exponent γ	Wheel	Exponent γ
60I8	0.185	60K8	0.185
60J8	0.154	60K7	0.184
60J8	0.187	60K6	0.171
60K8	0.185	60K5	0.144
60L8	0.196	60K5	0.220
60L8	0.221		
	Avg = 0.188		Avg = 0.181

There does not seem to be any systematic variation of γ with either wheel hardness or structure.

The foregoing tests show that the rate of metal removal, under constant normal force, varies as the 0.18 power of the curvature difference. In these tests the curvature difference was varied by changing essentially the work size R and wheel size a. It will be noted from Equations [5], [6], [7] that the speed ratio η also influences the curvature difference. In some earlier tests which had been run in ignorance of the curvature-difference effect, Fig. 8 was obtained, which shows, that under a constant force, the rate

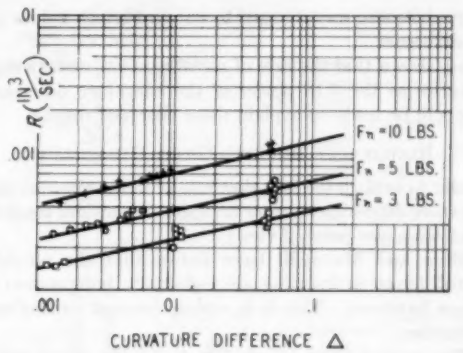

FIG. 7 RATE OF METAL REMOVAL VERSUS CURVATURE DIFFERENCE FOR SEVERAL VALUES OF NORMAL FORCE

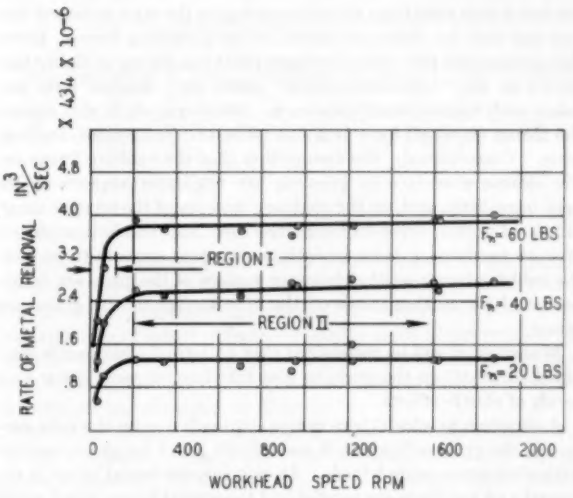

FIG. 8 RATE OF METAL REMOVAL VERSUS WORK SPEED; WORK—SAE 4150, 47-52C ROCKWELL, 3½ ID × 2 IN. WIDE; WHEEL—60L4, 2¾ IN. × 1¼ IN. × ⅞ IN.

of metal removal first varies linearly in Region I with work speed and later becomes nearly independent of work speed (Region II). The grinding in Region I is analogous to the usual plane-milling process in that rate of stock removal is determined by the table-feed rate. However, suppose the table-feed rate is increased to very large values. Assuming that the milling cutter did not break, the arbor would spring up somewhat and the cutter teeth would take consecutive gouges out of the work which would be spaced considerably in the direction of feed. Under these conditions the rate of metal removal would be independent of table-feed rate but would depend on cutter speed. Consequently, we should expect to find in grinding two regions, one in which the rate of metal removal is proportional to work speed and independent of wheel speed (Region I) and the other in which the rate of metal removal (barring and dulling effects) is proportional to wheel speed and independent of work speed (Region II).

Stated in another way, when the work speed is low (Region I) the wheel tends to grind its own curvature into the work and the curvature difference is very small. As work speed is increased the curvature difference increases and increased rate of metal removal results. The data of Fig. 8 when plotted on log-log paper against curvature difference yield a slope or exponent $\gamma = 0.17$ which is in good agreement with the previous data where the

geometric hole size was changed to obtain various values of curvature difference.

Having shown that the rate of metal removal, under a constant force, varies as the 0.18 power of the curvature difference, an attempt will be made to explain these observed results.

Resiliently Mounted Grain Hypothesis

In order to explain the fact that rate of metal removal depends on curvature difference it seems desirable to consider the grinding process from a new point of view:

(*a*) Shaw and Marshall[2] have shown that the normal and tangential forces in grinding are essentially independent of the workpiece hardness. This is in strong contrast to single-point-tool behavior.

(*b*) The normal force in grinding is usually about twice the tangential force,[2] whereas in single-point machining the reverse is true.

In single-point theory the assumption is usually made that the tool forces arise from the chip bearing on the rake surface of the tool and that the clearance surface is free of rubbing forces. Even this assumption falls down in single-point machining as Hahn[3] has shown in the "transition region" when very shallow cuts are taken with tools of small clearance. Furthermore, in this region the thrust (normal) force is about twice the (tangential) cutting force. Consequently, the assumption that the rubbing forces on the clearance surface in grinding are negligible appears to be very unrealistic, and, on the contrary, because of the relative magnitude of normal force to tangential force and the independence of work hardness, a more realistic assumption appears to be that the rubbing forces on the clearance surface of the grain are dominant and the cutting forces on the rake surface of the grain are minor.

Moreover, it will be recognized that no formal clearance is provided (dressed) on the grain so that interference must occur as a result of elastic effects.

A situation in which there are no cutting forces on the rake surface of the grain will occur, if one tries to grind tungsten carbide with aluminum-oxide wheels. In this case no metal at all is removed and yet there are normal and tangential forces which must originate entirely on the clearance surface.

In order to explain the curvature-difference effect it is necessary to consider not only the normal load to be carried on the clearance surface of the grain but, in addition, the elastic mounting of the grain. It is found that the modulus of elasticity of the bulk wheel is about $1/5$ that of steel and the modulus of the bond about $1/3$ that of steel while the modulus of the grain is nearly twice that of steel. Consequently, compared to steel, the wheel (vitreous bonded) behaves as a relatively flexible matrix with rigid grains embedded therein.

It will be assumed in the analytical work to follow that adjacent grains are mounted on springs but are uncoupled; i.e., force applied to one grain will not deflect an adjacent grain. A third feature to be considered is that in all probability the clearance surfaces of all surface grains of the wheel do not lie in exactly the same cylindrical surface; i.e., some will be a little high and some a little low. The asperities of surface roughness are known to follow a distribution curve of the type shown in Fig. 9, and it must be expected that the grains of a wheel follow a similar curve.

Now, to explain the fact that rate of metal removal increases with increasing curvature difference under the same normal force consider the following: When the curvature difference is small, the width of the interference or contact region is large and the load is supported by a certain number of outermost grains (grains lying near the point *A*, Fig. 9). When the curvature difference is large the width of the interference region is smaller and the number of outermost grains contacting the workpiece is less. Consequently, these grains deflect radially inward thereby allowing new lower-disposed grains such as at *B*, Fig. 9, to come into contact. The actual number of "working grains" per unit of wheel area is therefore greater in the latter case.

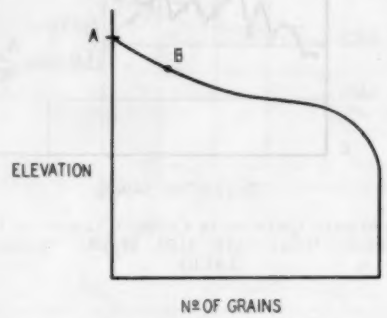

Fig. 9 Distribution in Elevation of Grains Relative to True Cylindrical Surface

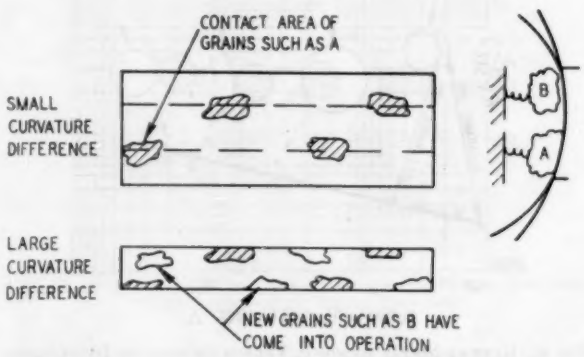

Fig. 10 Grain Density in Interference Area

Fig. 10 represents a plan view of the interference region for small and large curvature difference. In view of the foregoing there are more active grains in a wheel when the curvature difference is large than when small even though the same normal force is placed upon the wheel and it is, presumably, for this reason that rate of metal removal increases.

Analytical Considerations

It will be the objective of this section to develop a formula relating the rate of metal removal to the normal force and curvature difference.

Consider first a grinding wheel with the grains disposed relative to a datum cylinder according to Fig. 9. In any cross section of this wheel we will find some outermost grains such as at *A* and considerably more lower set grains such as at *B*. For purposes of analysis we may consider a hypothetical wheel in which the high grains have been shifted toward one end and the low grains toward the other end of the wheel, giving a rearranged wheel of the shape shown in Fig. 11(*a*). This rearranged wheel will have load-carrying and stock-removing characteristics equivalent to the actual disarranged wheel. As the normal force is increased, more and more of the right-hand portion of the wheel will cut;

[2] "Forces in Dry Surface Grinding," by E. R. Marshall and M. C. Shaw, Trans. ASME, vol. 74, 1952, pp. 51–59.

[3] "Metal-Cutting Chatter and Its Elimination," by R. S. Hahn, Trans. ASME, vol. 75, 1953, pp. 1073–1080.

in other words the effective width of the wheel becomes variable.

Fig. 11 (*b* and *c*) show the wheel penetrating the workpiece by the amount p_{oz}. The penetration is taken as a linear function of z with slope h as shown. The interference region *A-E-B-D* is shown.

In actual grinding we will suppose that m grains (where $m = 2\pi a\sigma dz$) of the wheel in some elemental section dz, on the average traverse some locus such as *A-C-B* but for analytical purposes we will consider that νm grains are very dull and traverse the path *A-E-B* and serve to support the normal load. The remaining $(1 - \nu)m$ grains we consider to be exceedingly sharp and to traverse the path *A-D-B* and serve to remove stock.

By using the concept of a rearranged wheel and the idea of "pure" load-carrying grains and pure stock-removing grains it is possible to derive a relation involving the rate of stock removal and the normal force and curvature difference.

The thickness of the interference region is found to be

$$\xi = p_{oz} - \frac{x^2}{2}\,\Delta \qquad [9]$$

where

$$p_{oz} = p_o - hz \qquad [10]$$

The width of any element dz is given by

$$b = 2\sqrt{\frac{2p_{oz}}{\Delta}} \qquad [11]$$

The load supported is found from

$$F_n = 2\int_0^{z=\frac{p_o}{h}} \int_0^{x=\frac{b_o}{2}} k\xi\nu\sigma\, dx\, dz \qquad [12]$$

Using Equations [9] and [10], integrating and eliminating b_o with the aid of Equation [11], gives

$$F_n = \frac{\sqrt{2}}{3}\,\frac{k\nu\sigma}{h}\,\frac{p_o^{5/2}}{\Delta^{1/2}} \qquad [13]$$

Next, consider the volume swept out by a stock-removing grain of triangular profile Fig. 10 (*d*). The volume of a scratch at any section z is

$$V_s = 2\int_0^{\frac{b}{2}} \xi^2 \tan\theta\, dx \qquad [14]$$

Using Equations [9] and [11] and integrating gives

$$V_s = \frac{16\sqrt{2}}{15}\tan\theta\,\frac{(p_{oz})^{5/2}}{\Delta^{1/2}} \qquad [15]$$

for the volume of an individual grain scratch.

The rate of metal removal is found by

$$\Re = N\int_0^{\frac{p_o}{h}} (1-\nu)\sigma 2\pi a\, V_s\, dz \qquad [16]$$

which gives, using Equations [15] and [10], after integration

$$\Re = \frac{32\sqrt{2}}{105}(2\pi aN)\,\frac{(1-\nu)\sigma}{h}\,\frac{\tan\theta}{\Delta^{1/2}}\,p_o^{7/2} \qquad [17]$$

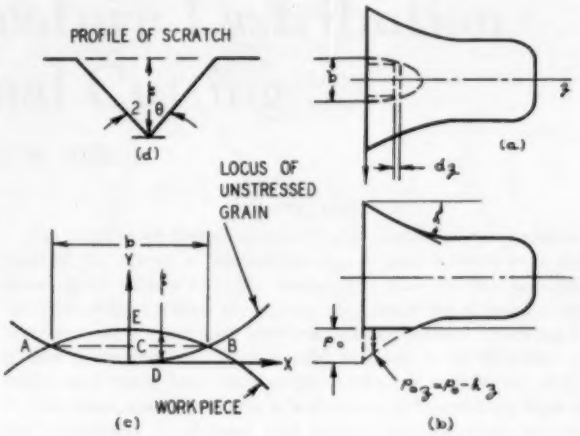

FIG. 11 HYPOTHETICAL REARRANGED WHEEL

By eliminating p_o from Equations [13] and [17] there results

$$\Re = \frac{32\sqrt{2}}{105}(2\pi aN)\,\frac{(1-\nu)\sigma}{h}\tan\theta\left[\frac{3}{\sqrt{2}}\,\frac{h}{k\nu\sigma}\right]^{7/5} F_n^{1.4}\Delta^{0.2}$$

or

$$\Re = KF_n^{1.4}\Delta^{0.2} \qquad [18]$$

Equation [18] relates the rate of metal removal to the normal force and the curvature difference. The surprising result is that the theoretical expression shows the rate of metal removal varying with the curvature difference raised to the 0.20 power while the experimental work shows the power to be 0.18. The fact that such close agreement is obtained must mean that the underlying hypothesis has some degree of truth.

It will be noted, however, that $\Re$ varies with the normal force to the 1.4 power. This is contrary to experiment where the exponent is unity. Consequently, a more perfect theory should yield

$$\Re = KF\Delta^{0.2} \qquad [19]$$

It may be that the assumption of uncoupled grains and the assumption that the rake surface forces are negligible are not exactly true.

CONCLUSION

From the experimental work it would seem that the cause for the different grinding action in holes and externally is due to the curvature difference, where the curvature of the actual trochoidal path is considered. Also, there appear to be two types of grinding, Region I where the process is similar to milling and Region II where it is not.

By assuming the clearance surface of the grain to be under load and the rake surface essentially free of force, at least in the normal or radial direction, and by considering a rearranged wheel with load-carrying grains and stock-removing grains, surprisingly good agreement is found with experiment relating the rate of metal removal to the curvature difference.

Shear-Plane Temperature Distribution in Orthogonal Cutting

By J. H. WEINER,[1] NEW YORK, N. Y.

An analytical solution is presented for the temperature distribution along the shear plane in orthogonal cutting. The principal assumption made is that the heat transferred by conduction in the direction of motion of the workpiece or chip may be neglected. The nature of the error involved in this assumption is investigated. The over-all fraction of shear-plane heat transferred into the workpiece is also computed and compared with previous results.

Nomenclature

The following nomenclature is used in the paper:

- k = thermal conductivity of metal, Btu/in. sec deg F
- ρ = density of metal, lb/cu in.
- c = specific heat of metal, Btu/lb deg F
- α = thermal diffusivity of metal, $k/\rho c$, in^2/sec
- t = depth of cut, in.
- L = length of shear plane, in.
- ϕ = shear angle
- ψ = tan ϕ
- q = heat release over shear plane, Btu/in^2 sec
- W = cutting velocity, ips
- V = chip velocity, ips
- x = distance from leading edge of shear plane in direction of workpiece motion, in.
- y = distance from leading edge of shear plane perpendicular to direction of workpiece motion, in.
- $z = y - \psi x$
- ξ = distance from leading edge of shear plane along shear plane, in.
- $\sigma = W\xi/2\alpha$
- $\lambda = WL/2\alpha$
- $C = \frac{1}{2}\psi\sqrt{\frac{W}{\alpha}}$
- u = temperature rise above initial temperature, deg F
- $T = W\rho cu/q$
- $Y = W\xi\psi^2 \cos\phi/4\alpha$
- $Y_L = WL\psi^2 \cos\phi/4\alpha$
- $f(x)$ = net fraction of shear-plane heat transferred into workpiece at x
- β = over-all fraction of shear-plane heat transferred into workpiece
- R_t = thermal number, Wt/α
- erf x = error function, $\frac{2}{\sqrt{\pi}}\int_0^x e^{-u^2}\,du$
- erfc x = complementary error function, $1 - \text{erf } x$
- $K_0(x)$ = modified Bessel function of second kind of zero order

[1] Assistant Professor, Department of Civil Engineering and Engineering Mechanics; Assistant Technical Director, Heat and Mass Flow Analyzer Laboratory, Columbia University.

Contributed by the Research Committee on Metal Processing and presented at the Annual Meeting, New York, N. Y., November 28–December 3, 1954, of The American Society of Mechanical Engineers.

Note: Statements and opinions advanced in papers are to be understood as individual expressions of their authors and not those of the Society. Manuscript received at ASME Headquarters, July 21, 1954. Paper No. 54—A-65.

Introduction

The cutting of metals involves large inelastic deformations, most of the energy of these appearing as heat released over the shear plane. Even with the assumption that the rate and distribution of heat release are known, the calculation of shear-plane temperatures is a complex heat-conduction problem involving as it does a moving-band heat source, inclined to its direction of travel, and losing heat both to the workpiece and to the chip. Furthermore, the chip moves in a direction different from that of the workpiece. It appears that drastic simplifications are required before a mathematical solution may be obtained.

Four analyses of the temperature distribution along the shear plane in orthogonal metal-machining operations have appeared recently: Hahn (1),[2] Chao and Trigger (2), Leone (3), Loewen and Shaw (4). The first two analyses start with the same simplified model of the process, namely, that of a band source of heat moving through an infinite medium, where the plane of the band source is inclined to its direction of motion. Hahn considers the temperature along the band source as representing directly the temperature along the shear plane, while Chao and Trigger multiply this temperature by an empirical constant representing the fraction of heat generated along the shear plane which flows into the workpiece. It is seen that Hahn's solution does not take into account the different directions of motion of chip and workpiece, while that of Chao and Trigger assumes that the fraction of heat generated which is transferred into the workpiece is constant along the length of the shear plane. The latter two studies are also similar to each other in that they consider only mean temperatures of shear plane and chip, equating these two quantities to determine the distribution of heat generated between workpiece and chip.

The present analysis avoids the just-mentioned simplifications, which it is felt introduce considerable error, at the expense of making a new simplification, which it is hoped does not. The simplification consists in neglecting the transfer of heat by conduction in workpiece and chip in the direction of their respective motions in comparison with the heat transferred by material transport in those directions and the heat conducted in the direction perpendicular to the direction of motion. This assumption results in considerable mathematical simplification, changing the character of the partial differential equations from elliptic to parabolic.

While this assumption is a common and understandable one in the study of heat transfer in a flowing fluid, it seems unusual when the moving medium has the high conductivity of a metal. In order to estimate the magnitude of the error introduced in this manner, the problem of the inclined band source moving through an infinite medium treated by Hahn, and Chao and Trigger is solved with this assumption, and the solution compared with that which includes the effect of conduction in the direction of motion. This comparison, made in the Appendix to this paper, indicates that for the conditions encountered in practice, the two solutions for this problem agree very well. Since this problem is similar to the metal-cutting process it seems reasonable to hope that there, too, the assumption introduces little error. It is recognized,

[2] Numbers in parentheses refer to the Bibliography at the end of the paper.

however, that reasoning by analogy in this manner is sometimes misleading. Rigorous upper bounds on the error introduced by this assumption appear to be difficult to obtain, but would be very valuable, particularly since the same procedure introduces considerable simplification in many other problems involving moving sources.

Mathematical Formulation of the Problem

There are two principal zones of heat generation in orthogonal cutting, zone A, Fig. 1, caused by friction between tool and chip, and zone B, caused by the energy released in the shear deformation. This paper is concerned only with the temperature distribution along the shear plane resulting from the heat generated in zone B.

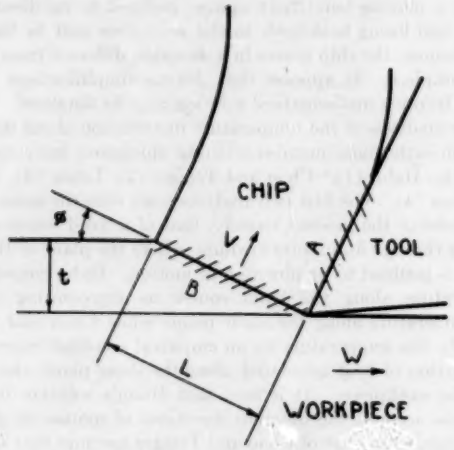

Fig. 1 Regions of Heat Generation

The following assumptions are made:

1 Heat is generated at a uniform rate q on the shear plane.
2 The thermal properties of workpiece and chip are constant.
3 The workpiece is considered semi-infinite in extent.
4 The heat flow is two-dimensional.
5 The free surfaces of the workpiece are perfectly insulated.
6 The quasi-stationary state has been reached; that is, the temperature distribution, referred to a co-ordinate system fixed with respect to the tool, is independent of time.
7 The chip velocity is perpendicular to the shear plane.
8 The transfer of heat by conduction in the direction of motion of the workpiece is small in comparison with the amount transferred by material transport and that conducted in the direction perpendicular to the direction of motion, and may be neglected. This assumption is also applied to the heat transferred in the chip in the direction of its motion.

The mathematical nature of assumption 8 may be seen more clearly by first considering the form of the partial differential equations and boundary conditions if it is not made. They then appear as follows

$$\alpha\left(\frac{\partial^2 u}{\partial x^2}+\frac{\partial^2 u}{\partial y^2}\right)-W\frac{\partial u}{\partial x}=0, \quad \text{in workpiece} \qquad [1]$$

$$\frac{\partial u}{\partial y}=0, \quad -\infty<x<0, \quad y=0 \qquad [2a]$$

$$\frac{\partial u}{\partial y}=0, \quad L\cos\phi<x<\infty, \quad y=t \qquad [2b]$$

$$k\left(\cos\phi\frac{\partial u}{\partial y}-\sin\phi\frac{\partial u}{\partial x}\right)+W\rho c\sin\phi\, u = -f(x)\,q, \quad 0<x<L\cos\phi, \quad y=\psi x \qquad [2c]$$

$$\lim_{y\to\infty} u = 0 \qquad [2d]$$

The Boundary Condition [2c] is obtained by a heat balance on a small triangular volume, Fig. 2. The heat entering the element

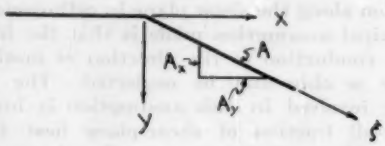

Fig. 2 Co-Ordinate Axes

from the shear plane through the area A, $Af(\bar{x})q$, is equal to the heat leaving the element through the area A_x

$$A_x\left(k\frac{\partial u}{\partial x}-W\rho cu\right)$$

and through the area A_y

$$-A_y\,k\frac{\partial u}{\partial y}$$

That is

$$Af(\bar{x})q=A_x\left(k\frac{\partial u}{\partial x}-W\rho cu\right)-A_y\,k\frac{\partial u}{\partial y}$$

where it is understood that all functions are defined at a suitably chosen mean co-ordinate. Dividing by A and taking the limit as the dimensions of the element go to zero, leads to Equation [2c].

The function $f(x)$, representing at each point of the shear plane the fraction of the heat generated which enters the workpiece, is initially unknown. It, and the temperature distribution, are determined by solving the problem given by Equations [1] and [2] simultaneously with the problem for the chip with the heat entering the chip at each point of the shear plane given by $[1-f(x)]q$.

In this form the problem is quite complex. Assumption 8 is now made. From the derivation of Equation [1] it is seen that this assumption corresponds to the omission of the term $\partial^2 u/\partial x^2$ and Equation [1] becomes

$$\alpha\frac{\partial^2 u}{\partial y^2}=W\frac{\partial u}{\partial x} \qquad [1']$$

Mathematically, this simplification is very valuable since it changes the character of the equation from elliptic to parabolic, in this case the simple one-dimensional heat equation, with the dimension x playing the role of time. Because of the change in character of the equation, the nature of the required boundary conditions also changes. It will be necessary to specify "initial conditions," that is $u(0, y)$, while it is necessary to specify the boundary conditions only over that range of x in which there is interest, that is, for $0<x<L\cos\phi$, since the boundary condition for $x>L\cos\phi$ will not affect the temperature distribution in the interval of interest.

Consistent with assumption 8, it is seen that the appropriate initial and boundary conditions are

$$u=0; \quad x=0, \quad 0<y<\infty \qquad [2'a]$$

$$-k\cos\phi\frac{\partial u}{\partial y}=q; \quad 0<x<L\cos\phi, \quad y=\psi x \qquad [2'b]$$

$$\lim_{y \to \infty} u = 0 \quad \ldots\ldots [2'c]$$

Boundary Condition [2′b] is obtained by again considering a heat balance on a small triangular volume, Fig. 2. Consistent with assumption 7, such a heat balance now yields

$$qA = -W\rho cuA_x - k\frac{\partial u}{\partial y}A_y + V\rho cuA$$

However, by means of a mass-flow balance, $W\rho A_x = V\rho A$, and therefore Equation [2′b] is obtained in the limit. It is to be noted that with this assumption the influence of the chip is given completely by the Boundary Condition [2′b] and it is not necessary to consider the chip further.

Solution of the Problem

As the first step in the solution of the problem given by Equations [1′] and [2′], the substitution $z = y - \psi x$ is made leading to

$$\alpha\frac{\partial^2 u}{\partial z^2} + W\psi\frac{\partial u}{\partial z} = W\frac{\partial u}{\partial x} \quad \ldots\ldots [1'']$$

$$u = 0; \quad x = 0, \quad 0 < z < \infty \quad \ldots\ldots [2''a]$$

$$-k\cos\phi\frac{\partial u}{\partial z} = q, \quad 0 < x < L\cos\phi, \quad z = 0 \quad \ldots [2''b]$$

$$\lim_{z \to \infty} u = 0 \quad \ldots\ldots [2''c]$$

By use of the Laplace transform with respect to the variable x

$$\bar{u}(s, z) = \int_0^\infty u(x, z)e^{-sx}\,dx$$

Equations [1″] and [2″] become

$$\alpha\frac{d^2\bar{u}}{dz^2} + W\psi\frac{d\bar{u}}{dz} - sW\bar{u} = 0 \quad \ldots\ldots [1''']$$

$$-k\cos\phi\frac{d\bar{u}}{dz} = q/s \quad \ldots\ldots [2''']$$

$$\lim_{z \to \infty} \bar{u} = 0$$

The solution of Equation [1‴] satisfying the Boundary Condition [2‴] is

$$\bar{u}(s, z) = \frac{2qCe^{-\sqrt{\frac{W}{\alpha}}(C+\sqrt{C^2+s})z}}{W\rho c\sin\phi[C + \sqrt{C^2 + s}]s} \quad \ldots\ldots [3]$$

where

$$C = \frac{1}{2}\psi\sqrt{\frac{W}{\alpha}}$$

Since the shear-plane temperatures are of primary interest, the substitution $z = 0$ is made in Equation [3] and the inverse transform of $\bar{u}(s, 0)$ is found using the known Laplace transform pair

$$\frac{1}{C + \sqrt{s}} \supset \frac{1}{\sqrt{\pi x}} - Ce^{C^2x}\operatorname{erfc}(C\sqrt{x}) \quad \ldots\ldots [4]$$

(reference 7), and the property of the Laplace transform, namely, that if $f(s) \supset F(x)$

$$\frac{1}{s}f(s + C^2) \supset \int_0^x e^{-C^2x}F(x)dx \quad \ldots\ldots [5]$$

(reference 8). In this manner the following expression for $u(x, 0)$ is obtained

$$u(x, 0) = \frac{2qC}{W\rho c\sin\phi}\left[\frac{1}{\sqrt{\pi}}\int_0^x \frac{e^{-C^2\xi}}{\sqrt{\xi}}\,d\xi - \frac{2C}{\sqrt{\pi}}\int_0^x\int_{C\sqrt{\xi}}^\infty e^{-u^2}du\,d\xi\right] \quad \ldots\ldots [6]$$

which becomes, after some manipulation

$$u(x, 0) = \frac{q}{W\rho c\sin\phi}\left[(1 + 2C^2x)\operatorname{erf} C\sqrt{x} + \frac{2C\sqrt{x}}{\sqrt{\pi}}e^{-C^2x} - 2C^2x\right] \quad \ldots\ldots [7]$$

or, introducing the dimensionless shear-plane temperature $T = (W\rho cu)/q$ and the dimensionless distance

$$Y = C^2x = \frac{W\xi\psi^2\cos\phi}{4\alpha}$$

$$T = \left\{(1 + 2Y)\operatorname{erf}\sqrt{Y} + \frac{2}{\sqrt{\pi}}\sqrt{Y}\,e^{-Y} - 2Y\right\}\csc\phi \quad \ldots [7']$$

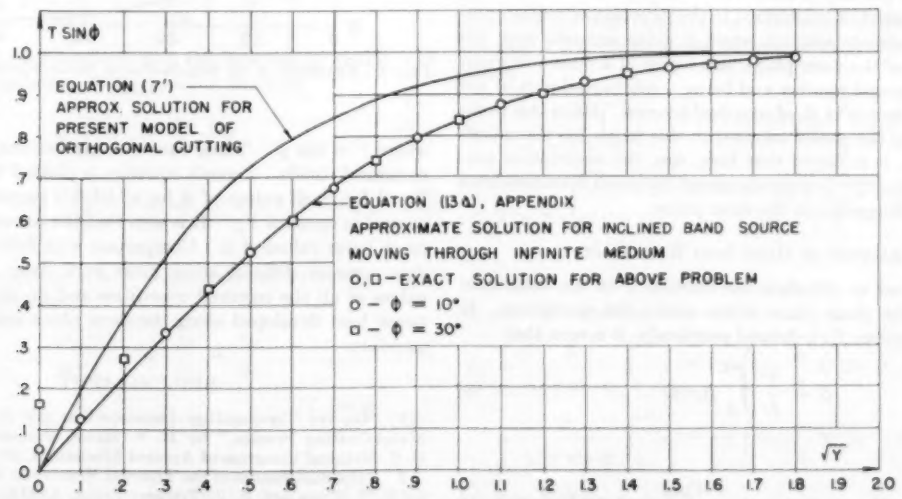

Fig. 3 Shear-Plane Temperature Distribution

Therefore the dimensionless combination $T \sin \phi$ obtained according to this analysis, can be plotted against the single dimensionless distance Y. This is done in Fig. 3.

In the Appendix the same simplification of neglecting conduction of heat in the direction of motion is made to obtain an approximate solution of the problem of an inclined band source moving through an infinite medium. The approximate solution found in this manner is $T \sin \phi = \text{erf} \sqrt{Y}$ and is plotted for comparison in Fig. 3.

It is seen that the solution, Equation [7′], for the model of the metal-cutting process adopted in this paper results in a more rapid rise of temperature along the shear plane than the model corresponding to an inclined band source moving through an infinite medium. This appears to result from the fact that there is no loss by conduction of shear-plane heat to the chip in the former model, while there is such loss in the latter. That there should be no or little loss by conduction to the chip appears reasonable when one considers the closely allied problem of a plane source in a moving medium with velocity perpendicular to the source. In this case there is no conduction to the rear or "chip side" of the source (5).

Comparison is also made in Fig. 3 of the exact solution of the inclined band-source problem, taking into account conduction in the direction of motion, and the approximate solution obtained by neglecting conduction. The numerical results of Chao and Trigger (2), evaluated for a source semi-infinite in length, $0 \leq \xi < \infty$, were used in computing the points shown for $\phi = 10$ and 30 deg. It is seen that the agreement between the approximate and exact solutions is very close except for a region in the vicinity of the leading edge of the source. This region of discrepancy becomes a smaller fraction of the total shear-plane length the larger the value of the thermal number R_t. For example, for $R_t = 10$, the distance from the leading edge at which the discrepancy becomes less than 2 per cent of the temperature there is approximately 10 per cent of the total length of the shear plane for either $\phi = 10$ or 30 deg. For larger values of R_t, the region of discrepancy will shrink proportionately; e.g., for $R_t = 20$ it will be 5 per cent of the total length of the shear plane.

There also will be a similar region of discrepancy in the vicinity of the trailing edge of the inclined band source in which the exact solution shows a slight decrease in temperature while the approximate solution does not. As shown in the Appendix, this region is of the same order of magnitude as the one just described.

Therefore, in the case of an inclined band source in a moving medium, the neglect of conduction in the direction of motion produces an approximate solution which is quite accurate over the central portion of the shear plane, this region of accuracy increasing with the thermal number and being a substantial part of the shear plane for values of R_t of practical interest. Since this problem is similar to the model adopted in this paper for the metal-cutting process, it is hoped that here, too, the assumption produces a solution which is accurate except for small distances from leading and trailing edges of the shear plane.

Fraction of Heat Into Workpiece

It is of interest to calculate the fraction β of the total heat generated on the shear plane which enters the workpiece. In terms of the function $f(x)$, defined previously, it is seen that

$$\beta = \frac{1}{L} \int_0^L f(x) dx \quad \ldots\ldots [8]$$

and that

$$[1 - f(x)]q = V\rho cu, \quad f(x) = 1 - \frac{V\rho cu}{q} = 1 - T \sin \phi \ldots [9]$$

By substitution of this value for $f(x)$ in Equation [8], using Equation [7′] for T, the following value of β is obtained

$$\beta = \frac{1}{4Y_L} \text{erf} \sqrt{Y_L} + (1 + Y_L) \text{erfc} \sqrt{Y_L} - \frac{e^{-Y_L}}{\sqrt{\pi}} \left(\frac{1}{2\sqrt{Y_L}} + \sqrt{Y_L} \right) \ldots [10]$$

where

$$Y_L = \frac{WL\psi^2 \cos \phi}{4\alpha} = \frac{Wt\psi}{4\alpha}$$

Numerical values of β are given in Fig. 4.

In their theoretical analyses, Leone (3) and Loewen and Shaw (4) obtain the respective formulas

$$\beta = \frac{1}{1 + 1.13r\sqrt{\frac{WL}{2\alpha}}}$$

and

$$\beta = \frac{1}{1 + \frac{1.07r}{(r^2 + 1)^{3/4}}\sqrt{\frac{WL}{2\alpha}}}$$

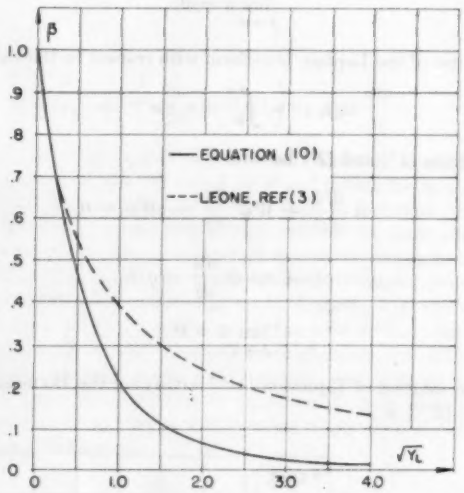

Fig. 4 Fraction β, of Shear-Plane Heat Flowing Into Workpiece

where $r = \sin \phi$. These formulas give substantially the same numerical results. Leone's equation is plotted for comparison in Fig. 4 for small values of ϕ for which his parameter may be expressed in terms of Y_L. It is seen that the present work indicates much lower values of β. Comparison with existing experimental data appears difficult since most such data do not give the values of all the required quantities and do not distinguish between heat developed along the shear plane and at the tool-chip interface.

BIBLIOGRAPHY

1 "On the Temperature Developed at the Shear Plane in the Metal-Cutting Process," by R. S. Hahn, Proceedings of the First U. S. National Congress of Applied Mechanics, 1951, pp. 661–666.

2 "The Significance of the Thermal Number in Metal Machining," by B. T. Chao and K. J. Trigger, Trans. ASME, vol. 75, 1953, pp. 109–120.

3 "Distribution of Shear-Zone Heat in Metal Cutting," by W. C. Leone, Trans. ASME, vol. 76, 1954, pp. 121–125.

4 "On the Analysis of Cutting-Tool Temperatures," by E. G. Loewen and M. C. Shaw, Trans. ASME, vol. 76, 1954, pp. 217–231.

5 Discussion by H. Blok and R. S. Hahn of reference (4), in particular Fig. 17(*b*), p. 227.

6 "A Treatise on the Theory of Bessel Functions," by G. N. Watson, Cambridge University Press, New York, N. Y., 1952.

7 "Modern Operational Mathematics in Engineering," by R. V. Churchill, McGraw-Hill Book Company, Inc., New York, N. Y., 1944, p. 297, transform pair No. 37.

8 Ibid., p. 294, operations 5 and 11.

Appendix

The purpose of this Appendix is to examine the nature of the error introduced by neglecting heat conduction in the direction of motion of workpiece and chip, respectively. This is done by using this assumption to obtain an approximate solution to a problem similar to that of metal cutting, the problem of an inclined band source moving through an infinite medium. This approximate solution is then compared with the exact solution to determine the error introduced in this case.

The mathematical formulation of this problem including conduction of heat in the direction of motion is as follows

$$\alpha\left(\frac{\partial^2 u}{\partial x^2}+\frac{\partial^2 u}{\partial y^2}\right)-W\frac{\partial u}{\partial x}=0 \qquad [11]$$

$$k\left[\lim_{\substack{y\to\psi x\\ y>\psi x}}\left(\cos\phi\frac{\partial u}{\partial y}-\sin\phi\frac{\partial u}{\partial x}\right)-\lim_{\substack{y\to\psi x\\ y<\psi x}}\left(\cos\phi\frac{\partial u}{\partial y}-\sin\phi\frac{\partial u}{\partial x}\right)\right]=q,\ 0<x<L\cos\phi \qquad [12]$$

The exact solution to this problem may be found to be, as in references (1) and (2), for the temperature along the source

$$T_{\text{exact}}=\frac{W\rho c u(\xi)}{q}=\frac{1}{\pi}\int_{-\sigma}^{\lambda-\sigma}e^{-u\cos\phi}K_0(|u|)du$$
$$=\frac{1}{\pi}\int_0^{\sigma}e^{u\cos\phi}K_0(u)du+\frac{1}{\pi}\int_0^{\lambda-\sigma}e^{-u\cos\phi}K_0(u)du \qquad [13]$$

where

$$\sigma=\frac{W\xi}{2\alpha},\quad \lambda=\frac{WL}{2\alpha}$$

With the neglect of conduction in the direction of motion, the approximate formulation of the problem becomes

$$\alpha\frac{\partial^2 u}{\partial y^2}-W\frac{\partial u}{\partial x}=0 \qquad [11a]$$

$$k\left(\lim_{\substack{y\to\psi x\\ y>\psi x}}\frac{\partial u}{\partial y}-\lim_{\substack{y\to\psi x\\ y<\psi x}}\frac{\partial u}{\partial y}\right)=q\sec\phi,\quad 0<x<L\cos\phi \qquad [12a]$$

With the substitution $z=y-\psi x$, and $t=x/W$, Equations [11*a*] and [12*a*] become

$$\alpha\frac{\partial^2 u}{\partial z^2}+W\psi\frac{\partial u}{\partial z}=\frac{\partial u}{\partial t} \qquad [11b]$$

$$k\left(\lim_{\substack{z\to 0\\ z>0}}\frac{\partial u}{\partial z}-\lim_{\substack{z\to 0\\ z<0}}\frac{\partial u}{\partial z}\right)=q\sec\phi,\quad 0<t<\frac{L\cos\phi}{W} \qquad [12b]$$

It is seen that these equations describe the problem of the temperature due to a continuous plane source of strength $q\sec\phi/\rho c$ released at $z=0$ for the time interval $0<t<L\cos\phi/W$ in a medium with thermal diffusivity α, flowing with velocity $W\psi$ in the direction of the negative z-axis. With this interpretation, the solution to Equations [11*b*] and [12*b*] may be written down immediately as

$$u(z,t)=\frac{q\sec\phi}{2\sqrt{\pi\alpha}\,\rho c}\int_0^t\frac{\exp\left[-\dfrac{[z+W\psi(t-\tau)]^2}{4\alpha(t-\tau)}\right]}{\sqrt{t-\tau}}d\tau$$

Setting $z=0$

$$t=\frac{x}{W}=\frac{\xi\cos\phi}{W}$$

the temperature along the inclined source is found to be, after some manipulation

$$T_{\text{approx}}=W\rho c u(\xi)/q=\csc\phi\,\operatorname{erf}\left(\frac{\psi}{2}\sqrt{2\sigma\cos\phi}\right)$$
$$=\csc\phi\,\operatorname{erf}\sqrt{Y} \qquad [13a]$$

The discrepancy between Equations [13] and [13*a*] will now be examined. It is noted that the length L of the band source does not appear in the approximate solution, Equation [13*a*]. Therefore the form of the exact solution Equation [13] is first examined when the source is semi-infinite in length, occupying the interval $0\le\xi<\infty$. The effect of the finite length of the source will be examined in the following:

When L becomes infinite, Equation [13] becomes

$$T_{\text{exact}}=\frac{1}{\pi}\int_0^{\sigma}e^{u\cos\phi}K_0(u)du+\frac{1}{\pi}\int_0^{\infty}e^{-u\cos\phi}K_0(u)du=I_1+I_2$$

From reference (6),[3] it is found that

$$I_2=\frac{\phi}{\pi\sin\phi}$$

The integral representation of the Bessel function[4]

$$K_0(u)=\frac{e^{-u}}{\sqrt{2u}}\int_0^{\infty}e^{-x}x^{-1/2}\left(1+\frac{x}{2u}\right)^{-1/2}dx$$

is used in the first integral I_1, and the order of integration is interchanged. Carrying out the integration with respect to u, I_1 becomes

$$I_1=\frac{\csc\phi/2}{2\sqrt{\pi}}\int_0^{\infty}x^{-1/2}e^{-x\cos^2\phi/2}\operatorname{erf}\left(\sin\frac{\phi}{2}\sqrt{2\sigma+x}\right)dx$$
$$-\frac{\csc\phi/2}{2\sqrt{\pi}}\int_0^{\infty}x^{-1/2}e^{-x\cos^2\phi/2}\operatorname{erf}\left(\sin\frac{\phi}{2}\sqrt{x}\right)dx$$
$$=I_{11}-\frac{\phi}{\pi\sin\phi}$$

I_{11} may be rewritten

$$I_{11}=\frac{2}{\sqrt{\pi}\sin\phi}\int_0^{\infty}e^{-u^2}\operatorname{erf}\left(\sin\frac{\phi}{2}\sqrt{2\sigma+u^2\sec^2\phi/2}\right)du$$
$$=\frac{2}{\sqrt{\pi}\sin\phi}\int_0^{\infty}e^{-u^2}\operatorname{erf}\left(\sin\frac{\phi}{2}\sqrt{2\sigma}\right)du$$

[3] Page 388, equation [9].

[4] Reference (6), p. 206.

$$+\frac{2}{\sqrt{\pi}\sin\phi}\int_0^\infty e^{-u^2}\left[\operatorname{erf}\left(\sin\frac{\phi}{2}\sqrt{2\sigma+u^2\sec^2\phi/2}\right)-\operatorname{erf}\left(\sin\phi/2\sqrt{2\sigma}\right)\right]du$$

$$=I_{111}+I_{112}$$

$$I_{111}=(\csc\phi)\operatorname{erf}\left(\sin\frac{\phi}{2}\sqrt{2\sigma}\right)$$

$$=\csc\phi\left\{\operatorname{erf}\left(\frac{\psi}{2}\sqrt{2\sigma\cos\phi}\right)-\left[\operatorname{erf}\left(\frac{\psi}{2}\sqrt{2\sigma\cos\phi}\right)-\operatorname{erf}\left(\sin\frac{\phi}{2}\sqrt{2\sigma}\right)\right]\right\}$$

$$0<\operatorname{erf}\left(\frac{\psi}{2}\sqrt{2\sigma\cos\phi}\right)-\operatorname{erf}\left(\sin\frac{\phi}{2}\sqrt{2\sigma}\right)$$

$$=\frac{2}{\sqrt{\pi}}\int_{\sin\frac{\phi}{2}\sqrt{2\sigma}}^{\frac{\psi}{2}\sqrt{2\sigma\cos\phi}}e^{-u^2}du<2\sqrt{\frac{\sigma\sin\phi}{\pi}}\left(\sqrt{\tan\frac{\phi}{2}}-\sqrt{\tan\frac{\phi}{2}}\right)e^{2\sigma\sin^2\frac{\phi}{2}}$$

$$I_{112}=\frac{4}{\pi\sin\phi}\int_0^\infty e^{-u^2}\int_{\sin\frac{\phi}{2}\sqrt{2\sigma}}^{\sin\frac{\phi}{2}\sqrt{2\sigma+u^2\sec^2(\phi/2)}}e^{-v^2}dv\,du$$

$$<\frac{4\sin\frac{\phi}{2}\,e^{-2\sigma\sin^2\frac{\phi}{2}}}{\pi\sin\phi}\int_0^\infty e^{-u^2}\left[\sqrt{2\sigma+u^2\sec^2\frac{\phi}{2}}-\sqrt{2\sigma}\right]du$$

But

$$\left[\sqrt{2\sigma+u^2\sec^2\frac{\phi}{2}}-\sqrt{2\sigma}\right]<\frac{u^2\sec^2\frac{\phi}{2}}{2\sqrt{2\sigma}}$$

Therefore

$$0<I_{112}<\frac{2\sin\frac{\phi}{2}\sec^2\frac{\phi}{2}\,e^{-2\sigma\sin^2\frac{\phi}{2}}}{\pi\sin\phi\sqrt{2\sigma}}\int_0^\infty u^2e^{-u^2}du$$

$$=\frac{\tan\frac{\phi}{2}\cos\frac{\phi}{2}\,e^{-2\sigma\sin^2\frac{\phi}{2}}}{2\sin\phi\sqrt{2\pi\sigma}}$$

Combining the foregoing integrals and inequalities, it is seen that

$$T_{\text{exact}}=T_{\text{approx}}+E(\sigma,\phi)$$

where

$$|E(\sigma,\phi)|<\max\left[\frac{\sin\frac{\phi}{2}\sec^2\frac{\phi}{2}\,e^{-2\sigma\sin^2\frac{\phi}{2}}}{2\sin\phi\sqrt{2\pi\sigma}},\ 2\sqrt{\frac{\sigma}{\pi\sin\phi}}\left(\sqrt{\tan\frac{\phi}{2}}-\sqrt{\tan\frac{\phi}{2}}\right)e^{-2\sigma\sin^2\frac{\phi}{2}}\right]$$

where, by the notation max $[f_1(\sigma,\phi), f_2(\sigma,\phi)]$ is meant the larger of the two functions for a particular set of values of σ and ϕ. It is seen that $E(\sigma,\phi)$ is small for large σ. From the actual numerical comparison made in Fig. 3 it is seen that the upper bound is generous and the error decreases more rapidly than it indicates.

To determine the error due to the finite length of the source, it is noted from Fig. 2 of reference (2) that

$$\int_0^{\lambda-\sigma}e^{-u\cos\phi}K_0(u)\,du$$

differs from

$$\int_0^\infty e^{-u\cos\phi}K_0(u)\,du$$

by less than 2 per cent of the value of T_{exact} for $\lambda-\sigma>1.0$.

Discussion

H. Blok.[5] By his ingenious refinements on methods at present available, the author has carried the computational determination of shear-plane temperature distribution a step further. Despite the author's conscientious efforts to verify the admissibility of his approximations, it is thought that a definite judgment can be established only by comparing the author's results with those to be deduced from an exact treatment that does not involve the approximations. To this end, it may well be worth while to settle the question once for all by carrying out, for a sufficient number of representative cases, computations on the basis of relaxational methods such as have recently been used by A. C. Rapier.[6]

B. T. Chao.[7] One of the major factors which have direct bearing on tool life is the tool-chip interface temperature. To a certain extent, the latter is influenced by the distribution of temperature along the shear zone. The author is to be commended for his timely contribution on the subject.

In the paper the author attempts to solve the rather complicated problem of heat conduction in orthogonal cutting by introducing certain assumptions. With speeds and feeds commonly employed in machining operations using carbide cutting tools, the simplification of neglecting the transfer of heat by conduction in workpiece and chip in the direction of their respective motions seems justifiable. On the other hand, the author's assumption of taking the chip-flow velocity vector perpendicular to the shear plane is not only unnecessary but also unrealistic. Under certain cutting conditions, it may introduce considerable error. The writer hereby offers a solution which is just as easy to derive as the one presented in the paper but without using the author's assumption 7.

From the geometry of chip formation, Merchant[8] has shown that for orthogonal cutting with type 2 chips, the ratio of the velocities V and W[9] is given by the following expression

$$\frac{V}{W}=\frac{\sin\phi}{\cos(\phi-\alpha)}\qquad[14]$$

where α is the rake angle of the tool. Equation [14] is, in effect, a relation required by the mass-flow balance. Unfortunately, the

[5] Professor of Mechanical Engineering, University of Technology, Delft, Holland.

[6] "A Theoretical Investigation of the Temperature Distribution in the Metal Cutting Process," by A. C. Rapier, *British Journal of Applied Physics*, vol. 5, 1954, pp. 400–405.

[7] Associate Professor of Mechanical Engineering, University of Illinois, Urbana, Ill.

[8] "Basic Mechanics of the Metal-Cutting Process," by M. E. Merchant, *Journal of Applied Mechanics*, Trans. ASME, vol. 66, 1944, p. A-168.

[9] Author's nomenclature is used in this discussion.

author used the relation $W\rho A_s = V\rho A$ instead. The latter implies

$$\frac{V}{W} = \sin \phi \quad \ldots\ldots [15]$$

Using Equation [14] of the discussion, the Boundary Condition [2″b] of the paper becomes

$$-k \cos \phi \frac{\partial u}{\partial z} + nWc\rho \sin \phi u = q, \quad 0 < x < L \cos \phi, \; z = 0 \quad \ldots\ldots [16]$$

where

$$n = \frac{1 - \cos (\phi - \alpha)}{\cos (\phi - \alpha)}$$

The author's analysis corresponds to the rather unrealistic condition of $\alpha = \phi$, and hence $n = 0$.

With the foregoing alteration in the boundary condition, the Laplace transform of the temperature function $u(x, z)$, for $z = 0$ becomes

$$\bar{u}(s, 0) = \frac{2qC}{Wc\rho \sin \phi} \frac{1}{s[C(1 + 2n) + \sqrt{C^2 + s}]} \ldots [17]$$

and the shear plane temperature is

$$u(x, 0) = \frac{q}{Wc\rho \sin \phi} \left\{ 2 \operatorname{erf} (C\sqrt{x}) + \frac{1 + 2n}{2n(1 + n)} \left[1 - e^{4n(1+n)C^2x} \operatorname{erfc} (1 + 2n) C\sqrt{x} - (1 + 2n) \operatorname{erf} (C\sqrt{x}) \right] \right\} \quad \ldots\ldots [18]$$

It may be remarked that on letting $n \to 0$ and using l'Hospital's rule, Equation [18] reduces to Equation [7] of the paper.

Introducing dimensionless temperature $T = Wc\rho u/q$ and distance

$$Y = C^2x = \frac{W\psi^2 \cos \phi}{4\alpha} \xi$$

as defined by the author, Equation [18] of this discussion, becomes

$$T = \left\{ 2 \operatorname{erf} \sqrt{Y} + \frac{1 + 2n}{2n(1 + n)} \left[1 - e^{4n(1+n)Y} \operatorname{erfc} (1 + 2n) \sqrt{Y} - (1 + 2n) \operatorname{erf} \sqrt{Y} \right] \right\} \csc \phi \ldots [19]$$

Using the data given in the author's reference (2), for the machining of SAE 52100 steel with a carbide tool of negative 2-deg rake, $\phi = 22.8$ deg when $R_t = 70$. Under these conditions, n has been found to be 0.101.

The author correctly points out the discrepancy between the approximate solution presented in the paper and those given in his references (1) and (2). This, indeed, is consistent with the simplification introduced in the analysis which changes the elliptic differential equation to the parabolic type. Physically, the condition $u = 0$, at $x = 0$, and $0 < y < \infty$ cannot exist. Likewise, the supply of heat for $x > L \cos \phi$, at $z = 0$ will also exert an influence. It may therefore be expected that the present method of solution will yield a temperature distribution which is too low at A and too high at O (Fig. 5 of this discussion). Strictly speaking, the discontinuous temperature solution which is inherent in the present mathematical treatment cannot be a physical reality. It could yield reasonable results for the distribution of shear plane temperature for regions not at the immediate vicinity of the trailing edge (A) and leading edge (O) of the shear zone. Unfortunately, in so far as the tool-chip interface temperature is concerned, the temperature distribution in the neighborhood of the leading edge (O) is actually of primary importance.

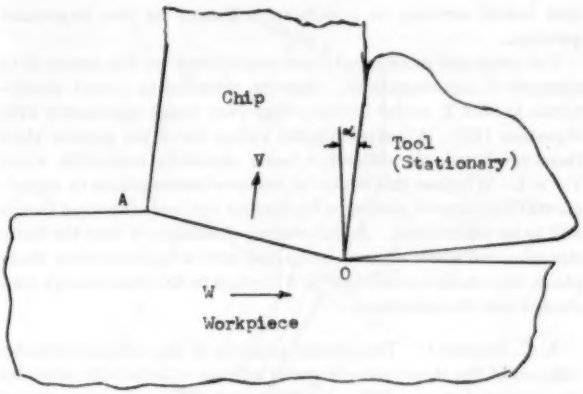

FIG. 5 TEMPERATURE DISTRIBUTION

E. G. LOEWEN.[10] The author has made an important and interesting contribution to metal-cutting theory. There is no doubt that the previously published analysis contained many approximations and that the assumptions involved in the present paper are more readily justified.

It was surprising to discover that Vieregge (see separate discussion) quite independently, of course, had been working on the same problem in Germany. Making similar, though not identical, assumptions and using a step-by-step difference method rather than purely analytical calculations, he had arrived at practically the same conclusions. The only noticeable difference is in the temperatures at the end of the shear plane ($\sqrt{Y_L} < 0.6$) which the author finds slightly higher. This is not an important difference since neither analysis claims high accuracy in this region.

Although the author's analytical solution is simpler to apply in practice, Vieregge's step-by-step method has the advantage of showing also the temperature at points outside of the shear plane itself.

Since the presentation of this paper still another approach to the problem has been published.[8] Using relaxation methods, and the same basic assumptions, Rapier gives just three values for β: 0.627, 0.499, 0.698, for Y_L values of 0.083, 0.167, 0.0417, respectively. These results are 5 to 10 per cent above the corresponding values from Equation [10] of the paper.

With several theoretical attacks on the shear-plane energy problem on hand now, we should consider how the results can be verified experimentally. This turns out to be quite difficult. No one since Schwerd[11] has tackled the problem of measuring the temperature distribution in and around the shear plane which would be a check on Fig. 3 of the paper. Schwerd's one useful publication seems to indicate shear-plane temperatures close to those predicted in this paper at the end of the shear plane ($\xi = 0$), but much higher temperatures near the cutting edge of the tool. One obvious conclusion is that the shear energy q is perhaps not distributed uniformly over the shear plane; but we need far more

[10] Assistant Professor, Mechanical Engineering Department, Massachusetts Institute of Technology, Cambridge, Mass. Mem. ASME.

[11] "Über die Bestimmung des Temperaturfeldes beim Spanablauf," by F. Schwerd, *Zeit. VDI*, vol. 77, 1933, pp. 211–216.

data before arriving at a definite judgment on this important question.

The other and more simply performed check on this theory is to measure β experimentally. Results obtained in recent experiments at M.I.T. so far indicate only very rough agreement with Equation [10]. All experimental values for β are greater than those predicted, the difference being especially noticeable when $Y_L > 1$. Whether this is due to incorrect assumptions or experimental inability to eliminate friction on the tool-clearance face is still to be determined. An interesting possibility is that the finite size of a real shear zone as compared with a mathematical shear plane, may make a considerable difference in the shear energy conducted into the workpiece.

A. C. Rapier.[12] The present analysis of the temperatures developed at the shear plane in metal cutting undoubtedly provides the best analytical solution yet proposed. The errors introduced by neglecting conduction in the direction of motion have been examined analytically, but it is perhaps simpler to appreciate the significance of the simplification by considering the over-all temperature distribution. The errors introduced are zero where the isotherms are parallel to the direction of motion and a maximum where the isotherms are perpendicular to the direction of motion. The same simplification was used by the writer for the solution of the temperature distribution in the chip under conditions where the temperature gradients in the direction of motion are relatively small.[6]

Examination of the complete temperature distribution in the workpiece (e.g., Fig. 8[6]) shows that the isotherms are approximately parallel to the direction of motion in only a small proportion of the whole area. For the higher values of Y_L ($= R \tan \phi/4$) they tend to become parallel to the shear plane over most of the region. Under these conditions the ratio of the heat conducted from the source in the X-direction to the total heat supplied by the source is $\sin^2 \phi$. Thus for the values of ϕ which are obtained in metal cutting the neglect of the conduction in the X-direction introduces relatively small errors and would be expected to give values of β which are slightly too small.

Fig. 6, herewith, shows the variation of β with $\sqrt{Y_L}$ as predicted by the present analysis compared with those obtained from solutions due to Loewen and Shaw, Hahn (mean values) and a suggested correction of Hahn's results given by the writer.[6] The results of individual relaxation solutions due to the writer are given by crosses. The agreement between the present solution, the corrected Hahn solution, and the relaxation solution is seen to be very good. Agreement would not be expected with the Loewen and Shaw solution since this type of solution is not applicable to the problem.[6]

G. Vieregge.[13] The author has made a valuable contribution to metal-cutting theory by showing how the distribution of the heat energy from the shear plane can be found by purely mathematical methods.

For a tool engineer the value of such an analysis does not lie in quantitative values of the heat going into the workpiece or in the absolute temperature of the shear plane. These can be found experimentally simpler and more accurately. The purpose of a

[12] Plasticity Division, Mechanical Engineering Research Laboratory, East Kilbride, Glasgow, Scotland.

[13] Doctor of Engineering, Deutsche Edelstahlwerke, Krefeld, Germany.

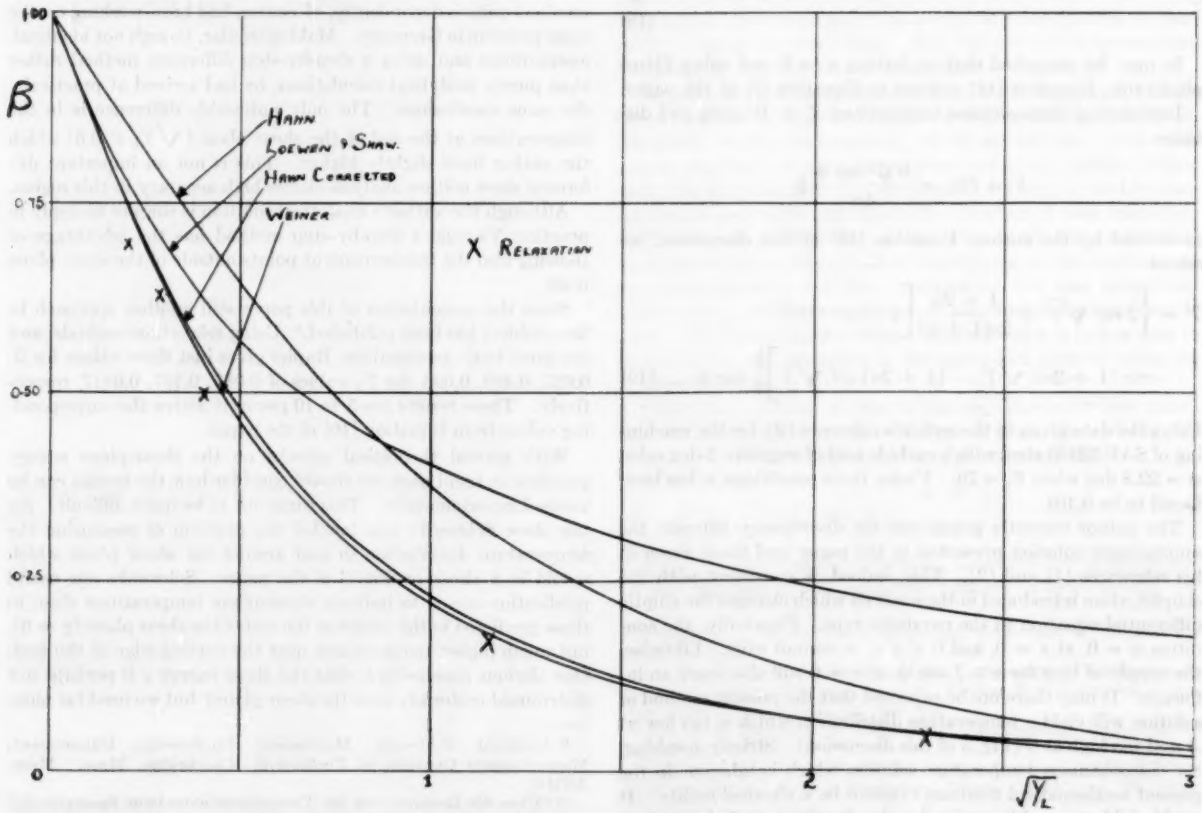

Fig. 6 Variation of β With $\sqrt{Y_L}$

mathematical analysis is to establish the important variables and to estimate their relative importance.

The writer treated this problem in a 1953 paper.[14]

Shear-plane and workpiece temperatures, and the energy going into the workpiece, were calculated using the same basic assumptions as the author's. Assumptions 1 to 6 agree completely with the writer's. As regards points 7 and 8 the following assumptions were made by the writer:

7 The chip can flow in any arbitrary direction.

8(a) Heat from the shear plane is removed as (1) stored heat in the chip, and (2) conducted toward the workpiece, perpendicular to the shear plane.

8(b) Heat is supplied to the shear plane from the stored energy in the workpiece approaching the shear plane.

The resulting temperature field and the energy flow into the workpiece were calculated by a method based on the difference method of Schmidt.[15]

Calculations were based on the following values:

Shear energy converted into heat q = 242,000 in-lb/in.,^{3} corresponding to a maximum possible shear-plane temperature u_{max} of 750 F

Thermal diffusivity:	α	= 0.0155 in^2/sec
Cutting speed:	W	= 183 fpm
Depth of cut:	t	= 0.0126 in.
Shear angle:	ϕ	= 30 deg

[14] "Energieverteilung und Temperatur bei der Zerspannung," by G. Vieregge, *Werkstatt und Betrieb*, vol. 86, 1953, pp. 691–703.

[15] "Das Differenzverfahren zur Lösung von Differenzialgleichungen der Nichtstationaren Warmeleitung, Diffusion und Impulsausbreitung," by E. Schmidt, *Forschung Ingenieurwesens*, vol. 13, 1942, p. 177.

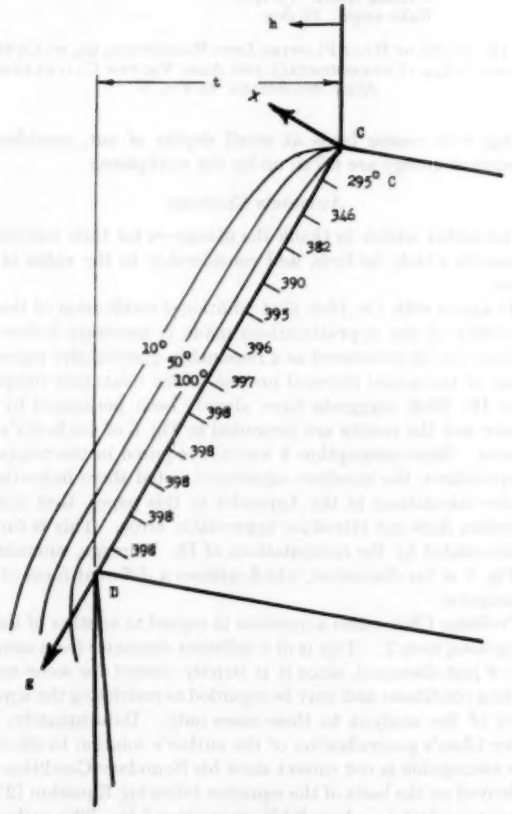

FIG. 7 TEMPERATURE FIELD NEAR SHEAR PLANE WHEN CUTTING STEEL WITH THE FOLLOWING VALUES: q = 170 KG/MM^2 (u_{max} = 400 C); α = 10 MM^2/SEC; ϕ = 30 DEG; t = 0.32 MM; w = 1000 MM/SEC

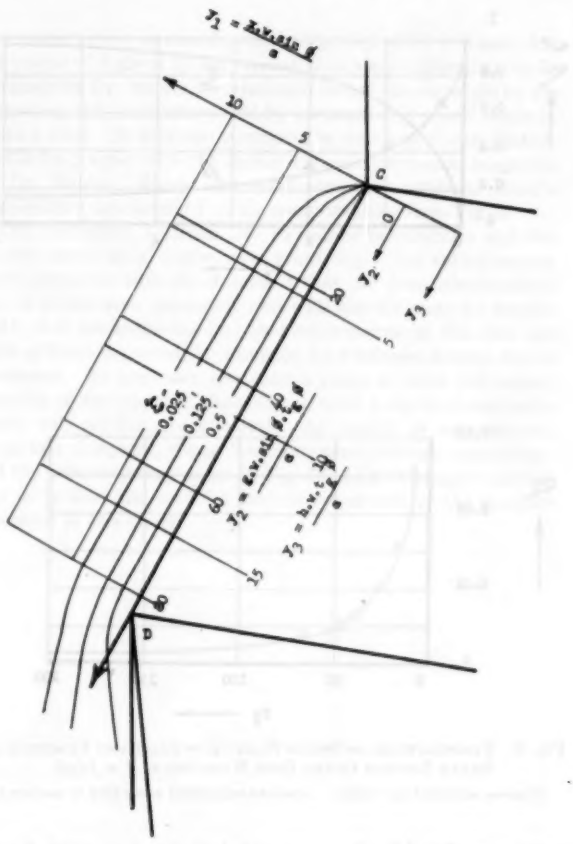

FIG. 8 TEMPERATURE FIELD NEAR SHEAR PLANE IN DIMENSIONLESS CO-ORDINATES; $\xi = f_1(y_2, y_3)$

This special case is typical for cutting steel. It leads to a temperature distribution shown in Fig. 7 of this discussion and repeated in Fig. 8 in dimensionless form.

The shear-plane temperature u_s can be written in dimensionless form

$$\frac{u_s}{u_{max}} = \xi_s = f_2\left(y_2 = \frac{hW \tan \phi}{\alpha}\right) \quad \ldots\ldots\ldots [20]$$

The energy remaining in the workpiece depends only on the position of point D, Fig. 8. It is represented in dimensionless form by

$$\frac{Q_w}{Q_s} = \beta = f_3\left(y_3 = \frac{tW \tan \phi}{\alpha}\right) \quad \ldots\ldots\ldots [21]$$

Both these functions are plotted in Fig. 9.

In his calculations the author finds the energy to the workpiece a function of the same quantities. His Equation [10] is also shown in Fig. 9 and shows complete agreement with the function $f_3(y_3)$.

One can see from Fig. 8 of this discussion that taking the maximum temperature gradient perpendicular to the shear plane is valid over almost its whole length. Although the author has taken the maximum gradient to be perpendicular to the direction of cut, the resulting difference between his and the writer's results is so small that it cannot even be seen in a graphical presentation. However, as he points out, neither assumption is correct near the workpiece surface, point C, because the approaching material must be heated up. At the lower end of the shear plane,

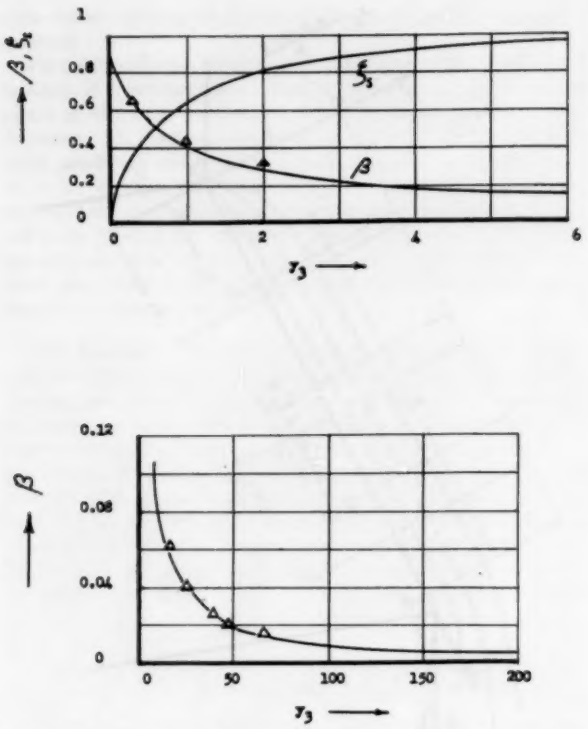

FIG. 9 TEMPERATURE OF SHEAR PLANE $\xi_s = f_2(y_3)$ AND FRACTION OF SHEAR ENERGY GOING INTO WORKPIECE, $\beta = f_3(y_3)$
(Curves obtained by writer. Δ-points calculated according to author.)

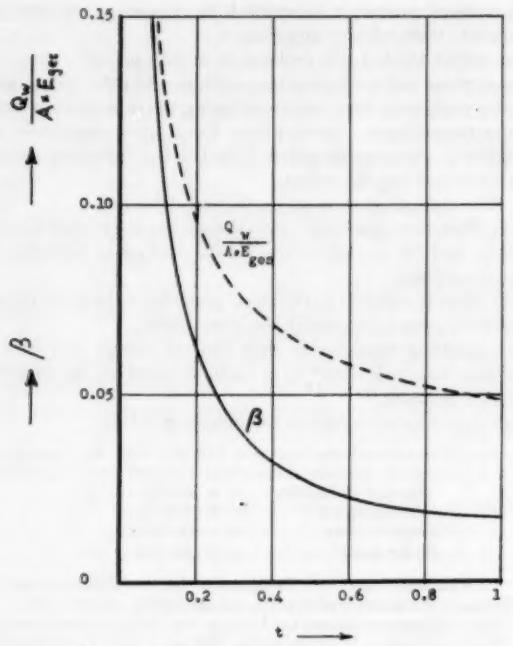

Orthogonal cutting
Material: Steel, 140,000 psi tensile strength
Cutting speed: 1.3 fpm
Rake angle: 10 deg

FIG. 10 RATIO OF HEAT FLOWING INTO WORKPIECE, Q_w, TO CUTTING ENERGY AE_{gcs} (EXPERIMENTAL) AND ALSO VALUES CALCULATED AS $f_3(y_3)$ ACCORDING TO FIG. 9

near point D, while there are no calculating errors, the initial assumptions do not hold. A second deformation due to separation of the chip from the workpiece is superimposed so that q increases sharply. The shear-plane temperature increases rapidly from point C on toward D, reaching the approximate temperature u_{max} in a few ten thousandths of an inch. In the direction of the workpiece the temperature drops very rapidly so that the zone heated is very small. The maximum workpiece temperature is reached in the immediate vicinity of the cutting edge. It is also the maximum surface temperature of the machined surface. As soon as the tool has passed, the surface heat is conducted into the workpiece, so that the surface temperature drops very quickly.

The heat remaining in the workpiece has been measured by A. O. Schmidt[16] as well as the writer. Schmidt found that 8 to 15 per cent of the total cutting energy remained in the workpiece. One should take account here of the fact that the shear process accounts for only about 70 per cent of the total energy. Experimental results of the writer are shown in Fig. 10 of this discussion. The energy retained by the workpiece is thus considerably greater than that predicted in Fig. 9. It becomes even greater in ordinary turning where the same surface meets the tool every revolution. This discrepancy can be explained by the separation and friction energies not taken into account, the spreading of a shear zone perpendicular to the shear plane, conduction along the side cutting edge unless one cuts under orthogonal conditions, and friction along the clearance face. Deformation and conduction along the side cutting edge contribute noticeably to heating of the workpiece. This can be seen from the fact that, when cutting with coarse feeds at small depths of cut, considerable amounts of energy are taken up by the workpiece.

[16] "Heat in Metal Cutting" by A. O. Schmidt, American Society for Metals, 1950.

AUTHOR'S CLOSURE

The author wishes to thank the discussers for their interesting comments which, he feels, add considerably to the value of the paper.

He agrees with Dr. Blok that additional verification of the admissibility of the approximations made is necessary before the solution can be considered as a reasonably quantitative representation of the actual physical process. The relaxation computations Dr. Blok sugggests have already been performed by Dr. Rapier and the results are presented in Fig. 6 of the latter's discussion. Since assumption 8 was not required in the relaxation computations, the excellent agreement noted there indicates, as do the calculations in the Appendix to this paper, that this assumption does not introduce appreciable error. This is further substantiated by the computations of Dr. Vieregge, summarized in Fig. 9 of his discussion, which utilizes a different form of this assumption.

Professor Chao raises a question in regard to another of the assumptions, item 7. This is of a different character from assumption 8 just discussed, since it is strictly correct for some metal-cutting conditions and may be regarded as restricting the applicability of the analysis to these cases only. Unfortunately, Professor Chao's generalization of the author's solution to eliminate this assumption is not correct since his Boundary Condition [16] is derived on the basis of the equation following Equation [2′c] of the paper which is only valid if assumption 7 is. The author believes that his solution is applicable with little error even when the chip velocity is not exactly orthogonal to the shear plane but further work is necessary to substantiate this. In connection

with the errors in the computed temperature distribution at points A and O, Fig. 5, it should be noted that while these errors are inherent in the present method of analysis, their magnitude decreases with increasing cutting velocity and, for practical conditions, are quite negligible.

Professor Loewen's statement that experiments in this field are in progress at M.I.T. is indeed welcome since, in the final analysis, a theory is only valuable if it can predict, in a reasonable quantitative manner, the results of experiments. If the discrepancies between his experiments and the present theory persist, then it will be necessary to conclude that some of the assumptions made in its development are too restrictive and a solution should be attempted under broader conditions. Perhaps, as Professor Loewen suggests, consideration of a shear zone of finite thickness may be necessary, although it would seem that, if some of the shear zone extends into the chip region, even lower values of β would result.

The interpretation of assumption 8 given by Dr. Rapier is very interesting It is the author's belief, however, based upon the calculations in the Appendix to this paper, that the fractional error in β introduced by it is less than $\sin^2\phi$. This belief is further borne out by an examination of Fig. 6 in which it is seen that the values of β given by the present theory are higher than those obtained by Dr. Rapier by relaxation techniques, whereas by his reasoning, the error introduced by assumption 8 would result in lower values. It was also surprising to find how closely Hahn's results for β agree with the author's when corrected as suggested by Dr. Rapier. Would this same correction apply to Hahn's temperature distribution? This seems unlikely from Fig. 3.

The agreement between Dr. Vieregge's calculations and the present theory is, of course, most gratifying. The author cannot agree, however, with his statement that the quantities involved can be found more accurately and with less difficulty by experiment; it is his understanding that experiments in this field are quite difficult, as noted, for example, by Professor Loewen in his discussion. In any case, one cannot claim to have full understanding of any physical phenomenon until a theory is available which will predict quantitatively the results of experiments. From this viewpoint, the lack of agreement between experiment and the present theory noted in Fig. 10 of Dr. Vieregge's discussion underlines the need for further refinement of the analysis presented in this paper.

Stresses and Strains in Cold-Extruding 2S-O Aluminum[1]

By E. G. THOMSEN[2] and J. FRISCH,[3] BERKELEY, CALIF.

2S-O aluminum was extruded at room temperature in an inverted extrusion process from a 4.3-in-diam cylindrical billet, into a 1.5-in-diam solid cylindrical bar. Steady-state particle-velocity vectors were determined from gridded, split billets during incremental extrusion steps. These velocity patterns were compared with those obtained previously for lead extrusions having the same billet and die geometry and the same high degree of lubrication; it was found that the patterns for these two metals were identical. The aluminum velocity pattern appeared not to be affected by extrusion load, but the extrusion load was a strong function of the extent of deformation. It was estimated that the extrusion load becomes constant after a reduction of billet length by approximately 2.4 in., the distance the plastic zone of the metal extends upstream from the orifice. The axial-stress distribution in the billet, determined from strain rates and natural strains, taking into account work hardening, had the same shape as that determined with lead. The wall pressure or radial stress in the plastic zone was found to be lower than the average pressure, but both pressures tend to approach each other beyond the plastic zone.

Nomenclature

The following nomenclature is used in the paper:

V = metal particle velocity, ipm
V_B = velocity of base end of billet, ipm
u, v = particle velocity components in the z and r-directions, respectively, ipm
z = axial distance measured upstream from orifice or die, in.
r = radial position of any particle, in.
α_s = angle between extrusion axis and principal strain-rate direction, deg
$\dot{\epsilon}_z, \dot{\epsilon}_r, \dot{\epsilon}_\theta$ = instantaneous normal plastic strain-rate components referred to current state of deformation in the z, r, and θ-cylindrical co-ordinate directions, in/in. per min
$\dot{\gamma}_{zr}$ = shear strain-rate component measurable on a meridian plane, which occurs on the z-plane and in the r-co-ordinate direction, min^{-1}
$\sigma_z, \sigma_r, \sigma_\theta$ = true normal stress components on z, r, and θ-planes, respectively, psi
τ_{zr} = shear stress on z-plane and in r-direction, psi
$\bar{\epsilon}$ = effective strain rate, min^{-1}
$\bar{\sigma}$ = effective stress, psi
$\Delta\bar{\epsilon}$ = increment of small effective strain
$\bar{\epsilon}_n$ = effective natural strain
l_o, l = original and final length of fibers, respectively, for uniform deformation, or gage length of test bar, in.
D_o, D = original and final diameters of test bars, respectively, or billet diameter and extruded bar diameter, in.
ϵ = small or engineering strain, in/in.
L = extrusion load, lb
K_s = constant axial stress reference datum, psi
$\Delta\sigma_z$ = increment of axial stress evaluated from experimental strain rates and effective natural strains for increments of r and constant z-positions, psi
ΔA_r = incremental mean area of billet which is equal to an annular ring having a mean radius r on which $\left(K_s + \sum_0^r \Delta\sigma_z\right)$ acts, sq in.

Introduction

In a recent series of articles (1 to 5)[4] an experimental method was discussed for obtaining particle-velocity vectors and distribution of stress and strain rate in the plastic portion of a metal during steady-state deformation. This method of analysis was called visioplasticity and was applied to extrusions of a 1.5-in-diam cylindrical bar (3), and to a tubular product (5), both extruded from a 4.3-in-diam solid cylindrical billet of commercially pure lead. The extrusion processes were carried out at room temperature at an approximate area reduction of 87.8 per cent. The particle-velocity vectors were determined on a meridian plane from the movement of marked particles in the form of intersections of grid lines by incremental extrusion steps, thereby permitting particle location at any stage of deformation. The external billet surfaces were relubricated before each additional incremental deformation step was taken. This prevented metal welding to the extrusion chamber and die surfaces, thereby carrying out the extrusion processes with negligible external friction. It was found that the stress and strain-rate distributions were not uniform across the section of the billet. It was further found that strain rates (4) did not affect the flow pattern nor the strain-rate distribution, but that the extrusion load increased approximately linearly with increasing extrusion speeds for the range of speeds investigated. It also was found that wall-pressure (3, 4, 5) measurements were in substantial agreement with calculated mean pressures if corrections for the condition necessary to establish plastic flow were made.

The investigations on lead were restricted to deformation processes where work hardening was essentially absent. However, in cold-deformation processes in the range of temperatures below their recrystallization temperatures, metals and alloys remember their undeformed state, and hence a solution requires the additional knowledge of the instantaneous state of strain as well as the strain path. It was pointed out (3) that the visioplasticity

[1] This investigation was sponsored by the National Science Foundation under Grant G-1002.

[2] Professor of Mechanical Engineering, University of California. Mem. ASME.

[3] Assistant Professor of Engineering Design, University of California. Assoc. Mem. ASME.

Contributed by the Research Committee on Metal Processing and presented at the Annual Meeting, New York, N. Y., November 28–December 3, 1954, of The American Society of Mechanical Engineers.

Note: Statements and opinions advanced in papers are to be understood as individual expressions of their authors and not those of the Society. Manuscript received at ASME Headquarters, September 10, 1954. Paper No. 54—A-161.

[4] Numbers in parentheses refer to the Bibliography at the end of the paper.

technique can be used for these cases since work hardening can be incorporated in the analysis. Hence the present paper will discuss the incremental cold extrusion of 2S-O aluminum and an analysis of stresses and strains will be presented. It is hoped that the information given will have practical value, and will aid in understanding forming operations in the work-hardening range of metal deformation.

Experimental Technique

The 2S-O aluminum cylindrical billets used in the present investigation were machined from a 6-in-diam commercial extrusion. These billets had a diameter of 4.300 in. and a length of 4 in. and were split on a meridian plane containing the axis. One of these split surfaces was provided with a square grid network machined into the surface at an approximate depth of 0.008 to 0.010 in. The extrusion apparatus was a portable composite cylinder consisting of two SAE 4140 heat-treated cylindrical rings which were assembled with a shrink fit. The bore of this composite cylinder was 4.305 in. and the external diameter was 14 in. A 1.5-in-diam square-edged split die and die holder were supported by a hollow ram to permit extrusions up to 11 in. in length. The extrusion load was obtained from the University of California's 4,000,000-lb Baldwin-Southwark testing machine. The diameter of the billet and the size and shape of the die were identical with those of lead extrusions used in earlier experiments (3) in order to permit direct comparison of results. The subsequent comparisons which will be made with lead refer to the results reported in reference (3).

The billets were lubricated on all external surfaces with molybdenum-disulphide grease (Molykote) before assembling into the extrusion apparatus. The extrusion load was then applied at a constant rate giving deformation rates in the plastic range for the incremental steps of approximately 0.045 ipm billet reduction which corresponds to a rate of bar extrusion of 0.37 ipm and an area reduction of 87.8 per cent. While the extrusion loads, to be discussed later, exceeded 1,000,000 lb (500 tons), the push-out load for removal of the billet was less than 3000 lb. No welding occurred between cylinder wall and billet during the initial extrusion step, and hence the extrusion process was carried out under conditions of negligible external friction.

Some difficulties were encountered when reloading billet 1 into the extrusion apparatus since the diameter of the billet had expanded during the first extrusion step to a diameter approximately 0.007 in. larger than the cylinder bore. In spite of the fact that the end of the cylinder bore was chamfered most of the lubricant was scraped off during reloading. This resulted in an extrusion load appreciably higher than before and considerable metal welding occurred. The push-out load was in the neighborhood of 500,000 lb; hence the push-out load was considerably higher than that in the first step.

An examination of the grid pattern showed much more local distortion than was observed in the initial extrusion step. In order to assure properly lubricated billets, thenceforth all billets used for the plastic-flow studies were relubricated after each incremental extrusion step and chilled to approximately —100 F in liquid nitrogen before replacing in the extrusion chamber. This permitted the billet to be assembled into the chamber without force. After reassembly of the cold billet into the chamber, a waiting period of 15 min, as determined by thermocouple measurements, brought the billet and cylinder temperature to within 5 deg F of room temperature.

All experimental results reported in the following sections of this paper were obtained by reloading a lubricated chilled billet into the extrusion chamber after each extrusion step, followed by a 15-min waiting period before applying the extrusion load.

Results and Discussion

Fig. 1 shows typical photographs of distorted grid lines on the meridian plane for incremental extrusion steps varying from 0.020 to 0.100 in. of billet reduction. These patterns appear to be identical with those obtained with lead reported earlier in spite of the fact that the extrusion load had increased by a factor of 10. The only obvious difference appears to be in the somewhat increased widening of the grid lines along the extrusion axis which can be attributed to the variation in depth of these machined lines, the aluminum grid lines apparently having been cut to a slightly greater depth than those on the lead billets.

After each incremental extrusion step the grid pattern was photographed and the ten times enlarged image of this pattern was projected on a screen. The instantaneous position of metal particles as represented by the intersection of grid lines was then plotted as dots on this screen. Consecutive plotting of positions of intersecting grid lines during eight incremental extrusion steps permitted the determination of instantaneous velocity vectors, i.e., direction and magnitude as described in the earlier paper. Inasmuch as the distorted grid patterns of Fig. 1 are symmetrical, only one half of the billet pattern was analyzed. All subsequent figures showing the complete meridian plane were obtained by a mirror-image method.

Fig. 2 shows the composite graph of the particle-flow directions during all eight incremental extrusion steps. While the load increased continuously during these extrusion steps, the particle-flow directions at any given point and stage of deformation were invariant. Hence it is possible to construct from this flow pattern streamlines or flow tubes as shown in Fig. 3. These streamlines were used, as will be shown later, for the determination of plastic strains since they permit integration of the strain-rate equations.

The dimensionless velocity ratios V/V_B, where V is the particle velocity and V_B is the corresponding velocity of the base end of the billet, are shown in Fig. 4 as constant velocity-ratio lines. These lines were obtained from cross plots of the experimentally determined velocity ratios as functions of axial position z from the orifice. The results represented in Figs. 2 or 3 and Fig. 4 permit the determination of the instantaneous velocity vectors as well as the axial and radial components of these vectors.

Comparing these figures with those obtained with lead, it is found that the instantaneous directions are identical and the velocity-ratio plots show no differences in the pattern, but minor differences in the position of these constant ratio lines. These minor differences may be attributed to experimental errors in determining and averaging the velocity ratios. To the extent to which this investigation permits, therefore, it may be concluded that lead and aluminum have an identical velocity-vector pattern in an inverted extrusion process, for the same geometrical shape and the same degree of boundary lubrication. These observations may have profound theoretical as well as practical significance, since they indicate that the flow pattern may be independent of the mechanical properties of the metal.

The principal strain-rate directions calculated from the equation

$$\tan 2\alpha_z = \frac{\dot{\gamma}_{zr}}{\dot{\epsilon}_z - \dot{\epsilon}_r} \qquad [1]$$

are given in Fig. 5. The crosses show the maximum and minimum principal directions for more than 400 calculated points on one side of the center line at spacings of 0.1 in. in both the radial r and axial z-directions. The strain rates are calculated from the velocity vectors by means of the equations

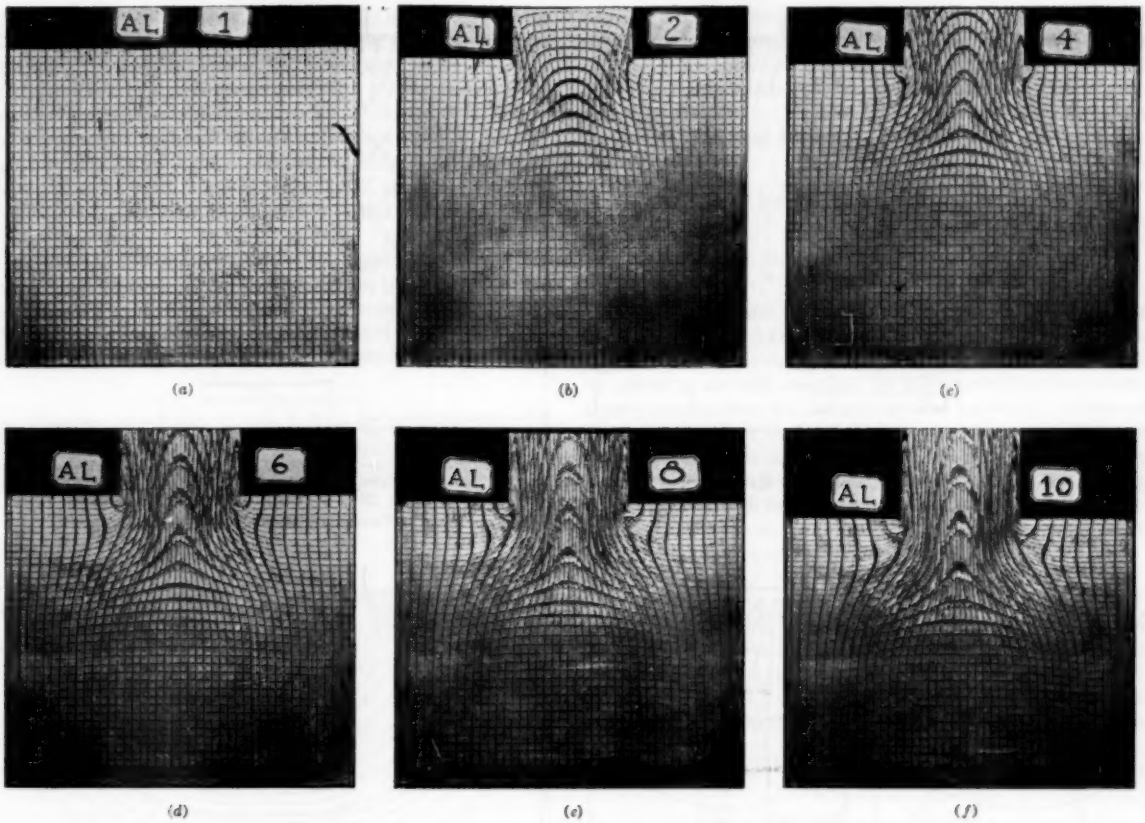

FIG. 1(*a–f*) DEFORMED ORIGINALLY SQUARE GRID LINES WHEN EXTRUDING SAME 2S-O ALUMINUM BILLET IN INCREMENTAL STEPS IN AN INVERTED EXTRUSION PROCESS

(Billet diam = 4.3 in., bar diam = 1.5 in., extrusion ratio = 8.25; reduction in area = 87.8 per cent; extruded at room temperature, cylinder wall and die friction $\simeq 0$.)

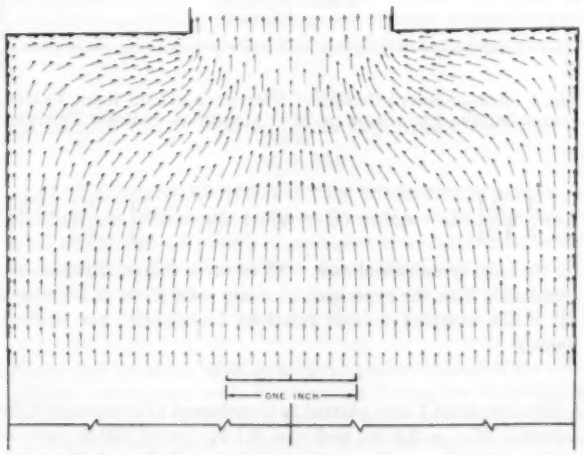

FIG. 2 STEADY-STATE PARTICLE-FLOW DIRECTIONS DURING EXTRUSION OF 2S-O ALUMINUM AT ROOM TEMPERATURE

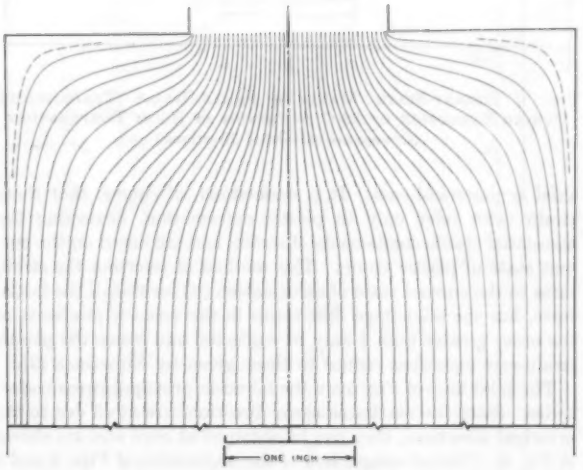

FIG. 3 FLOW TUBES OR STREAMLINES DURING EXTRUSION OF 2S-O ALUMINUM AT ROOM TEMPERATURE

$$\left.\begin{aligned} \dot{\epsilon}_z &= \frac{\partial u}{\partial z}, \quad \dot{\epsilon}_r = \frac{\partial v}{\partial r} \\ \dot{\gamma}_{zr} &= \frac{\partial u}{\partial r} + \frac{\partial v}{\partial z} \end{aligned}\right\} \quad \ldots\ldots\ldots\ldots [2]$$

at each of the more than 400 co-ordinate points by obtaining the slopes from curves at each reference point of the axial velocity component u, and the radial velocity component v, as functions of z and r. These components of plastic strain rates $\dot{\epsilon}_z$, $\dot{\epsilon}_r$, and $\dot{\gamma}_{zr}$ completely describe the instantaneous rate of straining for the

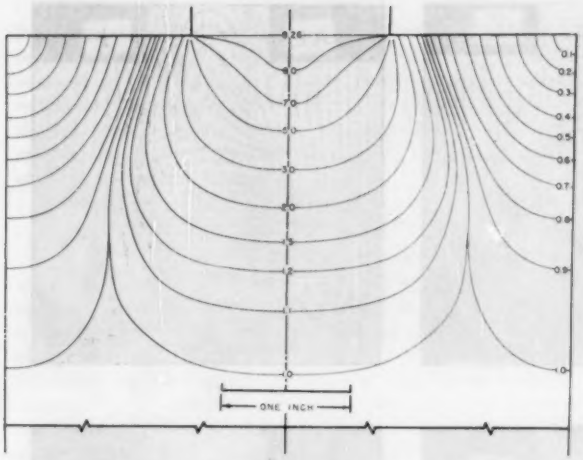

FIG. 4 CONSTANT STEADY-STATE VELOCITY RATIO LINES DURING EXTRUSION OF 2S-O ALUMINUM AT ROOM TEMPERATURE

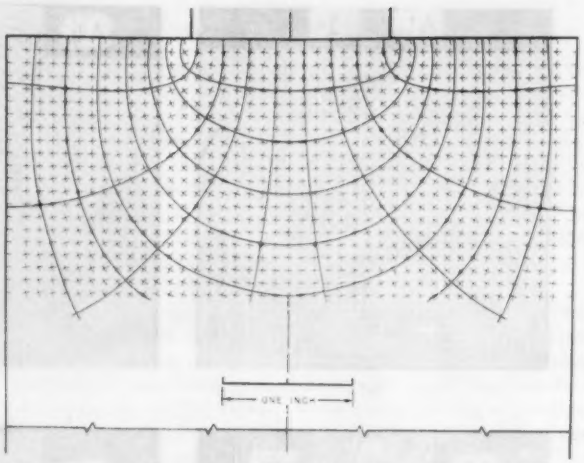

FIG. 5 STEADY-STATE PRINCIPAL STRESS TRAJECTORIES DURING EXTRUSION OF 2S-O ALUMINUM AT ROOM TEMPERATURE
(Crosses are calculated directions.)

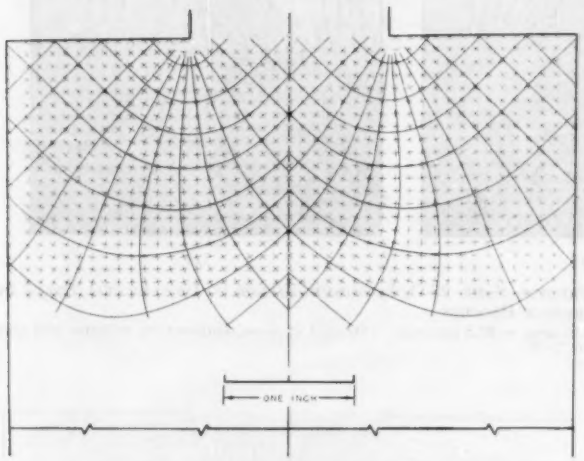

FIG. 6 STEADY-STATE MAXIMUM SHEAR-STRESS TRAJECTORIES DURING EXTRUSION OF 2S-O ALUMINUM AT ROOM TEMPERATURE
(Crosses are calculated directions.)

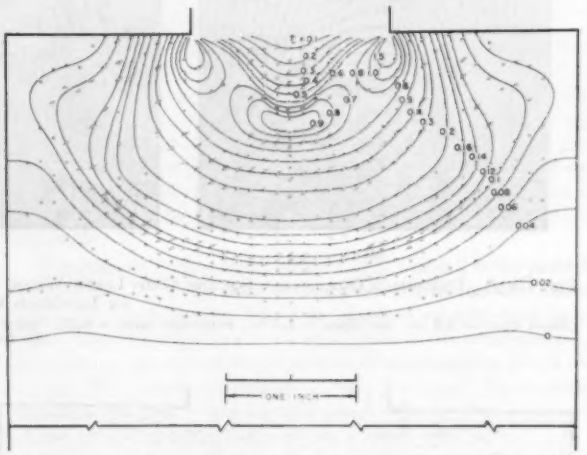

FIG. 7 STEADY-STATE CONSTANT EFFECTIVE STRAIN-RATE TRAJECTORIES DURING EXTRUSION OF 2S-O ALUMINUM AT ROOM TEMPERATURE

axial symmetrical case. It is understood, of course, that these strain rates refer only to plastic deformation, neglecting the associated elastic components of strain, and are based on the current state of plastic strain. This method of referring the strain rates to the current state of deformation (6) instead of the initial state, has the advantage that terms in the velocity gradients of the order greater than 1 may be neglected and hence the plastic strain-rate equations reduce to those given by Equations [2].

The solid lines of Fig. 5 are the faired-in principal stress trajectories. Since the maximum shear directions are at 45 deg to the principal directions, they can be obtained at once and are shown in Fig. 6. Critical comparison of the trajectories of Figs. 5 and 6 with those obtained with lead again reveal that they are essentially identical. Small differences again may be attributed to experimental errors in determining magnitude and direction of the particle velocities as well as the determination of the velocity gradients of Equations [2].

The effective strain rate $\dot{\bar{\epsilon}}$ which is a measure of the rate of plastic deformation is a complex strain-rate quantity and is given by

$$\dot{\bar{\epsilon}} = \frac{2}{3}\sqrt{\frac{1}{2}\left[(\dot{\epsilon}_z - \dot{\epsilon}_r)^2 + (\dot{\epsilon}_r - \dot{\epsilon}_\theta)^2 + (\dot{\epsilon}_\theta - \dot{\epsilon}_z)^2\right] + \frac{3}{4}\dot{\gamma}_{zr}^2} \quad [3]$$

for the axial symmetrical case. All terms in this equation are determinable from the experimental strain rates given in Equations [2] if the constant volume relations (continuity) are utilized, namely

$$\dot{\epsilon}_z + \dot{\epsilon}_r + \dot{\epsilon}_\theta = 0 \quad [4]$$

The calculated $\dot{\bar{\epsilon}}$ were plotted as functions of z for constant r, for intervals of $z = 0.1$ in. and $r = 0.1$ in., for all 400 or more coordinate positions. Curves were then faired through the calculated points and constant values of $\dot{\bar{\epsilon}}$ were subsequently taken from these curves and plotted in Fig. 7. Constant strain-rate lines were then faired through the plotted points. These effective strain rates have units of time (min^{-1}) and are analogous to instantaneous strain rates for uniform deformation usually given in in/in. per min.

It must be kept in mind, however, that the strain rates are referred to the current stage of deformation instead of the initial

undeformed state as is the usual practice. It may be noted from this figure that the strain rate is highest near the die corner and goes through a maximum rate along the extrusion axis. Comparison of the effective strain-rate pattern with that of lead again reveals that they are essentially identical. It is also of interest to note that the plastic zones for both aluminum and lead extend approximately 2.4 in. upstream from the orifice. Owing to the difficulty encountered in determining small strain rates by the present method, however, the boundary of this plastic zone is not precisely known.

Inasmuch as aluminum work-hardens during plastic deformation the total strains must be known in order to permit the determination of the stress distribution. The total effective natural strains $\bar{\epsilon}_n$ consequently have been calculated along the dotted flow paths of Fig. 8 and are shown by symbols; constant strain

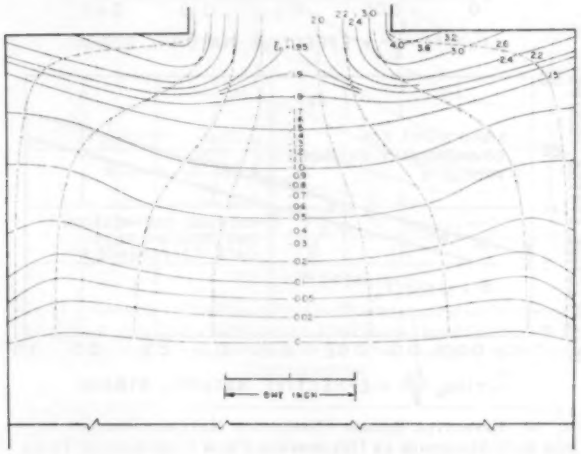

FIG. 8 STEADY-STATE EFFECTIVE NATURAL STRAIN TRAJECTORIES DURING EXTRUSION OF 2S-O ALUMINUM AT ROOM TEMPERATURE

trajectories were then faired through the points. The following procedure was used in determining the effective natural strains: Consider an infinitesimal effective plastic strain at a point as given by

$$d\bar{\epsilon} = \dot{\bar{\epsilon}}dt \quad \ldots\ldots [5]$$

Equation [5] can be replaced by the approximate equation

$$\Delta\bar{\epsilon} = \dot{\bar{\epsilon}}\Delta t \quad \ldots\ldots [6]$$

where Δt is a small increment of time required for a particle to move a small distance Δs along its flow path. The $\Delta\bar{\epsilon}$ is now a small effective strain, which is analogous to a small strain as defined by the equation for uniform deformation, namely

$$\epsilon = \frac{l - l_o}{l_o} \quad \ldots\ldots [7]$$

except that the small effective strain $\Delta\bar{\epsilon}$ takes account of the nonuniform deformation actually occurring during the deformation process. Another difference is that the equivalent original length l_o of any fiber as given by Equation [7] is an instantaneous length at any particular stage of plastic deformation and does not refer to a fiber of length l_o in the undeformed state. As with small strains in uniform deformation, small effective strains cannot be added; hence it is necessary to convert small strains to natural strains before additions can be performed. In uniform deformation processes a natural strain is defined as

$$\epsilon_n = \int_0^{\epsilon_n} d\epsilon_n = \log_e \frac{l}{l_o} = \log_e (1 + \epsilon) \quad \ldots\ldots [8]$$

where l_o and l are the initial and final lengths of fibers during uniform deformation processes, as, for example, in a tension test up to the maximum load. In this case l_o and l could refer to the initial and final gage length of the test bar and ϵ is the engineering strain as given by Equation [7]. Hence an effective natural strain can be formed analogously as the natural strain of Equation [8], namely

$$\left.\begin{aligned} \Delta\bar{\epsilon}_n &= \log_e (1 + \Delta\bar{\epsilon}) = \log_e (1 + \dot{\bar{\epsilon}}\Delta t) \\ \bar{\epsilon}_n &= \sum_0^t \log_e (1 + \dot{\bar{\epsilon}}\Delta t) \end{aligned}\right\} \quad \ldots\ldots [9]$$

In order to perform the integration it was necessary to calculate the times at which a particle occupied a certain position along the flow paths shown as dotted lines in Fig. 8. This was accomplished by assuming average velocities for incremental displacements of these particles along the flow paths. The increments of time were then added to yield the total time required for a particle to move from the zero strain line or plastic zone boundary to the particular position in question. Small errors involved in totaling times due to uncertainties in the location of the plastic-zone boundaries were ignored because the initial plastic strains are small as compared with those occurring in the central region of the billet or near the die edge.

It is of interest to note that the time required for a particle to cross the plastic zone (i.e., 2.4 in.) takes approximately $^1/_2t$ along the center line and more than $2^1/_2t$ along the cylinder wall to reach the orifice, if t is the time required for the butt end of the billet to move a distance of 2.4 in. It is obvious from this that particles originally located in the same cross section of the billet, e.g., sur-

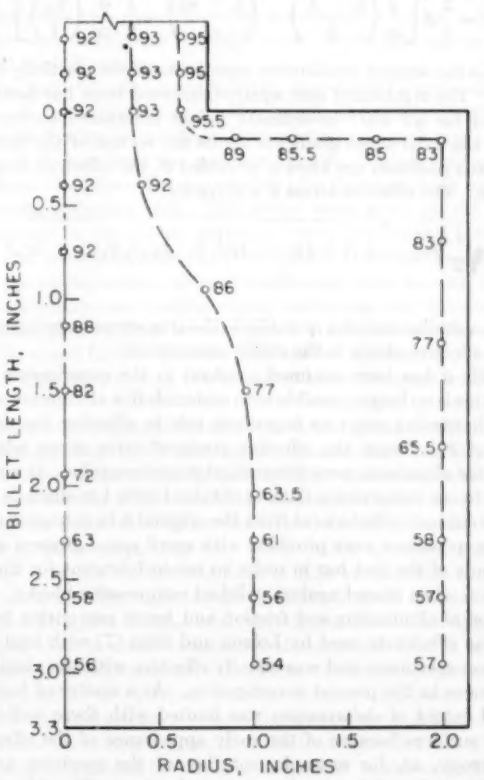

FIG. 9 ROCKWELL H HARDNESS NUMBERS (60 KG, $^1/_8$-IN. STEEL BALL) ON SURFACE OF SPLIT ALUMINUM BILLET AFTER EXTRUSION; REDUCTION OF BILLET LENGTH AT ROOM TEMPERATURE WAS $^3/_4$ IN.

face and center, will be found far removed from each other in the extruded bar.

The integration or summing up of the incremental times in Equation [9] was performed graphically and the calculated points shown in Fig. 8 were obtained from plots of total strains as functions of position s along the strain paths. It can be observed from Fig. 8 that the effective natural strains in the extruded bar are lowest ($\bar{\epsilon}_n = 1.95$) on the center line and become increasingly larger at the die edge ($\bar{\epsilon}_n > 4.0$). This is partially confirmed in practice since high grain deformation and residual stresses are found in the surface layers of extruded bars.

When comparing the effective natural strains in the extruded bar with those calculated by assuming that the same reduction in area takes place but under condition of uniform deformation, i.e.

$$\bar{\epsilon}_n \text{ (uniform)} = \log_e \left(\frac{D_o}{D}\right)^2 = \log_e \left(\frac{4.3}{1.5}\right)^2 = 2.1 \ldots [10]$$

it is found that only the central portion of the billet is subjected to these lower strains. Confirmation of the existence of this strain pattern also may be gained by comparing the hardness pattern of Fig. 9 obtained from hardness readings on a partially extruded billet, with those of Fig. 8. Only a degree of correspondence was achieved, however, because the billet had been reduced in length by only $^3/_4$ in. and hence the hardness readings along the surface of the extruded bar were lower than would be the case had the surface been fully work-hardened. It becomes at once evident that simple deformation theories cannot be used for describing accurately nonuniform deformation processes.

It has been shown in earlier papers (2, 3, 4, 5) that the equation

$$\frac{\partial \sigma_z}{\partial r} = \frac{2}{3}\bar{\sigma}\left[\frac{\partial}{\partial r}\left(\frac{\dot{\epsilon}_z - \dot{\epsilon}_r}{\dot{\bar{\epsilon}}}\right) - \left(\frac{\dot{\epsilon}_r - \dot{\epsilon}_\theta}{r\dot{\bar{\epsilon}}}\right) - \frac{1}{2}\frac{\partial}{\partial z}\left(\frac{\dot{\gamma}_{rz}}{\dot{\bar{\epsilon}}}\right)\right] \ldots [11]$$

satisfies the statical equilibrium equations and the plasticity equations. The right-hand side square-bracketed term has been calculated for all 400+ co-ordinate points mentioned earlier and hence the axial-stress gradients across the section of the billet at various z-positions are known, provided $\bar{\sigma}$, the effective stress, is known. The effective stress $\bar{\sigma}$ is given by

$$\bar{\sigma} = \sqrt{\frac{1}{2}\left[(\sigma_z - \sigma_r)^2 + (\sigma_r - \sigma_\theta)^2 + (\sigma_\theta - \sigma_z)^2\right] + 3\tau_{rz}^2} \quad \ldots\ldots [12]$$

and is a similar complex quantity in the true-stress components, as is the effective strain in the strain components.

While $\bar{\sigma}$ has been assumed constant in the experiments with lead, this is no longer possible with materials like aluminum, where work hardening plays an important role in affecting the magnitude of $\bar{\sigma}$. Hence the effective strain-effective stress relationships for aluminum were determined experimentally. It was decided to use compression data as obtained with 1-in-diam × 1-in-long solid test cylinders cut from the original 6-in-extrusion diam.

The specimens were provided with small spiral grooves at the flat ends of the test bar in order to retain lubricant for the end surfaces when placed against polished compression blocks. This method of eliminating end friction and hence preventing barreling was effectively used by Loizou and Sims (7) with lead compression specimens and was equally effective with the aluminum specimens in the present investigation. As a matter of fact, the useful extent of deformation was limited with these well-lubricated surfaces because of the early appearance of the effects of anisotropy, as, for example, rotation of the specimen axis or transformation of the circular cross section to an ellipsoid; whichever of the phenomena occurred depended on the specimen orientation in the original extrusion.

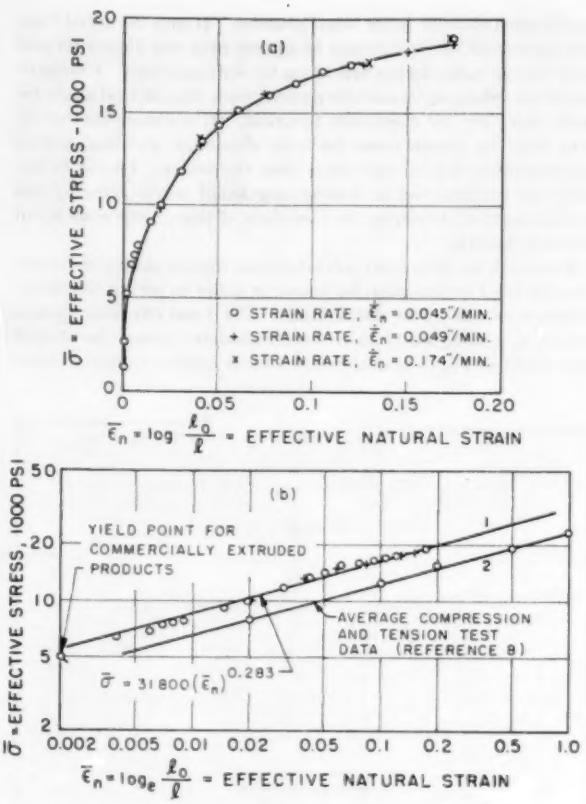

FIG. 10 EFFECTIVE STRESS—EFFECTIVE NATURAL STRAIN CURVES FOR 2S-O ALUMINUM AS DETERMINED FROM COMPRESSION TESTS

The compression data for three constant strain rates varying from $\dot{\bar{\epsilon}}_n = 0.045$ to 0.174 ipm for a limited range of deformations are shown in Fig. 10(a). The effective stress $\bar{\sigma}$ is the true axial stress and the effective natural strain $\bar{\epsilon}_n$ is equal to

$$\bar{\epsilon}_n = \log_e \left(\frac{D}{D_o}\right)^2 = \log_e \left(\frac{l_o}{l}\right)$$

since no barreling of the specimen occurred; l and D being the instantaneous specimen length and diameter, respectively, while l_o and D_o are those prior to deformation. As was to be expected, $\bar{\sigma}$ was found to be a function only of effective natural strain and independent of strain rate. Because of the limited deformation achieved with the compression specimens of the present investigation, however, these results were compared with those from an earlier investigation (8) for which larger strains were available.

Those data have been replotted as Curve 2 in Fig. 10(b) and are the average results of compression tests and tension tests on 0.505-in-diam specimens machined from $^3/_4$-in. extruded 2S-O aluminum rounds. The tension stresses were corrected for necking by using the Bridgman method of correction which takes account of the nonuniform stress distribution across a necked section. The present compression test data also can be plotted as a straight line on log-log paper and this line is essentially parallel with Curve 2.

The reasons for differences in magnitude of stress for any given strain for these data were not determined but are attributable to differences in the initial states and the chemical composition of these specimens. The equation $\bar{\sigma} = 31{,}800\ \bar{\epsilon}_n^{0.283}$ for the extrapolated curve was used to calculate $\bar{\sigma}$ for values of $\bar{\epsilon}_n$ within the extrusion.

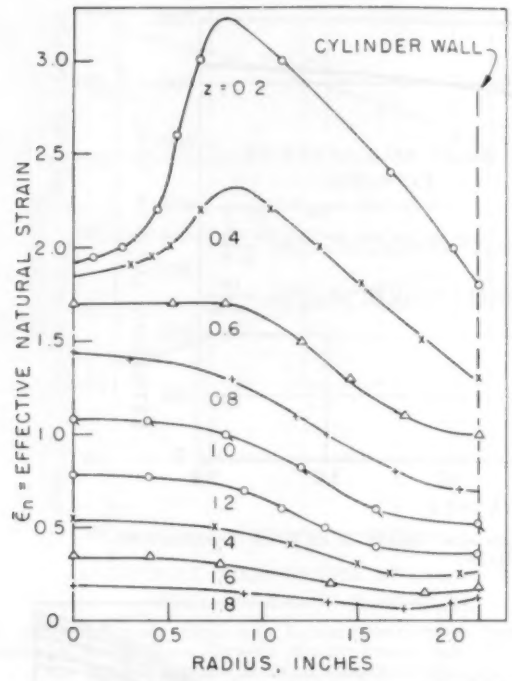

FIG. 11 EFFECTIVE NATURAL STRAIN DISTRIBUTION AS FUNCTION OF RADIUS AND FOR VARIOUS SECTIONS UPSTREAM FROM ORIFICE OR DIE DURING STEADY-STATE EXTRUSION OF 2S-O ALUMINUM AT ROOM TEMPERATURE

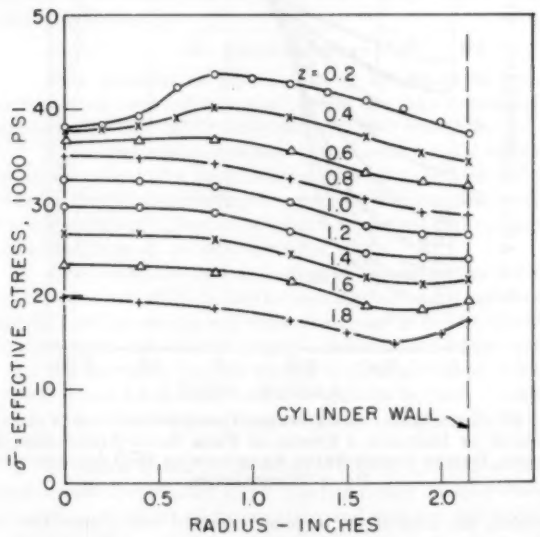

FIG. 12 EFFECTIVE STRESS DISTRIBUTION AS FUNCTION OF RADIUS FOR VARIOUS SECTIONS UPSTREAM FROM ORIFICE OR SHARP-EDGED DIE DURING STEADY-STATE EXTRUSION OF 2S-O ALUMINUM AT ROOM TEMPERATURE

The effective natural strain and effective stress distributions as functions of r for various z-positions are shown in Figs. 11 and 12, respectively. It is of interest to note that the large variation of strains across the section at $z = 0.2$ in., i.e., near the orifice, results in relatively small variations of $\bar{\sigma}$. However, $\bar{\sigma}$ varies appreciably with upstream distance z even though the variation at any particular cross section is small. The $\bar{\sigma}$ values obtained from Fig. 12 can now be used to solve for the stress gradients of Equation [11]. The integration of Equation [11] across the section at constant z can be performed by joining of slopes to obtain a continuous curve, or, if sufficient points are available, by transforming Equation [11] into a finite-difference equation, namely

$$\Delta\sigma_z = \frac{2}{3}\bar{\sigma}\,[f(\text{strain ratios})]\Delta r \quad \ldots\ldots\ldots [13]$$

where the square-bracketed terms of Equations [11] and [13] are identical.

If Δr is chosen as a small quantity, the errors in the determination of the increments of axial stress are small and may be ignored. Since the numerical values of the square-bracketed term of Equation [11] or [13] were available for intervals of 0.1 in., it was decided to use $\Delta r = 0.1$ in. Substituting $\Delta r = 0.1$ in. in Equation [13], the total variation of the axial stress was determined for several sections z.

Inasmuch as the total extrusion load at any section z was constant because of negligible wall friction it was possible to calculate the magnitude of the axial stress as follows: Let L equal the axial load and K_z a constant unknown stress; then equilibrium demands that

$$L = K_z\pi r_o^2 + \sum_{0}^{r_o}\left[\sum_{0}^{r}(\Delta\sigma_z)\right]\Delta A_r \quad \ldots\ldots\ldots [14]$$

from which σ_z at any radius r is given by

$$\sigma_z = K_z + \sum_{0}^{r}(\Delta\sigma_z) \quad \ldots\ldots\ldots [15]$$

Hence Equation [14] permits the evaluation of K_z at any particular distance z from the orifice provided the load L is known. Under these conditions the axial stress distribution can be determined from Equation [15].

The loads for billet 2 extruded in incremental lengths as functions of the instantaneous billet length are shown in Fig. 13. Only the loading curves have been plotted and each new loading curve is started from the measured length. This length was determined after the billet was removed for photographing from the preceding extrusion step. The strain rates given on the figure correspond to the plastic portion of each incremental extrusion step and were kept essentially constant. It should be observed that the plastic portion of each loading curve can be used to construct a continuous loading curve, indicating that the stepwise extrusion process may be considered a continuous process. It may be noted further that the load has not assumed as yet a constant value even though the length of billet 2 was reduced by 1.2 in.

Effects of extrusion rates also were investigated and the results are shown in Fig. 14. The extrusion rates as shown on this figure varied from 0.045 to 0.575 ipm of billet reduction, which corresponds to rates of bar extrusion varying from 0.37 to 4.75 ipm. It may be noted that all curves follow the solid loading line of billet 2, taken from Fig. 13. Even billet 1, which was previously extruded under conditions of high surface friction to the state shown in Fig. 14, followed the billet 2 and 3 loading curves closely. It is also evident from this figure that longer billets are required than those investigated if the extrusion load is to reach constancy. Unfortunately, the present extrusion equipment cannot be used for this purpose and the constant load value must be obtained by extrapolation; hence the dashed curve is the extrapolated load curve and it is assumed that at least 2.4 in. of billet reduction is required for the load to level off as shown in Fig. 14. For purposes of the subsequent evaluation of axial stresses a constant extrusion load of 1,300,000 lb was assumed.

With the foregoing load substituted in Equation [14] the axial-

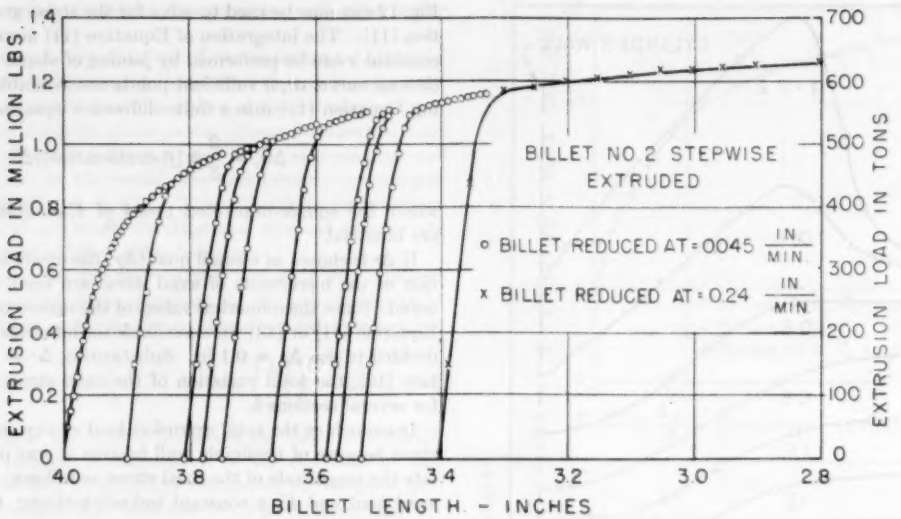

FIG. 13 LOADING CURVES DURING EXTRUSION OF 2S-O ALUMINUM (BILLET 2) AT ROOM TEMPERATURE IN INCREMENTAL STEPS

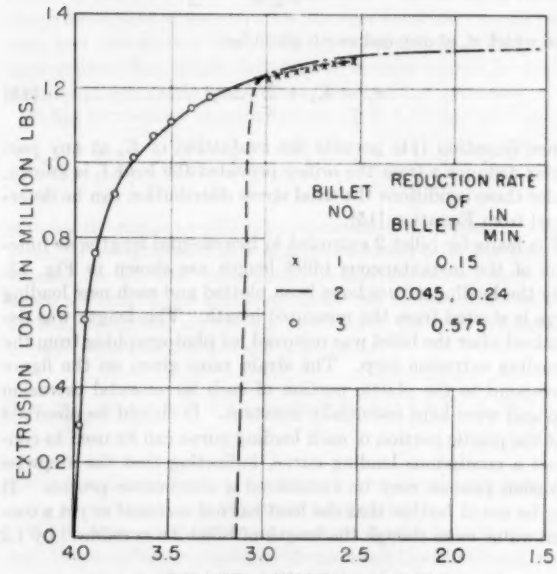

FIG. 14 EFFECT OF EXTRUSION SPEED ON EXTRUSION LOAD DURING EXTRUSION OF 2S-O ALUMINUM AT ROOM TEMPERATURE WITH 87.8 PER CENT AREA REDUCTION
(Inverted process with zero wall friction.)

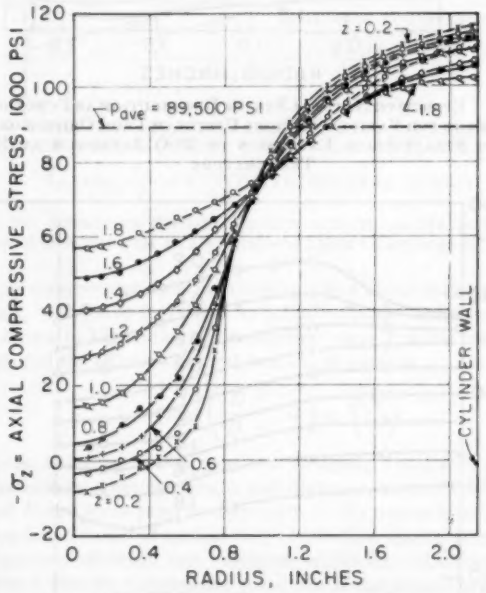

FIG. 15 CALCULATED AXIAL-STRESS DISTRIBUTION, FOR VARIOUS SECTIONS AT DISTANCE z UPSTREAM FROM SHARP-EDGED DIE OR ORIFICE, DURING STEADY-STATE EXTRUSION OF 2S-O ALUMINUM AT ROOM TEMPERATURE

stress distributions were calculated and are shown in Fig. 15. The shapes of these curves agree closely with those obtained with lead but some differences exist. While for lead a compressive stress existed near the extrusion axis for section $z = 0.2$ and 0.4 in., the stresses obtained for aluminum were tensile stresses. Whether or not this condition actually exists, or if it is due to inaccuracy of load determination or to difficulty of determination of strain rates and strains in the region of high particle velocities, is presently not known. Attention is drawn to the fact that the axial-stress curves tend to approach the average stress as given by the load divided by the billet cross-section area at z-positions quite removed from the orifice. Indeed, the trend of the curves appears to be such that outside of the plastic zone, as might be expected, the axial stress becomes constant and a condition of hydrostatic pressure prevails.

It is possible also to calculate other stress components from combinations of the plasticity equations as, for example, the radial stress σ_r, as given by the following equation

$$\sigma_r = \sigma_z - \frac{2}{3}\bar{\sigma}\left(\frac{\dot{\epsilon}_z - \dot{\epsilon}_r}{\dot{\bar{\epsilon}}}\right) \quad \ldots\ldots\ldots\ldots [16]$$

The calculated axial and radial-stress components at the cylinder wall are shown in Fig. 16. It is noted again that the stresses tend toward the average pressure $p_{avg} = 89{,}500$ psi. It is also of interest to note that the radial stress σ_r in the plastic zone, which corresponds at the cylinder wall to the wall pressure,

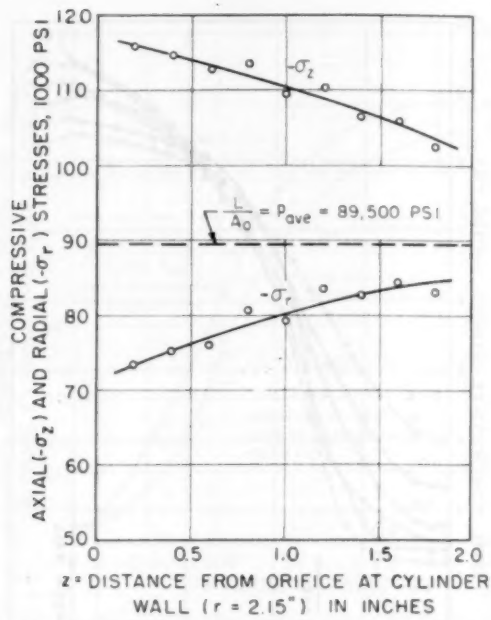

FIG. 16 CALCULATED AXIAL AND RADIAL COMPRESSIVE STRESSES ALONG CYLINDER WALL DURING STEADY-STATE EXTRUSION OF 2S-O ALUMINUM AT ROOM TEMPERATURE

is below the average pressure p_{avg} and agrees with earlier observations made with lead extrusions. Hence the average pressure p_{avg} appears to be a safe pressure for use as a design pressure for extrusion cylinders.

CONCLUSIONS

1 Flow patterns as represented by instantaneous velocity vectors in an inverted extrusion process of a solid cylindrical bar appear to be identical for both lead and 2S-O aluminum.

2 The correspondence of flow patterns for a metal influenced by strain rates and a metal subject to work hardening indicates that the flow is characterized by geometry and degree of external friction and gives indication of being independent of the properties of the metals or alloys being extruded.

3 Effective strain rates and effective natural strains are highest at the corner of the die and hence indicate nonuniform distribution of work hardening and residual stresses in the extruded bar. Highest metal deformation occurs at the extruded-bar surface.

4 The extrusion load for the 4.3-in-diam aluminum billet extruded into a 1.5-in-diam solid bar appears to reach a constant value only after a 2.4-in. or greater billet length reduction has occurred.

5 Extrusion speeds in the range of 0.37 to 4.75 ipm of bar extrusion were investigated and it was found that the load was only a function of extent of deformation and was not influenced by extrusion speed.

6 The axial compressive stresses, as in the case of lead extrusions, were lowest at the extrusion axis and highest at the cylinder wall but tended to a uniform distribution as the nonplastic zone, approximately 2.4 in. upstream from the billet, was approached. The general shapes of the stress curves of lead and 2S-O aluminum were similar, except that the stresses in the aluminum billet near the orifice were small tensile stresses.

7 The radial stresses in the plastic zone, which are equivalent to wall pressure in the extrusion chamber, are below the average pressure as determined by the extrusion load divided by the billet cross-sectional area. Radial stress and average pressure, however, appear to coincide at a distance greater than 2.4 in. upstream from the orifice, which is beyond the plastic zone. Hence design bursting pressures appear to be safe for the present extrusion processes reported when based on average pressure.

ACKNOWLEDGMENTS

The authors wish to thank the National Science Foundation for making funds available, and the University of California for its research grants for the support of this project. They also wish to thank the Division of Civil Engineering at the University of California for the use of the 4,000,000-lb testing machine and the Division of Mechanical Engineering at the University of California for offering shop facilities and mechanic's time for construction of test equipment and preparation of billets. They also wish to thank Mr. Lockrem, Senior Mechanician, University of California Production Laboratory, for his continuous interest and aid in the carrying out of the experimental work.

BIBLIOGRAPHY

1 "Plastic Flow in a Lead Extrusion," by C. T. Yang and E. G. Thomsen, Trans. ASME, vol. 75, 1953, p. 575.

2 "Experimental Stress Determination Within a Metal During Plastic Flow," by E. G. Thomsen and J. T. Lapsley, Jr., Proceedings of the Society for Experimental Stress Analysis, vol. 11, no. 2, 1954, p. 59.

3 "An Experimental Investigation of the Mechanics of Plastic Deformation of Metals," by E. G. Thomsen, C. T. Yang, and J. B. Bierbower, University of California Publications in Engineering, vol. 5, no. 4, 1954, pp. 89–144.

4 "An Experimental Study of Metal Extrusions at Various Strain Rates," by J. Frisch and E. G. Thomsen, Trans. ASME, vol. 76, 1954, p. 599.

5 "A New Approach to Metal-Forming Problems—Experimental Stress Analysis for a Tubular Extrusion," by E. G. Thomsen, Trans. ASME, vol. 77, 1955, pp. 515–522.

6 "Theory of Perfectly Plastic Solids," by W. Prager and P. G. Hodge, John Wiley & Sons, Inc., New York, N. Y., 1951, pp. 120–121.

7 "The Yield Stress of Pure Lead in Compression," by N. Loizou and R. B. Sims, *Journal of the Mechanics and Physics of Solids*, London, England, vol. 1, 1953, p. 234.

8 "Investigation of the Validity of an Ideal Theory of Elasto-Plasticity for Wrought Aluminum Alloys," by E. G. Thomsen, I. Cornet, I. Lotze, and J. E. Dorn, NACA TN 1552, Washington, D. C., July, 1948, p. 1.

Discussion

P. G. HODGE, JR.[5] The authors are to be congratulated on a fine piece of experimental work in computing the strains due to extrusion. One cannot help but be impressed by the close similarity between the results obtained for aluminum and those previously obtained by Thomsen, Yang, and Bierbower[6] for lead despite the fact that the two materials have quite different stress-strain characteristics. The writer would like to suggest that some figures from the earlier report be included so that the reader may see this striking similarity.

The technique of visioplasticity for interpreting the experimentally observed results appears to be quite valuable. However, while experiments are an indispensable tool in analysis and design (indeed, it is doubtful if any theory could predict this close agreement between two different materials), there is no question but that it is expensive and time-consuming. Therefore the authors' experimental work would be even more valuable if it could be related to a theory which would enable further predictions to be made.

With this in mind, the writer would like to emphasize not only the agreement between the stress fields for aluminum and lead,

[5] Associate Professor of Applied Mechanics, Department of Aeronautical Engineering, Polytechnic Institute of Brooklyn, N. Y. Mem. ASME.

[6] See authors' Bibliography (3).

but also the rather close agreement of both with a simple theoretical solution for plane strain of Lee.[7] This agreement was pointed out in the earlier paper,[8] but for some reason was not mentioned here.

The theoretical solution is not identical with the experimental one, the primary difference being the extent of the region of plastic flow. However, the writer would like to suggest to the authors that they take this theoretical stress solution, and compute the corresponding velocity pattern for an ideal material. This velocity pattern can then be used in exactly the same way as the experimentally obtained pattern to obtain the various quantities of interest, using the real material properties of aluminum. Finally, if the quantities so computed turn out to be in good agreement with each other, a really valuable analysis and design tool will have been provided for the extrusion process.

E. S. Howarth.[9] This paper is a worth-while contribution to the science of metalworking. The authors are to be congratulated on having so carefully carried out the tedious experimental work and so clearly presented the analytical results. Their efforts have resulted in a better understanding of the stresses and strains which develop during the extrusion operations. Confidence developed through the application of this method to their simplified conditions of relatively slow indirect extrusion, thorough lubrication, and a commercially pure strain-hardening metal should encourage the application of the method to more complex extrusion problems.

In the commercial extrusion of many aluminum alloys the maximum permissible extrusion speed for a given extrusion temperature is limited to that which will result in a high-quality surface on the product. Exceeding this speed results in an unsatisfactory checked, cracked, or broken surface. Qualitatively, it has been known that such unsatisfactory surfaces result from the tensile stresses developed as the extrusion emerges from the cylinder. This paper reveals the magnitude of these stresses for 1100-O aluminum (2S-O). Although these stresses were low it is significant that they were tensile in nature as compared to the compressive stresses which existed in the previous work by the authors employing lead. For other higher-strength aluminum alloys the tensile stresses in the vicinity of the die may be much greater. It would, therefore, be worth while to determine these stresses for a high-strength aluminun alloy which is more subject to the type of surface failure mentioned than is commercially pure aluminum.

Authors' Closure

The authors wish to take this opportunity to thank Professor Hodge and Mr. Howarth for their thought-provoking discussions of the paper.

Inclusion of certain curves from the lead extrusion experiments reported in reference (3) was considered at the time of preparation of the paper; having in mind the policy of the ASME, it was felt that elaboration would be avoided in the interest of brevity. However, inasmuch as Professor Hodge feels that it would be desirable to include some of the results for comparison, the axial-stress distribution for lead, given in Fig. 17, is included. These results have been discussed in the text of the paper where it was pointed out that the axial stress along the extrusion axis and near the orifice is compressive rather than tensile.

Professor Hodge's comments regarding comparison of theory with experiment are well taken since no reference was made to the fact that three solutions to the extrusion problem were compared in a companion paper, presented to the panel discussion of the ASME Research Subcommittee on plastic working of metals[9] at the same 1954 Annual Meeting in New York, N. Y., of the Society. These are the present visioplasticity solutions for axial stress and pressure distribution at $z = 0.8$ in., the slip line or Hencky plastic-sector solution for an ideal solid, and the work-of-deformation solution reproduced in Fig. 18. It is seen that the Hencky plastic-sector solution for the axial-stress distribution is in good agreement with experiment, although it requires some extrapolation into the region where the metal is supposed to be rigid. This extrapolation has been shown as a dotted line following the general shape of this curve, while in reality, it should be a horizontal line since the stress is assumed to be constant beyond the plastic sector. It may be noted also that the axial stress as predicted from the work-of-deformation method, also shown in Fig. 18, assuming uniform deformation, gives an axial-stress distribution which is in substantial error. Hence uniform-deformation theories cannot be used to get detailed knowledge of the distribution of stress when a metal is deformed nonuniformly. This does not infer, however, that the work-of-deformation method of solution always leads to wrong results. To the contrary, it was shown in the same paper[9] by evaluating the work of deformation from the experimental strains and mechanical properties of the aluminum alone, i.e., by integrating all infinitesimal work

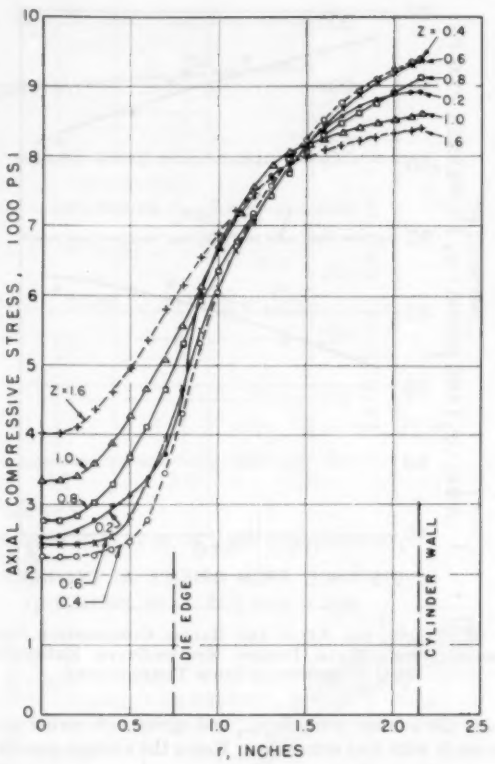

Fig. 17 Calculated Axial-Stress Distribution, for Various Sections at Distance z Upstream From Sharp-Edged Die or Orifice, During Steady-State Extrusion of Commercially Pure Lead at Room Temperature

[7] See authors' Bibliography (6).

[8] Chief, Mechanical Engineering Division, Aluminum Research Laboratories, New Kensington, Pa. Mem. ASME.

[9] "Plasticity Equations and Their Application to Working of Metals in the Work-Hardening Range," by E. G. Thomsen, presented December, 1954, at Panel Discussion of the ASME Research Subcommittee on Plastic Working of Metals, 1954 Annual Meeting of the ASME.

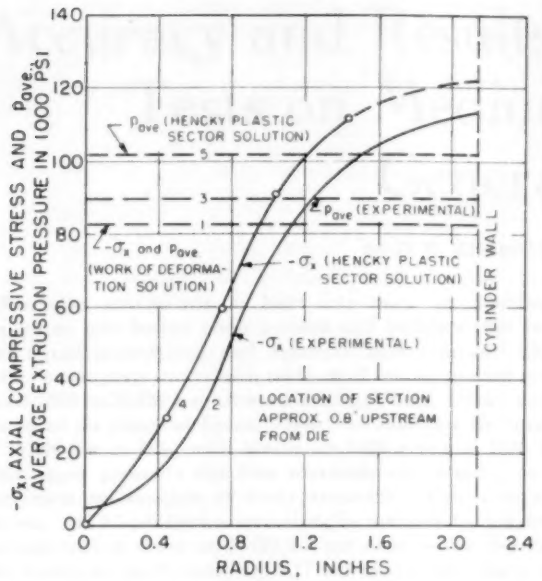

FIG. 18 COMPARISON OF SOLUTIONS FOR A 4.3-IN-DIAM SOLID CYLINDRICAL BILLET OF 2S-O ALUMINUM EXTRUDED INTO A 1.5-IN-DIAM SOLID CYLINDRICAL BAR AT ROOM TEMPERATURE AND WITH NEGLIGIBLE CYLINDER WALL AND DIE FRICTION

quantities along the actual particle-flow paths and summing them up over the whole section, an extrusion pressure of 95,000 psi could be predicted, which is in substantial agreement with the observed pressure of 89,500 psi. The equation used was

$$p_{ave} = \frac{1}{A_0 l_0} \int_0^V \int_0^{\bar{\epsilon}_n} \bar{\sigma} dV d\bar{\epsilon}_n = \frac{1}{A_1} \sum_0^{A_1} \left[\frac{31800}{1.283} \bar{\epsilon}_n^{1.283} \right] \Delta A_1$$

where A_0 and A_1 are billet and bar cross-sectional areas, dV is infinitesimal volume of annulus in billet which transforms at constant volume into another annulus in bar, ΔA_1 is a particular incremental cross-sectional area of a transformed annulus in bar which has been deformed to an effective strain $\bar{\epsilon}_n$.

A more comprehensive comparison of stress fields in an extrusion as obtained from experiments with those obtained from plane strain and axial symmetrical solutions is now available,[10] and comparison of velocity fields will soon be made available when experimental plane-strain studies now in progress have been completed. It should be noted here[9] that the visioplasticity technique is valuable in obtaining a specific solution for a given forming problem but is not intended to supplant theoretical solutions. It offers rather a means of checking these solutions. Detailed experimental study of large deformation and stress distribution is virtually an unexplored territory. In answering his own question as to whether slip-line field results are correct, Ford[11] says: "There are hardly any experiments which are conclusive because most investigators have used small deformations and have tried to observe the first yielding of material, which is so much dependent upon the elastic behavior and the transition from the elastic to the plastic region."

The extrusion of higher-strength-aluminum alloys as suggested by Mr. Howarth has been considered by the authors, but not carried out, since it requires the construction of new extrusion equipment in order to withstand the increased loads. While strain-rate effects for low-strain rates for both lead (4) and aluminum did not seem to affect the velocity patterns, an effect must be present if in commercial extrusion processes a limiting extrusion velocity for sound products exists. The authors can make no conclusive statement at this time, but it is possible that wall friction is a factor and that the extrusion speed may affect the temperature distribution in the billet in hot-forming. Recent extrusion experiments with maximum wall and die friction (as may be predicted from the slip-line theory) yield an appreciably different velocity pattern than those for negligible wall friction.

[10] "Comparison of Slip Line Solutions With Experiment," by E. G. Thomsen. Paper submitted to Applied Mechanics Division of ASME, May 1, 1955.

[11] "The Theory of Plasticity in Relation to Its Engineering Applications," by Hugh Ford, *Zeitschrift für angewandte Mathematik und Physik*, vol. 5, Fas. 1, 1954, p. 19.

Accuracy and Results of Steam-Consumption Tests on Medium Steam Turbine-Generator Sets

By D. E. KIMBALL,[1] WEST LYNN, MASS.

Precision steam-rate or heat-rate tests on turbine-generator sets insure their owners and builders that the sets equal guaranteed and expected performance. The writer's company made such tests on 22 medium-sized sets rated 2500 to 18,750 kw between 1946 and 1952. Most were tested at its plant at Lynn, Mass., on facilities for loads of 15,000 kw or less, with steam up 1500 psig and 1000 F. This paper presents the test methods and results, emphasizing an analysis of their accuracy. This analysis shows: (*a*) 0.5 per cent uncertainty in manufacturing and factory-testing these sets; (*b*) 0.3 per cent as the day-to-day uncertainty of tests; (*c*) 0.17 per cent uncertainty to be charged to the instrumentation of factory tests; (*d*) probably 0.5 per cent poorer performance of tests in the owner's plants than in factory tests. This analysis confirms our belief of many years that it is proper to accept or reject a turbine-generator set on the basis of precision tests, with no allowance for test error.

Introduction

PRECISION steam-rate or heat-rate tests on turbine-generator sets provide the best possible assurance to their owners and builders that such equipments are equaling guaranteed and expected performance. The author's company made such tests on 22 medium-sized sets, rated 2500 to 18,750 kw, between 1946 and 1952. Most tests were made in the factory at Lynn, Mass., on facilities for tests at 15,000 kw or less, with steam up to 1500 psig, 1000 F; the other four were tested in the owner's plants.

All these tests were made with great care and thoroughness to allow reliance on the results. These precautions included the following:

1 Testing five sets of duplicate turbines.

2 Measuring most data on two or more identical instruments duplicating each other.

3 Retesting certain runs on the same turbine.

4 Making certain that no different standard for design, manufacturing, or inspection is applied to the turbines to be tested than to the untested ones.

These precision tests serve three purposes:

1 A few tests were required by the turbine purchasers.

2 As a quality-control measure, the other turbines were tested to make certain that our turbines, in general, have suitable margin above guaranteed performance.

3 To obtain engineering data; most tests included more runs than are required simply to determine the margin above guarantees.

This paper presents the methods of making these tests and the test results with particular emphasis on the analysis of their accuracy.

The results and methods of similar tests in the owner's plants on large steam turbine-generator sets built by the company are presented in references (1, 2, 3).[2]

Summary

The test performance of each turbine was equal to or better than guaranteed, as originally assembled, before these precision tests.

The analysis of the accuracy of these tests shows that they have the following "errors" or "uncertainties"; these are measures of the tendency of test variations in these types of data to cause deviations of the results of individual tests from the average of many tests:

(*a*) 0.8 per cent[3] for designing, building, and precision-testing a turbine of these sizes, based on the scatter of the margins of these tests above predicted performance.

(*b*) 0.5 per cent for manufacturing and factory-testing a turbine, based on tests on five sets of duplicate turbines.

(*c*) 0.3 per cent for the day-to-day error of testing, based on duplicate runs on eight turbines.

(*d*) About 0.17 per cent as the combined error of the instrumentation that is used for calculating the performance of factory tests, based on the duplication in that instrumentation; this is the square root of the sum of the squares of the following effects on over-all performance from the errors in the different types of data:

	Per cent
Flow by weighed condensate	0.12
Generator output	0.10
Initial temperature	0.02
Initial pressure	0.02
Exhaust pressure	0.07

The error for throttle flow by weighed condensate may be significantly less than this 0.12 per cent; it will not exceed 0.20 per cent.

The analysis also shows 0.5 per cent as the probable amount by which performance in the owner's plants is poorer than in factory tests; possibly this difference is only 0.1 per cent.

The analysis shows the following errors for the supplementary instrumentation that is not used for calculating the performance of factory tests on turbines of this size:

---

[1] Supervisor, Turbine Thermodynamic Development Engineering, Medium Steam-Turbine Department, General Electric Company. Mem. ASME.

Contributed by the Power Division and presented at the Annual Meeting, New York, N. Y., November 28–December 3, 1954, of The American Society of Mechanical Engineers.

Note: Statements and opinions advanced in papers are to be understood as individual expressions of their authors and not those of the Society. Manuscript received at ASME Headquarters, November 8, 1954. Paper No. 54—A-253.

[2] Numbers in parentheses refer to the Bibliography at the end of the paper.

[3] These errors are root-mean-square errors, corresponding to about the central 68.2 per cent of a large group of tests; hence about one test in a group of six will be poorer than the group's average by more than these errors, and one in six will be that much better than average. See Root-Mean-Square Errors in the Appendix.

(*a*) 0.35 per cent for an uncalibrated precision steam-flow nozzle; 0.31 per cent if calibrated.

(*b*) Possibly 0.24 per cent for a calibrated precision condensate-flow nozzle.

(*c*) Possibly 0.62 per cent for the enthalpy-drop efficiency of noncondensing tests.

This analysis of precision tests confirms our belief of some 30 years that it is proper to accept or reject a turbine-generator set on the basis of the direct comparison of guaranteed performance with the performance of precision tests, with no allowance for test error. However, the analysis of approximate tests using mostly station instruments confirms our belief that such tests are not a proper basis for rejecting a unit unless its performance is at least 1.5 per cent poorer than guaranteed.

Test Results

The primary results of these tests are their margins above guaranteed steam rates or heat rates. Fig. 1 plots these results versus date of test. For each test of this period, this plot presents the average of its margins at $^2/_4$, $^3/_4$, and $^4/_4$ loads. The average of the margins of all 22 sets is 2.5 per cent better than guaranteed, with average margins for individual turbines varying from 0.0 per cent to +4.2 per cent. These are the results of the precision tests on these turbines as originally assembled with usual design and manufacturing standards.

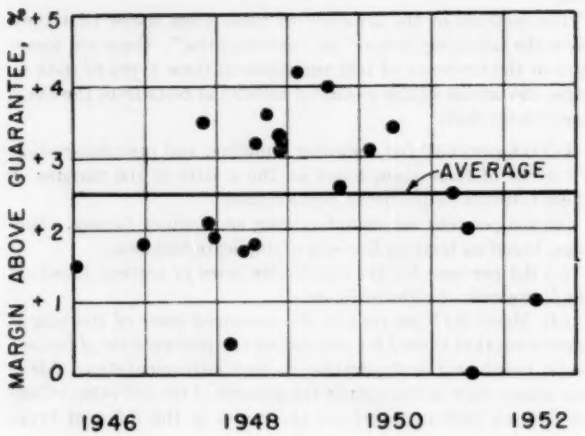

Fig. 1 Test Margins Above Guarantees—All Medium Land Turbine-Generator Tests

But a plot of margin above guarantees is inadequate for technical analysis. It involves significantly more scatter than can be charged to manufacturing and testing: For instance, each turbine must be built with an integral number of stages; thus, when we design certain turbines, we expect they will have more margin above guarantees than others.

Hence, for technical use, we present the test results as margins above predicted performance. In Fig. 2, we plot these margins for the 22 sets versus date of test. This shows that they average 1.2 per cent better than predicted, the two best turbines being 2.5 per cent better than predicted; the three poorest about 0.3 per cent below predicted. But we are interested in a more specific measure of the scatter of these tests from their average. The statisticians say that we can express the scatter of a group of data by δ,[4] its standard deviation; this is the root-mean-square deviation of the individual units in the group from their average; it is calculated by Equation [1] in the Appendix.

[4] The nomenclature is listed in the Appendix.

The standard deviation of the margins of these 22 tests above predicted performance is 0.82 per cent. This implies that about 15.8 per cent, or 3.5 of the 22, will be below the average for the 22 by more than 0.82 per cent, and 3.5 will be that much better than average. Observation of Fig. 2 indicates that approximately this distribution exists.

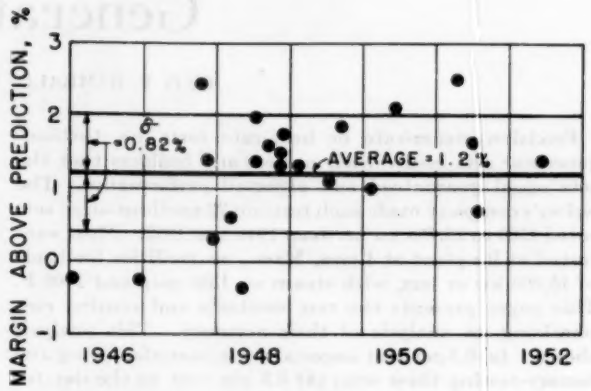

Fig. 2 Test Margins Above Predictions—All Medium Land Turbine-Generator Tests

As expected, this 0.82 per cent standard deviation for the margins above predictions is much less than 1.2 per cent, the standard deviation for the margins above guarantees.

Units Tested

Table 1 presents the turbines tested, listing them in order of testing, and presenting their ratings, contract and test-steam conditions, and test flows.

The first was tested in the owner's plant in 1946. For it, special inspection instructions were applied, obtaining measurements of the shaft packing clearances before and after the factory "spin" test. After its field steam-rate tests, it was opened and the measurements were repeated. This was the only turbine to which any special manufacturing or inspection instructions were applied before its test.

Hence the test margins above predictions represent the average performance of our turbines whether they are tested or not.

Factory Test Facilities

Table 2 lists the factory test facilities for steam-rate tests. They are suitable for precision tests on turbine-generator sets at 15,000 kw or less, with 1500 psig steam at 1000 F, exhausting to 1.5 in. Hg abs.

Figs. 3 and 4 show an 11,500-kw and an 18,750-kw set during factory steam-rate tests.

Accuracy of Test Results

General. These tests furnish us with several measures of their error or uncertainty:

1 They include five sets of duplicate turbines.

2 Each of eight turbines had one or more runs duplicating some previous run on it.

3 All tests had considerable duplication by identical instruments.

4 A precision steam-flow nozzle checks the weighed condensate flows of each factory test.

5 Enthalpy-drop efficiencies check the weighed-flow-output efficiencies of noncondensing tests.

TABLE 1 TURBINE-GENERATOR SETS TESTED

Test No.	Type of Test	Date of Test	Rating KW	Steam Conditions		Avg. Test Throttle Flow, #/Hr
				Contract	Test	
Factory Condensing Tests						
2	Steam Rate	Dec. '46	5,000	400#G, 750 F, 1.5 in. Hg	400#G, 763 F, 1.51 in. Hg	39,600
3	Steam Rate	Oct. '47	3,000	280#G, 700 F, 1.23 in. Hg	266#G, 692 F, 1.09 in. Hg	21,400
4	Steam Rate	Nov. '47	2,500	350#G, 750 F, 2 in. Hg	350#G, 724 F, 2.00 in. Hg	19,000
5	Steam Rate	Dec. '47	3,500	400#G, 750 F, 1.5 in. Hg	400#G, 751 F, 1.45 in. Hg	25,900
6	Steam Rate	Mar. '48	3,000	400#G, 750 F, 2 in. Hg	401#G, 666 F, 2.02 in. Hg	23,700
7 (6)*	Steam Rate	July '48	3,000	400#G, 750 F, 2 in. Hg	400#G, 705 F, 1.98 in. Hg	22,700
8	Steam Rate	July '48	5,000	600#G, 825 F, 1.5 in. Hg	569#G, 776 F, 1.56 in. Hg	33,800
9 (8)	Steam Rate	Sept. '48	5,000	600#G, 825 F, 1.5 in. Hg	571#G, 759 F, 1.62 in. Hg	34,200
10	Steam Rate	Nov. '48	7,500	275#G, 620 F, 2 in. Hg	272#G, 621 F, 2.05 in. Hg	62,000
11	Steam Rate	Feb. '49	11,500	600#G, 825 F, 1.5 in. Hg	512#G, 786 F, 1.29 in. Hg	75,300
12 (11)	Steam Rate	July '49	11,500	600#G, 825 F, 1.5 in. Hg	563#G, 823 F, 1.98 in. Hg	84,500
13	Steam Rate	Sept. '49	4,000	400#G, 700 F, 2 in. Hg	400#G, 706 F, 2.00 in. Hg	34,200
14	Steam Rate	Feb. '50	18,750	850#G, 900 F, 2.25 in. Hg	783#G, 840 F, 2.06 in. Hg	84,600
15	Both	Apr. '51	15,000	850#G, 900 F, 1.5 in. Hg	842#G, 905 F, 1.52 in. Hg	91,600
Field Condensing Tests						
1	Steam Rate	Jan. '46	5,000	400#G, 750 F, 1.5 in. Hg	398#G, 754 F, 1.49 in. Hg	35,400
16	Both	June '51	7,500	600#G, 825 F, 2 in. Hg	600#G, 806 F, 2.00 in. Hg	50,000
17 (15)	Heat Rate	July '51	15,000	850#G, 825 F, 1 in. Hg	835#G, 797 F, 1.41 in. Hg	101,600
18 (15)	Heat Rate	June '52	15,000	850#G, 900 F, 1.5 in. Hg	845#G, 887 F, 1.56 in. Hg	106,700
Factory Noncondensing Tests						
1 NC	Steam Rate	May '48	4,000	585#G, 700 F, 215#G	389#G, 723 F, 139#G	96,200
2 NC	Steam Rate	Nov. '48	2,500	600#G, 700 F, 265#G	520#G, 759 F, 221#G	95,500
3 NC	Steam Rate	Nov. '51	7,500	400#G, 700 F, 40#G	316#G, 721 F, 27.8#G	108,000
4 NC(2NC)	Steam Rate	Dec. '48	2,500	600#G, 700 F, 265#G	502#G, 705 F, 213#G	98,500

*** Numbers in parentheses are numbers of duplicate turbine previously tested.**

TABLE 2 STEAM-RATE TEST FACILITIES AT LYNN PLANTS

Steam generating:
- 3 650 lb, 850 F boilers: total flow, 425,000 lb/hr
- 2 1500 lb, 900 F boilers: total flow, 120,000 lb/hr

Steam superheating:
- 1 separately fired superheater: flow, 120,000 lb/hr at 1000 F

Condensing:
- 1 8900 sq ft condenser for 120,000 lb/hr at 1.5 in. Hg abs
- 1 3500 sq ft condenser for 40,000 lb/hr at 1.5 in. Hg abs

Test bases:
- 1 for 20,000-kw turbine-generator sets
- 2 for 3000-kw turbine-generator sets

Load-absorbing equipment:
- 2 3-phase, 14,400-volt, water rheostats: total capacity, 15,000 kw

Condensate-weighing equipment:
- 2 10,000-lb tanks with automatic timing, weighing, and printing equipment; capacity, 200,000 lb/hr
- 2 3400-lb tanks similarly equipped; capacity, 68,000 lb/hr

Other valuable comparisons include:

1 Factory tests versus field tests.

2 Seven duplicate turbines tested with station instruments.

Tests on Duplicate Turbines. For the five sets of duplicate turbines, Fig. 5 presents a plot versus rating of the deviation of over-all performance of each of two or more duplicate turbines from their average.

The three 15,000-kw turbines form a set which includes one turbine with both factory steam-rate and heat-rate tests, the performance of this turbine being 1.4 per cent better than consistent with factory tests on other turbines; the other two turbines had heat-rate tests in their owner's plants. For these three turbines, the average deviation from their average performance is 0.64 per cent.

Each of the other four sets of duplicate turbines consists of two turbines with factory tests. Their deviation from average performance averages 0.29 per cent, varying from 0.1 per cent to 0.7 per cent among the sets.

We must stop a minute before comparing the deviations of these duplicate tests with the errors derived from other measures of the accuracy of our tests; we must use a precise and somewhat statistical method.

First, statisticians would probably persuade us to use a root-mean-square average of these deviations, getting 0.37 per cent, as $\sqrt{\Sigma\Delta^2/n}$, in place of the direct average of 0.29 per cent. Further, they would note that in each set these deviations are

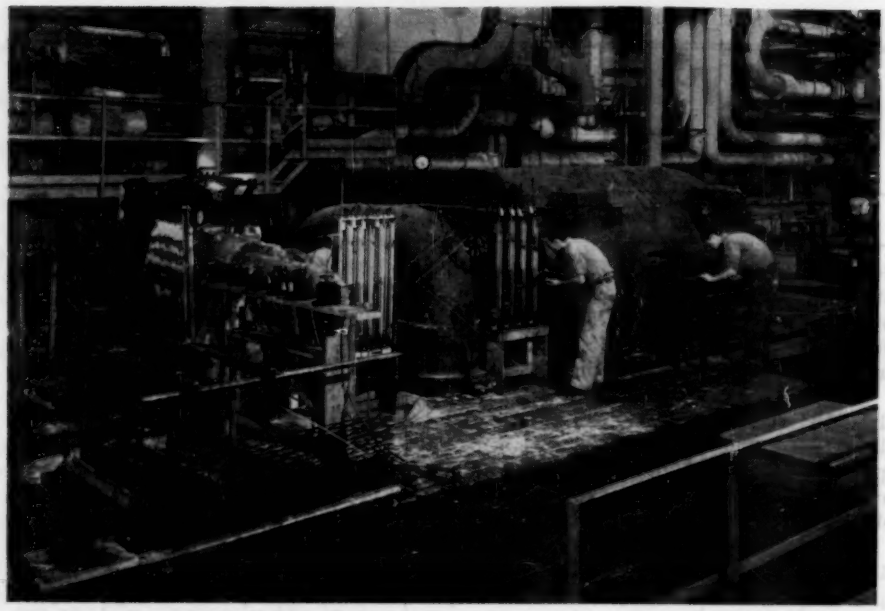

FIG. 3 11,500-KW STEAM TURBINE-GENERATOR DURING FACTORY STEAM-RATE TEST

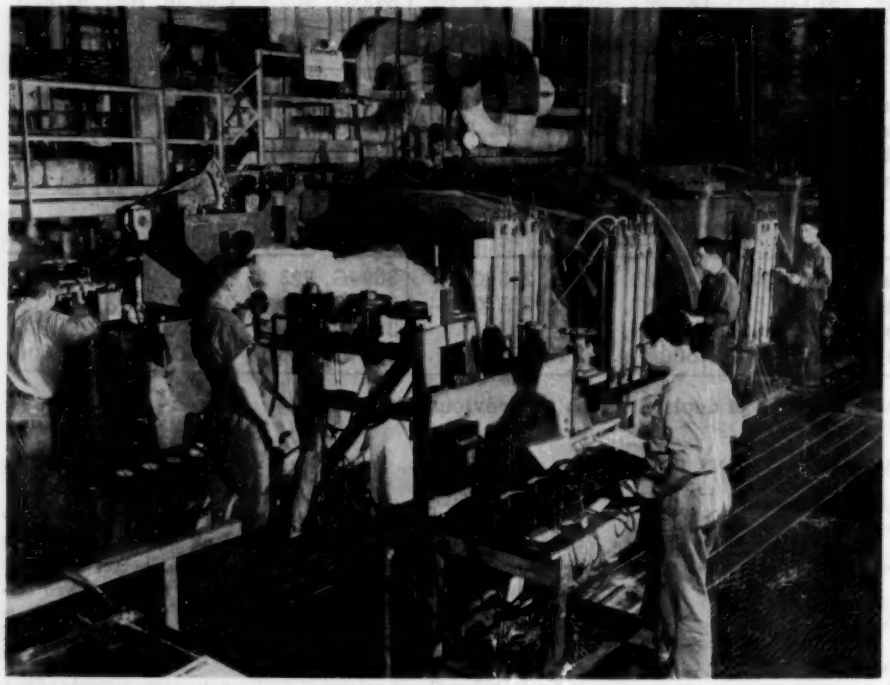

FIG. 4 18,750-KW STEAM TURBINE-GENERATOR DURING FACTORY STEAM-RATE TEST

referred to the average for the set, thus "losing one degree of freedom" and getting smaller deviations than we should use; to correct for this, they multiply by $\sqrt{n/(n-1)}$, where n is the quantity in the set. Thus the 0.37 per cent for the factory tests is increased further to 0.37 $\sqrt{2}$ or 0.53 per cent (the 0.64 per cent for the three 15,000-kw tests becomes 0.89 per cent). They might call 0.53 per cent the root-mean-square deviation of individual tests from average performance. We will call it the root-mean-square error, as a measure of the uncertainty of the average performance of a turbine.

We believe this 0.53 per cent is a fair measure of the error of manufacturing and factory-testing turbines of this size, as derived from factory tests on duplicate turbines. (We believe the 0.89 per cent is a somewhat unsound basis for conclusions.)

Duplicate Runs. These are our next measure of accuracy. We have noted that eight turbines had one or more runs which duplicate the load and steam conditions of a previous run on the same turbine. These duplicate runs were tested 4 hours to 17 days apart; thus they are a measure of the day-to-day variation of test results.

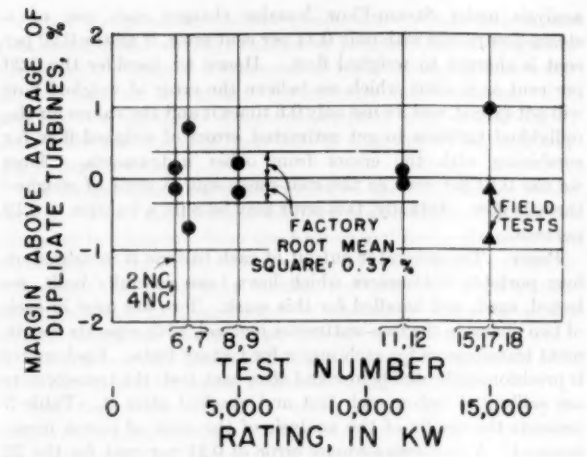

FIG. 5 TESTS ON DUPLICATE TURBINES: TEST MARGIN OF EACH INDIVIDUAL TURBINE ABOVE AVERAGE WITH ONE OR TWO DUPLICATE TURBINES

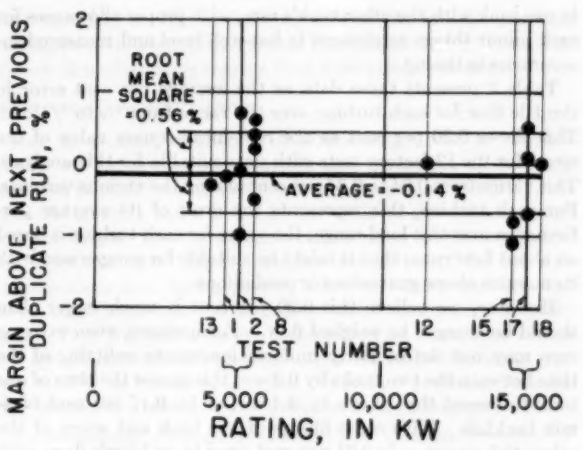

FIG. 6 DUPLICATE RUNS: TEST MARGIN OF EACH INDIVIDUAL RUN ABOVE NEXT PREVIOUS DUPLICATE RUN ON SAME TURBINE

Fig. 6 plots the margin of each of these runs above the performance of the next previous duplicate run on that turbine. This shows that six of the 16 duplicating runs had better performance than the previous run by 0.1 to 0.7 per cent, two showed no change, and eight were poorer by 0.1 per cent to 1.1 per cent; these margins average —0.14 per cent, implying a slight deterioration.

However, we are interested in a measure of the error of these runs, that is, in the magnitude of the uncertainty of each run, whether or not it was better or poorer than its predecessor. We can use 0.56 per cent, the standard deviation of these margins referred to their average, but we must adjust it: First, divide it by 2.0 (to change the difference between a pair of runs to the deviation of each run from their average), and then multiply by $\sqrt{n/(n-1)}$ or $\sqrt{2}$ (to correct from averages based on only two runs), getting a net multiplying factor of 0.707. Thus we get 0.40 per cent as the root-mean-square error of an individual run.

But this error for a run cannot be compared with the 0.53 per cent error for manufacturing and factory-testing a turbine, as just derived from the analysis of tests on duplicate turbines: The 0.53 per cent is based on the differences in performance of turbines over their load range, based on about three runs each for the duplicate turbines. We estimate that the three-run effect reduces the 0.40 per cent to 0.30 per cent.

This 0.30 per cent is a measure of the day-to-day error of the test results of a turbine, expressed as a deviation from its average performance on many days.

DUPLICATE INSTRUMENTATION

General. Our next measure of accuracy of testing is more extensive and more complicated to analyze.

Duplicate instrumentation has several important advantages:

1 It is commonly used to obtain the average of data which varies with location, such as pressure in an exhaust-flange opening.

2 It has often been very valuable to detect a faulty instrument or auxiliary, thus allowing immediate action to eliminate the fault and to reject and replace the test.

3 It always improves the accuracy of the test data: The ratio of the error of several instruments individually to the error of their average tends to equal the square root of their quantity; thus one instrument involves twice the error of the average of four.

4 It measures the accuracy of instruments and their probes, thus permitting proper improvement of test arrangements.

All of our instruments for steam-rate tests are rugged enough for use on a turbine base, yet they are of laboratory accuracy. They are carefully developed, selected, and reserved for steam-rate testing; before and after each test, they are carefully calibrated against laboratory standards which are checked periodically with national standards. There is little need to include in our analysis a significant allowance for the "systematic" error which is not detected by comparing duplicate instruments.

Yet, we find it worth while to include duplicate instrumentation for most types of the basic data used to calculate the performance of most tests. These include:

1 Two tanks weighing condensate for equal alternate periods.
2 Two wattmeters in each generator phase.
3 Two thermocouples measuring initial temperature.
4 Four manometers measuring condensing exhaust-flange pressure.
5 Two dead-weight gages measuring noncondensing exhaust pressure.

Also, we have the following precision checks on the basic data:

1 A steam-flow nozzle to check the weighed flow of each factory test.
2 Enthalpy-drop efficiency to check the flow-output efficiency of noncondensing tests.
3 A precision absolute-pressure gage to check the barometer-manometer exhaust pressure of condensing factory tests.
4 Dead-weight gages measuring the pressure in adjacent passages as checks on the dead-weight gage measuring initial pressure.

For each type of instrument, we have analyzed the average difference between duplicate instruments on each turbine and the variation of this difference from run to run. This analysis obtains the error of measurement of that type of data on each turbine, and it obtains the combined effect on each turbine of the error in all these types of instruments. Similarly, it furnishes the average effect of each type of data on each type of turbine. The Appendix presents the method of this analysis. We will now discuss its results, which Table 3 presents.

Weighed Throttle Flow. On each factory test, the condensed throttle flow for equal alternate periods is weighed in two tanks on precision, carefully adjusted and calibrated scales with precision automatic-timing devices. We compare the rate of flow

in one tank with the other tank's rate, with proper allowances for such minor things as changes in hot-well level and measured inaccuracies in timing.

Table 3 presents these data as the average per cent error in throttle flow for each turbine over the range from 1/2 to 4/4 load. This shows 0.20 per cent as the root-mean-square value of the errors for the 12 factory tests with data suitable for this analysis. This varies from 0.04 to 0.34 per cent among the various turbines. For each turbine, this represents the error of its average performance over this load range; the value for each turbine is based on about four runs; thus it might be suitable for comparison with its margins above guarantees or predictions.

However, we believe this 0.20 per cent is much larger than should be charged to weighed flow. For instance, even extreme care may not detect fairly uniform inaccurate splitting of the time between the two tanks by 0.2 sec; this causes the time of one tank to exceed the other's by 0.4 sec, or by 0.17 per cent of 4-min tankfuls. With eight fillings of one tank and seven of the other, this causes only 0.01 per cent error in an hour's flow; with equal quantities of tankfuls, as in many runs, it causes no error. Thus this would account for most of the 0.20 per cent, but would cause very little error in a turbine's flows. Also, the analysis under Steam-Flow Nozzles charges each use of a steam-flow nozzle with only 0.11 per cent error, if all the 0.20 per cent is charged to weighed flow. Hence we consider the 0.20 per cent as a value which we believe the error of weighed flow will not exceed, and we use only 0.6 times it and the values for the individual turbines to get estimated errors of weighed flow for combining with the errors from other instruments. Thus we use 0.12 per cent as the root-mean-square error of weighed throttle flow. Actually, this error may be only a fraction of 0.12 per cent.

Power. The generator output of each turbine is measured on four portable wattmeters which have been carefully built, selected, aged, and handled for this work. Two are used in each of two phases in the two-wattmeter method, with separate instrument transformers for each meter for factory tests. Each meter is precision-calibrated before and after each test; the transformers are calibrated before each test and checked after it. Table 3 presents the results of the analysis of the error of power measurement: A root-mean-square error of 0.11 per cent for the 22 turbines, with individual turbines from 0.03 to 0.21 per cent. Root-mean-square values for factory and field tests are 0.10 and 0.14 per cent, respectively.

TABLE 3 ERRORS FROM INSTRUMENTATION

Test No.	Error in Weighed Throttle Flow	Over-all Effect of Error in Generator Output	Error in Initial Temp.	Over-all Effect of Error in Initial Temp.	Error in Initial Pressure		Over-all Effect of Error in Initial Pressure	Error in Exhaust Pressure in. Hg or psi		Over-all Effect of Error in Exhaust Pressure	Combined Over-all Effect of Errors in All Instrumentation
	%	%	F	%	psi	%	%	in. Hg	%	%	%
Factory Condensing Tests											
2	0.20,(0.34)*	0.07	0.12	0.010	0.71	0.160	0.011	0.017	1.11	0.10	0.23
3	0.10,(0.16)	0.16	0.08	0.006	0.66	0.213	0.021	0.012	1.02	0.11	0.22
4	0.10,(0.17)	0.11	0.31	0.023	0.19	0.047	0.004	0.016	0.78	0.08	0.17
5	0.11,(0.19)	0.18	0.10	0.008	0.06	0.014	0.001	0.024	1.59	0.11	0.24
6	0.13,(0.22)	0.06	0.22	0.017	0.08	0.016	0.001	0.017	0.84	0.07	0.16
7	0.07,(0.12)	0.10	0.88	0.067	0.11	0.024	0.001	0.014	0.72	0.06	0.15
8	0.04,(0.06)	0.06	0.22	0.017	0.43	0.072	0.004	0.016	0.76	0.06	0.10
9	. . . . .	0.19	0.21	0.016	0.17	0.029	0.002	0.014	0.92	0.08	. . .
10	0.13,(0.21)	0.05	0.08	0.007	0.34	0.072	0.005	0.019	0.96	0.09	0.17
11	0.06,(0.10)	0.06	0.11	0.009	0.07	0.013	0.001	0.017	1.15	0.07	0.11
12	0.02,(0.04)	0.04	0.04	0.003	0.11	0.020	0.001	0.010	1.01	0.06	0.07
13	0.14,(0.23)	0.07	0.18	0.015	0.05	0.013	0.001	0.018	0.92	0.08	0.18
14	0.09,(0.15)	0.06	0.17	0.013	0.16	0.022	0.001	0.021	0.94	0.07	0.13
15	0.03,(0.05)	0.04	. . .	0.016	. . .	. . . .	. . . .	0.013	0.89	0.05	0.07
Field Condensing Tests											
1	. . . . .	0.21	0.19	0.015	. . .	. . . .	. . . .	. . . .	. . .	. . .	. . .
16	. . . . .	0.14	. . .	. . . .	. . .	. . . .	. . . .	. . . .	. . .	. . .	. . .
17	. . . . .	0.04	0.23	0.019	. . .	. . . .	. . . .	. . . .	. . .	. . .	. . .
18	. . . . .	0.13	0.73	0.056	. . .	. . . .	. . . .	. . . .	. . .	. . .	. . .
Factory Noncondensing Tests								psi			
1NC	0.20,(0.33)	0.03	0.41	0.041	0.03	0.009	0.007	0.01	0.02	0.01	0.21
2NC	0.16,(0.26)	0.12	0.05	0.005	0.08	0.016	0.018	0.03	0.02	0.02	0.20
3NC	0.09,(0.15)	0.14	0.26	0.025	0.22	0.048	0.017	0.02	0.08	0.03	0.17
4NC	0.13,(0.22)	0.10	0.30	0.033	0.37	0.081	0.086	0.17	0.02	0.02	0.19
Minimum	0.02,(0.04)	0.03	0.04	0.003	0.03	0.009	0.001	0.01	0.02	0.01	0.07
Maximum	0.20,(0.34)	0.21	0.88	0.067	0.71	0.213	0.086	0.17	1.59	0.11	0.23
Root-Mean-Square:											
Factory Cond.	0.11,(0.18)	0.10	0.29	0.022	0.32	0.082	0.007	0.017	0.99	0.08	0.16
Field Cond.	. . . . .	0.14	0.46	0.035	. . .	. . . .	. . . .	. . . .	. . .	. . .	. . .
Factory Noncond.	0.15,(0.25)	0.11	0.29	0.029	0.22	0.048	0.045	0.09	0.04	0.02	0.19
All Tests	0.12,(0.20)*	0.11	0.32	0.025	0.31	0.075	0.023	. . . .	. . .	0.07	0.17

Each value represents the error in the average data of a turbine-generator set from 1/2 to 4/4 load, as a measure of the effect of that error to cause the deviation of the individual test from the average performance of several tests.

* For errors in weighed throttle flow, values in parentheses are upper limits. We tabulate also estimated values 0.6 times these, for comparing and combining with errors from other instruments.

Initial Temperature. Initial temperature measurements use two selected and carefully calibrated precision thermocouples in finned ASME wells in a low-velocity pipe, measuring their voltages on separate precision potentiometers and auxiliaries. The analysis of these shows a root-mean-square error of 0.32 deg F, with individual turbines from 0.04 to 0.88 deg F; factory, 0.29 deg F; field, 0.46 deg F.

But we are interested in the effect on the performance of the turbine. From the effects of temperature on the test efficiencies of similar turbines and from the Keenan and Keyes steam tables, we obtain factors to convert this error in temperature, in degrees Fahrenheit, to an error in turbine performance, in percentage effect on steam rate, heat rate, or efficiency. Thus we obtain an error which can be compared with the deviations of test over-all performance from predicted, and which can be combined with the errors from flow, power, and other steam conditions.

Thus the root-mean-square error caused by inaccuracy in temperature measurement is 0.025 per cent of over-all performance, varying from 0.003 to 0.067 per cent.

Initial Pressure. Initial pressure measurements on each turbine use a calibrated precision deadweight gage connected to a carefully made hole in the low-velocity inlet pipe. These gages have been so trouble-free and accurate that we rarely use two to measure initial pressure. However, Table 3 presents the results of the analysis of pressures measured on two of these deadweight gages before the steam-flow nozzle in the inlet pipe of most factory tests; this analysis yields a measure of the accuracy of the use of deadweight gages on each of these tests. This shows a root-mean-square error of 0.31 psi, with individual turbines varying from 0.03 to 0.71 psi. As in temperature measurement, we derive factors to convert these errors to per cent of over-all performance. The root-mean-square error in over-all performance for factory condensing tests is 0.007 per cent varying from 0.001 to 0.021 per cent; for noncondensing, 0.045 per cent, 0.007 per cent, and 0.086 per cent. The noncondensing percentages are higher than condensing because their energy ranges are shorter.

Condensing Exhaust Pressure:

Factory Tests. The exhaust pressures of factory condensing tests are measured in four carefully made holes in the walls of an exhaust adapter of the same shape and area as the exhaust-flange opening and about 6 ft long; these pressures are measured on precision manometers with $^1/_2$-in-ID tubes, riders with verniers, and engraved scales. Atmospheric pressure is measured on a calibrated precision mercury barometer in the test building. On four turbines, the pressure near one of the manometer holes was measured on a calibrated precision absolute-pressure gage. We analyzed the variation among the four manometer pressures on each test as a measure of their accuracy and of whether their pressure holes were proper for obtaining the correct average pressure. Also, we analyzed the difference between the barometer-manometer pressure and the pressure by the absolute-pressure gage, as a measure of the error of the barometer; in this analysis, we charged the barometer with only $1/\sqrt{6}$ times the direct difference, assuming that it was much more accurate and more carefully read than the manometer and the absolute-pressure gage. This showed an average error between the absolute-pressure gage and the barometer-manometer pressure of 0.028 in. Hg. So we have charged the barometer with an error of 0.011 in. Hg for all tests.

Table 3 presents the results of the analysis of the errors of exhaust pressure. The errors include the error of the barometer combined with the error in the barometer-manometer pressure as the square root of the sum of the squares. The root-mean-square error in exhaust pressure is 0.017 in. Hg varying from 0.010 to 0.024 in. Hg, or 0.99 per cent of the exhaust pressure varying from 0.72 to 1.59 per cent. These convert to 0.08 per cent of over-all performance varying from 0.05 to 0.11 per cent.

Condensing Exhaust Pressure:

Test in Owners' Plants. For condensing tests in owner's plants, we use similar manometers and barometer to measure pressures in basket tubes in the exhaust-flange opening and pressures in carefully made holes in the walls of the exhaust hood near the flange. The barometer is calibrated at the factory before and after the test. These pressures are corrected for the differences measured during factory tests on similar turbines between these holes and the average of the exhaust adapter pressures. Thus the field tests are corrected to the equivalent of the average exhaust-adapter pressure measured in factory tests, but they tend to be less accurate than the factory pressures because they involve the inaccuracy of both factory and field pressures.

Noncondensing Exhaust Pressure. The exhaust pressure of each noncondensing test is measured on two calibrated precision dead-weight gages, each connected to a separate carefully made hole located in the side of an exhaust adapter immediately below the exhaust flange and having the same area and shape. Table 3 presents the analysis of the differences between the readings of these gages, the root-mean-square error of the individual turbines being 0.09 psi, varying from 0.01 to 0.17 psi. These convert to an average of 0.02 per cent in over-all performance, varying from 0.01 to 0.03 per cent.

Combined Error of Instrumentation. For each turbine, we combine the effects on over-all performance of errors in the various types of test data, adding them as the square root of the sum of the squares. Thus we obtained a measure of the error of test results as indicated by the differences between duplicate instruments. For each type of data, we combine the errors from the individual turbines, as the square root of the sum of their squares. Table 3 includes a summary of these combined errors. For the factory condensing tests, the root-mean-square combined error is 0.16 per cent, varying from 0.07 to 0.24 per cent among the turbines; for the noncondensing tests, the root-mean-square and extreme errors are 0.19, 0.17, and 0.21 per cent, respectively. The 0.12 per cent error in weighed flow accounts for much of the combined error.

Steam-Flow Nozzles. This is the first type of instrumentation that is used as a check on the basic instrumentation for calculating the test performance.

As just noted, the error in throttle flow of these tests accounts for much of their combined error from instrumentation. Also, even extreme care may fail to detect significant leaks from the steam and condensate piping, or into it. Hence, in each of our factory tests, we use a flow nozzle in the inlet steam line as a check on the weighed throttle flow. These are long-radius, low-diameter-ratio, throat-tap nozzles, built with extreme care to the ASME specifications, and carefully installed with a resistance straightener in the approach pipe. Their initial pressure is measured on a calibrated precision dead-weight gage; for pressures less than 600 psig, two differential pressures are measured on precision manometers with riders and verniers; for higher pressures, two initial pressures and two throat pressures are each measured on a calibrated precision dead-weight gage. This type of nozzle has been calibrated carefully, but each specific nozzle has not been, except that several nozzles have been used on about three tests each.

We use these flow-nozzle flows, not to calculate the test performance, but rather to assure us and the turbine owner that the weighed condensate is an accurate measure of throttle flow.

Fig. 7 presents the average apparent discharge coefficient for

each of these 18 factory tests. For each turbine, this is calculated as the average ratio of the throttle flow by weighing to that by the flow nozzle, with adjustment for the measured minor leakages. $\hat{\sigma}_{i-L}$, the standard deviation of average discharge coefficients of the individual turbines from their line, is 0.37 per cent. This is a measure of the combined error of measuring the throttle flow by weighing and by the flow nozzle. Table 3 shows that a directly calculated value of the root-mean-square error of weighed flow is 0.20 per cent. When we subtract this as the square root of the difference of the squares, we get 0.31 per cent, which we will consider tentatively as the error of measuring flow by an uncalibrated steam-flow nozzle.

Fig. 8 presents these same discharge coefficients with lines connecting the tests which used the same flow nozzle. This shows five nozzles with two to five tests each. $\hat{\sigma}_{i-N}$ the root-mean-square standard deviation of each of these tests from the average for all the tests using its flow nozzle is 0.23 per cent; this is our best measure of the combined error of measuring flow by weighing condensate and by a calibrated steam-flow nozzle. Subtracting the 0.20 per cent error of weighed flow leaves 0.11 per cent as a tentative measure of the error each time we use a calibrated steam-flow nozzle, whether for measuring flow during a steam-rate test or for calibrating the nozzle. And the error of measuring flow by a once-calibrated flow nozzle is

$$\sqrt{0.11^2 + 0.20^2 + 0.11^2}$$

or 0.25 per cent, if the nozzle is used with equal accuracy in the calibration and the test.

Under weighed flow, we estimated that 0.12 per cent is more suitable than 0.20 per cent for the error of weighed flow. If so, the error for a steam-flow nozzle each time it is used is $\sqrt{0.23^2 - 0.12^2}$ or 0.20 per cent; and the error for measuring throttle flow by a once-calibrated steam-flow nozzle is $\sqrt{0.20^2 + 0.12^2 + 0.20^2}$ or 0.31 per cent.

With 0.12 per cent as the error of weighed flow, the error for measuring flow by an uncalibrated steam-flow nozzle is $\sqrt{0.37^2 - 0.12^2}$ or 0.35 per cent.

Enthalpy-Drop Efficiency. Enthalpy-drop efficiency is available as a check on the flow-output efficiency of noncondensing tests. By nature, it is a simple test; it requires precise measurements in only initial and final temperatures and pressures. However, it requires a good measure of generator output to determine the load at which to compare test and guaranteed performance. Also, we need accurate measures of generator losses, bearing losses, heat lost from the turbine shell and piping, and net packing leakage. Further, the test temperatures must be unusually uniform to avoid inaccuracy in the allowance for the heat which is added to the metal of the turbine and piping during a run whose temperatures rise even slightly.

On three noncondensing tests, enthalpy-drop efficiency was carefully measured; each included generator-loss tests and a blocked-rotor test for heat loss. Table 4 presents a summary of the comparison of enthalpy-drop and weighed-flow-output efficiencies. It shows 0.65 per cent as the root-mean-square combined error of these two types of efficiency, varying from 0.21 to 0.85 per cent. Allowing for the 0.17 and 0.09 per cent errors of weighed flow and generator output for these three tests leaves 0.62 per cent as the root-mean-square error of enthalpy-drop efficiency. We believe that possibly many enthalpy-drop tests might show that their error is significantly less than this 0.62 per cent.

Tests in Owner's Plants

One measure of the acceptable performance of any equipment

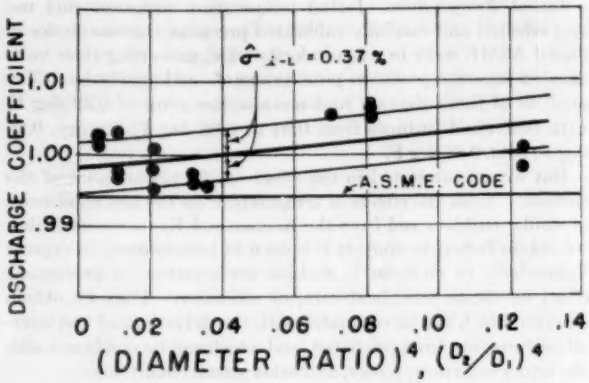

Fig. 7 Steam-Flow-Nozzle Apparent Discharge Coefficients From Factory Steam-Rate Tests on Individual Turbine-Generator Sets

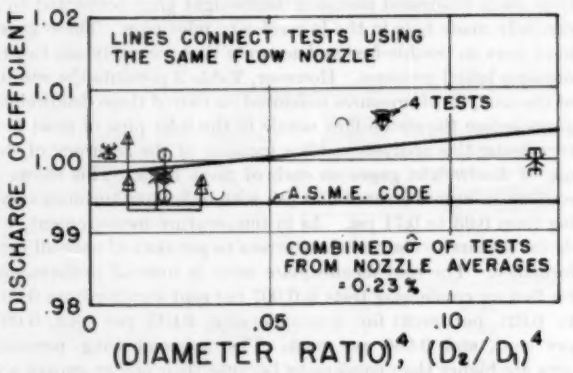

Fig. 8 Steam-Flow-Nozzle Apparent Discharge Coefficients for Individual Flow Nozzles From Factory Steam-Rate Tests

TABLE 4 COMPARISON OF ENTHALPY-DROP AND WEIGHED-FLOW-OUTPUT EFFICIENCIES

	Test	1NC	2NC	4NC	Root mean square
1	Combined error of enthalpy-drop and weighed-flow-output efficiencies, per cent	0.71	0.85	0.21	0.65
2	Error of weighed flow, per cent	0.20	0.16	0.13	0.17
3	Error of generator output, per cent	0.03	0.12	0.10	0.09
4	Error of enthalpy-drop efficiency = $\sqrt{(1)^2 - (2)^2 - (3)^2}$, per cent	0.68	0.83	0.16	0.62

is its record in the owner's plant; hence we made four of these tests in the field.

By nature, field tests are less accurate than factory tests. This is because many field tests need extraction for feed heating. This means a more complicated test to run and calculate: Many more flows, temperatures, and pressures to measure; many valves in the extraction and feed-heating system to check for adjustment or tightness; the high accuracy of weighed flows is not available; there is little chance to observe the steam path after the tests to detect deposits or other unsatisfactory conditions.

However, most of the precision instruments of factory tests are suitable. And in one field test, we measured the condensate on two flow nozzles in series to check each other. Analysis of this one test shows an 0.11 per cent error of the average of the flows of the two nozzles, as used to calculate this turbine's performance or 0.16 per cent error for one nozzle, as usually used. These errors of 0.11 and 0.16 per cent, as derived from one test, should

be increased to 0.16 and 0.24 per cent for two calibrated precision condensate-flow nozzles in series, and for one, respectively, before being compared and combined with the errors of other types of instruments as derived from several tests.

Field Test Versus Factory Tests

We compared the field-test results with factory tests in three ways.

Fig. 9 presents again the margins of the 22 tests above guaranteed performance, but it shows the field and factory tests by different symbols. On it, the four field tests average 1.7 per cent poorer than the 18 factory tests. But this comparison is blurred and warped by differences in the margins of predictions above guarantees. Hence, in Fig. 10, we present margins above predictions, showing the field tests averaging 0.5 per cent poorer than factory tests. We believe that this is a reasonable difference.

However, we are not certain that this 0.5 per cent difference exists, particularly in the larger of these turbines. It will be noted in Fig. 10 that the 0.5 per cent depends principally on the first field test made in 1946. Fig. 11 presents the third comparison, showing six factory steam-rate tests with three field heat-rate tests, all being rated between 5000 kw and 18,750 kw. This analysis was made to determine how consistent these two types of tests might possibly be with each other and within each type. Here, we plot test margin above calculated performance versus a size function. This shows the following:

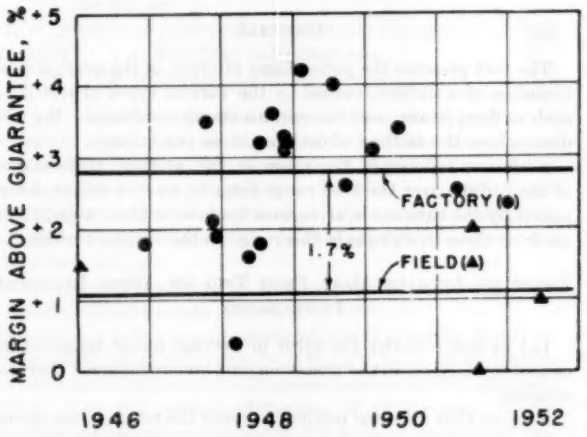

Fig. 9 Test Margins Above Guarantees: All Field and Factory Medium Land Turbine-Generator Tests

1 Five of the six factory tests have a standard deviation of 0.12 per cent from their line.

2 The sixth factory test is 1.4 per cent better than the five turbine line, and far enough inconsistent with their scatter to consider dropping it (see reference 6).

3 The three field tests average only 0.10 per cent below the factory line and have a standard deviation of 0.37 per cent from their line.

Thus, in turbines of this size, it is possible that field tests may not be significantly poorer than factory tests and may have a somewhat larger scatter.

Approximate Tests

Now let us illustrate the accuracy of approximate tests, that is, those using station instruments mostly.

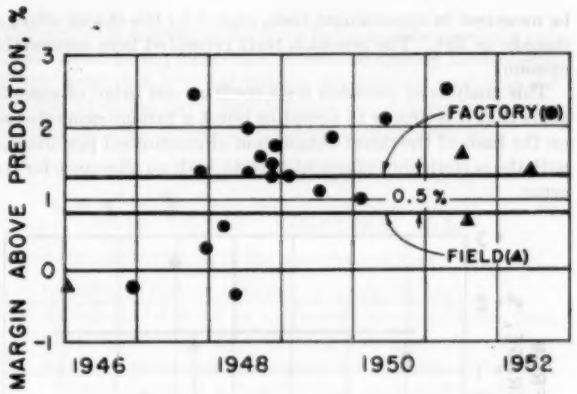

Fig. 10 Margins Above Predictions: Field and Factory Medium Land Turbine-Generator Tests

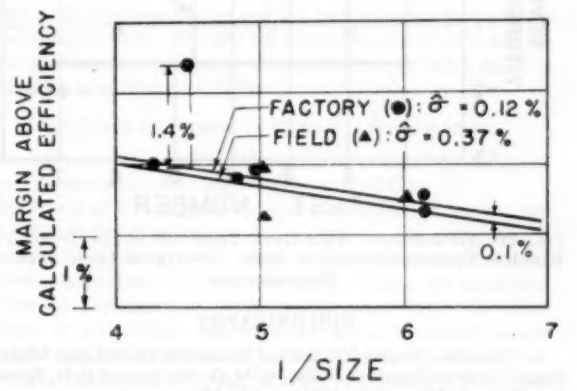

Fig. 11 Margins Above Calculated Efficiencies: Field and Factory Tests on Turbines 5000 to 18,500 Kw

During the period from 1948 to 1950, we made such tests on seven duplicate, clean and new 4000-kw turbine-generator sets. Each had about five runs over a 5-day period, all near rated load. They used calibrated station instruments except:

1 Initial temperature measured with a calibrated precision thermocouple.

2 Generator output measured on a polyphase watthour meter.

3 Exhaust pressure measured in one hole on one or two calibrated precision absolute-pressure gages.

Fig. 12 presents the results: The standard deviation of the seven turbines from their average performance is 1.6 per cent varying from 2.6 per cent above average to 2.0 per cent below it.

We noted before that the error of manufacturing and factory-testing a turbine is about 0.5 per cent. Subtracting this (as the square root of the difference of the squares) leaves 1.5 per cent. Hence practically all of this 1.6 per cent standard deviation is the additional error of these approximate tests.

Conclusions

We often receive data from similar approximate tests. Brief analysis indicates that their errors are often significantly larger than 1.5 per cent, coming usually from flow measurement and from pressures of noncondensing turbines.

On the other hand, for many years, we have believed that we can predict the performance of a turbine more closely than it can

be measured in approximate tests, except for the chance effect of damage or dirt. The precision tests presented here confirm this opinion.

This analysis of precision tests confirms our belief of some 30 years that it is proper to accept or reject a turbine-generator set on the basis of the direct comparison of guaranteed performance with the performance of precision tests, with no allowance for test error.

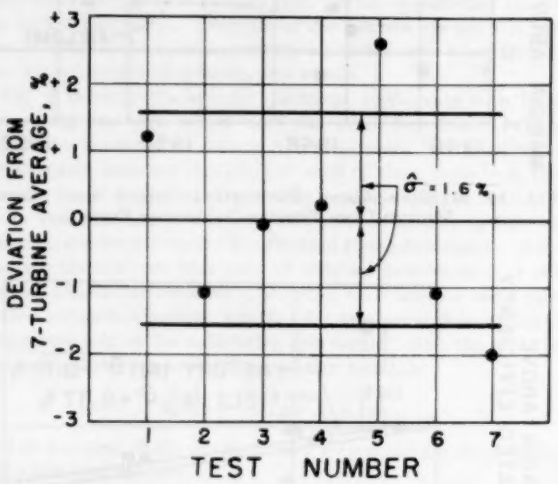

FIG. 12 APPROXIMATE HEAT-RATE TESTS ON SEVEN DUPLICATE 4000-KW TURBINE-GENERATOR SETS: DEVIATION FROM AVERAGE PERFORMANCE

BIBLIOGRAPHY

1 "Relative 'Engine Efficiencies' Realizable From Large Modern Steam Turbine-Generator Units," by G. B. Warren and P. H. Knowlton, Trans. ASME, vol. 63, 1941, pp. 125–135.

2 "Comparative Efficiencies of Central-Station Reheat and Nonreheat Steam Turbine-Generator Units," by C. W. Elston and P. H. Knowlton, Trans. ASME, vol. 74, 1952, pp. 1389–1399.

3 "Experience in Testing Large Steam Turbine-Generators in Central Stations," by E. M. Kratz, published in this issue, pp. 1369–1375.

4 "Describing Uncertainties in Single-Sample Experiments," by S. J. Kline and F. A. McClintock, *Mechanical Engineering*, vol. 75, 1953, pp. 3–8.

5 "Industrial Statistics," by H. A. Freeman, John Wiley & Sons, Inc., New York, N. Y., 1942.

6 "Treatment of Experimental Data," by A. G. Worthing and J. Geffner, John Wiley & Sons, Inc., New York, N. Y., 1944.

Appendix

NOMENCLATURE

The following nomenclature is used in the text and Appendix:

$\hat{\sigma}$ = standard deviation of individual members of a group from average of an infinite group

$$= \sqrt{\frac{\Sigma\Delta^2}{n-1}}$$

Δ = deviation of an individual unit in a group from group's average

n = quantity of units in a group

$\hat{\sigma}_{i-L}$ = standard deviation of individual units in a group from a line representing group; line usually is a least-squares line

$\hat{\sigma}_{i-N}$ = root-mean-square (or equivalent) standard deviation of individual units in several groups from their group averages

ϵ_t = error, or uncertainty, of test results; this is used in this paper as a root-mean-square value representing uncertainty of average performance of a turbine over load range from $^1/_2$ to $^4/_4$ load

ϵ_0 = the uncertainty caused by average difference between two duplicate instruments

ϵ_r = uncertainty caused by error of average difference between two duplicate instruments

ϵ_a = uncertainty caused by deviations from average of data for runs used to calculate average performance of turbine

q_r = quantity of runs used to calculate error of average difference between two duplicate instruments

q_a = quantity of runs used to calculate average performance of turbine

q_s = quantity of instruments used to calculate error of instrumentation

q_c = quantity of instruments used to calculate average performance of turbine

f = quantity of degrees of freedom lost because of referring deviations of individual units in a group to average data for group or to lines based on that data

GENERAL

The text presents the percentages of error, in the average performance of a turbine, caused by the various types of test data such as flow, power, and the various steam conditions. We will discuss here the method of deriving these percentages.

Each one represents the error in the average performance of the turbine over the load range from $^3/_4$ to $^4/_4$ load, as determined by the runs made at various loads over that range; there are from three to six runs in this range on the various turbines.

ERROR IN AVERAGE DATA FROM TWO OR MORE IDENTICAL INSTRUMENTS

Let us first consider the error in average initial temperature caused by the error in the measurements on two adjacent thermocouples.

Suppose that for some unknown reason the temperature measured on the upstream thermocouple averages 0.4 deg F more than the downstream temperature for each run tested. The statisticians analyze this to mean that the standard deviation (or root-mean-square error) of the temperature by one individual thermocouple alone can be calculated as

$$\hat{\sigma} = \sqrt{\frac{\Sigma\Delta^2}{n-1}} \quad \ldots\ldots\ldots\ldots\ldots\ldots [1]$$

or 0.28 deg F, where Δ is the deviation of one thermocouple from the average for the two; the denominator includes —1 to allow for the "loss of one degree of freedom" because the deviation of each individual thermocouple is referred to the average of the two being considered. Further, they say that the standard deviation of the average of the temperatures by the two thermocouples is their standard deviation individually divided by the square root of their quantity or $0.28/\sqrt{2}$ or 0.2 deg F. Thus the standard deviation of the average data shown by one value on each of two instruments is half the difference between them.

Let us now consider a more likely case: Suppose this average difference of 0.4 deg F represents runs where the difference varies from —0.2 to +0.7 deg F. Many of the turbines we are considering have several load runs outside the $^3/_4$ to $^4/_4$ range we are analyzing. All these runs cannot reduce the effect of the 0.4 deg F average difference by dividing it by the square root of their

quantity. Hence the average difference between the two thermocouples causes an initial error of

$$\epsilon_0 = \sqrt{2\Delta_0^2} \quad \ldots\ldots [2]$$

where

ϵ_0 = error caused by average of differences between two thermocouples
Δ_0 = average difference of each thermocouple from average for two

However, having several runs can allow for the error caused by the uncertainty of this average difference. This allowance can be made by the following equation

$$\epsilon_r = \sqrt{\frac{\Sigma[\Delta_i - \Delta_0]^2}{(q_r - 1)q_r}} \quad \ldots\ldots [3]$$

in which

ϵ_r = root-mean-square error of average temperature by one thermocouple
Δ = difference of each thermocouple from average of two for one run
q_r = quantity of runs used in calculating this error of average
subscripts i = data from individual runs
0 = average data from q_r runs

Term $q_r - 1$ is included in the denominator under the radical to average the squared deviations and correct for loss of one degree of freedom because we are considering the difference of the individual Δ from the average Δ.

Term q_r is included in the denominator under the radical to change the average error of the individual differences into the error of their average.

Thus we let all the runs at various loads on a turbine allow for the error of the average difference.

But we report the average performance of a turbine based on the three to six runs in the range from $^3/_4$ to $^4/_4$ load. Each of these runs has some deviation of the difference between its thermocouple readings from the average difference of all its runs. These deviations contribute specifically to the error of the average performance of the turbine. We express this as

$$\epsilon_a = \sqrt{\frac{\Sigma[\Delta_i - \Delta_0]^2}{q_a}} \Big/ q_a^2 \quad \ldots\ldots [4]$$

in which

ϵ_a = error from runs used to get average performance of turbine
q_a = quantity of runs so used

This equation includes q_a^2 in the denominator under the radical to divide by q_a once to get the average squared deviation with no loss of freedom, and by q_a again to get the error of the average.

We can combine these three errors to find the error for a turbine as one error in initial temperature as

$$\left.\begin{aligned} \epsilon_i &= \sqrt{\frac{1}{q_c}}\ \sqrt{\epsilon_0^2 + \epsilon_r^2 + \epsilon_a^2} \\ \epsilon_t &= \sqrt{\frac{1}{q_c}}\ \sqrt{2(\Delta_0)^2 + \frac{\Sigma[\Delta_i - \Delta_0]^2}{q_r} \Big/ (q_r - 1)q_r + \frac{\Sigma[\Delta_i - \Delta_0]^2}{q_a} \Big/ q_a^2} \end{aligned}\right\} \quad \ldots [5]$$

in which

ϵ_t = error of measuring temperature for a turbine
q_c = quantity of instruments of this type used in calculating performance of a turbine

This equation represents the error in the performance of a turbine as caused by the inaccuracy of two duplicating instruments.

When more than two instruments are used for analyzing the error, and when the deviations between two instruments have a consistent variation along a line, the equation expands to

$$\epsilon_t = \sqrt{\frac{1}{q_c}}\ \sqrt{\frac{\Sigma\Delta_0^2}{q_s} \Big/ q_s - 1 + \frac{\Sigma\ \Sigma\Delta_i^2}{q_s\ q_r} \Big/ q_s(q_r - f)q_r + \frac{\Sigma\ \Sigma\Delta_i^2}{q_s\ q_a} \Big/ q_s\, q_a^2} \quad \ldots\ldots [6]$$

in which the nomenclature is the same except that

q_s = quantity of instruments used in analyzing error
Δ_i = deviation of data for an instrument for a specific run from line representing data for that instrument for all runs
f = quantity of degrees of freedom lost because of using Δ from the lines; it is "one" if lines are straight and horizontal, and are not likely to be curved or slanting; "two," if lines are straight and slanting; "three," if curved simply

This same equation can be applied to duplicating instruments for all types of data. Usually for measurements of data such as flows, powers, and pressures, the deviations are more suitable as fractions or percentages of them.

Conversion to Errors in Over-All Performance

Our purpose is to express the error in over-all performance caused by errors in measuring various types of data.

The errors in flow and power need no conversion, since 1 per cent error in either will cause 1 per cent error in performance. However, 1 per cent error in initial or final pressure or in initial absolute temperature will not necessarily cause 1 per cent error in over-all performance. From performance tests on these turbines or on similar ones or from general thermodynamic data the turbine designer can predict suitable conversion factors. For converting an error in initial temperature in degrees Fahrenheit to an error in over-all performance, we need a coefficient in units of 100 [(ΔKW)/KW]/F, that is, in per cent change in load per degree Fahrenheit change in initial temperature. Similarly, conversion factors for the effects of pressure need to be in [(ΔKW)/KW]/[(Δpsia)/psia], when the error in pressure is in per cent, and in 100 [(ΔKW)/KW]/[Δpsia] when the error is in psia.

Although we may at times wish an error in just the efficiency of the turbine rather than in its steam rate or heat rate, each conversion factor for the effect of steam conditions must be derived as (ΔKW)/KW rather than $(\Delta e)/e$; this is because the error in the test conditions causes us to refer the test output to the wrong input, and not just plot the test efficiency at the wrong steam conditions.

Combining Errors of Different Types

Further, we wish to find the combined error in over-all performance of a turbine as caused by the inaccuracy of its instrumentation. We can obtain such a combined error as

$$\epsilon_t = \sqrt{\epsilon_i^2 + \epsilon_{p0}^2 + \epsilon_{pf}^2 + \epsilon_f^2 + \epsilon_g^2} \quad \ldots\ldots [7]$$

when ϵ_t, ϵ_{p0}, ϵ_{pf}, ϵ_f, and ϵ_g are the errors in over-all turbine performance caused by errors in initial temperature, initial and final pressures, flow, and generator output, individually, and ϵ_t is their combined effect (4).

Root-Mean-Square Errors

We apply the term root-mean-square error to the errors or uncertainties of this paper. Someone may ask why we do not use the statistician's term "standard deviation" as used for

some of our data. Equations [5] and [6] for ϵ_i, the error of duplicate instrumentation, are complicated, and would be a serious extension and warping of the meaning of standard deviation. Hence we use the general word error to represent all the different kinds of data listed in the summary, whether they are derived as simply a standard deviation, as a root-mean-square value of several standard deviations, or by Equation [5] or [6].

The words root-mean-square describe these errors in two ways: By their derivation and by what fraction of a group they represent.

First, we combine errors of various types as the square root of the sum of their squares. Hence we believe it somewhat suitable to use the root-mean-square value of the errors of a specific type for the various turbines to represent that error.

The statisticians show that a range of plus or minus one times the standard (or root-mean-square) deviation each side of average performance for a group tends to include 68.2 per cent or two thirds of the group. This leaves one sixth of the group below average performance by more than one root-mean-square error and one that much above average, as noted in the footnote early in the text. A range of $\pm 2\ \hat{\sigma}$ leaves 2.2 per cent of the group at each extreme; $\pm\ 3\hat{\sigma}$, 0.14 per cent. We believe the range for the root-mean-square error is suitable for the analysis of this paper.

Discussion

N. R. Deming.[5] The author has made a rather thorough analysis of the various errors or uncertainties affecting the accuracy of tests on industrial-size steam turbine-generator sets. In the abstract of the paper he summarizes his findings with numerical values for each type of accuracy. While showing figures ranging from 0.2 to 0.5 per cent he reasserts his belief that it is proper to accept or reject a turbine-generator set on the basis of precision tests with no allowance for test error.

Now it would appear that this could be a satisfactory arrangement to a turbine manufacturer only if adequate margin were included in the design to cover the largest value of anticipated test error, thus insuring that all tests would meet the guarantee. For units designed with small margin this 0.5 per cent test uncertainty could become important. For units with plenty of design margin, an allowance for test error becomes unnecessary.

The writer concurs with the author that the use of station instruments increases greatly the uncertainties of a test. The author's figures, of course, assume a turbine in good mechanical condition free of blading deposits.

It should be emphasized that the steam-flow nozzles, used by the author for assurance that the weighed condensate is an accurate measure of throttle flow, are carefully built, low-diameter ratio, ASME type nozzles properly installed with flow straighteners in the approach pipe—hence the low apparent uncertainties involved. These figures would not apply to the ordinary station steam-flow-nozzle installation for which the apparent discharge coefficient, in the writer's experience, may vary from 0 to 2¼ per cent above published ASME data.

R. M. Johnson.[6] The author's discussion of methods for evaluating the reliability of turbine tests is of particular interest to members of the Society. He correctly lists five measures of uncertainty available in his analysis of test data.

1 Comparison of results from duplicate units.

2 Comparison of repeat test runs on the same unit.

3 The deviation of readings from duplicate instruments.

4 Comparison of alternate methods such as the flow nozzle versus the weighed condensate.

5 Comparison of enthalpy drop efficiency, with efficiency computed from measured power and steam flow.

There are other measures of test accuracy, not discussed, such as the deviation between test and specified operating conditions, and the fluctuation of operating conditions during any one test run. The magnitude of adjustments for deviation in load, throttle pressure, initial temperature, and back pressure cannot be ignored. Likewise, the magnitude of fluctuation in the instrument readings, due to drift or unsteady operating conditions, is the first index of test accuracy.

Probably the most significant contribution of this paper is the illustration of a method for expressing the various uncertainties of a test in precise numbers. Here a word of caution is necessary. Chances are the percentage figures do not mean what was thought at the first reading. The spread of the deviations is always greater than the average, and the average differs from the root mean square by a formula which gives weight to the number of values used. It is the writer's feeling that the method is of little value for comparing two or three tests as in Figs. 5 and 6. It has greater meaning when a larger number of tests are compared as in Fig. 2. The author's conclusions would have considerably greater value if they were supported by tables of the original test readings.

For obvious reasons, the author has averaged the steam rates for the range of ¾, ¾, and ¼ of rated load. There is some objection to this practice, in that it can distort the true picture of spread in plots Figs. 1 and 2.

In Table 1, the average steam flows for the tests on duplicate turbines differ by as much as 16 per cent and in several cases the indicated deviation in available heat is appreciable. The author should explain how these variations were handled.

The writer agrees with the author that it is proper to accept or reject a turbogenerator set on the basis of precision tests without allowance for test error, but from a slightly different approach. What else can be done in reality? If we define a precision test as the best there is available from the standpoint of instruments, control of operating conditions, trained personnel, and test procedure, regardless of the evaluated error, nothing can be done about it. The approximate test is always a compromise test and is likely to raise more questions than it settles.

W. A. Pollock.[7] This paper is a valuable contribution to a subject on which there has been very little published.

The author's conclusion that precision-turbine-test results conducted in the manufacturer's shop may be accepted with no allowance for test errors is of interest. This conclusion is arrived at based on experience with weighing tanks.

Field tests with weighing tanks and specially calibrated instruments can be equally accurate and the writer described how this was practical at low cost in a paper[8] presented at the 1953 Annual Meeting.

It has been the writer's experience that field tests can be equally as accurate as shop tests and that field tests may be conducted on very large turbines with complex cycles, including several stages of feedwater heating.

To obtain accuracy within 0.35 per cent with precision flow nozzles in field tests as mentioned by the author, it is necessary to install the flow nozzle just prior to testing in order that there is not time for deposits to build up and produce errors. It has

[5] Design Engineer, Thermodynamics Section, Steam Division Engineering Department, Westinghouse Electric Corporation, Lester, Pa. Assoc. Mem. ASME.

[6] Ingersoll Rand Company, Phillipsburg, N. J.

[7] Technical Engineer of Power Plants, Wisconsin Electric Power Company, Milwaukee, Wis. Mem. ASME.

[8] "Testing Large Steam Turbines With Weighing Tanks," by W. A. Pollock, ASME Paper No. 53—A-66.

been shown that very minute deposits on flow nozzles can result in sizable errors. Recently, a 7.0 per cent meter error was confirmed in one installation as being due to deposits on the flow nozzle.

Author's Closure

The author wishes to thank the discussers for their many comments. He notes with interest that no discusser takes strong exception to the belief that it is proper to apply no allowance for test error when using precision tests as the basis of accepting or rejecting a turbine-generator set.

Mr. Johnson notes his feeling that the method of expressing the various uncertainties in precise numbers is of little value for comparing two or three tests as in Figs. 5 and 6. For several years the author has used statistical methods with small samples cautiously. However, we have found such methods very valuable for drawing proper conclusions from small samples. And we have often found these conclusions still apply when we extend the analysis to include later data. Further, we must be prepared to obtain whatever sound conclusions can be drawn from tests on only a few pairs of turbines and a few more pairs of duplicate runs, as in these plots. Actually, we were somewhat amazed by how consistently the magnitudes of the various types of uncertainties decreased when arranged in logical order as in the summary of the paper.

Mr. Johnson notes that the deviations between test and specified operating conditions, the adjustments for such deviations, and the fluctuations of readings are measures of test accuracy. Actually, the effects of these variations are automatically included in the paper's comparisions of the over-all performance of two or more turbines which are based on Figs. 1, 2, 5, and 6 of the paper.

Mr. Johnson comments on the differences between the average test steam flows and steam conditions of duplicate turbines. Most of these differences were caused by having more runs at high loads on one turbine than on the other and by having somewhat different steam temperatures, pressures, and vacuums available. All tests of this paper were corrected to contract conditions by proper factors; each type of performance data for each turbine is the average of one value each for $^1/_2$, $^3/_4$, and $^4/_4$ loads.

The author believes that Mr. Pollock's 1953 paper[7] on weighed flow tests in the owner's plant is very interesting and valuable. There seems to be a slight misunderstanding in his discussion however: Mr. Pollock refers to the author's conclusion about accepting turbines with no allowance for test error as applying to tests in the manufacturer's shop and being based on weighed flows.

Certainly, 80 per cent of the tests reported here were weighed-flow factory tests. But the 20 per cent of them which were tested in the owner's plants have test uncertainties fairly consistent with the factory tests; and Mr. Kratz's 1954 paper on tests on large steam turbine-generator sets in their owner's plants shows comparable accuracy.

The author agrees with Mr. Deming that a test uncertainty of 0.5 per cent could become important for units designed with small margin. However, it seems out of order to make a guarantee on a turbine-generator and then qualify that guarantee to include an allowance of about 0.5 per cent for the uncertainty of precision tests.

Hence the author reaffirms his belief for many years that it is proper to accept or reject a turbine-generator set on the basis of the direct comparison of guaranteed performance with the performance of precision tests, with no allowance for test error.

Experience in Testing Large Steam Turbine-Generators in Central Stations

By E. M. KRATZ,[1] SCHENECTADY, N. Y.

Since 1930 the author's company has participated in the tests of 111 central station steam turbine-generators of 15,000 kw rating or larger. These were all tests in the owners' power plants, substantially under service conditions. The measurements were made with calibrated test instruments using the careful procedures which experience has proven necessary if reliable data are to be obtained. The purpose of this paper is to make the testing techniques established as a result of this experience available to the power industry and especially to those directly concerned with tests on central station equipment.

Introduction

PERFORMANCE tests on large steam-turbine-generators are made for a number of different reasons. They furnish owners with test heat rates over the load range for use in system-load scheduling and give detailed "bench-mark" data against which to compare future check tests to establish the condition of the unit. Some are acceptance tests to demonstrate that the machine meets its guaranteed performance. The author's company instigates a considerable number of tests to determine the performance of new turbine types or to evaluate design improvements, thus supplementing and confirming the data obtained in laboratory tests on components. A high degree of accuracy is desirable in tests conducted for any of these purposes, and is practically imperative in acceptance and design-evaluation tests.

Since it has been the practice in this country to apply no tolerance to the results of turbine-generator acceptance tests to allow for errors in measurement, the best methods available must be used to keep these errors as small as possible. Improvements expected from design changes are frequently small percentages and the most accurate testing techniques are required to measure these gains.

Because of its interest in these two areas, the author's company maintains a stock of precision-test equipment used by a group of engineers who plan, supervise, analyze, and report the results of tests on large steam turbine-generators in owners' power plants. The amount of experience possessed by this group is indicated by the large number of tests which have been conducted on a wide range of turbine types, ratings, steam conditions, and cycle arrangements. Since 1930 this group has participated in precision tests of 111 central-station steam turbine-generators of 15,000 kw rating or larger. The organization has been such that continuity of experience has been achieved, although the original group personnel has changed.

The range of ratings, inlet pressures, and inlet temperatures tested is shown in Figs. 1 and 2. One hundred and two of these units are single-shaft machines with the remaining nine being cross-compound units. Ninety nine are nonreheat units and twelve are reheat. Eighteen of the tests were on noncondensing turbines, the remainder on condensing units. Thirty seven of the tests on condensing turbines were run without extraction for feedwater heating. Twenty were tested with both nonextraction and extraction operation and the remaining thirty six were tested only with normal extraction to the feedwater heaters. The nonextracting-type tests were run only on nonreheat turbines since it is impractical to operate reheat machines without extraction for feedwater heating. The application of the data obtained from these tests to the prediction of turbine-generator efficiencies has been described.[2,3] The test methods and results of one of these tests have been presented.[4] The results and an analysis of the accuracy of similar tests run in the factory and in the owners' power plants on medium steam turbine-generators also have been presented.[5]

Over-All Results of Tests

Fig. 3 shows the comparison between test and guaranteed performance of the machines shown in Figs. 1 and 2. This comparison is an arithmetical average of $^1/_2$, $^3/_4$, and full load. A number of factors contribute to the scatter in this comparison between test and guarantee performance, including:

1 Quite a number of the tests are on turbines of new types considerably different from previous units tested.

2 The realization of efficiency improvements resulting from design changes which were expected because of prior laboratory-component tests but which were not fully capitalized in making the guarantees.

3 Margin in the guarantees to provide for uncertainties.

4 Uncertainties as to the existence of deposits in the steam path having a detrimental effect on performance.

5 Inaccuracies in testing.

A somewhat better indication of testing consistency is obtained from Fig. 4 which shows the test heat rates for four reheat turbines with the same rating, steam conditions, and substantially the same design details. Each unit was tested in a different station and planned and supervised by different members of the group mentioned previously. The results have been corrected for differences in the feedwater-heating cycles and show remarkable consistency at loads above 60,000 kw.

Fig. 5 shows satisfactory consistency between tests on two duplicate nonreheat turbines in the same station. We believe that the results shown in Figs. 4 and 5 are indicative of the con-

---

[1] Supervisor, Turbine Performance Engineering, Large Steam-Turbine Generator Department, General Electric Company.

Contributed by the Power Division and presented at the Annual Meeting, New York, N. Y., November 28–December 3, 1954, of The American Society of Mechanical Engineers.

Note: Statements and opinions advanced in papers are to be understood as individual expressions of their authors and not those of the Society. Manuscript received at ASME Headquarters, November 22, 1954. Paper No. 54—A-258.

[2] "Relative Engine Efficiencies Realizable From Large Modern Steam-Turbine-Generator Units," by G. B. Warren and P. H. Knowlton, Trans. ASME, vol. 63, 1941, p. 125.

[3] "Comparative Efficiencies of Central-Station Reheat and Nonreheat Steam-Turbine-Generator Units," by C. W. Elston and P. H. Knowlton, Trans. ASME, vol. 74, 1952, p. 1389.

[4] "Heat Rate Test Results of the 100,000-Kw Essex Turbine-Generator," by V. S. Renton and Stanford Neal, Trans. ASME, vol. 72, 1950, p. 267.

[5] "Accuracy and Results of Steam-Consumption Tests on Medium Steam Turbine-Generator Sets," by D. E. Kimball, published in this issue, pp. 1355–1367.

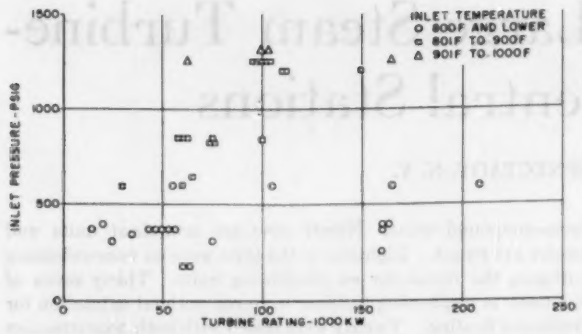

FIG. 1 TEST EXPERIENCE SINCE 1930—1800-RPM TURBINES

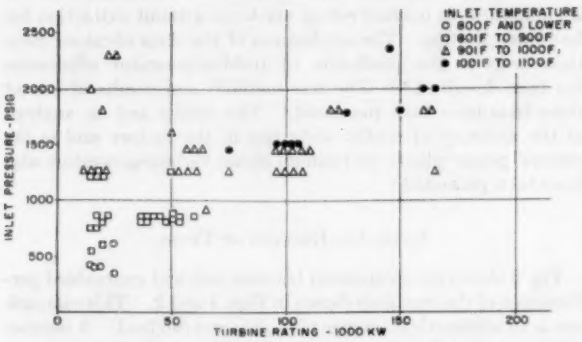

FIG. 2 TEST EXPERIENCE SINCE 1930—3600-RPM TURBINES

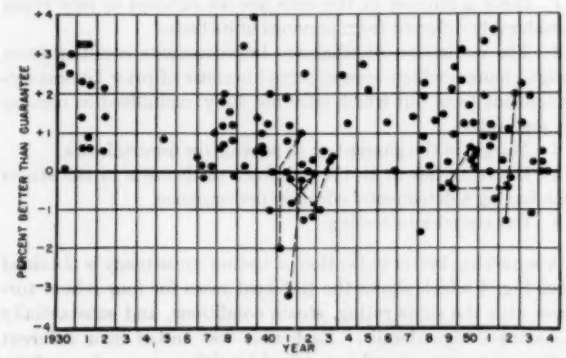

FIG. 3 TEST RESULTS ON TURBINE-GENERATORS 15,000-KW AND LARGER—AVERAGE OF 1/2, 3/4, AND FULL LOAD

sistency obtainable by very careful attention to testing procedures and the use of carefully calibrated instruments. It has been our experience that results comparable to these are generally not obtained where less than the care described in the following sections is used.

MEASUREMENTS

The ASME Power Test Code for steam turbines specifies the type of instruments, their application, and the procedure to be followed in testing a steam turbine-generator. The remainder of this paper will discuss and evaluate the results obtained with the different types of instrumentation and testing methods recommended by the ASME Code. In general, the type of instrument to be used must be selected after considering carefully the effect of

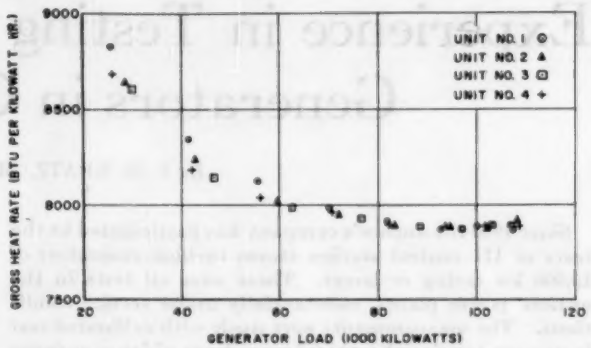

FIG. 4 TEST HEAT RATES—FOUR TANDEM-COMPOUND DOUBLE-FLOW-EXHAUST 3600-RPM REHEAT TURBINES—1450 PSIG, 1000/1000 F; 1.0 IN. HG

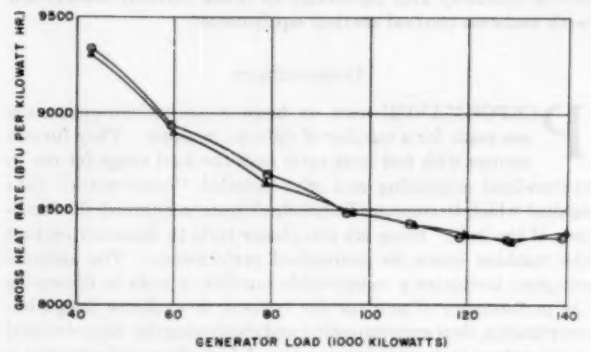

FIG. 5 TEST HEAT RATES—TWO TANDEM-COMPOUND TRIPLE-FLOW-EXHAUST 3600-RPM NONREHEAT TURBINES—1450 PSIG, 1000 F; 2.0 IN. HG

the measurement in question on the over-all results and the practicability of applying different instruments.

It is interesting to note that a turbine-generator test usually requires measurements from which the performance of other power-plant equipment can be determined with little or no additional instrumentation. For example, all of the data required to determine feedwater-heater performance is usually needed to measure the turbine performance, and condenser performance can be obtained with the addition of inlet and discharge circulating-water temperature measurements. Accurate steam and water flows must be established for the turbine-generator test and the same instruments or calibrations of station meters obtained from them may be used for boiler-efficiency tests.

FLOW MEASUREMENTS

An accurate measurement of the turbine throttle flow is of primary importance in any turbine-generator test. It has not been practical to use steam-flow nozzles or orifices to measure the throttle flow for turbine tests in central stations. Because of the high steam pressures and temperatures it would be very difficult to provide for inspection and cleaning of the primary element and it would be impractical to provide facilities for calibration under operating conditions. Therefore the throttle flow usually is obtained from an accurate measurement of condensate or boiler-feed flow.

The ASME Test Code recommends weighing as the most accurate method of measuring water flow; however, very few central stations are equipped with the facilities to weigh flow on modern turbines. The latest unit where such equipment was

available in this country in this group of machines was tested in 1944. Accordingly, a number of years ago the author's company started to accumulate a series of carefully built water flow nozzles, each assembled in its own section of test piping of adequate length and containing flow straighteners. Each of these flow nozzles with its accompanying piping has been calibrated carefully against weighed flow by Prof. W. S. Pardoe,[6] Prof. L. J. Hooper,[7] or Prof. E. F. Stover,[8] or with volumetric flow measurements by Prof. S. R. Beitler.[8] Several have been calibrated at two of the institutions to obtain cross-checks of the calibrations. These flow nozzles, with accompanying test-pipe sections, are then installed complete in the power plant and have been the basic flow measurement for about 60 per cent of the tests since 1949, shown in Fig. 3. On other units the owner has supplied a flow nozzle or orifice calibrated in a section of pipe with flow straighteners which he then has available for future tests on the unit.

The location of the nozzle in the feedwater piping depends upon the design of the heater cycle. In general it is best to have the flow nozzle measure directly the total flow from the turbine but this is not always practical. Since the nozzle should be readily available for inspection and cleaning if necessary, and since it may be desirable to remove it for recalibration if its condition is in question, it is usually installed on the low-pressure side of the boiler feed pumps. When extracting tests are being run, this may result in several of the highest pressure extraction flows being pumped to the boiler without being measured directly in the nozzle. In this case these flows are calculated from feedwater-heater heat balances.

The measurements required in an extraction test to obtain throttle flow based on a calibrated water nozzle or orifice are as follows:

1 Quantity of flow through the nozzle or orifice calculated from measurements of the pressure differential, the water temperature and pressure, and a calibration of the nozzle or orifice.

2 Temperature and pressure measurements on feedwater heaters to obtain extraction flows by heat balance if they are not included in the nozzle flow.

3 Measurement of extraneous flows such as pump leakages, flows to and from pump seals, turbine water seals, water for throttle, and reheat steam temperature control. These extraneous flows are usually measured by sharp-edged orifices, pitot tubes, positive-displacement meters, or by weight or volume.

4 Changes of stored water in the hot well, surge tank and feedwater heaters, drain tanks, etc.

Nonextraction tests require comparatively few flow measurements. These are measurement of the condensate flow from the hot well, change in the stored water in the hot well, and the extraneous flows such as air-ejector condenser drains to the main condenser and condensate-pump leakage.

In tests on noncondensing turbines, which top a number of older units of lower pressure and temperature, it is frequently impractical to obtain the throttle flow by measuring the condensate or feedwater flow. The performance of such turbines is usually established by the enthalpy-drop method. The measurements needed to calculate throttle flow using this method are as follows:

1 The enthalpy of the throttle and exhaust steam.

2 The generator output.

3 Generator losses.

4 Power absorbed by the turbine bearings, water seals, shaft-driven pumps, governor, etc.

5 Power absorbed by the exciter if it is driven by the turbine.

6 Quantity of the turbine shaft leakage flows and their enthalpies.

7 Heat loss from the turbine. For large units this is a small percentage of the total heat supplied and can be considered negligible.

Occasionally, it is possible to obtain test throttle-flow measurements on noncondensing turbines both by flow-nozzle measurement of condensate and by the enthalpy-drop method. This procedure, which provides an independent check of the throttle flow, has been carried out on three of the tests with the results shown in Fig. 6.

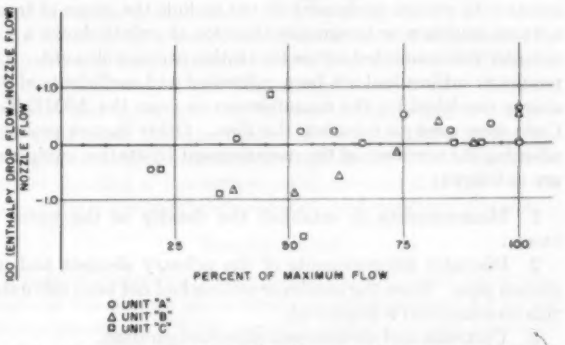

FIG. 6 COMPARISON OF THROTTLE FLOW BY HEAT BALANCE AND BY NOZZLES ON TWO HIGH-PRESSURE SECTIONS OF CROSS-COMPOUND UNITS AND ONE NONCONDENSING TURBINE

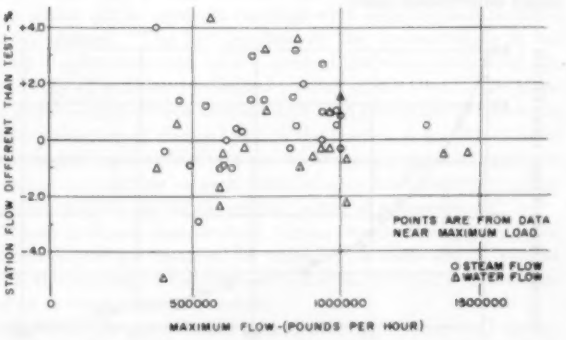

FIG. 7 COMPARISON OF FLOWS MEASURED BY STATION PRIMARY ELEMENTS WITH SAME FLOW FROM CALIBRATED TEST INSTRUMENTS (Data from 29 turbine-generator tests.)

Units A and B are the high-pressure units of cross-compound sets and unit C is a noncondensing topping turbine. Above 60 per cent flow the two methods agree within about 0.6 per cent for all three tests and the agreement is within 0.6 per cent for all points of the tests on unit A. Since the measurements used to obtain throttle flow by enthalpy drop are entirely independent of those used when the flow is based on a calibrated nozzle, it is possible to conclude that above 60 per cent maximum capacity the absolute magnitude was known within ±0.3 per cent for the three tests.

On a large proportion of the tests, data also have been taken from the regular station flow-measuring instruments. Although these data are not used in measuring the test performance of the unit, it is useful to the operator to have a check on the accuracy of his operating instruments. The consistency of the comparison of these flow measurements with the same flows as measured by the test instruments is also of value in checking for the adequacy of the testing procedures.

[6] University of Pennsylvania, Philadelphia, Pa.
[7] Worcester Polytechnic Institute, Worcester, Mass.
[8] Ohio State University, Columbus, Ohio.

Fig. 7 shows the comparison of steam and water flows measured with the station instruments to the same flow based on a water flow measured with a calibrated nozzle or orifice. Each point is the average of the data from the test points near the maximum output of the unit where the errors in flow measurement would be expected to be the smallest.

The flows measured by station instruments for the 49 points shown are from the tests of 29 turbine-generators. They include 28 throttle steam-flow measurements, 18 boiler feed-flow measurements, and the remaining 3 are condensate-flow measurements. There appears to be no significant difference in scatter between the three different types of flows measured. The flow measurements with station equipment do not include the errors of transmitters, recorders, or integrators since for all points shown a manometer was connected across the station primary element. The nozzles or orifices had not been calibrated and coefficients of discharge furnished by the manufacturer or from the ASME Test Code were used to calculate the flow. Other factors probably affecting the accuracy of the measurement by station equipment are as follows:

1 Measurements to establish the density of the water or steam.

2 Diameter measurements of the primary element and upstream pipe. Since the nozzles or orifices had not been calibrated this measurement is important.

3 Upstream and downstream pipe configuration.

4 Cleanliness and condition of the station primary element at the time of test is usually unknown.

5 Measurement of the pressure differential, particularly where small differentials exist.

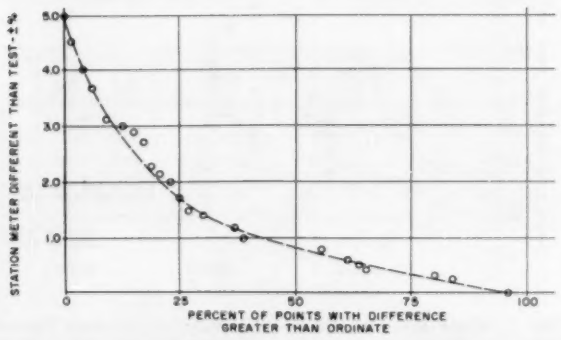

FIG. 8 COMPARISON OF FLOWS MEASURED BY STATION PRIMARY ELEMENTS WITH SAME FLOW FROM CALIBRATED TEST INSTRUMENTS

Fig. 8 is an accumulative percentage plot of the same data as shown in Fig. 7. It is interesting to note that in about 5 per cent of the tests the flow readings taken from station instruments, even with the possible errors of transmitters, recorders, or integrators eliminated, varied more than 3.5 per cent from the flows measured by the special test instruments. In about 40 per cent of the tests, the difference was greater than 1 per cent. We believe these data are indicative of the size of the errors present in flow measurements whenever special and careful provisions are not made.

Before leaving the subject of flow measurements, it should be pointed out that extreme care is required in establishing proper isolation of the turbine to be tested to prevent unmeasured flow into or out of the system during the test. Complete knowledge of the station piping and equipment is required for this purpose and to assure that the flows are not allowed to recirculate through or by-pass the flow nozzle.

TURBINE-GENERATOR OUTPUT MEASUREMENTS

The measurement of the turbine-generator output is equally important as the measurement of the throttle steam flow in obtaining the over-all performance. For tests of central-station units this involves the measurement of the electrical output of the generator and, if the excitation is supplied from a separate source, the power supplied to the motor-generator set. Since the latter is a small fraction of the total output, extreme accuracy of this power measurement is not required. The standards specified in the ASME Test Code have been followed for measuring the main generator output and also for the auxiliary generator if one is supplied. The three-wattmeter method is preferred for its simplicity and because all the meters operate at the generator-power factor. The instrument transformers are laboratory-calibrated with secondary burdens equivalent to those connected to them during the test. Where possible this burden is limited to the test instruments and leads. Indicating wattmeters have been used for all except one of the tests. Each meter is read at 1-min intervals. The possibility of observer error with the indicating meters is kept to a minimum by checking the observers carefully and by intercomparison.

The wattmeters are calibrated before and after the series of tests in the laboratory maintained by the author's company. These careful calibrations are made using precision-potentiometer equipment frequently compared to d-c standards of resistance and voltage maintained by the laboratory—which are certified by the National Bureau of Standards. The transfer from d-c standards to a-c power measurement is made with an astatic reflecting electrodynamometer element. Electrodynamometer-type "laboratory-standard" instruments are used for a-c current and voltage-calibration standards.

In addition to the calibrations in the laboratory, since 1948 the wattmeters have been calibrated in the field immediately after each test point with a portable d-c calibrating set which supplies a highly accurate and stable source of current and voltage. Direct and reverse readings are taken at scale points bracketing the test-meter reading by the same procedure used in the usual laboratory calibration of a-c wattmeters. The use of this equipment eliminates scale-subdivision errors and the possibility of changes in meter characteristics remaining unknown until a series of tests have been completed and the consequent question as to when the change occurred. This equipment has proved to be highly reliable and accurate. Current and voltage readings to obtain power factor are obtained with indicating meters which are calibrated in the laboratory before and after the tests.

On a large number of tests a photoelectric pickup has been supplied to count the revolutions of the station watthour meter during the test period. These data give the station operator an accurate calibration of his generator-output measurement and provide an additional check for consistency of measurements between tests. Percentage variations between test and station instruments for the load measurements are much less than for the flow measurements. A check of the data obtained near rated load on 23 tests shows that, in 74 per cent of the cases, power readings obtained by counting the revolutions of the station watthour meter were within 0.5 per cent of the data obtained by the calibrated test instruments. Maximum variation was 1.1 per cent. At lower loads the agreement was poorer with difference as large as 1.6 per cent. We have made no checks against station indicating wattmeters since these are usually not intended to be highly accurate instruments.

The use of watthour meters has not been encouraged in the past as they were not considered as reliable as the indicating meters. Recently, however, a set of accurate watthour-metering equipment has been developed by the General Engineering Lab-

oratory for turbine-generator tests. All mechanical indicating equipment has been removed from the meters and they are enclosed in a temperature-controlled case. The revolutions of each meter disk are counted electronically. The number of revolutions of each watthour meter against time as measured by a highly accurate tuning fork are recorded on a tape. The number of revolutions of each watthour meter disk also are indicated on a counter. Extensive calibrating of this equipment has been completed in the laboratory and trial runs have been made on several turbine tests in power stations. Generator-load measurements by the watthour meters have checked those measured at the same time by the indicating meters within 0.15 per cent. The use of this equipment in the future will eliminate the reading errors of observers and it is expected it will prove to be a highly satisfactory method of load measurement.

Pressure Measurements

All pressures which are significant in determining the over-all performance are measured with piston-type dead-weight gages or with mercury columns. These instruments are used because of their high accuracy and also, owing to their fundamental nature, they are the least susceptible to possible changes in calibration. The dead-weight-type gages are used for pressures above 35 psia and have a piston area of 0.125 sq in. with a clearance of 0.0002 to 0.0003 in. between the piston and cylinder. One gage which has been checked by the National Bureau of Standards serves to check all the others used in turbine tests. With the exception of the exhaust pressure of condensing turbines, which is measured by mercury absolute pressure gages, pressures below 35 psia are measured with mercury U-tubes. The accuracy of the measurement is dependent upon the density of the mercury, accuracy of the scale at ambient temperature, meniscus errors, reading errors, accuracy of the reference pressure measurement (usually atmospheric pressure), and corrections for water legs in the connecting lines. The latter correction is eliminated by purging the lines between the gage and pressure tap with a metered quantity of air. The flow of air is controlled and measured with small rotameters.

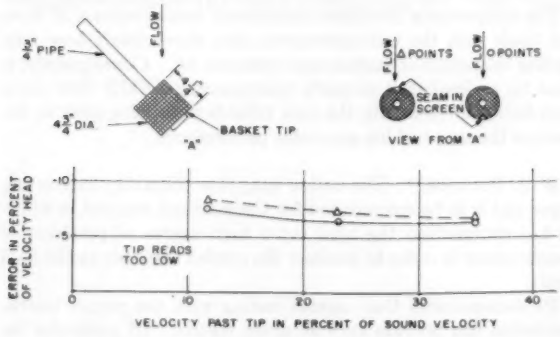

Fig. 9 Calibration of Basket Tip Used to Measure Condensing-Turbine Exhaust Pressure

Special pressure tips are installed at the plane of the turbine-exhaust flange for measuring the exhaust pressure of condensing turbines. The tips consist of a $^3/_4$-in. pipe with one end closed. Eighty $^1/_{16}$-in. holes are drilled in a spiral along 3 in. of the pipe at the closed end. This end of the pipe is then enclosed in a 7-mesh wire-screen basket. Tests of these tips have shown that when properly installed they read within 0.1 of a velocity head of the true static pressure. At 1.0 in. Hg exhaust pressure near rated load, the average velocity head at the exhaust flange of a 3600-rpm condensing turbine is about 0.05 in. Hg. The error is in a direction to cause the indicated pressure to be lower than the static pressure in the stream. Fig. 9 shows the calibration obtained on one of these tips. These pressure tips are relatively insensitive to the angle of the stream which is important because of the type of flow which occurs in the exhaust hoods of condensing turbines.

Accurate measurements of turbine-stage pressures during the initial period of operation with the turbine in good condition have proved to be of value to the operator for later periodic checks of performance. Consistent and accurate records of stage pressures frequently have made it possible to diagnose turbine troubles. The additional effort to obtain accurate measurements also has been justified during tests by helping to indicate poor instrumentation or testing procedures.

For instance, on a test of a reheat turbine the results were inconsistent and the performance poorer than expected. By checking the consistency of the relationship between stage pressures and flows and also comparing the pressures to design, it was possible to conclude that the data could be explained if steam was flowing from a certain extraction stage directly to the condenser. Further checking of the station piping revealed that this was the cause of the inconsistent data and poor performance of the unit.

Temperatures

The use of thermocouples for measuring steam and water temperatures has become the generally accepted practice for testing turbine generators. When properly constructed and calibrated they have proved to be satisfactory for temperatures up to 1050 F. Thermocouples with chromel-P and constantan wires are used because of the stability of their calibration over a period of time. Also, the change in emf with temperature is relatively large which allows accurate readings with semiprecision portable potentiometers. The hot junction of the thermocouple is enclosed in a stainless-steel tube to protect the wire and prevent the possibility of working the heated portion of the wire. The wires are continuous between the hot and cold junctions to eliminate the introduction of thermal emf in the leads. A supply of these instruments has been built up and by keeping a continuing record of repeat calibrations on each thermocouple it is possible to select the most stable ones for the critical points of measurement.

Where accurate temperature measurements are required the thermocouples are installed in wells. The wells should extend inside the pipe wall far enough to reduce the errors due to conduction to as low a value as possible.

Duplicate instrumentation is used at critical points such as initial steam, steam to and from the reheater, and feedwater out of the top heater. Where extraction flows must be obtained by heat balances to determine throttle flow, significant measurements around those heaters also are duplicated. Agreement within 1.0 deg F can be obtained between duplicate measurements by using carefully calibrated, stable instruments and sufficient care in applying them.

Where the best accuracy is not required and the installation of wells is not practical, pipe-wall temperatures are measured. By taking the proper precautions to prevent heat loss such measurements may be within a few degrees of the temperature measured in a well at the same location. It is usually necessary to bend the thermocouple wire near the hot junction when installing it in the pipe wall, and the presence of strains in the wire at a point with high-temperature gradients is a possible source of error. Experience has indicated that this method is not satisfactory for temperature measurements which require high accuracy.

A comparison between temperatures measured in the pipe wall and in wells was made at the throttle and exhaust on two non-condensing-turbine tests. On one unit with initial conditions of 1800 psig, 950 F the pipe-wall measurements at the throttle were

from 2.0 to 6.0 deg F lower than temperatures measured in the wells. On the other unit with initial conditions of 1250 psig, 950 F, the wall temperature was consistently about 4.2 deg F lower. Pipe-wall temperatures measured at the exhaust of the two units were from 0.5 to 3.0 deg F below well temperatures at the same location.

Conclusions

The company with which the author is associated has always followed the practice of testing many large steam turbine-generators in the owners' power plants. It has been our experience that consistent results can be obtained only by providing carefully calibrated instruments used with proper care and with adequate knowledge of the possible sources of error.

The measurement of throttle flow and generator load are of primary importance in establishing the input and output for the test of a turbine-generator. Throttle-flow measurements are the most frequent cause of inaccurate test data because of the difficulty in obtaining a precise basic measurement and the additional possible sources of error from miscellaneous flows and inadequate isolation.

Generator-load measurements are also frequently the source of significant errors but usually of a smaller magnitude. Reliable output measurements can be obtained by providing calibrated transformers and meters and careful consideration of possible errors from secondary burdens.

Accurate pressure and temperature measurements are required for reliable testing, although the direct effect on the over-all results is smaller than load and flow. Reliable pressure and temperature measurements are also of value for checking the condition of the unit and the adequacy of test procedures.

Acknowledgments

The author gratefully acknowledges the assistance of Miss A. MacCracken in the preparation of the material for this paper. It will be understood that these data have been accumulated over many years; the author has been supervisor of this work since 1951.

Discussion

F. J. Heinze.[9] This paper should be of great interest to the Central-Station industry—both users and manufacturers of power-generating equipment alike. It clearly stresses the points which have been emphasized by the writer's company for many years.

The performance tests conducted under most carefully set-up and controlled conditions will give accurate results which can be repeated even after fairly lengthy time intervals as long as the turbine-generator unit remains, or can be restored to a condition equivalent to new. The test results give the operating departments of the utilities a permanent bench mark against which the performance of the unit should be compared at regular intervals. Blade deposits are the main reason for efficiency losses in the turbines and the progressive deterioration can be charted, evaluated in dollars and cents, and outages can be scheduled at the most economic and convenient times. Actual test experiences have shown clearly that even slight deposits which had been considered at times as negligible will cause efficiency losses of more than 1 per cent. Medium to heavy deposits on the blades and under the shroud bands have affected the efficiency often as much as 3 per cent. Thus it can be well understood that the manufacturer desires to test the units as soon as possible after the initial start-up or after a turbine inspection which assures everybody of the good internal condition of the unit.

[9] Manager, Thermodynamics Section, Steam Division, Westinghouse Electric Corporation, Lester, Pa. Mem. ASME.

In so far as the test instrumentation is concerned, we fully agree with the author that it cannot be too elaborate, and only calibrated instruments of the best design should be used.

Since the throttle steam flow is usually obtained from an accurate measurement of the condensate or boiler-feed flow, the calibrated flow-measuring device is of prime importance. Owing to several experiences which our company had with condensate flow nozzles accumulating deposits in the short period between installation of the device and the test, its duration and the time interval before removing the test section, which affected the flow measurement as much as 1 per cent, we gradually have been replacing the flow nozzles by orifices.

In so far as the calibration of these devices is concerned, it is our opinion that the weighing method is more consistent than the volumetric method. Unfortunately, laboratories in this country have measuring capacities which fall far short of the flows encountered in modern large rating units. While the extrapolation of the calibration curves is on a sound scientific basis, it nevertheless would be desirable to cover the whole range of the test flows during the calibration.

In reheat turbines it is also of great importance to determine the reheat steam flow most accurately. In addition to measuring the various leakages which by-pass the reheater with calibrated orifices, we have determined in some cases the extraction steam quantities ahead of the reheater by measuring the heater drains, where the heaters were equipped with drain coolers. Whenever the installation of the calibrated flow-measuring device was in line with the test code the measured flows checked within 0.2 per cent the value determined by the heat-balance method.

To obtain reliable flow measurements, the steam conditions, load and flow conditions must be as stable as possible.

In so far as load measurements are concerned, we fully agree that the three-wattmeter method with instruments calibrated with the proper test burdens is most reliable. The comparison with the station watthour-meter data indicated that in the majority of the cases the station instruments gave low values.

Temperature and pressure measurements with calibrated instruments are well understood by everybody, although duplicate instrumentation at the vital points is not always fully appreciated.

The comparisons of station-instrument measurements of flows and loads with the test-instrument data show clearly how misleading the results of station-type tests can be. Consequently, it must be realized that properly instrumented ASME Test Code type tests are essentially the only reliable measuring stick to determine the true turbine-generator performance.

W. A. Pollock.[10] The author has presented a very interesting paper and is to be commended for the excellent manner in which he has summarized the need for a high degree of precision of measurement in order to produce the needed accuracy in the final result.

He demonstrates that careful testing with the proper instrumentation can provide very accurate results. Of particular interest are the tests described in Figs. 4 and 5, in which turbines of like design are shown to produce comparable results.

That accurate measurement of turbine-throttle flow is of utmost importance is properly stated. It is assumed that under Flow Measurements, the author refers to installations of his company's turbines when he states that no weighing tanks have been installed since 1944, because the writer reported in a paper[11] on an installation of weighing tanks at Oak Creek in 1953. The Oak Creek 120-mw cross-compound turbine was tested early this

[10] Technical Engineer of Power Plants, Wisconsin Electric Power Company, Milwaukee, Wis. Mem. ASME.

[11] "Testing Large Steam Turbines With Weighing Tanks," by W. A. Pollock, Trans. ASME. vol. 77, January, 1955, p. 79

year with weighing tanks and found to be 0.10 per cent better than guarantee. No difficulties occurred in manipulating these tanks which are large enough so the change-over between tanks needs be made at 15-min intervals. These tanks were installed at low first cost and will serve four units for tests as well as providing adequate cold condensate-storage capacity for the entire station.

The experience with station water and steam flowmeters shown in Fig. 7 is about the same as results found by the writer when water and steam flowmeters are compared with weighed-water values as was reported in a previous paper.[11]

C. A. Robertson.[12] The author is to be commended on the information presented in this paper relevant to accurate testing, together with comparison of commercial-station instruments with precision-testing equipment.

One of the important determinations is the measurement of steam flow to the turbine. The basic method is weighing the condensed steam; however, the next best is the use of nozzles in pipe sections calibrated as a unit, together with straightening vanes before the orifice or nozzle.

Power stations are usually equipped with commercial types of steam and fluid-metering equipment. The orifices or nozzles have registering or recording apparatus.

The writer is particularly interested in Fig. 7 which shows a comparison of flows measured by station primary elements with corresponding flow from calibrated test instruments. This graph shows the variations that may be expected when using commercial station instruments. This agrees, in general, with the writer's findings, and is another argument in favor of a more accurate means of steam-flow determination, by either weighing or use of calibrated orifices in special sections of piping, including straightening vanes.

The next important measurement is the load determination. This can be obtained best by high-grade precision-indicating wattmeters. This paper, however, mentions the inaccuracy of high-grade watthour meters, such as used in station installations. The poor showing of the accuracy of watthour meters, as indicated in the paper, appears rather high for calibrated instruments.

[12] Engineer, Steam Turbine Section, Power Department, Allis-Chalmers Manufacturing Company, Milwaukee, Wis. Mem. ASME.

Author's Closure

The author wishes to express his appreciation to the discussers for the time they have taken to review this paper.

Mr. Heinze's comments on the importance of deposits in the steam path on turbine performance are pertinent. Testing a unit as soon as possible is usually the most practical means of attempting to obtain a test on a turbine in good condition. It has been our experience that this is not always satisfactory, as appreciable deposits may accumulate during the several weeks required after initial operation to iron out the operating problems with associated equipment to the point where satisfactory tests can be made. As the presence of deposits may not be evident from the data or inspection through manholes, it may be necessary to open the unit to determine its condition. Mr. Heinze also commented on experience with deposits on test condensate-flow nozzles. We have had very little trouble with deposits when the nozzles were located in the condensate line ahead of all of the feedwater heaters and were in the line only during the turbine tests. When located after several heaters a light deposit has been found occasionally. Check calibrations to measure the effect on the flow measurement have shown no significant change in the coefficient. The deposits were very thin and coated the nozzle uniformly. The author would be interested in Mr. Heinze's reasons for expecting less trouble from deposits when using orifices for the flow measurement.

All of the testing experience reported in the paper was by the author's company. Mr. Pollock is therefore correct in that the statement regarding tests with weight-tank flow measurements referred only to tests of General Electric turbine-generators.

The differences between test and station-load measurements were not caused entirely by the watthour meters as inferred by Mr. Robertson. The station load was obtained by counting the watthour-meter revolutions and included any errors caused by not compensating correctly for transformer and secondary burden corrections as well as any inaccuracy from the watthour meter.

Heat and Mass Transfer in Spray Drying

By W. R. MARSHALL, JR.,[1] MADISON, WIS.

The heat and mass-transfer phenomena to and from droplets during spray drying are discussed. Evaporation from pure liquid drops and drops with solids present in quiescent and in moving air are considered. The problem of evaporation at high air temperatures is noted.

Nomenclature

The following nomenclature is used in the paper:

A = surface area of all drops in a spray created by atomization
A_h = area of droplet receiving heat
A_m = area of droplet losing mass
A_0 = initial or original surface area of bulk liquid prior to atomization; also area of drop of diameter x_0
B_0 = constant defined under Equation [14]
C_f = feed concentration
c_p = heat capacity of gas
c_s = humid heat of air-water vapor mixture, Btu/(deg F)(lb dry air)
D_p = dry-particle diameter
E = $w_l c_p / 4\pi k_f$
$(F_i)_\theta$ = fraction of mass of spray contained in the ith size class increment at time θ_n
g = acceleration due to gravity
h_c = heat-transfer coefficient for convection and conduction through the gas film, Btu/(hr)(sq ft)(deg F)
$(h_c)_0$ = heat-transfer coefficient for no relative air velocity
k_f = thermal conductivity of gas film surrounding drop, Btu/(hr)(deg F/ft)(sq ft)
k_g = mass-transfer coefficient, lb (mass)/(unit time) (unit area)(unit pressure diff)
$(k_g)_0$ = mass-transfer coefficient for no relative velocity
M = molecular weight
N_{Nu} = $h_c x / k_f$
N_{Pr} = $c_p \mu / k_f$
N_{Re} = $v_a x \rho_a / \mu$
N_{Sc} = $D_v \rho_a / \mu$
p_a = partial pressure of vapor in air surrounding drop
p_f = average partial pressure of nondiffusing or inert gas in film surrounding drop
p_s = vapor pressure corresponding to t_s
r = radius of any drop
R = gas constant
R_1 = radius of evaporating drop
R_2 = radius of outer limit of gas film surrounding drop
t_a = temperature of air surrounding drop, deg F
t_s = temperature of drop surface, deg F
t_1 = inlet-air temperature to drier
t_2 = outlet-air temperature
Δt = $(t_a - t_s)$, deg F
Δt_m = mean temperature between air and drop when air temperature experiences a large temperature change, deg F
T = absolute temperature
v_a = relative velocity between drop and air
v_f = terminal velocity in intermediate drag region
w = mass of water being evaporated
w_a = mass rate of air flow, lb/hr
w_l = rate of water removal in drier, lb/hr
x = drop diameter; also distance from drop center, Fig. 9
x_c = drop diameter corresponding to permanent crust formation on drop
x_0 = initial drop diameter
$\bar{x}_{vs}$ = mean drop diameter whose volume/surface ratio is same as that for entire spray (often referred to as Santer mean diameter)
λ_s = latent heat of evaporation corresponding to temperature t_s
μ = viscosity of gas film
ρ = density
ρ_a = air density
ρ_L = liquid density
σ = surface tension
θ = time

Introduction

The drying of droplets in a spray drier is a simultaneous heat and mass-transfer operation in which heat for evaporation is transferred by conduction and convection from a hot, gaseous atmosphere to the drop surface while vapor is transferred by diffusion and convection back into the gas stream. The mechanism of evaporation from pure liquid drops has been described by many workers. However, the much more complicated problem of evaporation from drops containing solids, the situation occurring in a spray drier, has received somewhat less attention, while the very complex problem of the evaporation of sprays or clouds of drops, in which a wide range of drop sizes occurs, has scarcely been touched.

The drying process for a drop containing solids is substantially the same as the drying process for wet, bulk solids; i.e., it is comprised of a short warm-up period, a period controlled by surface evaporation, and finally a period of subsurface evaporation. These periods are comparable to the usual constant-rate and falling-rate periods encountered in most drying operations. The most important and distinctive feature of evaporation from drops is the magnitude of the evaporation rate. Whereas the initial or constant rate of evaporation from the surface of bulk solids may range up to 1.0 lb water/(hr)(sq ft of drying surface), the surface rate of evaporation from a single droplet may range from 100 to 1000 times this value, depending on the drop size invol ed.

Furthermore, if one contrasts the evaporation rate from a bulk mass of liquid with the rate for this same mass of liquid after it has undergone atomization, it is found that heat and mass-transfer rates can increase nearly a millionfold over the rate for the original bulk of liquid. This is because the increase in surface area produced by atomization varies inversely with the diameter of the drop, while the coefficients of the transfer processes also increase inversely with drop diameter. Consequently, since the rate is proportional to the product of a transfer coefficient multiplied by the area of transfer, it will be proportional to the reciprocal of the square of the droplet diameter.

The increase in surface area resulting from atomization is given by

[1] Associate Director, Engineering Experiment Station, University of Wisconsin.

Contributed by the Process Industries Division and presented at the Annual Meeting, New York, N. Y., November 28–December 3, 1954, of The American Society of Mechanical Engineers.

Note: Statements and opinions advanced in papers are to be understood as individual expressions of their authors and not those of the Society. Manuscript received at ASME Headquarters, December 8, 1954. This paper was not preprinted.

$$A - A_0 = \pi x_0^2(1/\bar{x}_{vs} - 1/x_0) \quad [1]$$

where

A = new surface produced by atomization
A_0 = original surface of spherical liquid mass of diameter x_0
$\bar{x}_{vs}$ = diameter of droplet produced by atomization whose volume-to-surface ratio is the same as that for entire spray

The ratio of total-to-original surface produced by atomization is plotted versus the drop size in Fig. 1 to indicate how greatly

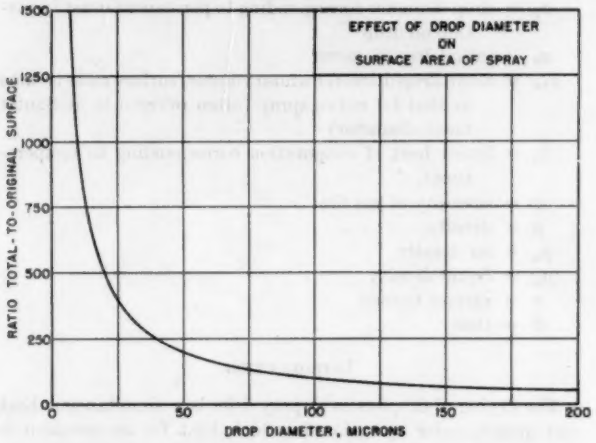

FIG. 1 EFFECT OF DROP DIAMETER ON SURFACE AREA OF SPRAY

the surface area of a liquid can be increased by dispersing it into small droplets. The curve in this figure assumes a monodisperse spray, i.e., a spray of uniform drop size, and is based on an original mass of liquid of spherical shape and 1 cm diam.

HEAT AND MASS TRANSFER IN DROPLET EVAPORATION

The properties of spray-dried products are markedly influenced, among other things, by the magnitudes of their drying rates. For example, if the drying rate is high, the dry particle is usually lighter and more friable than if it is dried at a lower rate. Further, rapidly dried, small particles may be overheated if they recycle into the hot-gas zone. Rapidly dried, film-forming materials may show "blow holes" where sudden vapor evolution ruptured the surface film.

In considering the drying process, it is convenient to treat the two periods of drying separately, as is usually done in other methods of drying. Thus, in droplet drying, the first period usually consists of evaporation from a wet surface which remains at some constant temperature. The rate can be expressed by heat or mass-transfer relationships as follows

$$\frac{dw}{d\theta} = \frac{h_c A_h (\Delta t)_m}{\lambda_s} \quad [2]$$

where Δt_m = mean temperature difference between air and drop surface = $(t_a - t_s)_m$, t_a and t_s being the air and drop temperatures, respectively, $dw/d\theta$ = evaporation rate, mass per unit time, h_c = heat-transfer coefficient for convection and conduction through the film surrounding the drop, A_h = surface area of drop receiving heat, λ_s = latent heat of evaporation corresponding to t_s.

Also, for mass transfer

$$\frac{dw}{d\theta} = k_g A_m (\Delta p)_m \quad [3]$$

where $(\Delta p)_m$ = mean vapor-pressure difference = $(p_s - p_a)_m$, p_s being the vapor pressure corresponding to t_s, and p_a is the partial pressure of vapor in the drying gas, k_g = coefficient of mass transfer, A_m = area of drop from which mass is transferred. It is usually assumed that the areas of heat and mass transfer are equal for the first period of drying; i.e., $A_h = A_m = \pi x^2$. This is not a valid assumption, however, for the later stages of drying.

Experimental studies have established empirical correlations for h_c and k_g. Representative of these are the following semi-empirical equations proposed by Ranz and Marshall (8),[1] which are useful for estimating heat and mass-transfer coefficients

$$\left(\frac{h_c x}{k_f}\right) = \left[2.0 + 0.60\left(\frac{v_a x \rho_a}{\mu}\right)^{1/2}\left(\frac{c_p \mu}{k_f}\right)^{1/3}\right] \quad [4]$$

or

$$\left(\frac{k_g x p_f}{D_v \rho_a}\right) = \left[2.0 + 0.60\left(\frac{v_a x \rho_a}{\mu}\right)^{1/2}\left(\frac{D_v \rho_a}{\mu}\right)^{1/3}\right] \quad [5]$$

where x = drop diameter, k_f = thermal conductivity of gas film around drop, D_v = diffusion coefficient of vapor, p_f = mean partial pressure of nondiffusing gas in gas film, v_a = relative velocity between drop and its surroundings, ρ_a = gas-film density, μ = gas-film viscosity, c_p = gas-film specific heat. Each group in parentheses is dimensionless.

For zero relative velocity, $v_a = 0$, Equations [4] and [5] reduce to the theoretical expressions for h_c and k_g as follows

$$(h_c)_0 = 2k_f/x \quad [6]$$

and

$$(k_g)_0 = \frac{2D_v \rho_a}{x p_f} \quad [7]$$

Equations [6] and [7] have considerable utility for approximate calculations. Equations [4] to [7] all show that the magnitudes of the coefficients increase inversely with the drop diameter x, other conditions remaining constant. However, since the drop Reynolds number $v_a x \rho_a/\mu$ decreases with x, only Equations [6] and [7] predict the inverse relationship at all times.

The significance of Equations [4] and [5] in terms of boundary-layer theory has been discussed by Froessling (5) and by Ranz and Marshall (8).

With reference to Equations [6] and [7] for still air or no relative velocity conditions, it is readily seen that Equations [4] and [5] may be rewritten as

$$h_c = (h_c)_0[1 + 0.30(N_{Re})^{1/2}(N_{Pr})^{1/3}] \quad [8]$$

$$k_g = (k_g)_0[1 + 0.30(N_{Re})^{1/2}(N_{Sc})^{1/3}] \quad [9]$$

where N_{Re}, N_{Pr}, and N_{Sc} have been written for the Reynolds, Prandtl, and Schmidt numbers, respectively. The terms in brackets may be thought of as average correction factors on the "still-air" coefficients due to the boundary layer around the drop.

Since the majority of drying operations deals with air-water-vapor mixtures, specific values of the dimensionless numbers for this system can be evaluated to give the following working equations for heat transfer:

For no relative velocity

$$(h_c)_0 = \frac{0.028}{x} \text{ Btu/(hr)(sq ft)(deg F)} \quad [10]$$

[1] Numbers in parentheses refer to the Bibliography at the end of the paper.

and for a finite relative velocity

$$h_c = \frac{0.028}{x}\left[1 + 0.27(N_{Re})^{1/2}\right] \quad [11]$$

Equation [11] is plotted in Fig. 2 as $h_c x$ for various values of N_{Re}. The ordinate values of this figure can be divided by the appropriate drop diameter to obtain the coefficients for other

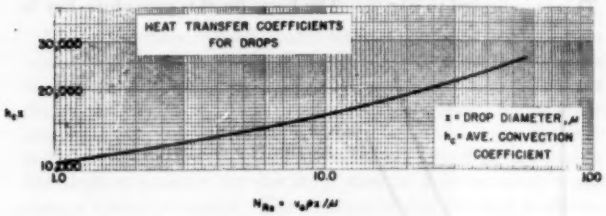

FIG. 2 HEAT-TRANSFER COEFFICIENTS FOR DROPS

diameters. Thus, for 100μ drops, the range will be from 85 to 300 Btu/(hr)(sq ft)(deg F). It is evident from this curve that the values of h_c for small drop diameters are exceedingly large in comparison with usual convection coefficients. For example, for 1-micron drops, convection coefficients can range from 8500 to 30,000 Btu/(hr)(sq ft)(deg F).

EVAPORATION TIMES FOR PURE LIQUID DROPS

Substitution of Equation [6] in Equation [2] and integration with respect to x and θ gives the following expression for the time to evaporate a drop from its initial diameter x_0 to x

$$\theta = \frac{\rho_L \lambda_s (x_0^2 - x^2)}{8k_f \Delta t_m} \quad [12]$$

Thus the time for complete evaporation of a drop in quiescent air is proportional to x_0^2.

When relative motion occurs between the drop and its surroundings, the evaporation time is given by

$$\theta = \frac{\rho_L \lambda_s}{4k_f \Delta t}\int_x^{x_0} \frac{x\,dx}{\left[1 + 0.3(N_{Re})^{1/2}(N_{Pr})^{1/3}\right]} \quad [13]$$

Integration of Equation [13] depends on the relationship between v_a and x as they appear in the Reynolds number. For the general case where x is continually changing and hence v_a also varies, a step-by-step integration is required. However, for certain limiting situations such as terminal velocity in the Stokes' law region or in the intermediate region, Equation [13] can be integrated to estimate the effect of relative velocity on the evaporation times. Such integrations have been made (4) and the results are given in the following equations

$$\theta = \frac{\rho_L \lambda_s x_0^2}{8k_f \Delta t}\left[1 - \frac{2B_0}{x_0^2}\int_{100}^{x} \frac{x^{2.08}dx}{(1 + B_0 x^{1.08})}\right] \quad [14]$$

where

$$B_0 = 0.3\left[0.153\left(\frac{g\rho_a(\rho_L - \rho_a)}{\mu^2}\right)^{0.71}\right]^{1/3}\left(\frac{c_p \mu}{k_f}\right)^{1/3}$$

Equation [14] is based on the assumption that the drop velocity would be at its terminal velocity in the intermediate region and can be expressed by

$$v_f = \frac{0.153 x^{1.14} g^{0.71}(\rho_L - \rho_a)^{0.71}}{\rho_a^{0.29}\mu^{0.43}} \quad [15]$$

Equation [14] further implies that for drop diameters less than

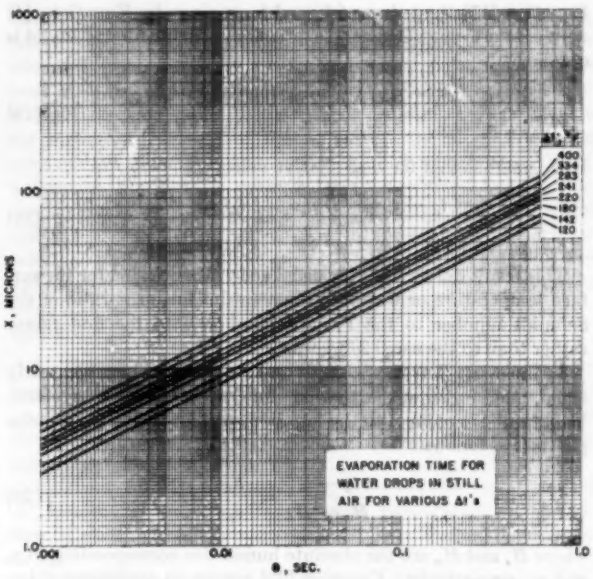

FIG. 3 EVAPORATION TIME FOR WATER DROPS IN STILL AIR FOR VARIOUS Δt's

100μ the effect of air velocity on the evaporation time becomes negligible and hence Equation [12] is sufficiently accurate. Equation [12] for an air-water vapor system is plotted in Fig. 3 to give some estimate of the time for complete evaporation of pure liquid drops in still air. This plot is based on several values of Δt. For other Δt it is simply necessary to multiply the time read from the curves by the appropriate Δt ratio. If it is desired to estimate the time required for the drop to evaporate from x_0 to some intermediate diameter x, it is necessary simply to subtract the time for complete evaporation of a drop of diameter x from the time for x_0. Fig. 3 was used in connection with the calculation of the evaporation of a spray of drops described in the following.

From Fig. 3 it is of interest to note the exceedingly short time required to evaporate drops of diameter less than 10μ, even in very humid air. Thus, for drops in the 1 to 5μ range, the evaporation rates in room-temperature air and 90 per cent relative humidity range from 162 to 32 lb/(hr)(sq ft), respectively, and the complete evaporation times are from 0.01 to 0.25 sec.

TEMPERATURES OF EVAPORATING DROPS

In estimating the evaporation times and evaporation rates for drops it is necessary to be able to specify or estimate the droplet surface temperature in order to evaluate the temperature driving force Δt_m. It is evident from Equations [2] and [3] that if a dynamic equilibrium between the rate of mass transfer and the rate of heat transfer is established, and if the heat transferred is essentially all consumed for evaporation, i.e., relatively low vapor concentration, the drop surface temperature t_s may be estimated from the following equality

$$\frac{\Delta t}{\Delta p} = \frac{k_g A_m \lambda_s}{h_c A_h} \quad [16]$$

and if $A_m = A_h$

$$\frac{t_a - t_s}{p_s - p_a} = \frac{k_g \lambda_s}{h_c} \quad [17]$$

which is the familiar expression for the wet-bulb temperature, if h_c is a pure convection coefficient. If there is substituted in

Equation [17] the values of k_g and h_g as given by Equations [4] and [5], the following general expression, suitable for any liquid is obtained

$$\frac{t_a - t_s}{p_s - p_a} = \frac{D_v \lambda_s \rho_a [2 + 0.60(N_{Re})^{1/2}(N_{Sc})^{1/3}]}{p_f k_f [2 + 0.60(N_{Re})^{1/2}(N_{Pr})^{1/3}]} \quad \ldots\ldots [18]$$

It is apparent that for zero relative velocity

$$\frac{t_a - t_s}{p_s - p_a} = \frac{D_v \rho_a x_s}{p_f k_f} = \frac{\lambda_s (N_{Sc}/N_{Pr})}{c_p p_f} \quad \ldots\ldots [19]$$

This result differs from the usual general expression for the surface temperature or wet-bulb temperature since the ratio of the Schmidt number to the Prandtl number is to the first power rather than to the usual 2/3 power.

In the event that the Schmidt and Prandtl numbers are nearly equal, the fortuitous situation for air-water-vapor systems, Equation [17] reduces to the familiar form for the wet-bulb temperature as follows

$$\frac{t_a - t_s}{H_s - H_a} = \frac{\lambda_s}{c_p} \quad \ldots\ldots [20]$$

where H_s and H_a are the absolute humidities corresponding to p_s and p_a, respectively. Equation [20] applies to conditions of low to moderate vapor concentrations. It is evident that Equation [20] corresponds to the equation of adiabatic saturation on a humidity chart, if $c_p = c_s$, where c_s is the humid heat. Thus the temperature of a water drop can be estimated from the air temperature and its humidity. From Equation [20] it is readily established that even at very high temperatures, droplets will evaporate at a substantially lower temperature than the air temperature, which is usually well below temperatures of degradation for most materials. This is a well-known advantage for spray drying. This may be visualized by considering three cases of hot air entering a spray drier for various values of absolute humidity. For hot-air temperatures of 150, 300, and 500 F, the wet-bulb temperature and hence the drop temperature for pure water, are plotted in Fig. 4 versus humidity. Also shown in this figure are the relative magnitudes of the temperature driving force Δt, producing evaporation. It is evident that a substantial increase in the drying temperature causes only a few degrees increase in drop temperature, and hence produces a marked increase in the evaporation rate.

When the drop contains solids in solution, the vapor pressure of the water is lowered and the drop temperature will be higher than that predicted from the wet-bulb temperature for water at its normal vapor pressure. By plotting on the usual humidity chart the humidity corresponding to the vapor pressure over the saturated solution of the material being dried, and using this line in place of the usual saturated humidity curve for water, the drop temperature can be estimated from the intersection of this line with the adiabatic saturation line for the air conditions involved. This is indicated in Fig. 5. The basis for this procedure lies in

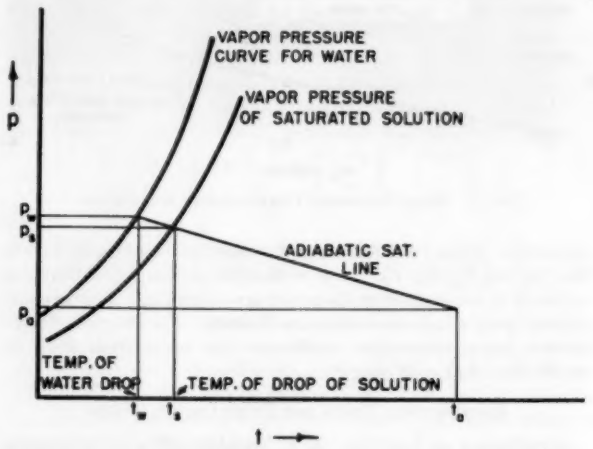

FIG. 5 METHOD FOR ESTIMATING TEMPERATURE OF A DROPLET OF A SOLUTION

a preliminary finding by Ranz and Marshall (8) that droplets of certain solutions, such as ammonium nitrate, evaporate with a surface temperature corresponding to that of the saturated solution even though the drop concentration is initially less than saturation. Charlesworth (1) has shown that this is not true for all solutions. However, it is a conservative estimate in most cases.

EFFECT OF CURVATURE ON VAPOR PRESSURE

The effect of curvature on the vapor pressure of a drop can be estimated from the thermodynamic relationship

$$\ln\left(\frac{p}{p_s}\right) = \frac{2M}{RT}\left(\frac{\sigma}{\rho_L r}\right) \quad \ldots\ldots [21]$$

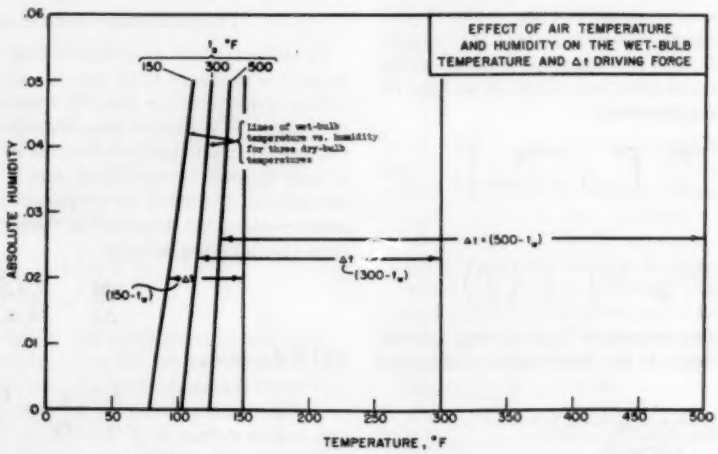

FIG. 4 EFFECT OF AIR TEMPERATURE AND HUMIDITY ON THE WET-BULB TEMPERATURE AND Δt DRIVING FORCE

where σ = surface tension, p_s = normal vapor pressure of liquid at absolute temperature T, p = actual pressure of vapor over drop surface, M = molecular weight, R = gas constant, r = drop radius, and ρ_L = liquid density. By substituting various values of r, drop radius, in this equation, it can be shown that the vapor pressure over the drop is not increased more than 1 per cent until a drop on the order of 0.2 micron is reached.

Evaporation From Sprays of Drops

One of the more difficult mathematical problems in connection with droplet evaporation is the computation of the over-all rate of evaporation for a spray of drops and the time variation in mean diameter of the spray. The problem is complicated, among other reasons, because of the nonlinear nature of the drop-size distribution function involved in the calculation. Further, the proper distribution function for the drop sizes in a given spray is not always known precisely. The solution of this problem is of considerable importance in combustion processes where complete evaporation is required and, in this connection, one published attempt has been made to solve the equations. Probert (7) assumed the drop-size distribution of a fuel spray fitted the Rosin-Rammler equation as follows

$$V_f = 1 - e^{-(x/x_p)^\delta} \quad \ldots\ldots\ldots\ldots\ldots\ldots [22]$$

where V_f = mass fraction of spray less than diameter x; x_p = a size parameter; and δ = a dispersion coefficient. For conditions of no relative velocity, Equation [6], Probert developed integrated expressions which predicted that a spray with a narrow size distribution would evaporate completely in a shorter time than one with a wide size distribution and large mass median diameter. However, the initial rate of evaporation for the spray with the wide size range would be greater. His calculation procedure ignored any change in the temperature driving force during evaporation.

Another procedure for estimating the effect of distribution of drop size on spray-drier performance can be used, which is based on calculating in a stepwise manner the evaporation times for various mass-fraction increments corresponding to various increments of drop size in a given spectrum of drops. Although the total drying time for a drop containing solids cannot be determined accurately from the calculations for drops of pure liquid, nevertheless, calculations for pure liquid drops are useful for illustrating the nature of the changes taking place. Thus suppose a spray entering a spray drier has an initial drop-size distribution corresponding to that shown in Fig. 6. Also, assume for purposes of illustration that the initial Δt = 400 F and the inlet-air temperature is 530 F. Then, with reference to Fig. 3, a stepwise procedure to estimate the time required to evaporate certain fractions of the spray can be developed. This procedure consists of calculating the change in mean drop diameter of selected size increments over short intervals of time on the assumption that all drops evaporate under the same constant Δt conditions for the short-time increment. The steps of the procedure are as follows:

1 From specified increments of drop diameter, select various mass fractions F_i, from the cumulative distribution curve, Fig. 6; i.e., establish a frequency distribution from the given cumulative distribution. Tabulate these mass fractions for corresponding, appropriate, average diameters.

2 From curves of θ versus x, Fig. 3, for the appropriate initial Δt, determine the time for complete evaporation as though this Δt would persist throughout the drier. Designate this time as θ_0.

3 Select a "suitable" time increment $\Delta\theta_1$ for estimating the first increment of evaporation. This might be selected such that the first two size classes are "evaporated" in the time increment.

4 Subtract $\Delta\theta_1$ from θ_0 and for this new time, $\theta_1 = \theta_0 - \Delta\theta_1$, find the corresponding value of x_1, the "reduced" diameter of the drop in each size fraction. This new drop diameter presumably is the diameter existing at time θ_1, if evaporation occurred essentially at a constant Δt. If a substantial change in Δt is found to occur, a precise calculation would require recalculating for a shorter-time interval.

5 Compute the ratio $(x_1/x_0)_i^3$ which will give numbers proportional to the fraction of the spray remaining in each size-class increment.

6 Multiply the individual $(F_i)_0$ as selected in 1 by $(x_1/x_0)_i^3$.

7 Take summation $\Sigma(F_i)_0(x_1/x_0)_i^3 = F_1$. Then F_1/F_0 = fraction of spray remaining and $1 - F_1/F_0$ = fraction evaporated. If F_0 is normalized, i.e., $F_0 = 1$, then F_1 is the fraction remaining.

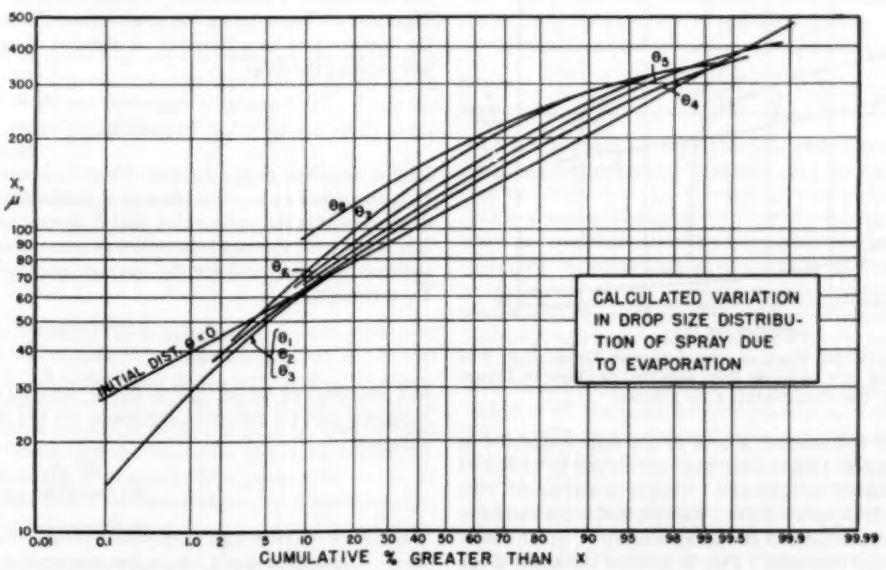

Fig. 6 Drop-Size Distributions for a Spray Undergoing Evaporation

Then, if

$$w_a c_p (t_1 - t_2) = w_l \lambda_s \quad [23]$$

$$(t_1 - t_2) \frac{c_p}{\lambda_s} \frac{w_a}{w_l} = 1 \quad [24]$$

where w_a = mass rate of air flow in drier, and w_l = over-all rate of evaporation, $(t_1 - t_2)$ = temperature drop through the drier. Thus the incremental temperature drop for time θ_1 is given by $(t_1 - t_2)(1 - F_1)$ where F_1 is the fraction of the spray remaining after the first time increment. The process is then repeated for the new distribution of $(F_i)_1$.

By following the foregoing procedure, the fraction of spray mass remaining at various times, as well as the variation of air temperature with time, were estimated for a hypothetical spray for the case of no relative velocity. The results are shown in Fig. 7.

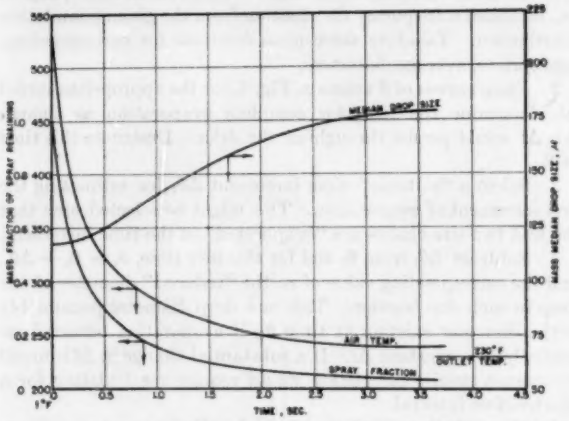

FIG. 7 VARIATION WITH TIME OF AIR TEMPERATURE, REMAINING MASS FRACTION OF SPRAY, AND MEDIAN DROP DIAMETER IN THE EVAPORATION OF A WATER SPRAY

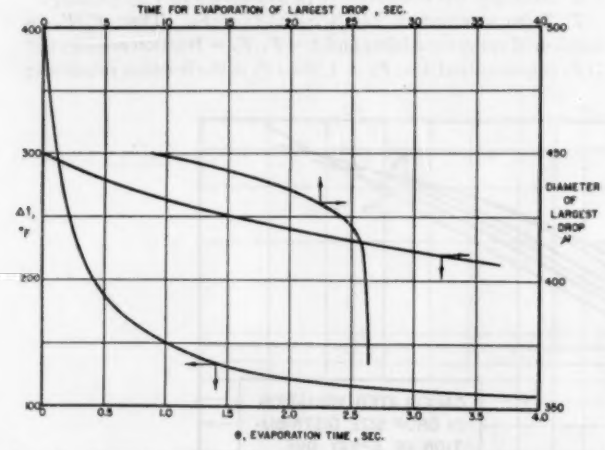

FIG. 8 VARIATION WITH TIME OF THE LARGEST DROP SIZE, THE TIME TO EVAPORATE THE LARGEST SIZE, AND THE Δt DRIVING FORCE IN THE EVAPORATION OF A SPRAY

It is observed that evaporation is over 90 per cent completed in 1.5 sec and that the air temperature has approached to within 30 deg F of its final outlet temperature. This is in agreement with measurements made on spray driers. Also plotted is the variation in the mass median diameter of the spray with time, which shows that this median size increases. This is because the small drops completely evaporate much more rapidly than the large ones.

In Fig. 8 are shown a plot of Δt versus time, a plot of the maximum drop size versus time, and a curve of the variation of the time for complete evaporation of the maximum drop size. The latter curve is especially interesting. It shows that the time of evaporation for the largest drop increases from 8 to 26 sec in 3.5 sec because of the rapid decrease in the Δt driving force. This confirms the fact that sprays with large drops will not dry completely in small size towers. It also suggests the need for designing a drier for the largest drops in the spray.

HEAT AND MASS TRANSFER AT HIGH TEMPERATURES

When very high temperatures are used for spray drying, the foregoing simplified picture of heat and mass transfer should be reinspected. The implication in Equation [2] is that all of the heat transferred from the gas to the drop is used in latent heat of evaporation. This concept neglects the sensible heat transferred to the vapors as they move out to the main gas stream. It also neglects any variation in the transport properties k_f, μ, and D_v caused by temperature and concentration gradients in the gas film surrounding the drop.

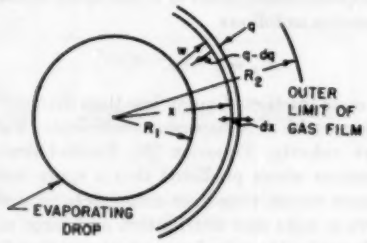

FIG. 9 HEAT AND MASS FLOW AROUND AN EVAPORATING DROP IN STILL AIR

With reference to Fig. 9, a heat balance written over a differential spherical shell through which heat is passing inward toward the drop while mass is passing outward results in the following differential equation

$$x^2 \frac{d^2t}{dx^2} + \left(2x - \frac{w_l c_p}{4\pi k_f}\right) \frac{dt}{dx} = 0 \quad [25]$$

For the boundary conditions $t = t_s$ at $x = R_1$, and $t = t_a$ at $x = R_2$, Equation [25] may be solved to give the following expression for the temperature as a function of distance through the gas film surrounding the drop

$$\frac{t - t_s}{t_a - t_s} = \frac{e^{-E/x} - e^{-E/R_1}}{e^{-E/R_2} - e^{-E/R_1}} \quad [26]$$

In this equation, $E = w_l c_p / 4\pi k_f$ where w_l is the rate of evaporation, mass/unit time. One obvious simplification in the foregoing development is the assumption that k_f is constant. Since this in fact is not true, k_f must be selected as some proper average value between t_s and t_a, and for the average composition of the film. By defining h_c as

$$\frac{q}{A_0 \Delta t} = \frac{k_f (dt/dx)_{R_1}}{\Delta t} \quad [26a]$$

and substituting for (dt/dx) at R_1 its value as determined from Equation [26] the following expression for the Nusselt number is obtained

$$N_{Nu} = \frac{h_c x_0}{k_f} = \frac{2E/R_1}{e^{E(1/R_1 - 1/R_2)} - 1} \quad [27]$$

When $E \to \infty$ (very high evaporation rates), $N_{Nu} \to 0$, and when $R_2 \to \infty$ and E is small, i.e., a low evaporation rate $N_{Nu} = 2.0$ in accordance with theory, Equation [6].

When $E = 0$, Equation [27] becomes

$$(N_{Nu})_{E=0} = \frac{2/R_1}{(1/R_1 - 1/R_2)} \quad [28]$$

and the ratio of N_{Nu} to $(N_{Nu})_{E=0}$ becomes

$$\frac{N_{Nu}}{(N_{Nu})_{E=0}} = \frac{E(1/R_1 - 1/R_2)}{[e^{E(1/R_1 - 1/R_2)} - 1]} \quad [29]$$

Upon expanding the exponent in the denominator

$$\frac{N_{Nu}}{(N_{Nu})_{E=0}} = \frac{1}{\left[1 + \frac{E}{2}(1/R_1 - 1/R_2) + \frac{E^2}{6}(1/R_1 - 1/R_2)^2 + \ldots\right]} \quad [30]$$

It is apparent from Equation [30] that when E is large (high evaporation rates) the actual Nusselt number can be substantially less than that for low evaporation rates. Godsave (6) reported experimental values of N_{Nu} when mass transfer occurred, which were only one fourth the predicted values for heat transfer alone.

From Equation [29], an expression for the actual heat-transfer coefficient can be written as follows

$$(h_c)_{act} = (h_c)_{app}\left(\frac{a}{e^a - 1}\right) \quad [31]$$

where

$$a = (w_l c_p/4\pi k_f)(1/R_1 - 1/R_2)$$

This expression is similar to that developed by Colburn and Drew (2) for the condensation of mixed vapors. If R_2 is on the order of twice the drop radius R_1, then

$$a = w_l c_p/8\pi k_f R_1 = w_l c_p/4\pi k_f x_0$$

Godsave (6) reported values of R_2 for burning droplets, which ranged up to three times the drop radius. On the other hand, if R_2 is very large, then

$$a = w_l/c_p/2\pi k_f x_0$$

For conditions of quite high air temperatures the value of a may range up to 4.0, depending on the liquid involved, for which the factor $a/(e^a - 1)$ has the value of about 0.075. Thus the actual heat-transfer coefficient can be as low as one tenth of the apparent coefficient.

From the definition of a and by substituting for w_l its equivalent in terms of the actual heat-transfer rate, an expression for a may be derived as follows

$$a = \ln\left[1 + \left(\frac{N_{Nu}}{2}\right)\left(\frac{\Delta t c_p}{\lambda}\right)\right] \quad [32]$$

where N_{Nu} is the Nusselt number computed for no mass transfer. It is evident for low relative velocities that $(N_{Nu}/2) = 1.0$, and hence the term $(\Delta t c_p/\lambda)$ determines the magnitude of a. This term is effectively the ratio of sensible heat transferred per unit mass of vapor to the latent heat, and it is evident that Δt must be large for this term to be significant. Equation [32] is plotted in Fig. 10. Also plotted in Fig. 10 is a curve of a versus $a/(e^a - 1)$. It is evident that this factor decreases rapidly as a increases, i.e., as the evaporation rate increases.

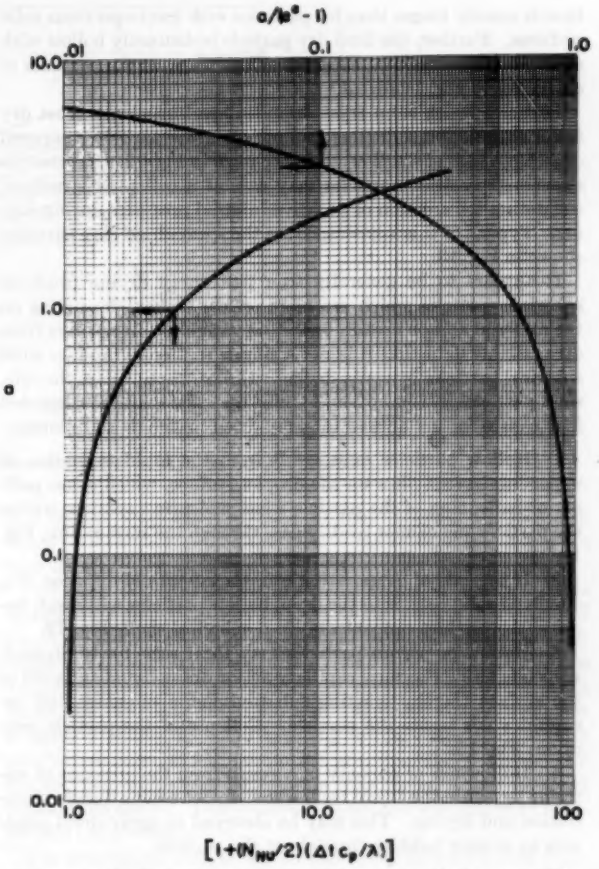

FIG. 10 VARIATION OF PARAMETER a, EQUATION [32], WITH N_{Nu} AND TEMPERATURE

EVAPORATION FROM DROPS CONTAINING SOLIDS

When an evaporating droplet contains a solid either in suspension or solution, the total evaporation or drying time is equal to the sum of the time for the surface evaporation period and the time for the subsurface evaporation period. The time for the first period is given by

$$\theta = \frac{2\lambda\rho_L}{\Delta t}\int_{x_0}^{x_0}\frac{dx}{h_c} \quad [33]$$

where h_c is given by Equation [4], with appropriate corrections for high temperatures, Equation [31], to be applied when required. Equation [12] is a special case of Equation [33].

An equation similar to [33] for the falling-rate period is not easy to establish since in this period the evaporation rate is governed by other factors than those governing the so-called constant-rate period. Since these other factors are largely associated with the solid phase in solution or suspension, it is exceedingly difficult to obtain a general law for the falling-rate period.

In general, the effect of the presence of a solid is to increase the time to remove the required moisture in contrast to the time required if all the moisture were present as a drop of pure liquid. Thus a solid in solution will cause a vapor pressure lowering during the initial period of surface evaporation, while during the second period it creates a solid phase through which liquid and vapor must pass in order to escape from the particle. The nature of this solid-phase resistance is extremely variable, and it has considerable influence on the properties of the dried particle. Thus, for materials which produce amorphous films on the drop surface, through which vapor escapes with difficulty, the drying

time is usually longer than for particles with less impervious solid surfaces. Further, the final dry particle is distinctly hollow with a characteristic smooth, homogeneous surface, as the particles of dry coffee in Fig. 11 reveal.[3]

Particles which form crystals and a less impervious crust dry faster and exhibit a distinct, hollow spherical particle composed of an aggregate of small crystals as shown in Fig. 12. In other instances spray-dried particles may exhibit a collapsed structure, suggesting the creation of negative internal pressures during drying. Typical of this appearance are the spray-dried clay particles shown in Fig. 13.

It appears to be generally true that spray drying produces spherical particles which are more or less hollow, depending on the material and on certain operating variables. It appears from all available data that it is not a simple matter to produce solid spherical particles by spray drying. Hollow particles are the rule, solid particles the exception. Duffie and Marshall (4) suggested four causes for hollowness in spray-dried materials as follows:

1 Hollow particles may result from the rapid formation of vapor-impervious films on the droplet surface, which cause puffing or ballooning of the particle when moisture vaporizes within the particle and cannot readily pass through the surface film, Fig. 11.

2 If the rate of evaporation exceeds the rate of diffusion of a dissolved solid back into the drop, hollow particles will result because the product concentrates in a spherical shell, Fig. 12.

3 Hollow or porous particles may form with finely divided, suspended solids because capillary action draws liquid and solid to the surface thereby creating subatmospheric pressures and resultant voids inside the particle. Collapse of the particle may occur, Fig. 13.

4 Hollowness or porosity may result from the presence of entrained gases in the liquid feed, which do not escape during atomization and drying. This may be observed in spray-dried products as minute bubbles throughout the particle.

The more hollow a particle, the lower the bulk density of the product and vice versa. Consequently, it is important to establish the range of hollowness together with the range of bulk density that reasonably can be achieved by varying the operating conditions.

Probably the most important single property of a spray-dried product, other than particle size, is its bulk density. Bulk density influences the size and cost of storage bins, the type and cost of containers, shipping costs, and marketing requirements. Following is a summary of the effects of particle size, drying air temperature, feed concentration, feed temperature, and air flow on bulk density:

Particle Size Distribution. In general, the bulk density of a given product will be greater if the size distribution is broad. This is due in part to the fact that the small particles fill the voids between the larger ones. Theoretically, a product of uniformly small particle size will have the same bulk density as a product of uniformly large particles, provided the particle density is the same in each case. However, recent studies by Crosby (3) have shown that the spray-dried particle density increases as the particle size decreases.

Drying Air Temperature. It appears to be generally true that the drying air temperature affects all materials the same; i.e., as the air temperature increases the bulk density decreases. This effect is attributed to an increase in particle size with air temperature, resulting in a decrease in particle wall thickness and hence in particle density. By designing a drier so that the hottest air does not immediately encounter the wet spray, the density

[3] Figs. 11, 12, and 13 were taken by Crosby (3). The particles were immersed in a mineral oil and photographed with transmitted light.

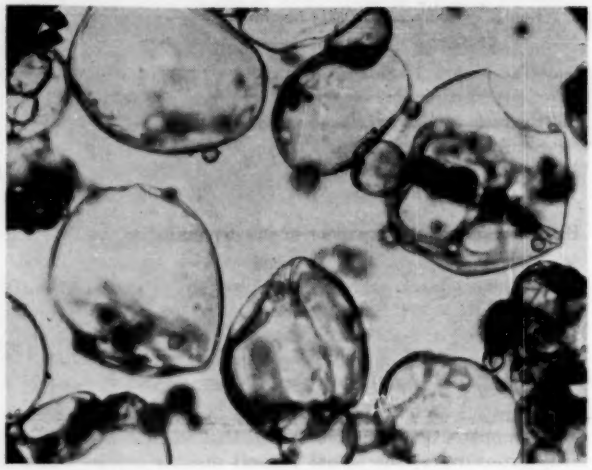

FIG. 11 PARTICLES OF SPRAY-DRIED COFFEE

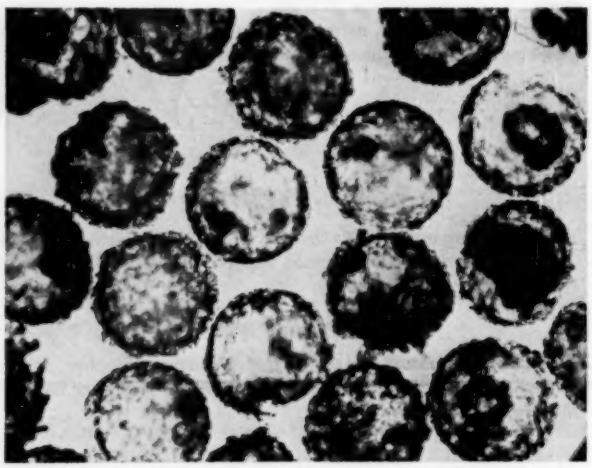

FIG. 12 PARTICLES OF SPRAY-DRIED SODIUM SULPHATE

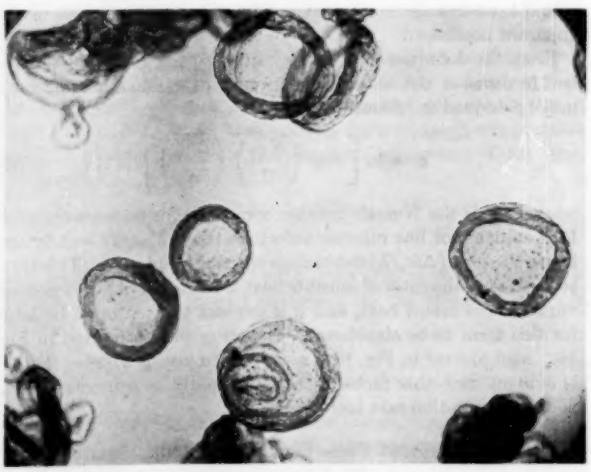

FIG. 13 COLLAPSED PARTICLES OF SPRAY-DRIED CLAY

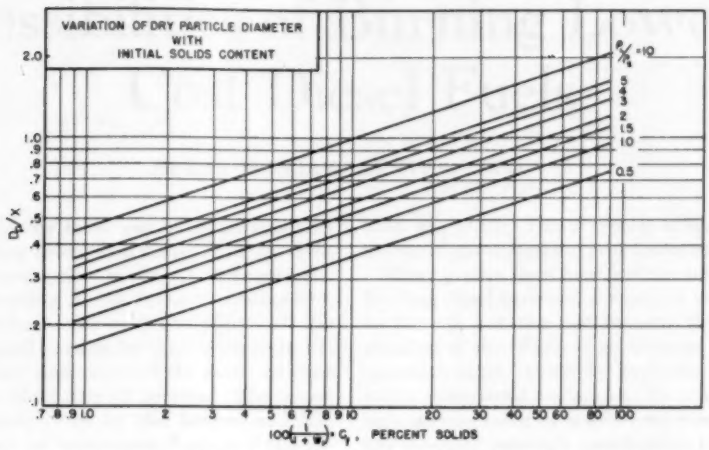

FIG. 14 VARIATION OF DRY-PARTICLE DIAMETER WITH INITIAL SOLIDS CONTENT

can be increased. Countercurrent flow accordingly can produce a denser product than co-current flow.

Feed Concentration. An analysis of the effect of feed concentration is complicated by its concomitant effect on atomization. Since feed concentration also influences the drop size produced by atomization, it is difficult to assess its separate effect on bulk density. From a weight balance on a droplet, the following expression for the ratio of densities for two feed concentrations can be derived

$$\frac{\rho_2}{\rho_1} = \frac{x_2^3 C_{f2}}{x_1^3 C_{f1}} \left(\frac{D_{p1}^3}{D_{p2}^3}\right) \quad [34]$$

where ρ_2 and ρ_1 are the particle densities corresponding to the feed concentrations, C_{f2} and C_{f1}, respectively; x refers to the liquid-drop diameter produced by atomization and D_p refers to the dry-particle diameter. It is evident from Equation [34] that if an increase in feed concentration increases x_2 more than D_{p2} or if $x = D_{p2}$, then the particle density surely will increase with concentration. As shown in Fig. 14, this is the case for most materials except at high solids content $C_f > 70$ per cent. If atomization can be so adjusted that x_1 and x_2 are nearly equal, then ρ_2 will depend on the ratio C_{f2}/D_{p2}^3. If this ratio is greater than D_{p1}^3/C_{f1}, then ρ_2 will decrease.

Available literature data on the effect of feed concentration on bulk density show conflicting trends. For some materials, the bulk density decreases with an increase in feed concentration, while with others this trend is reversed. All conclusions on the effect of this variable are based on the assumption that there is no aeration of the feed when the concentration is varied. However, aeration can easily occur if fines or dust from the collection system should be mixed into the feed. The result would be a lowering of the bulk density.

Feed Temperature. The effect of increasing the feed temperature in most instances is a slight reduction in the bulk density. However, this variable also affects atomization since an increase in temperature lowers the liquid viscosity, and this in turn results in a smaller drop size from the atomizer. Heating the feed also tends to deaerate it, which would have the effect of increasing the bulk density.

Air Flow. It is possible in the spray drying of some materials to cause the hot air to flow counter to the spray. The spray of liquid droplets initially encounters partly cooled, moist air and hence the drying rate is low. As a result the individual particles are not puffed as much, and hence they are somewhat more dense than with co-current air flow. Agglomeration of particles is more probable in countercurrent drying since some of the smaller particles which have dried are recirculated upward by the air, thereby permitting collision with larger, wetter particles falling from above. This procedure is not too well suited to heat-sensitive materials.

The general problem of air flow in spray driers requires separate treatment. It is a most important phase of spray drying and warrants considerable attention from both the research and design viewpoints.

BIBLIOGRAPHY

1 D. H. Charlesworth, PhD thesis, University of Wisconsin, Madison, Wis., 1954.

2 "Condensation of Mixed Vapors," by A. P. Colburn and T. B. Drew, Trans. AIChE, vol. 33, 1937, p. 197.

3 E. J. Crosby, PhD thesis, University of Wisconsin, Madison, Wis., 1954.

4 "Factors Influencing Properties of Spray-Dried Materials," by J. A. Duffie and W. R. Marshall, Jr., *Chemical Engineering Progress*, vol. 49, 1953, pp. 417–423, 480–486.

5 "On the Evaporation of Falling Drops," by N. Froessling, *Gerlands Beitrage zür Geophysik*, vol. 52, 1938, pp. 170–216.

6 "The Burning of Single Drops of Fuel," by G. A. E. Godsave, National Gas Turbine Establishment, England, Report No. R88.

7 "Influencing of Spray Particle Size and Distribution in the Combustion of Oil Droplets," by R. P. Probert, *Philosophical Magazine*, vol. 37, 1946, pp. 94–105.

8 "Evaporation From Drops," by W. E. Ranz and W. R. Marshall, Jr., *Chemical Engineering Progress*, vol. 48, 1952, pp. 141–146, 173–180.

Possibilities of Burning Lower-Cost Diesel Fuels

By RAY McBRIAN,[1] DENVER, COLO.

The question of getting the most out of diesel fuel and the possibilities of burning lower-cost diesel fuels involves more than the operational price savings. It requires a knowledge and understanding of the facts of combustion as related to engine performance and the effects of the characteristics of fuels and means by which undesirable features can be recognized and corrections made so that fuels may be burned satisfactorily in service. The paper outlines the research carried out by the Denver and Rio Grande Western Railroad on lower-cost fuels and the resulting economies.

Introduction

IN the early 1940's when we first purchased our diesel locomotives, the virtue of the diesel economies was expressed principally as that effected by fuel savings. We were able to buy the so-termed "premium" diesel fuels for around 4½ cents per gal. Today it is approximately 10 cents per gal, a little over double the first cost. This subsequent rise has been reflected in increased operating costs, and it brought about the recognition that diesel-fuel research is one of the most fertile fields for reducing operating expenses of diesel locomotives inasmuch as the fuel cost represents about 50 per cent of the operating cost.

Economies Realized

For more than a year, through research and an understanding of fuel characteristics, the Denver and Rio Grande Western Railroad has been using lower-cost fuels on its entire fleet of diesel locomotives. This has reflected material savings without any appreciable increase in maintenance costs. It should be mentioned, however, that the control of diesel locomotives with the use of the spectrograph and the proper changing of oil and air filters and the proper study of diesel fuels has been necessary to secure such savings without increasing maintenance costs. As an example, Table 1 gives the unit costs for fuel for the first nine months in 1954.

TABLE 1 NINE MONTHS UNIT FUEL COSTS COMPARED

	Unit cost, 1954	Unit cost, 1953
Yard fuel	0.1188	0.1507
Train fuel, freight	0.241	0.264
Train fuel, passenger	0.034	0.036

The total savings for the Denver and Rio Grande Western Railroad in this period of time has been $243,536. In order that the mechanical cost might be understood, the average on a three-year overhaul period approximates $3,000 only per engine. Also the mechanical operating ratio, as an example, for the month of September, 1954, was 14.89 and for the month of September, 1953, was 15.93. This is typical of our operation since we began the use of the economy type or lower-cost fuels.

Many papers have been written relative to the supply of the low-cost diesel fuels and a study as to what might or might not be burned, but the fact remains that through proper understanding of the effects of combustion as related to diesel-engine operation there should be available in any territory fuels by which operational savings can be made. Railroads other than ours are now using fuels with properties different from the generally accepted premium specification type. The fuels which the Denver and Rio Grande Western Railroad is using are not the regular type of specified burner oils, but they are fuels which have been selected by the railroad and refiner from unstable stocks or from study of refinery streams whereby the refiners have been able also to reduce operational refining costs and share such savings with the railroad.

Fuel Requirements

Actual service performance tied in with the research studies has proved that such type fuels, by which price savings can be obtained, can be used successfully. The actual savings for each of the fuels selected for our use range from ¾ cent to 4¼ cents per gal. No restrictions have been placed upon the refiner except those of water and dirt content.

Our railroad in co-operation with the refiner's studies of the refinery streams of various combinations of thermal, catalytically cracked, and straight-run fuels, have been studied with the electron microscope of combinations of storage stability, particle size, and presence of unstable constituents. These are determined and are corrected by the addition of chemical stabilizing and dispersing additive materials using the electron microscope as the control tool.

The attention of the Rio Grande Laboratory was first directed toward the possibilities of fuel savings at the time when we were working with the U. S. Bureau of Mines, Rifle, Colorado, Oil Shale Plant. That fuel was unstable and had a typical analysis as given in Table 2.

TABLE 2 TYPICAL FUEL ANALYSIS

API gravity	35
Flash point, deg F	175
Pour point, deg F	+15
Viscosity @ 100 F Saybolt Universal	35.6
Conradson carbon 10% bottoms, per cent	0.50
Sulphur, per cent	0.90
Nitrogen, per cent	0.05
Cetane	45
Initial boiling point, deg F	454
50 per cent point, deg F	506
End point, deg F	665
Aniline point	126.7

The shale oil was dark in color, very unstable and sludged badly when exposed to light in less than 1 hr. Because of studies we had made previously on lubricating oils with the electron microscope, it was decided there was some possibility that fuels could be studied in a similar manner. It was found that this fuel had a tremendous particle size when so examined. On a service test, in a very few hours, the fuel completely clogged filters and stuck injectors.

[1] Engineer, Standards and Research, Burnham Laboratory, Denver and Rio Grande Western Railroad Company. Mem. ASME.

Contributed by the Railroad Division and presented at the Annual Meeting, New York, N. Y., November 28-December 3, 1954, of The American Society of Mechanical Engineers.

Note: Statements and opinions advanced in papers are to be understood as individual expressions of their authors and not those of the Society. Manuscript received at ASME Headquarters, November 4, 1954. Paper No. 54—A-250.

Electron Microscope Used to Study Oils

Because of the examination of satisfactory premium fuels using the electron microscope, in which it was found that the average particle size was less than 1/10 micron and which resulted in very low wear rates with no problem of filtration or injector sticking, it was decided that, if the shale-oil fuel could be prepared or conditioned in a similar manner, no operational troubles should be anticipated. Consequently, a test was conducted with an E-M-D switcher using 2 qt of a dispersant per 1000 gal. Approximately, 5027 gal of the shale oil, high in sulphur, was used during the test. The total service test ran for 715 hr.

Results of Service Test on Shale Oil. The injector ran the full test with no trouble; the interior was bright and free from gum, and the plunger worked freely. There was no indication of corrosion on any part of the injector assembly. The nozzle tip had a coating of carbon about $^1/_{32}$ in. thick which did not interfere with the spray pattern and was soft and easily removed. The piston head had no measurable deposit of carbon. The piston rings were free and clean. The valve stems had practically no carbon. The exhaust ports had a carbon build-up of $^3/_{16}$ in. Carbon build up before the test started was not determined.

The Fulflo waste filters which ran the full time were darker in color than normal but were not plugged. On a previous test of shale oil without any treatment this type filter lasted only 10 hr. Of the two sintered bronze filters, one was removed after nine days of service for inspection. About two thirds of the area was spotted with a black oil deposit which was not gummy or varnish-like and wiped off easily. The other filter was in service for the full test period and was totally covered with a similar black deposit, but had not failed in service. The deposit appears to be carbon with no evidence of gum. Of the two small by-pass bronze-nozzle filters, one was black but freely filtering, the other was metallic colored. The burning characteristics of the oil appeared to be satisfactory regarding smoke and power. There was no trouble with sparking.

Of two samples of this fuel (analysis shown in Table 1) which were sent to us in January, 1951, one sample sludged badly. The second sample of this fuel is a clear solution, prepared at the same time with the chemical dispersant. This has remained stable for three years.

Tests on Lower-Cost Fuels

Following the test of the oil shale in 1952, a year's extensive road test was made of lower-cost, lower-cetane fuels, both stable and unstable storage stocks. Refiners submitted for study a series of samples which, in general, were blends of straight run, catalytically cracked or thermal-cracked fuels from unstable stocks. These combinations had not been used previously as commercial fuels because of instability and incompatibility, especially when mixed with other fuels. Service tests of these fuels were satisfactory.

It should be mentioned, too, that the Denver and Rio Grande Western Railroad is using the electron microscope in the study and evaluation of all fuels used by our own railroad and its subsidiaries and also for other companies. Our studies have included the following types of fuels: High-octane gasoline, gasolines, diesel fuels, kerosenes, jet fuels, and residual types of fuels, such as Bunker C.

Our evaluation of fuels then has begun with the general premise, which was believed true before studies with the electron microscope began, that the petroleum fuels are true solutions. Therefore, if they are true solutions, the optimum in engine combustion should be obtained and excellent engine performance should be attained. If, however, on examination of these fuels with the electron microscope, particles are in evidence on a fluorescent screen, when studied at ×1500, they are not true solutions but colloidal, and the particles should be considered in relation to combustion problems.

Evaluating Diesel-Fuel Combustion

Our basis for evaluating diesel-fuel combinations depends upon the actual relationship between the electron microscope and service performance. The procedure adopted for the electron-microscopic evaluation is to examine and study diesel fuels as received from the refiner with this instrument, then to place a small amount of this fuel in a bottle and expose it to light in a window. After two weeks, the fuel is compared with the "as-received" sample and if the fuel has developed large agglomerates and particle size and has definite chain-forming constituents present, it is considered to be unstable and will develop service trouble. Fuels are then treated with dispersants and studied. This applies to premium specification fuels as well as to the evaluation of lower-cost fuels. Our principal requirement is that a fuel, treated or untreated, as received and after the aging test should not develop any unstable constituents that will average over $^1/_{10}$ micron in size.

Research Theory of Combustion of Fuel

Based upon correlation with our findings in actual service conditions, our research theory regarding combustion of fuels is as follows:

1 To have proper and even combustion without excessive ring wear, deposits and liner wear, and to prevent contamination of the lubricating oil with depletion of additive, there should be no particles larger than an average of $^1/_{10}$ to $^1/_4$ micron in size in a diesel fuel.

2 There must be no chain formation present which is evidence of unstableness, nor should gum-forming constituents appear.

3 Fuels must not deteriorate in storage and must be compatible when mixed with other fuels.

4 If the particles and unstable chains can be dispersed and stabilized by additives, they must remain well dispersed during the storage time.

In applying these to operation, we found that, like coal when used with stokers, these particles when broken up into certain sizes would give the most efficient combustion of the diesel fuel. We also found that it was possible to prepare these unstable fuels by the use of chemical dispersants and condition them so that the engine would give efficient combustion.

We learned then that the diesel engine does not recognize specification terms, and therefore we have no specifications for diesel fuels. Fig. 1, an electron micrograph at 6750 diameters, represents a stable, satisfactory premium fuel typical of a mid-continent low-sulphur, base-stock, straight-run fuel, small particle size, which we had used on our railroad for ten years without any operational difficulty. Fig. 2 is an electron micrograph at 6750 diameters of another premium diesel fuel which was unsatisfactory in service. Note that the particle size in this sometimes exceeds 1 micron. It is these colloidal particles which we have found to be unburned, resulting in smoke, incomplete combustion, and wear rates, especially of the compression rings and liner ring-belt zones.

Typical analyses of the economy-type fuels used by the Denver and Rio Grande Western Railroad are given in Table 3.

In addition to the fuels being successfully used on our railroad, other railroads also are using economy-type distillate fuels as shown in Table 4.

Laboratory Engine Test

To demonstrate the effect of dispersancy and particle size on

TABLE 3 ANALYSES OF FIVE ECONOMY-TYPE UNSTABLE DIESEL FUELS SUCCESSFULLY DISPERSED AND USED BY THE D&RGW WITH SAVINGS OF 1/2 TO 4 CENTS PER GAL

Type	A	B	C	D	E	F
Gravity	29.4	35	36.7	34.7	30.5	39
Flash point, deg F	176	175	220	160	175	165
Pour point, deg F	−5	+15	+66	−10	−15	+30
Viscosity @ 100 F SSU	35.6	35.6	44.8	34.2	34.3	34.1
Conradson carbon 10 bottoms, per cent	0.13	0.50	0.10	0.15	0.28	0.10
Sulphur, per cent	1.23	0.90	0.12	0.34	0.48	0.27
Nitrogen, per cent	Trace	0.05	Trace	Trace	Trace	Trace
Cetane	34.3	45	60	43	35	50
Initial boiling point, deg F	378	454	436	366	399	394
50 per cent point, deg F	490	506	571	486	482	500
End point, deg F	590	665	760	636	588	710
Aniline point	125.1	126.7	176.7	140.4	...	...

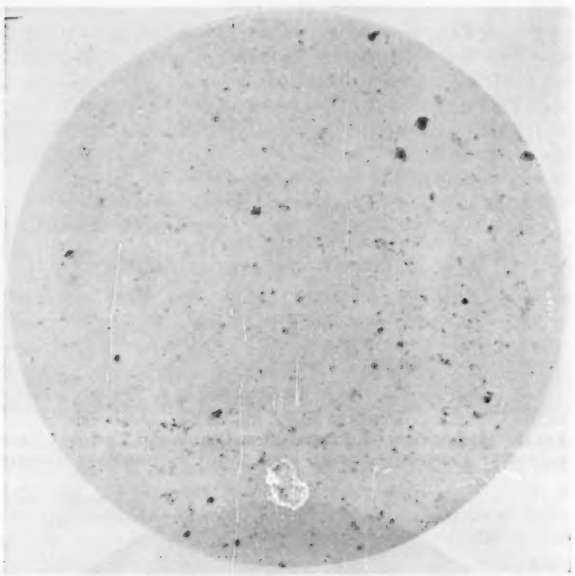

FIG. 1 ELECTRON MICROGRAPH AT ×6750 OF A STABLE, SATISFACTORY PREMIUM, MID-CONTINENT LOW-SULPHUR, BASE-STOCK, STRAIGHT-RUN FUEL

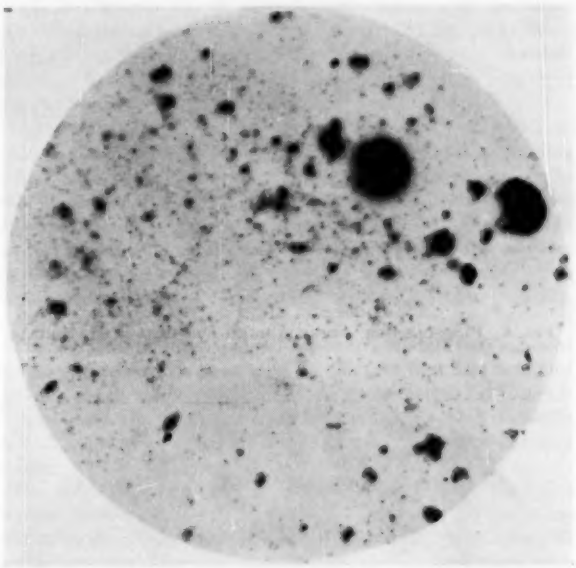

FIG. 2 ELECTRON MICROGRAPH AT ×6750 OF AN UNSATISFACTORY PREMIUM DIESEL FUEL

TABLE 4 ANALYSES OF TYPICAL FUELS USED BY OTHER RAILROADS

Gravity	24.5	26.0	25.5
Flash point, deg F	230	165	170
Pour point, deg F	+55	+15	+10
Viscosity @ 100 F SSU	72	37	37.4
Conradson carbon 10% bottoms, per cent	0.36	0.40	0.30
Sulphur, per cent	0.90	0.50	0.84
Nitrogen, per cent	...	...	...
Cetane	48	35	35
Initial boiling point, deg F	518	370	365
50% point, deg F	672	560	555
End point, deg F	744	720	730

wear reduction, the results of an engine-running test will be given. A premium fuel was used, having the following analysis: Sulphur 0.29 per cent, API gravity 37.6, end point 620, cetane 57, with a particle size shown in Fig. 3. The oil had been stored in light for two weeks. With the addition of dispersant materials, the particle size is as shown in Fig. 4. The test was run on a General Motors 1-71 engine with the results given in Table 5.

TABLE 5 FUEL TESTS

Wear	No additive	With additive dispersant and corrosion inhibitor
Top compression ring:		
Weight loss, grams	0.62	0.31
Gap increase, in.	0.023	0.011
Total compression ring:		
Weight loss, grams	1.51	0.62
Gap increase, in.	0.066	0.032

It will be observed from these tests that a 50 per cent or more reduction in wear has been made as well as a similar decrease in gap-ring increase. Our theory is that wear reduction was

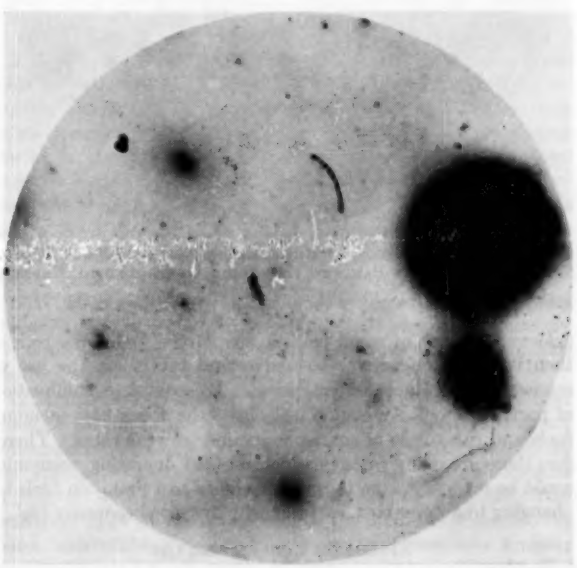

FIG. 3 PARTICLE SIZE OF A PREMIUM FUEL HAVING ANALYSIS: SULPHUR 0.29 PER CENT, API GRAVITY 37.6, END POINT 620, CETANE 57

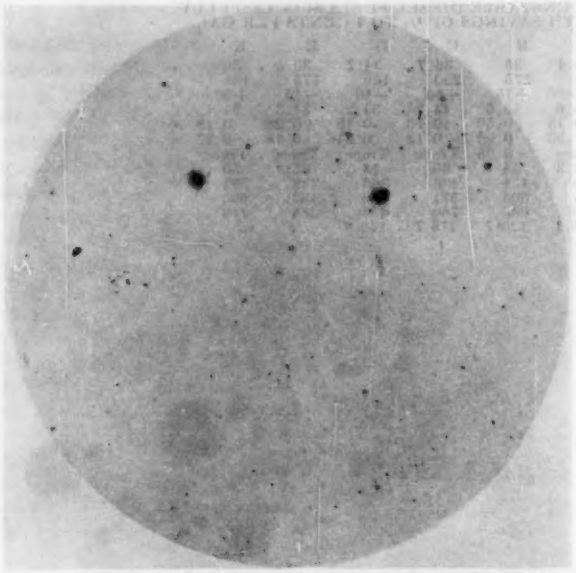

FIG. 4 PARTICLE SIZE AFTER ADDING DISPERSANT MATERIALS

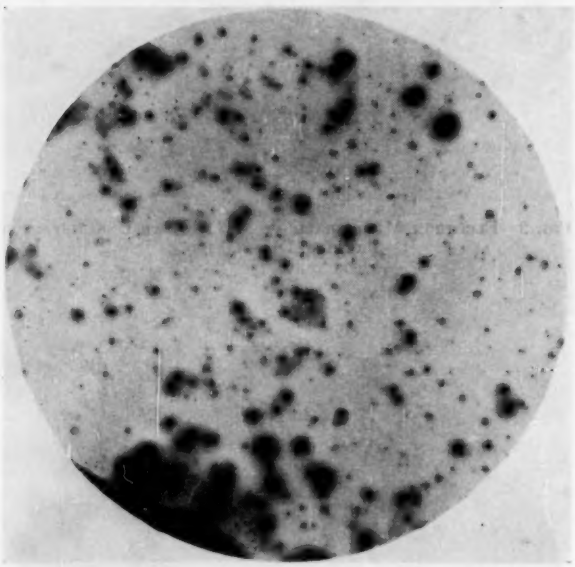

FIG. 6 MICROGRAPH OF LUBRICATING OIL AFTER 30,000 MILES, IN WHICH DISPERSANCY PATTERN HAD BEEN DESTROYED BY UNSATISFACTORY FUEL

achieved because of small particle size of the fuel. We believe then it is most necessary to understand this when the use of economy diesel fuels is considered. By complete combustion of particles the diesel engine will digest the lower-cost economy fuels and can result in similar reduction in wear rates. Therefore there are many cases in which decided operating economies could be made with the burning of higher-cost premium fuels by changing to a lower cost, satisfactorily dispersed economy fuel.

EFFECT ON LUBRICATING OIL

The effect of the carry-over of unburned fuel particles in lubricating oil is most important in considering the use of economy-type fuels. Fig. 5 is a micrograph of a lubricating oil removed

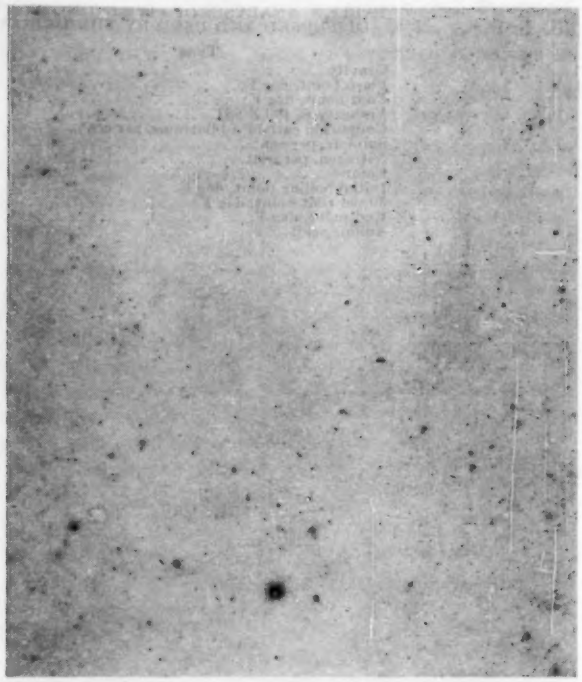

FIG. 5 MICROGRAPH OF LUBRICATING OIL AFTER USE OF A SATISFACTORILY DISPERSED DIESEL FUEL AND CALCIUM-BASE ADDITIVE

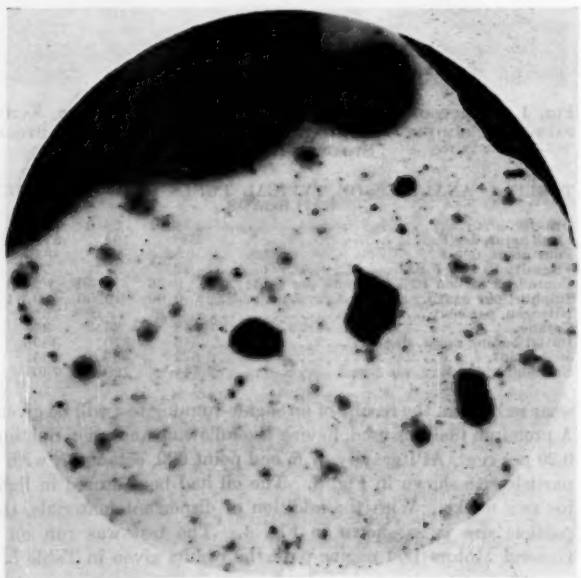

FIG. 7 MICROGRAPH OF FUEL SUPPLIED FOR CASE IN FIG. 6

from one diesel locomotive after use of a satisfactorily dispersed diesel fuel and a calcium-base additive with an ash content of not over 0.20 per cent. After 100,000 miles of operation without an oil change and only make-up oil added, the dispersancy pattern is as follows:

Fig. 6 shows a micrograph of a lubricating oil removed from a diesel-locomotive unit after 30,000 miles, in which the dispersancy pattern has been destroyed and several operating problems have arisen. The fuel supplied to this locomotive is shown in Fig. 7.

It will be noticed that particle sizes of over 1 micron result from incomplete fuel combustion, resulting in loss of additive and dispersancy. Similarly, it has been our experience in the study of fuels that high-sulphur fuels invariably are found to contain these large unstable hydrocarbon particles.

It is our theory that, if these particles can be broken up to $^1/_{10}$ micron size or less, the sulphur will be burned to SO_2 and go out the stack as such without serious damage to the engine. However, if the large particles, which either contain sulphurous compounds or hydrocarbons that act as a sponge and retain SO_2, should work past the compression rings SO_3 is formed, resulting in acid or sulphur wear. We now have under test fuels to which we are adding activated sulphur in various amounts. The activated sulphur is supplied by the Atomic Energy Commission through Tracerlab, Inc., and the National Aluminate Corporation of Chicago is furnishing the agent to disperse sulphur in the fuel. We hope to obtain the same pattern of wear reduction as shown in Table 3. If this can be accomplished, then we have a means by which we can evaluate and predict the performance of higher-sulphur diesel fuels and satisfactorily prepare them for use in diesel locomotives.

Some of the Problems

Included among economy-type diesel fuels are the high pour-point fuels, the low-cetane-type fuel, the high-sulphur fuels, mixtures of residual fuels with blends of either catalytically cracked or straight run, mixtures of thermal catalytically cracked with straight run, which can result in instability. Local conditions in refineries will determine which of the various combinations of so-called economy fuels may be more available. Diesel manufacturers of necessity must have restrictions on fuels and lubricating oils that can be used in their engines. Without a basic understanding of the combustion characteristics of fuels and how to prepare and condition them properly, the use of improper fuel can only result in very high operational cost, high wear rates, and possibly serious damage to locomotives. In other words, one cannot rush out and ask for a lower-cost diesel fuel and plan to use it successfully just because of the fact that he has secured a price saving.

In territories where pour point is a problem, it should be recognized that adequate fuel-heating facilities, both on the locomotive and in storage tanks, must be installed. It also must be recognized that various makes of locomotives react differently to different fuels. For example, it is possible to secure a fuel having a very high paraffinic content in which the pour point may be around 60 or 65 F. However, when mixed with a zero-point fuel, a plus 10 pour-point fuel will be secured but the cloud point will be plus 20 to 25, also a cetane of plus 50. In cold territories operating around zero, where the cooling-water temperature will remain less than 100 F, certain types of switches will put out a white fog which is not smoke but a finely dispersed paraffin mist. Filters will operate satisfactorily without clogging. Here the high-cetane value is not enough to insure the ignition at low operating temperatures. It is therefore necessary either to raise the operating temperature so that ignition is secured for proper combustion or to use some additive which will ignite the fuel satisfactorily.

Economy fuels with higher Btu content probably will make it necessary to change rack settings because of the danger of burning heads and the like. Each diesel fuel submitted as a lower-cost fuel should first be studied by load test, the burning characteristics observed, the horsepower determined, and if any changes are to be made they can be so regulated.

It also should be remembered that, when these lower-cost or economy fuels are used in Clarkson boiler heaters, it is necessary to change the burner settings so as to avoid excessive deposits and failures in service. We have found that storage and filtration problems are directly related to dispersibility of the fuel. If the fuel is conditioned properly with the dispersant, these problems should be overcome satisfactorily. When not so conditioned, some of these lower-cost fuels may become unstable where metallic filter elements of various compositions are in use and react with the fuel. Filter systems should be observed closely. Use of a fuel not of the proper particle size causes lubricating oil rapidly to lose its dispersancy pattern and detergency, and wear conditions to result. The use of higher additive level lubricating oils may improve such a condition temporarily but will not result in satisfactory operation. In general, smoke levels with lower-cost fuels will be higher than with premium fuels, but tests can be made of smoke-density readings at various throttle positions to determine the effect of the use of a finely dispersed fuel as compared with the one of the larger particle size.

Heaters in fuel lines, tanks, and on locomotives may be necessary. However, another approach to the cold-weather handling of fuel is to add a pour-point depressant plus a dispersant to prevent the macrowax crystalline formation in tanks and lines. Even at the cost of $^1/_2$ cent per gal where high pour-point fuels can be secured at a substantial savings, the use of a pour-point depressant can be justified.

A Fertile Field for Research

The Rio Grande's research studies as to fuel, and fuel relationship to engine performance, confirm the fact that fuel behavior has been poorly understood and that this is a fertile field for additional research. Opportunities for savings by both the railroad and the refiner are available through such co-operative studies.

The use of the electron microscope by the Denver and Rio Grande Western Railroad in evaluation of fuels has given reproducible results; it has confirmed operating experience. It can be used to prepare satisfactory fuels for railroad usage with dispersant additives. It permits the purchase of fuels without specification requirements.

Hence the use of lower-cost diesel fuels requires research and co-operation by the user, the refiner, and the engine builder.

Discussion

J. L. Broughten.[2] Utilization of economy locomotive diesel fuels by many U. S. railroads has provoked much thought regarding storage stability and engine performance. Information on service performance of straight-run diesel fuels obtained since the early days of locomotive dieselization, presents an ideal basis for comparing the performance of these lower-cost diesel fuels. The author and the D.&R.G.W. Railroad have always paid a great deal of attention to the engine wear and deposit conditions of their locomotives. There is no doubt that this has been a factor in the most favorable operating ratios of the D.& R.G.W. Railroad. In having firm ideas regarding the operating characteristics of straight-run fuels in diesel-electric locomotives, the author is in an excellent position with respect to evaluating the heavier economy diesel fuels.

Circumstances prevailing during the early days of railroad dieselization led to the use of high-cetane, low-sulphur, and low boiling-range, high-quality diesel fuels. Based on the satisfactory performance of these fuels, locomotive diesel-fuel specifications in general were drawn up to obtain the highest quality fuel available. The author's approach to the purchase of locomotive diesel fuels without regard to any set or conceivably limiting specifications is a much-needed rebellion against overly restrictive

[2] Research Division, Union Oil Company of California, Brea, Calif.

locomotive diesel-fuel specifications. We do feel, however, that a very broad specification containing certain necessary values such as viscosity, flash point, pour point, cetane number, impurities, and distillation can be drawn up without presenting undue restrictions on materials purchased under the specifications. It is felt that some limitation for these characteristics is necessary to enable the railroad to make definite plans regarding the utilization of fuels.

For example, a certain viscosity range should be established so that it can be determined whether or not fuel preheaters will be necessary on the locomotives to provide optimum viscosity at the injectors. A flash-point value is necessary for safety reasons. In the event that steam-heated storage and transportation facilities are available, as well as engine fuel-tank heating equipment, no provision for pour-point limitation is necessary. Diesel engines have critical cetane-number requirements which should be recognized. Fuel cleanliness, particularly in regard to abrasive material, is of paramount importance and must be considered in the specifications. It is definitely established with certain types of locomotive engines that oils containing materials above certain distillation ranges will result in excessive smoke and soot formation, thereby indicating a need for a distillation-range requirement.

Regarding the performance of economy locomotive diesel fuels, we concur with the author that it is possible to obtain engine conditions very similar to those experienced with the use of straight-run fuels. Examination of engine parts after approximately seven months of service with a 35-cetane-number, 735 deg F end-point fuel showed that critical engine-area conditions were approximately the same as had been previously noted with higher cetane, lower end-point fuels. Figs. 8 and 9 of this discussion show the comparison between a piston operated approximately six months on straight-run diesel and a piston operated seven months on the heavy, economy, low-cetane-number diesel fuel in the same type of engine under similar operating conditions. This relationship has been similarly demonstrated in controlled laboratory engine tests. Tables 6 and 7, herewith, present comparative ring and cylinder-liner wear data obtained under simulated service conditions. It is noted that there is very little difference in top compression ring and cylinder-liner wear.

Our experience shows that utilization of properly formulated lubricating oils is necessary with these higher soot-forming economy fuels to provide acceptable engine conditions with respect to wear and deposits.

The use of stabilizing or dispersant additives in certain economy diesel fuels is a must to obtain optimum engine-filter life. We have found that several of the commercially available additives of this type do an excellent job in dispersing fine hydrocarbon sediment to the point where the majority of the particles will

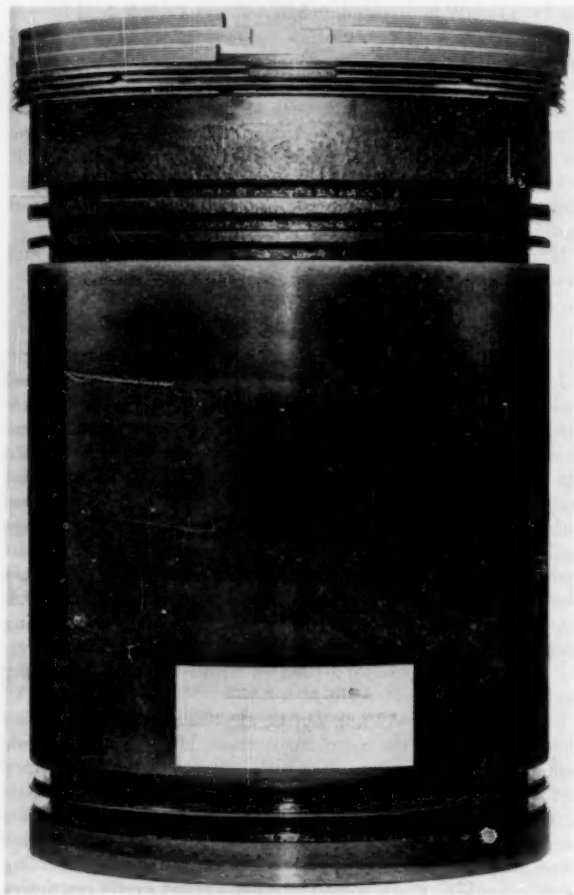

FIG. 8 PISTON AFTER SIX MONTHS' SERVICE WITH STRAIGHT-RUN DIESEL FUEL

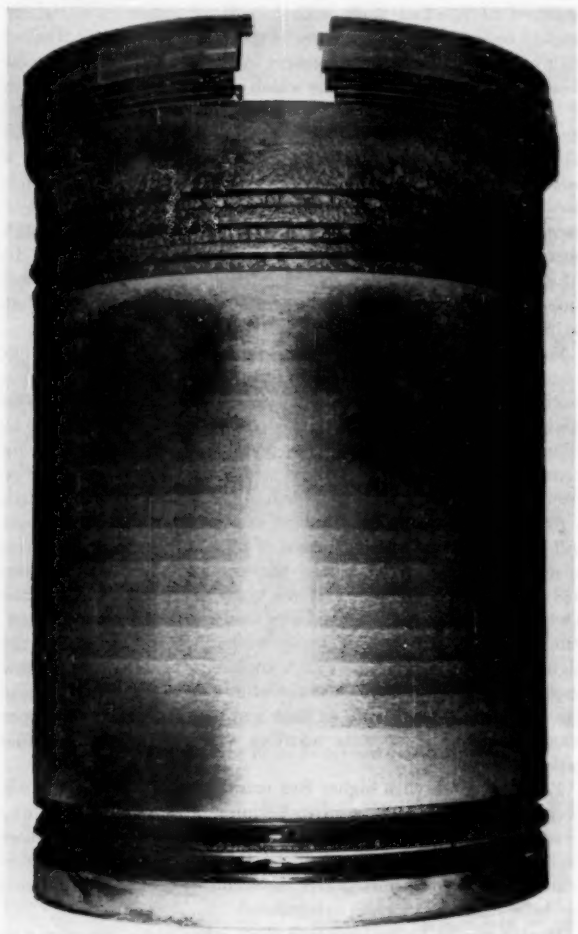

FIG. 9 PISTON AFTER SIX MONTHS' SERVICE WITH HEAVY ECONOMY DIESEL FUEL

TABLE 6 RING-WEAR DATA OBTAINED IN HEAVY DIESEL-FUEL-ENGINE TESTS

Fuel	Lube oil	Stabilizing additive	Gooch filter sediment, mg gal	Top compression ring wt loss, mg gal
Straight-run	A	None	10	0.103
LDF-760	A	None	320	0.055
LDF-760	A	None	442	0.119
LDF-760	B	550 ppm additive X	142	0.135
LDF-760	D	550 ppm additive Y	119	0.185
LDF-760	50% A + 50% B	None	400	...

TABLE 7 CYLINDER-WEAR DATA OBTAINED IN HEAVY DIESEL-FUEL-ENGINE TESTS

Fuel	Lube oil	Stabilizing additive	Gooch filter sediment, mg gal	Cylinder-liner wear, 0.001 in/100 hr	
				Long.	Transv.
Straight-run	A	None	10	0.17	0.19
LDF-760	A	None	320	0.14	0.13
LDF-760	A	None	442	0.19	0.19
LDF-760	B	550 ppm additive X	142	0.10	0.36
LDF-760	D	550 ppm additive Y	119	0.26	0.36
LDF-760	50% A + 50% B	None	400	0.23	0.13

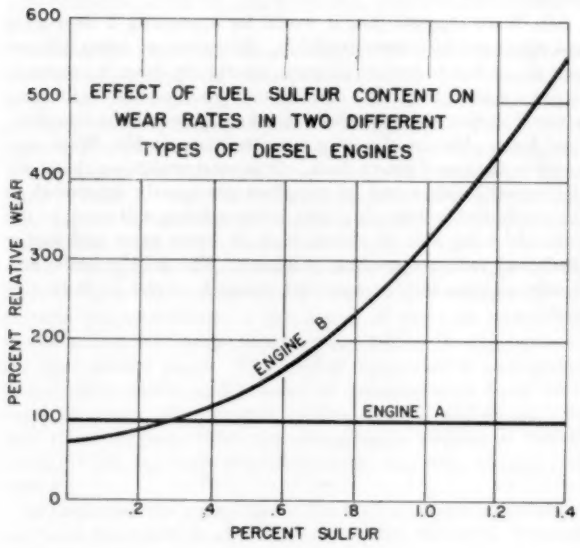

FIG. 10

pass through the filtering medium. The injection of the fine hydrocarbon sediment into the combustion chamber presents the question of the effect of the hydrocarbon sediment on the engine-combustion process and consequently the effect on engine wear and deposits. It is conceivable that, if these hydrocarbon particles are small enough and well dispersed, they will be burned much the same as atomized fuel droplets. It is also possible that if these particles are of sufficient size they will not be burned completely and might impinge on combustion-chamber walls before the exhaust cycle begins. In the case of the large particles, the author has presented information which indicates that higher engine wear will occur under this condition.

From our past experience with various types of diesel engines, both two-cycle and four-cycle, we are inclined to believe that engines are like individual human beings and that as such, each engine behaves differently in regard to the combustion of fuel. For example, Fig. 10 of this discussion shows the effect of fuel-sulphur content on wear rates in two different types of diesel engines. Engine A digests low and high-sulphur fuels to a similar degree, producing about the same effect on engine wear. In contrast, Engine B shows a significant difference in engine wear between the high-sulphur and low-sulphur fuels. Since it has been proved that the effect of sulphur on engine-wear rates is related to the chemical state of the sulphur from the combustion reactions, it can then be assumed that different types of engines will behave differently to injected hydrocarbon sediment. In Tables 6 and 7 we have presented wear data obtained in heavy-diesel-fuel engine tests which show that, in this particular type of engine, insoluble sediment had very little conclusive effect on engine wear and deposits.

The dispersion of fine hydrocarbon particles in diesel fuels with additives definitely may reduce smoke formation and soot in the combustion chamber in certain types of diesel engines. The question of just how much of an effect these unburned particles have on engine wear, deposits, and lube-oil performance poses a question which is of the utmost importance in the utilization of economy locomotive diesel fuels. If, in certain types of diesel engines, these unburned end products do cause unwanted conditions, it is conceivable that adequate lubricating oils can be formulated to meet this demand.

J. R. WARE.[3] The author is to be congratulated on his pioneering of tests to improve the performance of the diesel locomotive when cheaper, lower-grade fuels are used. His report of tests and electron-microscope studies on the effects of dispersant additives in fuel oil will stimulate further investigations to find the maximum gain that can be realized in use of cheaper fuel oils.

This subject is a timely one and of great interest to the railroads, which are now looking for further economies in operation of diesel locomotives. Interest in cheaper diesel-fuel oils started a number of co-operative test programs on the railroads several years ago. The oil companies and engine builders worked closely with the railroads to determine the performance and maintenance problems that might develop. The possibility that these problems can be reduced greatly by use of fuel additives is of great interest to the engine builder as well as the locomotive user.

The paper reports satisfactory locomotive operation on off-specification fuels that include some with 35-cetane rating, some with about 1 per cent sulphur, and several with boiling range end point over 700 F. In many of these fuels the Conradson carbon value also exceeded specification values. The author also reports a reduction in wear rate of rings tested in a Model 1-71 diesel-engine test, when a dispersant additive was used to reduce colloidal particle size in the fuel.

It would be interesting if liner- and ring-wear data were available on some of the Denver and Rio Grande Western locomotive tests to compare with tests run under Coordinating Research Council auspices several years ago. The fuels used then were not as much off specification as the Denver and Rio Grande Western economy fuels since they were 40 to 45 cetane with 1 per cent sulphur, and had a normal boiling range. However, the fuels were tested without use of dispersant additives or ignition improvers, and some increase in liner and ring wear was indicated by these tests.

It is our opinion that much additional test work on the part of the railroads, the oil companies, and the engine builders should be carried out to evaluate the author's theory that, if the size of colloidal particles in fuel oil is kept below $^1/_4$ micron, then combustion will be more complete, and ring and liner wear, deposits, and contamination of the lube oil will be greatly reduced. The decrease in maintenance costs and improved ability to burn

[3] Chief Mechanical Engineer, Engineering Department, Electro-Motive Division, General Motors Corporation, La Grange, Ill.

cheaper fuels that could be obtained if this theory is correct would justify the test program. This is, of course, based on low cost of the dispersant additive in relation to fuel-price reduction of the lower-quality fuels.

After reviewing this subject of lower quality, cheaper fuels with many railroads and oil companies, we also feel that much of this cheaper-fuel test program should be directed at even lower-quality fuels which promise cost reduction of 2 to 4 cents per gal. These fuels will be more closely tied to the price of coal in competitive markets because they are the heavy distillates or residuals. Many of the cheaper fuels tested have been only slightly off specification and are burner oils or fuel oils of limited availability. The bigger saving available in the heavy fuels or blends of heavy fuel and regular diesel fuel merits a thorough test program.

Since these heavier fuels will create additional filtering and handling problems and require heating on the locomotive, their use would require some railroad investment in additional facilities. Therefore the test program must prove that locomotive operation on this type of fuel is satisfactory with a minimum increase in wear rates, deposits, and lube-oil deterioration.

A few railroads already have been testing this type of heavy fuel, as well as some stationary and marine-engine operators. Some of these test fuels are as low as 25 and 19 in API gravity and are over 760 F in boiling-range end point. Their cetane rating ranges from 35 to 42, sulphur from 0.2 to 1.0 per cent, and Conradson carbon from 0.76 to over 12.0. The burning characteristics of fuels like these can be tested in laboratory-test engines to check values of peak combustion pressure, ignition lag, uncontrolled and controlled rate of pressure rise, thermal efficiency, and smoke. But the final performance rating of the fuel must be determined by extensive locomotive operation to judge operating and filtering problems, deposit-forming conditions, and engine wear.

As the author states, these tests must be run with proper control of air, oil, and fuel-filter maintenance, and proper laboratory control of lube-oil conditions. We have found in many tests that the effect on wear by abrasives in air or oil far exceeded the effect of lower-grade fuels.

We agree with the author that the behavior of diesel fuel is a fertile field for research. It is known that fuel additives can lower the pour point of fuels or raise the cetane rating, but much test work remains to determine to what extent the performance of the other cheaper fuels can be improved by the use of dispersant or other types of additives. As an engine builder we are greatly interested in a test program that will find means to reduce engine problems caused by the use of high-sulphur fuels, unstable fuels, or blends of residual fuels.

Author's Closure

Mr. Broughten's studies confirm our findings in service. We agree that a well-formulated additive and finely dispersed lubricating oil is most necessary to assure success in the utilization of these types of fuels. In addition, close attention to lubricating-oil filters must be adhered to and a satisfactory lubricating-oil filter used.

Mr. Ware suggests that it would be interesting if liner-wear and ring-wear data were available. Since we are using 100 per cent of our fuel to supply all units, we did not deem it necessary to run a control test. We can say that we have had no increase in our liner and ring wear since starting the use of the economy-type fuels. We are directing our attention, as Mr. Ware suggests, to the use of heavy fuels. It is most gratifying that both the engine builders and oil suppliers are greatly interested in the problem of fuel supply; this, in my opinion, will result in the railroads' being able to secure fuels at lower costs and higher Btu's and reduce operating problems. The field is fertile and it only requires such co-operative research studies for it to succeed.

Thermal Conductivity of Gases[1]

By F. G. KEYES,[2] CAMBRIDGE, MASS.

A paper[3] presented before the Heat Transfer Division at the 1953 Annual Meeting contains a description of the below-ice-point temperature apparatus for measuring thermal conductivities of gases and liquids, and a few results for neon were reported. During the past year low-temperature measurements have been made on the remainder of the rare gases, and also on other gases. Reliable results from thermal-conductivity measurements now appear to be forthcoming with the high-temperature apparatus to temperatures of 1380 F.

THE author's paper[3] reported data for neon at four temperatures below 0 deg C and to about the boiling point of oxygen. Data also were tabulated from measurements for Argon, hydrogen, nitrous oxide, methane, ammonia, ethane, ethylene, ethyl chloride, Freon 12, and Freon 114, over a range of pressure 0 deg C.

During the past year measurements have been largely confined to completing the measurements in the low-temperature range on the following substances: Argon krypton, xenon, nitrogen, oxygen, carbon dioxide, and methane. The data for these gas measurements were made over a pressure range, and where possible for the liquid phase also. The results are tabulated in Table 1. In Table 2 the constants for an empirical equation used to correlate thermal-conductivity data are given, and in Table 3 the equations for the pressure effects.

Our attempts to obtain measurements at high temperatures have hitherto not been successful. A fourth revision of the apparatus was undertaken in the course of the year embodying modifications and design changes suggested by the experience of the past several years. The revised apparatus is now giving reproducible results and a series of measurements have been made on argon, air, nitrogen, carbon dioxide, and steam. At this time (August, 1954) the temperature reached is 750 C (1382 F) and the apparatus temperature has been advanced to 1650 F.

In perfecting the apparatus for the high-temperature measurements we have had the able assistance of Mr. Robert G. Vines of Melbourne, Australia, whose unfailing patience and skill have brought this long-continued effort to the present promising status.

Acknowledgment

It is a pleasure to acknowledge the financial assistance in this investigation of The American Society of Mechanical Engineers, the Permanent Science Fund of the American Academy of Arts and Sciences, and Project Squid, acting for the United States Navy, Air Force, and Army, and the Engineering Foundation.

[1] This research was conducted under the auspices of Project Squid, jointly sponsored by the Office of Naval Research, the Office of Scientific Research (Air Force), and the Office of Ordnance Research (Army), under Contract No. N5ori-105 Task Order III, NR 098-038.

[2] Professor Emeritus and Lecturer, Department of Chemistry, Massachusetts Institute of Technology. Mem. ASME.

[3] "Thermal Conductivity of Gases," by F. G. Keyes, Trans. ASME, vol. 76, 1954, p. 809.

Contributed by the Research Planning Committee and presented at the Annual Meeting, New York, N. Y., November 28–December 3, 1954, of The American Society of Mechanical Engineers.

Note: Statements and opinions advanced in papers are to be understood as individual expressions of their authors and not those of the Society. Manuscript received at ASME Headquarters, October 22, 1954. Paper No. 54—A-235.

TABLE 1 NEW MEASUREMENTS

(Calories 4.186 ij per sec per cm per deg C)

	P atm	$10^6\lambda$	t, deg C
Argon (gas phase)	11.0	4.02	0
	7.7	3.98	0
	4.6	3.95	0
	1.0	3.92	0
	4.6	2.77	— 94.7
	2.9	2.73	— 94.7
	1.0	2.71	— 94.7
	1.0	2.02	—142.6
	3.7	1.72	—168.4
	1.0	1.64	—168.4
	.33	1.62	—168.4
(Liquid phase)	10.2	22.4	—161.3
	10.2	25.9	—173.8
	4.5	25.8	—173.8
	10.2	29.0	—186.3
	2.2	28.9	—186.3
Krypton (gas phase)	10.7	2.18	0
	7.4	2.15	0
	5.8	2.13	0
	4.3	2.12	0
	1.7	2.10	0
	1.0	2.09	0
	10.7	1.57	—101.8
	7.3	1.48	—101.8
	4.1	1.42	—101.8
	1.0	1.36	—101.8
	1.8	1.09	—142.1
	0.28	1.05	—142.1
(Liquid phase)	11.2	9.9	—111.2
	4.6	17.9	—129.8
	1.05	21.1	—150.1
Xenon (gas phase)	10.7	1.32	0
	7.5	1.29	0
	4.1	1.25	0
	1.3	1.21	0
	1.0	1.21	0
	1.0	1.21	0
	5.6	1.05	— 58.9
	1.1	0.97	— 58.9
	0.46	0.73	—118.4
(Liquid phase)	5.5	13.9	— 72.9
	1.3	16.8	—101.2
	.25	19.5(±4%)[a]	—127.2
Nitrogen (gas phase)	10.6	5.86	0
	7.6	5.82	0
	3.9	2.23	—181.1
	1.0	2.08	—181.1
Oxygen (gas phase)	10.1	5.94	0
	1.0	5.85	0
	4.9	2.95	—145.1
	1.1	2.86	—145.1
	1.0	2.15	—175.6
(Liquid phase)	10.5	29.8	—162.8
	7.4	37.2	—187.5
Carbon dioxide (gas phase)	1.0	3.47	0
	0.94	2.42	— 66.5
Methane (gas phase)	9.0	7.42	0
	1.2	7.24	0
	6.5	4.67	—101.9
	1.2	4.49	—101.9
	1.1	3.14	—152.7

[a] Convection was evident at this temperature.

TABLE 2 EQUATION CONSTANTS FOR HEAT CONDUCTIVITY AT LOW PRESSURE

$$\lambda_0 = \frac{c_0\sqrt{T}}{1 + c_T/10^{c_1 T}}$$

	$c_0 \times 10^6$	c	c_1	Temp range, deg K
A	0.384	178.8	8	90–620
Kr	0.225	240.0	12	130–580
Xe	0.154	378.0	25	155–273
N_2	0.615	235.5	12	90–823
O_2	0.606	206.2	6	86–373

TABLE 3 PRESSURE-COEFFICIENT EQUATIONS

Krypton $\lambda = \lambda_0(1 + 5580P_r^{2.6})$

Xenon $\lambda = \lambda_0(1 + 11{,}750P_r^{2.6})$

Oxygen $\lambda = \lambda_0(1 + 136P_r^{2})$

It is again a privilege to acknowledge the assistance of the Linde Air Products Division of Union Carbide and Carbon Corporation in supplying facilities which have greatly aided our progress.

In the past year's work that company generously has supplied large quantities of high-purity argon, krypton, and xenon without which it would not have been possible to obtain measurements of thermal conductivity of the liquid phase. The "Freons," highly purified, were supplied through the kindness of Dr. R. C. McHarness of the "Kinetic" Laboratory of E. I. du Pont de Nemours & Company.

The loyal and skilled contributions of the author's co-workers, Mrs. Ruth McDonald, Miss Elizabeth Vander Pol, and Mr. B. G. Humphrey, Jr., have made a happy and productive year.

Some Technical Aids for Engineers

Problems and Control of
AIR POLLUTION

The twenty-five papers in this book were presented at the First International Congress on Air Pollution. Collectively they mirror the experience with atmospheric pollution problems in the United States and elsewhere, and focus attention on the gaps in our understanding of the biological effects of air pollution, the researches in progress and some of their findings, areas for further investigations, the need for governmental regulation, mass toxicity from atmospheric pollution within plants, and processes developed for removal of sulphur dioxide from gases.

1955 — $7.50

Safety Code for
ELEVATORS, DUMBWAITERS, AND ESCALATORS

Completely rewritten and expanded, this 1955 Code provides an up-to-date set of safety requirements relating to the design, construction, installation, operation, inspection, maintenance, alteration, and repair of hydraulic, power, and hand sidewalk elevators, dumbwaiters, escalators, private residence elevators, and inclined lifts and their hoistings. Appendixes offer a considerable amount of data and information useful in the application of the rules.

A17.1—1955 — $3.50

CODE FOR PRESSURE PIPING

Requirements prescribed are for the design, fabrication, materials, installation, and testing of the following systems and piping components: Power piping systems, Industrial gas and air piping systems (includes piping and component parts not covered by Section 8), Refinery and oil transportation piping systems, and District heating piping systems. The alterations and improvements incorporated in the requirements for the types of services covered herein and the new rules on expansion and flexibility in the section on Fabrication Details bring this code in line with the best current practice.

B31.1—1955 — $3.50

MANUAL ON CUTTING OF METALS

Gives useful information on the mechanical characteristics and structures of metals to be cut; the influence of the composition and microstructure of each metal on cutting tool wear and surface finish, types and function of cutting fluids; forces, power, and speeds for specific cutting condition; and tabular data on feeds, speeds, and depths of cut to be used when turning steels and cast irons.

1952 — $10.00

METALS PROPERTIES

Supplies designers with a vast amount of data on more than 500 metals, including the chemical composition of each metal; its brittleness; heat treatment and other characteristics; industrial uses; and treatment temperatures for forging, annealing, quenching, etc. Additionally, there is a fund of working data from the end-quench hardenability of steel to the weldability of aluminum alloys and hot working temperature of copper alloys.

1954 — $11.00

METALS ENGINEERING-DESIGN

A book of vital data on the properties, testing, inspection, and selection of metals. Specific items covered are high temperature considerations, elasticity, residual stresses, vibration, fatigue, shot peening, cold working, nitriding, flame strengthening, impact, corrosion, nondestructive testing, surface finish and mass production, and design procedures.

1953 — $10.00

SMALL PLANT MANAGEMENT

This is the guide-book to consult for sound advice on organizing and operating the small plant; technical research; rating products; selecting a process; controlling manufacturing expense; obtaining best facilities, materials, productivity, and labor relations; how to do and use accounting; and how to pay and save on taxes.

1950 — $7.00

Published by

THE AMERICAN SOCIETY OF MECHANICAL ENGINEERS

29 W. 39th St., N. Y. 18

DESIGN DATA AND METHODS

Includes stress and deflection methods applied to circular and rectangular plates; analysis of circular beams; information on hydrostatic testing and variable-section column problems; design data for piping; data on stress concentrations, torsion, helical compression and tension springs, thermal stresses, stresses in pressure vessels, shrinkfitted assemblies, and thick-walled cylinders. There are also numerical solutions of gas flow problems, information on two-dimensional supersonic flow; bearing calculations; and methods of solving vibration problems.

1953 — $4.00

DYNAMICS OF AUTOMATIC CONTROLS

Studies the functional elements of a control, describes mathematical methods for handling control problems, deals with important components of the control loop and special control problems, examines causes of nonlinearities in the control loop, and treats the off-on regulator and its field of application.

1948 — $6.00

Elevated Temperature Properties of: **I. CHROMIUM-MOLYBDENUM STEELS**
II. SELECTED SUPERSTRENGTH ALLOYS

Each of these Reports graphically summarizes elevated temperature strength data and presents summary curves for tensile and yield strength, elongation and reduction of area, rupture, and creep rates. Report I gives data for 23 steels and also the chemical composition, processing data, heat-treatment, and other pertinent information about the steels included in the survey. Report II gives the data for 13 selected superstrength alloys and includes brief descriptions of each alloy along with chemical composition, recommended heat-treatment, and processing.

I—1953 II—1954
$4.75 each; $3.50 to ASME members

VISCOSITY OF LUBRICANTS UNDER PRESSURE

Reviews twelve experimental investigations on 148 lubricants comprising twenty-five fatty oils, seventeen compounded oils, and twelve other lubricants. Data collected are co-ordinated by means of sixty tables in which the results originally appearing in diversified units are compared. The methods proposed for correlating viscosity-pressure characteristics of oils with properties determined at atmospheric pressures are reviewed and illustrated. Pertinent topics such as experimental work on heavily loaded bearings, lubrication calculations, and additional techniques for viscosity are covered.

1954 — $5.00

Effect of temperature on
THE BRITTLE BEHAVIOR OF METALS
With Particular Reference to Low Temperatures

The twenty-seven papers in this book cover the following broad fields: The evaluation of brittle failures in ships and engineering structures, criteria of metal behavior for design engineers, metallurgical and mechanical factors, notched toughness test significance and reliability, and certain aspects of current research, including new data on titanium, quenched and tempered steels at high strength levels, and several types of cast irons.

1954 — $7.50; $5.65 to ASME members

POWER TEST CODES

Centrifugal, Mixed-Flow, and Axial-Flow Compressors and Exhausters 1949	$1.50
Centrifugal Pumps 1954	$1.50
Displacement Compressors, Vacuum Pumps and Blowers 1954	$2.00
Evaporating Apparatus 1955	$1.50
Feedwater Heaters 1955	$1.50
Solid Fuels 1954	$2.50
Steam Condensing Apparatus 1955	$2.00

20% DISCOUNT TO ASME MEMBERS